Jingtao Wang
Wenjia Wu *Editors*

Functional Membranes for High Efficiency Molecule and Ion Transport

Science Press
Beijing

Springer

Functional Membranes for High Efficiency Molecule and Ion Transport

Jingtao Wang · Wenjia Wu
Editors

Functional Membranes for High Efficiency Molecule and Ion Transport

Science Press
Beijing

Springer

Editors
Jingtao Wang
School of Chemical Engineering
Zhengzhou University
Zhengzhou, Henan, China

Wenjia Wu
School of Chemical Engineering
Zhengzhou University
Zhengzhou, Henan, China

ISBN 978-981-19-8154-8 ISBN 978-981-19-8155-5 (eBook)
https://doi.org/10.1007/978-981-19-8155-5

Jointly published with Science Press
The print edition is not for sale in China mainland. Customers from China mainland please order the print book from: Science Press.

This Springer imprint is published by the registered company Springer Nature Singapore Pte Ltd.
The registered company address is: 152 Beach Road, #21-01/04 Gateway East, Singapore 189721, Singapore

Foreword

Over the past few decades, membrane technology has attracted increasing interests in a broad range of applications like energy, environment, water, food, and medicine, because of its high energy efficiency, easy scalability and small capital investment, as well as environmental friendliness. Membranes, acting as selective barriers that allow the preferential permeation of certain chemical species, determine the efficiency, cost, and stability of membrane technology. Although remarkable progresses have been achieved in membrane technology, the trade-off between selectivity and permeability of membranes remains a great challenge. To this end, intensive research efforts have been dedicated to developing novel membrane materials and membrane structures, including novel building blocks (block copolymer, polymer of intrinsic microporosity (PIM), porous organic cage (POC), porous aromatic framework (PAF), metal-organic framework (MOF), covalent organic framework (COF), *etc.*), inorganic zeolite and ceramic membranes, nanophase-separated membrane, composite membrane, and lamellar membrane, among others.

This book reviews the design, fabrication, structure manipulation, and mass transfer mechanism exploration of several kinds of membranes, including hybrid membrane, composite membrane, nanofiber composite membrane, and 2D lamellar membrane, for applications as organic solvent nanofiltration (OSN) membrane, proton exchange membrane (PEM), and separator/electrolyte in lithium battery.

The book is composed of seven chapters. Chapter 1 gives a brief introduction to membranes, including the category, definition, design strategy, and application, with an emphasis on OSN membrane, PEM, and separator/electrolyte for lithium battery. Chapter 2, contributed by Wenpeng Li, Shiyuan Liu, and Jingjing Chen, introduces the fabrication as well as the structure and performance control of polymer-based composite membranes for OSN, which mainly concentrate on manipulating the structure of active layer with nanofillers. Chapter 3, contributed by Xiaoli Wu, Yifan Li, and Jingtao Wang, introduces the fabrication as well as the structure and performance control of inorganic-nanosheet-based lamellar membranes for OSN, which mainly concentrate on manipulating the structure of interlayer channel by anchoring or intercalating functionalized species. Chapter 4, contributed by Guoli Zhou, Jingchuan Dang, and Jingtao Wang, introduces the fabrication as well as the structure and

performance control of polymer-based composite membranes as PEM for hydrogen fuel cell, which mainly concentrate on manipulating the structure of transfer channel with nanofillers and ionic liquid. Chapter 5, contributed by Jianlong Lin, Wenjia Wu, and Jingtao Wang, introduces the fabrication as well as the structure and performance control of inorganic nanosheet-based lamellar membranes and polymer nanofiber-based composite membranes as PEM for hydrogen fuel cell, which mainly concentrate on manipulating the structure of interfacial transfer pathway by inducing functional group rearrangement. Chapter 6, contributed by Weijie Kou, Jiajia Huang, and Wenjia Wu, introduces the fabrication as well as the structure and performance control of polymer-based separators for lithium–sulfur battery, which mainly concentrate on decorating the commercial separators with nanofibers and inorganic nanosheets. Chapter 7, contributed by Jie Zhang, Yafang Zhang, and Jingtao Wang, introduces the fabrication as well as the structure and performance control of polymer-based composite solid-state electrolyte for lithium ion battery, which mainly concentrate on manipulating the structure of mass transfer channel with nanofillers.

This book is a valuable reference for designing and fabricating high-performance membranes for applications in OSN, hydrogen fuel cell, and lithium battery and is suitable for broad scientific communities including chemical engineers, chemists, materials scientists and biomedical engineering researchers, as well as the graduate students in related fields.

Zhongyi Jiang
Tianjin University
Tianjin, China

Contents

Chapter 1
Introduction to Membrane

Jingtao Wang and Wenjia Wu

In the past decades, membrane technology has been widely utilized in various separation processes, because of their low-energy consumption, low-cost, reliability, and scalability when compared with conventional separation processes like distillation, extraction, or crystallization [1, 2]. In order to further increase the competitiveness, intensive efforts have been made from improving the separation efficiency of existing membrane processes to exploring new applications. As the core part, membrane materials with high permeability, high selectivity, and high stability are extremely desired since they can significantly accelerate the practical application of membrane technology [3, 4]. To date, plenty of membranes with different pore sizes have been developed, such as polymer membrane, ceramic membrane, two-dimensional (2D) lamellar membrane, molecule sieving membrane, hybrid membrane, and composite membrane [5–10]. These membranes have been widely used for different separation processes including, microfiltration, ultrafiltration, nanofiltration, reverse osmosis, gas separation, and proton/ion conduction, etc. [11, 12].

For each category of membrane, the physical and chemical environments of transfer channels are of great importance in manipulating the comprehensive properties. The physical environments are dictated by the connectivity, tortuosity, and size of transfer channels, while the chemical environments are dictated by the type, amount, and distribution of functional groups within transfer channels [13]. Generally, ideal transfer channels should integrate the following attributes: (i) they should be short with appropriate transfer environment to endow membranes with high permeability, (ii) the channel size distribution should be narrow to endow membranes with high

J. Wang (✉) · W. Wu
School of Chemical Engineering, Zhengzhou University, Zhengzhou 450001, P. R. China
e-mail: jingtaowang@zzu.edu.cn

W. Wu
e-mail: wenjiawu@zzu.edu.cn

J. Wang
Henan Institute of Advanced Technology, Zhengzhou University, Zhengzhou 450003, P. R. China

J. Wang and W. Wu (eds.), *Functional Membranes for High Efficiency Molecule and Ion Transport*, https://doi.org/10.1007/978-981-19-8155-5_1

selectivity, and (iii) the chemical and mechanical stability should be high to endow membranes with long-term operation stability [14]. Currently, polymers are the dominant membrane materials, due to their easy processability and high scale-up capability. For conventional polymer membranes, breaking the permeability–selectivity or permeability–stability trade-off remains a challenge. The great progress in polymer membranes over the past decades has brought about the booming of novel kinds of structured membranes including, hybrid membrane, composite membrane, and phase-separated membrane, which push the separation performances of polymer membranes to new records [15–18].

Hybrid membrane is an intricately structured membrane configuration, owing to its merit of coupling the good flexibility and processability of polymers with the regular topological structure as well as the tunable functionality of fillers [19, 20]. Impermeable fillers such as silica particles, graphene oxide (GO) nanosheets, and organic/inorganic nanorods can induce a distortion of chain alignment to improve the free volume property or induce the construction of long-range, ordered transfer channels in membrane [21, 22]. Permeable fillers such as metal–organic frameworks (MOFs), covalent organic frameworks (COFs), and zeolite can afford additional transfer pathways and mechanisms to membrane including, molecule sieving, and selective adsorption [23, 24].

Composite membrane for molecule transfer is generally a heterogeneous membrane with dense separation layer and porous support layer, where the separation layer and the support layer can be separately optimized to achieve simultaneously high separation performance and stability [25, 26]. Particularly, the fabrication of composite membrane with an ultrathin separation layer is deemed as a delicate strategy to achieve highly permeable membrane, which is one of the most important pursuits for membrane technology [27, 28]. At present, researches related to composite membranes mainly focus on the precise manipulation of physical structure and chemical component of separation layer; however, these remain challenging due to the pursuit of ultrathin thickness. For proton/ion separation, electrospinning is increasingly recognized as a powerful mean for introducing unique phase-separated architectures into composite membranes [29]. Indeed, it allows the elaboration of composite membranes with a rather facile mean to control of the long-range organization/distribution/percolation of hydrophilic and hydrophobic domains of the ionomer by adjusting the type of electrospun material, the volume fraction of nanofibers, and the experimental conditions [30]. Moreover, electrospinning can impart uniaxial alignment of polymer chains within nanofibers, resulting in enhanced mechanical properties. Importantly, it can promote the formation of interconnected transfer channels, which facilitate the improvement in proton/ion conduction [31].

In recent years, 2D nanosheets, with a thickness of one to a few atoms, have become the promising building blocks for advanced membranes [32]. Moreover, the nanosheets can be designed with precise pore size along with targeted chemical functionality, enabling their extraordinary physical or chemical selectivity [33]. Through a facile filtration process, 2D lamellar membranes can be fabricated with either porous or nonporous nanosheets. The transfer channels based on nonporous nanosheets refer to the interlayer channels of lamellar membranes, differing from

the pores of porous nanosheet-based lamellar membranes [34]. To date, a large number of nonporous nanosheets have been developed including, graphene oxide (GO), hexagonal boron nitride (h-BN), MXenes, transition metal dichalcogenides (TMDs), layered double hydroxides (LDHs), etc., most of which are easy to fabricate. For 2D lamellar membranes fabricated with nonporous nanosheets, the researchers are mainly concentrated on controlling the physical structure and chemical component of interlayer channels. However, the interlayer channel is usually tortuous. To this end, intrinsically porous nanosheets are developed. The transfer channels based on this kind of nanosheet refer to the channels from the intrinsic pores on nanosheets [35]. Intrinsically porous nanosheets can be 2D zeolites, 2D MOFs, 2D COFs, etc.

In this work, we focus on the application of membrane technology on organic solvent nanofiltration, hydrogen fuel cell, and lithium ion battery. We prepared several kinds of membranes, including hybrid membrane, composite membrane, nanofiber composite membrane, and 2D lamellar membrane, and the microstructure and performance of membrane were efficiently manipulated. In addition, the relevant transfer/separation mechanisms were deeply studied, and the transfer model equations were established. For organic solvent nanofiltration, the category of membrane mainly contains hybrid membrane, composite membrane, and 2D lamellar membrane. For hydrogen fuel cell, the category of membrane mainly includes hybrid membrane, nanofiber composite membrane, and 2D lamellar membrane. With respect to lithium ion or lithium–sulfur battery, hybrid membrane and 2D lamellar membrane are investigated in detail. The microstructures and performances as well as the structure-performance relationships of membranes are systematically investigated. Based on this, we preliminarily disclose the mass transfer mechanism in confined spacing and obtain a series of high-performance membranes and membrane materials. Hopefully, this work will offer some guidance on the design of advanced membranes with diverse transfer channels for applications in separation, catalysis, energy conversion, and storage, etc.

References

1. D.S. Sholl, R.P. Lively, Seven chemical separations to change the world. Nat. News **532**, 435–437 (2016)
2. L. Yang, S. Qian, X. Wang, X. Cui, B. Chen, H. Xing, Energy-efficient separation alternatives: metal-organic frameworks and membranes for hydrocarbon separation. Chem. Soc. Rev. **49**, 5359–5406 (2020)
3. H. B. Park, J. Kamcev, L. M. Robeson, M. Elimelech, B. D. Freeman, Maximizing the right stuff: the trade-off between membrane permeability and selectivity. Science, **356**, eaab0530 (2017)
4. S. Wang, L. Yang, G. He, B. Shi, Y. Li, H. Wu, R. Zhang, S. Nunes, Z. Jiang, Two-dimensional nanochannel membranes for molecular and ionic separations. Chem. Soc. Rev. **49**, 1071–1089 (2020)
5. A.C. Balazs, T. Emrick, T.P. Russell, Nanoparticle polymer composites: where two small worlds meet. Science **314**, 1107–1110 (2006)

6. A. Kusoglu, A.Z. Weber, New insights into perfluorinated sulfonic-acid ionomers. Chem. Rev. **117**, 987–1104 (2017)
7. L. Chen, G. Shi, J. Shen, B. Peng, B. Zhang, Y. Wang, F. Bian, J. Wang, D. Li, Z. Qian, G. Xu, G. Liu, J. Zeng, L. Zhang, Y. Yang, G. Zhou, M. Wu, W. Jin, J. Li, H. Fang, Ion sieving in graphene oxide membranes *via* cationic control of interlayer spacing. Nature **550**, 380–383 (2017)
8. H. Wang, M. Wang, X. Liang, J. Yuan, H. Yang, S. Wang, Y. Ren, H. Wu, F. Pan, Z. Jiang, Organic molecular sieve membranes for chemical separations. Chem. Soc. Rev. **50**, 5468–5516 (2021)
9. S. Karan, Z. Jiang, A.G. Livingston, Sub-10 nm polyamide nanofilms with ultrafast solvent transport for molecular separation. Science **348**, 1347–1351 (2015)
10. M.Y. Jeon, D. Kim, P. Kumar, P.S. Lee, N. Rangnekar, P. Bai, M. Shete, B. Elyassi, H.S. Lee, K. Narasimharao, S.N. Basahel, S. Al-Thabaiti, W. Xu, H.J. Cho, E.O. Fetisov, R. Thyagarajan, R.F. DeJaco, W. Fan, K.A. Mkhoyan, J.I. Siepmann, M. Tsapatsis, Ultra-selective high-flux membranes from directly synthesized zeolite nanosheets. Nature **543**, 690–694 (2017)
11. T. Matsuura, Synthetic membranes and membrane separation processes (CRC Press, 2020)
12. H. Strathmann, Membrane separation processes: current relevance and future opportunities. AIChE J. **47**, 1077–1087 (2001)
13. G. He, Z. Li, J. Zhao, S. Wang, H. Wu, M.D. Guiver, Z. Jiang, Nanostructured ion-exchange membranes for fuel cells: recent advances and perspectives. Adv. Mater. **27**, 5280–5295 (2015)
14. L. Wang, M.S. Boutilier, P.R. Kidambi, D. Jang, N.G. Hadjiconstantinou, R. Karnik, Fundamental transport mechanisms, fabrication and potential applications of nanoporous atomically thin membranes. Nat. Nanotechnol. **12**, 509–522 (2017)
15. D.W. Shin, M.D. Guiver, Y.M. Lee, Hydrocarbon-based polymer electrolyte membranes: importance of morphology on ion transport and membrane stability. Chem. Rev. **117**, 4759–4805 (2017)
16. E.B. Trigg, T.W. Gaines, M. Maréchal, D.E. Moed, P. Rannou, K.B. Wagener, M.J. Stevens, K.I. Winey, Self-assembled highly ordered acid layers in precisely sulfonated polyethylene produce efficient proton transport. Nat. Mater. **17**, 725–731 (2018)
17. Y. Cheng, Y. Ying, S. Japip, S.D. Jiang, T.S. Chung, S. Zhang, D. Zhao, Advanced porous materials in mixed matrix membranes. Adv. Mater. **30**, 1802401 (2018)
18. J. W. Barnett, C. R. Bilchak, Y. Wang, B. C. Benicewicz, L. A. Murdock, T. Bereau, S. K. Kumar. Designing exceptional gas-separation polymer membranes using machine learning. Sci. Adv. **6**, eaaz4301 (2020)
19. R.D. Noble, Perspectives on mixed matrix membranes. J. Membr. Sci. **378**, 393–397 (2011)
20. T.C. Merkel, B.D. Freeman, R.J. Spontak, Z. He, I. Pinnau, P. Meakin, A.J. Hill, Ultrapermeable, reverse-selective nanocomposite membranes. Science **296**, 519–522 (2002)
21. R. Kannan, B.A. Kakade, V.K. Pillai, Polymer electrolyte fuel cells using Nafion-based composite membranes with functionalized carbon nanotubes. Angew. Chem. Int. Ed. **47**, 2653–2656 (2008)
22. B.G. Choi, J. Hong, Y.C. Park, D.H. Jung, W.H. Hong, P.T. Hammond, H. Park, Innovative polymer nanocomposite electrolytes: nanoscale manipulation of ion channels by functionalized graphenes. ACS Nano **5**, 5167–5174 (2011)
23. L. Xiang, L. Sheng, C. Wang, L. Zhang, Y. Pan, Y. L. Amino-functionalized ZIF-7 nanocrystals: improved intrinsic separation ability and interfacial compatibility in mixed-matrix membranes for CO_2/CH_4 separation. Adv. Mater. **29**, 1606999 (2017)
24. H. Dou, M. Xu, B. Wang, Z. Zhang, G. Wen, Y. Zheng, D. Luo, L. Zhao, A. Yu, L. Zhang, Z. Jiang, Z. Chen, Microporous framework membranes for precise molecule/ion separations. Chem. Soc. Rev. **50**, 986–1029 (2021)
25. H. Fan, Q. Shi, H. Yan, S. Ji, J. Dong, G. Zhang, Simultaneous spray self-Assembly of highly loaded ZIF-8-PDMS nanohybrid membranes exhibiting exceptionally high biobutanol-permselective pervaporation. Angew. Chem. Int. Ed. **126**, 5684–5688 (2014)
26. J.E. Gu, S. Lee, C.M. Stafford, J.S. Lee, W. Choi, B.Y. Kim, K.Y. Baek, E.P. Chan, J.Y. Chung, J. Bang, J.H. Lee, Molecular layer-by-layer assembled thin-film composite membranes for water desalination. Adv. Mater. **25**, 4778–4782 (2013)

27. R.W. Baker, J.G. Wijmans, Y. Huang, Permeability, permeance and selectivity: a preferred way of reporting pervaporation performance data. J. Membr. Sci. **348**, 346–352 (2010)
28. H. Li, Z. Song, X. Zhang, Y. Huang, S. Li, Y. Mao, H.J. Ploehn, Y. Bao, MYu. Ultrathin, Ultrathin molecular-sieving graphene oxide membranes for selective hydrogen separation. Science **342**, 95–98 (2013)
29. R. Sood, S. Cavaliere, D.J. Jones, J. Rozière, Electrospun nanofibre composite polymer electrolyte fuel cell and electrolysis membranes. Nano Energy **26**, 729–745 (2016)
30. S. Cavaliere, Electrospinning for advanced energy and environmental applications (CRC Press, 2015)
31. M.V. Kakade, S. Givens, K. Gardner, K.H. Lee, D.B. Chase, J.F. Rabolt, Electric field induced orientation of polymer chains in macroscopically aligned electrospun polymer nanofibers. J. Am. Chem. Soc. **129**, 2777–2782 (2007)
32. G. Liu, W. Jin, N. Xu, Two-dimensional-material membranes: a new family of high-performance separation membranes. Angew. Chem. Int. Ed. **55**, 13384–13397 (2016)
33. H.W. Kim, H.W. Yoon, S.M. Yoon, B.M. Yoo, B.K. Ahn, Y.H. Cho, H.J. Shin, H. Yang, U. Paik, S. Kwon, J.-Y. Choi, H.B. Park, Selective gas transport through few-layered graphene and graphene oxide membranes. Science **342**, 91–95 (2013)
34. L. Ding, Y. Wei, L. Li, T. Zhang, H. Wang, J. Xue, L. Ding, S. Wang, J. Caro, Y. Gogotsi, MXene molecular sieving membranes for highly efficient gas separation. Nat. Commun. **9**, 1–7 (2018)
35. C. Zhang, B.H. Wu, M.Q. Ma, Z. Wang, Z.K. Xu, Ultrathin metal/covalent-organic framework membranes towards ultimate separation. Chem. Soc. Rev. **48**, 3811–3841 (2019)

Chapter 2
Composite Membrane for Organic Solvent Nanofiltration

Wenpeng Li, Shiyuan Liu, and Jingjing Chen

2.1 Introduction

Organic solvents (e.g., alkanes, aromatics, alcohols, ketones, and esters) are utilized in a wide range applications including pharmaceuticals, petroleum refining and food industry, the consumption of which is just less than that of water [1]. Different from water obtained directly from nature, organic solvents are yielded by processes with complex energy conversion and harsh operating conditions [2, 3]. Therefore, it is a crucially important issue to separate and recycle organic solvents to reduce pollution and save resources. Compared with the traditional technologies such as flash chromatography [4], distillation [5], and extraction [6], organic solvent nanofiltration (OSN), which employs a solvent permselective membrane, is considered as a prospective candidate as it is operated under no-phase transformation condition that can save energy [7]. For OSN process, high flux, satisfactory rejection, and strong stability are highly needed for practical applications. Specially, polymeric membranes with acceptable permeance and high rejection have drawn increasing attention in OSN field. Besides, thin-film composite (TFC) membranes which possess hierarchical architecture: the porous support layer ensures excellent mechanical strength and the ultra-thin active layer holds high flux and adequate rejection, are promising to achieve high performance [8–11]. Particularly, interfacial polymerization (IP) technology, which can manufacture highly cross-linked polyamide on the porous support layer, tremendously promotes the development of TFC membranes. This technology controls independently the amount of monomers in aqueous and organic phases to prepare 10 ~ 100 nm-thick nanofilms, which is benefited from the unique self-inhibition effects during film-forming process [12–16].

However, TFC membranes usually suffer from serious permeation and rejection trade-off effect due to the motion of polymer chains in organic solvents, which leads to

W. Li (✉) · S. Liu · J. Chen
School of Chemical Engineering, Zhengzhou University, Zhengzhou 450001, P. R. China
e-mail: liwenpeng@zzu.edu.cn

J. Wang and W. Wu (eds.), *Functional Membranes for High Efficiency Molecule and Ion Transport*, https://doi.org/10.1007/978-981-19-8155-5_2

the exist of wide distribution free volume cavities in membrane matrix. In addition, to ensure high rejection, the nanofilm is generally dense with highly cross-linked structure, while the narrow nanochannels give high resistance for molecule transport. Besides, the thickness of nanofilm is often thick (> 200 nm) to maintain the integrity of nanofilm, thus collectively bringing low molecule permeance (< 5 L m^{-2} h^{-1} bar^{-1}) [17, 18]. Several methods have been exploited to overcome this tricky trade-off effect, including hybridization and precise control of cross-linking degree [19, 20]. Especially the former, the fabrication of nanocomposites by incorporating inorganic fillers in the polymer matrix has proven to be a simple and efficient method for the following reasons: (i) the presence of impermeable fillers will significantly hinder the transport of large solutes, and then enhance the rejection [21]; (ii) the fillers, through steric effects and/or interfacial interactions, inhibit the movement of polymer chains and pack near the polymer-filler interface, thus providing a narrow free volume distribution.

In addition, if the filler surface possesses desired functional groups, extra pathways would be built along the filler surface, where solvent molecules transport selectively [22]. In this case, the permeability of small-sized solvent molecules can be maintained or even enhanced despite steric hindrance effect from inorganic fillers. Specifically, particles (MOFs [23], silica [24], zeolite [25]) and nanosheets (MXene [14], GO [26]) with size from nanoscale to microscale have been embedded into OSN membrane. For example, Wu and co-workers incorporated MXene nanosheets into polymer matrix to construct alcohol-selective nanochannels along MXene nanosheet surface utilizing the –OH groups, resulting in a 30.2% increase for isopropanol flux [14]. Together with the highly elevated rejection of solutes by the physical hinder of nanosheets, this novel hybrid membrane could overcome the trade-off effect to a certain extent.

Besides, preparing ultrathin (< 100 nm) and defect-free nanofilm provides a promising method to enhance molecule permeance as the reduced thickness obviously shortens the transport path. Recently, two significant advances have been achieved by smoothening support layer or slowing down the reaction rate. Karan and co-workers coated 1.8 nm $Cd(OH)_2$ nanowires on substrate to construct a smooth nanostrand interlayer with ordered nanopores, supporting a continuous, uniform interface between aqueous phase and organic phase. Defect-free ultrathin nanofilm (< 30 nm thickness) was obtained by IP, which achieves high flux (> 100 L m^{-2} h^{-1} bar^{-1} for acetonitrile) with a rejection of 99% for acid fuchsin (~ 580 g mol^{-1}) [12].

In contrast, Jimenez-Solomon et al. chose rigid, contorted phenol monomers (e.g., 5,5′, 6,6′-tetrahydroxy-3,3,3′,3′-tetramethylspirobisindane) to reduce the reaction rate of IP process, and thus integrate thin film with thickness of ~ 20 nm was obtained. Such film achieved satisfactory rejection (> 95%) for dyes with molecular weight larger than 300 [15]. However, the sophisticated nanomachining steps were required in manufacture process, and available monomers were expensive and rare, seriously impeding the development and practical application of this preparation method.

In this study, TFC membranes with fillers incorporated into nanofilms were prepared by adsorption-assisted IP technology, and ultrathin nanofilms with thickness below 70 nm were synthesized. Nanomaterials, including carbon dots (CDs) [27] and MXene ($Ti_3C_2T_x$) [14, 28], were selected as active fillers and polyethyleneimine (PEI) polymer was used as matrix to prepare TFC membranes. The uniformly distributed fillers with various functional groups act as active sites to selectively facilitate the transport of solvents, and meanwhile impede the flow of large solutes by physical steric hindrance. This structure effectively relieves the trade-off effect for TFC membranes. Additionally, hydrophilic monomers such as PEI, diethylenetriamine (DETA), and ethanediamine (EDA) were used to prepare ultrathin nanofilms (< 30 nm) assisted by dopamine sublayer, achieving fast molecule transport for polar solvents [29, 30]. Furthermore, amphipathic CDs with tunable functional groups (–NH–/–NH_2 and –OH) and carbonized nanodomains were synthesized to prepare ultrathin nanofilms [31]. The resulted TFC membranes give highly enhanced permeance for both polar and non-polar solvents because the amphipathic membrane surface permits favorable dissolution and the nanopores allow fast diffusion. Therefore, this work provides a new pathway to understand IP procedure and design advanced nanofiltration membranes for fast molecule transport and highly efficient separation.

2.2 Composite Membrane with $Ti_3C_2T_x$-Incorporated Active Layer

$Ti_3C_2T_X$ nanosheets were prepared by an effective strategy of extracting Al layer from Ti_3AlC_2 using 50% HF ($Ti_3AlC_2 + 3HF = AlF_3 + 3/2H_2 + Ti_3C_2T_x$), and next intercalated by dimethyl sulfoxide (DMSO) to exfoliate the stacked $Ti_3C_2T_x$ [32]. The specific procedure of synthesizing $Ti_3C_2T_x$ is illustrated in Fig. 2.1. The Ti_3AlC_2 powders were prepared by mixing TiH_2, TiC_2, and Al powders, which were ball milled for 12 h. Subsequently, the homogenized mixture was heated and kept at 1450 °C for 2 h. Next, HF aqueous solution (50%) was used to treat $Ti_3C_2T_x$ powder for 12 h to obtain multilayered $Ti_3C_2T_x$ powder. $Ti_3C_2T_x$ powder was then stirred within DMSO solution at room temperature for 18 h. The colloidal suspension was centrifuged to obtain the intercalated powder that was separated from the liquid DMSO. After decantation of the supernatant, deionized water was added to the precipitate, and the weight ratio of precipitate to water was 1:500. After an ultrasonic treatment for 4 h, it was centrifuged. The precipitate was dried in air for 3–4 days, and the resulting powder was named as $Ti_3C_2T_x$.

As shown in Fig. 2.2, the preparation process of PEI-based composite membrane contains three steps. The first step was the fabrication of PEI-based composite membranes. $Ti_3C_2T_x$ was dispersed into water and then ultrasonically exfoliated. Subsequently, $Ti_3C_2T_x$ solution was dropped into PEI solution under agitation, followed by ultrasound. Then, PEI-$Ti_3C_2T_x$ solution was coated on the surface of

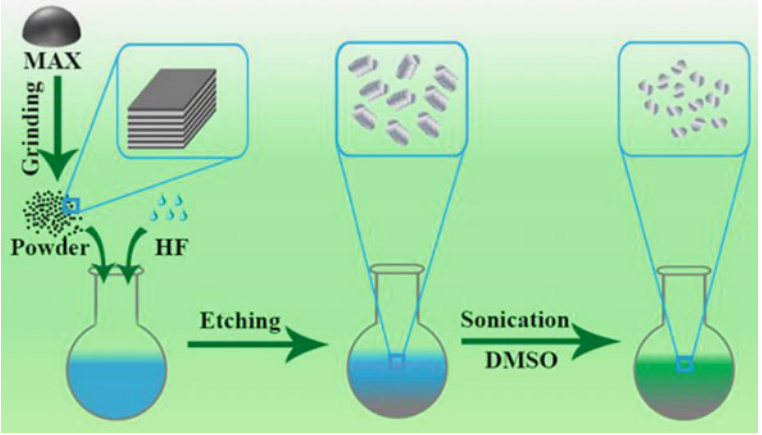

Fig. 2.1 Diagram of $Ti_3C_2T_x$ synthesis. Copyright (2016), Elsevier [14]

PAN support layer by drop coating method. After removing the excess solution, the mixture solution (TMC and *n*-hexane) was casted to the PEI-$Ti_3C_2T_x$ layer. Finally, the membrane was dried in air before being placed in an oven. The prepared membranes were named as PAN/PEI-$Ti_3C_2T_x$-*X*, where *X* ($X = 1$, 2, 3, and 4) represents the mass ratio of $Ti_3C_2T_x$ to PEI.

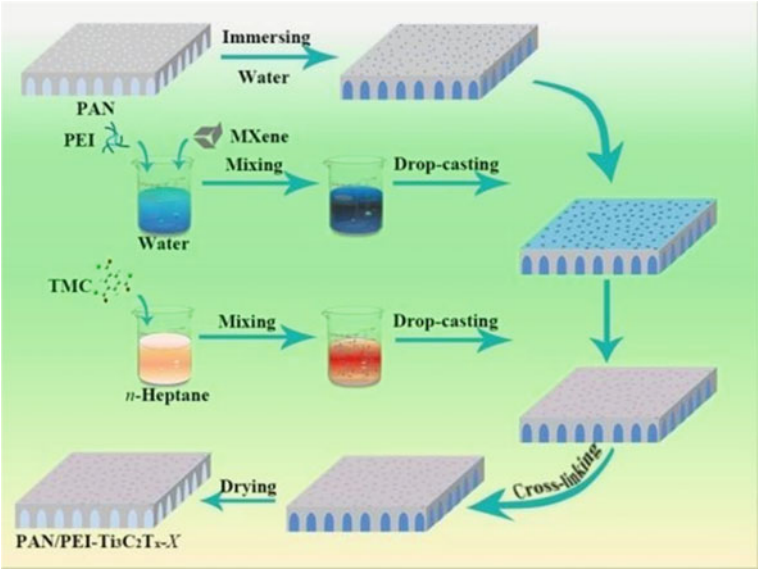

Fig. 2.2 Schematic diagram of synthesis of PAN/PEI-$Ti_3C_2T_x$-*X*. Copyright (2016), Elsevier [14]

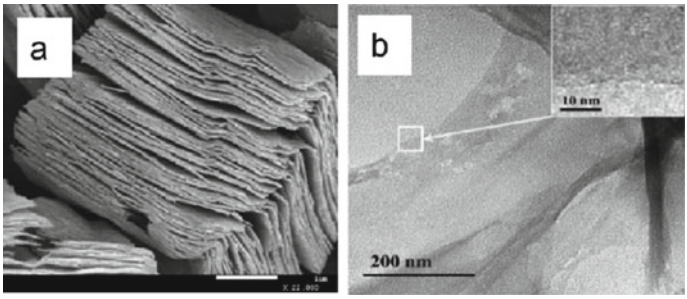

Fig. 2.3 The **a** SEM and **b** TEM images of $Ti_3C_2T_x$ nanosheets. Copyright (2016), Elsevier [14]

Scanning electron microscopy (SEM) image in Fig. 2.3a reveals that Ti_3AlC_2 is successfully etched into laminated nanosheets with thickness ranging from a few nanometers to 45 nm. As shown in Fig. 2.3b of transmission electron microscope (TEM) images, $Ti_3C_2T_x$ can be stripped into single nanosheets with transverse sizes ranging from several hundred nanometers to several microns by simple ultrasonic processing with the assistance of solvent DMSO that was inserted between layers. X-ray diffraction (XRD) results in Fig. 2.5a show that the increased layer spacing along the *c*-axis is caused by the removal of Al atoms, while some prominent (00*l*) ($l = 2, 4$, etc.) diffraction peaks of $Ti_3C_2T_x$ are located at 2θ angle lower than Ti_3AlC_2.

The $Ti_3C_2T_x$ nanosheets were uniformly dispersed into PEI solution to obtain hybrid active layer, which was then coated on PAN support layer to prepare composite OSN membrane. In order to obtain the same thickness of active layer, identical amount of PEI and preparation process were used in this experiment. The morphologies of membranes are observed by SEM, as shown in Fig. 2.4. Figure 2.4a illustrates that the surface of PAN/PEI is smooth and homogeneous without obvious defects or voids. After the addition of $Ti_3C_2T_x$, PAN/PEI-$Ti_3C_2T_x$-3 has a rough surface with some flaky wrinkles (Fig. 2.4b), similar to other lamellar membranes [33]. In addition, the entire surface of the composite film is uniform without exposing the nanosheet, and the good compatibility of $Ti_3C_2T_x$ and PEI polymer is inferred by hydrogen bonding (H-interaction) [34]. As shown in Fig. 2.4c, this interaction drives the PEI chain to cover the surface of $Ti_3C_2T_x$ without exposing the nanosheet to membrane surface. This also indicates that the nanosheets are mostly horizontally arranged in polymer matrix due to their large transverse area and small thickness [35].

The chemical structure of the membrane was detected using fourier transform infrared spectroscopy (FTIR) and illustrated in Fig. 2.5b. PAN shows a typical stretching vibration of C≡N at 2243 cm^{-1}. Apparently, coating PEI layer leads to the disappearance of this peak, indicating that the active layer was full covered [36]. In addition, PAN/PEI displays three new bands at 1355, 1546, and 1612 cm^{-1}, corresponding to the tensile vibration of –C–N, –N–H and C=O, respectively. The excellent compatibility between PEI and $Ti_3C_2T_x$ makes PAN/PEI-$Ti_3C_2T_x$-3 show similar FTIR spectra as compared to the PAN/PEI. However, the characteristic band

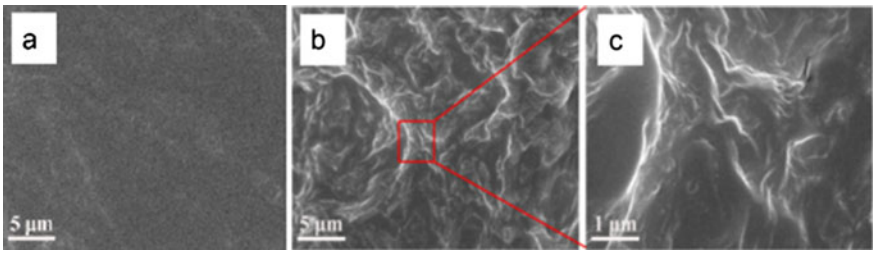

Fig. 2.4 The surface of SEM images of **a** PAN/PEI, **b** and **c** PAN/PEI-$Ti_3C_2T_x$-3. Copyright (2016), Elsevier [14]

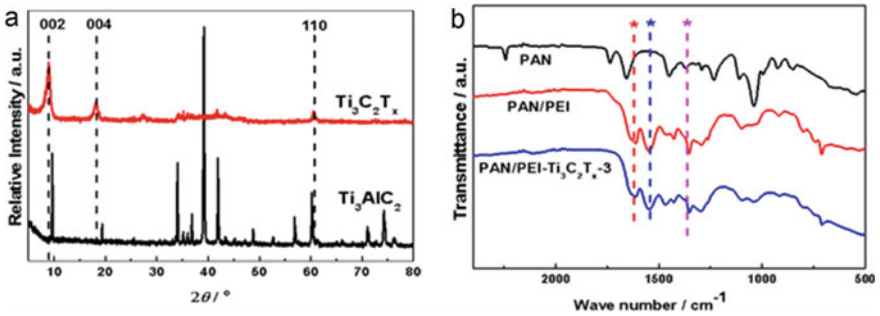

Fig. 2.5 **a** XRD curves of $Ti_3C_2T_x$ and Ti_3AlT_2. **b** FTIR spectra of PAN, PAN/PEI, and PAN/PEI-$Ti_3C_2T_x$-3. Copyright (2016), Elsevier [14]

intensity becomes weaker after incorporating $Ti_3C_2T_x$ [37]. And, this brings abundant hydrophilic groups to composite membrane, and the reduced strength is attributed to the reduction of PEI content [38]. $Ti_3C_2T_x$ has changed its morphology to further influence the chains' motion and packing, which is proved by XRD as pictured in Fig. 2.6a. The well-aligned accumulation of cross-linked PEI polymer segments produces a wide crystal band at $2\theta = 9 \sim 28°$, while $Ti_3C_2T_x$ generates additional bands for PAN/PEI-$Ti_3C_2T_x$-*X* at $2\theta = 6.6°$, and its band strength increases followed by the increase of $Ti_3C_2T_x$ content. This band is triggered by the esterification reaction between –OH on $Ti_3C_2T_x$ and –COCl on TMC, and the crystal band of $Ti_3C_2T_x$ is transferred at $2\theta = 9.6 \sim 6.6°$. Furthermore, for this novel ligand, $Ti_3C_2T_x$ intervention on PEI chains results in a slight decrease in the strength of PAN/PEI-$Ti_3C_2T_x$-*X* at $2\theta = 9 \sim 28°$.

Thermogravimetric analysis (TGA) demonstrates the thermal properties of the membranes, and the results are shown in Fig. 2.6b, showing that all membranes undergo three stages of weightlessness: the first stage of the membrane is water evaporation (about 30 ~ 300 °C); and the second stage of the membrane is side chain pyrolysis (about 350 ~ 450 °C); and the third stage of PEI and PAN is the skeleton degradation (about 500 ~ 660 °C). PAN/PEI-$Ti_3C_2T_x$-*X* membranes present comparable degradation mechanism to that of PAN/PEI because of the non-existence of covalent

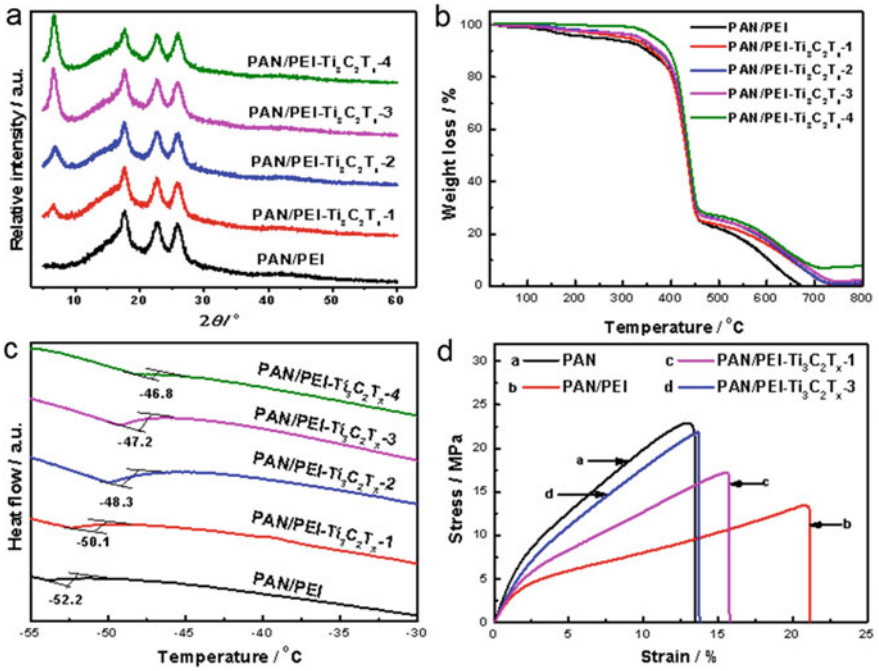

Fig. 2.6 **a** XRD curves, **b** TGA curves, and **c** DSC curves of PAN/PEI and PAN/PEI-$Ti_3C_2T_x$-*X*. **d** Stress–strain curves of PAN, PAN/PEI, PAN/PEI-$Ti_3C_2T_x$-1 and PAN/PEI-$Ti_3C_2T_x$-3. Copyright (2016), Elsevier [14]

bond between $Ti_3C_2T_x$ and PEI. However, the appearance of strict from $Ti_3C_2T_x$ and the interfacial interactions with PEI change the initial temperature of sidechain decomposition to a slightly higher value for PAN/PEI-$Ti_3C_2T_x$, yielding stronger char appearance at 800 °C, notably in high $Ti_3C_2T_x$ ingredients. For example, T_d (specific temperature at 5% weight loss) of PAN/PEI is 232.4 °C, which boosts to 295.9, 334.1, 336.2, and 365.8 °C after cultivating 1, 2, 3, and 4 wt% $Ti_3C_2T_x$ nanosheets into the matrix, separately. Differential calorimetry curves (DSC) of the membranes in Fig. 2.6c indicate that the glass transition temperature (T_g) for PAN/PEI is around − 52.2 °C, but the moist PEI chain shift allows the corresponding T_g of membranes finally pick up to − 50.1, − 48.3, − 47.2, and − 46.8 °C. In the case of stress–strain curves, the mechanical properties of the membranes are depicted in Fig. 2.6d, which proves that the PAN support obtains a mechanical stability with Young's modulus of 488.4 MPa and then extends the tensile strength of 22.9 MPa. The coating of the cross-linked PEI layer improves the flexibility of the PAN support, as provided by the longer elongation of 21.15% for PAN/PEI. This should start with inserting PEI molecules into the PAN nanopores, which disrupts the intrinsic compaction of the PAN chains and enhance the chain flexibility. Incorporation of $Ti_3C_2T_x$ nanosheets improves the stiffness of composite membranes [39]. For example, adding $Ti_3C_2T_x$ with weigh increases from 1 to 3%, Young's modulus and tensile strength enhance

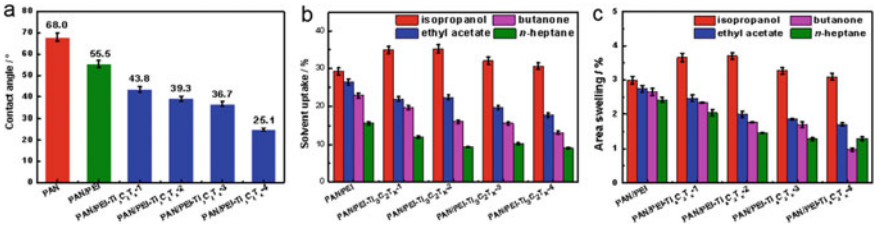

Fig. 2.7 **a** Contact angles of PAN, PAN/PEI, and PAN/PEI-$Ti_3C_2T_x$-*X*. **b** Solvent uptake and **c** area swelling of PAN/PEI and PAN/PEI-$Ti_3C_2T_x$-*X*. Copyright (2016), Elsevier [14]

from 201.7 MPa and 15.5 to 282.2 MPa and 21.8 MPa, respectively. In addition, the elasticity of the composite membrane has been improved, as confirmed by the apparent increase in length.

Since the wetting capacity of the OSN membrane plays an important role in determining the dissolution capacity, the contact angle of the membranes with water is shown in Fig. 2.7a. The contact angle decreases from 63.8° for PAN support to 55.5° for PAN/PEI. On the other hand, different from the general phenomena that embedding inorganic fillers would increase the water contact angle [40], the embedding of hydrophilic $Ti_3C_2T_x$ nanosheets provides reduced contact angles for PAN/PEI-$Ti_3C_2T_x$-*X* due to the multiple –OH groups. The rough surface also helps to reduce the contact angle by increasing the directional force for the propagation of droplets by the multi-gradient effect [41]. This effect can be further strengthened by increasing the $Ti_3C_2T_x$ content, and the contact angle gradually decreases from 43.8° to 25.1° as the $Ti_3C_2T_x$ content varies from 1 to 4 wt%. The low contact angle of < 45° permits PAN/PEI-$Ti_3C_2T_x$-X a high absorption capacity for polar molecules but a low inflammatory potential for non-polar molecules [42].

During operation, the membrane remains structurally stability and the free volume cavities required for mass transfer occur due to adequate solvent uptake and expansion of polymer chains [43]. Of these, four solvents (ethyl acetate, isopropanol, butanone, and n-heptane), with dipole moments of 6.27×10^{-30}, 1.66×10^{-30}, 8.97×10^{-30} and 0 Cm, respectively, were selected as representatives to evaluate solvent resistance. Solvent uptake and swelling features play important roles in OSN performance as they reflect the dissolution resistance of the membrane. As shown in Fig. 2.7b, PAN/PEI displays the solvent uptakes of 15.6%, 22.8%, 26.4%, and 29.3% for n-heptane, butanone, ethyl acetate, and isopropanol, respectively. However, the swelling degree of the membrane is less than 3.7%, indicating that soluble molecules are mainly stored in the pores of the PAN support (Fig. 2.7c). Due to the dense and uniform active layer, the membrane's thickness increases due to the expansion by solvent uptaking. With the exception of isopropanol, the inclusion of $Ti_3C_2T_x$ nanosheets reduces the solvent absorption and area inflammation of PAN/PEI-$Ti_3C_2T_x$-*X* for other solvents, especially membranes with higher nanosheet content. This is ascribed to the inhibition of chain motion that reduce solvent storage and diffusion within membrane. For example, when $Ti_3C_2T_x$ content

elevates from 1 to 4 wt%, solvent absorption and area swelling of membrane for butanone decrease from 19.6% to 13.1% and from 2.3% to 1.0%, respectively. In contrast, for isopropanol, with the nanosheet contents are 1, 2, 3, and 4 wt%, the solvent uptake growth rates are 19.3%, 20.4%, 9.5%, and 4.7%, respectively. These results show that embedding $Ti_3C_2T_x$ nanosheets can form additional interfaces with hydrophilic domains. Here, PEI and $Ti_3C_2T_x$ nanosheets bear hydrophilic –NH_2/–NH– and –OH groups, respectively. Thus, this domain serves as an additional storage space for isopropanol solvents. And, the PEI chain kinetics is facilitated with the help of H-interaction and give a strong solution effect for isopropanol. Under similar conditions, solvent absorption and area swelling of the composite membrane follows the order of n-heptane < butanone < ethyl acetate < isopropanol. Considering the molecular dimensions (butanone < ethyl acetate < isopropanol < n-heptane) and dipole moments (n-heptane < butanone < ethyl acetate < isopropanol), we believe that small and polar molecules can be easily absorbed into the membrane. While it is difficult for large and non-polar molecules to dissolve into membrane. In general, PEI-based membranes have good solvent resistance as compared to commercial membranes and other OSN membranes in literature [44].

Four solvents were chosen as indicators for testing membrane performance at transmembrane pressures of 4 bar and 10 bar (Fig. 2.8a and b). When the transmembrane pressure is increased from 4 to 10 bar, the solvent flux is greatly improved, for PAN/PEI, the flux of isopropanol, ethyl acetate, butanone, and n-heptane increased from 18.9, 15.6, 8.0 and 4.8 L m^{-2} h^{-1} to 25.8, 19.1, 15.1, and 6.4 L m^{-2} h^{-1}, respectively. It is important to note that the flux of PAN/PEI is comparable to that reported in literatures [45]. In comparison, the incorporation of $Ti_3C_2T_x$ nanosheets can reduce the flux of weak polar or non-polar solvents such as ethyl acetate, butanone, and n-heptane. For example, incorporation 1 wt% $Ti_3C_2T_x$ nanosheets into PEI matrix reduces the flux of butanone, ethyl acetate, and n-heptane to 16.8, 11.6 and 4.1 L m^{-2} h^{-1}, which are reduced by 16.1%, 22.3%, and 36.1%, respectively. The reducing degree of these solvents is in the order of their non-polar nature: butanone < ethyl acetate < n-heptane. In contrast to this, the transfer capacity of membrane to isopropanol is facilitated by incorporation $Ti_3C_2T_x$ nanosheets with a flux of 28.7 L m^{-2} h^{-1}, which is 11.3% flux improvement. This finding indicates that the –OH groups on the $Ti_3C_2T_x$ surface should be the main flux variation factor. In particular, the –OH groups interact with isopropanol via hydrogen bondings, making it the adsorption site for isopropanol. The horizontally aligned $Ti_3C_2T_x$ nanosheets form a dense layer that allows isopropanol transporting at overlapping intervals along the surface, whereas it acts as a barrier layer for non-polar solvents by preventing their transport (Fig. 2.9), as observed in the GO laminated membranes [46]. This can be confirmed by increasing the isopropanol flux by elevating the $Ti_3C_2T_x$ nanosheet content to 2 wt%, due to the increase in surface channels, the flux increased by 30.2% to 33.5 L m^{-2} h^{-1}. And meanwhile, the flux of isopropanol for PAN/PEI-$Ti_3C_2T_x$-3 and PAN/PEI-$Ti_3C_2T_x$-4 is 26.7 and 23.4 L m^{-2} h^{-1}, respectively. However, the eventual aggregation of $Ti_3C_2T_x$ when the content exceeds 4 wt% causes a slight decrease for isopropanol but is still higher than that of PAN/PEI. Different from isopropanol, the flux of weakly polar and non-polar solvents decreases with the

increase of $Ti_3C_2T_x$ content, which is due to the increase of the transfer barrier. For example, when $Ti_3C_2T_x$ content increases to 4 wt%, the flux of ethyl acetate, butanone and n-heptane reduces to 9.1, 6.0, and 2.1 L m^{-2} h^{-1}, respectively. Solvent flux through PAN/PEI-$Ti_3C_2T_x$-*X* increases in the order of n-heptane < butanone < ethyl acetate < isopropanol, well in accordance with the order of solvent uptake. This suggests that the transport of organic solvents through these membranes is in the "transition region" between the pore flow model and the solution-diffusion model. Although the incorporation of $Ti_3C_2T_x$ nanosheets reduced the fluxes of ethyl acetate, butanone and n-heptane to a certain extent, the permeation fluxes of PAN/PEI-$Ti_3C_2T_x$-*X* are acceptable compared with literature data [45]. In particular, it has a significant promoting effect on the transfer of isopropanol, holding promising to act as a organic solvent nanofiltration membrane to purify alcohols. This effect is different from the inhibitory effect of many other inorganic fillers reported in literature, such as GO [16], ZIF-7 [12], and carbon nanotubes [47].

The rejection capacity of OSN membranes is usually reflected by the molecular weight cut-off (*MWCO*) when the rejection reaches 90%. In this work, PEG

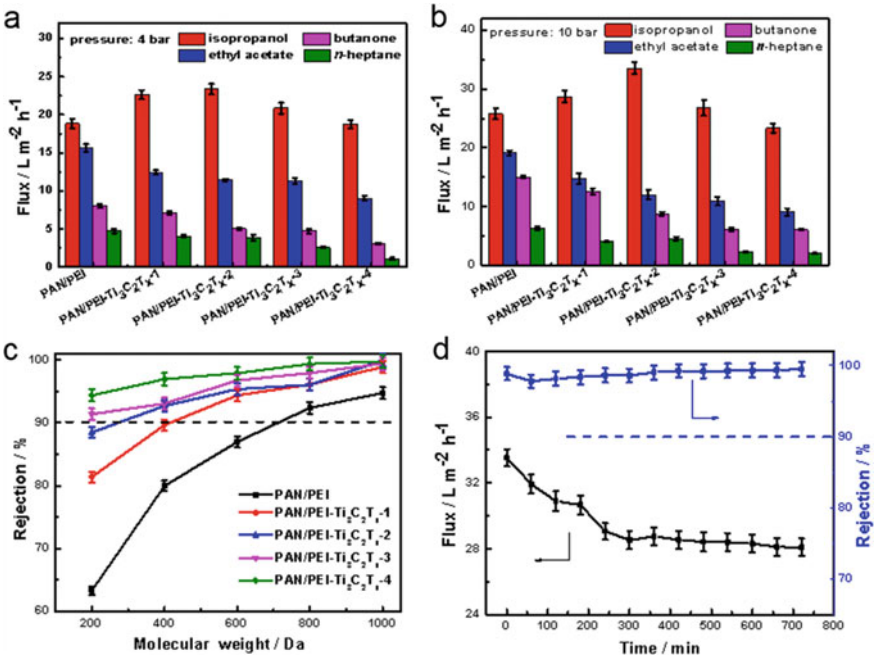

Fig. 2.8 The permeate flux of PAN/PEI and PAN/PEI-$Ti_3C_2T_x$-*X* for isopropanol, ethyl acetate, butanone, and n-heptane under the trans-membrane pressure of **a** 4 bar and **b** 10 bar at room temperature. **c** The rejection of PAN/PEI and PAN/PEI-$Ti_3C_2T_x$-*X* at room temperature. **d** The long-term operation performances of PAN/PEI-$Ti_3C_2T_x$-3 in isopropanol solution using PEG 1000 as solute at transmembrane pressure of 10 bar and room temperature. Copyright (2016), Elsevier [14]

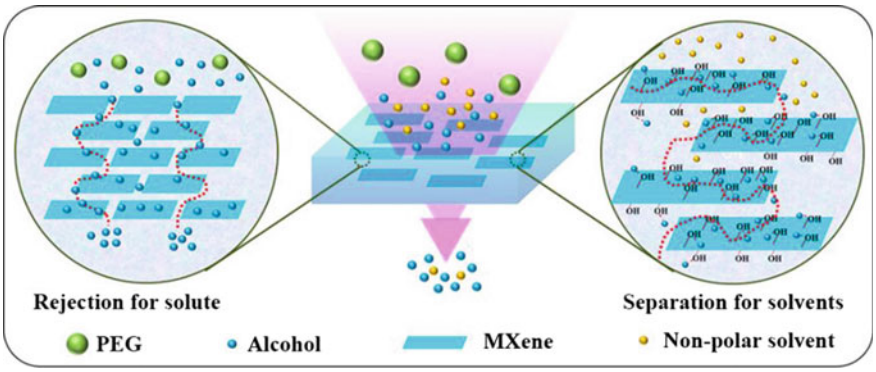

Fig. 2.9 Transfer and rejection mechanism of PAN/PEI-$Ti_3C_2T_x$-*X*. Copyright (2016), Elsevier [14]

(*Mw*: 200, 400, 600, 800, 1000 Da) is used as the solute, and isopropanol is used as the solvent due to the highest flux among the four chosen solvents to investigate the rejection ability of membrane, as shown in Fig. 2.8c. Just as we expected, the rejection capacity of each membrane increases with increasing PEG molecular weight. The *MWCO* of PAN/PEI provided by the cross-linked PEI network is 726 Da, which is comparable to the reported value in literature [48]. The horizontally aligned $Ti_3C_2T_x$ nanosheets in PEI matrix block the transport of large-sized PEG molecules, significantly improving the *MWCO* of the composite membranes. For example, only the adding of 1 wt% $Ti_3C_2T_x$ nanosheets can achieve a *MWCO* of below 400 Da. And further increasing $Ti_3C_2T_x$ nanosheet content causes more blockage for PEG molecules, resulting in higher solute rejection. With the increase of $Ti_3C_2T_x$ content, the *MWCO* of PAN/PEI-$Ti_3C_2T_x$-3 and PAN/PEI-$Ti_3C_2T_x$-4 is even lower than 200 Da. The larger lateral area and horizontal stacking of nanosheets contribute to such effective improvement in membrane rejection. The rejection improvement for OSN membranes by 2D $Ti_3C_2T_x$ nanosheets is much higher than that by other inorganic fillers, such as hollow spheres [46], silicalite [49], and zeolite [44].

Considering the good comprehensive nanofiltration performance, the long-term stability was further studied with PAN/PEI-$Ti_3C_2T_x$-2 membrane as the typical sample. The isopropanol flux and PEG 1000 rejection are surveyed in dead-end filtration at 10 bar for 720 min. Interference from concentration polarization is attenuated by applying magnetic stirring. PAN/PEI-$Ti_3C_2T_x$-2 membrane was immersed in isopropanol for more than 48 h prior to measurement to reach a complete equilibrium. The result in Fig. 2.8d shows that the isopropanol flux decreases by 27.2% in the first 480 min, from 33.5 to 24.4 L m^{-2} h^{-1}, and then remains relatively stable at 24.3 L m^{-2} h^{-1}. This variation is attributed to the compaction of membrane structure and blocking of the pores by solvent molecules, which is also confirmed by a slight increase in PEG rejection from 98.8% to 99.2%. These phenomena are common observations for OSN membranes, and actually the favorable long-term operation

stability is achieved for the composite membranes in this work compared to the reported membranes in literature [50].

In conclusion, we present a series of composite OSN membranes containing $Ti_3C_2T_x$ nanosheets, a new source of nanosheet with rich –OH groups, in which a typical hydrophilic polymer PEI is used as the matrix. $Ti_3C_2T_x$ nanosheets have a large lateral area and nanometer thickness, thus arranging horizontally in the matrix and causing significant interference to the polymer chain movement. The structural stability and solvent resistance of the composite membrane are enhanced by inhibiting the motion of PEI chains. The hydrophilic –OH groups construct the polymer-$Ti_3C_2T_x$ interface region, which is conducive to the storage of polar solvents and creates a wide and long way to transport alcohol molecules with the –OH groups as the carrier. Therefore, compared with the weakly polar or non-polar solvents, the alcohol flux of composite membrane is increased by 30%. In addition, $Ti_3C_2T_x$ nanosheets can effectively block the transfer of large-sized PEG solute and enhance the rejection ability of PEI-based membrane. The similar functions of $Ti_3C_2T_x$ in the transfer properties of the PDMS matrix lead to the conclusion that the inclusion of $Ti_3C_2T_x$ nanosheets could be an approach to overcome the flux-rejection trade-off of polymer membranes for alcohol-based OSN. Along with acceptable operational stability, these composite membranes could potentially be used to separate alcohol-containing mixtures for drug purification and sewage treatment. In addition, surface modification of $Ti_3C_2T_x$ nanosheets by functional groups will be carried out to investigate the influence of functionalized $Ti_3C_2T_x$ nanosheets on the nanofiltration efficiency of composite membranes. These rudimentary studies would provide a new viewpoint into the applications of the MXenes nanosheets in the field of membrane separation.

2.3 Composite Membrane with Functionalized $Ti_3C_2T_x$-Incorporated Active Layer

The procedure for synthesizing $Ti_3C_2T_x$ is shown in Fig. 2.1. A typical preparation of $Ti_3C_2T_x$-*M* is shown in Fig. 2.10. Using the example of amine-modified $Ti_3C_2T_x$, $Ti_3C_2T_x$ was added to a mixture of ethanol, water, and aqueous ammonium solution with vigorous stirring for 24 h. APTES was then poured into the above mixture and stirred for a further 24 h. Finally, the APTES modified $Ti_3C_2T_x$ ($Ti_3C_2T_x$-NH_2) was centrifuged and then dried in a vacuum oven at 60 °C. $Ti_3C_2T_x$ bearing other groups (–COOR, $–C_6H_6$, and $–C_{12}H_{26}$) were prepared in a similar process using MPTMS, MATES, and DCTES as modifiers, which were designated as $Ti_3C_2T_x$-COOR, $Ti_3C_2T_x$-C_6H_6, and $Ti_3C_2T_x$-$C_{12}H_{26}$, respectively. The manufacture of PEI-based membranes is illustrated in Fig. 2.10.

SEM images of $Ti_3C_2T_x$ (Fig. 2.11a) show that removal of Al atoms from the $Ti_3C_2T_x$ block results in a laminated nanosheet structure with lateral size of up to a few micrometers [51]. The TEM diagram (Fig. 2.11b) shows that after mixing

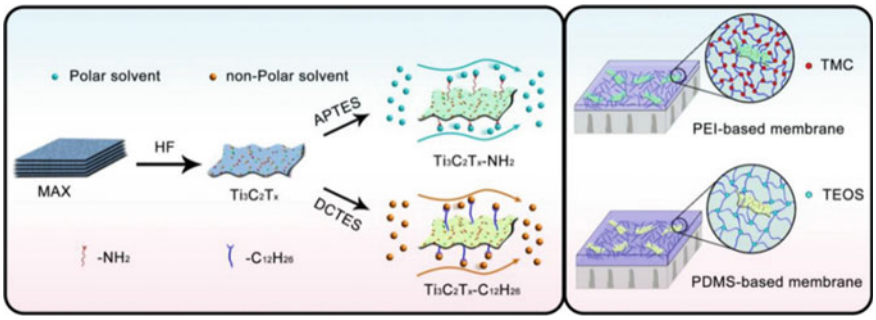

Fig. 2.10 The process of synthesis of $Ti_3C_2T_x$ and $Ti_3C_2T_x$-*M* and the microstructure of composite membranes. Copyright (2017), Elsevier [28]

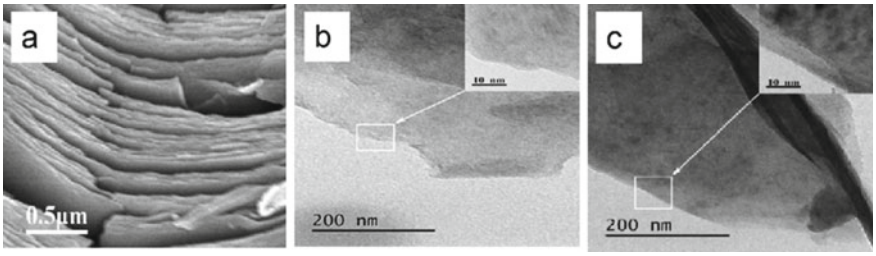

Fig. 2.11 **a** SEM image of $Ti_3C_2T_x$. TEM images of **b** $Ti_3C_2T_x$ and **c** $Ti_3C_2T_x$-NH_2. Copyright (2017), Elsevier [28]

the DMSO, these $Ti_3C_2T_x$ compounds were dispersed into individual nanosheets with thickness of several nanometers [52]. Figure 2.11c shows that the surface of $Ti_3C_2T_x$-NH_2 nanosheet appears darker as compared to that of $Ti_3C_2T_x$, implying the grafting of functional groups.

The FTIR curves (Fig. 2.12a) confirm that these $Ti_3C_2T_x$-based nanosheets show a clear band at 954 cm^{-1}, corresponding to the O–H elongation vibration due to the presence of –OH groups on $Ti_3C_2T_x$ nanosheet surface. Specifically, $Ti_3C_2T_x$-NH_2 nanosheets give a new feature band at 1501 cm^{-1} which assigned to the N–H [53]. And meanwhile, the spectrum of $Ti_3C_2T_x$-COOR shows a new band at 1730 cm^{-1}, associating with elongated vibration C=O [54]. For $Ti_3C_2T_x$-C_6H_6, the main band of the phenyl group from 1600 to 1400 cm^{-1} was determined on its spectrum [55]. The lamellar structure of $Ti_3C_2T_x$ and $Ti_3C_2T_x$-*M* is investigated by XRD and the results are shown in Fig. 2.12b. A typical diffraction band at $2\theta = 9.6°$ (interlayer distance, 0.91 nm) appears, with a slight decrease in intensity after functionalization [56].

$Ti_3C_2T_x$ or $Ti_3C_2T_x$-*M* nanosheets were respectively added into the PEI matrix on PAN supports to form composite OSN membranes. The composite nanofilms have the same thickness of the active layer due to the controlled amount of PEI and the same amount of fillers under identical preparation process. The morphologies of the nanofilms were characterized by SEM as shown in Fig. 2.13. Figure 2.13a

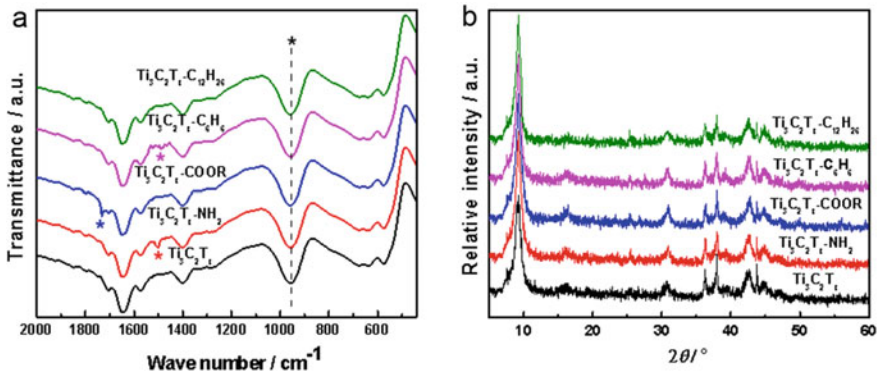

Fig. 2.12 **a** FTIR spectra and **b** XRD curves of $Ti_3C_2T_x$ and $Ti_3C_2T_x$-*M*. Copyright (2017), Elsevier [28]

shows that the surface of PAN/PEI membrane is smooth without visible cracks. The cross-sectional SEM image (Fig. 2.13b) shows that there is no visible nanosheets but some wrinkling, indicating that $Ti_3C_2T_x$ nanosheets are well bonded to the PEI matrix. The hydrogen bonding interactions (H-interaction) between $Ti_3C_2T_x$ and PEI polymer chains help the well compatible properties between PEI and $Ti_3C_2T_x$ nanosheets as shown in Fig. 2.13b. In addition, Fig. 2.13b shows an intact nanofilm with thickness of ~ 550 nm on the PAN support, which is agreed well with the structure reported in literature [14]. In addition, due to the incorporation of $Ti_3C_2T_x$ within nanofilm, it is difficult to obtain complete nanofilms with thicknesses below 200 nm.

FTIR spectra of composite membranes were obtained to demonstrate the chemical composition of prepared skin nanofilms (Fig. 2.14a). Typical correlations of –CN, –NH and C=O are observed on the spectra of PAN/PEI within the range at 1355, 1546, and 1612 cm^{-1}, which confirms the chemical reaction between PEI and TMC. Due to the small size of the nanosheets and the coating of the PEI matrix, there is no

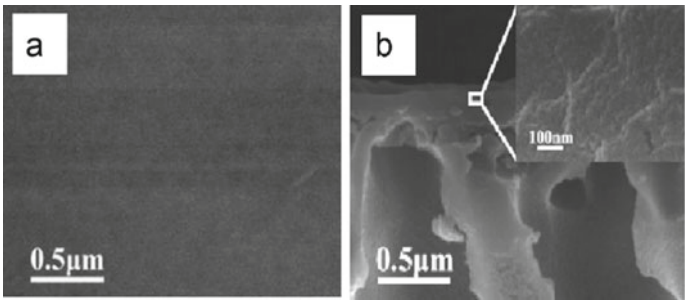

Fig. 2.13 SEM images of surface of **a** PAN/PEI, and cross-sectional image of **b** PAN/PEI-$Ti_3C_2T_x$. Copyright (2017), Elsevier [28]

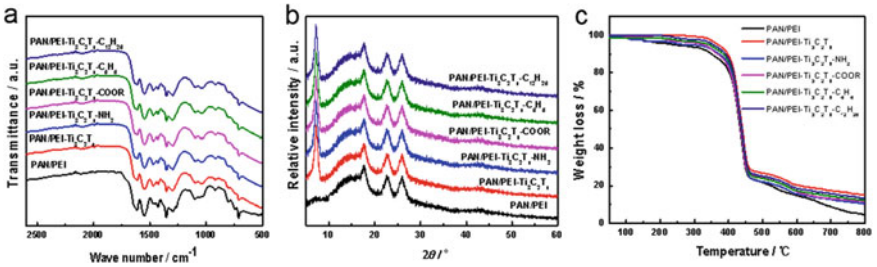

Fig. 2.14 **a** FTIR spectra, **b** XRD curves, and **c** TGA curves of PEI-based membranes. Copyright (2017), Elsevier [28]

new signals appeared on the spectra of PAN/PEI-$Ti_3C_2T_x$ and PAN/PEI-$Ti_3C_2T_x$-*M*. Changes in the microstructure affected by $Ti_3C_2T_x$ or $Ti_3C_2T_x$-*M* are further investigated by XRD. Figure 2.14b shows that the regulation of the PEI matrix in all membrane forms crystal bands at $2\theta = 9$–$28°$, and the addition of $Ti_3C_2T_x$ or $Ti_3C_2T_x$-*M* brings an additional sharp band at $2\theta = 7.0°$. Depending on the bond in $Ti_3C_2T_x$ or $Ti_3C_2T_x$-*M* at $2\theta = 9.6°$, the decrease of bond intensity may be due to the esterification reaction between –OH in $Ti_3C_2T_x$ and –COCl in TMC. The thermal properties of membranes are characterized by TGA as shown in Fig. 2.14c, which shows that all membranes undergo three stages of weight loss: the first stage is the evaporation of membrane-bound water (approximately 30 ~ 300 °C); the second stage is the degradation of branched chains on PEI and PAN polymer and grafted functional groups on nanosheets (approximately 350 ~ 460 °C), and the third stage is pyrolysis of PEI and PAN backbone (approximately 500 ~ 660 °C). Compared with PAN/PEI, the structure of $Ti_3C_2T_x$ or $Ti_3C_2T_x$-*M* are thermally stable and would not completely decompose into side chains, resulting in high carbon yields of up to 800 °C. Meanwhile, the TGA curves of PAN/PEI-$Ti_3C_2T_x$-*M* and PAN/PEI-$Ti_3C_2T_x$ give a similar behavior with that of $Ti_3C_2T_x$-*M* and $Ti_3C_2T_x$ nanosheets on the thermal properties.

Hydrophilicity/hydrophobicity of composite membranes was evaluated by the contact angles of water and diiodomethane. As shown in Table 2.1, the hydrophilicity of PEI results in a water contact angle of 55.4° for PAN/PEI [36]. The incorporation of $Ti_3C_2T_x$ nanosheets with a high content of –OH groups further enhances the hydrophilic property of the nanofilm, reducing the water contact angle to 36.6° for PAN/PEI-$Ti_3C_2T_x$. In addition, the rough surface of PAN/PEI-$Ti_3C_2T_x$ pushes the floating droplets with large guiding forces through multiple tilting effects, thus reducing the contact angle [57]. Conversely, due to the presence of hydrophilic groups of $–NH_2$ and –COOR, the water contact angles of PAN/PEI-$Ti_3C_2T_x$-NH_2 and PAN/PEI-$Ti_3C_2T_x$-COOR reduce to 28.2° and 31.7°, respectively. When grafting the hydrophobic $–C_6H_6$ and $–C_{12}H_{26}$ groups, the water contact angles of PAN/PEI-$Ti_3C_2T_x$-C_6H_6 and PAN/PEI-$Ti_3C_2T_x$-$C_{12}H_{26}$ are 41.5° and 45.3°, respectively. Another characteristic associated with diiodomethane (Table 2.1) is that the contact angle for PAN/PEI is 96.5°, which is expected to be higher than water. The inclusion

of hydrophilic $Ti_3C_2T_x$ nanosheets results in a higher contact angle (107.3°) for PAN/PEI-$Ti_3C_2T_x$, while PAN/PEI-$Ti_3C_2T_x$-NH_2 and PAN/PEI-$Ti_3C_2T_x$-COOR-NH_2 also have higher contact angles of 118.9° and 113.6°, respectively. In contrast, when the hydrophobic groups (–C_6H_6 and –$C_{12}H_{26}$) are grafted onto the surface of $Ti_3C_2T_x$ nanosheets, the contact angles of PAN/PEI-$Ti_3C_2T_x$-C_6H_6 and PAN/PEI-$Ti_3C_2T_x$-$C_{12}H_{26}$ decrease to 103.4° and 100.2°, respectively. We infer that the grafted groups on the nanosheets control the affinity of the composite membranes for polar and non-polar molecules.

The above assumption can be further confirmed by the solvent uptake and area swelling of the composite membranes as shown in Table 2.1. Four commonly used solvents are chosen as representatives, including two polar solvents (isopropanol and ethyl acetate) and two nonpolar solvents (toluene and n-heptane). PAN/PEI displays solvent uptake of 30.5% and 12.1% for isopropanol and n-heptane, respectively. The fraction of associated area swelling, are relatively small, only 3.2% and 2.0%. This phenomenon indicates that the solvent molecules are mainly conserved in the pores of the PAN support [58]. The incorporation of $Ti_3C_2T_x$ nanosheets results in lower solvent uptake and area swelling for solvents, except for isopropanol, which is due to the lack of swelling of $Ti_3C_2T_x$ nanosheets. However, the –OH groups on $Ti_3C_2T_x$ provide a strong affinity for isopropanol through H-interaction, thus facilitating the adsorption and storage. Similarly, membranes doped with $Ti_3C_2T_x$-NH_2 and $Ti_3C_2T_x$-COOR nanosheets exhibit higher solvent adsorption and area swelling for isopropanol and ethyl acetate but lower values for n-heptane and toluene as compared to PAN/PEI-$Ti_3C_2T_x$. In particular, the solvent adsorption for $Ti_3C_2T_x$-COOR retains the highest value to ethyl acetate, and this phenomenon must be due to the presence of ester groups. Conversely, membranes coated by $Ti_3C_2T_x$-C_6H_6 or $Ti_3C_2T_x$-$C_{12}H_{26}$ nanosheets exhibit high solvent uptake and low area swelling in non-polar solvents. This phenomenon means that the hydrophobic groups on $Ti_3C_2T_x$-C_6H_6 or $Ti_3C_2T_x$-$C_{12}H_{26}$ nanosheets, even in a hydrophilic matrix, can promote adsorption for non-polar solvents. As expected, the highest absorption and swelling rates for toluene and n-heptane are those grafted with hydrophobic functional groups. Surprisingly, compared with other OSN nanofilms, the nanofilms prepared in this work exhibit excellent solvent resistance (area swelling rate less than 3.5%) [59].

The membrane permeation flux tests were carried out at 4 bar and 10 bar, respectively, to test the pure solvent flux of the above four solvents. By comparing the change of solvent flux at different pressures (4 and 10 bar) (Fig. 2.15a), it can be found that increasing transmembrane pressure can significantly improve the solvent flux as mentioned in literature [37]. When $Ti_3C_2T_x$ is added into the matrix, the permeability of the composite membrane to solvent is decreased, but the flux for isopropanol is increased. This is due to the uniform dispersion of nanosheets in the active layer of membrane, which increases the transmembrane resistance and hinders the penetration of solvent molecules. It is found that the flux of isopropanol increases after the addition of $Ti_3C_2T_x$, where the –OH groups on $Ti_3C_2T_x$ nanosheets accelerate the migration of isopropanol molecules, acting as carrier sites for isopropanol transport. For composite membrane containing $Ti_3C_2T_x$-*M* nanofilm, this phenomenon is more significant, as shown in Fig. 2.15b. The flux of membranes with $Ti_3C_2T_x$-NH_2

Table 2.1 Contact angle, solvent uptake and area swelling of PEI-based membrances

Membrane	Contact angle (°)		Solvent uptake (%)		Area swelling (%)	
	Water	Diiodomethane	Isopropanol	*n*-heptane	Isopropanol	*n*-heptane
PAN/PEI	55.4	96.5	30.54	12.14	3.17	2.01
PAN/PEI-$Ti_3C_2T_x$	36.6	107.3	33.13	9.52	3.29	1.64
PAN/PEI-$Ti_3C_2T_x$-NH_2	28.2	118.9	36.32	7.95	3.48	1.53
PAN/PEI-$Ti_3C_2T_x$-COOR	31.7	113.6	34.51	8.24	3.32	1.52
PAN/PEI-$Ti_3C_2T_x$-C_6H_6	41.5	103.4	32.12	9.94	2.94	1.69
PAN/PEI-$Ti_3C_2T_x$-$C_{12}H_{26}$	45.3	100.2	31.59	10.79	2.74	1.74

or $Ti_3C_2T_x$-COOR nanofilms to polar solvents is significantly increased, which is due to the increase of affinity for polar solvents. Specifically, the number of carrier sites ($–NH_2$ groups) for isopropanol molecules increases greatly on $Ti_3C_2T_x$-NH_2 nanosheets, and the flux of isopropanol increases by 20% compared with PAN/PEI-$Ti_3C_2T_x$. In contrast, since the $–NH_2$ group does not accelerate the transport of non-polar solvent molecules, the addition of nanosheets within the active nanofilms actually increases the molecular migration resistance, resulting in a significant decrease in the fluxes for n-heptane (11%) and toluene (9%). Similarly, introducing $Ti_3C_2T_x$-C_6H_6 and $Ti_3C_2T_x$-$C_{12}H_{26}$ nanosheets into nanofilms can promote the transport of non-polar solvents, while increasing the transport resistance of polar solvents. Therefore, these phenomena indicate that the mass transfer resistance of OSN can be reduced by changing the solvent affinity with the nanofilm. Thus, it is possible to achieve highly selective permeation of a particular solvent. Incorporation $Ti_3C_2T_x$-NH_2, $Ti_3C_2T_x$-COOR, $Ti_3C_2T_x$-C_6H_6 and $Ti_3C_2T_x$-$C_{12}H_{26}$ nanosheets has the most significant flux increase percentage to isopropanol, ethyl acetate, toluene, and n-heptane, respectively, due to the grafted groups on nanosheets fill in the mixed matrix of membranes. Similarly, due to the hydrophilic PEI matrix as the main membrane body, the membrane exhibits high transport performance for polar solvents, and its flux obeys the order of n-heptane < toluene < ethyl acetate < isopropanol [60].

The rejection ability of OSN membranes is usually reflected by the *MWCO*, which indicates the molecular weight of the solute when its rejection reaches 90%. In this study, membrane rejection is tested using PEG (*Mw*: 200, 400, 600, 800 and 1000 Da) as solute under 10 bar and the results are shown in Fig. 2.15c. It shows the *MWCO* of PAN/PEI is more than 700 Da, which is close to the value reported in the literature [61]. In comparison, the incorporation of $Ti_3C_2T_x$ and $Ti_3C_2T_x$-*M* nanosheets improves the rejection ability of membranes with the *MWCO* of below 200 Da. This increase is caused by embedding nanosheets into the membrane, which blocks and expands the transport pathways for bulk PEG. It is interesting to note that membranes containing $Ti_3C_2T_x$-$C_{12}H_{26}$ and $Ti_3C_2T_x$-C_6H_6 nanosheets exhibit higher enhancement than membranes with $Ti_3C_2T_x$-NH_2 and $Ti_3C_2T_x$-COOR nanosheets. The hydrophilic $–NH_2$ or –COOR groups, compared to the $–C_6H_6$ or $–C_{12}H_{26}$, are suggested to aid in the transport of PEG through nanopores by forming weak bindings.

The actual running capacity and long-term stability of the membrane was evaluated by PAN/PEI-$TI_3C_2T_x$-NH_2. Dead-end filtration for 720 min was performed at 10 bar to measure the rejection capacity of PEG 1000 and the flux of pure isopropanol solvent. As shown in Fig. 2.15d, in the initial 480 min, the flux of isopropanol decreases by 29.3%, and the corresponding rejection of PEG 1000 increases from 97.1 to 99.3%. After this, the solvent flux and PEG rejection remain stable. This phenomenon is due to the compaction of membrane and the blockage of the nanopores by solute molecules [62]. Despite the compaction and clogging of OSN membranes, the prepared nanofilms possess the capability of enduring long-term operation process.

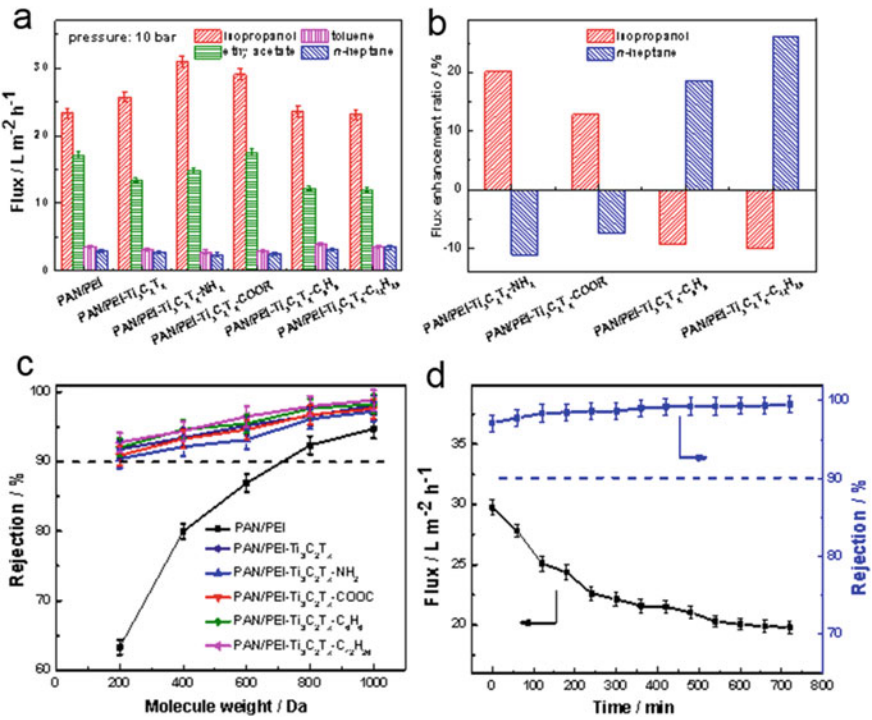

Fig. 2.15 **a** The fluxes of PEI-based membranes under 10 bar. **b** Flux enhancement ratio for isopropanol and n-heptane of PAN/PEI-$Ti_3C_2T_x$-*M* compared to PAN/PEI-$Ti_3C_2T_x$ under 10 bar. **c** The rejection of PEI-based membranes under 10 bar. **d** The long-term operation performances of PAN/PEI-$Ti_3C_2T_x$-NH_2 in isopropanol solution using PEG 1000 as solute under 10 bar. Copyright (2017), Elsevier [28]

In conclusion, four functional groups of $–NH_2$, –COOR, $–C_6H_6$, and $–C_{12}H_{26}$ are grafted onto $Ti_3C_2T_x$ by chemical grafting of organofunctional siloxane auxiliary functional groups to prepare $Ti_3C_2T_x$-*M* nanosheets, which are filled into PEI matrix to prepare novel nanofilm composite membranes. The grafted groups on the nanosheets significantly affect the hydrophilicity of PEI membrane, thus enhancing the selectivity of the nanofilm to solvents of different polarity. The grafted chemical groups can enhance the affinity of TFN nanofilm to the solvent through the interactions between the groups on PEI polymer chains and the polar groups of the solvent, thus reducing the mass transfer resistance and improving the flux. From this point of view, the grafted functional groups accelerate the transport of molecules across the thin nanofilm, and enhance the transport capacity of the corresponding polar molecules. Specifically, the membranes combining $Ti_3C_2T_x$-NH_2, $Ti_3C_2T_x$-COOR, $Ti_3C_2T_x$-C_6H_6 and $Ti_3C_2T_x$-$C_{12}H_{26}$ nanosheets acquire a significant increase in the flux of isopropanol, ethyl acetate, toluene and n-heptane, respectively. As expected, the participation of $Ti_3C_2T_x$-*M* nanosheets also effectively supports OSN

membrane rejection by increasing cellular transport pathways. In this way, $Ti_3C_2T_x$-*M* nanosheets are considered as novel nanoparticles to entered into OSN. We hope that this work can provide a clear and effective way of directing TFN membrane systems for multifunctional applications, e.g., OSN, pervaporation, and even gas separation.

2.4 Composite Membrane with Quantum Dot-Incorporated Active Layer

According to the method reported in literature, CDs were prepared by one-step pyrolysis under microwave [63]. Due to the difference of the reaction temperature and the composition of reaction solvents, CDs exhibit different carbonation degrees. Typically, the mixed solution of glycerol and ultra-purified water dissolved citric acid completely. DETA was added to the above mixture. The mixture was treated with ultrasonic at room temperature for 5 min and then heated in a 750 W microwave oven for another 5 min. As the reaction proceeded, the color of the solution changed from colorless to yellow and then to black. Subsequently, in order to purify samples, the products were washed with ethanol for three times to remove residual small molecules, and then dispersed in water. After centrifugation, CDs1 with the highest carbonation degree were obtained from the aqueous solution through freeze drying for 48 h. With the consumption of ultra-purified water increasing to 1.0 g, 1.5 g, and 2.0 g, meanwhile the corresponding consumption of glycerol decreased to 1.0 g, 0.5 g, and 0 g, respectively, CDs with lower carbonation degree were prepared by the same method. According to the decrease of carbonization degree, the synthesized CDs were successively named as CDs*M* ($M = 1$, 2, 3, and 4).

The PAN support was soaked in NaOH solution (1 M) at 50 °C for 1 h, which was cut into disk with a radius of 4.5 cm in advance. The hydrolyzed PAN support was rinsed with water to remove residual NaOH. Subsequently, it was stored in water for its subsequent use when the pH value of flushing water reached about 7.0.

A certain number of CDs were dispersed into water by whisking at room temperature for 1 h. PEI aqueous solution was prepared and whisked for 1 h. Then, the uniform PEI CDs solution was obtained by mixing both of the above solutions and stirring. Afterwards, the mixture was cast onto the surface of hydrolyzed PAN support and kept for 10 min. After removing the excess solution, the n-hexane solution with TMC was cast onto the PEI-CDs layer and maintained for 2 min for the cross-linking reaction. Afterwards, the membrane was firstly dried for 20 min in air and then in an oven at 60 °C for 2 h to evaporate the residual n-hexane and complete the cross-linking reaction. The composite membrane was called PAN/PEI-CDs*M*-10 by using 10 wt% loaded CDs*M* to ensure the dense thickness of the active layer. The other three membranes prepared by doping CDs2 were collectively referred to as PAN/PEI-CDs2-*X*, where *X* ($X = 2$, 5 and 30) represented the filler content.

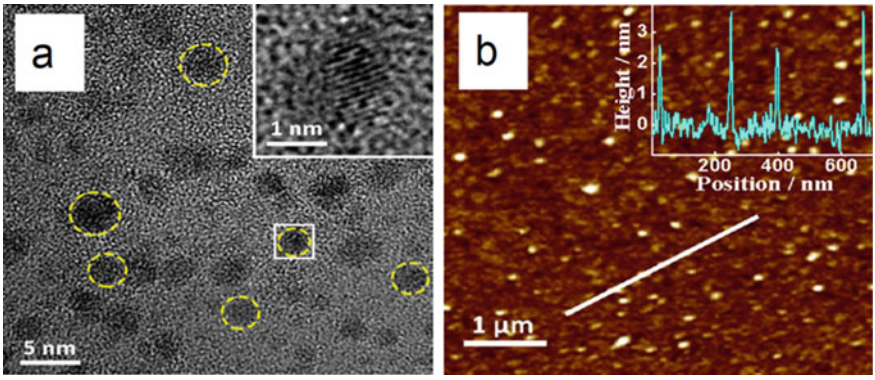

Fig. 2.16 **a** TEM image of CDs1 (inset: high-resolution TEM image) and **b** AFM image of CDs1 (inset: height profile along the white line on the image). Copyright (2018), Elsevier [27]

Taking CDs1 as an example, the morphology of CDs was measured by atomic force microscope (AFM). It is found that a single CDs1 has a typical 0D structure with a height of 2–4 nm (Fig. 2.16b). In addition, as shown in Fig. 2.16a, the clear morphology of CDs (CDs1, the highest carbonation degree) was detected by transmission electron microscopy (TEM). This situation is similar to that reported in literature [64]. Regardless of the degree of carbonization, CDs are uniformly dispersed without obvious aggregation, and the particle size is between 2 and 5 nm. Due to the decrease of hydrophilicity [65], high reaction temperature makes CDs1 form a high carbonate network structure (Fig. 2.16a).

As shown in Fig. 2.17a, the chemical composition of CDs was investigated by FTIR, respectively. The C content of CDs1 is higher, but the O content is lower. It is different that the O content of CDs1 is lower than that of CDs4. Furthermore, all the CDs show characteristic bands of O–H, N–H, and C=O at 1390, 1543, and 1720, and 1390 cm^{-1} (dashed lines), respectively, which is in consistent with the results in the literature [66, 67]. In addition, the thermal properties of CDs in Fig. 2.17b show that all CDs are thermally stable up to 200 °C, meeting the requirements of practical applications. In the first stage of water evaporation (25 ~ 250 °C), the weight loss rate of CDs4 is the highest (15.4%), because the strong hydrophilicity gives CDs4 high water absorption, while the weight loss rate of CDs1 is the lowest (7.5%). Then the oxygen-containing groups and some main chains are deoxidized thus significantly reduce the weight from 250 to 460 °C. At 800 °C, after the C–C bond is completely decomposed, the coke yield of all CDs is close to 29.6%.

A hybrid active layer was created by PEI matrix containing CDs as a composite membrane on hydrolyzed PAN support: PAN/PEI-CDs2-*X*. As shown in Fig. 2.18, the morphologies of above membranes are examined by SEM. The insert in Fig. 2.18a shows that the active layer on the PAN support is white, while the addition of 10 wt% CDs2 (black) changes the membrane color to light yellow (the insert in Fig. 2.18b). SEM in Fig. 2.18a shows clearer morphology, indicating that the surface of PAN/PEI (Fig. 2.18a) is smooth and homogeneous without obvious cavities or defects. In

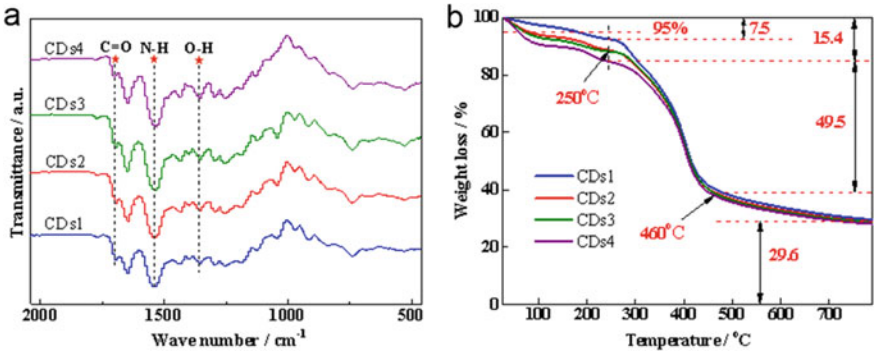

Fig. 2.17 **a** FTIR spectra and **b** TGA curves of the CDs. Copyright (2018), Elsevier [27]

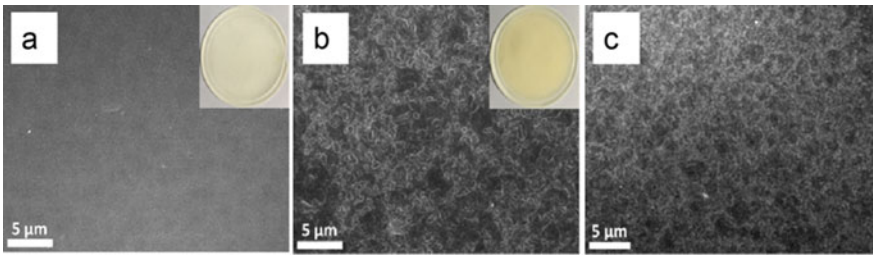

Fig. 2.18 Surface SEM images of **a** PAN/PEI, **b** PAN/PEI-CDs2-10, and **c** PAN/PEI-CDs2-30 (inset: photos of the corresponding object). Copyright (2018), Elsevier [27]

contrast, PAN/PEI-CDs2-10 (Fig. 2.18b) presents a relatively rough surface because of the presence of CDs in PEI bulk. Due to the good compatibility between sub-5 nm CDs and PEI chains, the PAN/PEI-CDs2-30 (Fig. 2.18c) forms a intact active layer without obvious defects despite aggregation when the loading increased to 30 wt%.

The affinity of membrane to solvent is crucial for membrane permeation and selectivity by determining membrane dissolution ability. The membrane contact angle was measured, and the results were shown in Fig. 2.19. The hydrophilicity of PEI reduces the contact angle of PAN/PEI to 56.3°, which is basically in consistent with the results reported in the literature [32]. On the other hand, the hydrophilicity of the membrane is further improved by the addition of CDs, and the contact angle reduces to less than 47.6°. The lower contact angle and the rougher membrane surface are conducive to the diffusion of droplets on membrane surface. As shown in Fig. 2.19a, the contact angle of the composite membranes varies with the type of CDs and follows the sequence of PAN/PEI-CDs1-10 (47.6°) > PAN/PEI-CDs2-10 (35.5°) > PAN/PEI-CDs3-10 (34.1°) > PAN/PEI-CDs4-10 (29.3°). The angle difference between membranes is huger than that of corresponding CDs, which may be a result of the increase of membranes roughness. It can be seen from Fig. 2.19b that the effect of CDs on the

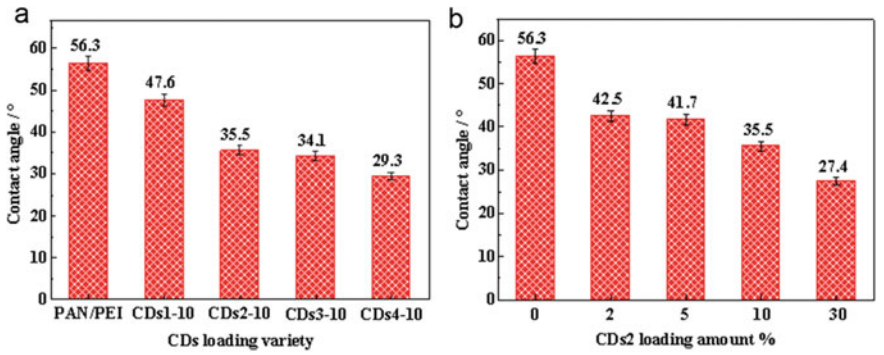

Fig. 2.19 Water contact angles of **a** PAN/PEI-CDs*M*-10 and **b** PAN/PEI-CDs2-*X*. Copyright (2018), Elsevier [27]

hydrophilicity of the membrane become stronger when the load of CDs2 increases from 2 to 30 wt%, and is testified by the further reduction of contact angle.

The OSN performance of membranes was evaluated by solvent flux, solute rejection, and operation stability according to the methods described in the literature [33]. The membrane performances were monitored at trans-membrane pressures of 4 and 10 bar using the above five solvents as indicators. Generally, increasing the trans-membrane pressure is an effective manner to improve the membrane transfer performance, which elevating transfer impetus. As shown in Fig. 2.20, the fluxes of n-heptane, toluene, acetone, ethyl acetate, and isopropanol for PAN/PEI are changed to 6.6, 8.8, 14.7, 19.5 and 27.6 L m^{-2} h^{-1} from 4.2, 5.9, 8.0, 16.1 and 19.2 L m^{-2} h^{-1}, respectively, when the pressure increases from 4 to 10 bar [45]. Although there are slight differences after CDs incorporation, the flux order of all composite membranes for all five solvents is identical. Because of the hydrophilic nature of PEI matrix, the flux of isopropanol, ethyl acetate and acetone is much higher. In addition, the order of the transfer rate (i.e., isopropanol > ethyl acetate > acetone > toluene > n-heptane) is similar to that of the solubility parameter (corresponding to polarity), rather than the solvent viscosity shown in Table 2.2. The solubility parameters of acetone and ethyl acetate are obviously similar. Adjoining with hydrogen bonding site, the size of $–CH_2CH_3$ of ethyl acetate is much larger than that of $–CH_3$ of acetone. Thus, there is no self-hydrogen bond cluster of the solvent, resulting in stronger swelling, this may explain the difference in permeability between the two solvents. These observations suggest that the solution-diffusion model probably is the main mechanism for solvent transport, which is in consistent with the observations of other PEI-based membranes [14, 68]. It is found that the CDs, which are filled in membranes, with different hydrophilic/hydrophobic properties can control the solvent permeation, especially for the non-polar and strong polar solvents. As clearly shown in Fig. 2.20a–c, the addition of CDs4 significantly increases the migration of isopropanol and ethyl acetate, but inhibits the migration of toluene and n-heptane. 10 wt% CDs4 increases isopropanol flux from 54.3% to 42.6 L m^{-2} h^{-1}, while n-heptane flux decreases from 29.8% to 4.6 L m^{-2} h^{-1}. These results also show that CDs4 can easily increase the

flux of polar solvents for OSN membranes. It is worth noting that CDs1 has the opposite effect on solvent migration, and PAN/PEI-CDs1-10 shows an increase in the permeability of non-polar solvents, while decrease in the permeability of polar solvents. As shown in Fig. 2.20c, when the weight percentage of CDs1 is 10%, the flux of n-heptane increases to 8.6 L m^{-2} h^{-1} with improvement of 31.2%, while the flux of isopropanol decrease by 4.6%, indicating that the non-polar solvent is easy to penetrate. Considering the significant changes in membrane swelling and solvent absorption, these results confirm that CDs effectively accelerate the transport of solvent molecules by promoting the dissolution of solvent molecules and providing transfer sites of functional groups. For instance, the –OH, $–NH_2$ and $–CO_2H$ groups in CDs4 help membrane preferentially adsorb polar molecules through hydrogen bond interactions, and then assist them continuous migration as jumping sites [69]. Hence, due to the decrease of functional group loading, the mobility of polar solvent on CDs within the membrane decreased. For example, for composite membranes containing CDs4, CDs3 and CDs2, the improvement degrees of isopropanol flux are 54.3%, 40.2%, and 37.4%, respectively.

In addition, in order to study the selectivity of different solvents to CDs, mixed solution was used to measure the flux and selectivity of representative membranes.

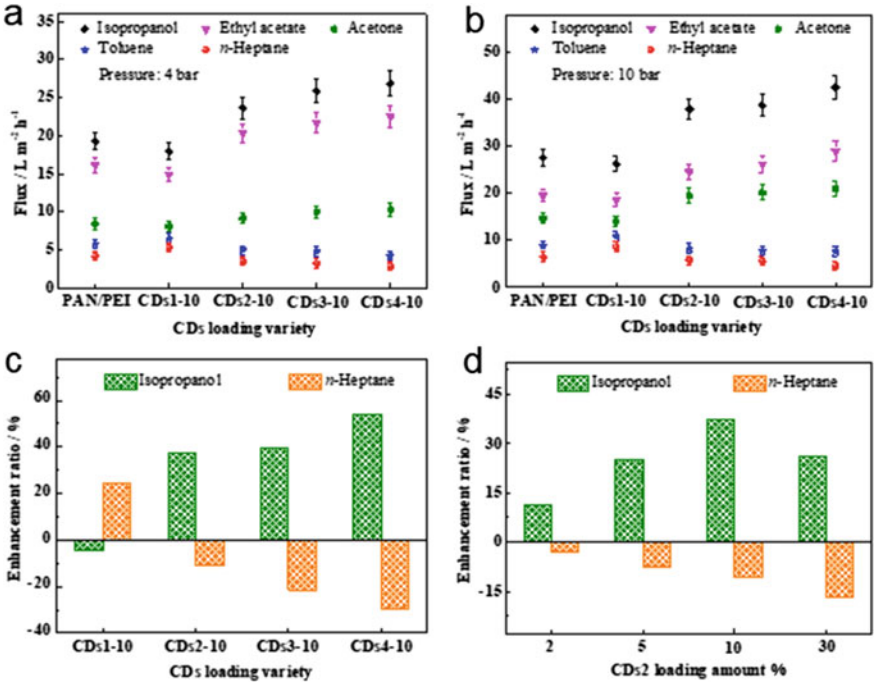

Fig. 2.20 The solvent fluxes of membranes under **a** 4 bar and **b** 10 bar at room temperature. **c** and **d** Flux enhancement ratios of isopropanol and n-heptane under 10 bar. Copyright (2018), Elsevier [27]

Table 2.2 The solubility parameter and viscosity of organic solvents

Solvent	Isopropanol	Ethyl acetate	Acetone	Toluene	*n*-Heptane
solubility parameter ($Cal^{1/2}/cm^{-3/2}$)	11.5	9.2	9.9	8.9	7.4
Viscosity (mPa. S)	2.37	0.46	0.33	0.59	0.41

Copyright (2018), Elsevier [27]

The mixed solution of isopropanol and n-heptane, with the greatest polarity difference and good mutual solubility was selected. As shown in Table 2.3, isopropanol and n-heptane for PAN/PEI at 10 bar gain the fluxes of 27.8 and 4.8 L m^{-2} h^{-1}, respectively, which means that the selectivity between isopropanol and n-heptane is 5.8. This finding stems from the hydrophilicity of PEI matrix. In contrast, the addition of 10% CDs4 not only increases the flux of isopropanol to 44.1 L m^{-2} h^{-1}, but also improves the selectivity to 9.5. This directly indicates the selective transfer ability of CDs4 to polar solvents due to its abundant hydrophilic groups. On the contrary, CDs1 displays the opposite function, and the selectivity is reduced to 3.2.

Rejection performance is another key parameter of OSN membrane. In order to obtain sufficient operation efficiency, a high rejection is required. Among them, PEG (*Mw*: 200, 400, 600, 800, 1000, 1500, and 2000) was used as the solute and isopropanol was used as the solvent for the rejection measurement. Figure 2.21a, b show the results as mentioned earlier, PEI-based membranes create small-sized networks after complete cross-linking, they achieve acceptable rejection capacity. The results show that the rejection of all membranes increases with the increasing of molecular weight of PEG. Furthermore, the molecular weight threshold is less than 800. Compared with PAN/PEI composite membrane, the solute rejection of composite membrane is basically the same. This finding proves that the solute transfer is physically prevented, which is completely different from the membranes with rejection significantly increased by hybridization of large-sized fillers. In contrast, the rejection of the composite membrane reduces slightly. These results show that CDs less than 5 nm can slightly change the overall structure of the PEI matrix, as CDs can promote the migration of oxygen-containing PEG, leading to the flow of PEG. Therefore, the rejection value of PAN/PEI-CDs4-10 is the lowest because the surface of CDs4 contains abundant hydrophilic groups. While for CDs with low group loading, the rejection of the composite membranes almost remain unchanged despite the increase of CDs2 content, especially when the molecular weight of PEG

Table 2.3 The flux and selectivity of mixed solvent

Membrane	PAN/PEI	PAN/PEI-CDs1-10	PAN/PEI-CDs4-10
Isopropanol flux/L m^{-2} h^{-1}	27.8	26.7	44.1
n-Heptane flux/L m^{-2} h^{-1}	4.8	8.3	4.6
Selectivity	5.8	3.2	9.5

Copyright (2018), Elsevier [27]

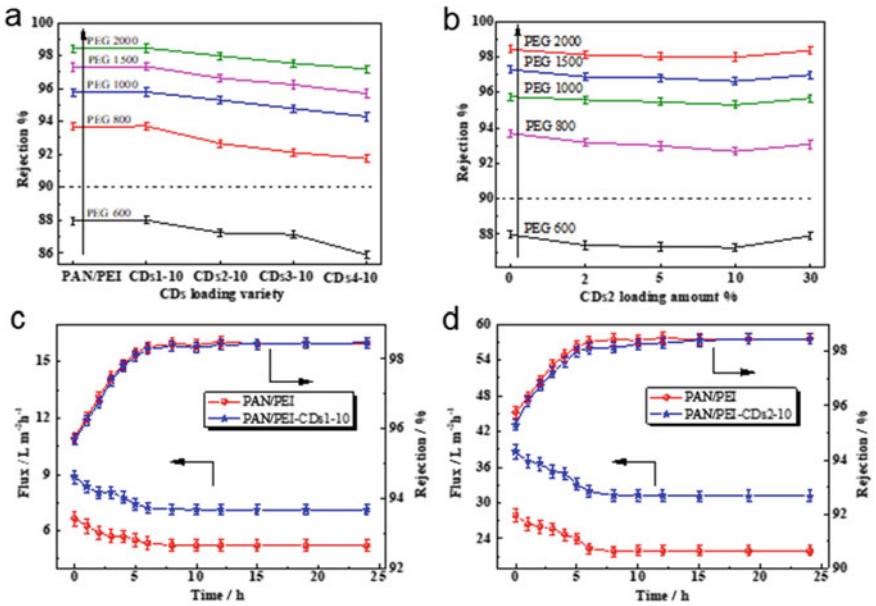

Fig. 2.21 Rejection of **a** PAN/PEI-CDs*M*-10 and **b** PAN/PEI-CDs2-*X*. The long-term operation performance of **c** PAN/PEI-CDs1-10 in n-heptane solution and **d** PAN/PEI-CDs2-10 in isopropanol solution with PEG 1000 under 10 bar. Copyright (2018), Elsevier [27]

is larger than 1000 (Fig. 2.21b). At the load of 30 wt%, the aggregation of CDs inhibites the transport of PEG, which improves the rejection of the membranes.

The operational stability assessment selected PAN/PEI and PAN/PEI-CDs2-10 (using isopropanol as solvent), PAN/PEI and PAN/PEI-CDs1-10 (using n-heptane as solvent) for measuring. The rejection (using PEG 1000 as solute) and flux were evaluated in a cross-flow device at 10 bar for 24 h. As shown in Fig. 2.21c, because of membrane compaction and pore plugging [32], the n-heptane flux of PAN/PEI decreases by 22.4% from 6.7 L m^{-2} h^{-1} to 5.2 L m^{-2} h^{-1} in the first 6 h. In contrast, the flux of PAN/PEI-CDs1-10 decreases by 20.2%, indicating that the addition of CDs1 mitigates the reduction of flux. Similarly, as shown in Fig. 2.21d, the addition of CDs2 can mitigate the decrease of isopropanol flux (19.2% vs. 21.3% for PAN/PEI). On the other side, membrane compaction and pore plugging slightly improve the retention rate of PEG 1000, reaching more than 98%. Although the flux decreases, the prepared membranes show potential operational stability in OSN applications.

In this study, novel OSN composite membranes are prepared on the basis of CDs polymer active layer. Sub-5 nm 0D carbon dots are added into the PEI matrix to prepare composite membrane, which is easy to synthesize using tail functional groups. The results display that the PEI matrix retains its inherent physical and chemical properties after hybridization with high loading CDs, and is not significantly disturbed by these fillers. The composite membranes have excellent solute rejection

(molecular weight threshold lower than 800), solvent resistance, and sufficient operation stability resulting from the cross-linked networks of PEI. Evenly distributed CDs are highly efficient and selective nano-accelerator for solvent transfer. More specifically, low carbonate cadmium can promote the migration of polar solvents in the membrane by providing binding sites. Specifically, the transfer of polar solvents through the membranes can be promoted by providing bonding sites of hydrophilic groups (–OH, $–CO_2H$, $–NH_2$) in low carbonated CDs. Taking the membrane embedded with CDs4 as an example, it reveals 54.3% increase in solvent flux and 40.5% increase in solvent absorption. In addition, these CDs can slightly inhibit the absorption and permeation of non-polar solvents, thus improving the permeability of OSN membrane for polar solvents. On the contrary, the hydrophobic domains on high carbonate CDs prevent the transport of polar solvent and accelerate the non-polar solvent at the same time. The distinctive hybridization strategy described in this paper herein may pave the way for well-designed nanocomposite or hybrid membranes so as to combine the advantages of fillers and polymers maximally.

2.5 Composite Membrane with Quantum Dot-Assembled Active Layer

One-step microwave-assisted pyrolysis was used to synthesize quantum dots. Specifically, PQDs were prepared by the following steps: CA and DETA were dispersed in water and treated with ultrasonic at ~ 22 °C for 5 min. Then, the mixture was heated in a microwave-oven at 750 W for 5 min. And, the products were dispersed in water and freeze-drying for 48 h, then residual small molecules were removed by washing with ethanol for several times. For GQDs with a higher degree of carbonation, an amount of glycerol was added to the solvent of water to provide higher reaction temperature of above 100 °C. When preparing GQD1 and GQD3, the mass of glycerol added into water is 1.0 g and 1.5 g, respectively.

As shown in Fig. 2.22, a free-standing QD/TMC membrane was prepared by IP at the free oil–water interface. For instance, a certain amount of GQD1 was dissolved into water to obtain a 2.0 wt% homogeneous solution. Meanwhile, a certain amount of TMC was dissolved in n-hexane to prepare organic solutions with concentrations of 0.25, 0.5, 0.75, 1.0, 1.5, and 2.0 wt%. Initially, the aqueous solution was poured into a petri dish to obtain a stable solution surface, and subsequently, the organic solution was gently added onto the upper surface for the polymerization reaction. After a period of time, and the two-phase solutions was carefully drained off when reaction formed a transparent and smooth film at the interface. The resultant film was washed with water for several times, and then transferred to anodic aluminum oxide (AAO) substrate or silicon wafer for further characterization.

The QD/TMC composite membranes supported by PAN were prepared as follows: firstly, PAN support was hydrolyzed with NaOH (1 M) solution for 1 h at 50 °C, and then the hydrolyzed PAN was soaked the water for 10 min. After the excess

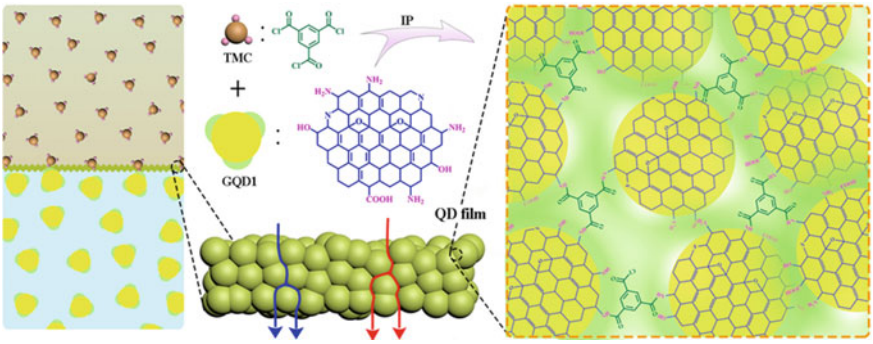

Fig. 2.22 Schematic diagram of QD/TMC composite membrane. Copyright (2019), American Chemical Society [31]

aqueous solution was drained, the TMC solution was gently covered on the QDs loaded PAN membranes for a certain time. Then the composite membrane was dried in the air for 10 min, and then in an oven at 60 °C for 10 min after the excess TMC solution was drained off. Lastly, the membrane was stored in water for the following characterization and performance measurement. The obtained membranes were named as QD/TMC, in which QD included GQD3, GQD1 and PQD. In addition, a typical polymer membrane, called (DETA-CA)/TMC, was directly prepared with DETA and CA as aqueous monomers, respectively.

As depicted in Fig. 2.23a, the TEM image illustrates that GQD has a typical 0D structure with size of 2 ~ 4 nm and height of (2.5 ± 0.3) nm [70]. The clear lattice structure of GQD1 is gradually emerged from the edge to the center with the increase of carbonization degree, the result is depicted in high-resolution transmission electron microscope (TEM) images [71]. This directly corroborates the amphipathic property of GQD1. In contrast, the higher the carbonization degree of GQD3 is, the clearer the center of lattice edge presented (Fig. 2.23a), while the carbonization-free PQD cannot be detected by TEM because of its aggregation and disordered aggregation. As shown in (Fig. 2.23b), this structure can be demonstrated by XRD, which shows a crystal band of about 21°. The intensity of band increases with the increase of carbonization degree, and the order is GQD3 > GQD1 > PQD. Here, the carbonation degree of GQD3 remains unchanged to ensure the presence of a certain amount of active groups such as –OH and –NH/–NH_2 (Fig. 2.23c), ready for following IP. Consequently, there are the characteristic bands of –OH and –NH/–NH_2 groups in the FTIR spectra of GQD3.

As shown in Fig. 2.24, FTIR was used to detect the chemical composition of the membrane. Because the FTIR penetration depth is about 450–550 nm [36], the spectra of all the membranes appeare a bond of 2244 cm^{-1}, which is the typical stretching vibration of –C≡N for PAN support. In addition, three new bonds corresponding to the stretching vibration of –C–N, –N–H, and –C=O are observed for the composite membranes at 1365, 1557, and 1647 cm^{-1}, respectively. These findings collectively confirm the formation of polyamide membranes. For QD/TMC

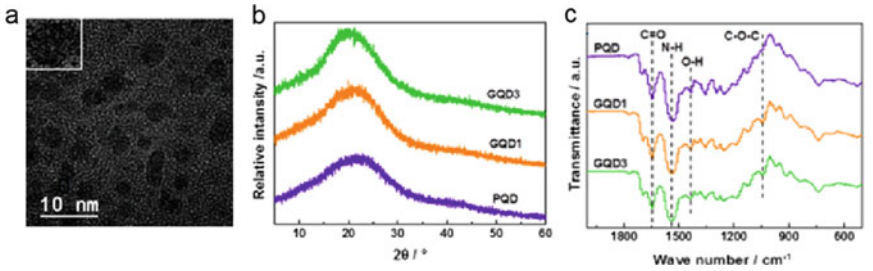

Fig. 2.23 **a** TEM image of GQD3 (inset: HRTEM image), reproduced with permission [72]. **b** XRD patterns and **c** FTIR spectra of QDs. Copyright (2019), American Chemical Society [31]

composite membrane, the group band intensity decreases with the increase of carbonization degree of QDs due to the decrease of group loading. These changes give the membranes selective affinity for non-polar and polar molecules. As shown in Fig. 2.24b, PQD/TMC and (DETA-CA)/TMC composite membranes with rich hydrophilic groups have strong affinity for polar molecules (water contact angle < 32°), but low affinity for non-polar molecules (contact angle of diiodomethane is about 100°). In contrast, hydrophobic composite membrane GQD3/TMC depicts strong affinity for non-polar molecules. It is worth noting that the GQD1/TMC composite membrane has good wettability for polar and non-polar molecules, and the contact angle of water and diiodomethane is less than 43°. This further confirms the amphiphilic structure of GQD1, including hydrophobic region and hydrophilic region. It is worth noting that due to the consumption of hydrophilic groups during interfacial polymerization, the water contact angle of all membranes is slightly higher than that of the corresponding quantum dots. This further confirms the amphipathic structure of GQD1, which contains both hydrophilic and hydrophobic domains.

Positron annihilation spectroscopy (PAS) and N_2 adsorption/desorption isotherms were used to detect the porous structure of membranes. The free volume properties (i.e. pore size) of thin membranes can be probed by PAS at the atomic scale. The depth distribution of defects can be characterized simultaneously by injecting positrons into intermediate energy samples. The characteristic of the spectrum is the *S* parameter. If the positron is captured in the open volume defect, the *S* parameter will be higher. The free volume characteristics of the membranes are shown in Fig. 2.24c. The membrane can be divided into three main areas: the upper membrane (Area I), the interface area (Area II) and the PAN support (Area III). For these composite membranes, the *S* parameter is usually increases from I to III. In area I, *S* parameter increases in the order of GQD3/TMC > GQD1/TMC > PQD/TMC > (DETA-CA)/TMC. This strongly proves that the free volume cavities in the membranes are gradually changing from dense structure to porous structure. Different from (DETA-CA)/TMC membrane, of which the *S* parameter increases, that of QD-based membranes exhibit increased volatility due to the porous structure of assembled nanoparticles. With the approach of the interface (area II), the *S* parameters of the membranes decrease significantly, indicating the good compatibility between the

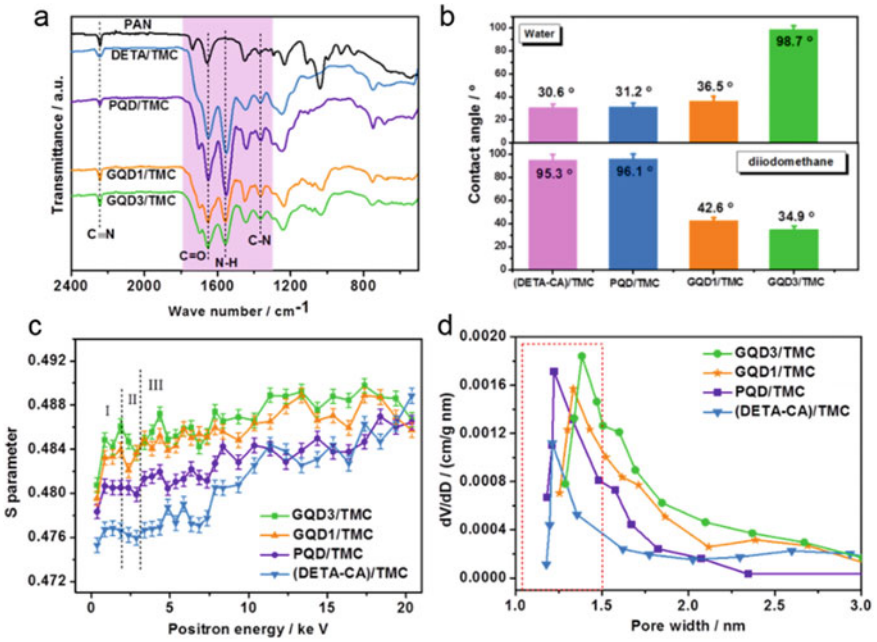

Fig. 2.24 **a** FTIR spectra, **b** water and diiodomethane contact angles, **c** PAS curves, and **d** pore-size distribution of membranes. Copyright (2019), American Chemical Society [31]

membranes and the support, which makes the membranes denser. In area III, the high *S* parameter stems from a typical finger-like hole in the support. The calculated aperture values provide further evidence (Fig. 2.24d). It can be expected that the dense cross-linked membrane, named (DETA-CA)/TMC composite membrane has a small pore size of 1.1 nm. The pore size of PQD/TMC composite membrane is 1.2 nm. It is worth noting that GQD3/TMC and GQD1/TMC composite membranes have a large pore size of about 1.4 nm, indicating that nanopores are formed between nanoparticles. Note that the pore sizes are less than 1.5 nm, belonging to the nanofiltration range [72].

In order to better understand the formation process of these nanoparticles, ethylamine is added into the reaction system, which artificially interrupts the interfacial reaction between GQD1 and TMC. Then the polymerization process stops at the required time as TMC molecules are rapidly consumed [73]. The SEM image (Fig. 2.25a) clearly shows that TMC monomers cross-link a certain amount of GQD1 and form a small irregular polyamide fragment at the beginning 2 s. At the time of 5 s, fragments gather together to form a larger one. Then, within 10 s, the nanoparticles are orderly assembled into the initial complete film. As high-resolution SEM image (Fig. 2.25b) depicts that the nanoparticles are uniform (size of 8.5 nm) without becoming larger with time. Since the single GQD1 is 2 ~ 4 nm, one nanoparticle contains 4–5 GQD1. Then, a large number of nanoparticles are assembled into a

complete nanofilm. This special growth manner may originate from its hydrophilic chemical groups on surface, that is, the unique chemical and physical properties of GQDs. After TMC cross-linking, the hydrophilic regions of GQDs tend to combine under the interaction and surface tension, forming multi quantum dots aggregated nanoparticles. The film-forming mechanism has not been verified by experiments, because the interfacial polymerization is rapid in kinetics at the initial stage of reaction. Combining to the theoretical proof in reference and observation in this study [12, 64–77], it is considered that the nanoparticle assembly structure of the quantum dot based film is the growth of polyamide assembled by nanoparticles at the oil–water interface. Figure 2.25c shows that GQD1 near the water surface rapidly moves to the oil phase and reacts with TMC to form an initial polyamide oligomer. These oligomers accumulate at the bottom of the oil phase because of their large size. Then, the newly broadcast GQD1 constantly react with the TMC. Because of the blocking of the large-sized oligomers, the newly formed nanoparticles accumulate next to the pre-polymerization and increase with the extension of polymerization time. It forms a continuous membrane at the interface with other similar oligomers, but this prevents the further penetration of GQD1, resulting in self-terminated polymerization.

In this research, the permeability of the composite membranes is tested with eight common organic solvents, such as methanol, 1-butanol, 2-propanol, ethanol,

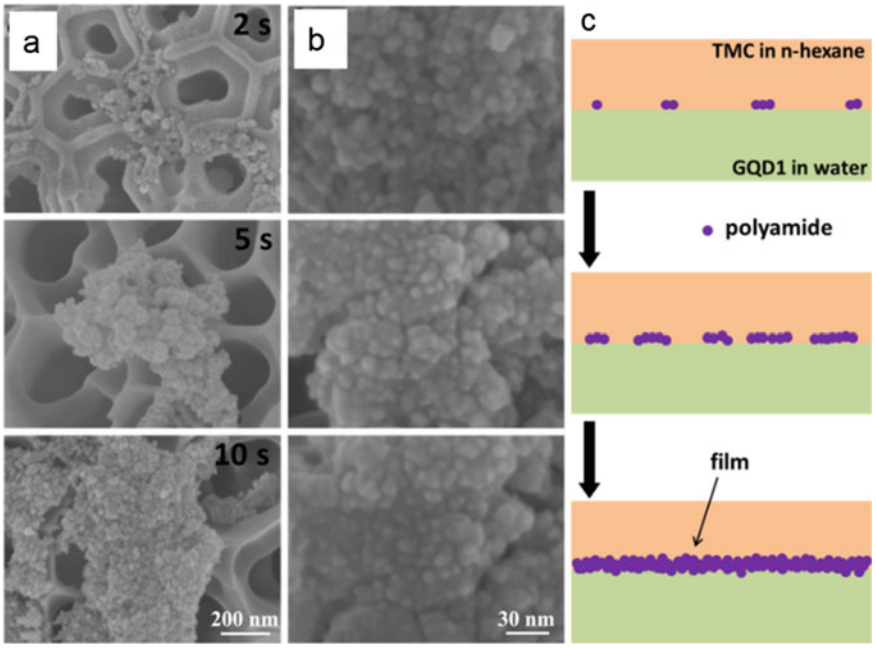

Fig. 2.25 **a** Low and **b** corresponding high-resolution SEM images of GQD1/TMC nanoparticles formed at different time. **c** Schematic of the polymerization procedure of GQD1/TMC film. Copyright (2019), American Chemical Society [31]

n-hexane, acetone, toluene, and acetonitrile. It can be expected that the permeability of the tightly cross-linked (DETA-CA)/TMC composite membrane to polar solvents is relatively low (less than 10 L m^{-2} h^{-1} bar^{-1}), shown in Fig. 2.26a. And low affinity makes it difficult for non-polar solvents to migrate, which is a common phenomenon for traditional membranes composed of hydrophilic polymer matrix [12, 29, 78, 79]. In contrast, QD/TMC composite membranes have higher molecular transport capacity. Take GQD1/TMC composite membrane as an example, the acetonitrile permeance is 46.9 L m^{-2} h^{-1} bar^{-1}, which is about three times of that of (DETA-CA)/TMC composite membrane. In addition to polar solvents, non-polar solvents also have ultrafast permeance. For instance, the permeance of n-hexane increases nearly 100 times to 50.8 L m^{-2} h^{-1} bar^{-1}. Polar and non-polar solvents have high permeability simultaneously, which is due to the formation of amphiphilic regions in GQD1/TMC composite membrane. As mentioned above, GQD1 has good affinity for polar and non-polar solvents simulationaly, because of its hydrophilic and hydrophobic regions. This helps the molecules dissolve into the membrane matrix. The nanopores between nanoparticles can obviously promote the molecular diffusion after they enter into the nanofilm. It is a common and effective method to promote molecular transport by constructing nanopores in membranes. Hence, the migration ability of membrane is greatly enhanced [80, 81]. These advantages gives GQD1/TMC composite membranes excellent properties, which are superior to most polymer nanofilms, and even reach the level of GO [82], MoS_2 [83], and other lamellar membranes. However, neither hydrophobic GQD3/TMC composite membrane nor hydrophilic PQD/TMC composite membrane can form amphiphilic channels. For PQD/TMC composite membranes, the carbonization-free PQD with rich hydrophilic groups bring the corresponding membranes good affinity for polar solvents and is not conducive to the dissolution of non-polar solvents. GQD3 is relatively hydrophobic because the strong carbonization process consumes most of the hydrophilic groups. Hence, GQD3/TMC membrane exhibits relative hydrophobicity, and shows good affinity for non-polar solvents compared with polar solvents. This can be proved by the difference in contact angle of GQD3/TMC membrane to diiodomethane (35°) and PQD/TMC membrane to water (31°). It is worth noting in Fig. 2.26a that although the permeability of PQD/TMC composite membrane is the lowest, its permeability is much higher than that of (DETA-CA)/TMC composite membrane due to its porous structure.

In order to study the influence of pore size on membrane permeability, the properties of composite membranes are compared. The results show that the solvent permeability follows the order of GQD3/TMC > GQD1/TMC > PQD/TMC, which is in consistent with the pore size order measured by PAS and BET. This circumstance shows that the assembled nanopores have a great effect on the molecular transfer of the composite membrane. For GQD3/TMC and GQD1/TMC composite membranes with large nanopores, the permeability of acetone is 57.5 and 45.4 L m^{-2} h^{-1} bar^{-1}, respectively. The PQD/TMC composite membrane with the smallest pore size (about 1.2 nm) has the lowest solvent permeance (acetone: 23.4 L m^{-2} h^{-1} bar^{-1}). In addition, these membranes also have good rejection capacity. Compared with other polymer

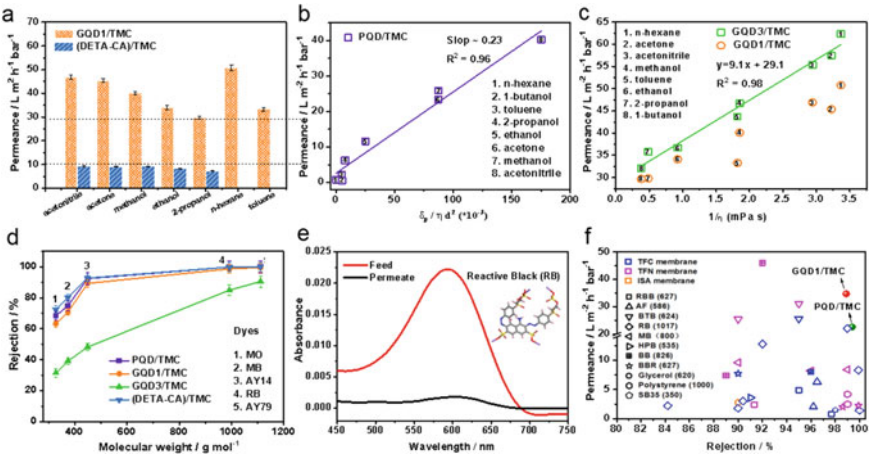

Fig. 2.26 **a** Solvent permeance and **d** dye rejection of composite membranes. Relationship between solvent permeance and solvent properties for **b** PQD/TMC and **c** GQD1/TMC and GQD3/TMC membranes. **e** UV/Vis absorption spectra of RB in ethanol before and after filtration by GQD1/TMC composite membrane. **f** Performance comparison between membranes in this work and reported ones in literatures. Copyright (2019), American Chemical Society [31]

OSN membranes [84–86], these membranes assembled by nanoparticle have good nanofiltration performance (Fig. 2.26f).

In addition, the solvent permeance of QD-based membranes can be easily adjusted by the thickness of the membrane. It can be seen from Fig. 2.27a that when the membrane thickness decreases from 86.3 to 33.4 nm, the acetone permeance of GQD1/TMC membrane gradually increases to 28.8 L m^{-2} h^{-1} bar^{-1}. In addition, it can be seen from Fig. 2.27a that the nanoparticle-assembled structure of the GQD1/TMC membrane is robust enough to withstand pressure up to 3.5 bar. The difference is that the (DETA-CA)/TMC membrane will not penetrate acetone until the pressure rises to 2.0 bar. With the increase of pressure, the increasing rate of permeance decreases gradually, indicating the densification of the membrane matrix. This is also demonstrated by the operational stability results in Fig. 2.27c. The acetone permeance of GQD1/TMC composite membrane remains almost unchanged within 24 h, while that of (DETA-CA)/TMC composite membrane decreases by 34.1%.

The separation ability of the membranes was tested by separating five industrial dyes from ethanol, the result was depicted in Fig. 2.26d. Compared with the reference value of (DETA-CA)/TMC composite membranes, it is found that GQD1/TMC composite membrane has considerable rejection capacity. As shown in Fig. 2.26e, the rejections of the high molecular weight dyes RB ($Mw = 991.8$) and AY 79 ($Mw = 1111.1$) are higher than 95%, while they are almost completely separated, which further proves the integrity of GQD1/TMC membrane. The rejection of low molecular weight dyes, such as MO ($Mw = 327.3$) and MB ($Mw = 373.9$) are 63% and 71%, respectively. The results show that the *MWCO* of GQD1/TMC composite membrane is about 460 Da, which is slightly higher than that of (DETA-CA)/TMC

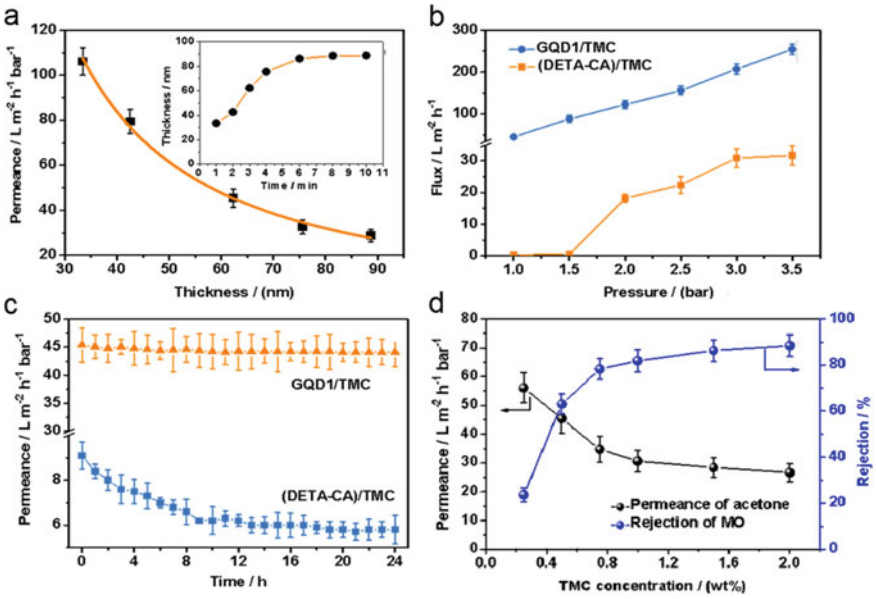

Fig. 2.27 **a** Acetone permeance as a function of film thickness for GQD1/TMC membrane, (insert is the thickness variation of GQD1/TMC film with polymerization time). **b** Acetone flux as a function of testing pressure. **c** Variation of acetone permeance with operation time. **d** Acetone permeance and MO rejection as a function of TMC concentration for GQD1/TMC composite membrane. Copyright (2019), American Chemical Society [31]

composite membrane (430 Da). The comparable rejection properties indicates that the membranes assembled by nanoparticles have no defects. The average pore size of GQD1/TMC composite membrane should be 1.5 ~ 2.0 nm, which depends on the molecular size of dye (2.0 nm for RB) and *MWCO*. Because of the swelling of the membrane in the solvent, this value is larger than the BET result (about 1.4 nm). Moreover, the rejection capacity of GQD1/TMC composite membrane can be adjusted by the concentration of TMC. As shown in Fig. 2.27d, when the TMC concentration increases from 0.25 to 2.0 wt%, the membrane can retain nearly 90% of MO. In contrast, PQD/TMC composite membrane also depicts good rejection, while *MWCO* reached 435 Da. However, the large pore size of GQD3/TMC composite membrane leads to poor dye rejection, as *MWCO* is about 1000 Da.

In order to investigate the molecular transfer mechanism of quantum dots-based membranes, the relationship between molecular physical parameters and permeability was established. There are some physical parameters regarded as the possible influence factors, such as viscosity (η, Pa s), molar diameter (d, m), and solubility parameter (δ, $Pa^{0.5}$). It can be seen from Fig. 2.26b, c that PQD/TMC composite membrane displays a clear relationship: $P = K_1\delta/\eta d^2$, where K_1 is the scale constant (m^3 $Pa^{-0.5}$). This equation is identical to the MPD membrane reported previously [59]. This confirms that molecular transport is usually described by solution-diffusion

theory in amorphous and dense polymer membranes. Molecules must be dissolved into the membrane surface firstly, and subsequently diffuse through the membrane, which mainly depends on molar diameter d and solubility parameter δ [87]. The difference is that the relation for GQD3/TMC membrane is $P = K_2/\eta$, where K_2 is also proportionality constant (L m^{-2}). The equation is the same as that of inorganic porous membranes with permanent nanopores and hydrophobic feature [82, 88]. Molecular transport is mainly controlled by the pore-flow model (i.e. Poiseuille's law), hence, the viscosity of the solvent is an important parameter affecting molecular transfer. The disordered accumulation of molecules and the weak interaction between membrane and solvent make the effect of δ and d on permeance negligibly. It is worth noting that the permeability of GQD1/TMC membrane is roughly determined by viscosity, and the other two factors δ and d also play important roles, as exhibited in the result in Fig. 2.26c. This is reasonable for GQD1/TMC membrane, because nanopore is the main transfer route; hence, the pore-flow mode controls the transfer behavior (η). At the same time, the membrane shows strong amphipathic for both polar and nonpolar molecules, leading to intermolecular interaction (δ), and then inducing molecular accumulation (d) [26, 89]. Therefore, the molecular permeance of GQD1/TMC membrane is not only controlled by the pore-flow model, but also affected by the solution-diffusion model. This process lies in between PQD/TMC and GQD3/TMC composite membranes.

Besides, QD/TMC composite membrane not only has excellent nanofiltration performance, but also shows reasonable operational stability in harsh environments. It can be seen from Fig. 2.28a that the change of n-hexane permeance and RB rejection is less than 4% after immersion in NaOH or HCl solution, even after ultrasonic treatment for 12 h. The results show that QD/TMC composite membrane has good structural stability. As shown in Fig. 2.28b, when GQD1/TMC membrane is continuously operated in solvent for 10 days, the cross-linking structure is quite stable, and the solvent permeance decreases by less than 23%. This discovery highlights the advantages of nano quantum dots-based membranes with high stability and performance, and has a practical industrial application prospect.

In conclusion, a novel nanoparticle-assembled TFC membrane is prepared by IP method using quantum dots as structural units. The defect free nanofilms are assembled by QDs cross-linked into nanoparticles, which have hydrophobic and hydrophilic regions. GQD1/TMC composite membrane has good affinity for non-polar and polar molecules due to its amphiphilic nature, which is conducive to their dissolution in the membrane. Moreover, it has excellent permeability to non-polar and polar solvents, because the nanopores between nanoparticles allow rapid molecular diffusion, which can greatly improve the transmission capacity of the membranes. Specifically, the permeability of acetonitrile and n-hexane is more than 3 and 100 times higher than that of traditional compact composite membranes, reaching 46.9 and 50.8 L m^{-2} h^{-1} bar^{-1}, respectively. In addition, the QD-based membranes display good rejection and favorable operational stability. What's more important, we explore the molecular transfer mechanism of quantum dots matrix membranes and propose their model equations, which paves the way for the design of efficient membranes for transport and separation.

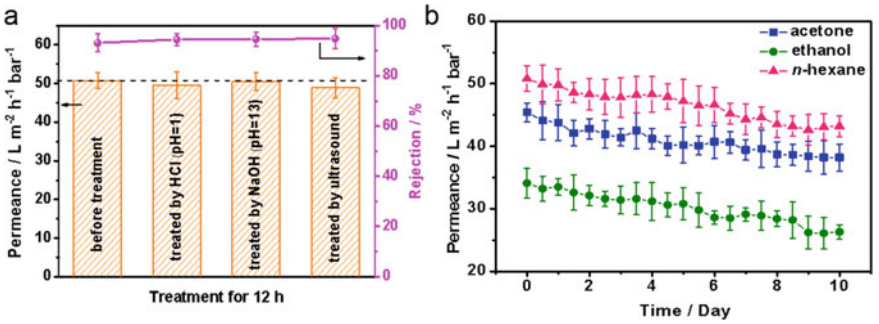

Fig. 2.28 **a** n-Hexane permeance and RB rejection of GQD1/TMC composite membrane treated by HCl, NaOH solution, and ultrasound for 12 h. **b** Solvent permeance with operation time for GQD1/TMC composite membrane. Copyright (2019), American Chemical Society [31]

2.6 Composite Membrane with Ultrathin Active Layer

First, PAN substrates were hydrolyzed with 1 M NaOH solution at 50 °C for 1 h, and then soaked and washed with deionized water for several times until the solution became neutral. It is then immersed in the freshly prepared dopamine solution at 25 °C for 15 min. It's worth noting that Tris buffer was used to adjust the pH value of above dopamine solution to 8.5, which was conducive to the self-polymerization of dopamine to produce a polydopamine (PDA) adsorption layer on the PAN surface [90–93]. And, the formed substrate was named as DPAN.

PEI aqueous solutions with concentrations of 1, 0.1, 0.01, 0.005, and 0.001% (w/v) were obtained by dissolving and diluting, respectively. Meanwhile, the cross-linking agent TMC was dissolved in n-hexane solvent as an oil phase with a weight concentration ratio of 1:1.25 to corresponding PEI monomer. Then, DPAN substrate was spread on the bottom of utensil with DPAN layer facing up, and enough PEI aqueous solution was injected to stand for 30 min to guarantee the full adsorption of amine monomer. The excess PEI solution was then discarded. Subsequently, the oil phase was slowly added to the utensil for polymerization for 60 s. Similarly, the excessive TMC solution was poured off, and the membrane surface was washed several times with n-hexane to remove residual unreacted monomers, followed by drying at 60 °C for 15 min (Fig. 2.29). The resulted TFC membranes were named as DPAN/PEI-*X*, where *X* represented the PEI solution concentration. Similarly, two other polyamide membranes were prepared with EDA and DETA as amine monomers and were named as DPAN/EDA-*X* and DPAN/DETA-*X*, respectively.

Here, the PAN substrate was hydrolyzed by NaOH solution and subsequently coated with a PDA layer to obtain a smoother surface with smaller pore size. The SEM image in Fig. 2.30a exhibits a uniform PDA layer with a roughness of only 24.7 nm. To directly measure the adsorption capacity for amine monomers, PAN and DPAN are immersed in dilute solutions of PEI, DETA and EDA with a concentration of 0.01% for 30 min, respectively. Next, the DPAN substrate adsorbs amine solution for

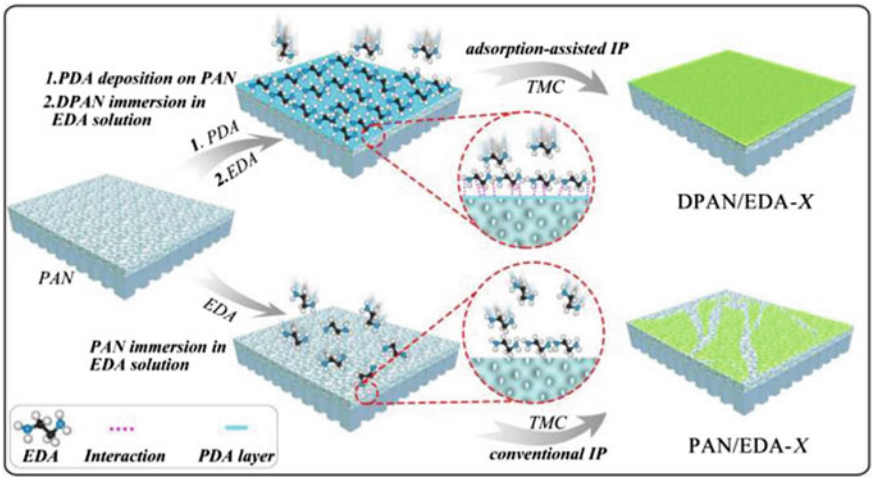

Fig. 2.29 Schematic illustration of membrane prepared by adsorption-assisted and conventional interfacial polymerization. Copyright (2018), American Chemical Society [29]

30 min, and then cross-linked by TMC to grow a polyamide layer. As demonstrated by the SEM images in Fig. 2.30b–d, the porous support is uniformly covered by an active layer with no pinholes or cracks detected. For DPAN/PEI-0.01, the outline of the substrate can still be seen due to the thin active layer. In addition, due to the outstanding film-forming capacity of interfacial polymerization technique, the obtained surface roughness of DPAN/PEI-0.01 is significantly decreased to 10.2 nm, which is an ideal morphology for nanofilms [94]. However, PAN/DETA-0.01 and PAN/EDA-0.01 present relatively rough surfaces with roughness of 17.5 and 58.2 nm, respectively, due to the larger kinetic energy of DETA and EDA molecules in solution and thus faster adsorption rate [95], which is prone to form disordered and dense packing. As demonstrated in Fig. 2.30c, d, bulk and granular surfaces are obtained for DPAN/DETA-0.01 and DPAN/EDA-0.01, respectively. This further confirms that defect-free ultrathin nanofilms (< 30 nm) can be obtained by adsorption-assisted IP, which is difficult to achieve for conventional IP.

The nanostructure of the active layer is then carefully tuned and characterized in detail. The TEM images of DPAN/PEI-0.01 in Fig. 2.31a visually reveal the ultrathin and even nanostructure of active layer with a thickness of about 25 nm, which is in consistent with the results of AFM (Fig. 2.31c, d). Distinct from the common TFC membranes prepared by traditional IP method [96], the interface between the active layer and DPAN substrate is clear but tightly bonded without obvious cracks for DPAN/PEI-0.01. TEM image of a free-standing active layer is further captured to probe its integrity, which displays that the membrane is defect-free and smooth over a large area ($16.2 \times 13.0\ \mu m^2$, Fig. 2.31b). This result also approves the remarkable function of PDA as a functional layer, capable of enriching polymerized monomers, while contributing to the formation of ultrathin, robust membranes. To demonstrate

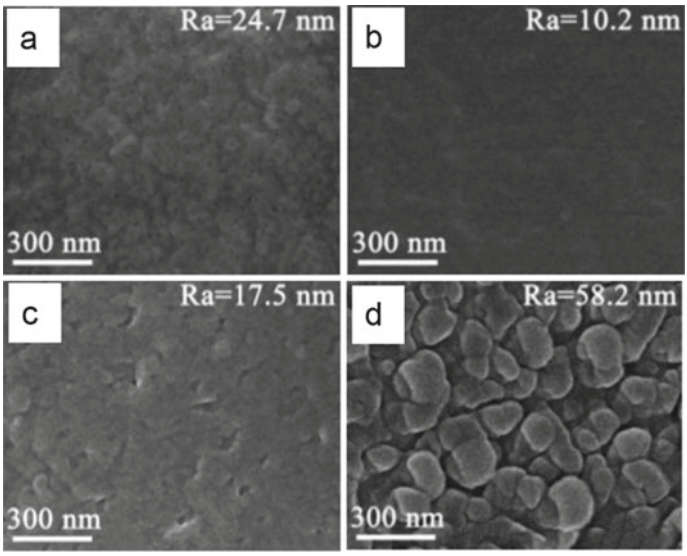

Fig. 2.30 Surface SEM images of **a** DPAN, **b** DPAN/PEI-0.01, **c** DPAN/DETA-0.01, and **d** DPAN/EDA-0.01 membranes. Copyright (2018), American Chemical Society [29]

this capability, dilute PEI solutions with concentrations of 0.005 and 0.001% are employed, which are unable to form a complete active layer by conventional IP. And as revealed in Fig. 2.31e, the thickness of DPAN/PEI-0.1 membrane is only increased to 25.1 nm by increasing the concentration of PEI solution from 0.01 to 0.1%. Furthermore, it is worth noting that the PAN/DETA-*X* and PAN/EDA-*X* membrane thickness is in accordance with that of DPAN/PEI-*X* in the range of amine concentration from 0.001 to 0.1%. While for concentration higher than 1%, the thickness of active layer increases significantly, especially for PAN/DETA-1 and PAN/EDA-1. This suggests that the thickness of active layer may be decided by the thickness of the stacked amine layer after achieving adsorption equilibrium. On the other hand, the amine molecules even in ultra-dilute solution can be effectively captured by PDA layer, significantly improving the utilization rate of monomers.

Positron annihilation spectroscopy (PAS) curves were probed to further evaluate the structure of active layer on molecular level, as shown in Fig. 2.32a. The membranes express a typical bilayer composite structure, where the low *S* parameter corresponds to the active layer, and the high *S* parameter implies a porous support. The *S* parameters vary little from the interface to membrane surface, implying that the active layer is formed by tightly packed molecules, which is in accordance with TEM result that displays a uniform active layer. In addition, this structure is different from that of active layer formed by traditional IP, which consists of asymmetric structures with loose top and dense bottom [97]. Such difference may originate from the pre-multilayer-stacking structure of amine monomers. The *S* parameter decreases sequentially in the order of PAN/PEI-*X* < PAN/DETA-*X* < PAN/EDA-*X*, which

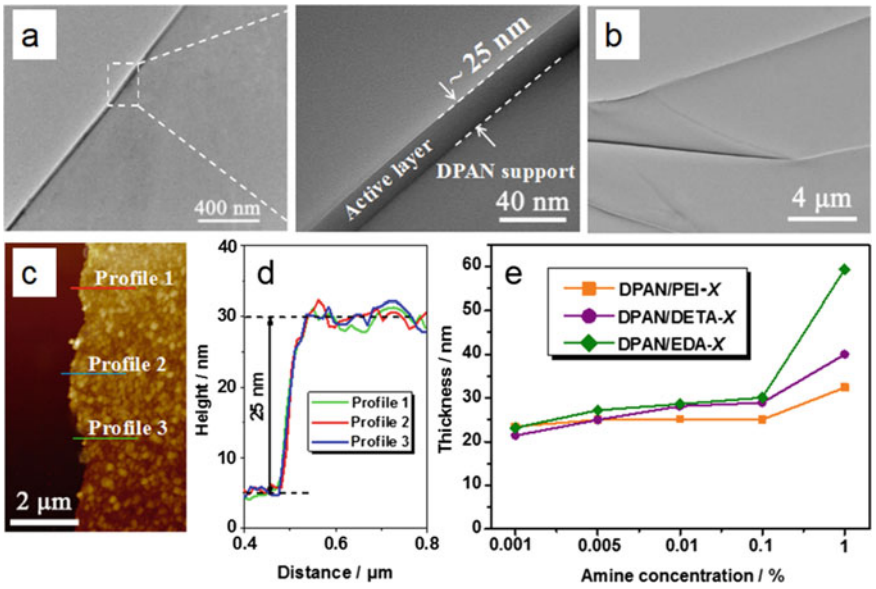

Fig. 2.31 **a** TEM and **b** SEM images, **c** AFM image and **d** corresponding height profiles of DPAN/PEI-0.01. **e** Active layer thickness of TFC membranes with different amine concentrations. Copyright (2018), American Chemical Society [29]

may be due to the fact that the small-sized DETA and EDA are able to produce more compact active layers and thus smaller free volume cavities. Due to the homogeneous porous structure within support layer, it shows significantly increased but constant *S* parameters at different probing depths.

Thereafter, to further tune the active layer structure, the cross-linking agent TMC was adjusted to TMC-AC composites with a series of molar ratios. Figure 2.32a shows that DPAN/PEI-0.01 (1:1) (1:1 represents the molar ratio of TMC:AC) and DPAN/PEI-0.01 (3:1) exhibit similar behavior with DPAN/PEI-0.01 (i.e., cross-linking agent is TMC), suggesting the presence of active layer with regular structure. The difference is that they exhibit higher *S* parameters than DPAN/PEI-0.01, which implies the presence of larger free volume cavities. This should be ascribed to the rigidity, small sized, and higher activity of TMC compared to AC [98], thus providing a relatively denser cross-linked network. This is why the *S* parameter of DPAN/PEI-0.01 (1:1) is higher than that of DPAN/PEI-0.01 (3:1). The efficacy of structure modulation is also confirmed by the degree of network cross-linking (DNC) calculated from X-ray photoelectron spectroscopy (XPS) results. Considering the simple and clear structure of EDA molecule, it is used here to concisely calculate the DNC of polyamide network. All samples exhibit the peaks for C1s, N1s, and O1s peaks at ~ 284.7, 399.4 and 530.9 eV (Fig. 2.32b), where the characteristic peak of N–C=O could be clearly detected after cross-linking reaction. The DNC can then be calculated from the O/N ratio and the relative values of N and O contents. The results in

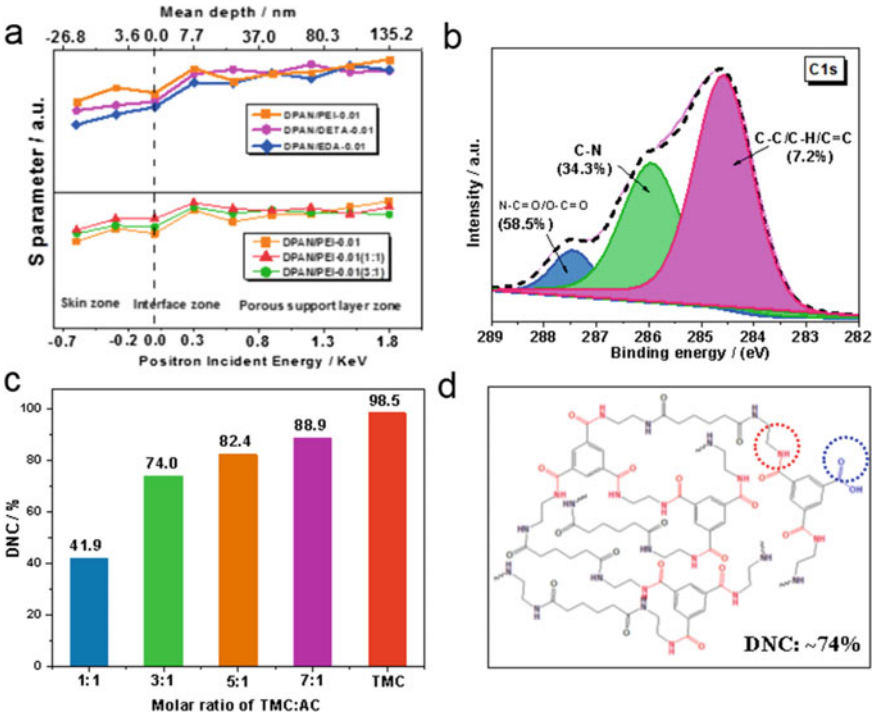

Fig. 2.32 **a** *S* parameter as a function of the positron energy for membranes with different cross linkers. **b** C 1 s spectra of DPAN/EDA-0.01. **c** DNC of DPAN/EDA-0.01 cross-linked by TMC-AC composites. **d** Illustration of the cross-linked network with ~ 74% DNC formed by EDA as amine and TMC-AC with 3:1 ratio as cross linker (red dotted circle represents the cross-linked amide bonds, and blue one means uncross-linked acyl chloride groups). Copyright (2018), American Chemical Society [29]

Fig. 2.32c depict that the highest DNC of 98.5% is obtained for DPAN/EDA-0.01. The DNC decreases from 88.9 to 41.9% as the TMC:AC ratio gradually changed from 7:1 to 1:1, confirming the effective modulation of the structure of active layer. Figure 2.32d describes the DNC at ~ 74% cross-linked structure, in which the amide bonds (red dotted circle) endow the polyamide layer with a steady network structure, and the hydrolyzed acyl chloride groups (blue dotted circle) produce hydrophilic active sites. Moreover, the DNC is close to 100% by using TMC only, far exceeding that formed by traditional IP (almost < 70%) [99]. This means that the surface-enriched multilayered amine on DPAN support is prone to cross-linking as well as forming dense active layers.

The permeation performance of resulted TFC membranes was tested on a home-made dead-end device after measuring several hours to acquire reliable data. Four polar (ethanol, isopropanol, acetone, and ethyl acetone) and two nonpolar (toluene and n-heptane) organic solvents were selected for permeance measurements. Figure 2.33a shows that the polyamide membranes with ultrathin active layers

allow ultrafast solvent permeation, more than ten times higher than commercial TFC membranes [68]. Specifically, for DPAN/PEI-0.01, acetone and ethyl acetone permeance are 54.4 and 43.8 L m^{-2} h^{-1} bar^{-1}, respectively. And, ethanol and isopropanol permeance are 40.2 and 28.8 L m^{-2} h^{-1} bar^{-1}, respectively, lower than that of acetone and ethyl acetone. However, the permeance of non-polar solvents is significantly reduces to 3.9 and 4.3 L m^{-2} h^{-1} bar^{-1} for n-heptane and toluene, respectively. The significant difference in permeance between polar and non-polar solvents should be originated from the hydrophilicity of active layer. Furthermore, the permeance of polar solvents exhibits an order consistent with solvent viscosity: acetone > ethyl acetone > ethanol > isopropanol, but not in the order of molecular dynamics diameters. This means that molecules possibly transport in an ultrafast viscous flow through a polyamide membrane with 25 nm-thick active layer, which is also confirmed in a carbon membrane with a 35 nm thickness [75]. In addition, the molecular weight cut-off (*MWCO*) of DPAN/PEI-0.01 is about 700 Da by measuring the rejection of SY 21. Considering the excellent permeation of membrane, such rejection for a specific application is acceptable. Furthermore, reducing the PEI concentration can significantly improve the solvent permeation. For example, the acetone permeance of DPAN/PEI-0.001 increases to 96.3 L m^{-2} h^{-1} bar^{-1}, distinct from that of 74.5 L m^{-2} h^{-1} bar^{-1} for DPAN/PEI-0.005. And, the isopropanol permeance also increases to 50.7 L m^{-2} h^{-1} bar^{-1}, but accompanied by an increase in *MWCO* of ~ 1000 Da. The increase in permeance is attributed to the decrease in thickness of active layer, which results in a shorter transport path and increase in free volume. Compared with other membranes with high permeance, the polyamide membranes fabricated by adsorption-assisted IP are not only about 50% more productive than advanced 8 nm-thick TFC membranes [38], but comparable to that of ultrathin laminar membrane with continuous 2-nm channels [56]. This result further validates the superiorities of adsorption-assisted IP method for preparing polyamide membranes with ultrathin, permeable characteristic active layers. Furthermore, despite increasing the concentration of amine monomer at the expense of membrane permeability, DPAN/PEI-1 still exhibits approving solvent permeance with an acetone permeance of 38.8 L m^{-2} h^{-1} bar^{-1}, maintaining the *MWCO* of 450 Da, which is superior to the commercial polyamide membranes (usually < 8 L m^{-2} h^{-1} bar^{-1}).

In addition to PEI-based polyamide membranes, EDA- and DETA-based TFC membranes also exhibit ultrafast organic solvent permeation. For instance, the acetone permeance of DPAN/EDA-0.001 and DPAN/DETA-0.001 is 42.9 and 68.9 L m^{-2} h^{-1} bar^{-1}, respectively, while keeping the *MWCO* of less than 480 Da. Even at 1% amine monomer concentration, the acetone permeance of the two membranes still reaches 18.4 and 25.0 L m^{-2} h^{-1} bar^{-1}, respectively, with their *MWCO* below 300 Da. Besides, they also exhibit viscous flow behavior, with the permeance order remaining inverse to viscosity as acetone > ethyl acetone > ethanol > isopropanol. In addition, their permeability for non-polar organic solvents is almost undetectable, as PEI-based membranes have a toluene permeance of less than 5.0 L m^{-2} h^{-1} bar^{-1}. In contrast, the low toluene permeability also confirms that these TFC membranes are intact without any defect structures. Compared to PEI-based polyamide membranes, EDA- and DETA-based membranes reduce the permeance of the selected solvents

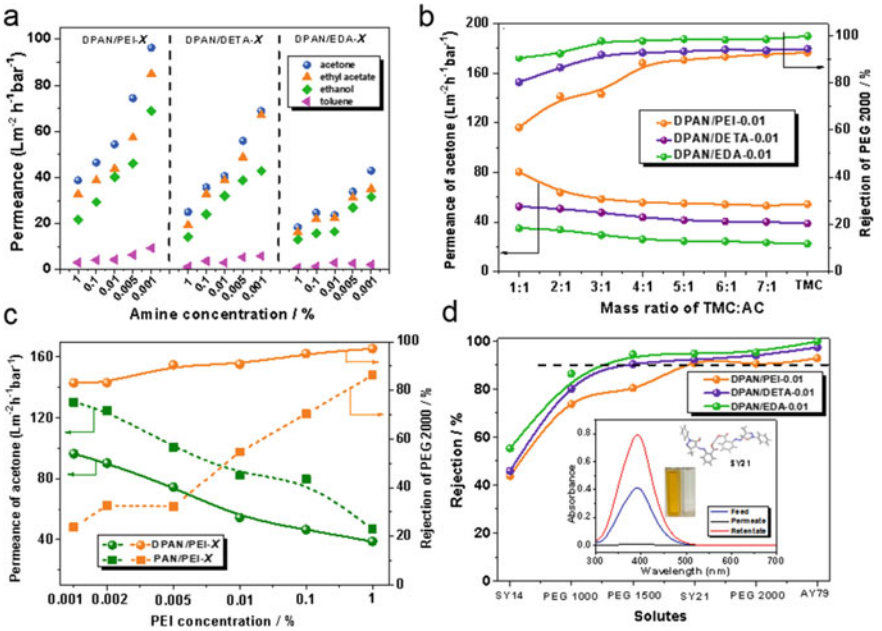

Fig. 2.33 **a** Solvent permeance, **b** acetone permeance and PEG 2000 rejection of DPAN/PEI-0.01, DPAN/DETA-0.01, and DPAN/EDA-0.01. **c** Acetone permeance and PEG 2000 rejection for DPAN/PEI-X and PAN/PEI-X with different PEI concentrations. **d** Rejection of SY 14, SY 21, AY 79, and PEG 1000, 1500, 2000 for DPAN/PEI-0.01, DPAN/DETA-0.01, and DPAN/EDA-0.01 (insert is UV–vis absorption spectra of SY 21 in acetone before and after filtration through DPAN/EDA-0.01). Copyright (2018), American Chemical Society [29]

by around 50% and 30%, respectively. This may be a result of the reduction of free volume cavity (i.e. transport pathways) created by molecular segment motion, consistent with the consequence demonstrated by PAS. Therefore, the permeability of membranes with cross-linked network structures prepared by IP will vary with DNC that is regulated by the TMC:AC ratio. For example, Fig. 2.33b shows that increasing the TMC:AC ratio from 1:1 to 7:1 induces a decrease in free volume, resulting in a decrease in the acetone permeance of DPAN/PEI-0.01 from 80.4 to 53.0 L m^{-2} h^{-1} bar^{-1}. Together, regulating the physical structure and chemical composition of polyamide layer can effectively adjust the solvent permeance of TFC membranes.

Rejection of dye molecules and PEG oligomers with different kinetic diameter or molecular weight by prepared TFC membranes was tested to assess the integrity of the active layer. Figure 2.33c shows that PAN/PEI-*X* cannot grow a defect-free polyamide membrane when the aqueous phase concentration is lower than 0.1%, which can be proved by the fact that rejection of PEG 2000 for PAN/PEI-0.001 is only 23.7%, while that of PAN/PEI-1 is effectively enhanced to 86.2%. But, the great difference is that DPAN/PEI-*X* shows distinct rejection behavior: 95.1% for DPAN/PEI-0.1,

and even 90.5% for DPAN/PEI-0.005. This result directly verifies the integrity of the active layer in DPAN/PEI-*X* and highlights the advantage of adsorption-assisted IP to prepare a complete active layer, even with ultra-dilute monomer solutions. In addition, we also tested the rejection of a series of dye molecules to evaluate the potential of these TFC membranes for practical applications, as shown in Fig. 2.33d. As for SY 14 with a molecular weight of 248 g mol^{-1}, about 50% of them can be sieved out by DPAN/PEI-0.01, while when the molecular weight expand to 694 g mol^{-1}, the membrane could reject 90.7% of SY 21. And the rejection even reaches 92.8% for the larger AY 79, a molecular weight of 1111 g mol^{-1}. In contrast, EDA- and DETA-based polyamide membranes show more satisfactory separation selectivity for dye molecules and PEG oligomers. Especially, DPAN/EDA-0.01 and DPAN/DETA-0.01 can absolutely separate AY 79 with almost 100% rejection. Such effective rejection should give the credit to the compact polymer packing within the cross-linked network, that is, the increased cross-linking degree.

To gain an in-depth understanding of this excellent nanofiltration performance, the transport resistance and permeability of polyamide layer were obtained, as displayed in Fig. 2.34a. The results show that the permeability of acetone is nearly ten times higher than that of toluene, indicating that the prepared ultrathin polyamide membrane gives a lower transmission barrier to polar solvents than non-polar solvents. This is directly evidenced by the obvious differences in energy barriers in the range of $X = 0.001$–0.1 for DPAN/PEI-*X*: 0.24–0.68 for acetone but 2.3–8.3 for toluene. The weak increase in acetone resistance here (0.24–0.68) may be due to the regularity and similar molecular structure in the cross-linked network. Likewise, the transport resistance of DPAN/EDA-*X* and DPAN/DETA-*X* for polar solvents is lower compared to non-polar solvents, and varies only slightly in the range of $X = 0.001$–0.1. Nevertheless, due to the apparent increase in the DNC of the cross-linked network by increasing the PEI concentration to 1%, the membrane displays > onefold increase in resistance to both acetone and toluene. This indicates that tuning the nanostructure of polyamide network enables to enhance the permeability or reduce the transport resistance of membranes to organic solvents [100].

Figure 2.34b summarizes the performance of OSN membranes formed by conventional techniques in literatures and compares them with those obtained in this study. It

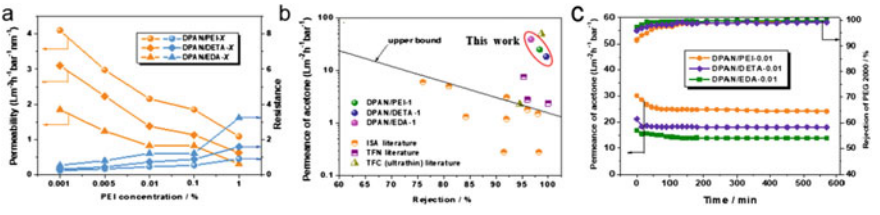

Fig. 2.34 **a** Permeability and resistance of acetone of membranes. **b** Acetone permeance versus AY79 rejection for reported OSN membranes and this study. **c** Acetone permeance and PEG 2000 rejection of membranes as a function of operation time. Copyright (2018), American Chemical Society [29]

can be found that although most nanofiltration membranes have an intractable trade-off between permeance and selectivity [101], the three membranes prepared in this work exceed the upper limit [15]. This is attributed to the ultrathin and defect-free structure, which allows low-resistance fast permeance and high rejection, conductive to alleviate the trade-off effect of TFC membranes. In addition to their remarkable capacity in separation, the as-prepared membranes also show excellent long-term operational stability, as shown in Fig. 2.34c. The three membranes display a slight decrease in permeance of < 18% during the first 40 min, which may be caused by the compaction of DPAN substrate. The reduction is comparable to that of other reported TFC membranes, generally not exceeding 20%, and the membrane displays an almost steady permeance for 500 min after this procedure, reaching a stable operating state. Compared to EDA- and DETA-base membranes with rigid and dense characteristics, PEI-based membranes with chain structure are loose and easily compressible during actual pressure operation, thus resulting in a faster decrease in permeability. In addition, the results from very thin structures demonstrate the strong practicality of the active layer obtained by adsorption-assisted IP. Additionally, membrane shrinkage helps achieve higher rejection efficiency (almost 100% for PEG 2000).

In conclusion, we prepare a polyamide membrane with superior nanofiltration performance by introducing PDA as an adsorption layer. The adsorption layer is able to capture amine monomers and enrich them on porous substrates from ultra-diluted aqueous solutions, thus endowing a unique adsorption-assisted interfacial polymerization. Therefore, defect-free and ultrathin films of only ~ 25 nm are acquired as active layers. The resulting novel TFC membranes brilliantly accomplish the selective rejection of both dye molecules and PEG oligomers, importantly, simultaneously achieve ultrafast permeation for polar organic solvents. Concretely, the acetone permeance reaches about 96.3 L m^{-2} h^{-1} bar^{-1} under the same conditions, which is nearly 10 times that of polyamide membranes fabricated by traditional interfacial polymerization. Furthermore, the versatility and simplicity of this strategy give it the potential to manipulate nanostructure for advanced membrane. More importantly, such polyamide membrane with ultrathin active layer effectively alleviates the inherent trade-off between permeance and selectivity of TFC membranes, rendering them one of the best TFC membranes for various separations. Uniform and ultrathin membranes formed by adsorption-assisted interfacial polymerization are not limited to membrane separation, but can also be universally applicable to other thin-film materials, such as, drug release, electrolyte-related devices, and catalysis.

2.7 Composite Membrane with Hierarchically-Structured Active Layer

In this study, dual-needle electrostatic atomization-assisted interfacial polymerization (IP) technology was employed to prepare hierarchically-structured polyamide membranes from PEI monomer and TMC cross-linking agent. As displayed in

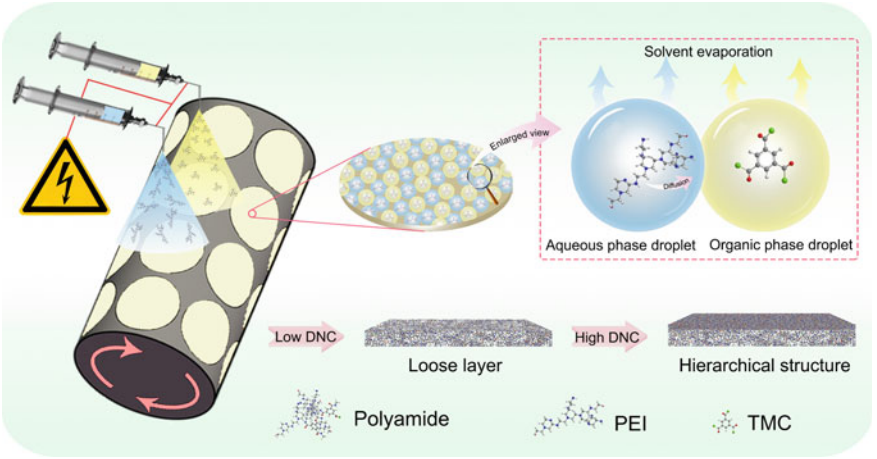

Fig. 2.35 Schematic illustration of preparing a hierarchically-structured membrane. Copyright (2020), Royal Society of Chemistry [30]

Fig. 2.35, PEI and TMC solutions were contained into two syringes connected with high-voltage power, respectively. Then quantified solutions were pumped and deposited together onto the pre-pasted nylon substrate and then reacted to form a polyamide layer after contacting with each other. Under the action of strong coulomb repulsion, the ejected droplets were broken into submicron-sized ones with many tiny interfaces, readily enabling a smooth IP membrane due to the dilute concentration. During this process, the thickness of polyamide layer was determined by the amount of atomized PEI and TMC, while its compactness was regulated by the TMC concentration through the degree of cross-linking. Therefore, hierarchical nanostructures with different degrees of cross-linking were constructed by varying the concentration of TMC cross-linking agent from an initial low concentration one to a later high one, without changing the PEI concentration.

$TMC_{0.001}$ membrane was first prepared with organic phase of 0.001% (w/v) and PEI solution at a concentration of 0.1% (w/v). The SEM image in Fig. 2.36a shows that the surface of $TMC_{0.001}$ membrane is smooth and defect-free, and the obvious micropores on the surface of nylon substrate are adequately covered. And as the amount of atomized monomer increases, the outline of the porous substrate gradually becomes blurred, indicating an increase in the thickness of generated polyamide layer. The dramatic decrease in surface roughness shown in AFM images verifies the result, where the average surface roughness of $TMC_{0.001}$ membrane is only 16.87 nm, much lower than that of nylon substrate (~ 198 nm). And, this compensation for roughness facilitates the formation of a ultrathin active layer, especially avoiding inevitable pore penetration [102]. Then, increaseing the concentration of TMC to 0.1% and keeping a constant PEI of 0.1% on top of the $TMC_{0.001}$ layer to continue to prepare a polyamide layer with a higher degree of cross-linking (Fig. 2.36b). The dense layer has a higher content of 14.3% compared to the 1.2% O content in the

loose $TMC_{0.001}$ layer. At the same time, under the excellent support of the $TMC_{0.001}$ layer, the roughness of the $TMC_{0.001}/TMC_{0.1}$ membrane is further reduced to only 5 nm, becoming one of the most ideal roughness values for TFC membranes [103]. For reference, a defect-free $TMC_{0.1}$ membrane with the same solution amount as the $TMC_{0.001}$ membrane is also prepared, with an active layer thickness of about 37.2 nm. It can be concluded that its physicochemical structure do not change much with the oil phase concentration by comparing the surface morphology of these prepared TFC membranes, unlike those prepared by traditional IP [104]. This may be because the monomer concentrations in atomized submicron-sized droplets are diluted, and thus the instantaneous reaction rate of polymerization is delayed to avoid the typical ridge-valley structure caused by local temperature inhomogeneity at the interface [105]. FTIR and XPS spectroscopies confirm the formation and chemical composition of the polyamide network. C 1 s spectra reveal the characteristic peaks of representative carboxyl and amide groups in Fig. 2.37. And the proportion of amide groups in $TMC_{0.001}$, $TMC_{0.1}$, and $TMC_{0.001}/TMC_{0.1}$ membranes is in accordance with the results from inserted energy dispersive spectroscopy (EDS).

Figure 2.36c shows the captured cross-sectional TEM image form $TMC_{0.001}/TMC_{0.1}$ membrane. No obvious gap between the loose support layer and dense layer is detected, that is, a seamless connection, which implies the good compatibility probably due to the similar chemical composition. The entire polyamide layer is even with a thickness of about 50 nm, exactly the sum of the dense and loose layers, in accordance with the results independently detected by

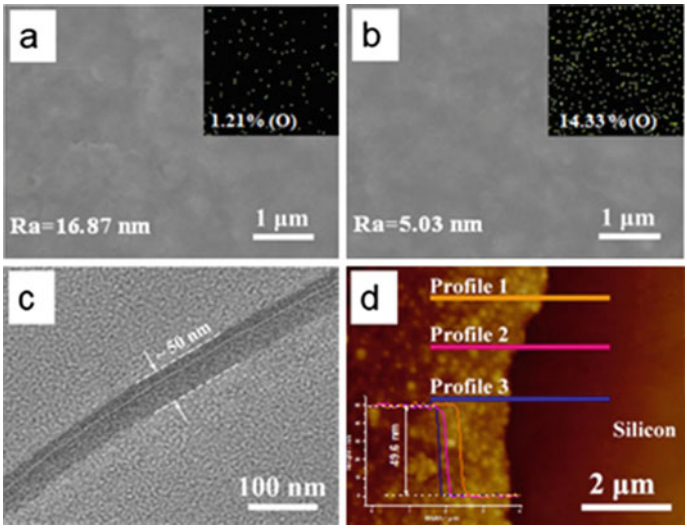

Fig. 2.36 Proofs of the hierarchically-structured membrane. SEM images of **a** $TMC_{0.001}$ and **b** $TMC_{0.001}/TMC_{0.1}$ membranes (insets: corresponding O elemental mappings). **c** Cross-sectional TEM and **d** AFM height image (inset: height profiles) of $TMC_{0.001}/TMC_{0.1}$ membrane. Copyright (2020), Royal Society of Chemistry [30]

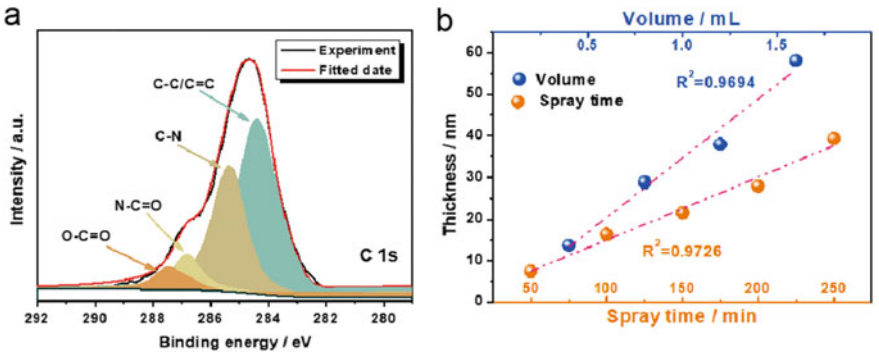

Fig. 2.37 Proofs of the hierarchically-structured membrane. **a** High resolution C 1 s spectra of $TMC_{0.001}$/$TMC_{0.1}$ membrane. **b** The thickness of active layer in $TMC_{0.1}$ membrane with spray volume and time. Copyright (2020), Royal Society of Chemistry [30]

AFM on silicon wafers in Fig. 2.36d. The thickness of the polyamide layer can be precisely controlled by the amount of monomer atomized by atomization-assisted IP technology. Taking the $TMC_{0.1}$ membrane as an example, Fig. 2.37b shows that the active layer thickness has a linear relationship with the spray amount and time (i.e. monomer amount). Therefore, in this work, an ultrathin active layer with a thickness of about 8 nm is prepared on the top surface of $TMC_{0.001}$ support layer by spraying for 50 min. And, this way of film growth is different from that of traditional IP, where the water–oil phase immiscibility forces monomers to react only at the water–oil interface, but once the initial membrane forms, subsequent monomers are blocked from contact, resulting in self-termination and uncontrolled growth [96]. On the contrary, the submicron-scale droplets provide an ultrahigh specific surface area, thereby significantly increasing the contact area of the two reactants, enabling full polymerization of the monomers, and improving the controllability of industrial economy and the reaction yield. For conventional IP, a large number of monomers cannot participate in subsequent polymerization.

Since the oxygen elements in polyamide layer are derived from TMC molecules, the oxygen content can usually reflect the degree of cross-linking of polyamide network to a certain extent. The XPS results (Fig. 2.38a) display that the $TMC_{0.001}$/$TMC_{0.1}$ and $TMC_{0.1}$ membranes have a comparable oxygen content of 14%, implying a cross-linking degree, compared to the 1.3% oxygen content of the $TMC_{0.001}$. For further quantitative study, *p*-phenylenediamine (PPD) with a clear chemical structure is chosen as the aqueous monomer instead of PEI. The results suggest that the polyamide network produced at 0.1% TMC concentration is approximately 1.7 times more cross-linked than at 0.001% concentration [12]. Therefore, a hierarchical structure with a dense top layer on the top of a loose inner layer is constructed by altering the concentration of TMC solution from 0.001 to 0.1%. Besides, the charge characteristics of membrane surface can further demonstrate the successful construction of this structure, because the more fully the TMC reacts, the less unreacted active amino groups are, which means the weaker the positive charge

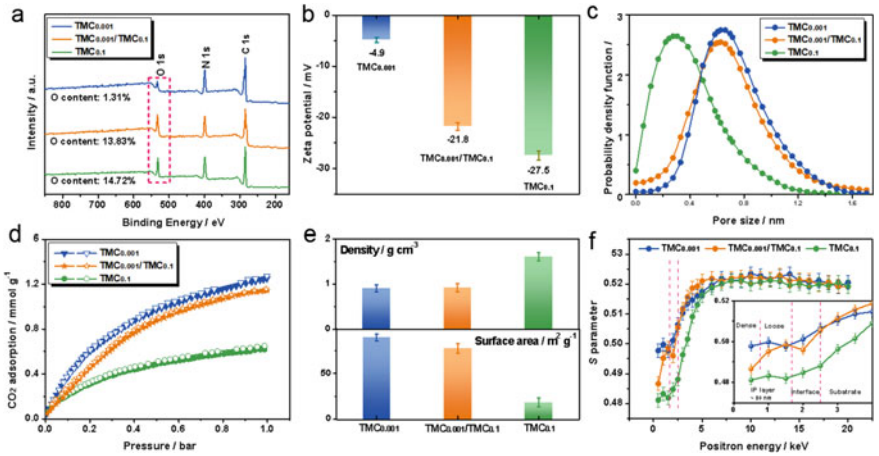

Fig. 2.38 Proofs of the hierarchical nanostructure. **a** XPS spectra, **b** Zeta potential at pH = 7.0, and **c** pore size distribution. **d** CO_2 sorption curves as well as **e** density and surface area of membranes. **f** *S* parameter as a function of the positron energy. Copyright (2020), Royal Society of Chemistry [30]

strength. Thus Fig. 2.38b shows that the $TMC_{0.1}$ and $TMC_{0.001}/TMC_{0.1}$ membranes show strong negative potentials, reaching – 27.5 and – 21.8 mV, respectively, compared to the $TMC_{0.001}$ membrane with the potential of – 4.9 mV. The dynamic contact angle tests are then performed on $TMC_{0.1}$ and $TMC_{0.001}/TMC_{0.1}$ membranes, it can be seen intuitively that the drop rate of the liquid on $TMC_{0.001}/TMC_{0.1}$ membrane surface is significantly faster than that on $TMC_{0.1}$ membrane, in spite of feel free to their initial contact angles are comparable. This result also suggests that the loose support layer within the $TMC_{0.001}/TMC_{0.1}$ membrane facilitates the transport of molecules across the membrane.

Next, based on the log-normal probability density function between molecular rejection and Stokes radius, the pore size distribution of polyamide layer was obtained to further probe its hierarchical structure. Figure 2.38c shows that the pore size distribution of active layer on $TMC_{0.001}$ membrane ranges from 0.2 to 1.4 nm, and that of the highly cross-linked active layer on $TMC_{0.1}$ membrane changes from 0.0 to 1.0 nm. Compared to the $TMC_{0.001}$ membrane, $TMC_{0.001}/TMC_{0.1}$ membrane displays a slight trend for small size distributions in the range 0.1–1.4 nm. In addition, the loose structure within the $TMC_{0.001}$ membrane also provides a larger specific surface area and thus N_2 adsorption capacity. Moreover, considering that CO_2 molecules with a kinetic diameter of 0.33 nm can access to the nanopores that are unreachable to N_2 with a kinetic diameter of 0.36 nm [106], CO_2 adsorption is also performed for precise assessment. Figure 2.38d shows that $TMC_{0.001}/TMC_{0.1}$ and $TMC_{0.001}$ membranes have higher CO_2 uptake ability than $TMC_{0.1}$ membranes, with normal steep uptake, especially at low relative pressure, confirming the loose layer with large free volume. Due to the existence of ultrathin dense layer, the CO_2 adsorption by $TMC_{0.001}$ membrane is slightly higher than that of $TMC_{0.001}/TMC_{0.1}$ membrane.

At the same time, by using the Langmuir model to analyze the CO_2 adsorption isotherm, Fig. 2.38e shows that $TMC_{0.001}/TMC_{0.1}$ and $TMC_{0.001}$ membranes obtain higher specific surface areas of about 80 and 90 $m^2\ g^{-1}$, respectively, much higher than that of dense $TMC_{0.1}$ membrane with 20 $m^2\ g^{-1}$ (Fig. 2.38e). Reasonably, a light density will inevitably be obtained for membranes with the large specific surface area. PAS is then performed to further directly confirm the hierarchical nanostructure, which clearly embodies the active layer, the interface between substrate and active layer as well as the substrate of a TFC membrane in Fig. 2.38f. The pore size of the active layer can be adjusted by the degree of cross-linking of polyamide network. The dense layer can effectively capture most of the injected positrons and thus show low S parameters, while the loose layer is the opposite [107]. Importantly, for $TMC_{0.001}/TMC_{0.1}$ membrane, although there are fewer positrons escaping at the beginning due to the ultrathin dense layer, the S parameter starts to increase after the first point due to the presence of the loose layer. Meanwhile, the positron injection depth (R, nm) is calculated by the formula $R = (40/\rho) \times E^{1.6}$ [108], where ρ is the density of active layer (g cm^{-3}) and E is the positron energy (keV). The obtained average implant depth is about 50 nm, i.e. the thickness of active layer, which matches well with the results of AFM and TEM.

Solvent permeance and dye rejection of membranes were tested in a home-made dead-end device. Measure at test pressure for several hours before reading data to ensure stable performance. In addition, microporous nylon substrates have no dye rejection but have ultra-high permeability (typically over 2000 L $m^{-2}\ h^{-1}\ bar^{-1}$). Figure 2.39a shows that the loosely structured $TMC_{0.001}$ membrane has the most advantageous permeance for polar solvents and non-polar solvents, while the $TMC_{0.1}$ membrane with dense structure has the lowest solvent permeance. It is worth noting that the $TMC_{0.001}/TMC_{0.1}$ membrane also shows satisfactory solvent permeability, surpassing that of $TMC_{0.1}$ membrane, and even close to that of $TMC_{0.001}$ membrane. Specifically, acetone achieves the highest permeance reaching 56.9 L $m^{-2}\ h^{-1}\ bar^{-1}$, followed by methanol permeance of 39.5 L $m^{-2}\ h^{-1}\ bar^{-1}$and water permeance of 23.7 L $m^{-2}\ h^{-1}\ bar^{-1}$, and even toluene permeance reaches 7.8 L $m^{-2}\ h^{-1}\ bar^{-1}$. These results emphasize the superiorities of this hierarchical membrane, in which the loose layer readily realizes rapid transfer for solvent molecules. And transfer resistance is then obtained according to the formula of $1/P_w$ [109] to verify above conclusion. As shown in Fig. 2.39d, the transport resistance of solvent molecules through $TMC_{0.001}$ and $TMC_{0.001}/TMC_{0.1}$ membranes is comparable, but the resistance of $TMC_{0.1}$ membrane is obviously higher than that of $TMC_{0.001}$ membrane by 158 ~ 248%. This further underlines the power of the loose layer to a polyamide membrane, which allows the $TMC_{0.001}/TMC_{0.1}$ membrane to surpass the permeance of conventional interfacial polymerization prepared TFC membranes (typically less than 5 L $m^{-2}\ h^{-1}\ bar^{-1}$) [94]. Furthermore, the performance is in accordance with most hydrophilic membranes, depending on molecular viscosity and solubility parameters [110], especially for polar solvents, thus following the order of acetone > methanol > water.

Next, dye rejection was measured under 3 bar to assess whether the loose interlayer was deselecting the $TMC_{0.001}/TMC_{0.1}$ membrane. Figure 2.39b shows that

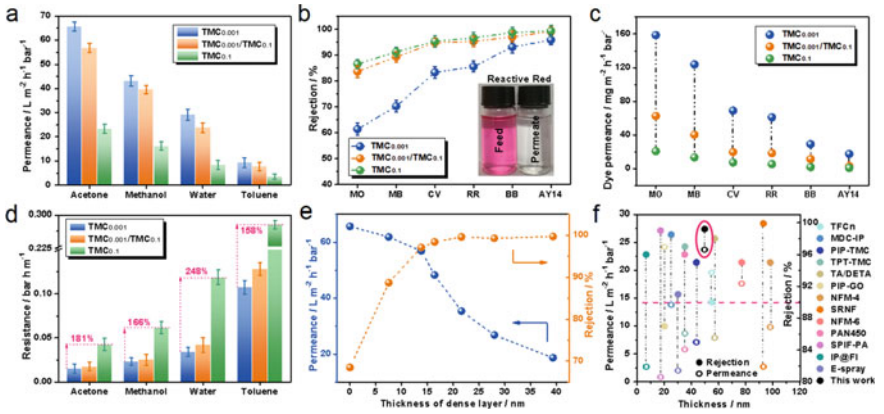

Fig. 2.39 **a** Solvent permeance, **b** dye rejection, **c** dye permeance, and **d** transport resistance of $TMC_{0.001}$, $TMC_{0.001}/TMC_{0.1}$, and $TMC_{0.1}$ membranes. **e** Acetone permeance and BB rejection of $TMC_{0.001}/TMC_{0.1}$ membranes with different dense layer thickness. **f** Water permeance and rejection of most reported ultrathin TFC membranes and in this study. Copyright (2020), Royal Society of Chemistry [30]

the $TMC_{0.001}$ membrane has poor dye rejection due to the loose overall cross-linked network, and thus can only effectively intercept the largest AY14 with a size of 1.9 nm, which is in sharp contrast to the $TMC_{0.1}$ membrane. In contrast, the $TMC_{0.001}/TMC_{0.1}$ membrane exhibits outstanding rejection for dyes, which is comparable to the $TMC_{0.1}$ membrane. For example, the rejection for dye MB with a size of 1.2 nm is close to 90%, and that even reaches 95% for CVs with an increase in size to ~ 1.5 nm. Furthermore, note that although the TMC0.001/TMC0.1 membrane is negatively charged, its ~ 95.3% rejection of negatively charged RR is only slightly higher than that of CV (~ 94.9%) with positive charge. Moreover, the UV–Vis absorption spectra of the dye solution before and after soaking membranes for 3 h are almost unchanged. These can be concluded that the electrostatic interactions of membranes with molecules and the adsorption of dyes by membranes have negligible effect on the rejection performance, which is mainly explained by the size sieving mechanism [70]. Therefore, the rejection selectivity is readily achieved by the dense top layer of as-prepared membrane with hierarchical structure. The dye permeance in Fig. 2.39c further confirms the advantage of $TMC_{0.001}/TMC_{0.1}$ membrane, in which compared with $TMC_{0.1}$ membrane, its high solvent permeability is accompanied by an increase in small dye permeance, while compared with $TMC_{0.001}$ membrane, complete separation of large dyes is achieved.

It is recognized that membrane thickness plays a decisive role in its permeability. Therefore, based on the conclusion in Fig. 2.37f, a series of $TMC_{0.001}/TMC_{0.1}$ membranes with different dense layer thicknesses were fabricated by varying the spraying time. Figure 2.39e shows that the acetone permeance continuously reduces from 60.9 to 18.7 L m^{-2} h^{-1} bar^{-1} as the thickness of dense layer increases from 8 to 40 nm. It is worth observing that in the thickness range of 8–13.8 nm, the dye

rejection keeps increasing, but when it exceeds 13.8 nm, the BB rejection is basically kept at a constant value of 95%, which means that the 13.8 nm-thick active layer has been able to achieve ideal selectivity for membranes. This phenomenon can be elucidated by the dissolution-diffusion mechanism of molecular transport [111]. The dissolution behavior of molecules is mainly determined by the chemical properties of membrane surface rather than the thickness, which mainly affects the molecular diffusion behavior. Increasing the membrane thickness would increase the molecular diffusion path length, resulting in a decrease in the diffusion coefficient. This also shows that accurately adjusting the thickness of the active layer can achieve controllable nanofiltration performance for TFC membranes. The TFC membranes reported in literatures with thicknesses of active layer below 100 nm are summarized in Fig. 2.39f. It is found that the $TMC_{0.001}/TMC_{0.1}$ membrane with a 13.8 nm-thick dense layer prepared in this paper shows obvious advantages with both high permeability and rejection performance. This confirms that a highly coordinated transfer behavior is achieved through constructing a membrane with hierarchical structure, featuring both fast permeation of molecules with low resistance and selective rejection, overcoming the ever-present trade-off effect.

Permeance against operation time of $TMC_{0.001}/TMC_{0.1}$ membrane was evaluated (Fig. 2.40). As shown in Fig. 2.40a, permeance against operation time was performed in typical 600 min. The result indicates that the permeance shows a little decline in the first hour because of membrane compaction for $TMC_{0.001}/TMC_{0.1}$ membrane, and then keeps steady for water, toluene, and acetone. The membrane compaction is benefited for dye rejection, like the most TFC membranes reported in the literatures [112, 113]. Then, pressure-dependent permeance was measured utilizing water and acetone as the represents of solvents. Figure 2.40b shows that the water and acetone fluxs have an increase linear relationship with the pressure (< 8 bar), suggesting the outstanding structural retention capability. Whereas when pressure is over than 8 bar, flux appears slight reduction owing to the intrinsic compaction of nylon substrate [114]. Moreover, $TMC_{0.001}/TMC_{0.1}$ membrane was measured after immersing in HCl solution (pH = 4.0) for a month, which would be suffered in some industrial operations. As shown in Fig. 2.40c, membrane with HCl treatment shows outstanding stability with slight permeance reduction compared to that without HCl treatment. Here, the outstanding interface compatibility would also be conducive to membrane operation and structure stability, which is certified by the low swelling of solvent. Except for stability, membrane fouling was also evaluated. $TMC_{0.001}/TMC_{0.1}$ membrane shows satisfactory anti-fouling property after four cycling measurement resulting from the smooth surface in Fig. 2.40d [115]. These results jointly certify excellent promising of this novel membrane for industrial processes.

In conclusion, the polyamide membrane with hierarchical structure is prepared, where dense layers formed on the top of loose layers. The density and thickness of polyamide membrane are precisely controlled by the double-needle electrostatic atomization method. An ultra-thin dense layer with a thickness of only 8 nm is achieved, enabling efficient dye selectivity (rejection). Meanwhile, the loose inside layer mainly acts as a support, giving the membrane good mechanical stability and achieving low resistance to molecular permeation. Importantly, high permeance of

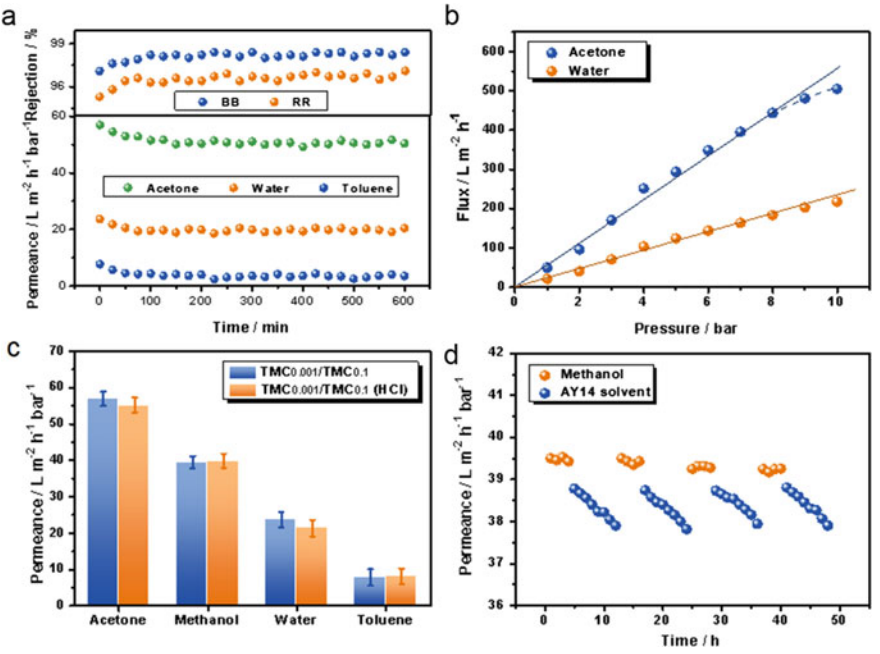

Fig. 2.40 Stability of $TMC_{0.001}/TMC_{0.1}$ membrane. **a** Long-term operation under 3 bar. **b** Acetone and water fluxes as a function of operation pressure. **c** Permeance before and after HCl treatment for one month. **d** Four-stage antifouling test. Copyright (2020), Royal Society of Chemistry [30]

56.9 L m^{-2} h^{-1} bar^{-1} for acetone and 23.7 L m^{-2} h^{-1} bar^{-1} for water is realized by $TMC_{0.001}/TMC_{0.1}$ membrane, which are superior to most traditional IP-based membranes. And, the high dye rejection is also achieved. The excellent performance of $TMC_{0.001}/TMC_{0.1}$ membrane overcomes the typical trade-off effect that is prevalent in most TFC membranes. Furthermore, benefited from the favorable architectural stability and interfacial compatibility of $TMC_{0.001}/TMC_{0.1}$ membrane, outstanding operational stability is achieved under extreme conditions such as high-pressure, prolonged operational conditions, and acid treatment. Additionally, electrostatic atomization-assisted method with high controllability provides novel ideas for rational design of nanocomposites, and opens the way for constructing new generation of TFC membranes.

References

1. L. Zhu, H. Yu, H. Zhang, J. Shen, L. Xue, C. Gao, B. Van der Bruggen, Mixed matrix membranes containing MIL-53 (Al) for potential application in organic solvent nanofiltration. RSC Adv. **5**, 73068–73076 (2015)
2. S.K. Lim, L. Setiawan, T.H. Bae, R. Wang, Polyamide-imide hollow fiber membranes

cross-linked with amine-appended inorganic networks for application in solvent-resistant nanofiltration under low operating pressure. J. Membr. Sci. **501**, 152–160 (2016)
3. C.J. Davey, Z.X. Low, R.H. Wirawan, D.A. Patterson, Molecular weight cut-off determination of organic solvent nanofiltration membranes using poly (propylene glycol). J. Membr. Sci. **526**, 221–228 (2017)
4. I.B. Valtcheva, S.C. Kumbharkar, J.F. Kim, Y. Bhole, A.G. Livingston, Beyond polyimide: crosslinked polybenzimidazole membranes for organic solvent nanofiltration (OSN) in harsh environments. J. Membr. Sci. **457**, 62–72 (2014)
5. L.M. Vane, Separation technologies for the recovery and dehydration of alcohols from fermentation broths. Biofuels Bioprod. Bioref. **2**, 553–588 (2008)
6. B.S. Chanukya, N.K. Rastogi, Extraction of alcohol from wine and color extracts using liquid emulsion membrane. Sep. Purif. Technol. **105**, 41–47 (2013)
7. A.K. Shukla, J. Alam, M. Alhoshan, L.A. Dass, M.R. Muthumareeswaran, Development of a nanocomposite ultrafiltration membrane based on polyphenylsulfone blended with graphene oxide. Sci. Rep. **7**, 41976 (2017)
8. L. Pérez-Manríquez, P. Neelakanda, K.V. Peinemann, Morin-based nanofiltration membranes for organic solvent separation processes. J. Membr. Sci. **554**, 1–5 (2018)
9. A. Liu, M.V. de Ruiter, W. Zhu, S.J. Maassen, L. Yang, J.J.L.M. Cornelissen, Compartmentalized thin films with customized functionality *via* interfacial cross-linking of protein cages. Adv. Func. Mater. **28**, 1801574 (2018)
10. Z. Wang, Z. Wang, S. Lin, H. Jin, S. Gao, Y. Zhu, J. Jin, Nanoparticle-templated nanofiltration membranes for ultrahigh performance desalination. Nat. Commun. **9**, 1–36 (2018)
11. S.P. Sun, T.A. Hatton, S.Y. Chan, T.S. Chung, Novel thin-film composite nanofiltration hollow fiber membranes with double repulsion for effective removal of emerging organic matters from water. J. Membr. Sci. **401**, 152–162 (2012)
12. S. Karan, Z. Jiang, A.G. Livingston, Sub-10 nm polyamide nanofilms with ultrafast solvent transport for molecular separation. Science **348**, 1347–1351 (2015)
13. M.B. Wu, Y. Lv, H.C. Yang, L.F. Liu, X. Zhang, Z.K. Xu, Thin film composite membranes combining carbon nanotube intermediate layer and microfiltration support for high nanofiltration performances. J. Membr. Sci. **515**, 238–244 (2016)
14. X. Wu, L. Hao, J. Zhang, X. Zhang, J. Wang, J. Liu, Polymer-$Ti_3C_2T_x$ composite membranes to overcome the trade-off in solvent resistant nanofiltration for alcohol-based system. J. Membr. Sci. **515**, 175–188 (2016)
15. M.F. Jimenez−Solomon, Q. Song, K.E. Jelfs, M. Munoz−Ibanez, A.G. Livingston, Polymer nanofilms with enhanced microporosity by interfacial polymerization. Nat. Mater. **15**, 760–767 (2016)
16. X. Yu, Z. Wang, Z. Wei, S. Yuan, J. Zhao, J. Wang, S. Wang, Novel tertiary amino containing thin film composite membranes prepared by interfacial polymerization for CO_2 capture. J. Membr. Sci. **362**, 265–278 (2010)
17. S. Darvishmanesh, J. Degrève, B. Van der Bruggen, Mechanisms of solute rejection in solvent resistant nanofiltration: the effect of solvent on solute rejection. Phys. Chem. Chem. Phys. **12**, 13333–13342 (2010)
18. W. Ogieglo, H. Van der Werf, K. Tempelman, H. Wormeester, M. Wessling, A. Nijmeijer, N.E. Benes, n-Hexane induced swelling of thin PDMS films under non-equilibrium nanofiltration permeation conditions, resolved by spectro-scopic ellipsometry. J. Membr. Sci. **437**, 313–323 (2013)
19. N. Stafie, D.F. Stamatialis, M. Wessling, Effect of PDMS cross-linking degree on the permeation performance of PAN/PDMS composite nanofiltration membranes. Sep. Purif. Technol. **45**, 220–231 (2005)
20. S. Basu, M. Maes, A. Cano-Odena, L. Alaerts, D.E. DeVos, I.F.J. Vankelecom, Solvent resistant nanofiltration (SRNF) membranes based on metal-organic frameworks. J. Membr. Sci. **344**, 190–198 (2009)

21. J. Campbell, R.P. Davies, D.C. Braddock, A.G. Livingston, Improving the permeance of hybrid polymer/metal-organic framework (MOF) membranes for organic solvent nanofiltration (OSN)-development of MOF thin films via interfacial synthesis. J. Mater. Chem. A **3**, 9668–9674 (2015)
22. K. Vanherck, A. Aerts, J. Martens, I. Vankelecom, Hollow filler based mixed matrix membranes. Chem. Commun. **46**, 2492–2494 (2010)
23. J. Campbell, G. Székely, R.P. Davies, Fabrication of hybrid polymer/metal organic framework membranes: mixed matrix membranes versus in situ growth. J. Mater. Chem. A **2**, 9260–9271 (2014)
24. Y. Zhang, R. Wang, Fabrication of novel polyetherimide-fluorinated silica organic-inorganic composite hollow fiber membranes intended for membrane contactor application. J. Membr. Sci. **443**, 170–180 (2013)
25. S.B. Teli, M. Calle, N. Li, Poly (vinyl alcohol)-H-ZSM-5 zeolite mixed matrix membranes for pervaporation separation of methanol-benzene mixture. J. Membr. Sci. **371**, 171–178 (2011)
26. L. Huang, J. Chen, T. Gao, M. Zhang, Y. Li, L. Qu, G. Shi, Reduced graphene oxide membranes for ultrafast organic solvent nanofiltration. Adv. Mater. **28**, 8669–8674 (2016)
27. Z. Yuan, X. Wu, Y. Jiang, Y. Li, J. Huang, L. Hao, J. Zhang, J. Wang, Carbon dots-incorporated composite membrane towards enhanced organic solvent nanofiltration performance. J. Membr. Sci. **549**, 1–11 (2018)
28. L. Hao, H. Zhang, X. Wu, J. Zhang, J. Wang, Y. Li, Novel thin-film nanocomposite membranes filled with multi-functional $Ti_3C_2T_x$ nanosheets for task-specific solvent transport. Compos. A Appl. Sci. Manuf. **100**, 139–149 (2017)
29. X. Wu, Y. Li, X. Cui, J. Wang, X. Cao, P. Zhang, L. Zheng, Adsorption-assisted interfacial polymerization toward ultrathin active layers for ultrafast organic permeation. ACS Appl. Mater. Interfaces. **10**, 10445–10453 (2018)
30. J. Chen, J. Zhang, X. Wu, X. Cui, W. Li, H. Zhang, J. Wang, X. Cao, P. Zhang, Accurately controlling the hierarchical nanostructure of polyamide membranes via electrostatic atomization-assisted interfacial polymerization. J. Mater. Chem. A **8**, 9160–9167 (2020)
31. X. Wu, G. Zhou, X. Cui, Y. Li, J. Wang, X. Cao, P. Zhang, Nanoparticle-assembled thin film with amphipathic nanopores for organic solvent nanofiltration. ACS Appl. Mater. Interfaces. **11**, 17804–17813 (2019)
32. X. Wang, X. Shen, Y. Gao, Z. Wang, R. Yu, Atomic-scale recognition of surface structure and intercalation mechanism of $Ti_3C_2T_x$. J. Am. Chem. Soc. **137**, 2715–2721 (2015)
33. L. Shao, X. Cheng, Z. Wang, J. Ma, Z. Guo, Tuning the performance of polypyrrole-based solvent-resistant composite nanofiltration membranes by optimizing polymerization conditions and incorporating graphene oxide. J. Membr. Sci. **452**, 82–89 (2014)
34. H. Siddique, E. Rundquist, Y. Bhole, L.G. Peeva, A.G. Livingston, Mixed matrix membranes for organic solvent nanofiltration. J. Membr. Sci. **452**, 354–366 (2014)
35. K. Varoon, X. Zhang, B. Elyassi, D.D. Brewer, M. Gettel, S. Kumar, J. Lee, S. Maheshwari, A. Mittal, C. Sung, M. Cococcioni, L.F. Francis, A.V. McCormick, K.A. Mkhoyan, M. Tsapatsis, Dispersible exfoliated zeolite nanosheets and their application as a selective membrane. Science **333**, 72–75 (2011)
36. M. Li, J. Xu, C. Chang, C. Feng, L. Zhang, Y. Tang, C. Gao, Bioinspired fabrication of composite nanofiltration membrane based on the formation of DA/PEI layer followed by cross-linking. J. Membr. Sci. **459**, 62–71 (2014)
37. H. Zhang, Y. Zhang, L. Li, S. Zhao, H. Ni, S. Cao, J. Wang, Cross-linked polyacrylonitrile/polyethyleneimine-polydimethylsiloxane composite membrane for solvent resistant nanofiltration. Chem. Eng. Sci. **106**, 157–166 (2014)
38. Y. Ying, Y. Xiao, J. Ma, X. Guo, H. Huang, Q. Yang, C. Zhong, Recovery of acetone from aqueous solution by ZIF-7/PDMS mixed matrix membranes. RSC Adv. **5**, 28394–28400 (2015)
39. Y. He, H. Zhang, Y. Li, J. Wang, L. Ma, W. Zhang, J. Liu, Synergistic proton transfer through nanofibrous composite membranes by suitably combining proton carriers from the nanofiber mat and pore-filling matrix. J. Mater. Chem. A **3**, 21832–21841 (2015)

40. H. Mao, H. Zhang, Y. Li, Y. Xue, F. Pei, J. Wang, J. Liu, Tunable solvent permeation properties of thin film nanocomposite membrane by constructing dual-pathways using cyclodextrins for organic solvent nanofiltration. ACS Sustain. Chem. Eng. **3**, 1925–1933 (2015)
41. N. Moumen, R.S. Subramanian, J.B. McLaughlin, Experiments on the motion of drops on a horizontal solid surface due to a wettability gradient. Langmuir **22**, 2682–2690 (2006)
42. P. Schmidt, T. Koese, P. Lutze, Characterisation of organic solvent nanofiltration membranes in multi-component mixtures: membrane rejection maps and membrane selectivity maps for conceptual process design. J. Membr. Sci. **429**, 103–120 (2013)
43. S. Darvishmanesh, F. Tasselli, J.C. Jansen, E. Tocci, F. Bazzarelli, P. Bernardo, P. Luis, J. Degrève, E. Drioli, B. Van der Bruggen, Preparation of solvent stable polyphenyl sulfone hollow fiber nanofiltration membranes. J. Membr. Sci. **384**, 89–96 (2011)
44. L.E.M. Gevers, I.F.J. Vankelecom, P.A. Jacobs, Zeolite filled polydimethylsiloxane (PDMS) as an improved membrane for solvent-resistant nanofiltration (SRNF). Chem. Commun. **19**, 2500–2502 (2005)
45. H. Siddique, L.G. Peeva, K. Stoikos, G. Pasparakis, M. Vamvakaki, A.G. Livingston, Membranes for organic solvent nanofiltration based on preassembled nanoparticles. Ind. Eng. Chem. Res. **52**, 1109–1121 (2013)
46. R. Ding, H. Zhang, Y. Li, J. Wang, B. Shi, H. Mao, J. Dang, J. Liu, Graphene oxide-embedded nanocomposite membrane for solvent resistant nanofiltration with enhanced rejection ability. Chem. Eng. Sci. **138**, 227–238 (2015)
47. C. Xue, G. Du, L. Chen, A carbon nanotube filled polydimethylsiloxane hybrid membrane for enhanced butanol recovery. Sci. Rep. **4**, 5925–5931 (2014)
48. Y. Han, Z. Xu, C. Gao, Ultrathin graphene nanofiltration membrane for water purification. Adv. Func. Mater. **23**, 3693–3700 (2013)
49. A. Dobrak-Van Berlo, I.F.J. Vankelecom, B. Van der Bruggen. Parameters determining transport mechanisms through unfilled and silicalite filled PDMS-based membranes and dense PI membranes in solvent resistant nanofiltration: comparison with pervaporation. J. Membr. Sci. **374**, 138–149 (2011)
50. W. Liu, S. Hu, G. Liu, F. Pan, H. Wu, Z. Jiang, B. Wang, Z. Li, X. Cao, Creation of hierarchical structures within membranes by incorporating mesoporous microcapsules for enhanced separation performance and stability. J. Mater. Chem. A **2**, 5267–5279 (2014)
51. O. Mashtalir, M. Naguib, V.N. Mochalin, Y. Dall'Agnese, H. Min, M.W. Barsoum, Y. Gogotsi, Intercalation and delamination of layered carbides and carbonitrides. Nat. Commun. **10**, 1–7 (2013)
52. Y. Yuan, X. Gao, Y. Wei, X. Wang, J. Wang, Y. Zhang, C. Gao, Enhanced desalination performance of carboxyl functionalized graphene oxide nanofiltration membranes. Desalination **405**, 29–39 (2017)
53. J. Gao, J. Zhu, J. Luo, J. Xiong, Investigation of microporous composite scaffolds fabricated by embedding sacrificial polyethylene glycol microspheres in nanofibrous membrane. Compos. A **91**, 20–29 (2016)
54. J. Farahbaksh, M. Delnavaz, V. Vatanpour, Investigation of raw and oxidized multiwalled carbon nanotubes in fabrication of reverse osmosis polyamide membranes for improvement in desalination and antifouling properties. Desalination **410**, 1–9 (2017)
55. X. Song, L. Wang, L. Mao, Z. Wang, Nanocomposite membrane with different carbon nanotubes location for nanofiltration and forward osmosis applications. ACS Sustain. Chem. Eng. **4**, 2990–2997 (2016)
56. J. Xuan, Z. Wang, Y. Chen, D. Liang, L. Cheng, X. Yang, Z. Liu, R. Ma, T. Sasaki, F. Geng, Organic-base-driven intercalation and delamination for the production of functionalized titanium carbide nanosheets with superior photothermal therapeutic performance. Angew. Chem. Int. Ed. **55**, 1–7 (2016)
57. K. Goh, W. Jiang, H. Karahan, S. Zhai, L. Wei, D. Yu, A. Fane, R. Wang, Y. Chen, All-carbon nanoarchitectures as high-performance separation membranes with superior stability. Adv. Func. Mater. **25**, 7348–7359 (2015)

58. Y. Zhang, H. Zhang, Y. Li, H. Mao, G. Yang, J. Wang, Tuning the performance of composite membranes by optimizing PDMS content and cross-linking time for solvent resistant nanofiltration. Ind. Eng. Chem. Res. **54**, 6175–6186 (2015)
59. X. Zhang, Y. Lv, H. Yang, Y. Du, Z. Xu, Polyphenol coating as an interlayer for thin-film composite membranes with enhanced nanofiltration performance. ACS Appl. Mater. Interfaces. **8**, 32512–32519 (2016)
60. S. Sun, S. Chan, W. Xing, Y. Wang, T. Chung, Facile synthesis of dual-layer organic solvent nanofiltration (OSN) hollow fiber membranes. ACS Sustain. Chem. Eng. **3**, 3019–3023 (2015)
61. Y. Su, C. Li, W. Zhao, Q. Shi, H. Wang, Z. Jiang, S. Zhu, Modification of polyethersulfone ultrafiltration membranes with phosphorylcholine copolymer can remarkably improve the antifouling and permeation properties. J. Membr. Sci. **322**, 171–177 (2008)
62. Q. Zhang, C. Deng, F. Soyekwo, Q. Liu, A. Zhu, Sub-10 nm wide cellulose nanofibers for ultrathin nanoporous membranes with high organic permeation. Adv. Func. Mater. **26**, 792–800 (2016)
63. X. Zhai, P. Zhang, C. Liu, T. Bai, W. Li, L. Dai, W. Liu, Highly luminescent carbon nanodots by microwave-assisted pyrolysis. Chem. Commun. **48**, 7955–7957 (2012)
64. Y. Sun, B. Zhou, Y. Lin, W. Wang, K.A. Shiral Fernando, P. Pathak, M. J. Meziani, B.A. Harruff, X. Wang, H. Wang, P.G. Luo, H. Yang, M.E. Kose, B. Chen, L. Monica Veca, S.Y. Xie. Quantum-sized carbon dots for bright and colorful photoluminescence. J. Am. Chem. Soc. **128**, 7756–7757 (2006)
65. J. Huang, M. Rong, M. Zhang, Preparation of graphene oxide and polymer-like quantum dots and their one-and two-photon induced fluorescence properties. Phys. Chem. Chem. Phys. **18**, 4800–4806 (2016)
66. S. Zhao, Y. Yao, C. Ba, W. Zheng, J. Economy, P. Wang, Enhancing the performance of polyethylenimine modified nanofiltration membrane by coating a layer of sulfonated poly (ether ether ketone) for removing sulfamerazine. J. Membr. Sci. **492**, 620–629 (2015)
67. Y. Hai, J. Zhang, C. Shi, A. Zhou, C. Bian, W. Li, Thin film composite nanofiltration membrane prepared by the interfacial polymerization of 1, 2, 4, 5-benzene tetracarbonyl chloride on the mixed amines cross-linked poly (ether imide) support. J. Membr. Sci. **520**, 19–28 (2016)
68. H. Zhang, H. Mao, J. Wang, R. Ding, Z. Du, J. Liu, Mineralization-inspired preparation of composite membranes with polyethyleneimine-nanoparticle hybrid active layer for solvent resistant nanofiltration. J. Membr. Sci. **470**, 70–79 (2014)
69. P. Marchetti, M.F. Jimenez Solomon, G. Solomon, A.G. Livingston, Molecular separation with organic solvent nanofiltration: a critical review. Chem. Rev. **114**, 10735–10806 (2014)
70. B. Liang, H. Wang, X. Shi, B. Shen, X. He, Z.A. Ghazi, N.A. Khan, H. Sin, A.M. Khattak, L. Li, Z. Tang, Microporous membranes comprising conjugated polymers with rigid backbones enable ultrafast organic-solvent nanofiltration. Nat. Chem. **10**, 961–967 (2018)
71. K.H. Thebo, X. Qian, Q. Zhang, L. Chen, H. Cheng, W. Ren, Highly stable graphene-oxide-based membranes with superior permeability. Nat. Commun. **9**, 1–8 (2018)
72. I. Gadwal, G. Sheng, R.L. Thankamony, Y. Liu, H. Li, Z. Lai, Synthesis of sub-10 nm two-dimensional covalent organic thin film with sharp molecular sieving nanofiltration. ACS Appl. Mater. Interfaces. **10**, 12295–12299 (2018)
73. J. Shi, D. Yang, Z. Jiang, Y. Jiang, Y. Liang, Y. Zhu, X. Wang, H. Wang, Simultaneous size control and surface functionalization of titania nanoparticles through bioadhesion-bssisted bio-ispired mineralization. J. Nanopart. Res. **14**, 1120 (2012)
74. R. Nadler, S. Srebnik, Molecular simulation of polyamide synthesis by interfacial polymerization. J. Membr. Sci. **315**, 100–105 (2008)
75. R. Oizerovich-Honig, V. Raim, S. Srebnik, Simulation of thin film membranes formed by interfacial polymerization. Langmuir **26**, 299–306 (2010)
76. V. Freger, Kinetics of film formation by interfacial polycondensation. Langmuir **21**, 1884–1894 (2005)
77. V. Freger, S. Srebnik, Mathematical model of charge and density distributions in interfacial polymerization of thin films. J. Appl. Polym. Sci. **88**, 1162–1169 (2003)

78. I.C. Kim, J. Jegal, K.H. Lee, Effect of aqueous and organic solutions on the performance of polyamide thin-film-composite nanofiltration membranes. J. Polym. Sci. B Polym. Phys. **40**, 2151–2163 (2002)
79. I.C. Kim, K.H. Lee, Preparation of interfacially synthesized and silicone-coated composite polyamide nanofiltration membranes with high performance. Ind. Eng. Chem. Res. **41**, 5523–5528 (2002)
80. Q. Zhang, S. Ghosh, S. Samitsu, X. Peng, I. Ichinose, Ultrathin freestanding nanoporous membranes prepared from polystyrene nanoparticles. J. Mater. Chem. **21**, 1684–1688 (2011)
81. X. Peng, J. Jin, Y. Nakamura, T. Ohno, I. Ichinose, Ultrafast permeation of water through protein-based membranes. Nat. Nanotechnol. **4**, 353–357 (2009)
82. Q. Yang, Y. Su, C. Chi, C.T. Cherian, K. Huang, V.G. Kravets, F.C. Wang, J.C. Zhang, A. Pratt, A.N. Grigorenko, F. Guinea, A.K. Geim, R.R. Nair, Ultrathin graphene-based membrane with precise molecular sieving and ultrafast solvent permeation. Nat. Mater. **16**, 1198–1202 (2017)
83. Z. Wang, Q. Tu, S. Zheng, J.J. Urban, S. Li, B. Mi, Understanding the aqueous stability and filtration capability of MoS_2 membranes. Nano Lett. **17**, 7289–7298 (2017)
84. X. Cheng, S. Ding, J. Guo, C. Zhang, Z. Guo, L. Shao, In-situ interfacial formation of TiO_2/polypyrrole selective layer for improving the separation efficiency towards molecular separation. J. Membr. Sci. **536**, 19–27 (2017)
85. X. Cheng, K. Konstas, C.M. Doherty, C.D. Wood, X. Mulet, Z. Xie, D. Ng, H.R. Hill, L. Shao, C.H. Lau, Hyper-cross-linked additives that impede aging and enhance permeability in thin polyacetylene films for organic solvent nanofiltration. ACS Appl. Mater. Interfaces **9**, 14401–14408 (2017)
86. X. Quan, Z. Xing, X. Jiang, T. Li, C. Hon, Z. Guo, J. Ma, L. Shao, Progress in materials science towards sustainable ultrafast molecular-separation membranes: from conventional polymers to emerging materials. Prog. Mater Sci. **92**, 258–283 (2018)
87. Z. Jiang, M. Nania, S. Karan, A.E. Porter, F. Foglia, J.T. Cabral, A.G. Livingston, R. Barker, Neutron reflectivity and performance of polyamide nanofilms for water desalination. Adv. Func. Mater. **27**, 1701738 (2017)
88. D.B. Shinde, G. Sheng, X. Li, M. Ostwal, A. Emwas, K. Huang, Z. Lai, Crystalline 2D covalent organic framework membranes for high-flux organic solvent nanofiltration. J. Am. Chem. Soc. **140**, 14342–14349 (2018)
89. S. Karan, S. Samitsu, X. Peng, K. Kurashima, I. Ichinose, Ultrafast viscous permeation of organic solvents through diamond-like carbon nanosheets. Science **335**, 444–447 (2012)
90. M. Emmrich, F. Huber, F. Pielmeier, J. Welker, T. Hofmann, M. Schneiderbauer, H. Ebert, Subatomic resolution force microscopy reveals internal structure and adsorption sites of small iron clusters. Science **348**, 308–311 (2015)
91. Y. Liu, K. Ai, L. Lu, Polydopamine and its derivative materials: synthesis and promising applications in energy, environmental, and biomedical fields. Chem. Rev. **114**, 5057–5115 (2014)
92. T.G. Barclay, H.M. Hegab, S.R. Clarke, M.G. Markovic, Versatile surface modifcation using polydopamine and related polycatecholamines: chemistry, structure, and applications. Adv. Mater. Interfaces **4**, 1601192–1601230 (2017)
93. L. Yu, Y. Zhang, B. Zhang, J. Liu, H. Zhang, C. Song, Preparation and characterization of HPEI-GO/PES ultrafiltration membrane with antifouling and antibacterial properties. J. Membr. Sci. **447**, 452–462 (2013)
94. M.J. Raaijmakers, N.E. Benes, Current trends in interfacial polymerization chemistry. Prog. Polym. Sci. **63**, 86–142 (2016)
95. Y.C. Chiang, Y.Z. Hsub, R.C. Ruaan, C.J. Chuang, K.L. Tung, Nanofiltration membranes synthesized from hyperbranched polyethyleneimine. J. Membr. Sci. **326**, 19–26 (2009)
96. H. Wu, X. Zhang, D. Xu, B. Li, Z. Jiang, Enhancing the interfacial stability and solvent-resistant property of PDMS/PES composite membrane by introducing a bifunctional aminosilane. J. Membr. Sci. **337**, 61–69 (2009)
97. F. Foglia, S. Karan, M. Nania, Z. Jiang, A.E. Porter, R. Barker, J.T. Cabral, Neutron reflectivity and performance of polyamide nanoflms for water desalination. Adv. Func. Mater. **27**, 1701738–2170174 (2017)

98. N.K. Saha, S.V. Joshi, Performance evaluation of thin film composite polyamide nanofiltration membrane with variation in monomer type. J. Membr. Sci. **342**, 60–69 (2009)
99. Y. Zhu, W. Xie, S. Gao, F. Zhang, W. Zhang, Z. Liu, J. Jin, Single-walled carbon nanotube film supported nanofiltration membrane with a nearly 10 nm thick polyamide selective layer for high-flux and high-rejection desalination. Small **12**, 5034–5041 (2016)
100. J.R. Werber, C.O. Osuji, M. Elimelech, Materials for next-generation desalination and water purification membranes. Nat. Rev. Mater. **1**, 16018–16034 (2016)
101. H.B. Park, J. Kamcev, L.M. Robeson, M. Elimelech, B.D. Freeman, Maximizing the right stuff: the trade-off between membrane permeability and selectivity. Science **356**, eaab0530 (2017)
102. G. Chen, H. Zhu, Y. Hang, Q. Liu, G. Liu, W. Jin, Simultaneously enhancing interfacial adhesion and pervaporation separation performance of PDMS/ceramic composite membrane via a facile substrate surface grafting approach. AIChE J. **65**, e16773 (2019)
103. M.R. Chowdhury, J. Steffes, B.D. Huey, J.R. McCutcheon, 3D printed polyamide membranes for desalination. Science **361**, 682–686 (2018)
104. B. Huang, Y. Tang, Z. Zeng, Z. Xu, Microwave heating assistant preparation of high permselectivity polypiperazine-amide nanofiltration membrane during the interfacial polymerization process with low monomer concentration. J. Membr. Sci. **596**, 117718 (2020)
105. S.H. Maruf, A.R. Greenberg, Y. Ding, Influence of substrate processing and interfacial polymerization conditions on the surface topography and permselective properties of surface-patterned thin-film composite membranes. J. Membr. Sci. **512**, 50–60 (2016)
106. S. Wang, Y. Wu, N. Zhang, G. He, Q. Xin, X. Wu, H. Wu, X. Cao, M.D. Guiver, Z. Jiang, A highly permeable graphene oxide membrane with fast and selective transport nanochannels for efficient carbon capture. Energy Eng. Sci. **9**, 3107–3112 (2016)
107. X. Cui, X. Wu, J. Zhang, J. Wang, H. Zhang, F. Du, L. Qu, X. Cao, P. Zhang, A loosely stacked lamellar membrane of irregular MoS_2 flakes for ultrahigh water and organics permeation. J. Mater. Chem. A **7**, 12698–12705 (2019)
108. B. Li, W. Liu, Z. Jiang, X. Dong, B. Wang, Y. Zhong, Ultrathin and stable active layer of dense composite membrane enabled by poly(dopamine). Langmuir **25**, 7368–7374 (2009)
109. X. You, H. Wu, R. Zhang, Y. Su, L. Cao, Q. Yu, J. Yuan, K. Xiao, M. He, Z. Jiang, Metal-coordinated sub-10 nm membranes for water purification. Nat. Commun. **10**, 4160 (2019)
110. P. Silva, S. Han, A.G. Livingston, Solvent transport in organic solvent nanofiltration membranes. J. Membr. Sci. **262**, 49–59 (2005)
111. X. You, H. Wu, Y. Su, J. Yuan, R. Zhang, Q. Yu, M. Wu, Z. Jiang, X. Cao, Precise nanopore tuning for a high-throughput desalination membrane via co-deposition of dopamine and multifunctional POSS. J. Mater. Chem. A **6**, 13191–13202 (2018)
112. T. Gao, H. Wu, L. Tao, L. Qu, C. Li, Enhanced stability and separation efficiency of graphene oxide membranes in organic solvent nanofiltration. J. Mater. Chem. A **6**, 19563–21956 (2018)
113. M.H. Farahani, D. Hua, T.S. Chung, Cross-linked mixed matrix membranes (MMMs) consisting of amine-functionalized multi-walled carbon nanotubes and P84 polyimide for organic solvent nanofiltration (OSN) with enhanced flux. J. Membr. Sci. **548**, 319–331 (2018)
114. V.E. Reinsch, A.R. Greenberg, S.S. Kelley, R. Peterson, L.J. Bond, A new technique for the simultaneous, real-time measurement of membrane compaction and performance during exposure to high-pressure gas. J. Membr. Sci. **171**, 217–228 (2000)
115. H. Mahdavi, A. Rahimi, Zwitterion functionalized graphene oxide/polyamide thin film nanocomposite membrane: towards improved anti-fouling performance for reverse osmosis. Desalination **433**, 94–107 (2018)

Chapter 3
Lamellar Membrane for Organic Solvent Nanofiltration

Xiaoli Wu, Yifan Li, and Jingtao Wang

3.1 Introduction

In recent years, two-dimensional lamellar membranes featuring the properties of highly selective permeation are promising for organic solvent nanofiltration (OSN) [1–3]. Graphene-based 2D materials, especially graphene oxide (GO) with the virtues of single-atomic thickness, plentiful oxygen-containing functional groups, and outstanding chemical stability, have become the candidate for lamellar membranes [4–6]. As an example, Shi et al. found that GO membrane was stable in most organic solvents, and the permeation of solvent was tunable by adjusting the size of nanochannels and the properties of membrane surface [7]. In addition, Nunes embedded in suit scattered sub-5 nm silica nanoparticles in the GO nanochannels to prepare GO membrane with alternating dual-spacing nanochannels. This membrane achieved high permeance and satisfactory dye rejection [8]. However, it is a great challenge that membranes achieve high permeation and precise sieving simultaneously [9–11]. Meanwhile, GO membranes are generally unstable in solvents due to the weak interaction between adjacent GO nanosheets [12]. This causes the GO membrane to swell or even disintegrate in the operating environment [13]. Therefore, how to overcome the defects of GO membranes and improve the performance have become urgent problems to be solved at present.

Therefore, researchers dedicate to improving the performance of membranes by various strategies [14–17]. On the one hand, the surface functionalization strategy provides a new pathway to solve the poor rejection and mechanical stability by maintaining the inner lamellar structure of membranes [14]. Primarily, hydrophilic/hydrophobic heterostructured lamellar membranes which were prepared

X. Wu · Y. Li · J. Wang (✉)
School of Chemical Engineering, Zhengzhou University, Zhengzhou 450001, P. R. China
e-mail: jingtaowang@zzu.edu.cn

X. Wu · J. Wang
Henan Institute of Advanced Technology, Zhengzhou University, Zhengzhou 450003, P. R. China

J. Wang and W. Wu (eds.), *Functional Membranes for High Efficiency Molecule and Ion Transport*, https://doi.org/10.1007/978-981-19-8155-5_3

by patterning functional polymer clusters onto membrane surface with adverse wettability were reported [18]. This novel heterostructured membrane achieved high molecule permeation and precise sieving. On the other hand, intercalating nanoparticles or macromolecular to enlarge the channel size can effectively decrease transport resistance. We report a graphene-based hybrid membrane utilizing the insertion of QDs in nanochannels to manipulate the microenvironment, significantly enhancing the nanofiltration performance [19]. These hydrophobic sites and hydrophilic regions allow both non-polar and polar solvents to dissolute into the membrane, whereas the enlarged nanochannel size promotes them to diffuse rapidly. In particular, the permeance of acetone reaches 173.5 L m^{-2} h^{-1} bar^{-1}, and that for n-hexane achieves 85.4 L m^{-2} h^{-1} bar^{-1}, which are 500% higher than primary GO membranes. Besides, ultrathin and stable organic–inorganic lamellar composite membranes are successfully prepared through dual-needle electrostatic atomization strategy [20]. This strategy utilizes thermal cross-linking of GO nanosheets and PEI polymer chains to achieve high structure, pressure, and operation stabilities.

Recently, MXene nanosheets (e.g., $Ti_3C_2T_x$) and MoS_2 nanosheets with large lateral size and rigidity have been elected to be prospective as the building block for constructing lamellar membranes [15–17, 21]. In recent years, Wang and co-workers successfully synthesized small-sized $Ti_3C_2T_x$ nanosheets to prepare $Fe(OH)_3$-intercalated lamellar membrane, reaching a high permeance (> 1000 L m^{-2} h^{-1} bar^{-1}) for water. This membrane possessed irregular nanochannels with widths of 2 ~ 5 nm, impeding the further improvement of permeation and rejection performance [15]. Next, the authors prepared larger-sized nanosheets by improving the synthesis method. The large nanosheets could construct regular nanochannels (~ 0.3 nm), reaching a remarkable high permeance and gas separation [22]. It is noted that ordered interlayer nanochannels and stable molecule transport are the requirements for high permeation. However, the molecule transport mechanism and relationship between physical parameter and permeance remain equivocal, and the quantitative model equations for describing molecule permeation under various conditions have not been established [21]. Here, we report an MXene lamellar membrane constructed by rigid, double-layered, and large-sized $Ti_3C_2T_x$ nanosheets with straight and regular inner nanochannels [23]. More importantly, the molecule transport mechanism through nanochannels is explored, and corresponding model equations that correspond to molecules with ordered and disordered configuration have been established for guiding the design of advanced lamellar membranes.

Furthermore, the MXene nanosheets are post-modified chemically by hydrophilic ($–NH_2$) and hydrophobic ($–C_6H_5$, $–C_{12}H_{25}$) functional groups to adjust nanochannel microenvironment [24]. Molecular dynamics (MD) simulations and experimental data certify that hydrophilic nanochannels ($–NH_2$) can form a strong interaction to polar molecules, thus inducing their alignment in order to form molecular aggregates. This study elucidates the ultrafast molecular penetration of two-dimensional layered membrane with nanochannels. This allows the aggregates to transfer in an ultrafast parallel way at high capillary pressures, achieving ultrahigh acetonitrile and methanol permeance of 3337 and 3018 L m^{-2} h^{-1} bar^{-1}, respectively. They are 2.8 and 3.8 times higher than that of hydrophobic nanochannels with disordered molecule

configuration, respectively. More importantly, molecules with different arrangement patterns show different transport mechanisms and molecule transfer model equations. In addition, by adjusting the interaction of adjacent nanosheets, the channel size changes slightly within angstroms scale, thus allowing precise molecule selectivity. These findings pave a way to the design of advanced separation materials with highly efficient mass transport.

3.2 Lamellar $Ti_3C_2T_x$ Membrane

TiC, TiH_2, and Al were evenly mixed in a molar ratio of 2:1:1.2 and then ball milled for 12 h. The mixture was placed in a porcelain boat and heated to 1450 °C for 2 h under flowing argon at a fixed heating rate of 10 °C min^{-1}. The obtained product ($Ti_3C_2T_x$) was ground into powder with a lateral size < 35 μm. Then, the $Ti_3C_2T_x$ powder (9.0 g) and aqueous HF (43 wt%, 150 mL) were stirred vigorously for 72 h under the temperature of 55 °C. The product (multilayer $Ti_3C_2T_x$) was washed with water to reach a neutral state. The delaminated $Ti_3C_2T_x$ was prepared by solvent intercalation and ultrasonic-assisted exfoliation methods. Particularly, the obtained $Ti_3C_2T_x$ (5.0 g) was dispersed in dimethyl sulfoxide solution (100 mL) and stirred for 48 h, and then the dispersion was centrifuged at 3000 rpm for 10 min to obtain $Ti_3C_2T_x$ power. Then, $Ti_3C_2T_x$ was added into water and sonicated for 20 min under N_2 atmosphere, and then, the solution was centrifuged at 2000 rpm for 0.5 h to obtain black supernatants for membrane preparation (Fig. 3.1).

Lamellar membranes were obtained by vacuum filtration of nanosheet dispersion onto a Nylon support. To improve the affinity between Nylon support and nanosheets, the Nylon support was pre-treated using dopamine aqueous solution (2 mg mL^{-1}) with 10 mM *tris*–HCl for 4 h to deposit a polydopamine (PDA) layer. Here, a certain

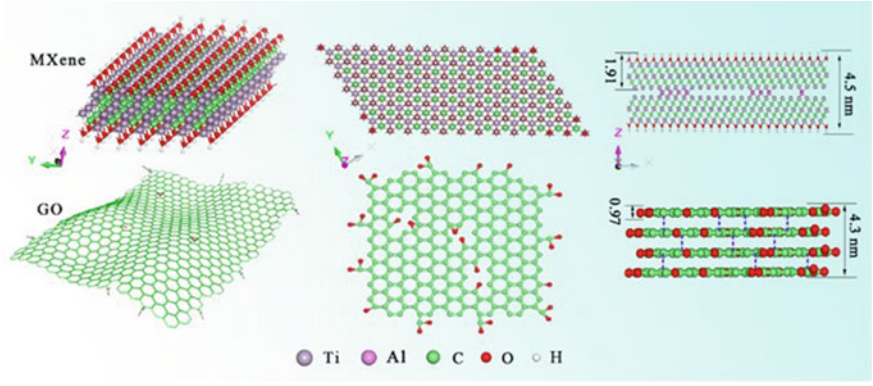

Fig. 3.1 Crystal structures of MXene and GO. Copyright (2018), John Wiley and Sons [23]

amount of MXene and GO nanosheet dispersion were then filtrated on the pre-treated Nylon support to prepare MXene and GO lamellar membranes, respectively. Subsequently, the resulted membranes were then immediately immersed in solvents to maintain a solvated state. And, the membranes with distinct thicknesses were obtained by controlling nanosheet loading. Moreover, to reduce the surface roughness of Nylon support, $Cd(OH)_2$ nanostrands were used to build sacrificial layer. In detail, the $Cd(OH)_2$ nanostrands were prepared by reacting $CdCl_2$ and 2-aminoethanol with equal volumes in dilute aqueous solutions. Subsequently, the nanostrand solution was filtrated on Nylon support to construct a smooth platform and the nanosheet dispersion was then stacked to build lamellar membranes. Then, dilute HCl solution was used to remove $Cd(OH)_2$ nanostrands and regular lamellar membrane was finally prepared.

$Ti_3C_2T_x$ nanosheets were prepared by etching Al layer of $Ti_3C_2T_x$ using hydrogen fluoride (HF) solution. To synthesize rigid $Ti_3C_2T_x$ nanosheets, a soft-etching low-power sonication procedure with a low concentration HF solution was performed for partial exfoliation. Scanning electron microscopy (SEM, Fig. 3.2a) and atomic force microscopy (AFM, Fig. 3.3a) images confirm that the $Ti_3C_2T_x$ nanosheet possesses typical sheet structure with a lateral size of > 3 μm and thickness of 4.5 nm. Considering the theoretical thickness of monolayer is 1.91 nm, the as-prepared $Ti_3C_2T_x$ nanosheets are mainly double-layered and bonded by intermittent Al layer. This can also be further proved by the energy dispersive spectroscopy (EDS) mapping of the amount of Al (31%) after etching (Fig. 3.2d). Transmission electron microscopy (TEM) image shows that MXene nanosheets display smooth nanosheet surface, confirming that the $Ti_3C_2T_x$ nanosheets have sufficient rigidity and free-standing morphology in SEM image (Fig. 3.2b). Besides, HRTEM image shows that the Ti layer of $Ti_3C_2T_x$ nanosheet surface displays clear lattice fringes and possesses rich hydroxyl and epoxy groups (Fig. 3.2c and e). For comparison, multilayer GO nanosheets were prepared by a comparable low-power ultrasonic procedure to enable an analogous morphology with $Ti_3C_2T_x$ nanosheets, such as micron-scale lateral size and a similar thickness of 4.3 nm (Fig. 3.3b) [25].

Next, low-pressure filtration procedure was used to ensure the uniform nanosheet stacking (MXene, GO) and regular lamellar structure is constructed as shown in Fig. 3.4a. Resulted membranes were then immersed in the tested solvents to maintain a solvated state. And, they were named as MXene-*X* and GO-*X*, respectively, where *X* represents the thickness of lamellar membranes. The image of SEM displays that lamellar membranes have smooth surface without detectable pinholes or cracks. HR-SEM image further indicates that the MXene membrane possesses typical lamellar structure with clear interlayer spacing (Fig. 3.4a and b).

X-ray diffraction (XRD) was used to investigate the regular degree of interlayer nanochannels in lamellar membrane [26]. To avoid the influence of Nylon support, amorphous anodic aluminum oxide (AAO) was utilized to prepare lamellar membranes for XRD detection [15]. The results are shown in Fig. 3.5a, a sharp diffraction peak at $2\theta = 12.9°$ is observed under solvated conditions for the MXene membrane, which is different from the intrinsic diffraction peak of the material ($2\theta = 9.4°$). In addition, the strong peak displays only slight broadening and intensity

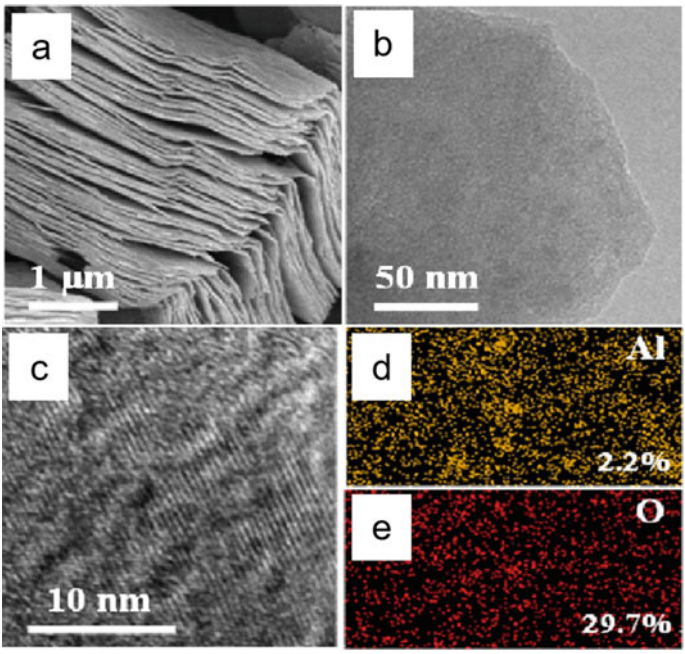

Fig. 3.2 **a** SEM, **b** TEM and **c** high-resolution TEM images of $Ti_3C_2T_x$. Elemental maps of **d** Al and **e** O for $Ti_3C_2T_x$. Copyright (2018), John Wiley and Sons [23]

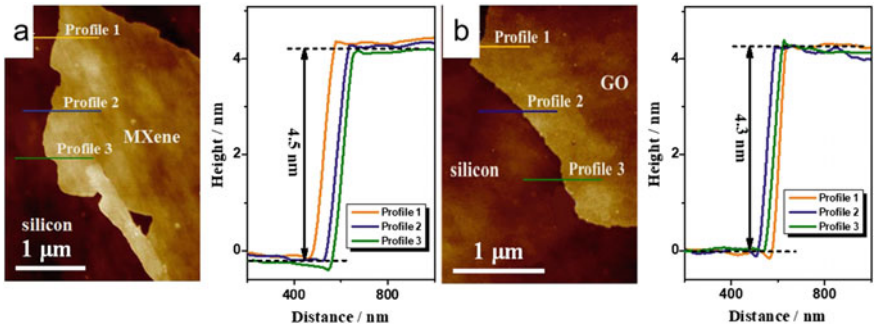

Fig. 3.3 AFM image (left side) and the corresponding height profiles (right side) of **a** MXene and **b** GO nanosheets. Copyright (2018), John Wiley and Sons [23]

enhancement during dehydration and rehydration processes. And, the characteristic peaks of MXene membrane in organic solvents and solvent evaporation are comparable to those in water (Fig. 3.5a), highlighting the rigid MXene nanosheet structure and regular interlayer nanochannels.

The bending test of free-standing membrane further proves that straight nanosheet form regular nanochannels, where MXene membrane gives much lower elongation

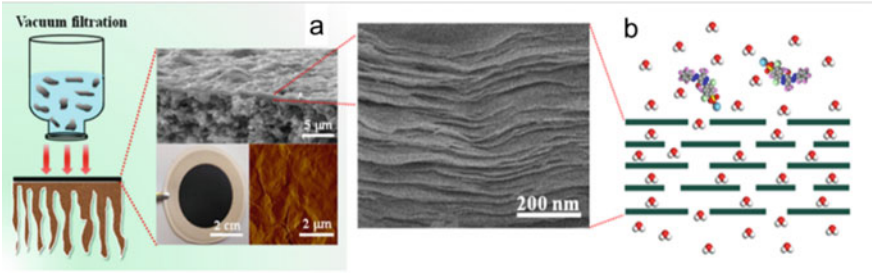

Fig. 3.4 **a** Schematic illustration of preparation for MXene lamellar membrane and the corresponding cross-sectional SEM, photo of real figure, and surface AFM image. **b** Schematic illustration of molecule through lamellar membrane. Copyright (2018), John Wiley and Sons [23]

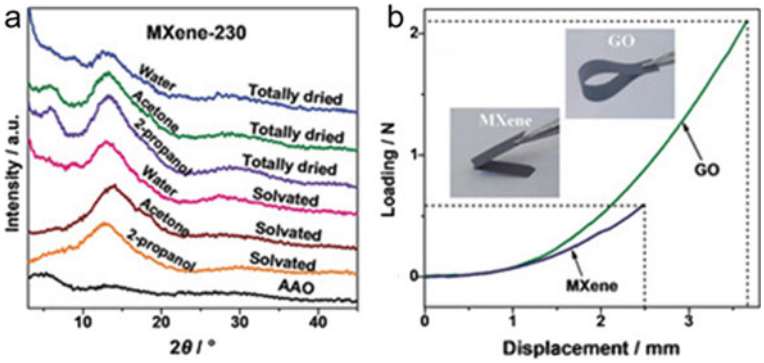

Fig. 3.5 **a** XRD patterns of MXene-230 membrane in different solvents (water, acetone, 2-propanol) and fully dried state. **b** The bending loading-displacement and the corresponding real figures of MXene and GO membranes. Copyright (2018), John Wiley and Sons [23]

at the break point than GO membrane (Fig. 3.5b). Importantly, the nanosheets are stacked directly to form natural nanochannels in this study, further indicating the superiority of rigid nanosheets during their stacking into desired regular and robust nanochannels.

The permeance of lamellar membrane was evaluated on the homemade device. Figure 3.6a reveals that the MXene-230 membrane shows an unparalleled water permeance of 2302 L m^{-2} h^{-1} bar^{-1}, surpassing that of the GO-210 membrane (257 L m^{-2} h^{-1} bar^{-1}) by more than 9 times. Even after dehydration and rehydrated, MXene-230 still displays ultrahigh water permeance of 1703 L m^{-2} h^{-1} bar^{-1}, which is enhanced by 12.2 times as compared to that of GO-230 membrane (129 L m^{-2} h^{-1} bar^{-1}). To obtain the permeation parameter (K') of water in MXene and GO membranes, water permeance is correlated with membrane thickness through Darcy's law [27]. The results are shown in Fig. 3.6b, the K' value of $10^{-8.5}$ for MXene membrane is more than five orders of magnitude higher than that of GO membrane

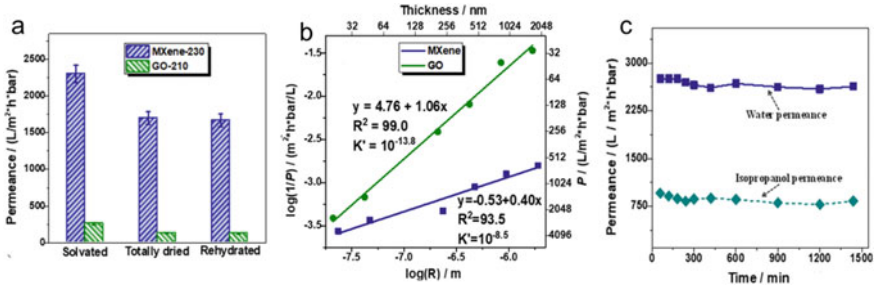

Fig. 3.6 **a** Water permeance in different states of MXene and GO membranes. **b** Water permeance against the membrane thickness. **c** Long-time operation performance of MXene-230 membrane in water and isopropanol. Copyright (2018), John Wiley and Sons [23]

($10^{-13.8}$), highlighting the ultrafast transfer feature of robust nanochannels. Considering the significant effect of small perturbations on water-bonded flow [28], the robust and regular nanochannels are critical to efficient and low-barrier molecular transfer. The robust nanochannels also confer stable molecular permeance, such as the permeance change of MXene membrane is less than 5% during the long-term operation process (1500 min).

Next, the transfer behavior of molecules through MXene membrane is studied by seven common solvents in industry. Results show that MXene-230 membrane gives an unparalleled ultrahigh permeance of > 5000 L m^{-2} h^{-1} bar^{-1} for polar acetonitrile and acetone. And, methanol achieves the third highest permeance (3563 L m^{-2} h^{-1} bar^{-1}). Meanwhile, other solvents also display excellent performance: 1916, 1616 and 983 L m^{-2} h^{-1} bar^{-1} for ethanol, dimethylformamide, and 2-propanol, respectively. Note that the same order of solvent permeance (from 3443 to 627 L m^{-2} h^{-1} bar^{-1}) is observed for MXene-470 membrane.

Four common dye molecules in industry with different sizes were used to evaluate nanochannel width of MXene membrane. The UV–Vis absorption spectra display that MXene-230 gives perfect rejection for acid yellow 79 (AY79, 2.8 nm) (Fig. 3.7b), while the rejection is only 32% for helianthin B (1.2 nm). Moreover, MXene membrane could only reject about half of acid yellow 14 (AY 14) with size of 1.9 nm. When the molecule size is increased to 2.0 nm (reactive black, RB), the nanochannels can sieve out almost all dyes with rejection rate of 96%. For much larger dye molecule, the rejection achieves almost 100%. Here, considering the influence of dye adsorption and electrostatic interaction, negatively charged dye molecules are used to filter through lamellar membranes. And, these interactions can promote rejection to a certain extent (< 3%). But the rejection mechanism is mainly derived from size sieving [29]. It is reasonable to deduce that the nanochannel width of MXene membrane is concentrated at about 2 nm with a narrow distribution. The nanochannels assembled by rigid MXene nanosheets are more regular than most of the reported interlayer nanochannels assembled by flexible nanosheets [30, 31]. These regular and stable interlayer nanochannels are usually achieved through the crystalline pores of metal–organic framework and zeolite membranes [32], enabling

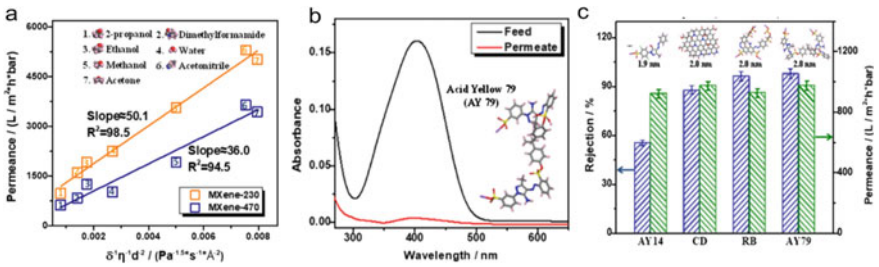

Fig. 3.7 **a** Solvent permeance as a function of solvent physical parameters for MXene-230 and MXene-470 membranes. **b** The UV–Vis absorption spectra of AY79 dye through MXene-230 membrane. **c** Dye rejection and the corresponding solvent permeance of MXene-230 molecules. Copyright (2018), John Wiley and Sons [23]

the application of assembled nanochannels as sieve path for gas, solvents, ions, and so on.

In Fig. 3.7a, we propose a phenomenological transport rate model according to the relationship for the permeance (P_s) of liquids with their physical parameters: $P_s = K/\delta_s \cdot \eta_s \cdot {d_s}^2$, where K, δ_s, η_s, and d_s represent proportionality constant ($bar^{0.5} \cdot Å^3$), solubility parameter ($Pa^{0.5}$), viscosity (mPa s), and molar diameter (Å), respectively. This model describes well molecule transfer in MXene-230 and MXene-470 membranes. The interesting thing is that this equation can only be established for membranes with robust and regular nanochannels. This model not only displays a quantitative relationship between solvent physical parameters and permeance, but clarifies the controversial conclusions reported so far for molecule transport in confined nanochannels [13]. Note that a comparable model has been established for uniform free-volume transfer path in thin polymers membranes: $P_s = K \cdot \delta_s / \eta_s \cdot {d_s}^2$ [33, 34]. This reveals that the physical properties of the molecule all influence the solvent transfer rate, while the function of δ_s is different. The inverse proportion relation between P_s and δ_s for MXene lamellar membranes should derive from the novel transfer behavior in regular nanochannels.

Considering that the molecule tends to form concerted orientations through intermolecular bonds in confined spacing, the MXene nanochannels with sub-2 nm may contain 4 ~ 5 layers of bonded monolayers. This continuous and stable fluid then leads to ultrafast molecular transfer under the function of capillary-like pressure and cohesive energy. This is the essential reason why low solubility (low friction force) favors molecular slip.

In a word, double-layered rigid $Ti_3C_2T_x$ MXenes were prepared by soft-etching low-power sonication methods and then as building blocks to assemble lamellar membranes. The rigid nanosheets ensure the formation of regular and straight nanochannels through a low-pressure vacuum filtration. Resulted nanochannels exhibit unparalleled molecule permeation and precise dye rejection. The permeance of water and organic acetone achieves about 2300 and 5000 L m^{-2} h^{-1} bar^{-1}, respectively, 2 and 20 times higher than that of reported lamellar membranes with similar rejection. Importantly, the molecule transfer mechanism is revealed, and the

corresponding equations are also established for 2D confined regular nanochannels. And, the establishment of equation clarifies the controversial conclusions of molecule transfer in confined nanochannels. The construction of regular nanochannels provides guidance for the design of efficient mass transfer lamellar membranes.

3.3 Lamellar Functionalized-$Ti_3C_2T_x$ Membrane

The modification procedure of $Ti_3C_2T_x$ (take amino modification as example): Firstly, to activate the surface hydroxyl groups of $Ti_3C_2T_x$, the $Ti_3C_2T_x$ and diluted HCl solution (1:1.39, m_{HCl}/m_{water}) were mixed at 25 °C and stirred for 6 h. The obtained product was washed with water until close to neutral. Then, the $Ti_3C_2T_x$ solution was added to methanol with volume ratio of 1:10 and stirred at a constant speed for 2 h. A certain amount of APTES was dispersed into methanol of 25 mL under 110 °C, and then refluxed for 2 h under argon. Next, to remove the unreacted APTES, the amino modified $Ti_3C_2T_x$ solution was centrifuged at 5000 rpm for 10 min and redispersed in water for the preparation of lamellar membranes. Likewise, DCTES and MATES were utilized to graft dodecyl and phenyl groups onto the $Ti_3C_2T_x$ surface, which were designed as $Ti_3C_2T_x$-$C_{12}H_{25}$ and $Ti_3C_2T_x$-C_6H_5, respectively. And, they were dispersed into n-hexane for membrane preparation (Fig. 3.8).

Lamellar membranes were prepared by assembling nanosheets on Nylon support. To achieve high-quality lamellar membrane, the $Ti_3C_2T_x$ or $Ti_3C_2T_x$-*X* dispersion solution was diluted. Resulted membranes were then immersed in solvents (water, acetone, methanol, and so on) to maintain a solvated state, and the membrane thickness can be regulated by controlling the nanosheet loading.

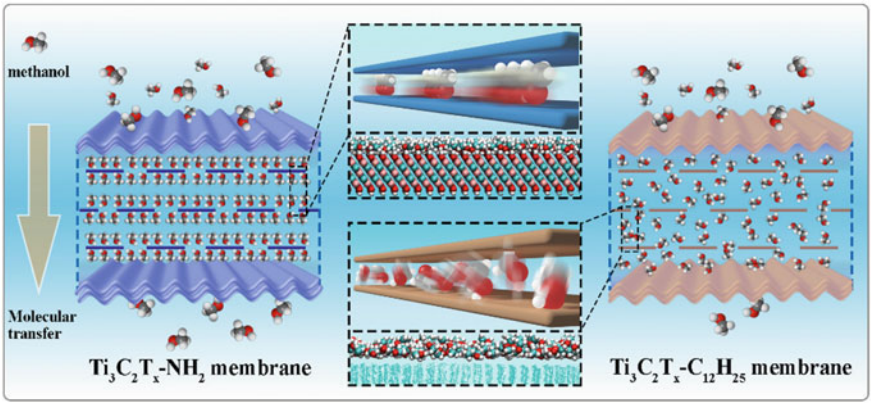

Fig. 3.8 Schematic diagram of molecule transfer through lamellar membranes. Copyright (2019), John Wiley and Sons [24]

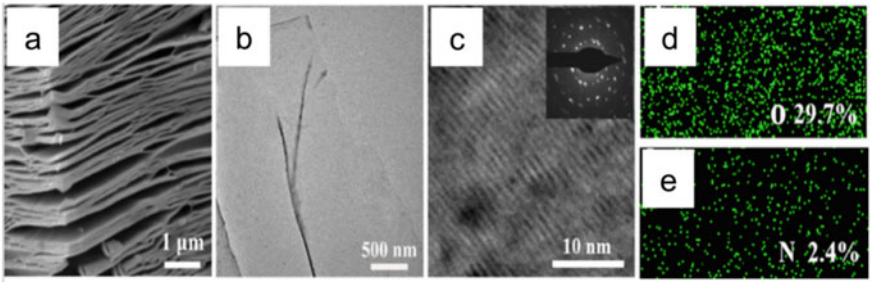

Fig. 3.9 Characterization of $Ti_3C_2T_x$ nanosheet. **a** SEM image of $Ti_3C_2T_x$ power. **b** TEM and **c** high-resolution TEM images of $Ti_3C_2T_x$ nanosheets. The elemental mappings of **d** O for $Ti_3C_2T_x$ nanosheet, and **e** N for $Ti_3C_2T_x$-NH_2 nanosheet. Copyright (2019), John Wiley and Sons [24]

The monolayer nanosheets with large lateral size and abundant hydroxyl groups were preapred by a moderate etching method. As shown in Fig. 3.9a and b, resulted nanosheets possess smooth surface and rigid structure properties with large lateral size of about 3 μm. And, the aboundant and uniform hydroxyl groups can also be directly proved by high oxygen ratio of 29.7% (Fig. 3.9d). This further confirms that moderate etching process ensures the typical nanosheet structure and clear lattice fringes of Ti layer on nanosheet surface (Fig. 3.9c).

Functionalized nanosheets with $–NH_2$, $–C_6H_5$, $–C_{12}H_{25}$ groups were named as $Ti_3C_2T_x$-NH_2, $Ti_3C_2T_x$-C_6H_5, $Ti_3C_2T_x$-$C_{12}H_{25}$, respectively. Note that modification process ensures well nanosheet structure and uniform group distribution. This can be further indicated by smooth nanosheet surface and uniform elemental distribution (Fig. 3.9e). Meanwhile, the charge characteristics and wettability are efficiently regulated.

Low pressure filtration imparts well membrane structure. This can be proved by smooth surface without detectable cracks and regular nanochannnels (Fig. 3.10a and b). The regularity of nanochannels is primarily derived from the nanosheet rigidity. And, sharp peak of (002) membrane with distinct wettability further indicates the order of nanochannels. Moreover, XRD patterns show a slight change of nanochannel size due to electrostatic interaction of adjacent nanosheets. For instance, the raw $Ti_3C_2T_x$ membrane shows a strong interlayer peak of 6.5° and the corresponding channel size is 1.38 nm, while the nanochannel size increases to 1.51 and 1.66 nm for $Ti_3C_2T_x$-$C_{12}H_{25}$ and $Ti_3C_2T_x$-C_6H_5 membranes, respectively. In contrast, the $Ti_3C_2T_x$-NH_2 nanochannel size is reduced to 1.28 nm. Considering the strong negative potential of original $Ti_3C_2T_x$ nanosheets, the enlargement of the nanochannel size should come from stronger electrostatic repulsion of adjacent nanosheets. After modifying the $–NH_2$ groups, the electrostatic repulsion of interlayer channels drops and then reduces nanochannle size.

The precise dye rejection further proofs nanochannel regularity and size difference of lamellar membranes (Fig. 3.11a) [16]. Considering the slightly enhanced rejection of membrane surface due to electrostatic repulsion, the dye rejection mainly depends

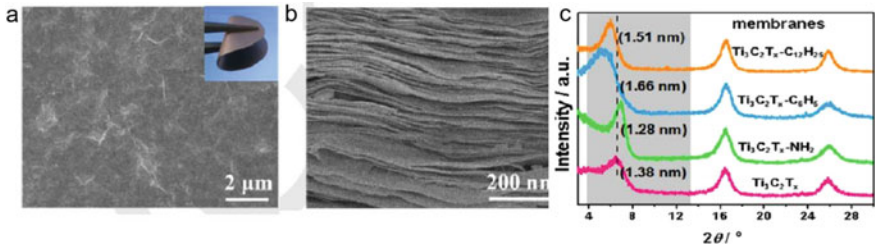

Fig. 3.10 Proofs for the membrane integrity and channel regularity. **a** SEM surface (inset: the photo of membrane), and **b** cross-sectional SEM images for $Ti_3C_2T_x$-NH_2 membrane. **c** XRD patterns of different function membranes. Copyright (2019), John Wiley and Sons [24]

on the size sieving mechanism. The rejection results are shown in Fig. 3.11a, $Ti_3C_2T_x$-NH_2 membrane can only reject 73% of the dye molecule with size of 1.2 nm (methyl orange, MO). When the size of dyes is slightly increased to 1.3 nm, the rejection rate can achieve 92% (methylene blue, MnB). For larger dye, it can almost reach 100% and separate reactive black (RB, 2.0 nm) from mixed solution with MO. By contrast, the nanochannel sizes are 1.4, 1.5, and 1.7 nm for $Ti_3C_2T_x$, $Ti_3C_2T_x$-$C_{12}H_{25}$, and $Ti_3C_2T_x$-C_6H_5 membranes, respectively, highlighting the tunable nanochannel sizes.

It is well known that weak nanochannel–molecule interactions between polar solvent and hydrophobic nanochannel usually display low frictional resistance and high solvent penetration [35, 36]. Therefore, higher transfer efficiency should be the main factor for ultrahigh permeance. As shown in Fig. 3.11b, the permeation parameter (K) of $10^{-6.7}$ for hydrophilic nanochannel is more than two orders of magnitude higher than that of hydrophobic nanochannel ($10^{-8.9}$). And, the polar molecules show higher diffusion coefficient (D) in hydrophilic nanochannels than that in hydrophobic nanochannels (Fig. 3.11c). For instance, $Ti_3C_2T_x$ nanochannels achieve over 2 times higher D for methanol than in $Ti_3C_2T_x$-$C_{12}H_{25}$ nanochannels. These phenomena show that the microenvironment of nanochannel, that is nanochannel–molecule interactions, significantly affect molecule alignment, thus affecting molecule transfer efficiency in two-dimensional confined nanochannels. To prove our conjecture, a

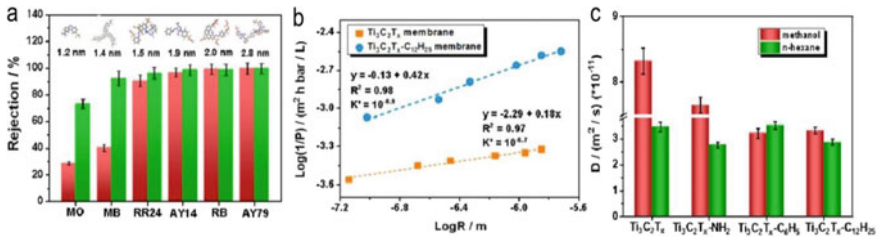

Fig. 3.11 **a** Dye rejection with vrious sizes for $Ti_3C_2T_x$-NH_2 (green) and $Ti_3C_2T_x$-$C_{12}H_{25}$ (pink) membranes. **b** Methanol permeance against membrane thickness of $Ti_3C_2T_x$ and $Ti_3C_2T_x$-$C_{12}H_{25}$. **c** Diffusion coefficient of polar methanol and non-polar n-hexane for distinct membranes. Copyright (2019), John Wiley and Sons [24]

heterogeneous membrane with hydrophobic $Ti_3C_2T_x$-$C_{12}H_{25}$ surface and hydrophilic $Ti_3C_2T_x$ inner nanochannels is prepared to avoid the effects of the dissolution process on molecule permeantion. Results show that $Ti_3C_2T_x$-$C_{12}H_{25}$/$Ti_3C_2T_x$ membrane achieves more than 20% enhancement of methanol permeance than through $Ti_3C_2T_x$-$C_{12}H_{25}$ membranes. This is probably due to the change in molecular configuration from initial disordered state to ordered state, corresponding to hydrophobic and hydrophilic nanochannels, respectively.

To further prove this point, molecular dynamic simulations were performed to demonstrate molecular configuration changes. The results are shown in Fig. 3.12a1, polar methanol molecules in $Ti_3C_2T_x$ nanochannels form an oriented and stable aggregation state. Considering that interaction energy is the sum of Lennard–Jones interactions and short-range interactions, the interaction energy of channel wall with molecule is used to reveal the origin of molecular arrangement (Fig. 3.12d). The results display that high channel–molecule interaction energy (–35.4 kJ mol^{-1}) induces methanol to form ordered molecule layer, and the second layer methanol molecules are also further induced to stay near the surface of first methanol layer. These ordered molecule layers can effectively reduce collisions of molecule–molecule and molecule–channel wall. This transfer behavior is comparable to "molecule-wire" of water in nanotubes, endowing strong cohesive energy among molecules and then driving molecule diffusion fast in hydrophilic nanochannels. Moreover, subnanometer channels provide extremely high capillary forces, promoting the parallel transfer of orderly aligned aggregate along the channel wall and then achieving ultrafast molecule transfer. Similarly, $Ti_3C_2T_x$-NH_2 nanochannels with moderate interaction energy (–23.8 kJ mol^{-1}) also endow orderly aligned molecule (Fig. 3.12b1). In contrast, weak channel–molecule interactions (low interaction energy) fail to drive molecules into ordered state, and then lead to lower solvent permeance. For instance, Fig. 3.12c1 shows that $Ti_3C_2T_x$-$C_{12}H_{25}$ nanochannel displays a disordered molecule configuration, and this state is similar to solvents in the bulk phase. Note that the average location of methanol molecule is further away from the $Ti_3C_2T_x$-$C_{12}H_{25}$ nanochannel surface as compared to $Ti_3C_2T_x$ nanochannel. This is due to repulsion effect between hydrophobic nanochannel and polar molecule and weak interaction energy (–2.4 kJ mol^{-1}). Meanwhile, as expected, the $Ti_3C_2T_x$, $Ti_3C_2T_x$-NH_2, and $Ti_3C_2T_x$-$C_{12}H_{25}$ nanochannels give disordered aligned of non-polar n-hexane (Fig. 3.12a2, b2, and c2). Comparing with polar solvents, non-polar solvents with uniformly dispersed state could possess excellent chemical structure stability, thus bringing weak channel–molecule interactions. The disordered aligned molecules maintain their arbitrary motion in all directions, which results in violent collisions of molecule–molecule and molecule–channel walls. And, the violent collisions significantly reduce molecule transfer rate and induce some molecules to move in the opposite direction from the main flow, which is a common phenomenon in other applications, such as gas diffusion, solvent transfer, and ion exchange. These phenomena show that the ordered molecule alignment is the origin of ultrafast transfer for molecules in regular nanochannels.

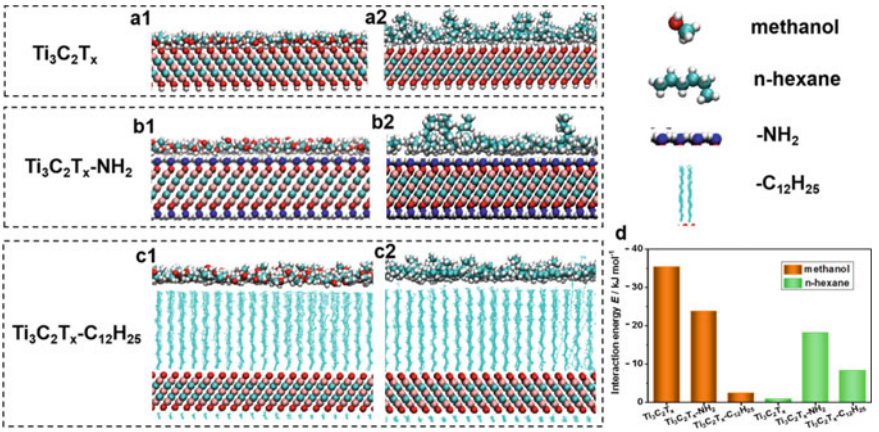

Fig. 3.12 MD simulations in distinct channels. Molecule configuration of methanol and n-hexane in **a** $Ti_3C_2T_x$, **b** $Ti_3C_2T_x$-NH_2, and **c** $Ti_3C_2T_x$-$C_{12}H_{25}$ channels. Spheres in red, cyan, white, and pink blue represent nitrogen, carbon, hydrogen, oxygen, and titanium atoms. **d** The interaction energy of molecule-channel. Copyright (2019), John Wiley and Sons [24]

The solubility parameter and molecular kinetic diameter should be the main factor determining molecule transfer efficiency due to regulated molecular alignment by channel–molecule interactions [37]. Here, a phenomenological transport model that well correlates permeance (P_s) of polar solvent s and the parameters of molecules is established for hydrophilic $Ti_3C_2T_x$ and $Ti_3C_2T_x$-NH_2 nanochannels. The equation can be expressed as $P_s = A\delta_s/\eta_{ls}{d_s}^2$, where A, δ_s, η_{ls}, d_s represent proportionality constant (m^3 $Pa^{-0.5}$), Hansen solubility parameter ($Pa^{0.5}$), molecule viscosity (Pa s), and molecule diameter (m), respectively (Fig. 3.13a). Note that this equation is different from the previously reported equation in 2.0 nm-channels for $Ti_3C_2T_x$ membrane: $P_s = K/\delta_s\eta_{ls}{d_s}^2$ [23]. The relationship between P_s and δ_s is inverse proportion for 2.0 nm nanochannels but positive proportion in sub-1.4 nm nanochannels. This may be due to larger hydrophilic nanochannels induce more polar molecules to form an ordered arrangement by strong channel–molecule interactions, and then, this strong interaction energy act as friction force for large aggregate to transfer within nanochannels [38]. In contrast, a certain number of molecules in a relatively narrow nanochannel possess moderate interactions with channel wall and transfer along channel wall [39]. Interestingly, the above equation is similar to the transfer mechanism of molecule through small-sized channel of < 1.0 nm in polymer membranes [33], while solvent molecules in hydrophobic nanochannels show a disordered configuration, and the corresponding equation is also established as follows: $P_s' = A'/\eta_{ls}$, where A' represents proportionality constant ($L\ m^{-2}$) (Fig. 3.13b). This indicates that molecule transfer is controlled by η_{ls} and obeys typical Hagen–Poiseuille's equation [40]. This phenomenon has also been reported through MD simulations that weak channel–molecule interactions bring disordered molecule configuration; thus,

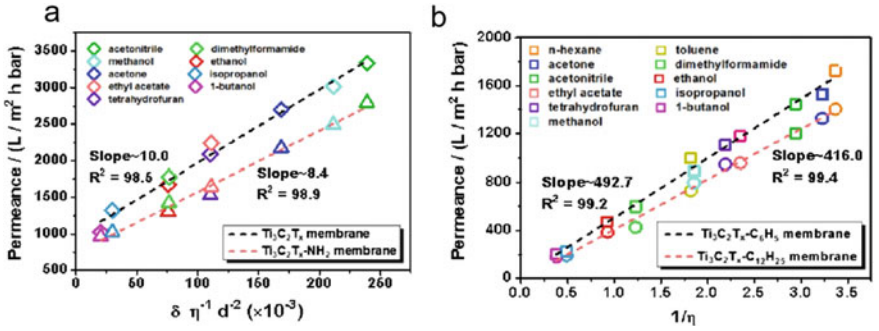

Fig. 3.13 Nanofiltration permeance of membranes. **a** Solvent permeance as a function of molecule parameters for $Ti_3C_2T_x$ membrane and $Ti_3C_2T_x$-NH_2 membrane. **b** Solvent permeance as a function of the viscosity for $Ti_3C_2T_x$-C_6H_5 membrane and $Ti_3C_2T_x$-$C_{12}H_{25}$ membrane. Copyright (2019), John Wiley and Sons [24]

the effects of molecule δ_s and d_s are negligible for molecule transfer in 2D nanochannels. Understanding of transfer mechanism that ordered arrangement drives solvents transfer fast clearly resolves controversial conclusions.

MXene lamellar membranes with well-designed nanochannels were prepared by assembling rigid $Ti_3C_2T_x$ nanosheets. The nanochannel size (from 1.28 to 1.66 nm) and wettability were effectively regulated by using hydrophilic (–NH_2) and hydrophobic (–C_6H_5, –$C_{12}H_{25}$) groups. Hydrophilic lamellar membranes with –NH_2 and –OH groups display ultrahigh solvent permeance of 3337 and 3018 L m^{-2} h^{-1} bar^{-1} for polar acetonitrile and methanol, respectively. This is more than 3 times higher than that of regular hydrophobic membranes. Importantly, the potential molecular transport mechanism is revealed, and the corresponding transfer models are also established. The polar molecules are induced to form orderly aligned aggregates in hydrophilic nanochannels. This ordered alignment significantly reduces collisions of molecule–molecule and molecule–channel wall and then endows the ultra-low-resistance transfer of polar molecule layer, while non-polar solvents display disordered configuration and molecular agglomerations in nanochannels due to weak channel-molecule interations. The obove findings prove that molecular arrangement is primary cause of efficient transport in two-dimensional nanochannels. Elaborating molecular transfer mechanism in two-dimensional confined nanochannels provides a theoretical guidance for the design of efficient separation membranes and other fields, such as gas capture, energy conversion, drug delivery, and so on.

3.4 Lamellar MoS_2 Membranes with Loosely Stacked Structure

Asymmetrical MoS_2 nanosheets with a series of thickness were fabricated by ultrasound-assisted exfoliation method [41]. 0.01 g MoS_2 solid substances were added to 100 mL of the ethanol and water (7:3 V/V), which were mixed and stirred for 12 h. In addition, the retained mixed liquid was carried out to ultra-sonication with power of 300 W for 6 h. Furthermore, centrifugation was performed at 3500 rpm for 20 min and the gray solution was kept for membrane preparation.

Procedure with temperate-exfoliation and low-power ultra-sonication is carried out to gain multilayer MoS_2 flakes in different series kinds of thickness. SEM images (Fig. 3.14a, b) explain that the MoS_2 nanosheets remain the irregular shape due to the MoS_2 powder treating in exfoliation procedure. AFM images (Fig. 3.14c) show MoS_2 flakes with congruous landscape dimension size of ~ 500 nm, but the most utilized flakes in the literature (usually 2 ~ 5 μm) [42] is larger than it. Furthermore, there are four heights (i.e., nanosheet thickness) of 0.9, 1.7, 2.6, and 3.6 nm for MoS_2 flakes. At the same time, TEM image (Fig. 3.14d) gives sufficient reasons for further appearance of these multi-laminate MoS_2 flakes, which apparently shows the rigid and smooth surface of flakes.

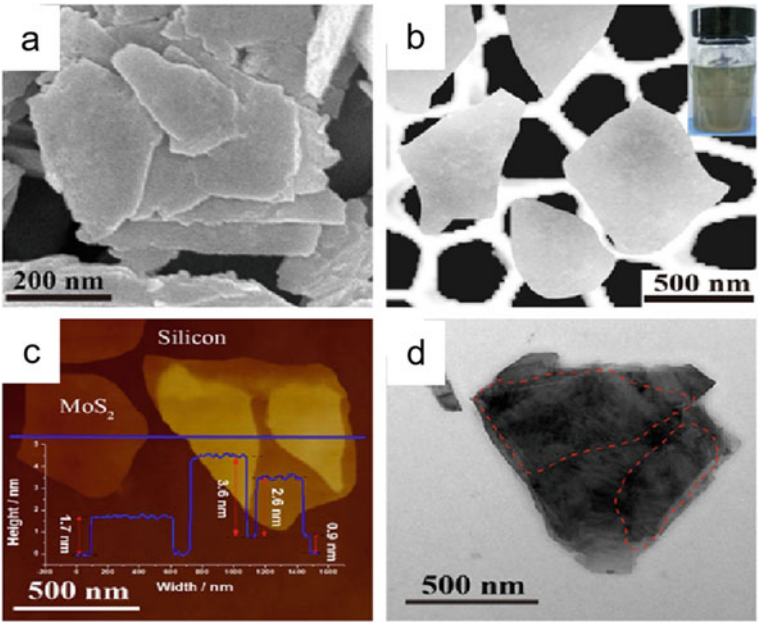

Fig. 3.14 Proofs for the result of irregular MoS_2 nanosheets in various thickness. The images of SEM **a** powder of MoS_2, **b** MoS_2 nanosheets with AAO supporting. **c** MoS_2 flakes of AFM and **d** TEM images. Copyright (2019), Royal Society of Chemistry [22]

With the assistance of Nylon support, the loosely stacked MoS_2 membranes were made via vacuum filtration of MoS_2 solution. Nylon support and MoS_2 flakes retain the well affinity, due to the fact that Nylon support was pre-processed by dopamine aqueous solution (2 mg mL^{-1}, pH = 8.5) for 4 h to form a PDA layer deposition. MoS_2 membranes with different kinds of thickness were prepared by adjusting the volume of MoS_2 flake dispersion, i.e., flake loading. At the end of filtration, the gained membrane maintains its solvated state by immersing in water or organic solvents for further characterization and testing.

A sluggish filtration process is employed to ensure uniform and defect-less buildup of MoS_2 flakes on the support. The images of SEM and AFM, which are shown in Fig. 3.15a and b, clarify that the lamellar structure of the surface of MoS_2 membrane is wrinkled and undamaged [43]. Apparently, while cross-sectional SEM images (Fig. 3.15c and e) approve that the MoS_2 flakes are loosely stacked with irregular interlocking structure. The results can be elucidated by the rigid, tiny, and unusual structure of MoS_2 nanosheets, which can provide a convenient way to achieve a disordered stacking behavior during filtration. This loose sheet-like stacking structure differs from the traditional inter-channel structure, which possesses ordered nanochannels by ultrathin nanosheets.

As shown in Fig. 3.16c, the structure of the stacking of these membranes is further explained by XRD [26]. Herein, to reduce the interference from Nylon support, an amorphous anode AAO is used as a support [15]. The results show that the MoS_2 membrane also displays a sharp (002) band at $2\theta = 14.4°$, which is almost

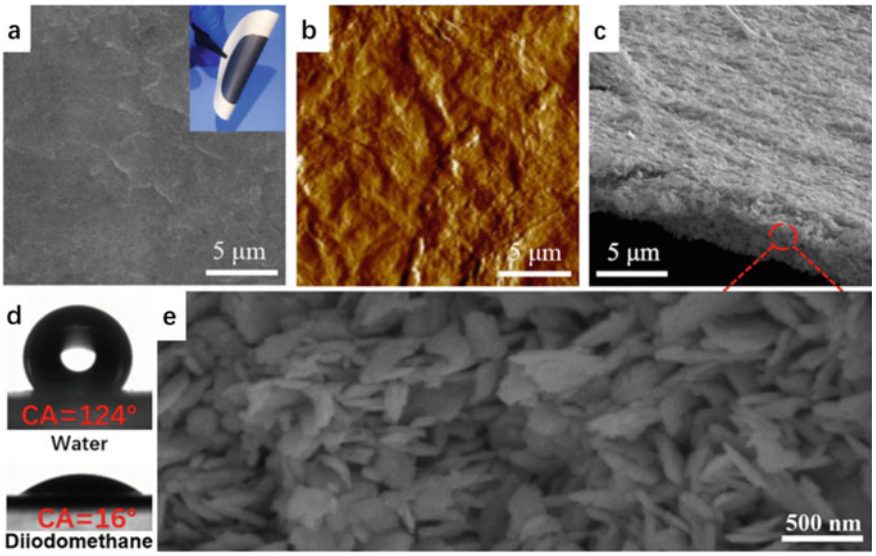

Fig. 3.15 Proofs for the preparation of the membrane of MoS_2 flake. **a** The MoS_2 membrane of the surface SEM picture. **b** of AFM image **c** of cross-sectional SEM images **e** is a partial enlargement of d). **d** The contact angle of MoS_2 nanosheets. Copyright (2019), Royal Society of Chemistry [22]

the same as that of MoS_2 nanosheets. In addition, the spacing between layers is concluded to be only 0.61 nm. Being proved that the thickness of S-Mo-S triple layer is 0.32 nm [44], however, it is too narrow for molecules to pass through the interlayer channels, because the channels are only 0.29 nm. Thus, the rapid transfer of molecules is due to the multilayered channels that exist inside this loosely stacked MoS_2 membrane. This channel is formed by the interlocking structure of irregular nanosheets, consisting of large cavities between narrow gaps and stacked nanosheets at the contact edges of the nanosheets. The specific surface area test analysis and pore size distribution (Fig. 3.16b) show the presence of bimodal apertures at 1.8 nm and 8.3 nm, respectively, further demonstrating the hierarchical channel structure. It is reasonable due to the disordered stacking of the flakes, which provides an aperture range of pore size. According to the SEM image morphology, these results demonstrate that the channels contain narrow gaps (~ 1.8 nm) and bigger cavities (~ 8.3 nm, Fig. 3.16a). In addition, the space and sizes of gaps and spacing of membranes are controlled by the thickness of the membrane. Thin membrane really shows highly loose stacking structure with bigger spacing and gaps, due to compaction effect, their sizes will be reduced with their increasing membrane thickness. When the film thickness is bigger than the stable value of 2.3 μm, the membrane structure is performed uniform with stable morphology.

The permeance of eight solvents and rejection of seven dyes used in industry were measured, to ensure a stable performance, the permeances of solvents that consist of water and organic are measured on a homemade device over several hours. Figure 3.17a shows that MoS_2 membrane performs unparalleled permeability to both water and organics. The permeance of water for 2.3-μm-thick lamellar is approximately up to 1430 L m^{-2} h^{-1} bar^{-1}; moreover, the permeances of n-hexane and acetone are approximately 5000 L m^{-2} h^{-1} bar^{-1}, separately. Acetonitrile shows the permeance of 4725 L m^{-2} h^{-1} bar^{-1}. Other solvents also achieve ultrahigh permeability; for example, methanol permeance is 3790 L m^{-2} h^{-1} bar^{-1} and toluene permeance is 2246 L m^{-2} h^{-1} bar^{-1}. Increasing membrane thickness causes the decreased molecule permeance. Such as, the permeance of n-hexane reduces from 5680 to 2640 L m^{-2} h^{-1} bar^{-1}, and the water permeability reduces from 1430 to

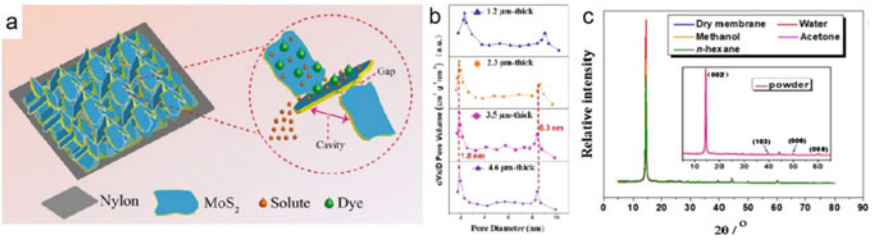

Fig. 3.16 **a** Schematic of a hierarchical transmission channel inside the membrane. **b** The distribution of pore diameter in the layered channels carried out through BET. **c** XRD evidences of MoS_2 membranes that soaked in various solvent environment. Copyright (2019), Royal Society of Chemistry [22]

610 L m^{-2} h^{-1} bar^{-1} when thickness increases to ~ 4.7 μm. Therefore, the molecular permeance of MoS_2 membrane can be adjusted by tuning the thickness of membrane (Fig. 3.17c). Apparently, the reduction of solvent permeability along with the increase of thickness ought to be attributed to the empty size in the membrane becomes smaller. As reaching the size of 2.3 μm, the reduction rate of permeability gets lower. When the membrane thickness reaches 2.3 μm, it should be ascribed to that the channels achieve an even and rigid building structure.

Furthermore, Fig. 3.17a clarifies that the permeability increases when the solvent viscosity decreases, which obeys $P = K\,\eta^{-1}$ (η, mPa s), where K is a proportional constant (L Pa m^{-2} bar^{-1}). This explains that the molecular transfer rate is judged by the viscosity, which is in accordance to the Hagen–Poiseuille equation [33]. It should be noted that such an equation differs from the equation established by a regular channel membrane, in which the molecules are arranged in an orderly manner due to the interaction of the channel walls. The parameter of solubility and the diameter of the pore also influence the transfer rate of molecules in this condition [38]. However, molecules tend to accumulate disorderly in irregular transfer channels, while the

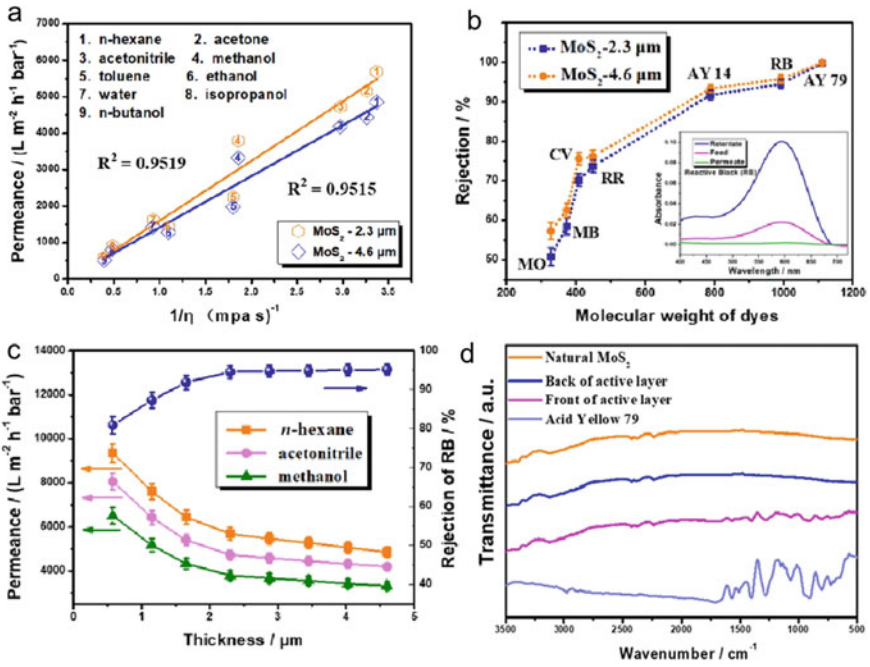

Fig. 3.17 Performance in nanofiltration to the MoS_2 membrane that is stacked loosely. **a** Permeability of solvents of MoS_2 membrane films of different thicknesses to the properties of the combined solvent. **b** Interception of dye molecules in MoS_2 membrane membranes. **c** Permeability and the rate of rejection at different membrane thickness. **d** FTIR curves of MoS_2 membrane in different states. Copyright (2019), Royal Society of Chemistry [22]

hydrophobicity of the channels reduces channel–molecule interactions and allowing low-resistance slip [45].

Seven dye molecules with apparently different sizes were decentralized in methanol and transformed among MoS_2 membrane so as to assess the width of channels. In Fig. 3.17b, it shows the factors of the charge, molecular dimension, and molecular weight of dyes are different. MoS_2 membrane can reject molecules with size smaller than 1.9 nm, such as crystal violet (CV, 1.5 nm, which rejection is 70%) and methyl orange (MO, 1.2 nm, which rejection is 51%). When the molecular size increasing up to 1.9 nm, the membrane channels can sift the most dye molecules, as the rejection of acid yellow 14 (AY 14, 1.9 nm) is above 90%. At the same condition, the rejection reaches almost 100% for much larger acid yellow 79 (AY 79, 2.8 nm).

As shown in Fig. 3.18a, framework stability of the loosely stacked MoS_2 membrane was performed, where the constant solvent permeance and dye rejection during long-term operation verify the strong structural stability of the nanochannels. Moreover, such channels can withstand the hard environments existed in industrial production. After sonication for 20 min (Fig. 3.18c) or immersion in acid solution for more than 24 h (Fig. 3.18d), the solvent permeance has changed less than 3%. As showed in Fig. 3.18b, MoS_2 membranes are able to withstand pressures up to 3.5 bar without structural collapse. When the pressure was further increased to 5.0 bar, weak compaction occurred, as was the slight decrease in solvent permeability by about 5%. Then, the solvent permeance remains stable when the pressure is reduced from 5.0 to 1.0 bar due to the stability of structure. Above all, these results confirm the excellent stability of the loosely stacked MoS_2 membrane.

In conclusion, we present the application of rigid irregular MoS_2 flakes as building blocks to fabricate novel lamellar membranes by loose stacking. The resultant MoS_2 flakes are disorderly stacked to build hierarchical transport channels through slow vacuum filtration, unlike the conventional lamellar membranes with compact in-plane channels. The narrow gap (~ 1.8 nm) at the contact edge of the nanosheet and the large cavity (~ 8.3 nm) between the stacked nanosheets together comprise the hierarchical transfer channel. The large spacing permits low-resistance permeation of molecules accompanied with fast permeance: over 1430 and 5000 L m^{-2} h^{-1} bar^{-1} for water and organics, respectively. The accurate dye rejection is mainly achieved by size screening in the presence of the narrow gap: over 90% for dyes with a size of lager than 1.9 nm. Moreover, dynamic simulation results explain that the transfer resistance of molecules in fastigiated channel is much lower than that in horizontal channel. Then, the corresponding model equations that describe the transfer of molecules in this channel are established. Moreover, this MoS_2 membrane shows rigid structural stability in ultrasonic and acid environments, showing the potential for long-term operation.

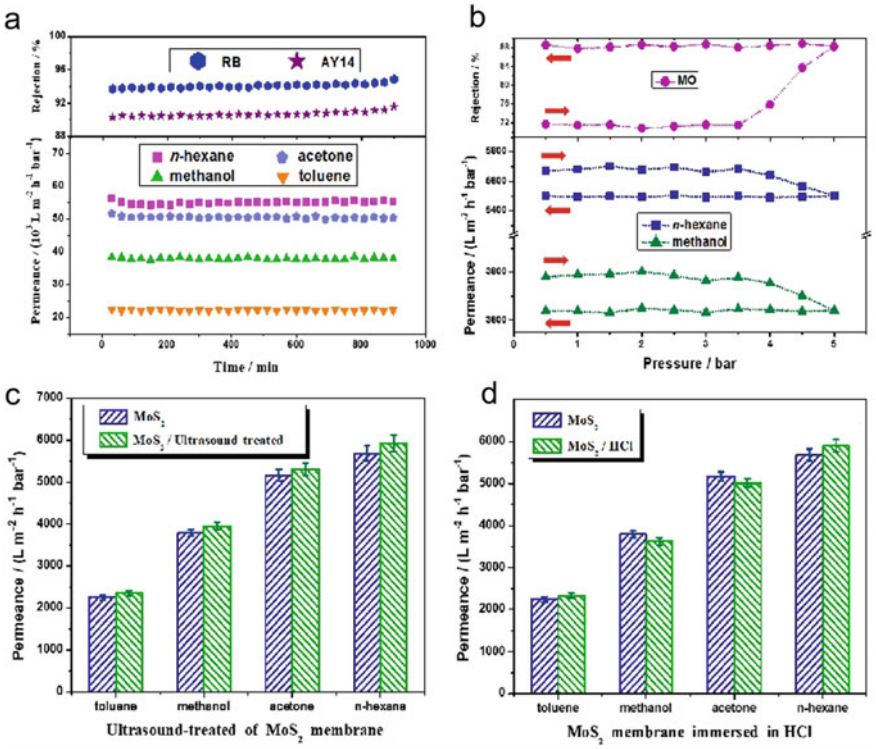

Fig. 3.18 Proofs for the stability of loosely stacked MoS_2 membrane. **a** Permeability and retention properties of MoS_2 film on solvents under pressure of 1 bar, for instance, permeability of n-hexane, acetone, methanol, toluene, and long-term operating performance in the interception of RB and AY14. **b** The permeability and rejection of MoS_2 membrane under various trans-membrane pressure. Permeability of methanol, toluene, acetone and n-hexane in MoS_2 membrane changed after **c** Treating it in HCl solution for 24 h at pH = 4 and **d** ultrasound 20 min in the environment of the test solution. Copyright (2019), Royal Society of Chemistry [22]

3.5 Lamellar GO Membrane with Polymer Cluster-Patterned Surface

Herein, GO and reduced GO (RGO) nanosheets were prepared by conventional methods [12]. The irregular wrinkles of TEM (Fig. 3.19a) and AFM (Fig. 3.19c) images explain the flexible characteristics of GO that possesses typical 2D structure. As shown in the AFM, the lateral size estimated is about 3 μm and the thickness of GO is 1.1 nm. In the literature, the thickness of the single-layer graphene oxide is 0.8 nm [46], while the water molecules are adsorbed to form a binding layer on the GO surface due to the rich oxygen-containing functional groups. This is pictured by the X-ray photoelectron spectroscopy (XPS) (Fig. 3.20c) which performs high O/C ratio of 53%. In addition, GO nanosheets were reduced to RGO nanosheets

by moderate Wallace's assistance. The structure and size of the nanosheets are well maintained during the reduction process, and the thickness of the RGO formed after the reduction is reduced to ~ 0.5 nm, as shown in Fig. 3.19b and d. And, the oxygen-containing functional groups decrease sharply during the reduction process with an O/C ratio of 13%, which means that the hydrophilic groups are reduced by about 75% (Fig. 3.20c). These results show that GO nanosheets are hydrophilic and RGO nanosheets are hydrophobic.

Herein, the heterostructured laminar membranes were prepared by multi-needle electrostatic atomization method. As pictured in Fig. 3.20a, flexible GO nanosheets were uniformly deposited on AAO substrate without folding. Due to the strong electrostatic repulsion generated by the high-voltage field and the shear force from the rotating receiver, the nanosheets are flattened and ordered layer by layer to form a laminar structure with regular interlayer channels. As shown in Fig. 3.20b, the SEM image apparently predicts the ordered stacking structure of GO and RGO nanosheets.

By the inspiration of beetle's backbond, hydrophilic/hydrophobic heterostructured laminar membranes are constructed by patterning functional polymer clusters onto an ordered lamellar structure, which have opposite wettability. As shown in the SEM image of Fig. 3.21a, the roughness (R_a) shows a slightly increase range from ~ 110 to 130 nm due to the formation of islanded polymer clusters (Fig. 3.21b). This

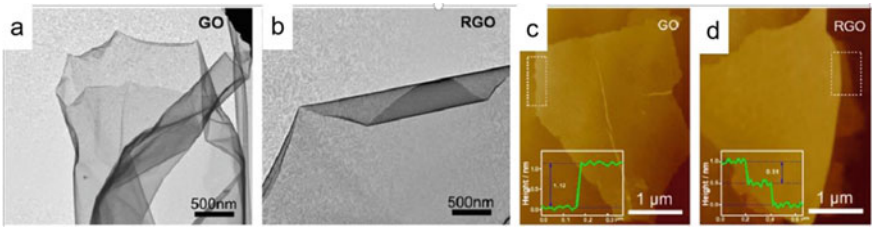

Fig. 3.19 Images of TEM of **a** GO and **b** RGO. Images of AFM along the dashed rectangle of with height profiles **c** GO and **d** RGO. Copyright (2019), John Wiley and Sons [18]

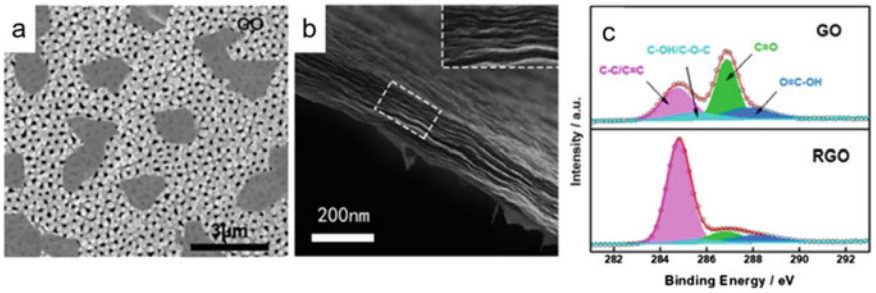

Fig. 3.20 **a** Image of SEM of GO nanosheet on AAO support. **b** Cross-sectional SEM picture of GO membrane using electrostatic atomization. **c** XPS spectra for C 1 s of RGO and GO. Copyright (2019), John Wiley and Sons [18]

result is due to the high pressure forcing the polymer solution to form fine droplets deposited on the surface of the laminar structure. At the same time, the solvent (mainly ethanol) evaporates rapidly, further avoiding the diffusion of the polymer into the membrane.

Moreover, the presence of a nanoscale bumpy morphology on the surface of nanosheet, which can be directly observed by the TEM images of the composite nanosheets (Fig. 3.22a) because the low concentration of the polymer solution ensures the formation of nanoscale clusters rather than films. Thus, the nanoscale tracks are evenly formed on the surface of nanosheets, which is intuitively reflected by the composite nanosheets of TEM image (Fig. 3.22a). As shown in Fig. 3.22b, the AFM result implies that the uneven surfaces have a width and height of ~ 20 nm and ~ 1.2 nm, respectively, the same as stenocara beetle. In addition, it is well noted that the deposited polymer clusters are mainly assembled on the surface of the lamellar membrane without immersing into the interlayer, as unchanged peak values and intensities in Fig. 3.22c.

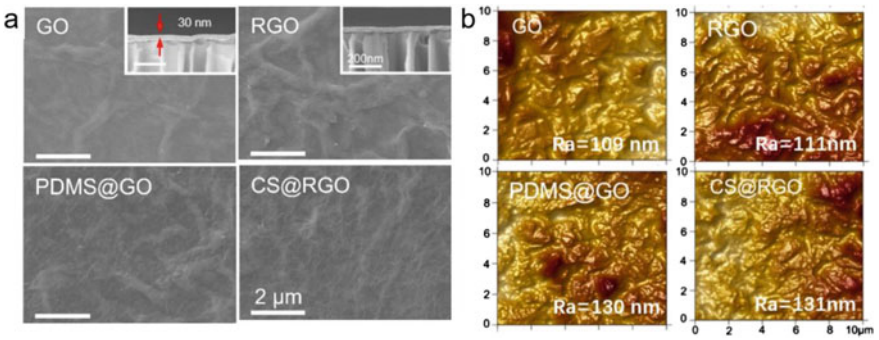

Fig. 3.21 **a** SEM images of membranes of GO, PDMS@GO, RGO, and CS@RGO. Insert shows that the thicknesses of GO and RGO membranes are carried out to be about 30 nm. **b** Images of AFM of GO, PDMS@GO, RGO, and CS@RGO membranes. GO nanosheet anchored by PDMS groups (A-GO). Copyright (2019), John Wiley and Sons [18]

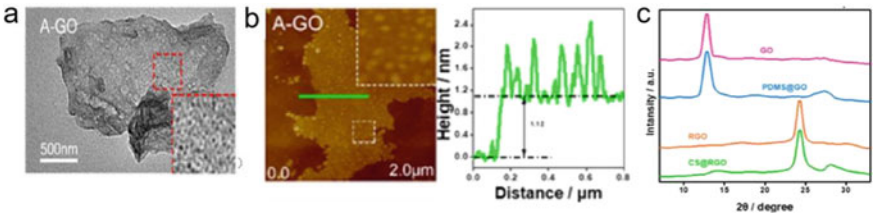

Fig. 3.22 **a** TEM image with height profile **b** AFM image with height profile Insert exhibits PDMS clusters on GO nanosheet. **c** XRD patterns of GO, PDMS@GO, RGO, and CS@RGO membranes in fully dried. Copyright (2019), John Wiley and Sons [18]

The nanofiltration performance was estimated according to the solvent permeance, dye rejection, and operational stability of the resultant membranes. Notably, nylon substrates have a pore size of about o.2 μm and typically have excellent solvent permeance of over 2000 L m^{-2} h^{-1} bar^{-1}, but invalid rejection for dyes. In this work, 12 commonly used solvents were selected for performance evaluation at a pressure of merely 1.0 bar. As expected, for common polar solvents, such as acetone, ethyl acetate, acetonitrile, DMF, methanol, ethanol, and water, GO membrane exhibits ultrahigh permeance, while the non-polar solvents (n-hexane, n-pentane, n-heptane, n-octane, and toluene) have a lower transport rate. Apparently expressed in Fig. 3.23a, the high permeance of water and acetone is 36.2 L m^{-2} h^{-1} bar^{-1} and 48.4 L m^{-2} h^{-1} bar^{-1}, respectively. However, the permeance of n-hexane is merely 19.0 L m^{-2} h^{-1} $bar^{-1}$and toluene is only 10.4 L m^{-2} h^{-1} bar^{-1}. However, notably, patterning PDMS clusters increases the permeation ability of almost non-polar solvents. For example, the permeance is increased by 7.6 times to 143.6 L m^{-2} h^{-1} bar^{-1} for n-hexane and is increased from 10.4 to 111.0 L m^{-2} h^{-1} bar^{-1} for toluene. In contrast to non-polar solvents, the permeation of polar solvents is inhibited by PDMS clusters. The reduced permeance is presented with 12.0 and 40.6 L m^{-2} h^{-1} bar^{-1} for water and acetone, respectively. These results should be ascribed to the formation of a heterostructured structure assembled from PDMS clusters and GO laminates. In this way, a highly synergistic transport process is constructed, featuring enhanced dissolution and ultra-low-barrier diffusion. This is very similar to the role of the bumps and grooves on the beetle's back. As shown in Fig. 3.23, pressure-dependent permeance was carried on and the results ought to further corroborate it. The results express that the permeance of n-hexane booms from 19.0 to 73.2 L m^{-2} h^{-1} bar^{-1} through GO membrane against the pressure increases from 1.0 to 6.0 bar, correspondingly, as the permeance of acetone changes from 48.4 to 54.4 L m^{-2} h^{-1} bar^{-1}. Furthermore, it is noted that the island-like distribution of PDMS bumps also allows the GO domains to dissolve polar molecules, resulting in a slight decrease in permeance for polar solvents.

To further demonstrate the superiority of the clustered surface of functional polymers, more polymer solution with more (~ 21 mL) was sprayed to form an intact PDMS film, and the corresponding membranes are named as PDMS/GO. As shown in Fig. 3.23c, after coating the polymer film, the permeance of both the polar and the non-polar solvents is reduced. For example, the n-hexane permeance drop by 21.9% and toluene permeance drop by 24.0% for PDMS/GO membrane coated with a PDMS film, comparing to PDMS@GO membrane with PDMS clusters.

To estimate the interlyer spacing of nanosheet laminates, dye molecules with diverse sizes were filtrated through the prepared membranes. Herein, to avoid dye adsorption on the membrane, negatively charged dyes were selected designedly. As shown in Fig. 3.23d, the molecule with a size of smaller than 1.4 nm can easily pass through GO membrane, for example, only 35% rejection for methyl orange (MO, 1.0 nm). However, as for rose bengal (RosB) with a size of 1.2 nm, almost half were rejected when passing through the interlayer channels, while the size of molecule is blooming up to 1.4 nm, the rejection of channels is about 99%, in which almost all

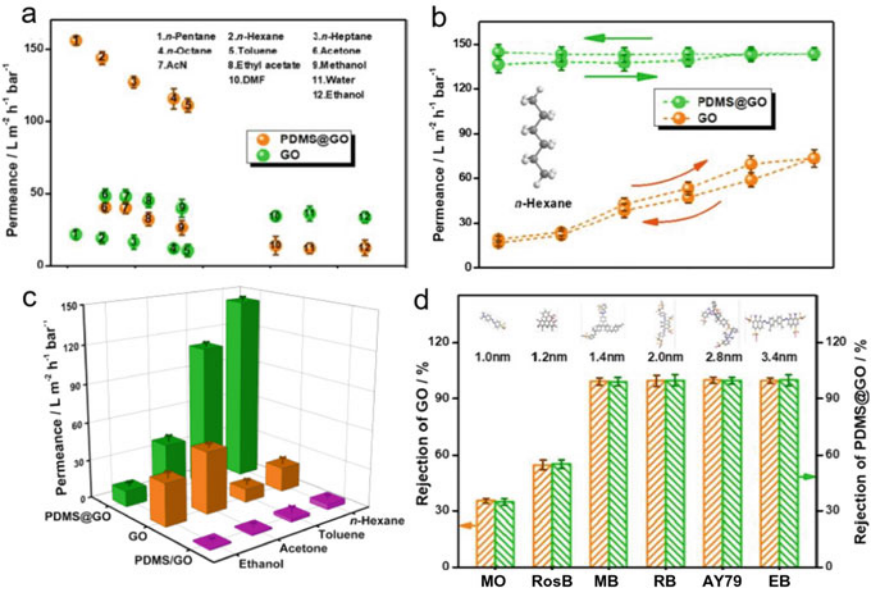

Fig. 3.23 **a** Solvent permeability along with the viscosity for GO, PDMS@GO. **b** Solvent permeance against a cyclic pressure for GO, PDMS@GO membranes. **c** The permeability comparation of the GO, PDMS/GO, PDMS@GO. **d** The property of the rate of rejection in several dyes in methanol versus their molecular size. The sort of the dyes: methyl orange (MO), rose bengal (Ros B), methyl blue (MB), reactive black (RB), acid yellow 79 (AY79), and evans blue (EB). Copyright (2019), John Wiley and Sons [18]

methyl blue (MB) could not pass through. Moreover, the rejection of much larger dyes reaches nearly 100%.

As shown in Fig. 3.24, the operating and mechanical stability of the heterostructured lamellar membranes was further measured. As pictured in Fig. 3.24a, after undergoing 48 h of continuous operation, the solvent permeance only decreases slightly within the first 10 h, which indicates that both GO and PDMS@GO membranes have good structural stability. And, the degree rate of reduction (below 6%) is lower than that of polymer membranes (usually more than 20%) [47]. Furthermore, the consistent behaviors are also detected for RGO and CS@RGO membranes. In addition, heterostructured lamellar membranes experienced the ultrasonic treatment and immersion treatment in DMF, hydrochloric acid, and sodium hydroxide solutions, which are unavoidable in many industrial processes. As shown in Fig. 3.24b, the membrane structure is stable with negligible changes in permeance (less than 4%). This is mainly due to the highly ordered flake accumulation and covalent cross-linking of polymer groups.

For the first time, a hydrophilic/hydrophobic heterostructured lamellar membrane with excellent permeation and separation performance is prepared by imitating the hierarchical structure of the beetle back. Electrostatic atomization technology is carried out to facilely construct orderly stacked lamellar structure and pattern polymer

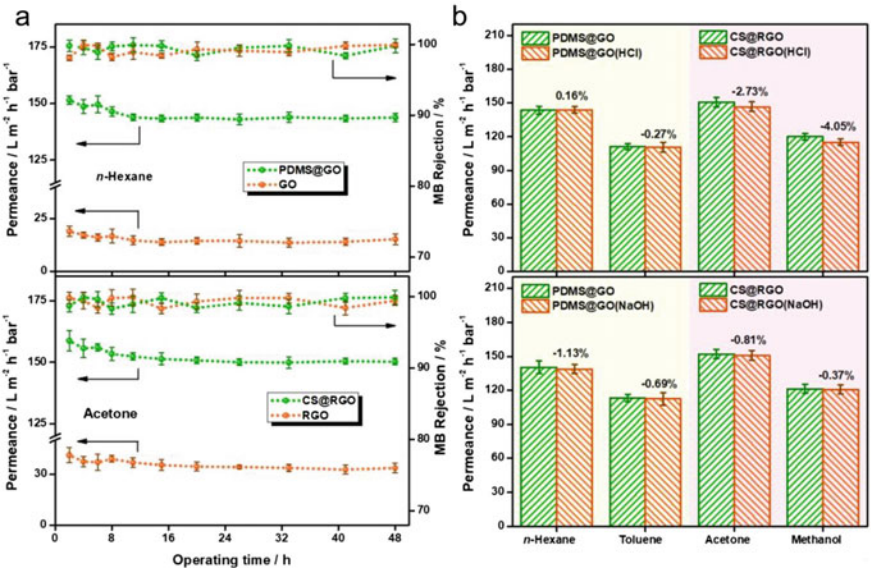

Fig. 3.24 **a** The performability of solvent of membrane, for instance, GO, PDMS@GO, RGO and CS@RGO membranes under operation time. **b** Solvent permeability of PDMS@GO and CS@RGO nanosheet membranes before and after the treatment of HCl (1 M) and NaOH (1 M) last for 20 min. Copyright (2019), John Wiley and Sons [18]

clusters on laminate surface with reversed wettability. Functional polymer clusters achieve rapid dissolution, while lamellar channels with weak affinity to solvents achieve ultra-low-resistance diffusion, which together greatly enhance permeance (more than 7 times that of nanosheet laminates). This enhancement is achieved while completely maintaining the rejection of the sheet laminate. Among them, the permeance of n-hexane in the PDMS@GO membrane reaches 143 L m^{-2} h^{-1} bar^{-1}, and the screening size is calculated to 1.4 nm. The water permeance of 98.1 L m^{-2} h^{-1} bar^{-1} is achieved by CS@RGO membrane, and its screening size is 1.2 nm. Furthermore, the as-prepared membranes exhibit remarkable stability under ultrasonic and strongly alkaline or acidic environments. Moreover, the bio-inspired heterostructure, highly synergized two materials with opposite chemical property, permits the potential applications for hybrid or composite materials in catalysis, separation, sensor, electrolyte-relevant devices as well.

3.6 Lamellar GO-PEI Membrane

GO nanosheets were prepared from natural graphite powders on the basis of modified Hummers' method [4, 48]. The obtained GO powder was dispersed in the mixed

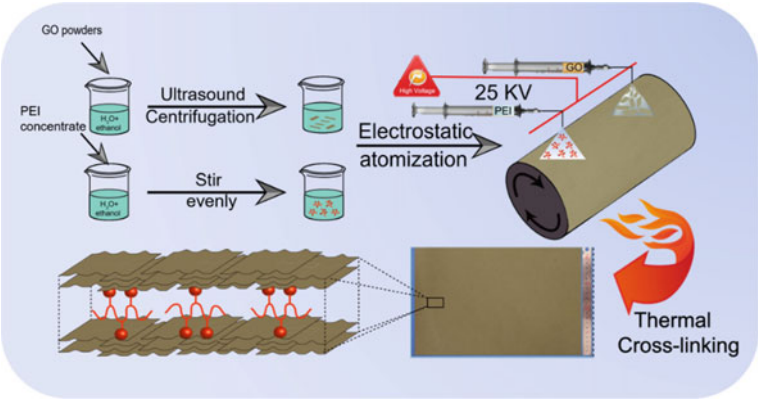

Fig. 3.25 Preparation process of GO-PEI membrane. Copyright (2020), Elsevier [20]

solution of ethanol and water (3:2, v/v) by ultrasound-assisted method, and centrifugation for 10 min at 6000 rpm and 15 min at 8000 rpm to obtain uniformly dispersed GO supernatant [5, 22].

Polymeric PEI was selected to cross-link adjacent GO layers that was used as build blocks. PEI (0.1 wt%) was dissolved in the mixture of ethanol and water with the volume ratio of 3:2. GO powder was also uniformly dispersed in the above mixture. By electrostatic atomization method, the resultant two solutions of 120 mL were respectively pumped with 25 kV and 15 cm from the tip to the collector at a rate of 0.005 mm min^{-1} to prepare the novel lamellar composite membranes (22 cm × 33 cm), as shown in Fig. 3.25. The highly ordered GO-PEI structure can be rapidly constructed using a dual-needle electrostatic strategy. Finally, these composite membranes were attained by thermally cross-linking at 80 °C for 2 h.

To detect stacking condition, the identical process was used to deposit the nanosheets on the AAO support. As shown in Fig. 3.26a, smooth deposition guarantees highly ordered laminates with regular interlayer channels. The inserted is optical image of GO membrane, and the macroscopic surface of the membrane is smooth and uniform, no obvious defects. Moreover, N elemental mapping (Fig. 3.26b) of membranes manifests that PEI is evenly distributed within interlayer channels. This is also proved by XPS spectra (Fig. 3.26c) of GO-PEI membrane with a clear N 1 s peak and a content of 21.5%.

Cross-sectional SEM images of GO membrane exhibit distinct lamellar structure, while GO-PEI membrane results in the fuzzy lamellar structure owing to the cross-linked PEI to interlayer channels (Fig. 3.27a). In addition, controlling the time of atomization as well as the amount of GO and PEI can achieve precise control of membrane structure such as thickness of membrane. Thus, these lamellar composite membranes with identical structure but different thickness of 32, 61, and 89 nm were prepared.

In addition, thermal cross-linking significantly improves the mechanical properties of GO-PEI membranes. As illustrated in Fig. 3.28a, Young's modulus (11.46 ×

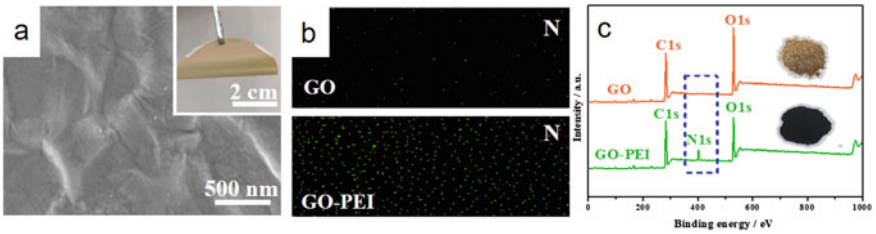

Fig. 3.26 **a** Surface SEM image of GO-PEI membrane (insert is the optimal photo of GO-PEI membrane). N elemental mapping of **b** GO membrane and GO-PEI membrane. XPS patterns of **c** GO membrane and GO-PEI membrane. Copyright (2020), Elsevier [20]

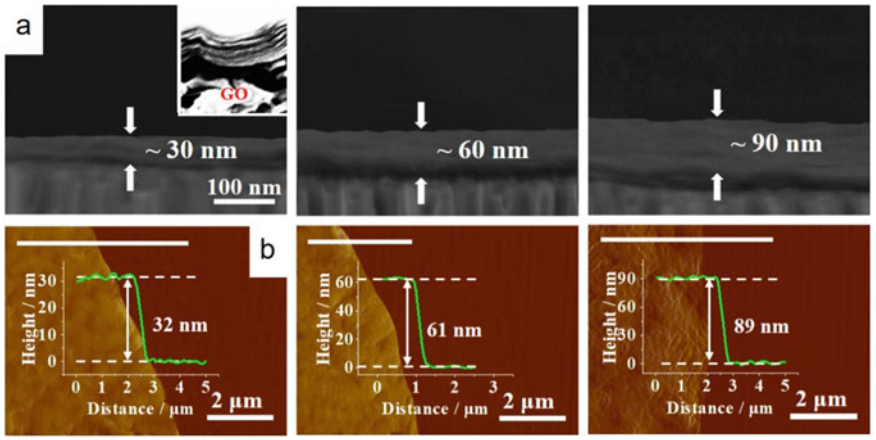

Fig. 3.27 **a** Cross-sectional SEM image of different thicknesses of GO-PEI membrane. (insert is the cross-sectional SEM image of GO membrane). **b** AFM images of GO-PEI membrane of different thicknesses with height profile along the dotted rectangle. Copyright (2020), Elsevier [20]

10^4 MPa) and the tensile strength (43.7 MPa) of cross-linked GO-PEI membrane are higher than that of GO membrane (6.14×10^4 MPa, 35.8 MPa) and no cross-linked GO-PEI membrane (7.24×10^4 MPa, 37.2 MPa). Importantly, thermal cross-linking gives GO-PEI membranes the ability to maintain ordered lamellar structures in harsh solvent environments. As shown in XRD results of Fig. 3.28b, the layer-by-layer stacked construction of GO-PEI membrane basically remains unchanged and the location of (002) peak does not shift before and after immersing toluene, DMF, water, and n-hexane for 24 h.

Then, nanofiltration performance was evaluated by the solvent permeance and dye rejection. And, the referenced GO membrane is made by vacuum filtration method [49, 50]. Water and eleven organic solvents were selected for permeance evaluation at 1.0 bar pressure. PEI (Mw = 300 Da) was inserted into GO membrane and thermally cross-linked with adjacent GO nanosheets to prepare stable layered composite membranes. The addition of PEI not only significantly improves the

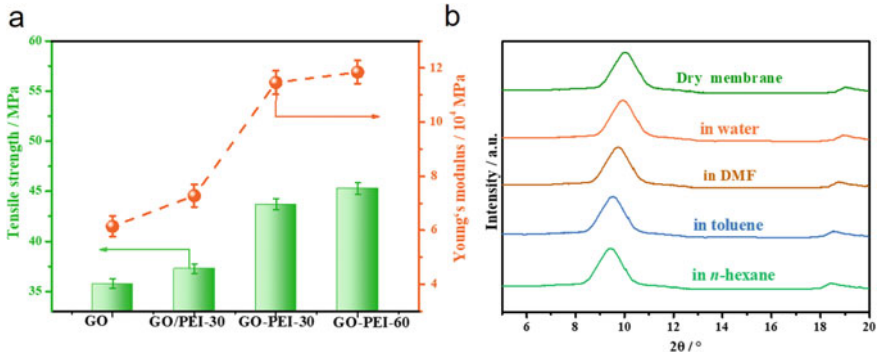

Fig. 3.28 **a** Young's modulus and tensile strength of GO membrane and GO-PEI membranes. **b** XRD spectra of GO-PEI membrane in various organic solvents for 24 h. Copyright (2020), Elsevier [20]

stability of membrane, but also enhances the mass transfer capacity. As a result, the permeance of GO-PEI membrane to polar solvent molecules was significantly improved. The permeance of acetone and water can reach 146.8 L m^{-2} h^{-1} bar^{-1} and 46.2 L m^{-2} h^{-1} bar^{-1}, respectively (Fig. 3.29a), which conforms to the viscous flow equation [51]. From Fig. 3.29b, it can be indicated that the addition of hydrophilic PEI enlarges the interlayer space of the lamellar membrane. Therefore, polar solvents are more likely to enter the membrane and hold higher solvent uptake (Fig. 3.29c). Meanwhile, the regular and continuous transfer pathways formed through GO-PEI membrane allow efficiently transport of solvent molecules and reduce cross-layer transfer barrier. Then, to determine channel spacing, dye molecules of different sizes were separated using GO and GO-PEI membranes. Figure 3.29b reveals that both GO and GO-PEI membranes are poorly to reject small-size methyl orange (MO, 1.0 nm) with rejection below 38%, while for larger brilliant blue (BB) with a size of 1.6 nm, its rejection can reach more than 96%, and for much larger size dyes, it can reach 100%.

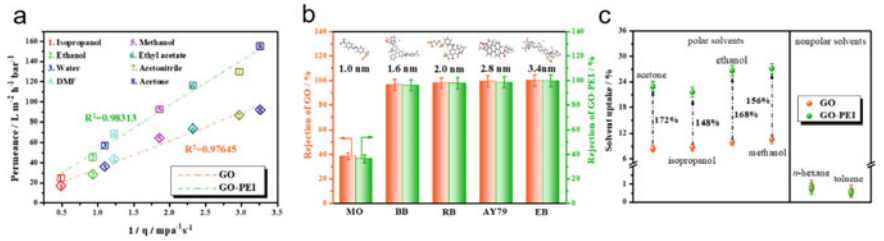

Fig. 3.29 Nanofiltration performance of membrane. **a** Solvents permeance versus the viscosity for GO and GO-PEI membranes. **b** Rejection of dyes in methanol against their molecular size. **c** Solvent uptake of GO membrane and GO-PEI membranes. Copyright (2020), Elsevier [20]

The structure stability evaluation of this novel lamellar composite membrane was shown in Fig. 3.30. After five-stage antifouling measurements of GO-PEI membrane with 1000 ppm of humid acid (HA), bovine serum albumin (BSA) and sodium alginate (SA) solution as feed (Fig. 3.30a), the permeance of acetone declines slightly only after the first stage. Furthermore, Fig. 3.30b reveals that the molecule permeance elevates slightly after ultrasonic treatment, proving that the membrane can withstand certain mechanical damage. Figure 3.30c indicates that owning to the membrane compaction solvent permeance of all GO-PEI membranes only slightly decline in the first 3 h, and then, the permeance remains almost unchanged during long-term stable operation of 36 h. Moreover, to satisfy the needs of industrial processes, GO-PEI membranes with a thickness of 30 nm were soaked in HCl solution (pH = 1.5) and NaOH solution (pH = 11) for 20 min (Fig. 3.30b). The results show that the membrane has excellent stability and the permeance change can be ignored compared with the membrane without treatment. Moreover, pressure-dependent permeation was verified using water as solvent. As can be seen in Fig. 3.30d where the water permeance increases linearly when pressure increase, showing excellent anti-pressure capacity.

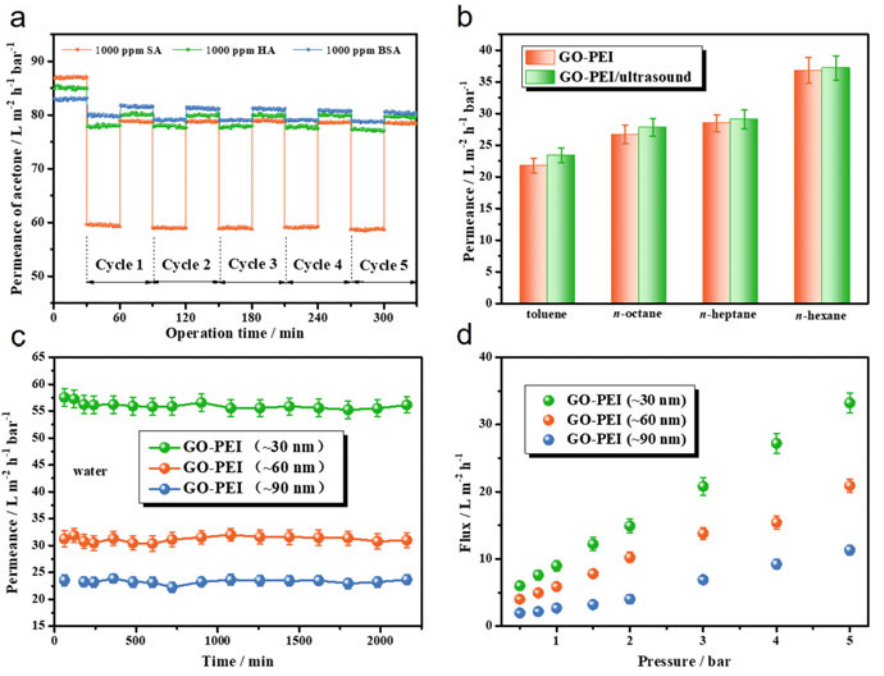

Fig. 3.30 Stability performance of membranes. **a** Measurements of five-stage antifouling for GO-PEI membrane. **b** Permeance comparison of methanol, toluene, n-hexane and n-octane for GO-PEI membrane after ultrasonic treatment for 20 min. **c** Water performance of GO-PEI membrane with different thicknesses versus operation time. **d** Solvent permeance versus different pressure for different membrane thicknesses. Copyright (2020), Elsevier [20]

An ultrathin and stable lamellar composite membrane was synthesized by covalently cross-linking of PEI and GO nanosheets. The highly ordered layer-by-layer PEI-GO structure was constructed for the first time by dual-needle electrostatic atomization. In this way, PEI was uniformly intercalated into GO interlayer and thermally cross-linked the adjacent GO nanosheets, and simultaneously performed as transfer sites for polar molecules. Thus, compared with GO membrane, GO-PEI membrane achieves the high permeance of 146.8 L m^{-2} h^{-1} bar^{-1} for acetone with the enhanced structural stability. Furthermore, the ordered interlayer channels provide precise size sieving for industrial dyes with size larger than 1.6 nm and the rejection rate more than 96%. Notably, this lamellar composite membrane exhibits excellent pressure, operation, and cycling stabilities, thus holding great potential for industrial applications.

3.7 Lamellar GO-Quantum Dot Membrane

GO nanosheets were prepared from natural graphite powders on the basis of modified Hummers' method in the literature [52]. RGO was reduced from GO by Wallace's method [53]. Typically, PQDs were synthesized as follows: under ultrasonic treatment, DETA (540 μL) and CA (0.9606 g) were dissolved in ultra-purified water (2.0 g) at room temperature for 5 min. Then, the mixture was heated in a microwave oven for 7 min to carry out the reaction. Thereafter, the products were repeatedly washed with ethanol to remove residual small molecules and then dispersed in water and freeze-dried for 48 h. For the preparation of highly carbonized GQDs, ultrapurified water as the reaction solvent was replaced by a mixture solvent of glycerol (1.5 g) and water (0.5 g) to provide a higher reaction temperature above 100 °C.

Different amounts of GQD solution (50 mL, 100 mL, 150 mL, 200 mL, 1 mg mL^{-1}) and GO solution (50 mL, 1 mg mL^{-1}) were mixed and then diluted to 500 mL to prepare the lamellar composite membrane. The GO and GQDs were completely mixed and further stirred overnight at 70 °C for reaction. Then, the dispersion was filtrated through a D-nylon support in a vacuum filter tank, and the resultant lamellar composite membrane was named GQD@GO membrane. Similarly, PQD@RGO membrane was prepared by inserting PQDs into RGO nanochannels. For comparison, GO and RGO membranes were fabricated by an identical process without GQD/PQD addition.

TEM images (Fig. 3.31a) show that GO nanosheets own typical flexible nanosheet structure with irregular folds. The lateral dimension and thickness of GO are ~ 3 μm and ~ 1.4 nm, respectively. As the theoretical thickness of a monlayer GO is 0.8 nm [54], one or two water layers are absorbed on the surface of nanosheet, which is due to the hydrophilic oxygen-containing functional groups.

The degree of carbonization of GQDs is regulated to ensure that there are a few groups on their surface to react with GO. And, TEM image (Fig. 3.31b) suggests that GQDs are typical 0 D materials with a small size between 2 and 5 nm, and they own distinct lattice fringes since the high carbonization, while TEM could not detected

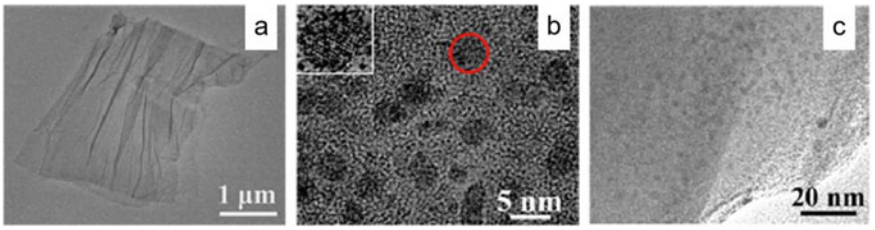

Fig. 3.31 TEM images of **a** GO nanosheet, **b** GQD and **c** GQD@GO composite. Copyright (2020), Elsevier [19]

the carbonization-free PQDs because of their disordered stacking and aggregation. In addition, XPS (Fig. 3.32b) and FTIR (Fig. 3.32c) results distinctly illustrate the diversity of hydrophilic groups exist in both PQDs and GQDs, while the strength of C–N and –C=O bonds in GQDs is much weaker than that in PQDs.

Next, GO reacts with GODs to prepare GQD@GO composites. Figure 3.32c reveals that QDs still firmly and equably anchored to the surface of nanosheet after ultrasonic treatment for over 20 min. Here, in order to identify the covalent bonding between QDs and nanosheets more easily, the composite of PQD@GO was synthesized accordingly and their chemical compositions were characterized by XPS. As shown in Fig. 3.32, GO nanosheets possess the typical XPS spectra as reported in the literature [9, 31], which contain four components corresponding to the carbon atoms in carbonyl, epoxy, hydroxyl, and carboxyl groups. After reacting with PQDs, the O/C atomic ratio reduces from 53% of primary GO to 44% for PQD@GO composite, although PQDs are rich in oxygen-containing groups, possessing a high O/C atomic

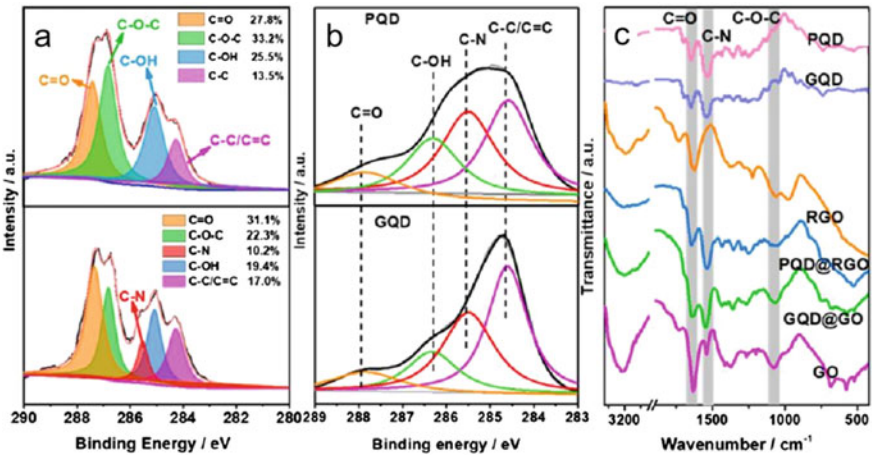

Fig. 3.32 **a** XPS pattern of GO power (upper) and PQD@GO composite (below). **b** C 1 s spectra of PQDs (upper) and GQDs (below). **c** FTIR patterns of PQDs, GQDs, GO, RGO and GQD@GO and PQD@RGO composites. Copyright (2020), Elsevier [19]

ratio of 56%. This observation strongly suggests that the functional groups on GO are reduced by PQDs to form covalent bonds. Under the same conditions, GQDs and PQDs can covalently bond on the GO and RGO surfaces respectively. This cross-linking reaction can be further demonstrated by FTIR spectroscopy (Fig. 3.32c). Compared with GO and RGO nanosheets, the GQD@GO and PQD@RGO composites show a stronger peak at 1533 cm^{-1}, corresponding to the stretching vibration of the amide group (–C–N–). This peak can also be observed in the spectra of PQDs and GQDs, but it is much weaker, whereas the weak peak in the GO spectrum should be caused by impurities introduced during the preparation of GO. This increase in peak strength confirms that the carboxyl group on the nanosheet covalently binds to the amide group of the QDs to form more amide groups. In addition, the peak intensity of the –C=O and C–O–C groups on the spectrum of nanosheet was significantly reduced compared with that of the composite material, indicating that these groups were consumed during the reaction with the QDs. Together, these evidences confirm the strong covalent interactions between nanosheets and QDs in GQD@GO and PQD@RGO composites. In addition to covalent interaction, hydrogen bonding and π–π interaction also exist between nanosheets and QDs, which jointly promote the stability of GQD@GO and PQD@RGO composites.

The precise morphologies are identified by SEM. Figure 3.33a shows that pristine GO membrane surface is relatively flat with many wave-like wrinkles, which well match with the observation in the literature [55, 56], while Fig. 3.33b reveals that, after intercalating GQDs, the surface becomes smoother and the wrinkles are reduced. This discovery should be due to the cross-linking effect of GQDs that firmly anchors adjacent GO layers and thereby drags these wrinkles into plain regions. Moreover, the existence of GQDs is further confirmed by EDS (Fig. 3.33c), and it was found that the surface of GQD@GO membrane exists a large amount of N elements from GQDs. Cross-sectional SEM image (Fig. 3.33d) shows the ordered layer-by-layer structure of GO membrane with the thickness of ~ 500 nm as reported in the literature [57]. GQDs were inserted into GO layers, retaining their lamellar structure and smoothing the wave-like wrinkles (Fig. 3.33e) substantially, which matches the results of surface SEM image. Considering the favorable nanofiltration performance and excellent structural stability, the membrane with a thickness of ~ 500 nm was selected for the characterization and performance assessment. As depicted in Fig. 3.33f, the structure of membranes is further detected by XRD. The sharp diffraction peak appeared in membranes confirms the orderly stacked nanosheets, which is in good agreement with SEM results. In particular, GO membrane has a peak at 10.5°, corresponding to a channel size of 0.84 nm [58], while this peak significantly shifts to 6.6°, indicating the size of the GQD@GO membrane is increased to 1.35 nm. Similarly, the size of RGO membrane increases from 0.38 to 0.95 nm for the PQD@RGO membrane. According to the larger interlayer distance, the GQDs/PQDs act as spacers embedded in adjacent GO/RGO nanochannels.

The OSN performance of membrane was evaluated by solvent permeance, rejection of dyes, and stability. It is noteworthy that the D-nylon supports with large pores (around 200 nm) own high water permeance (~ 2000 L m^{-2} h^{-1} bar^{-1}) but negligible rejection of dyes. Figure 3.34a displays that the permeance of

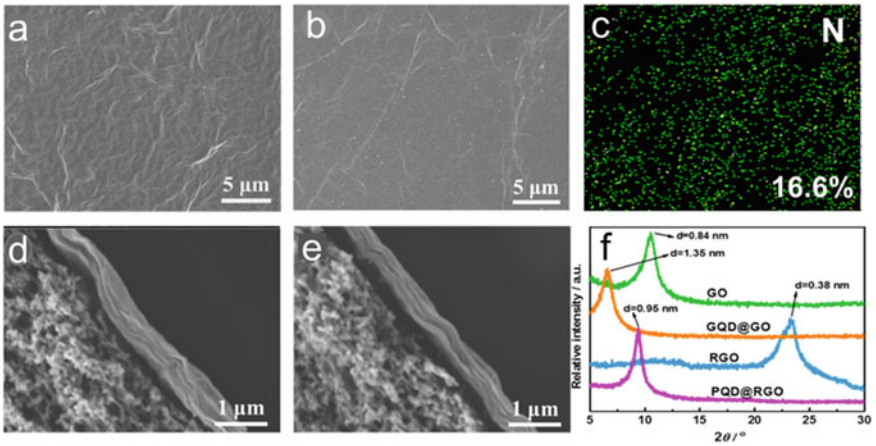

Fig. 3.33 SEM images of **a**–**b** GO membrane and GQD@GO membranes. N elemental mapping of **c** GQD@GO membranes. Cross-sectional SEM images of **d** GO membrane and **e** GQD@GO membranes. **f** XRD spectra of GO, GQD@GO, RGO and PQD@RGO membranes. Copyright (2020), Elsevier [19]

hydrophilic GO membrane to polar solvents is much higher than that of non-polar solvents. For instance, acetonitrile and acetone acquire the highest permeance of 30.3 L m^{-2} h^{-1} bar^{-1} and 32.1 L m^{-2} h^{-1} bar^{-1}, respectively, while toluene and n-hexane only have the permeance of 2.3 L m^{-2} h^{-1} bar^{-1} and 2.8 L m^{-2} h^{-1} bar^{-1}, respectively. In contrast, intercalation of QDs notably boosts the permeance of both polar and non-polar solvents. Moreover, the permeance for methanol and acetone achieves 146.7 L m^{-2} h^{-1} bar^{-1} and 173.5 L m^{-2} h^{-1} bar^{-1}, respectively. Specially, the permeance for n-hexane increases over 30 times (85.4 L m^{-2} h^{-1} bar^{-1}) and toluene permeance is also pronouncedly increased from 2.3 to 63.6 L m^{-2} h^{-1} bar^{-1}. Additionally, Fig. 3.34c indicates that the n-hexane permeance of GQD@GO membrane (85.4 L m^{-2} h^{-1} bar^{-1}) is much higher than that of PQD@GO membrane (30.6 L m^{-2} h^{-1} bar^{-1}). These results directly illustrate the crucial influence of appropriate chemical affinity on superior solvent permeance, which determines the ease of molecular solubilization and entry into the membranes.

GQD@GO membrane that displays excellent permeance for polar/non-polar solvents should be attributed to the optimized nanochannels on physicochemical microenvironments. As explained above, the GQD-modified GO nanochannels hold both hydrophilic and hydrophobic domains, showing excellent affinity for polar and non-polar solvents. It would be conducive to the dissolution of solvent in the membrane, and the increase of channel size promotes the rapid transport of solvent along the nanochannel. Thus, an efficient co-transport process is established with excellent permeance to both polar and non-polar solvents. Likewise, embedding hydrophilic PQDs into hydrophobic RGO nanochannels allows the evaluation of the affinity of RGO membrane for polar solvents and enhances their permeance (Fig. 3.34b and d).

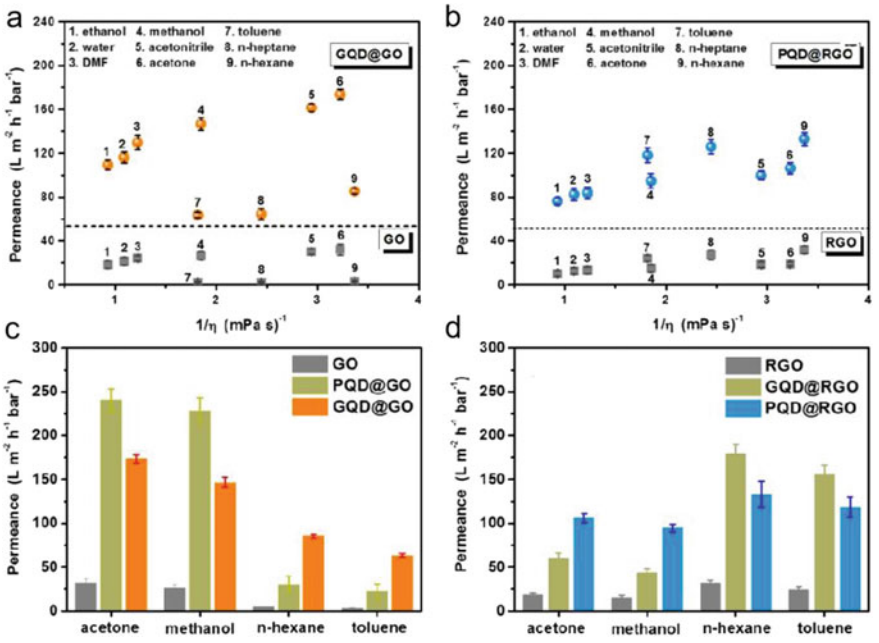

Fig. 3.34 Solvent permeation as a function of the viscosity for **a** GO membrane and GQD@GO membranes, **b** RGO membrane and PQD@RGO membranes. Solvent permeance of **c** GO, PQD@GO and GQD@GO membranes, and **d** RGO, PQD@RGO and GQD@RGO membranes. Copyright (2020), Elsevier [19]

Figure 3.35a and b illustrate that GQD@GO membrane with amplified channel sizes has a lower rejection for dyes smaller than 1.4 nm, only 42.4% for MB, compared to the primary GO membrane. Further increase dye size to 2.0 nm, the membranes can reject most of the RB with a rejection of over 95%. For larger dyes, the rejection achieves almost 100%. In addition, PQD@RGO membrane also exhibits a similar rejection. Compared with original GO membrane and RGO membrane, the corresponding composite membranes achieve a similar rejection capacity for the dyes with size > 2.0 nm. The small channel size of lamellar composite membranes should is mainly factor for precise dye rejection. And, the inserted QDs would also enhance dye rejection due to steric hindrance effect. Besides, the adjacent nanosheets with strong π−π interaction can also facilitate dye rejection. Note that the resulted membranes can meet the requirement of rejection ability during nanofiltration process, providing a promising prospect for OSN applications [59].

QDs were embedded into graphene-based lamellar membranes nanochannels to adjust the microenvironment and strengthen the nanofiltration performance. GQDs were introduced into the nanochannels of GO lamellar membranes to create hydrophobic sites within hydrophilic nanochannels to improve the affinity between membrane and non-polar solvents. The amphipathic nanodomains that are well-designed readily promote both polar and non-polar solvents to dissolute into

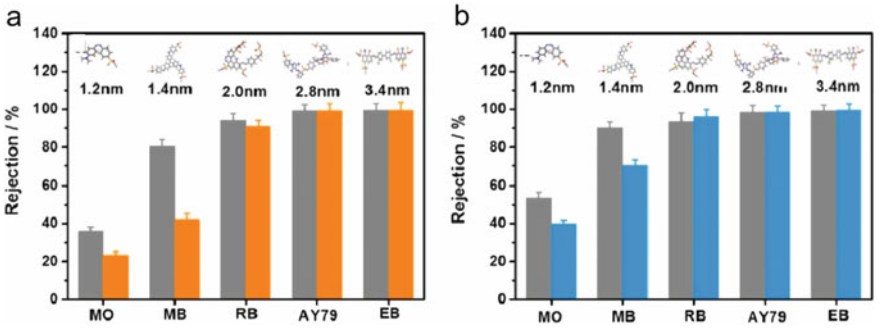

Fig. 3.35 **a** and **b** Dye rejection performance of (gray stripes are original GO membrane and RGO membrane, orange stripes are GQD@GO membrane, and blue stripes are PQD@RGO membrane). Copyright (2020), Elsevier [19]

membrane, and the enlarged channel size (from 0.84 to 1.35 nm) facilitates rapid molecule permeation driven by pressure. This highly coordinated transport process results in excellent solvent permeance: 85.4 L m^{-2} h^{-1} bar^{-1} and 173.5 L m^{-2} h^{-1} bar^{-1} for n-hexane and acetone, respectively. Accordingly, it is proved that the chemical affinity is the primary factor that determines permeance of solvents as it controls molecules to enter into nanochannels. To validate this observation, similar effect was achieved by inserting hydrophilic PQDs into hydrophobic RGO nanochannels. Besides, the as-prepared graphene-based lamellar membranes show satisfactory rejection for large dyes (> 2.0 nm). And, these membranes show excellent structural stability even in harshly acidic or alkaline environments. This strategy to control microenvironments of nanochannels provides new approaches for the design of advanced lamellar membranes in practical applications.

References

1. R.P. Lively, D.S. Sholl, From water to organics in membrane separations. Nat. Mater. **16**, 276–279 (2017)
2. J. Shen, G. Liu, Y. Ji, Q. Liu, L. Cheng, K. Guan, M. Zhang, G. Liu, J. Xiong, J. Yang, W. Jin, 2D MXene nanofilms with tunable gas transport channels. Adv. Func. Mater. **28**, 1801511 (2018)
3. G. Liu, W. Jin, N. Xu, Two-dimensional-material membranes: a new family of high-performance separation membranes. Angew. Chem. Int. Ed. **55**, 13384–13397 (2016)
4. N. Ahmad, P. Goh, K. Wong, A. Zulhairun, A. Ismail, Enhancing desalination performance of thin film composite membrane through layer by layer assembly of oppositely charged titania nanosheet. Desalination **476**, 114167 (2020)
5. L. Chen, G. Shi, J. Shen, B. Peng, B. Zhang, Y. Wang, F. Bian, J. Wang, D. Li, Z. Qian, G. Xu, G. Liu, J. Zeng, L. Zhang, Y. Yang, G. Zhou, M. Wu, W. Jin, J. Li, H. Fang, Ion sieving in graphene oxide membranes *via* cationic control of interlayer spacing. Nature **550**, 380–383 (2017)
6. X. Zhang, H. Liu, L. Jiang, Wettability and applications of nanochannels. Adv. Mater. **31**, 1804508 (2019)

7. L. Huang, Y. Li, Q. Zhou, W. Yuan, G. Shi, Graphene oxide membranes with tunable semipermeability in organic solvents. Adv. Mater. **27**, 3797–3802 (2015)
8. Q. Yang, Y. Su, C. Chi, C.T. Cherian, K. Huang, V.G. Kravets, F.C. Wang, J.C. Zhang, A. Pratt, A.N. Grigorenko, F. Guinea, A.K. Geim, R.R. Nair, Ultrathin graphene-based membrane with precise molecular sieving and ultrafast solvent permeation. Nat. Mater. **16**, 1198–1202 (2017)
9. K.H. Thebo, X. Qian, Q. Zhang, L. Chen, H. Cheng, W. Ren, Highly stable graphene-oxide-based membranes with superior permeability. Nat. Commun. **9**, 1486 (2018)
10. H. Zhang, Ultrathin two-dimensional nanomaterials. ACS Nano **9**, 9451–9469 (2015)
11. L. Zhang, B. Chen, A. Ghaffar, X. Zhu, Nanocomposite membrane with polyethylenimine-grafted graphene oxide as a novel additive to enhance pollutant filtration performance. Environ. Sci. Technol. **52**, 5920–5930 (2018)
12. Y. Zheng, S. Zheng, H. Xue, H. Pang, Metal-organic frameworks/graphene-based materials: preparations and applications. Adv. Func. Mater. **28**, 1804950 (2018)
13. S. Karan, S. Samitsu, X. Peng, K. Kurashima, I. Ichinose, Ultrafast viscous permeation of organic solvents through diamond-like carbon nanosheets. Science **335**, 444–447 (2012)
14. Q. Zhang, J. Teng, G. Zou, Q. Peng, Q. Du, T. Jiao, J. Xiang, Efficient phosphate sequestration for water purification by unique sandwich-like MXene/magnetic iron oxide nanocomposites. Nanoscale **8**, 7085–7093 (2016)
15. H. Li, Z. Song, X. Zhang, Y. Huang, S. Li, Y. Mao, H.J. Ploehn, Y. Bao, M. Yu, Ultrathin molecular-sieving graphene oxide membranes for selective hydrogen separation. Science **342**, 95–98 (2013)
16. L. Ding, Y. Wei, Y. Wang, H. Chen, J. Caro, H. Wang, A two-dimensional lamellar membrane: MXene nanosheet stacks. Angew. Chem. Int. Ed. **56**, 1825–1829 (2017)
17. M. Naguib, M. Kurtoglu, V. Presser, J. Lu, J. Niu, M. Heon, L. Hultman, Y. Gogotsi, M.W. Barsoum, Two-dimensional nanocrystals produced by exfoliation of Ti_3AlC_2. Adv. Mater. **23**, 4248–4253 (2011)
18. J. Wang, Z. Yuan, X. Wu, Y. Li, J. Chen, Z. Jiang, Beetle-inspired assembly of heterostructured lamellar membranes with polymer cluster–patterned surface for enhanced molecular permeation. Adv. Func. Mater. **29**, 1900819 (2019)
19. X. Wu, S. Liu, X. Cui, J. Lin, H. Zhang, J. Zhang, J. Wang, Manipulating microenvironments of nanochannels in lamellar membranes by quantum dots for highly enhanced nanofiltration performance. Chem. Eng. Sci. **228**, 116001 (2020)
20. Q. Wang, X. Wu, J. Chen, W. Li, H. Zhang, J. Wang, Ultrathin and stable organic-inorganic lamellar composite membrane for high-performance organic solvent nanofiltration. Chem. Eng. Sci. **228**, 116002 (2020)
21. H. Huang, Z. Song, N. Wei, L. Shi, Y. Mao, Y. Ying, L. Sun, Z. Xu, X. Peng, Ultrafast viscous water flow through nanostrand-channelled graphene oxide membranes. Nat. Commun. **4**, 2979 (2013)
22. X. Cui, X. Wu, J. Zhang, J. Wang, H. Zhang, F. Du, L. Qu, X. Cao, P. Zhang, A loosely stacked lamellar membrane of irregular MoS_2 flakes for ultrahigh water and organics permeation. J. Mater. Chem. A **7**, 12698–12705 (2019)
23. J. Wang, P. Chen, B. Shi, W. Guo, M. Jaronie, S. Qiao, A regularly channeled lamellar membrane for unparalleled water and organics permeation. Angew. Chem. Int. Ed. **57**, 6814–6818 (2018)
24. X. Wu, X. Cui, W. Wu, J. Wang, Y. Li, Z. Jiang, Elucidating ultrafast molecular permeation through well-defined 2D nanochannels of lamellar membranes. Angew. Chem. Int. Ed. **58**, 18524–18529 (2019)
25. I. Jung, M. Pelton, R. Piner, D.A. Dikin, S. Stankovich, S. Watcharotone, M. Hausner, R.S. Ruoff, Simple approach for high-contrast optical imaging and characterization of graphene-based sheets. Nano Lett. **7**, 3569–3575 (2007)
26. J. Shen, G. Liu, K. Huang, Z. Chu, W. Jin, N. Xu, Subnanometer two-dimensional graphene oxide channels for ultrafast gas sieving. ACS Nano **10**, 3398–3409 (2016)
27. Z. Jalilvand, F.Z. Ashtiani, A. Fouladitajar, H. Rezaei, Computational fluid dynamics modeling and experimental study of continuous and pulsatile flow in flat sheet microfiltration membranes. J. Membr. Sci. **450**, 207–214 (2014)

28. G. Hummer, J.C. Rasaiah, J.P. Noworyta, Water conduction through the hydrophobic channel of a carbon nanotube. Nature **414**, 188–190 (2001)
29. L. Huang, J. Chen, T. Gao, M. Zhang, Y. Li, L. Dai, L. Qu, G. Shi, Reduced graphene oxide membranes for ultrafast organic solvent nanofiltration. Adv. Mater. **28**, 8669–8674 (2016)
30. L. Sun, Y. Ying, H. Huang, Z. Song, Y. Mao, Z. Xu, X. Peng, Ultrafast molecule separation through layered WS_2 nanosheet membranes. ACS Nano **8**, 6304–6311 (2014)
31. J. Abraham, K.S. Vasu, C.D. Williams, K. Gopinadhan, Y. Su, C.T. Cherian, J. Dix, E. Prestat, S.J. Haigh, I.V. Grigorieva, P. Carbone, A.K. Geim, R.R. Nair, Tunable sieving of ions using graphene oxide membranes. Nat. Nanotechnol. **12**, 546–550 (2017)
32. S. Qiu, M. Xue, G. Zhu, Metal–organic framework membranes: from synthesis to separation application. Chem. Soc. Rev. **43**, 6116–6140 (2014)
33. S. Karan, Z. Jiang, A.G. Livingston, Sub-10 nm polyamide nanofilms with ultrafast solvent transport for molecular separation. Science **348**, 1347–1351 (2015)
34. M. Alhabeb, K. Maleski, B. Anasori, P. Lelyukh, L. Clark, S. Sin, Y. Gogotsi, Guidelines for synthesis and processing of two-dimensional titanium carbide ($Ti_3C_2T_x$ MXene). Chem. Mater. **29**, 7633–7644 (2017)
35. Z. Li, H. Zhang, J. Han, Y. Chen, H. Lin, T. Yang, Ultrahigh carbon dioxide-selective composite membrane containing a γ-CD-MOF layer. Adv. Mater. **30**, 1706981 (2018)
36. G. Liu, W. Jin, N. Xu, Graphene-based membranes. Chem. Soc. Rev. **44**, 5016–5030 (2015)
37. D.B. Shinde, G. Sheng, X. Li, M. Ostwal, A. Emwas, K. Huang, Z. Lai, Crystalline 2D covalent organic framework membranes for high-flux organic solvent nanofiltration. J. Am. Chem. Soc. **140**, 14342–14349 (2018)
38. X. Zou, G. Zhu, Microporous organic materials for membrane-based gas separation. Adv. Mater. **30**, 1700750 (2018)
39. H.W. Kim, H.W. Yoon, S.M. Yoon, B.M. Yoo, B.K. Ahn, Y.H. Cho, H.J. Shin, H. Yang, U. Paik, S. Kwon, Selective gas transport through few-layered graphene and graphene oxide membranes. Science **342**, 91–95 (2013)
40. J.A. Willcox, H.J. Kim, Molecular dynamics study of water flow across multiple layers of pristine, oxidized, and mixed regions of graphene oxide. ACS Nano **11**, 2187–2193 (2017)
41. Y. Yao, L. Tolentino, Z. Yang, X. Song, W. Zhang, Y. Chen, C. Wong, High-concentration aqueous dispersions of MoS_2. Adv. Func. Mater. **23**, 3577–3583 (2013)
42. X. Wang, H. Tang, S. Huang, L. Zhu, Fast and facile microwave-assisted synthesis of graphene oxide nanosheets. RSC Adv. **4**, 60102–60105 (2014)
43. S.H. Aboutalebi, M.M. Gudarzi, Q.B. Zheng, J. Kim, Spontaneous formation of liquid crystals in ultralarge graphene oxide dispersions. Adv. Func. Mater. **21**, 2978–2988 (2011)
44. K. Ai, C. Ruan, M. Shen, L. Lu, MoS_2 nanosheets with widened interlayer spacing for high-efficiency removal of mercury in aquatic systems. Adv. Func. Mater. **26**, 5542–5549 (2016)
45. Y. Wang, L. Li, Y. Wei, J. Xue, H. Chen, L. Ding, J. Caro, H. Wang, Water transport with ultralow friction through partially exfoliated g-C_3N_4 nanosheet membranes with self-supporting spacers. Angew. Chem. Int. Ed. **56**, 8974–8980 (2017)
46. K. Goh, W. Jiang, H.E. Karahan, S. Zhai, L. Wei, D. Yu, A.G. Fane, R. Wang, Y. Chen, All-carbon nanoarchitectures as high-performance separation membranes with superior stability. Adv. Func. Mater. **25**, 7348 (2015)
47. Z. Yuan, X. Wu, Y. Jiang, Y. Li, J. Huang, L. Hao, J. Zhang, J. Wang, Carbon dots-incorporated composite membrane towards enhanced organic solvent nanofiltration performance. J. Membr. Sci. **549**, 116001 (2018)
48. H. Abadikhah, E.N. Kalali, S. Behzadi, S.A. Khan, X. Xu, M.E. Shabestari, S. Agathopoulos, High flux thin film nanocomposite membrane incorporated with functionalized TiO_2@reduced graphene oxide nanohybrids for organic solvent nanofiltration. Chem. Eng. Sci. **204**, 99–109 (2019)
49. L. Ding, L. Li, Y. Liu, Y. Wu, Z. Lu, J. Deng, Y. Wei, J. Caro, H. Wang, Effective ion sieving with $Ti_3C_2T_x$ MXene membranes for production of drinking water from seawater. Nat. Sustain. **3**, 296–302 (2020)

50. D. Emadzadeh, T. Matsuuraa, M. Ghanbaric, A. Ismail, Hybrid forward osmosis/ultrafiltration membrane bag for water purification. Desalination **468**, 114071 (2019)
51. Y. Feng, M. Weber, C. Maletzko, T. Chung, Fabrication of organic solvent nanofiltration membranes *via* facile bioinspired one-step modification. Chem. Eng. Sci. **198**, 74–84 (2019)
52. S. William, J. Hummers, E.R. Offeman, Preparation of graphitic oxide. J. Am. Chem. Soc. **80**, 1339–1339 (1958)
53. D. Li, M.B. Müller, S. Gilje, R.B. Kaner, G.G. Wallace, Processable aqueous dispersions of graphene nanosheets. Nat. Nanotechnol. **3**, 101–105 (2008)
54. J. Zhu, J. Hou, A. Uliana, Y. Zhang, M. Tiana, B. Van der Bruggen, The rapid emergence of two-dimensional nanomaterials for high-performance separation membranes. J. Mater. Chem. A **6**, 3773–3792 (2018)
55. S. Wang, D. Mahalingam, B. Sutisna, S.P. Nunes, 2D-dual-spacing channel membranes for high performance organic solvent nanofiltration. J. Mater. Chem. A **7**, 11673 (2019)
56. M. Cheng, L. Huang, Y. Wang, Y. Zhao, J. Tang, Y. Wang, Y. Zhang, M. Hedayati, M.J. Kipper, S.R. Wickramasinghe, Synthesis of graphene oxide/polyacrylamide composite membranes for organic dyes/water separation in water purification. J. Mater. Sci. **54**, 252–264 (2019)
57. W. Wang, E. Eftekhari, G. Zhu, X. Zhang, Z. Yan, Q. Li, Graphene oxide membranes with tunable permeability due to embedded carbon dots. Chem. Commun. **50**, 13089–13092 (2014)
58. J. Yang, D. Gong, G. Li, G. Zeng, Q. Wang, Y. Zhang, G. Liu, P. Wu, E. Vovk, Z. Peng, X. Zhou, Y. Yang, Z. Liu, Y. Sun, Self-assembly of thiourea-cross-linked graphene oxide framework membranes toward separation of small molecules. Adv. Mater. **30**, 1705775 (2018)
59. L. Prozorovska, P.R. Kidambi, State-of-the-art and future prospects for atomically thin membranes from 2D materials. Adv. Mater. **30**, 1801179 (2018)

Chapter 4
Composite Proton Exchange Membrane for Hydrogen Fuel Cell

Guoli Zhou, Jingchuan Dang, and Jingtao Wang

4.1 Introduction

Fuel cell, converting chemical energy into electrical energy, has been regarded as promising next generation energy conversion devices [1, 2]. Among various kinds of fuel cells, proton exchange membrane fuel cell (PEMFC), i.e., hydrogen fuel cell, has attracted extensive research interests because of the merits of environmental friendliness, high energy density, easy fuel handling, and feasibility of mobile and transport applications [3–6]. As the vital content of PEMFC, proton exchange membrane (PEM) is demanded to effectively transfer protons, block fuels (i.e., methanol, hydrogen), and possess acceptable structure stability for practical application [7–9].

The commercial PEM is the state-of-the-art perfluorosulfonic acid-based membrane (Nafion) in virtue of their high proton conductivity and stable physicochemical properties [3, 10]. In particular, as a representative of commercial PEMs, Nafion possesses prototypical bicontinuous nanostructure with parallel-cylindrical or locally-flat interconnected hydrophilic ionic nanophases in a hydrated state. This gives Nafion a significantly high proton conduction ability (~0.1 S cm^{-1} conductivity) [11–13]. However, the ionic nanophases are highly solvent dependent that shrink and even collapse with solvent loss—resulting in significantly decreased performance [14, 15]. The conductivity of Nafion decays by more than three orders of magnitude following water loss [16, 17]. In view of this, tremendous efforts have been devoted to the modification of Nafion or development of alternative membrane materials at present.

Among all the approaches for improving the properties of PEM, organic–inorganic hybridization approach to prepare hybrid/composite membranes has become a

G. Zhou · J. Dang · J. Wang (✉)
School of Chemical Engineering, Zhengzhou University, Zhengzhou 450001, P. R. China
e-mail: jingtaowang@zzu.edu.cn

J. Wang
Henan Institute of Advanced Technology, Zhengzhou University, Zhengzhou 450003, P. R. China

J. Wang and W. Wu (eds.), *Functional Membranes for High Efficiency Molecule and Ion Transport*, https://doi.org/10.1007/978-981-19-8155-5_4

hot topic among researchers, combining the advantages from the inorganic fillers and organic polymer matrix [18, 19]. To date, inorganic fillers, including 0D quantum dots, 1D tubes, 2D sheets, and 3D irregular spheres and metal–organic frameworks, have been incorporated into the membrane [20, 21]. For example, Kim et al. obtained a 60% increase in proton conductivity for Nafion [from 6.5 to 10.4 mS cm^{-1} at 80 °C and 25% relative humidity (RH)] with the inclusion of 1 wt% phosphotungstic acid modified graphene oxide (GO) [21]. In addition, with the gradual awareness of the inherent relationship between interfacial structures and proton conductivities of membranes, increasing attentions have been paid to the design of surface-modified inorganic fillers, so as to tailor the structures and performances of composite membranes. According to extensive studies reported [22–25], the available functional groups, which provide the sites to construct paths, are required for the modification of filler surface to enhance their proton conduction ability. In this chapter, composite PEMs with different functional fillers are introduced, including functionalized GO, ionic liquid, polymer microcapsule, and quantum dots. The microstructure and physicochemical properties of those composite membranes are investigated in detail, and their performances are evaluated in terms of proton conduction, structural stability, and application for hydrogen fuel cell.

4.2 Composite Membrane with Polymer Layer-Functionalized GO

GO nanosheets were fabricated by oxidizing natural graphite according to the method in literature [26]. SGO was prepared through distillation-precipitation polymerization method [27]: GO (5.0 g) was added into the mixture of water (20 mL), aqueous solution of ammonium (15 mL), and ethanol (180 mL) with vigorous stirring at 25 °C for 24 h. Afterward, 3-(trimethoxysilyl) propyl methacrylate (MPS) (2.0 mL) was incorporated into the resultant mixture. After stirring for another 24 h, the MPS-modified GO was purified by centrifugation and then drying in a vacuum oven. AIBN (0.02 g), St (0.50 mL), crosslinker divinylbenzene (DVB) (0.50 mL), and MPS-modified GO (0.30 g) were dissolved by ultrasonic in acetonitrile (80 mL). The mixture was heated and kept boiling until half acetonitrile was distilled out. Afterward, the modified GO was purified and dried for sulfonation. The resultant modified GO was sulfonated by concentrated sulfuric acid (94%) at 40 °C for 2 h or 4 h to obtain S2GO or S4GO, respectively.

CS (1.2 g) was dissolved in acetic acid aqueous solution (30 mL) and stirred for 2 h at room temperature. Simultaneously, a certain amount of GO or SGO was dispersed into water (30 mL) with ultrasonic treatment for 24 h. Afterward, these two solutions were mixed together and stirred vigorously for another 24 h. The resultant homogenous solution was cast onto a clear glass plate and dried at 30 °C for 72 h to obtain a hybrid membrane. The obtained membrane was then immersed in 1.0 M sulfuric acid solution for 24 h to completely crosslink the CS matrix, following

by extensively rinsing with water to remove the residual acid. After being dried, the hybrid membranes were obtained and designated as CS/GO-*X*, CS/S2GO-*X,* or CS/S4GO-*X* representing GO, S2GO, or S4GO as the nanofillers, where *X* (*X* = 0.5, 1.0, 1.5, 2.0, and 2.5) represented the weight percentage of the nanofillers to CS. CS control membrane was fabricated in exactly the same way as described above without incorporating any nanosheets. The average thickness of the dry membranes fell in the range of 60 ~ 68 μm.

The preparation process of SGO includes mainly three steps, as shown in Fig. 4.1: The first step was grafting MPS on the surface of GO to introduce reactive vinyl groups; the second step was forming polymer layer (poly(DVB-*co*-St)) through distillation-precipitation polymerization, where St provided phenyl groups and DVB acted as crosslinker; the third step was grafting sulfonic acid groups on polymer layer through the sulfonation of phenyl groups. During the third step, the loading amount of sulfonic acid group was adjusted by sulfonation time, and the two kinds of SGO with different loading amount were designated as S2GO and S4GO.

The morphology of GO, S2GO, and S4GO was detected by transmission electron microscopy (TEM), as shown in Fig. 4.2. Different from graphite, GO is exfoliated into nanosheet, which agglomerated driven by the strong interlayer attractions (Fig. 4.2a). Due to the sulfonation reaction mainly occurs on poly(DVB-*co*-St) layer, the morphology of nanosheets is slightly altered after sulfonation, and S2GO (Fig. 4.2b) and S4GO (Fig. 4.2c) remain the sheet structure. For SGO, the presence of $-SO_3H$ groups weakens the interlayer interaction, therefore preventing the stacking and reducing the contact area.

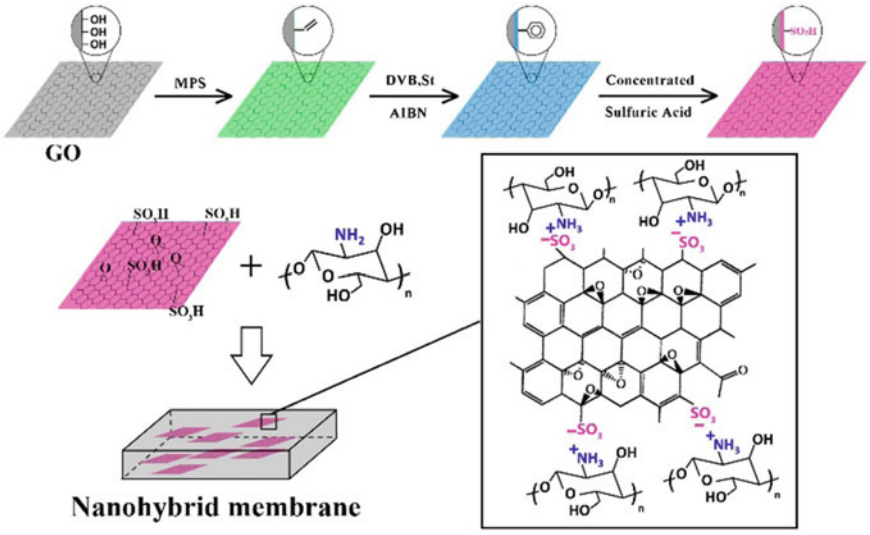

Fig. 4.1 Preparation of SGO and hybrid membrane. Copyright (2014), Elsevier [28]

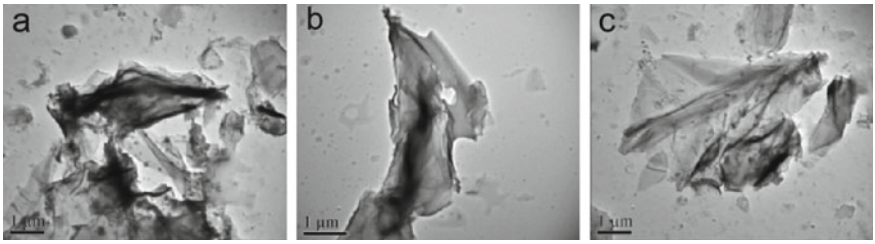

Fig. 4.2 TEM images of nanosheets: **a** GO, **b** S2GO, and **c** S4GO. Copyright (2014), Elsevier [28]

The as-prepared GO, S2GO, and S4GO were then incorporated into CS matrix to prepare hybrid membranes via solution-casting method. To better investigate the interfacial interaction between CS and nanosheet, FTIR of CS, CS/GO-1.5, CS/S2GO-1.5, and CS/S4GO-1.5 was conducted and displayed in Fig. 4.3a. Three characteristic peaks around 3260, 1628, and 1527 cm^{-1} are observed for all the membranes, which are related to the characteristic peaks of CS, viz., hydroxyl, amide I, and amide II groups, respectively. The peak at 1151 cm^{-1} is assigned to C–O stretching vibrations of C–OH in CS chain. The intensity of these characteristic peaks in hybrid membranes becomes weak as compared to CS control membrane, implying the generation of interfacial attractions (e.g., hydrogen bonding and electrostatic interactions) between –OH/–NH_2 groups of CS and acid groups of nanosheets. Compared with GO-incorporated membrane, SGO-incorporated membranes give rise to a new peak at 898 cm^{-1} (dashed line), corresponding to the symmetric stretching of –S–O^- group. This group should result from the deprotonation of –SO_3H on SGO driven by –NH_2 in CS matrix. In this manner, acid–base pairs (–$SO_3^-\cdots{}^+{}_3$HN–) are formed along SGO surface. The influence of nanosheet content on interfacial interaction was probed, and the results were shown in Fig. 4.3b. It could be found that the intensity of the characteristic peaks for CS gradually decreases with the increase of S2GO content from 0.5 to 2.5%, which is attributed to the increase of acid–base pairs and hence the interfacial attractions.

The microstructure of hybrid membranes was detected using scanning electron microscopy (SEM) images of cross-section. Figure 4.4a shows that CS control membrane is dense and smooth, without obvious crack or pinhole. In comparison, the cross-sections of hybrid membranes become rougher and display obvious wrinkles due to the presence of nanosheets (assigned in Fig. 4.4b–d). Besides, the overall morphology of hybrid membranes is uniform without crack. This observation suggests that the nanosheets (GO, S2GO, and S4GO) are well dispersed within CS matrix because of the strong interfacial interactions, making a good compatibility between CS and nanosheets. For hybrid membranes, SGO-incorporated membranes possess more wrinkles than GO-incorporated membrane, inferring much better dispersion of SGO. The well dispersion of SGO would provide more continuous pathways for proton migration.

As a key indicator of PEM, proton conductivity is the performance-limiting parameter which determines the operational voltage and current output of a fuel cell [29].

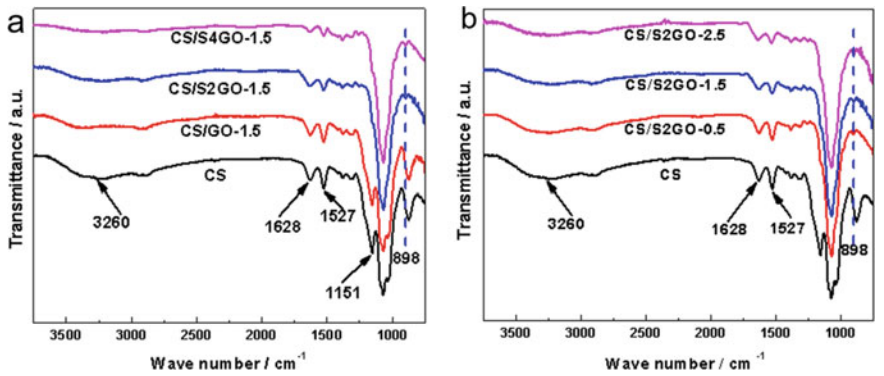

Fig. 4.3 FTIR spectra of CS control membrane and hybrid membranes. Copyright (2014), Elsevier [28]

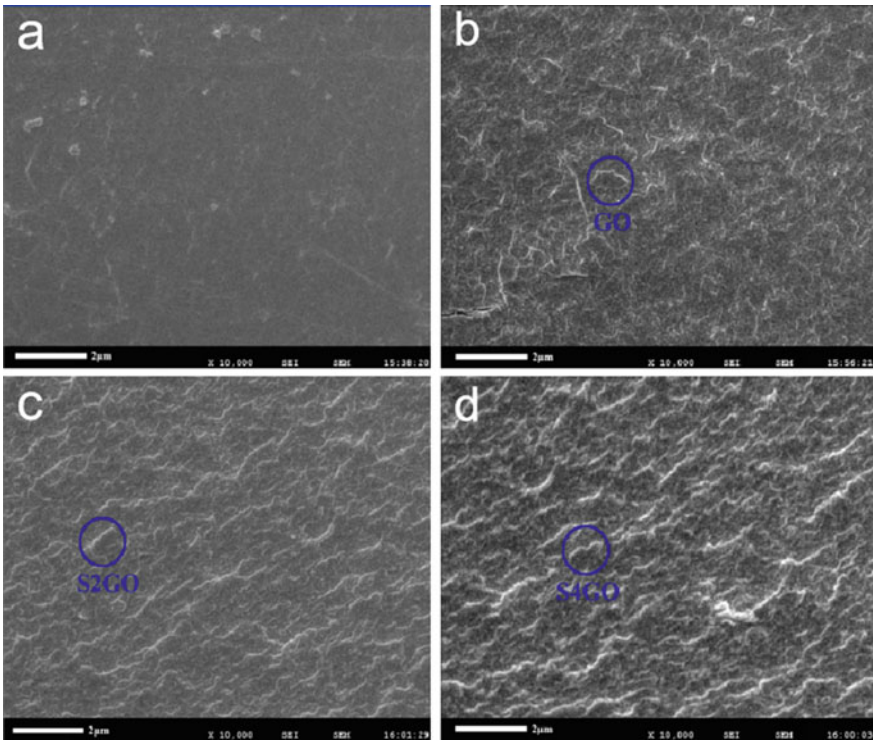

Fig. 4.4 SEM images of the cross-section of **a** CS, **b** CS/GO-1.5, **c** CS/S2GO-1.5, and **d** CS/S4GO-1.5. Copyright (2014), Elsevier [28]

Proton conductivities under hydrated (100% RH) conditions were conducted for better understanding the effect of SGO on proton transfer. The conductivity at 25 °C and 100% RH is shown in Fig. 4.5a. It is found that CS control membrane attains a conductivity of 0.0117 S cm^{-1}. The incorporation of SGO nanosheets significantly promotes the proton transfer through hybrid membranes, giving the conductivity of 0.0174 or 0.0182 S cm^{-1} with elevation of 49% or 56% when incorporating 0.5% S2GO or S4GO, respectively. As mentioned in water uptake, proton transfer through PEM obeys vehicle mechanism and/or Grotthuss mechanism. Vehicle mechanism is related to the proton diffusing in the form of H_3O^+, $H_5O_2^+$, or $H_9O_4^+$, while Grotthuss mechanism is related to the proton hoping from one hopping site to the adjacent one [30, 31]. Considering the fact that the incorporation of SGO reduces the water uptake and area swelling of hybrid membranes, which in turn would reduce the vehicle-type transporting proton, the enhanced conductivities should be attributed to the increase of Grotthuss-type transporting proton. The transfer is reasonably promoted by: (i) the abundant sulfonic acid groups within membrane, which act as additional proton-hoping sites; (ii) the formation of acid–base pairs ($-SO_3^- \cdots {}^+{}_3HN-$), which serve as low-barrier proton-hoping sites, and (iii) the sheet structure with high specific surface area, which allows SGO to create wide and continuous pathways. Figure 4.5a indicates that the proton conductivity of hybrid membrane could be effectively enhanced by increasing the sulfonic acid group loading or content of SGO. Notably, CS/S4GO-2 achieves the highest conductivity of 0.0267 S cm^{-1}, 222.5% of that of CS control membrane. When further increasing the S4GO content to 2.5%, a reduction of conductivity is observed, due to the agglomeration of nanosheet. Under identical conditions, GO nanosheets display similar effect on elevating the conductivity of hybrid membrane through the conducting $–CO_2H$ groups.

The temperature-dependent conductivities under hydrated condition were shown in Fig. 4.5b–d. It is found that all the membranes exhibit gradual increase of conductivity with the temperature varying from 25 to 85 °C, resulting from the enhanced motion of polymer chains and water molecules at high temperature. For instance, the conductivity of CS control membrane increases from 0.0117 to 0.0253 S cm^{-1}. By comparison, the hybrid membrane possesses higher conductivity than CS control membrane under every testing temperatures, meanwhile following the order of CS < CS/GO-X < CS/S2GO-X < CS/S4GO-X. For another, as the temperature increases from 25 to 85 °C, conductivity elevations from 0.0195 to 0.0450, from 0.0226 to 0.0549, and from 0.0233 to 0.0612 S cm^{-1} are obtained for CS/GO-1.5, CS/S2GO-1.5, and CS/S4GO-1.5, with elevation rate of 130.7%, 142.9%, and 162.6%, respectively. These results indicate that the conduction ability of acid–base pair could be improved by increasing temperature, as the activated motion of acid–base pairs makes the enthalpy change smaller during proton hoping at elevated temperatures.

Considering the unique advantages of elevated-temperature PEMFC, the single cell performances were conducted under elevated temperature conditions. Due to the good comprehensive performances of proton conductivity and structural stability, CS/GO-2, CS/S2GO-2, CS/S4GO-2, and CS control membrane were chosen as representative and then measured under 120 °C. Similar thickness was utilized for each membrane to ensure a good comparison. Figure 4.6 reveals that CS control

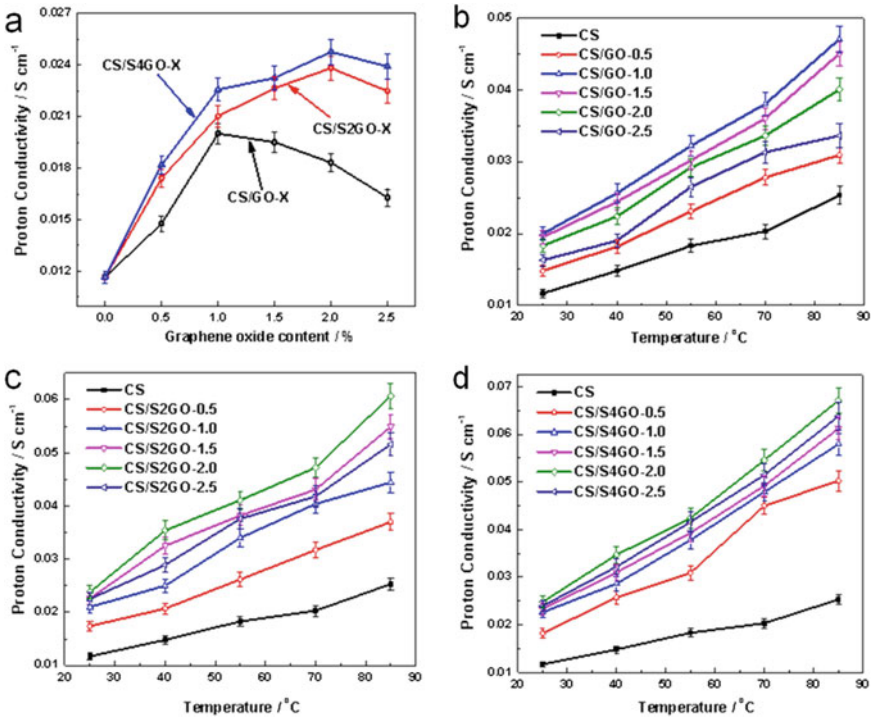

Fig. 4.5 **a** Proton conductivity at 25 °C and 100% RH. Temperature-dependent conductivity of **b** CS/GO-X, **c** CS/S2GO-X, and **d** CS/S4GO-X at 100% RH. Copyright (2014), Elsevier [28]

membrane attains the open-circuit voltage (OCV) of 0.95 V, inferring a good H_2 barrier ability. Meanwhile, the anhydrous conduction ability affords the control membrane acceptable cell performances with the maximum current density and power density of about 284.0 mA cm^{-2} and 81.2 mW cm^{-2}, respectively. Compared with the control membrane, the hybrid membranes acquire much better cell performances. The OCVs are elevated to 0.97, 0.98, and 0.99 V for CS/GO-2, CS/S2GO-2, and CS/S4GO-2, respectively. The increased OCVs indicate that the presence of GO/SGO within CS matrix increases the transfer pathways for H_2 molecules, thus enhancing the H_2 resistance abilities of hybrid membranes. In addition, it is found that incorporating 2% S2GO could provide a 58% increase of the maximum current density (448.7 mA cm^{-2}) and a 64% increase of the maximum power density (132.9 mW cm^{-2}). The enhanced proton conductivity should be the main factor for the elevated performances, which could reduce the electrolyte resistance of MEAs and facilitated the reduction reaction in cathode [32, 33]. For the hybrid membranes, the cell performances increase in the order of CS/GO-2 < CS/S2GO-2 < CS/S4GO-2, in accordance with the order of their proton conductivities. This finding supports the fact that proton conductivity of PEM plays a critical role in its cell performances. It should be noted that CS/S4GO-2 achieve the highest current density (459.3 mA cm^{-2})

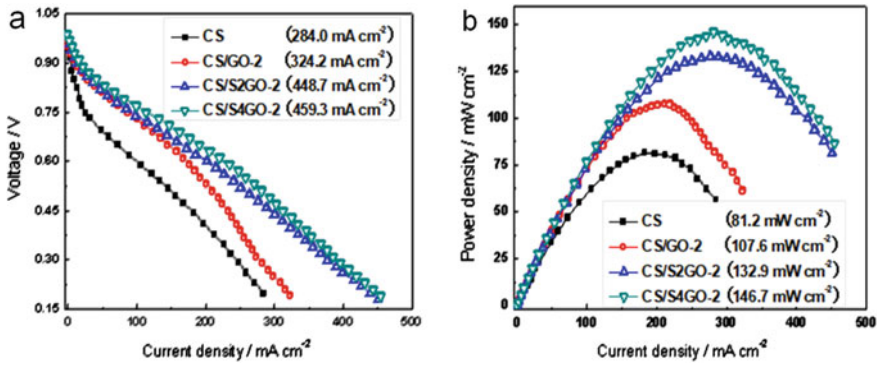

Fig. 4.6 Single cell performance of CS control membrane and hybrid membranes under 120 °C: **a** polarization curves and **b** power density–current density curves. Copyright (2014), Elsevier [28]

and power density (146.7 mW cm^{-2}), and these datas are also higher than those of Nafion under similar conditions [34]. Clearly, these results indicate that the SGO gives obvious enhancement in the cell performances of CS-based PEM. Together with the low cost of CS, the as-prepared hybrid membranes might have potential applications for PEMFC.

In this study, we report an attempt for highly conductive hybrid membrane by incorporating SGO nanosheets into CS matrix. SGO nanosheets with tunable sulfonic acid group loading amount are synthesized via the facile approach of distillation-precipitation polymerization. The conductivity measurements prove that SGO donates significant enhancement in proton conductivity to the hybrid membranes under hydrated conditions by means of (i) the generation of acid–base pairs at CS-SGO interface, which work as facile proton-hoping sites, and (ii) the nanosheet structure and high specific surface area of SGO, which allow the hoping sites form continuous and wide pathways, affording efficient proton migration to the SGO-filled membrane. Moreover, increasing the sulfonic acid group loading amount or content of SGO provide more transfer pathways and thereby further enhance the proton conductivity. The stable structure of the hybrid membrane contributes to stable proton transfer behaviors over days under both hydrated conditions. Benefiting from the enhanced proton conductivity, the hybrid membrane achieves much higher H_2/O_2 PEMFC performances than those of the control membrane and Nafion under elevated temperature. Considering the facile preparation process, the present study might provide a potential strategy on the rational design and preparation of highly conductive proton conductors under various conditions.

4.3 Composite Membrane with Polymer Brush-Functionalized GO

GO was synthesized from flake graphite based on the method in literature. Two types of SP-GO were fabricated via a crosslinker-free distillation-precipitation polymerization method [35, 36]: GO (5.0 g) was dispersed in the mixture of ethanol (180 mL), water (20 mL), and aqueous solution of ammonium (15 mL) with vigorous stirring at room temperature for 24 h. MPS-modified GO (0.30 g), azodiisobutyronitrile AIBN (0.02 g), St (0.50 mL), and SS (0.50 mL) were dissolved into acetonitrile (80 mL) in a dried two-necked flask under ultrasonic bathing. The above mixture was heated and kept boiling until 40 mL acetonitrile was distilled out. Afterward, the modified GO was purified by centrifugation with washing by acetonitrile. The resultant modified GO was treated with 0.1 M HCl to exchange the Na^+ in $–SO_3Na$ with H^+. Then, sulfonated polymer brush-modified GO was obtained after being dried in a vacuum oven at 60 °C till constant weight. The as-synthesized SP-GO was designated as SGO. Another distillation-precipitation polymerization process was performed with the synthesized SGO as initial seed, by using exactly the same method as the case for MPS-modified GO. The as-synthesized SP-GO was designated as SSGO.

Sulfonated poly(ether ether ketone) (SPEEK) was obtained via post-sulfonation of PEEK as follows [17]: PEEK pellets (20.0 g) were dispersed into 98 wt% sulfuric acid solution (147 mL) at 25 °C. The obtained mixture was first stirred vigorously for 10 h at 45 °C, cooled to room temperature, and then added into excessive water under continuous agitation. The precipitated SPEEK was completely washed with water until the pH reached 7.0. Then, it was dried first at room temperature for 2 days followed by drying at 60 °C under vacuum for 24 h. The sulfonation degree of SPEEK was 65.0% as determined by titration method.

A certain amount of fillers (GO, SGO, or SSGO) were dispersed into DMF (8.0 g) under ultrasonic treatment and stirred for 8 h at room temperature, respectively. Afterward, SPEEK (0.7 g) was added into the above solution and stirred vigorously for another 12 h. The resultant solution was cast onto a clear glass plate and dried first at 60 °C for 12 h, then at 80 °C for 12 h. The composite membranes were designated as SPEEK/GO-*X*, SPEEK/SGO-*X*, or SPEEK/SSGO-*X*, representing GO, SGO, or SSGO as the fillers, where *X* ($X = 2.5, 5, 7.5$, or 10) represented the weight percentage of the fillers to SPEEK. SPEEK control membrane was fabricated in exactly the same way as above without incorporating fillers. It should be pointed out that the average thickness of the dry membranes was in the range of 80 ~ 91 μm.

The fabrication process of SGO mainly includes three steps as illustrated in Fig. 4.7: The first step is grafting MPS on the surface of GO to introduce reactive vinyl groups; the second step is the grafting sulfonated polymer brushes (poly(SS-*co*-St)) through distillation-precipitation polymerization, in which SS provides sulfonate sodium groups while St is used to promote the polymerization of SS; the third step is exchanging the Na^+ in sulfonate sodium with H^+ to obtain sulfonated polymer brushes. Moreover, SSGO with longer brush and higher $–SO_3H$ group loading was fabricated by repeating the polymerization process.

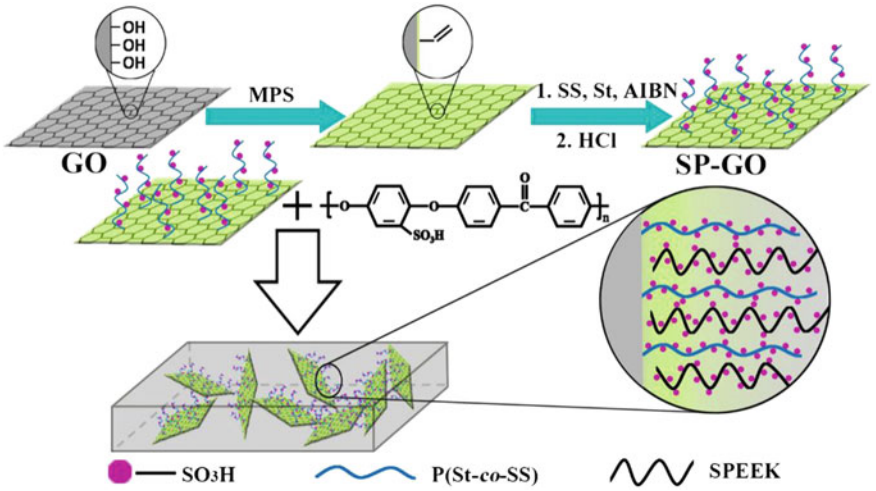

Fig. 4.7 Fabrication of SGO and the composite membrane. Copyright (2015), Elsevier [37]

The morphology of GO, SGO, and SSGO was detected by TEM, and the images were displayed in Fig. 4.8. It can be seen that GO appears as an exfoliated sheet with some wrinkles (Fig. 4.8a), which is close to the morphology in literature [18, 19]. These wrinkles should originate from the GO agglomeration driven by the strong interlayer attractions. Compared with GO, the sulfonic acid-containing polymer brushes weakens the interlayer interactions of SGO and SSGO, thus facilitating SGO and SSGO to exfoliate into individual sheets. Moreover, the sheet structure is maintained for both SGO (Fig. 4.8b) and SSGO (Fig. 4.8c) without obvious destruction since the polymerization occurs mainly at the vinyl groups of MPS on GO surface.

Ion-exchange capacity (*IEC*), as an indicator of the number of ion exchangeable groups and available protons, strongly affects proton conduction [23]. *IEC* values measured by the classical titration method are shown in Fig. 4.9, which reveals that SPEEK control membrane attains an *IEC* value of 1.765 mmol g^{-1}. By comparison, the lower *IEC* values of GO than SPEEK decrease the $-SO_3H$ concentration in SPEEK/GO-*X*, thereby yielding reduced *IEC* values. For example, the *IEC* value

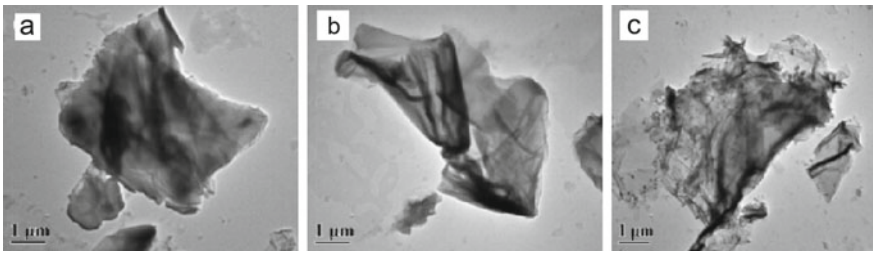

Fig. 4.8 TEM images of **a** GO, **b** SGO, and **c** SSGO. Copyright (2015), Elsevier [37]

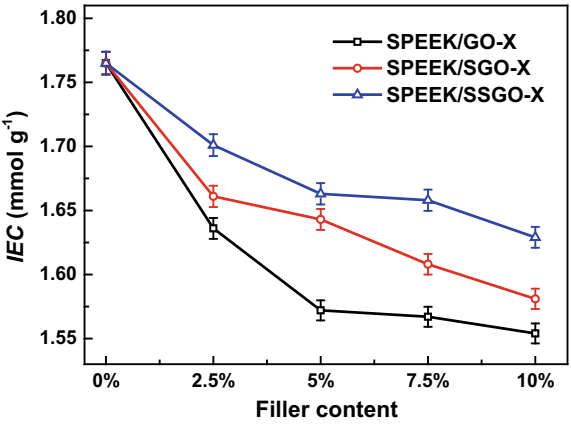

Fig. 4.9 *IEC* values of SPEEK control and composite membranes at 25 °C. Copyright (2015), Elsevier [37]

of SPEEK/GO-5 is about 1.572 mmol g^{-1}. When compared with SPEEK/GO-*X*, SGO and SSGO donate higher *IEC* values to SPEEK/SGO-*X* and SPEEK/SSGO-*X* membranes. For instance, *IEC* values of 1.643 and 1.662 mmol g^{-1} are acquired when adding 5% SGO and SSGO, respectively. The increased *IEC* values reasonably result from the sulfonic acid groups in the polymer brushes. In addition, *IEC* values of the composite membranes decrease continuously with the filler content. Taking SPEEK/SSGO-*X* as an example, increasing the SSGO content from 2.5% to 10% gives a decrease of *IEC* from 1.701 to 1.629 mmol g^{-1}.

Proton conductivity, determining the operational voltage and current output of a fuel cell, is the most essential property for a PEM fuel cell. At a molecular level, the proton conduction in PEMs obeys two mechanisms [29]: one is Grotthuss mechanism, which is related to the proton hopping from one solvent molecule or conducting carrier to a neighboring one; the other is vehicle mechanism, which assumes that proton combines with solvent molecules to yield hydronium ions, such as H_3O^+, $H_5O_2^+$, $H_9O_4^+$, and then diffuses as a whole across the membrane.

To fully understand the function of SGO and SSGO on proton transfer, proton conductivities of the membranes under both hydrated (100% RH) and anhydrous (0% RH) conditions were measured. The hydrated conductivities in Fig. 4.10a reveal that SPEEK control membrane attains a conductivity of about 0.0150 S cm^{-1} at 25 °C and 100% RH, close to the result in literature [24]. Compared with SPEEK control membrane, the incorporation of GO, SGO, or SSGO significantly facilitates the proton transfer through composite membranes, yielding the conductivity of 0.0171, 0.0197, or 0.0215 S cm^{-1} with the enhancement of 14%, 31.3%, or 43.3% when incorporating only 2.5% GO, SGO, or SSGO, respectively. Considering the reduced ionic cluster size and *IEC* of composite membranes, both of which would lead to lower proton transfer, the conductivity enhancement is reasonably attributed to the following reasons: (i) the sheet structure and high aspect ratio of the fillers interconnect the sulfonic-aggregated ionic clusters, especially the dead ends in SPEEK matrix; (ii) the increased water uptake and area swelling of the composite

membranes would provide additional proton carriers and H-networks, facilitating the proton transfer. When compared with GO, SGO and SSGO give much higher proton conductivities to the composite membranes. This should be ascribed to the sulfonated polymer brushes on SGO and SSGO, which insert into SPEEK matrix and then serve as additional and wider pathways for proton transfer via the interconnected SP-GO sheets [36]. Besides, proton conductivities of composite membranes can be effectively enhanced by increasing the length of brushes or content of fillers, as seen in Fig. 4.10a. The highest conductivity of 0.0335 S cm^{-1} is achieved for SPEEK/SSGO-10, which is 123% of that of SPEEK control membrane. The temperature-dependent conductivities under hydrated condition are shown in Fig. 4.10b–d. It can be found that the proton conductivity for control membrane is increased from 0.0150 to 0.0347 S cm^{-1} with the temperature increasing from 25 to 65 °C. By comparison, much higher proton conductivities are achieved by the composite membranes under elevated temperatures, and the conductivities elevated in the order of SPEEK < SPEEK/GO-*X* < SPEEK/SGO-*X* < SPEEK/SSGO-*X*. For instance, the conductivities are elevated from 0.0194 to 0.0422 S cm^{-1} for SPEEK/GO-5, from 0.0226 to 0.0487 S cm^{-1} for SPEEK/SGO-5, and from 0.0246 to 0.0523 S cm^{-1} for SPEEK/SSGO-5 as the temperature increases from 25 to 65 °C. Such results probably arise from the promoted motion of conducting sites and the enhanced activity of hydronium ions at high temperature.

PEMFCs, operating at high temperature and low humidity condition, have attracted much attention due to the compelling advantages: (i) enhanced electrochemical kinetics; (ii) improved carbon monoxide tolerance of Pt electrode, and (iii) easier water and heat management [29–31]. However, most of the developed PEMs suffer from conductivity decline at elevated temperature due to the evaporation of water. Therefore, it is much important and impending to develop highly conductive membrane under anhydrous condition. As shown in Fig. 4.11a, SPEEK control membrane displays a conductivity of about 1.17 mS cm^{-1} at 120 °C and anhydrous condition, much lower than the 0.015 S cm^{-1} under hydrated condition, implying the critical role of water in proton transfer. Compared with SPEEK control membrane, SPEEK/GO-*X* achieves an enhancement of conductivity from 1.25 to 1.61 mS cm^{-1} with the content increasing from 2.5 to 10%. The conductivity enhancement is probably attributed to the anhydrous conducting groups (−OH, $-CO_2H$) on GO surface. By comparison, the incorporation of SGO and SSGO gives much higher conductivities to the composite membranes. For example, SPEEK/SGO-*X* acquires the conductivities of 1.750 ~ 2.59 mS cm^{-1}, corresponding to the SGO content of 2.5% ~ 10%. Moreover, the conductivity can be tailored by the brush length and sulfonic acid loading amount, and higher brush length endows faster proton conduction. The highest conductivity up to 3.53 mS cm^{-1} is achieved by SPEEK/SSGO-10, higher than that of Nafion (0.1 mS cm^{-1}) under identical conditions [29]. The sulfonated polymer brushes on SGO and SSGO should contribute to the enhanced conduction ability, which make the fillers work as additional proton-conducting pathways and meanwhile interconnected ionic clusters (i.e., transfer pathways) in SPEEK matrix. Figure 4.11b–d shows the temperature-dependent conductivity of as-prepared membranes ranging from 30 to 150 °C under anhydrous condition. Similar to the

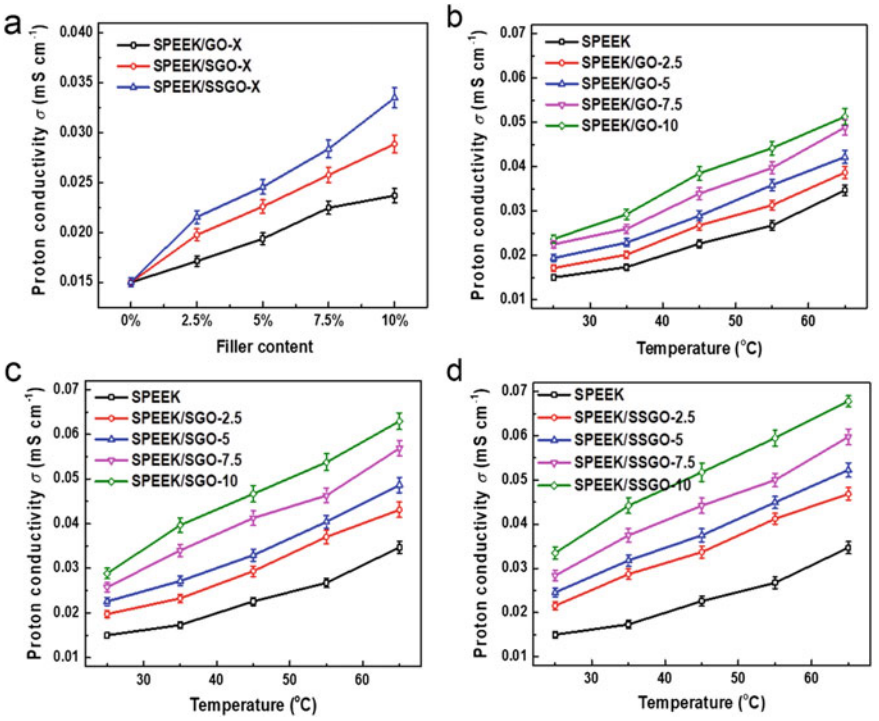

Fig. 4.10 **a** Proton conductivity of SPEEK control and composite membranes at 25 °C and 100% RH. Temperature-dependent conductivity of **b** SPEEK/GO-*X*, **c** SPEEK/SGO-*X*, and **d** SPEEK/SSGO-*X* under 100% RH. Copyright (2015), Elsevier [37]

behaviors under hydrated condition, it can be found that all the membranes display continuous increase of conductivity with the temperature. For instance, the conductivities elevate from 0.148 to 1.50 mS cm^{-1} for SPEEK control membrane, from 0.258 to 1.69 mS cm^{-1} for SPEEK/GO-5, from 0.442 to 2.71 mS cm^{-1} for SPEEK/SGO-5, and from 0.635 to 3.66 mS cm^{-1} for SPEEK/SSGO-5, when the temperature increases from 30 to 150 °C.

Considering the unique advantages of the elevated-temperature PEMFC and the acceptable anhydrous proton transport property of composite membrane, the single cell performances were examined under 120 °C and anhydrous conditions. Due to the comprehensive performances of proton conductivity and structural stability, SPEEK control membrane, SPEEK/GO-5, SPEEK/SSGO-5 were chosen as representatives. The thickness of these three membranes was kept almost the same, and the electrodes were also fabricated in the same manner for all the MEAs to ensure a good comparison. As shown in Fig. 4.12, the open-circuit voltages (OCVs) for all the cells are above 0.94 V, indicating that the obtained membranes have low gas (H_2 and O_2) crossover [38], in accordance with the results of H_2 permeability. SPEEK control membrane attains the maximum current density and power density of about

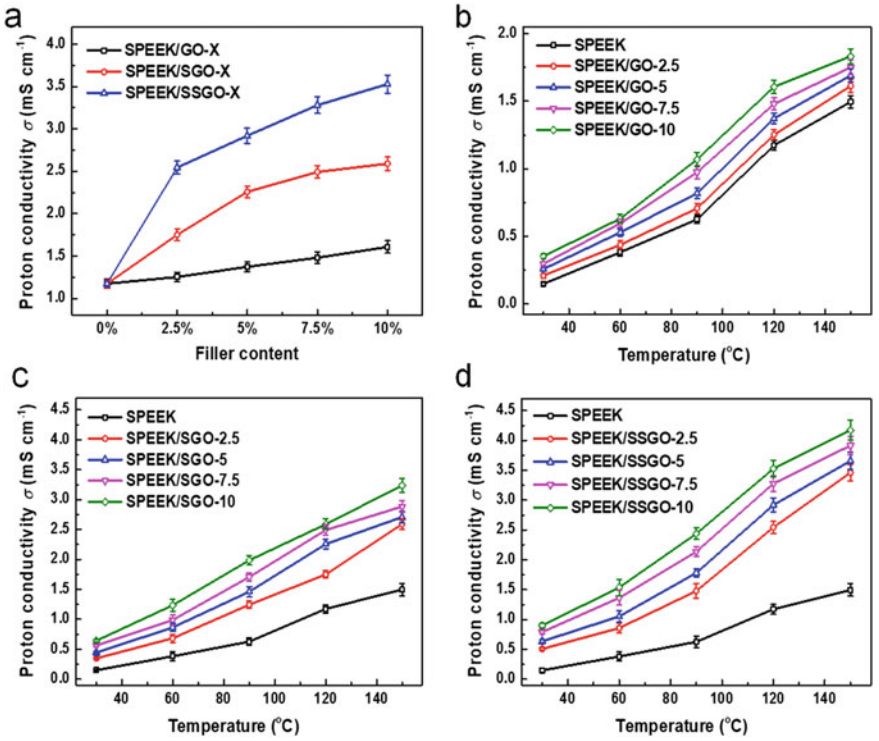

Fig. 4.11 **a** Proton conductivity of SPEEK control and composite membranes at 120 °C and anhydrous condition. Temperature-dependent conductivity of **b** SPEEK/GO-*X*, **c** SPEEK/SGO-*X*, and **d** SPEEK/SSGO-*X* under anhydrous condition. Copyright (2015), Elsevier [37]

318.4 mA cm^{-2} and 86.9 mW cm^{-2}, respectively. By comparison, the PEMFC performances of the composite membranes are enhanced after GO/SSGO incorporation. It is found that incorporating 5% SSGO affords a 27% increase in maximum current density (403.3 mA cm^{-2}), together with a 37% increase in maximum power density (119.6 mW cm^{-2}). This enhancement is reasonably ascribed to the enhanced proton conduction ability of SPEEK/SSGO-5, which reduces the electrolyte resistance and meanwhile accelerates the cathode reaction. Similar observations have been reported in other composite PEMs [12, 39]. Compared to SSGO, GO displays similar function in elevating the cell performances of SPEEK-based membrane, and SPEEK/GO-5 acquires the maximum current density of 395.9 mA cm^{-2} and the maximum power density of 96.7 mW cm^{-2}. Collectively, SPEEK/SSGO membrane offers significant promise as a proton exchange membrane for PEMFC application under anhydrous and elevated temperature conditions, and the obtained results are comparable to the data of Nafion and some other membranes in literature [40, 41].

In this study, two kinds of SP-GO with tunable sulfonated polymer brush length (i.e., SGO and SSGO) were synthesized via a facile distillation-precipitation

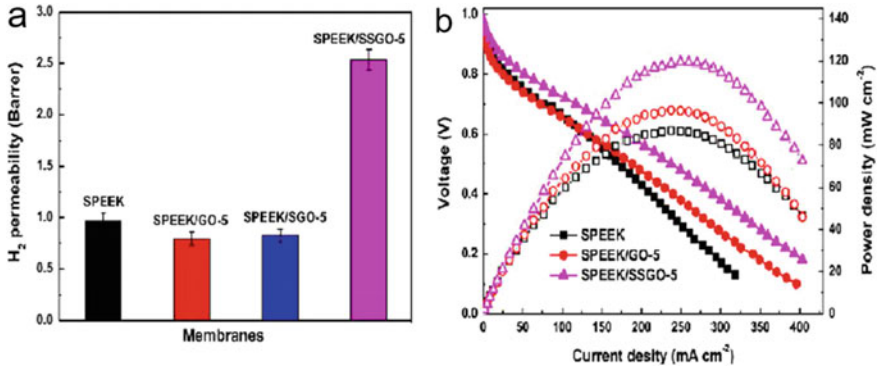

Fig. 4.12 Single PEMFC performances of SPEEK control membrane, SPEEK/GO-5, and SPEEK/SSGO-5 with anhydrous H_2/O_2 operated under 120 °C and anhydrous conditions. The flux rate of H_2 and O_2 is 150 and 200 mL min^{-1}, respectively. Copyright (2015), Elsevier [37]

polymerization technique and then incorporated into SPEEK matrix to prepare composite membranes. Compared to GO, SGO and SSGO as the fillers in the corresponding composite membranes possessed the following advantages: (i) improving the filler dispersion to form interconnected structure; (ii) generating wide and continuous conducting pathways via the sulfonated polymer brushes on SP-GO surface. Helped by these advantages, the SP-GO-filled membranes achieved higher proton conductivity and lower transfer-energy barrier than the control membrane and GO-filled membrane. Additionally, increasing the length of polymer brushes and filler content could further enhance the proton conduction ability. Particularly, the composite membrane with 10 wt% SSGO acquired the highest proton conductivity of 0.0678 S cm^{-1} at 65 °C under hydrated condition and 4.17 mS cm^{-1} at 150 °C under anhydrous condition, 95.5% and 178% higher than that of SPEEK control membrane, respectively. Moreover, low H_2 permeability was obtained for the composite membranes by incorporating the fillers. Benefiting from the enhanced proton conductivity and low H_2 permeability, the composite membranes achieved higher PEMFC performances than Nafion under elevated temperature and anhydrous conditions. This study might provide instructive information about constructing proton transfer highways within composite membrane by rational manipulation of the interfacial structures.

4.4 Composite Membrane with Block Copolymer Brush-Functionalized GO

The synthesis process of FGO was elucidated in Fig. 4.13. Firstly, GO was fabricated from natural graphite through the improved Hummers method [29]. Then, the GO water solution (25 mL, 0.2 mg mL^{-1}) was incorporated into 200 mL ethanol,

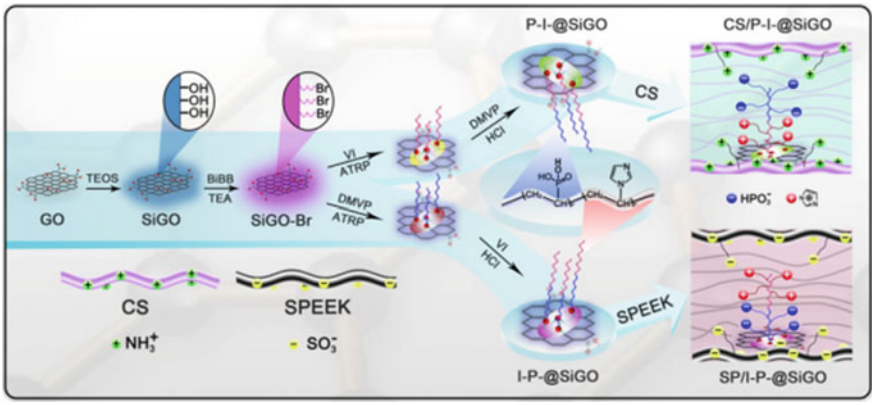

Fig. 4.13 Schematic preparation of acid–base copolymer brush functional GO and composite membrane. Copyright (2017), Elsevier [42]

followed by incorporating 1 g PVP. After stirring at 25 °C for 0.5 h, 2.5 mL tetraethyl orthosilicate (TEOS) was added into the above mixture. Meanwhile, the pH value of solution was adjusted to ~ 9.0 with ammonia. The mixture was ultrasonicated for 0.5 h to acquire a homogeneous solution. Afterward, the solution was strongly stirred at 25 °C for 24 h. Finally, the reaction mixture was washed and centrifuged with ethanol for several times, then dried and named as SiGO.

SiGO (0.6 g) was added in a round-bottom flask (100 mL) with tetrahydrofuran THF (30 mL), and ultrasonicated for 0.5 h. Then, 6 mL triethanolamine (TEA) was added, followed by adding 5 mL 2-bromoisobutyryl bromide (BIBB) dropwise addition with ice bath. The reaction system was Vaseline sealed to prevent ambient water from entering and reacted for 24 h at 25 °C with magnetic agitation. The target product, SiGO-Br, was collected by washing and centrifugation with alcohol for three times and dried with vacuum oven at 60 °C for 72 h.

Then, a schlenk flask (100 mL) was incorporated with 1 g SiGO-Br, 0.021 g $CuBr_2$, 0.029 g BPy, 1.5 g DMVP, and 40 mL methanol. The mixture was ultrasonicated to obtain a homogeneous solution. Next, certain amount of AIBN methanol solution (0.014 mmol mL^{-1}) was incorporated into the Schlenk flask. The flask was degassed immediately through three cycles of freeze–pump–thaw with N_2, and the system was then heated to 75 °C and maintained for 24 h under reflux condition. After polymerization, the final product was attained by filtration, washing with methanol and ethanol for several times, and vacuum drying at 60 °C for 24 h. The modified GO was dispersed in excess HCl aqueous solution (10 M) and reacted at 100 °C for 24 h to convert phosphonate into phosphonic acid. After rinsing with water for removing the residual acid, the final product was dried in vacuum oven at ambient temperature. The product was named as P-@SiGO. I-@SiGO was fabricated in the same way except the HCl treatment process (reaction condition and amounts of the reactants: SiGO-Br: 1 g, monomer VI: 0.80 g, 8.44 mmol). Two kinds of block copolymer brush-grafted GO (acid–base and base–acid) were conducted by tandem approach

in the same procedure: I-P-@SiGO and P-I-@SiGO. The former utilized P-@SiGO (1 g) as seed and VI (0.80 g) as monomer, while the latter utilized I-@SiGO (1 g) as seed and DMVP (1.5 g) as monomer.

SPEEK-based membrane: Certain amount of FGO was added into 3.5 g DMF with ultrasonic treatment and stiring for 4 h at room temperature. Then, 0.7 g SPEEK was incorporated into 3.5 g DMF, and vigorously stirred until SPEEK was totally dissolved. The above two solution was then mixed and treated with ultrasoic and stirring for attaining a homogeneous solution. Then, the solution was casted onto a glass plate and dried at 60 °C for 12 h, followed by drying at 80 °C for another 12 h. The prepared membranes were named as SP/I-@SiGO-*X*, SP/P-@SiGO-*X*, SP/I-P-@SiGO-*X*, and SP/P-I-@SiGO-*X*, where *X* ($X = 0.5$, 2.5, 5.0, 7.5, or 10) was the weight ratio (wt%) of nanosheet to SPEEK. For comparison, SPEEK control membrane (designated as SP) was prepared with the same procedure.

CS-based membrane: Certain amount (0.5, 2.5, 5.0, 7.5, and 10 wt%) of nanosheet was incorporated to chitosan-acetic acid solution (ρB: 2%). After fully dispersing, the solution was casted on glass plate and dried at 30 °C for 24 h. The membrane was then peeled from the plate and immersed in 1.0 M sulfuric acid solution for 24 h for cross-linking the CS chain, followed by rinsing with water several times to remove the residual sulfuric acid. Finally, the composite membrane was attained after drying. CS-based composite membrane with four types of nanosheet (P-@SiGO, I-@SiGO, I-P-@SiGO, and P-I-@SiGO) was named as CS/P-@SiGO-*X*, CS/I-SIGO-*X*, CS/I-P-@SiGO-*X*, and CS/P-I-@SiGO-*X*, where *X* ($X = 0.5$, 2.5, 5.0, 7.5, or 10) was the weight ratio (wt%) of nanosheet to CS. CS control membrane (labeled as CS) was prepared through the same procedure.

Functional GO was incorporated into SPEEK matrix to prepare composite membrane. SEM images in Fig. 4.14a–e displays that, different from the smooth cross-section of SP, the addition of FGO makes the cross-section of composite membrane rough with some wrinkles. Grafting polymer brush improves the interfacial compatibility and confers uniform FGO distribution, better than the poor compatibility of SPEEK –GO composite. In addition, the presence of polymer brush also assists FGO to form a perpendicular packing, similar to the finding in literature [33]. For composite membrane, it could be found that SP/I-@SiGO-5 (Fig. 4.14c) and SP/I-P-@SiGO-5 (Fig. 4.14e) exhibit better compatibility with low roughness than those of SP/P-@SiGO-5 (Fig. 4.14b) and SP/P-I@SiGO-5 (Fig. 4.14d). These should be attributed to outer basic imidazole groups in I-@SiGO and I-P-@SiGO, which drive the polymer brush to insert into SPEEK matrix and thus permit a well coverage by polymer matrix. The chemical component of membrane is detected by FTIR (Fig. 4.14f), which reveals that all membranes possess similar FTIR spectra with characteristic peaks of $–SO_3H$ at 1224, 1079, and 1022 cm^{-1}. The physical mixture and well compatibility between FGO and SPEEK bring no new peak to composite membrane.

The amphipathic property of SPEEK chain gives typical nanophase-separation structure to the prepared membranes, wherein the aromatic backbone form hydrophobic domain, which can be confirmed by WXRD, and the $–SO_3H$ groups aggregate into ionic clusters, which can be confirmed by SAXS. Figure 4.15a reveals

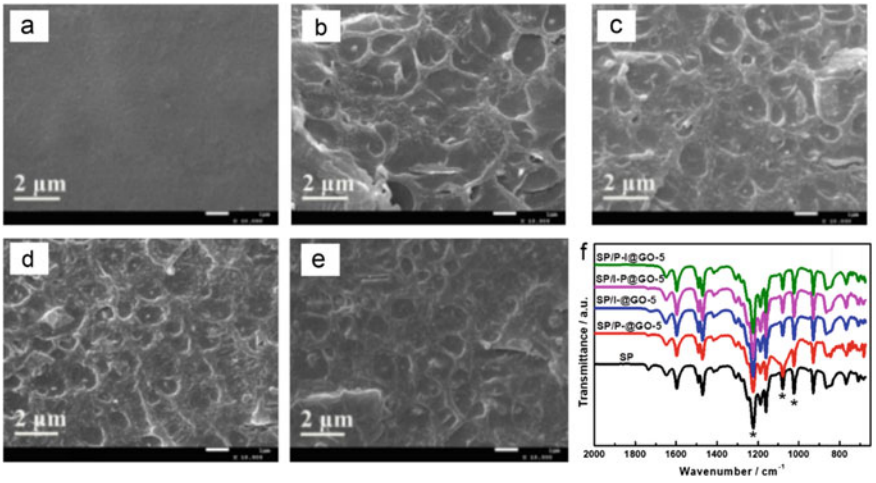

Fig. 4.14 Cross-sectional SEM images of **a** SP, **b** SP/P-@SiGO-5, **c** SP/I-@SiGO-5, **d** SP/P-I-@SiGO-5, and **e** SP/I-P-@SiGO-5. **f** FTIR spectra of as-prepared membranes. Copyright (2017), Elsevier [42]

that the lack of strong interaction between FGO and SPEEK matrix makes the composite membrane display similar WXRD patterns with SP, with the typical crystalline band at $2\theta = 12 \sim 22°$ for hydrophobic domain [40]. In comparison, the presence of FGO affects the ionic cluster structure as verified by the shifted q in SAXS pattern. Although all membranes show characteristic peak of ionic cluster at $q = 0.21 \sim 0.31$ nm^{-1} (Fig. 4.15b), the peak for composite membrane shifts to higher values, that is, smaller ionic cluster. This is probably resulted from the interfacial interaction, like electrostatic attraction (between imidazole group of basic brush and sulfonic acid group of SPEEK) and hydrogen-bonding interaction (between phosphoric acid group of acidic brush and sulfonic acid group of SPEEK), which hampers the assembly of sulfonic acid groups into ionic cluster through retarding chain motion. For practical application, SAXS data of wet state are more important since PEM operates under humidified environment. Figure 4.15c shows that the q value of membrane left-shifts after hydration, indicating the increase of ionic cluster size. This phenomenon is probably ascribed to the enrichment of water in ionic cluster, which enlarges the size. Similar to dry state, composite membranes attain lower q value than SP under wet state. Additionally, the presence of imidazole groups makes the q value of related composite membranes higher than those of P-@SiGO incorporated membranes, possibly because of the stronger interfacial interaction. Furthermore, the long brush helps I-P-@SiGO, and P-I-@SiGO gives stronger interaction and therefore higher q value to composite membranes than those of P-@SiGO and I-@SiGO. This speculation can be confirmed by the Δq value (q value gap between dry and wet state), and Δq value of composite membranes containing imidazole-FGO is smaller than that of SP/P-@SiGO-5. SP attains the highest Δq value because there is no interference from FGO.

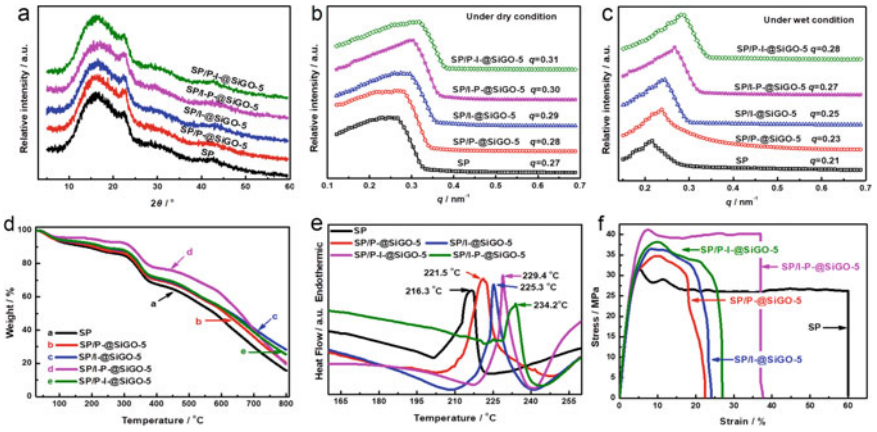

Fig. 4.15 **a** XRD pattern of as-prepared membranes. SAXS pattern of as-prepared membranes under **b** dry and **c** wet condition. **d** TGA curves, **e** DSC curves, and **f** stress–strain curves of as-prepared membranes. Copyright (2017), Elsevier [42]

The unique structure also brings different thermal and mechanical property to composite membranes, and Fig. 4.15d shows that composite membrane displays analogous degradation process to that of control membrane due to the absence of covalent bond. The polymer brush inserting and interfacial interaction, however, make the onset temperature shift to higher value for composite membranes. This can be verified by DSC curve in Fig. 4.15e, where all the membranes display endothermic peak ranging 216 ~ 234 °C for the relaxation process of structural reorganization. Close to the value in literature, the transition temperature (T_d) of SP is 216.3 °C, and the incorporation of FGO gives higher T_d of over 220 °C to composite membrane. Like the trend of SAXS, the T_d value obeys the order of SP/I-P-@SiGO-5 > SP/P-I-@SiGO-5 > SP/I-@SiGO-5 > SP/P-@SiGO-5, originating from the difference in interfacial interaction. The presence of FGO also improves the mechanical stability of composite membranes (Fig. 4.15f).

High proton conductivity will confer better fuel cell performance, especially under elevated temperatures and low humidity conditions. Under above operation conditions, fuel cell possesses obvious superiority like fast electrode reaction kinetic, eliminated CO poisoning of platinum electrocatalyst, simplified heat and water management [43]. In this study, proton conductivity at both hydrated (100% RH, 25 ~ 55 °C) and anhydrous (0% RH, 25 ~ 120 °C) conditions was tested and shown in Fig. 4.16. Figure 4.16a displays that SP attains a conductivity of 0.015 S cm^{-1} at 25 °C and 100% RH, close to the value in literature [40]. For SP/P-@SiGO-X, the presence of phosphoric acid groups provides more proton-hopping sites (reflected by *IEC*) along the nanosheet surface and larger free volume (reflected by FFV) near ionic cluster, which jointly endow enhanced proton conduction property to composite membranes. For instance, the addition of 5 wt% P-@SiGO confers a 93.3% augment with the conductivity of 0.029 S cm^{-1}. Although the addition of I-@SiGO brings lower *IEC*

and close FFV, it gives surprisingly high conductivity enhancement to the composite membrane, which is even superior to the function of P-@SiGO. For example, SP/I-@SiGO-5 obtains a conductivity of 0.051 S cm^{-1} with the increment of 240.0%. This phenomenon reasonably stems from the well inserted imidazole brush in the form of acid–base pair. As found in other reported acid–base composites, the acid–base pairs can work as low-energy-barrier proton-hopping sites with the sulfonic groups as proton donors and imidazole groups as proton acceptors. In this way, broad and long-range proton conduction networks are constructed along FGO surface. For FGO with acid–base block copolymer brush, it is anticipated that the co-existence of phosphoric acid brush and imidazole brush will generate significant promoting effect on proton conduction to composite membrane. And the addition of 5 wt% I-P-@SiGO and P-I-@SiGO confers the increment of 486.7% (0.088 S cm^{-1}) and 346.7% (0.067 S cm^{-1}) to the related composite membranes. It could be found that although I-P-@SiGO and P-I-@SiGO possess similar brush structure, they generate different promotion degree on proton conduction. The difference of interface structure should be the main reason, and the outer imidazole brush on I-P-@SiGO may drive the inner phosphoric acid brush to stretch and insert into SPEEK matrix as far as possible. In this manner, broader interface transfer path and hence better synergistic effect are achieved with SP/I-P-@SiGO-*X*, as compared with the situation for SP/P-I-@SiGO-*X*. This speculation can be further confirmed by the anhydrous conductivity in Fig. 4.16b. Through comparison, it is found that anhydrous conductivity of all the membranes is lower than those under hydrated conditions by two orders of magnitude. This implies that the loss of water generates serious influence on the conduction property of SPEEK-based membranes by reducing the amount of vehicle-type carriers and shrinking the ionic cluster. Meanwhile, the conduction property of sulfonic acid group is obviously restrained due to the suppressed H^+ protonation and deprotonation [44]. Compared with the control membrane, the conductivity of SP/P-@SiGO-*X* slightly increases because of the better self-ionization ability of phosphoric acid group. Again, the FGO bearing imidazole brush (I-@SiGO, I-P-@SiGO, and P-I-@SiGO) brings significant promotion on proton conduction, originating from the continuous hopping between proton donors (acid groups) and accepters (base groups). Similar to the behavior at hydrated condition, the anhydrous conductivity of the composite membranes obeys the order of SP/I-P-@SiGO-X > SP/P-I-@SiGO-X > SP/I-@SiGO-X.

Figure 4.16 also reveals that the conductivity of composite membrane could be tuned by FGO loading amount. Figure 4.16a and b shows that the conductivity at both hydrated and anhydrous conductions could be effectively improved by increasing FGO loading amount. For example, varying I-P-@SiGO loading amount from 0.5 to 10 wt% increases the conductivity from 0.025 mS cm^{-1} to 0.093 S cm^{-1} at hydrated condition and from 0.54 mS cm^{-1} to 1.24 mS cm^{-1} at anhydrous condition. Figure 4.16c and d reveals that the proton conductivity of membrane elevates with temperature, indicating that proton transfer is a thermally activated process [22]. Under elevated temperatures, the improved polymer chain motion and proton kinetic energy facilitate proton migration. Taking SP and SP/I-P-@SiGO-5 as example, with the temperature elevates from 20 to 120 °C, their anhydrous conductivity elevates from 0.37 mS cm^{-1} to 1.56 mS cm^{-1} (increment of 322%)

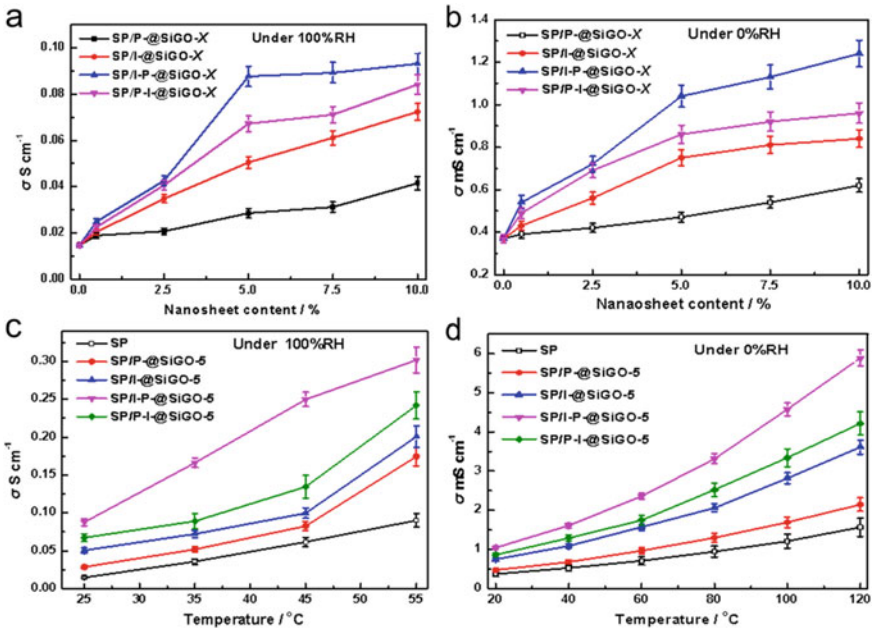

Fig. 4.16 Proton conductivity of membranes as a function of nanosheet loading amount at 25 °C under **a** hydrated and **b** anhydrous conditions. Temperature-dependent proton conductivity of membranes under **c** hydrated and **d** anhydrous conditions. Copyright (2017), Elsevier [42]

and from 1.04 mS cm^{-1} to 5.89 mS cm^{-1} (increment of 466%), respectively. This also indicates that composite membrane is more suitable as temperature-sensitive conductor because of the formation of continuous proton-hopping pathways. With the temperature-dependent conductivity curve, E_a value at anhydrous condition is calculated and shown in Table 4.1. The E_a values of composite membranes are a little higher than that of SP, but fall in the scale of Grotthuss mechanism. The constructed interface transfer paths should be responsible for increased E_a value by enabling more protons to transfer through Grotthuss mechanism, in accordance with the finding in literature [35]. Close to the conductivity results, the broad interface hopping paths bring SP/I-P-@SiGO-5 the highest E_a value of 16.59 kJ mol^{-1}.

In this work, FGO with polymer or copolymer brush is used to construct interface transfer highway for efficient proton transfer. In the above part, a common acid polymer (SPEEK) with nanophase-separation structure is selected as membrane matrix, and it is found that the generated strong attraction drives the basic brush to insert into SPEEK matrix, which also drives other segment in, forming long-range paths along FGO surface. To investigate and verify the universality of this finding, a typical base polymer (CS, without naonphase separation) is chosen as matrix to fabricate another series of composite membranes.

SEM images in Fig. 4.17a–e reveal that CS control membrane is dense and void free. For compsosite membranes, FGOs are uniformly distributed in CS matrix

Table 4.1 Young's modulus, T_d, area swelling, proton conductivity, and E_a of as-prepared membranes

Membrane	Young's modulus (MPa)	T_d (°C)	Area swelling[a] (%)	*IEC*[a] (mmol g^{-1})	σ (mS cm^{-1})		E_a (kJ mol^{-1})
					55 °C 100%RH	120 °C 0%RH	0%RH
SP	543.2	217	15.4	1.44	60.1	1.51	13.5
SP/P-@SiGO-5	875.2	222	10.4	1.62	174.4	2.15	14.5
SP/I-@SiGO-5	978.6	227	9.1	1.33	200.7	3.61	15.1
SP/I-P-@SiGO-5	1054.3	234	6.9	1.65	301.9	5.89	16.6
SP/P-I-@SiGO-5	994.6	229	8.3	1.71	242.0	4.30	15.4
CS	718.3	226	47.7	0.26	27.0	0.62	15.8
CS/P-@SiGO-5	1424.6	228	42.2	0.45	61.8	2.51	16.0
CS/I-@SiGO-5	1576.4	227	37.8	0.22	43.5	2.16	15.5
CS/I-P-@SiGO-5	1884.6	230	35.3	0.34	72.7	4.08	16.1
CS/P-I-@SiGO-5	2049.8	232	25.0	0.41	83.1	4.59	16.2

[a]is measured at 25 °C

without obvious defect. Likewise, the interfacial interaction may contribute to this excellent dispersion by giving well compatibility between CS and FGO. Because of the long polymer brush, CS chain wraps up I-P-@SiGO and P-I-@SiGO and generates obvious nacre-like structure and rough cross-section to CS/I-P-@SiGO-5 (Fig. 4.17d) and CS/P-I-@SiGO-5 (Fig. 4.17e). Interfacial interaction also slightly changes the FTIR spectra of membranes (Fig. 4.17f). All the membranes display the characteristic peaks for CS at 3268 (hydroxyl group), 1637 (amide I group), and 1530 cm^{-1} (amide II group). In comparison, the peak intensity of composite membrane becomes weaker, especially for CS/P-@SiGO-5 and CS/P-I-@SiGO-5.

The nanosheet loading/temperature-dependent proton conductivity of membranes at hydrated and anhydrous conditions is displayed in Fig. 4.18. Figure 4.18a reveals that CS control membrane obtains a conductivity of 1.92×10^{-4} S cm^{-1} at 25 °C and 100% RH, much lower than that of SP because of the lack of sufficient proton-hopping site and continuous ionic cluster. In comparison, the incorporation of FGO confers remarkable improvement in proton conduction. For example, the conductivity elevates by 3.7 times (5.5×10^{-3} S cm^{-1}), 2.6 times (3.6×10^{-3} S cm^{-1}), 6.3 times (6.2×10^{-3} S cm^{-1}), and 6.7 times (7.9×10^{-3} S cm^{-1}) when adding 5 wt% of P-@SiGO, I-@SiGO, I-P@SiGO, and P-I-@SiGO, respectively. These remarkable improvements should be, again, resulted from the constructed interface transfer paths by the inserted brush and polymer matrix, where the conductive groups act as rapid hopping sites for efficient proton transfer among FGO and polymer. As FGO loading amount elevates, the promotion effect strengthens because of the increase of interface transfer paths, endowing gradually increased conductivity. The conductivity of CS/P-@SiGO-*X* increases from 0.9×10^{-3} S cm^{-1} to 6.9×10^{-3} S cm^{-1} with nanosheet

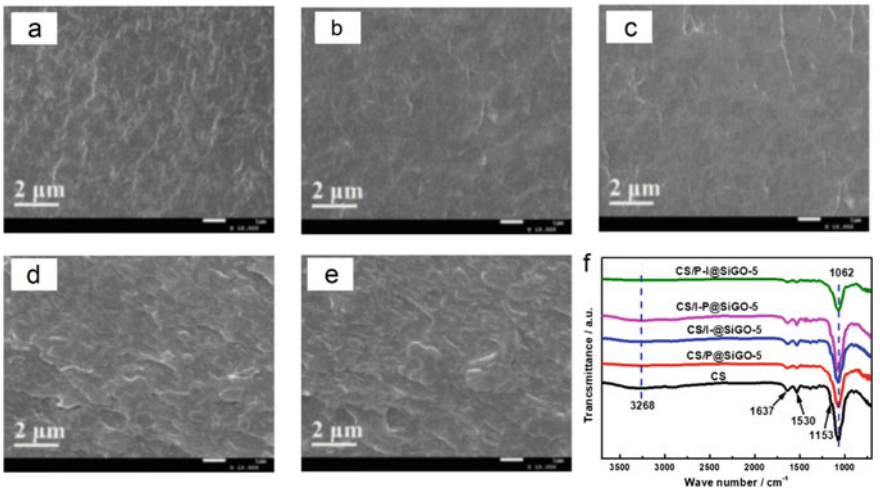

Fig. 4.17 Cross-sectional SEM images of **a** CS, **b** CS/P-@SiGO-5, **c** CS/I-@SiGO-5, **d** CS/I-P-@SiGO-5, and **e** CS/P-I-@SiGO-5. **f** FTIR spectra of as-prepared membranes. Copyright (2017), Elsevier [42]

loading amount elevating from 0.5 to 10 wt%. Additionally, the promotion effect of FGO on conductivity follows the order of P-I-@SiGO > I-P@SiGO > P-@SiGO > I-@SiGO, a little different from that of SPEEK-based membranes. Although the long acid–base copolymer brush helps P-I-@SiGO and I-P@SiGO achieve stronger promotion effect for both CS- and SPEEK-based composite membranes, FGO with phosphoric acid brush imparts higher conductivity to basic CS membrane, like that of imidazole brush to acidic SPEEK membrane. This is due to that acidic groups can afford better insertion of polymer brush through the formation of acid–base pair, providing broad and low-energy-barrier proton-hopping paths. In this way, the outer acidic brush makes P-I-@SiGO construct broader interface proton transfer paths and therefore gives higher conductivity than that for I-P@SiGO. The anhydrous conductivity in Fig. 4.18b displays that the conductivity of all membranes is much lower than those in hydrated condition because of the water loss, but still obeys the order of CS/P-I-@SiGO-X > CS/I-P@SiGO-X > CS/P-@SiGO-X > CS/I-@SiGO-X > CS. Taking FGO loading amount of 5 wt% as example, the conductivity of related membranes is 0.85, 0.76, 0.56, and 0.43 $\times$ 10^{-3} S cm^{-1}, 6.1, 5.3, 3.7, and 2.6 times higher than that of CS. These findings suggest that the interface transfer paths could generate promotion effect on conductivity at both hydrated and anhydrous conditions. The temperature-dependent conductivity of membrane is shown in Fig. 4.18c and d. The proton conductivity of all membranes increases with temperature at both hydrated and anhydrous conditions, resulted from the improved chain motion and proton kinetic energy. The composite membrane displays higher conductivity than CS control membrane at every temperature, especially at anhydrous condition. It is speculated that the constructed interface transfer paths are more effective for

proton transfer via Grotthuss mechanism with the formed acid–base pairs and/or imidazole groups. As a result, the composite membrane possesses more Grotthuss-type proton transport, which gives composite membrane higher E_a value than CS control membrane (Table 4.1). Note that the intermolecular proton transfer between protonated imidazole and neat imidazole results in a slight reduction of E_a for CS/I-@SiGO-5 (15.5 vs. 15.8 kJ mol^{-1} for CS). Collectively, these results demonstrate that strong interaction will drive the groups or segments to insert into membrane matrix, enabling the transfer between polymer and filler in composite membrane. For composite PEM, grafting acid–base copolymer brush may be an idea and universal strategy for modifying filler surface for obtaining excellent proton conduction.

In conclusion, we demonstrate the construction of controllable interface proton transfer paths in polymer membrane with polymer brush-grafted GO (P-@SiGO, I-@SiGO, P-I-@SiGO, and I-P-@SiGO), and acidic SPEEK and basic CS are chosen as representative membrane matrix. Interestingly, it is found that the acidic groups or basic groups in polymer brush could effectively drive the brush to insert into CS matrix or SPEEK matrix through electrostatic attraction, which (if at outer segment) could drag the inner segment to insert into matrix for P-I-@SiGO and I-P-@SiGO. The inserted brush constructs well-connected networks using the acid/base groups

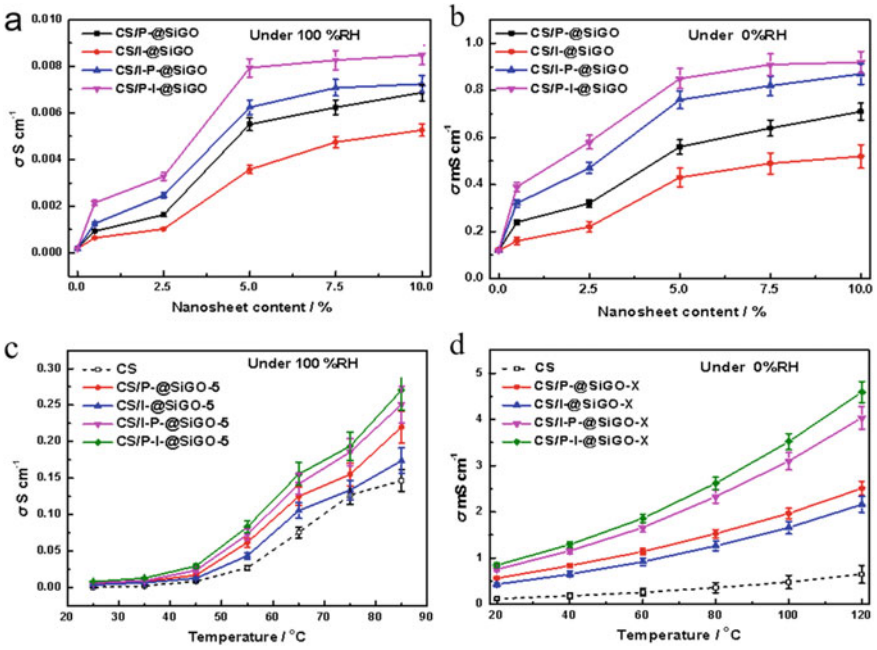

Fig. 4.18 **a** Hydrated and **b** anhydrous conductivity of as-prepared membrane as a function of nanosheet loading amount. Temperature-dependent **c** hydrated and **d** anhydrous conductivity of as-prepared membranes. Copyright (2017), Elsevier [42]

from FGO and polymer chain, triggering synergic promotion effect on proton conduction of composite membrane. In this way, broad and long-range transfer paths are constructed along FGO surface, and the acid–base pairs act as low-energy-barrier hopping sites, which then imparts several times enhancement of proton conductivity, especially at anhydrous condition. The acid–base copolymer brush brings broader paths to composite membranes, and thus stronger promotion effect. As expected, the enhancement degree on proton conduction for SPEEK-based membrane obeys the order of I-P-@SiGO > P-I-@SiGO > I-@SiGO > P-@SiGO, while for CS-based membrane, the order is P-I-@SiGO > I-P-@SiGO > P-@SiGO > I-@SiGO. These findings imply the dexterous regulation property of polymer brush and unique function of interface transfer paths on proton transfer in composites.

4.5 Composite Membrane with Ionic Liquid

SPEEK was synthesized through post-sulfonation of PEEK. DS of SPEEK was regulated by controlling the reaction time, and four kinds of SPEEK with DS of 43%, 54%, 62%, and 75% were synthesized and named as SP-43, SP-54, SP-62, and SP-75, respectively. The SPEEK was then used to prepare SPEEK control membrane by solution-casting method: 0.7 g SPEEK was added in 10 mL DMF at 25 °C and stirred vigorously for 12 h. The resultant solution was casted on a glass plate and dried at 60 °C for 12 h and another 8 h at 80 °C.

The SPEEK control membrane (4.0 cm^2 × 4.0 cm^2) was then utilized for preparing composite membrane. As shown in Fig. 4.19, SPEEK control membrane was immersed in ionic liquid at a certain temperature and/or ultrasonic power. After treatment in IL for a certain time, the membrane was taken out, and the surface IL was removed, followed by drying in vacuum oven at 60 °C until a constant weight.

SPEEK, containing hydrophilic side chains (terminated with sulfonic acid groups) and hydrophobic aromatic backbone, possesses distinct nanophase-separation structure. The side chain aggregates into ionic clusters, whereas the aromatic backbone forms hydrophobic phase for mechanical strength [44]. The morphology of the as-prepared membrane was detected by SEM and SAXS. It can be seen in Fig. 4.20

Fig. 4.19 Schematic synthesis of composite membrane by IL-swollen method. Copyright (2015), Elsevier [45]

that the morphology of all membranes is uniform without obvious crack or defect. For SPEEK control membrane, no macroscopic channel is observed in Fig. 4.20a. In comparison, the addition of IL gives distinct continuous channels to composite membrane, and elevating the IL content will increase the channel size and the connectivity of channels (Fig. 4.20b–d). These phenomena indicate that IL may be mainly located in the ionic cluster driven by the generated electrostatic interaction from $–SO_3H$ groups, and the enrich of IL broadens the cluster to interconnected channels.

SAXS is a powerful technique to detect ionic cluster, which derives from the nanophase separation between ionic side chain and hydrophobic main chain. The location and intensity of SAXS peak could be utilized to evaluate the size and number of ionic cluster, respectively [46–48]. Therefore, SAXS was used to further investigate the structure of as-prepared membranes, and the results were shown in Fig. 4.21a. It is found that typical scattering peak at q value range of 0.50 ~ 0.56 nm^{-1} is observed for all membranes, implying the presence of nanophase-separation structure and ionic cluster [49]. In comparison with SPEEK control membrane (0.56 nm^{-1}), incorporating IL increases the cluster size of composite membrane, as verified by the reduction in q value to 0.53, 0.53, 0.52, and 0.50 nm^{-1} with IL loading amount of 16%, 25%,

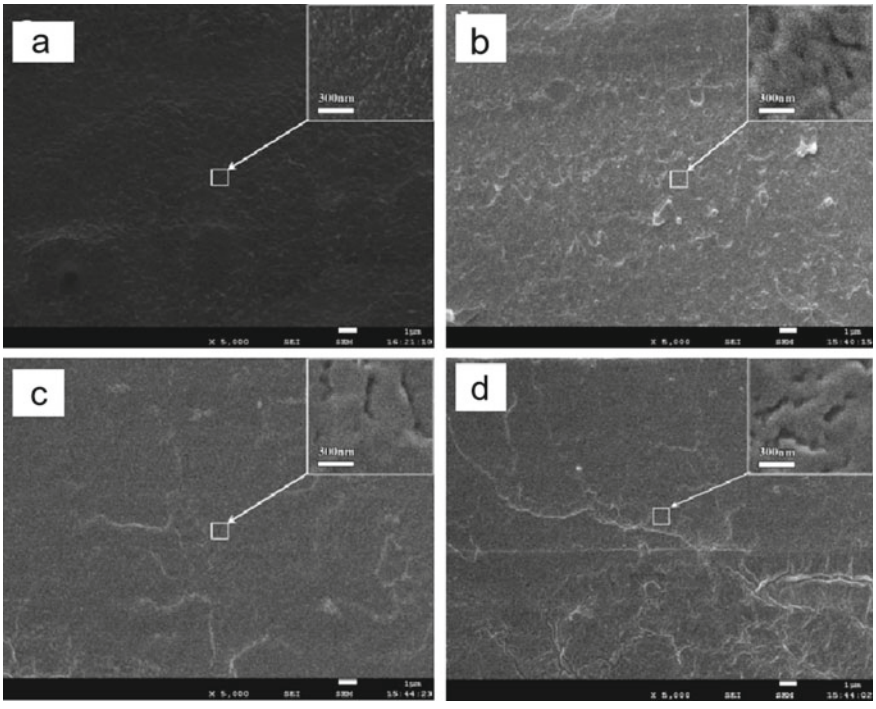

Fig. 4.20 Cross-sectional SEM images of as-prepared membranes: **a** SP-62, **b** SP-62-IL-16, **c** SP-62-IL-25, and **d** SP-62-IL-32. Copyright (2015), Elsevier [45]

32%, and 43%, respectively. The Bragg spacing (d) is related to q based on the equation: $d = 2\pi/q$, and d is related to the "center to center distance" between two clusters and indicates the size of ionic cluster [50]. Therefore, the reduction in q value implies the increase of cluster size. This phenomenon should be attributed to the enrichment of IL in ionic cluster, which is in accordance with the results in SEM. Meanwhile, incorporating IL also enhances the peak intensity of composite membrane, implying the increase in ionic cluster number. Jointly, the increased cluster size and number corporately contribute to the increase of connectivity of ionic cluster, and the IL-enriched continuous channels would provide facile paths for proton hopping through the carrier sites (i.e., imidazole, ionic liquid, and acid–base pairs). To further investigate the influence of IL on the morphology of SPEEK matrix, the membranes were subjected to WXRD. Figure 4.21b reveals that all membranes exhibit broad crystalline band at $2\theta = 12 \sim 25°$, related to the ordered stacking of hydrophobic backbone [51]. In comparison with SPEEK control membrane, the intensity reduction of band for composite membrane should be resulted from the plasticizing effect of IL on the hydrophobic backbone of SPEEK. The plasticizing effect weakens the interaction among backbone and thus destroys the ordered stacking, making the composite membrane more flexible.

High anhydrous conductivity is indispensable for fuel cell operated at elevated temperatures. Considering the structure/mechanical stability, the IL content was controlled below 43% in conductivity tests. Anhydrous proton conductivity of as-prepared membranes at 40 ~ 140 °C was tested, and the results were shown in Fig. 4.22a. It is found that SPEEK control membrane exhibits a low conductivity of 0.17 mS cm^{-1} at 120 °C, three orders of magnitude lower than that at hydrated condition [52]. This phenomenon confirms that water plays pivotal role in proton conduciton in $–SO_3H$ groups by generating solvated species to dissociate H^+ from the acid groups, where the resulting acid radical ion ($–SO_3^-$) can act as proton carriers. Therefore, the $–SO_3H$ group in SPEEK control membrane may lose conduction ability without water. In comparison, incorporating IL gives significant augment in

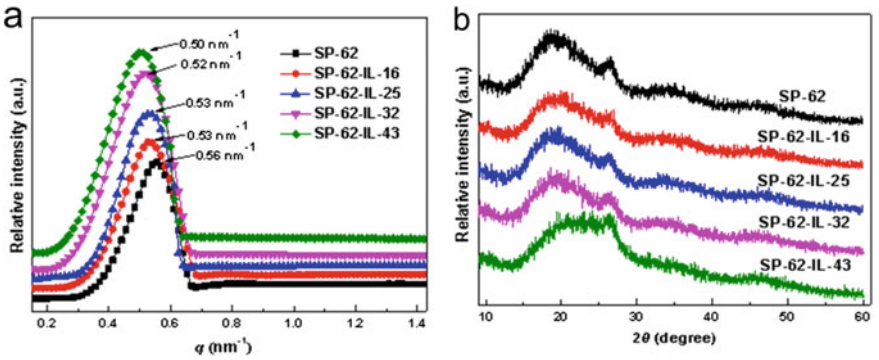

Fig. 4.21 **a** SAXS and **b** WXRD patterns of as-prepared membranes. Copyright (2015), Elsevier [45]

proton transfer ability to composite membrane, affording a 20 times enhancement of conductivity (3.6 mS cm^{-1}) when incorporating 16% IL. Increasing IL content can further improve the transfer ability of composite membrane. For example, the conductivity gradually increases to 5.4, 6.6, and 7.7 mS cm^{-1} as the IL content elevates to 25%, 32%, and 43%, respectively. These phenomena indicate that the strong promotion effect of imidazole-type ionic liquid on the proton conduction property of acidic polymer matrix. The presence of imidazole type in ionic channels will (i) give ample anhydrous hoping sites (i.e., imidazole and ionic liquid, Fig. 4.23B and C) for proton hopping and (ii) form acid–base pairs (sulfonic acid-imidazole, Fig. 4.23A) along the channel surface, which construct low-energy-barrier transfer pathways. Through the interconnected channels, these hopping sites create continuous paths for efficient proton conduction. In this way, the conduction property of $–SO_3H$ is activated in the form of acid–base pair. With the increase of IL content, the size and connectivity of transfer channels increase, affording gradually enhanced anhydrous conductivity. For another, Fig. 4.22a also reveals that all membranes display continuous increase of anhydrous conductivity with the testing temperature. For example, the conductivity of SP-62-IL-32 increases from 0.93 to 7.4 mS cm^{-1} when the temperature elevates from 40 to 140 °C. The facilitated mobility of proton carrier should be the main contributor for this conductivity enhancement. Note that SP-62-IL-43 achieves the maximum anhydrous conductivity of 9.3 mS cm^{-1} at 140 °C, which is about 52 times of that of SPEEK control membrane (0.18 mS cm^{-1}).

To further investigate the effect of IL on proton conduction, E_a for proton transport through the membrane was computed via Arrhenius equation from temperature-dependent conductivity (Fig. 4.22b). Similar to the results in literature, SPEEK control membrane attains a Grotthuss-type E_a of 26.9 kJ mol^{-1} [45, 53]. In comparison, the incorporation of IL lowers the E_a value of composite membrane; the E_a value reduces to 26.1, 25.2, 22.8, and 21.6 kJ mol^{-1} when the IL content is 16%, 25%, 32%, and 43%, respectively. The increased hopping site and channel size as well as the generated acid–base pair should contribute to the transfer barrier reduction. In conclusion, the decreased E_a together with the elevated conductivity further

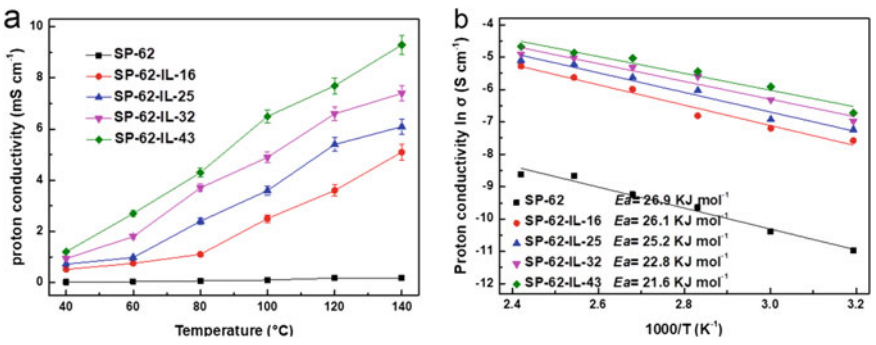

Fig. 4.22 **a** Temperature-dependent anhydrous conductivity and **b** the Arrhenius plots of as-prepared membranes. Copyright (2015), Elsevier [45]

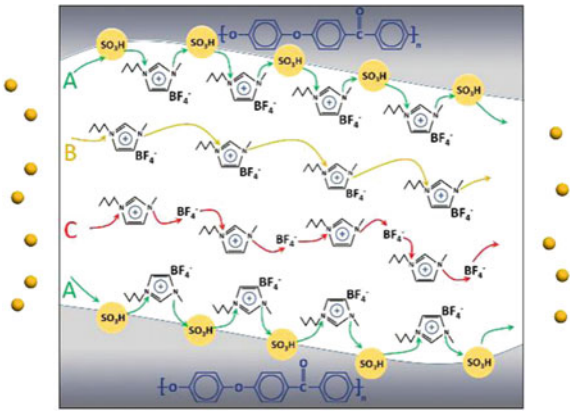

Fig. 4.23 Possible proton transfer mechanism in composite membrane: A proton hopping via acid–base pair; B proton hopping via imidazole molecule; C proton hopping via ionic liquid. Copyright (2015), Elsevier [45]

confirms the distinct conduction promption property of imidazole-type ionic liquid in acid polymer, which constructs facile paths for Grotthuss-type proton transfer.

Generally, IL leaching is a serious issue for IL-incorporated composite membrane because it would result in the decline of proton conductivity. During the operation of PEMFC at elevated temperature and anhydrous condition, water molecules will generate at cathode in the form of steam, part of which might lead to IL leaching from PEM. To detect the IL retention property of composite membrane, IL loss and IL retention were measured under an extreme condition (immersing the membrane into water). Figure 4.24a depicts the IL loss curves of composite membrane as a function of time. It is found that all the composite membranes display fast IL release at the beginning 50 min because of the leaching of IL in free form. Like free water, the free-form IL has weak interaction with membrane matrix and mainly locates in the center of ionic channels. After this stage, the IL content in composite membrane keeps almost constant with the testing time, and the retained IL should be in bound form. Like bound water, the bound-form IL has strong attraction with $–SO_3H$ groups along channel surface. For composite membrane, high IL content is related to large IL-enriched channels, affording more free-form IL. Therefore, SP-62-IL-43 displays higher IL loss (79%) during the first stage than SP-62-IL-16 (72%). Figure 4.24b shows the time-dependent IL retention of composite membrane. Similar to the results in Fig. 4.24a, the IL retention decreases obviously at the beginning 50 min and then reaches a constant value. Although SP-62-IL-43 suffers from a fast IL loss, the increase of ionic channels (SEM results) will provide more space for interacting with IL. Accordingly, the retained IL in SP-62-IL-43 at equilibrium (9.0%) is higher than that in SP-62-IL-16 (4.6%). The IL leaching will reduce the amount of proton-hopping sites and thus decrease the proton conductivity of composite membrane. Figure 4.24c shows the conductivity of composite membrane during IL release. Similar to the behavior of IL retention, the serious IL release leads to obvious reduction of proton conductivity during the beginning 50 min. For example, the conductivity of SP-62-IL-16 and SP-62-IL-43 decreases from 5.1 to 1.8 mS cm^{-1} and from

9.3 to 2.9 mS cm^{-1} during this stage, respectively. The high IL retention endows SP-62-IL-43 higher proton conductivity than that of SP-62-IL-16. After equilibrium, the retained IL is mainly in bound form, which transports proton via acid–base pair in a low-energy-barrier manner. Consequently, the constant conductivity of composite membrane (above 1.8 mS cm^{-1}) after leaching is still much higher than that of SPEEK control membrane (0.18 mS cm^{-1}) at 140 °C. At low humidity, the IL leaching result of composite membrane is more useful for its practical application in fuel cell. SP-62-IL-43, which contains relatively high IL content among the composite membranes, is selected as representative for investigating the IL retention ability at 80 °C and 10% RH. Figure 4.24d displays a similar IL loss trend with that in water: the IL loss increases at first and then reaches a constant value. Compared with the data in Fig. 4.24a, it can be found that the IL leaching from composite membrane at low humidity is obviously reduced because of the absence of water. For instance, the constant IL loss of SP-62-IL-43 at 10% RH is only 8.1% after 168 h, about 1/10 of that in water after testing 150 min. As a result, the retained IL in SP-62-IL-43 at 10% RH (39.5%) is much higher than that in water (9.0%). Collectively, these results imply that the as-prepared membranes possess acceptable IL retention property, especially at low humidity.

Anhydrous conductivity of casting membrane at temperature range of 40–140 °C is shown in Fig. 4.25a. Similarly, incorporating IL gives additional hopping sites in the form of acid–base pair, brings enhanced conductivity to composite membrane. For example, the anhydrous conductivity of SP-62-IL-16, SP-62-IL-25, SP-62-IL-32, and SP-62-IL-43 at 120 °C is 2.3, 3.6, 4.9, and 6.2 mS cm^{-1}, respectively. For another, the anhydrous conductivity of all membranes increases with temperature. Figure 4.25b depicts the temperature-dependent conductivity of composite membranes prepared by IL-swollen method and solution-casting method containing identical IL content. It is found that the swollen membrane possesses better proton transfer property than that of casting membrane at all temperatures. For example, the conductivity of SP-62-IL-16 at 120 °C is 3.6 and 2.3 mS cm^{-1} for swollen membrane and casting membrane, respectively, and the value of SP-62-IL-43 is 7.7 and 6.2 mS cm^{-1}. The random distribution of IL in casting membrane should be the main factor for the low conductivity, which makes the membrane lack of continuous transfer paths and therefore high transfer resistance.

The IL retention property of casting membrane in terms of IL loss and IL retention was measured, and the results were shown in Fig. 4.26a–b. It is found that the casting membrane displays similar trend with swollen membrane: fast IL release at the beginning 50 min and then reaching a constant value. In comparison with the swollen membrane, the casting membrane attains higher IL retention. For instance, the retained IL content at equilibrium of the casting membrane is 5.0% and 10.8% for SP-62-IL-16 and SP-62-IL-43, respectively, higher than those of swollen membranes. This phenomenon should be resulted from the random distribution of IL in casting membrane, which allows more IL to interact with SPEEK and thus forms more bound-form IL. Figure 4.26c shows that the conductivity of casting membrane continuously decreases during the IL release. Through comparison, it is surprising to find that the swollen membrane attains higher proton conductivity than those of casting ones under

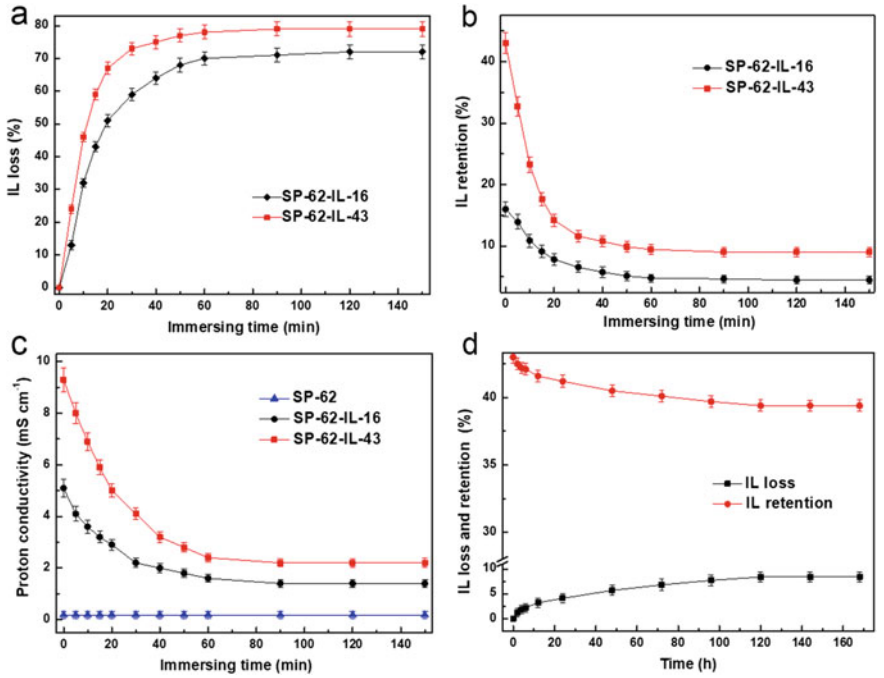

Fig. 4.24 Time-dependent **a** IL loss and **b** IL retention of the composite membranes (immersing in water). **c** Time-dependent anhydrous conductivity of the composite membranes after immersing in water (conductivity was measured at 140 °C). **d** IL loss and IL retention of SP-62-IL-43 at 80 °C and 10% RH. Copyright (2015), Elsevier [45]

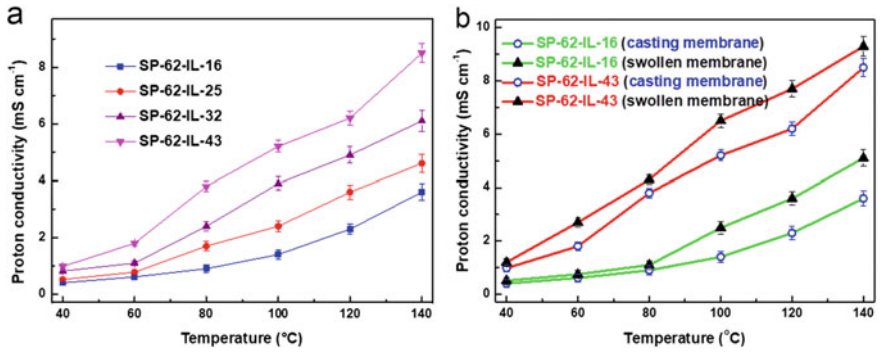

Fig. 4.25 **a** Temperature-dependent conductivity of casting membrane at anhydrous condition. **b** The comparison of temperature-dependent anhydrous conductivity of swollen membrane and casting membrane. Copyright (2015), Elsevier [45]

identical condition. For example, the constant conductivity of casting membrane is 0.9 and 1.8 mS cm^{-1} for SP-62-IL-16 and SP-62-IL-43, respectively, while those of swollen ones are 1.4 and 2.2 mS cm^{-1}. Considering the low IL retention of swollen membrane, the high proton conductivity should result from the interconnected channels, which serve as continuous proton transfer paths. Furthermore, the IL retention property and corresponding conductivity of casting membrane at 80 °C and 10% RH were performed, and the results were shown in Fig. 4.26d. The high IL retention confers composite membrane high proton conductivity. The constant conductivity of casting SP-62-IL-43 at 80 °C and 10% RH (after testing for 168 h) is 3.5 mS cm^{-1}, while this value for the membrane immersing in water is 1.8 mS cm^{-1} (after testing for 150 min). Compared with the casting membrane, the swollen membrane displays higher anhydrous conductivity at 80 °C and 10% RH, originating from the continuous proton transfer paths. Collectively, these results suggest that the swollen membrane may be superior to the casting membrane.

In conclusion, a facile approach for developing high-performance anhydrous PEM is proposed through the incorporation of imidazole-type ionic liquid into acid polymer matrix via IL-swollen method. During the preparation process, IL content

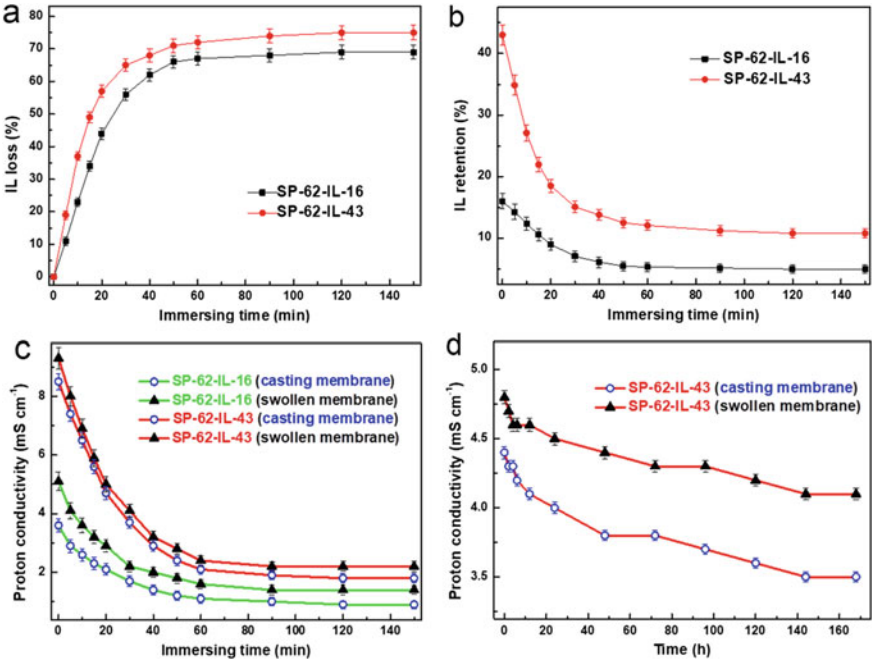

Fig. 4.26 Time-dependent **a** IL loss and **b** IL retention of the casting membranes (immersing in water). **c** The comparison of time-dependent conductivity of swollen membrane and casting membrane after immersing in water (testing at 140 °C). **d** The comparison of time-dependent conductivity of swollen membrane and casting membrane at 80 °C and 10% RH. Copyright (2015), Elsevier [45]

is accurately controlled by tuning the preparation condition, including ultrasonic power, treatment temperature, and treatment time. In addition, this approach allows IL to enrich in the ionic cluster of SPEEK membrane, forming interconnected proton transfer channels, and increasing IL content can elevate the size and connectivity of channels. Conductivity measurement results reveal that the presence of IL gives significant augment in anhydrous conductivity of SPEEK membrane, through the following multiple roles: the imidazole and ionic liquid provide ample anhydrous hopping sites to the membrane; the imidazole forms acid–base pair with sulfonic acid group, which serves as low-energy-barrier paths along channel surface. The continuous paths enable the efficient proton conduction through these hopping sites. Particularly, a 51 time increased conductivity of 9.3 mS cm^{-1} at 140 °C is attained with the IL content of 43% IL. Additionally, the electrostatic interaction confers the composite membrane acceptable IL retention property at low humidity. In comparison with swollen membrane, casting membrane exhibits random IL distribution and fails to form continuous proton transfer path, thus displaying low anhydrous conductivity. Considering the facile preparation method, tunable IL content, and continuous proton transfer path, the present study might offer promising way for designing high-performance proton-conducting materials, especially for utilization at anhydrous and elevated temperature condition.

4.6 Composite Membrane with Ionic Liquid and Functionalized GO

GO was exfoliated from natural graphite based on the improved Hummers' method [29]. FGO was fabricated by distillation-precipitation polymerization [54]. 0.3 g MPS-modified GO, 1 mL VI or SS, and 0.02 g AIBN were dissolved in 80 mL acetonitrile in a dried two-necked flask with ultrasonic. The mixture was heated until 40 mL acetonitrile was distilled out. Then, the reaction was ended, and the functional GO was purified by three cycles of ultracentrifugation, decanting, and resuspension in acetonitrile. For SS functional GO, the attained product was then treated with 0.1 M HCl to exchange the Na^+ in $–SO_3Na$ with H^+. Finally, the vinyl imidazole and p-styrenesulfonic acid functional GO were named as VGO and SGO, which bear basic imidazole group and acidic $–SO_3H$ group on surface, respectively. SPEEK was synthesized through post-sulfonation of PEEK [33]. The DS of SPEEK in this study was ~ 62% (Fig. 4.27).

SPEEK control membrane was fabricated via solution-casting method: 0.75 g SPEEK was dispersed in 10.0 g DMF at ambient temperature. After stirring vigorously for 12 h, the mixture was casted onto a glass plate and dried first at 60 °C for 12 h, then at 80 °C for 12 h. The resultant membrane was named as SP.

IL-free membrane: certain amount of GO, VGO, or SGO was dispersed in 10.0 g DMF by ultrasonic for 8 h at room temperature. Then, 0.75 g SPEEK was dissolved in above solution and stirred vigorously for another 12 h at room temperature. The

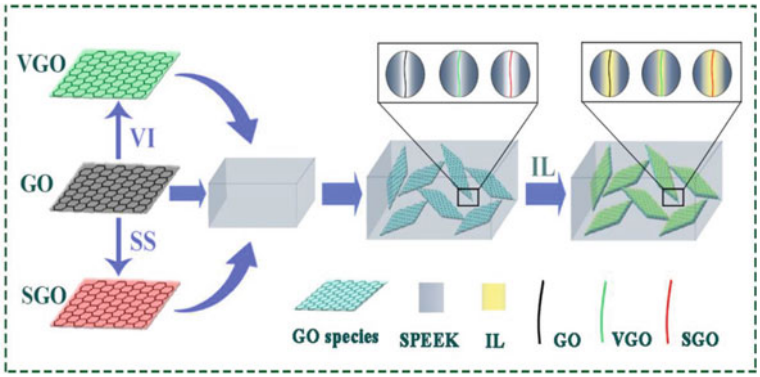

Fig. 4.27 Schematic preparation of nanocomposite membrane. Copyright (2016), American Chemical Society [50]

resultant mixture was casted onto a glass plate and dried at 60 °C for 12 h followed by at 80 °C for another 12 h. The resultant membranes were named as SP-GO-*X*, SP-VGO-*X*, or SP-SGO-*X*, representing GO, VGO, or SGO as filler, where *X* (*X* = 2.5, 5, 7.5, or 10) was the weight ratio of filler to SPEEK.

The as-prepared membrane (4.0 cm^2 × 4.0 cm^2) was utilized to prepare IL-filled nanocomposite membrane. The IL-free membrane was immersed in ionic liquid at a given temperature and ultrasonic power. After immersing in IL for a certain time, the membrane was taken out and wiped with lens tissue to remove the surface IL, Afterward, it was dried in vacuum oven at 60 °C until a constant weight. According to the pre-experiment, the treatment time was set as 72 h under the ultrasonic power of 100 W and 55 °C.

VGO and SGO were prepared by distillation-precipitation polymerization with vinyl imidazole and sodium p-styrenesulfonate as grafting monomers, respectively, as shown in Fig. 4.29. The morphology of GO, VGO, and SGO was detected with TEM and displayed in Fig. 4.28a–c. GO displays typically 2D sheet-like structure with some wrinkles (Fig. 4.28a), similar to the morphology in literature [55]. Since the polymerization mainly occurs at the vinyl group of MPS on GO surface, both VGO (Fig. 4.28b) and SGO (Fig. 4.28c) retain the sheet structure without obvious change. In comparison with GO, VGO and SGO appear much darker in color, implying the presence of polymer brush. The chemical structure of grafted brush on VGO and SGO was determined by FTIR. Figure 4.28d reveals that GO shows three characteristic peaks at 1736, 1628, and 1386 cm^{-1}, which are ascribed to the vibration of C=O stretching, adsorbed water bending, and C–O deformation, respectively. In comparison, VGO gives rise to three new peaks at 1568, 1447, 745 cm^{-1}, which are related to the stretching vibration of C=N, the vibration of C–N bond in imidazolium group, and the bending vibration of imidazolium ring, respectively. For SGO, although the major vibration peak related to $–SO_3H$ group (overlapped by the band in 1170 cm^{-1} of GO) can not be observed, a new peak at 2923 cm^{-1} corresponding to –SOH group is observed [29]. To verify the finding in FTIR, XPS was utilized to detect the

component and content on FGO. In XPS spectra, two major peaks at binding energy of 285.6 and 533.9 eV are observed (Fig. 4.28e) for GO, related to C1s and O1s, respectively. The relative C/O atom ratio of GO was 2.98, inferring the existence of oxygen-containing groups. VGO and SGO give rise to N 1 s peak (402.4 eV, 5.33 at.%) and S $2p^3$ peak (169.6 eV, 2.68 at.%) in their spectra, respectively. This indicates that certain amount of imidazole and sulfonic acid groups is grafted on VGO and SGO surface, respectively. To further confirm the surface grafting, TGA is conducted and displayed in Fig. 4.28f. All the fillers undergo three-stage weight loss, including the evaporation of moisture (mainly bond water) in the first stage (30 ~ 120 °C), the deoxygenation of GO (mainly oxygen-containing functional groups) in the second stage (160 ~ 300 °C), and the decomposition of GO backbone in the third stage (300 ~ 750 °C). In comparison, it is found that the polymer brushes confer improved water retention ability to VGO and SGO, related to the higher weight loss in the first stage. Meanwhile, the strong bonding ability of $–SO_3H$ group to water offers SGO higher weight loss than that of VGO during this stage. In the second stage, the coverage of polymer brushes inhibit the deoxygenation of GO [56], thus conferring VGO and SGO lower weight loss. And the weight loss for VGO and SGO during this stage is ascribed to the decomposition of imidazole and sulfonic acid groups in polymer brush. During the third stage, the pyrolysis of polymer brush, oxygen-containing functional group, and GO backbone co-contribute to a higher weight loss for VGO and SGO in comparison with GO.

GO, VGO, and SGO were added into SPEEK to prepare membrane, followed by impregnating with IL through swollen method. The dispersion of filler within membrane was detected by SEM as shown in Fig. 4.30. It is found that SPEEK control membrane (Fig. 4.30a) is dense, uniform, and defect free. The addition of

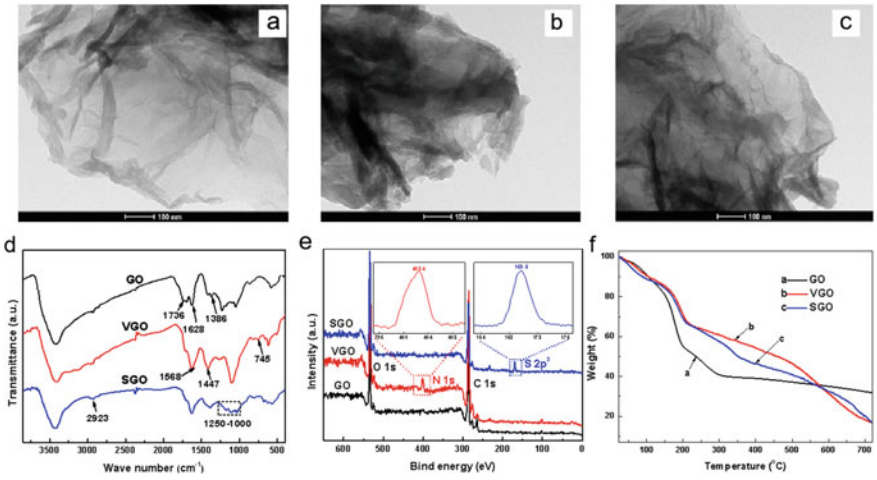

Fig. 4.28 Characterization of fillers: TEM image of **a** GO, **b** VGO, and **c** SGO; **d** FTIR spectra, **e** XPS spectra, and **f** TGA curves of fillers. Copyright (2016), American Chemical Society [50]

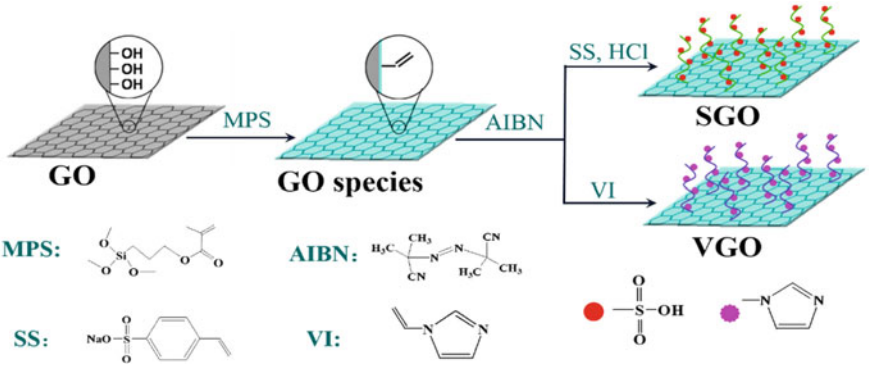

Fig. 4.29 Schematic synthesis and chemical structure of FGO. Copyright (2016), American Chemical Society [50]

GO makes SP-GO-5% (Fig. 4.30b) becomes rough with wrinkles and even some pinholes. However, SP-VGO-5% (Fig. 4.30c) and SP-SGO-5% (Fig. 4.30d) exhibit uniform filler distribution with a little wrinkles. This should be attributed to the enhanced mutual interaction between VGO/SGO and SPEEK because of the grafted polymer brushes, which improve the interfacial compatibility. Additionally, SP-VGO-5% displays better compatibility as compared with SP-SGO-5%, implying the stronger interaction between VGO (basic imidazole group) and SPEEK (acidic –SO_3H group). After incorporating with IL, large number of short-range channel could be discerned in SP-IL (Fig. 4.30e), due to the aggregation of IL in ionic cluster, which broadens them to be macroscopic. In comparison with SP-IL, new long-range channels along filler–polymer interface are detected for SP-GO-5%-IL, SP-VGO-5%-IL, and SP-SGO-5%-IL in Fig. 4.30f, g and h, respectively. These are possibly originated from the diffusion of IL into the interfacial domain, which broadens them to interconnected channel. In this way, long-range transfer paths form at polymer-filler interface. Note that, compared with SP-VGO-5%-IL, the newly formed channels for SP-SGO-5%-IL are more clear and roomy, and ILs are mainly enriched in the interfacial channel rather than in ionic cluster of SPEEK. These are possibly due to that, for SP-VGO-5%-IL, the strong electrostatic attraction between polymer and VGO makes the interface difficult to swollen, and therefore, the probability of IL diffusion, while for SP-SGO-5%-IL, the inherent loose interface together with the electrostatic attraction between –SO_3H group and IL give stronger driving force for IL diffusion, making the channel more broad and suitable for IL storage. These findings imply that the IL distribution within nanocomposite membrane can be effectively regulated by tuning the interfacial microstructure and interaction.

Free volume characteristic (i.e., FFV and density) of as-prepared IL-free membrane was estimated by buoyancy method (Table 4.2) [35, 55]. SPEEK control membrane possesses a density of 1.359 g cm^{-3} together with a FFV of 0.223%. In comparison, incorporating GO increases the FFV to the range of 0.225–0.233% for SP-GO-X (X = 2.5, 5, and 7.5%). Considering the reduced ionic cluster size, the

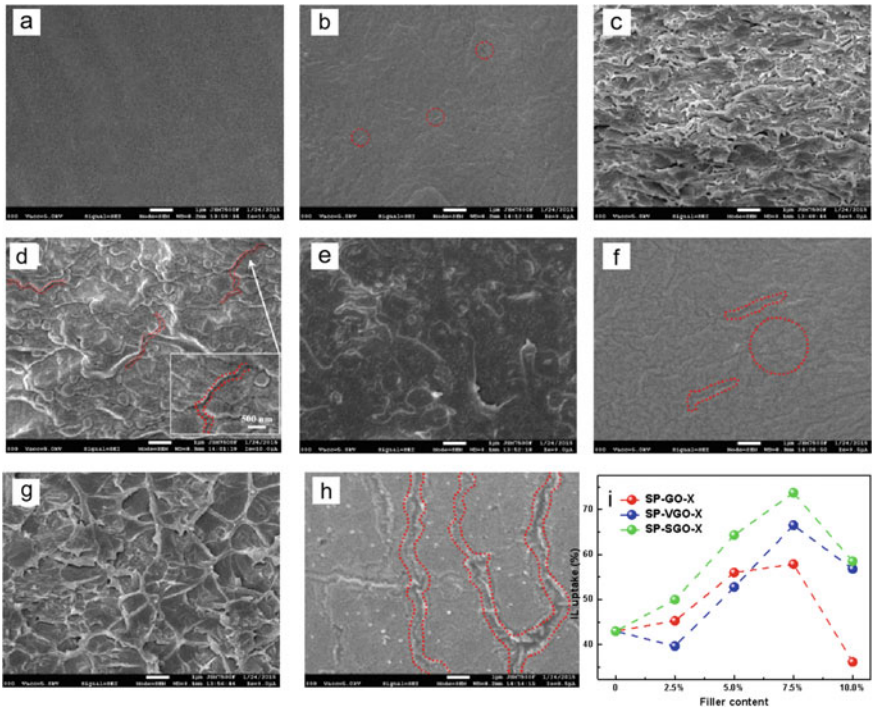

Fig. 4.30 Cross-sectionAL SEM image of **a** SP, **b** SP-IL, **c** SP-GO-5%, **d** SP-GO-5%-IL, **e** SP-VGO-5%, **f** SP-VGO-5%-IL, **g** SP-SGO-5%, and **h** SP-SGO-5%-IL. **i** IL uptake of the membrane. Copyright (2016), American Chemical Society [50]

elevated FFV should stem from the newly formed domain along polymer-filler interface. The obvious reduction of FFV for SP-GO-10% (0.219%) is possibly because of the aggregation of GO, which reduces the interfacial domain. For SP-VGO-*X*, the small ionic cluster size together with the dense interface co-contributes to the low FFV (0.221 and 0.229%) at low filler loading amount (2.5 and 5%). Benefitted from the good compatibility, VGO-incorporated membrane attains higher FFV (0.239 and 0.230%) at high filler loading amount (7.5 and 10%) as compared with GO-incorporated membrane. Note that SP-SGO-*X* achieves the FFV of 0.227%, 0.236%, 0.241%, and 0.233% when the filler loading amount is 2.5%, 5%, 7.5%, and 10%, respectively, which is the highest among IL-free membranes under identical condition. The loose interface and good compatibility (as seen in SEM) should be the main factor for this phenomenon. Collectively, the efficient regulation of free volume characteristic may be beneficial for fine-tuning IL uptake and distribution.

For Grotthuss-type proton transfer, the dominant mechanism for water-free condition, sufficient hopping sites, and continuous distribution is vital for satisfactory conductivity. In this work, IL is used to act as proton-hopping sites along transfer

Table 4.2 Density and FFV of the membrane determined by buoyancy method

Sample	ρ_B (g cm^{-3})	FFV (%)
SP	1.359 ± 0.005	0.223 ± 0.007
SP-GO-2.5%	1.281 ± 0.007	0.225 ± 0.008
SP-GO-5%	1.206 ± 0.009	0.231 ± 0.008
SP-GO-7.5%	1.146 ± 0.007	0.233 ± 0.007
SP-GO-10%	1.110 ± 0.008	0.219 ± 0.006
SP-VGO-2.5%	1.271 ± 0.006	0.221 ± 0.005
SP-VGO-5%	1.179 ± 0.006	0.229 ± 0.007
SP-VGO-7.5%	1.094 ± 0.007	0.239 ± 0.007
SP-VGO-10%	1.045 ± 0.005	0.230 ± 0.006
SP-SGO-2.5%	1.255 ± 0.006	0.227 ± 0.007
SP-SGO-5%	1.158 ± 0.009	0.236 ± 0.007
SP-SGO-7.5%	1.079 ± 0.008	0.241 ± 0.008
SP-SGO-10%	1.026 ± 0.007	0.233 ± 0.005

channel. The IL content in nanocomposite membrane is regulated by tuning the interfacial microstructure through incorporating functional GO nanosheets. Figure 4.30i shows that SPEEK control membrane attains the IL uptake of 43.0%. In comparison, the incorporation of GO affords nanocomposite membrane-elevated IL uptake, and increasing the GO content will strengthen the effect. For instance, SP-GO-2.5%-IL and SP-GO-5%-IL attain IL uptake of 45.3% and 56.0%, respectively. Considering the smaller ionic cluster size (SPEEK phase) and larger FFV (interfacial domain), the elevated IL uptake should originate from the domain along polymer-filler interface, which provides additional space for IL storage. However, when GO content exceeds 5.0%, the growth rate in IL uptake for nanocomposite membrane becomes slow and even sharply reduces (57.9% for SP-GO-7.5%-IL and 36.2% for SP-GO-10%-IL). Such findings are possibly due to the aggregation of GO, which makes fillers unable to efficiently create interfacial domain (as seen in FFV) for IL storage. Similar to the change of FFV, VGO-incorporated membrane exhibits lower IL uptake (39.7 and 52.8%) when the filler content is 2.5 and 5.0%, but higher IL uptake (66.5 and 56.8%) when the filler content is 7.5 and 10%. The incipient low IL uptake for SP-VGO-*X*-IL should result from the narrow interfacial domain at SPEEK-VGO interface. And the retral high IL uptake should originate from the good dispersion of VGO, creating abundant polymer-filler interfacial domain. Note that, SGO-incorporated nanocomposite membrane achieves the highest IL uptake at all filler content. For instance, the IL loading amount of SP-SGO-*X*-IL ($X = 2.5\%$, 5%, 7.5%, and 10%) is 50.0%, 64.3%, 73.7%, and 58.5%, respectively. The high IL uptake should be ascribed to the $-SO_3H$ groups on SGO, which (i) enables enhanced filler dispersity, creating more interfacial domain; (ii) generates repulsive interaction with SPEEK, making the domain loose and easy to swollen; (iii) generates strong electrostatic attraction with imidazole-type IL, providing strong driving force for IL diffusion deep into the

interfacial domain. Through comparison, a correlation between FFV and IL uptake is observed, confirming the storage function of interfacial domain for IL. Collectively, the above result of membrane microstructure and IL uptake implies that the main interaction between SPEEK and SGO is repulsive interaction, while there is mainly electrostatic attraction between SPEEK and VGO. For nanocomposite membrane, the sulfonic acid groups in SPEEK facilitate the diffusion of imidazole-type IL by attractive interaction.

Anhydrous conductivity of as-prepared membrane at 30 ~ 150 °C was shown in Fig. 4.31. It is found that SPEEK control membrane exhibits a relatively low conductivity of 0.47 mS cm^{-1} at 120 °C, which is much lower than that at hydrated condition (about 100 mS cm^{-1}). The incorporation of GO, VGO, and SGO slightly enhances the conduction property, and the conductivity is all below 2 mS cm^{-1} because proton transfer notably relies on water molecules to form structure diffusion and hydration shell. Thus, the proton donors in membrane may lose their conduction ability in water-free condition. Meanwhile, the close *IEC* value for SPEEK control and GO/FGO-filled membrane should be another reason for the similar conductivity (Fig. 4.31a). In comparison, the incorporation of IL confers much higher conductivity to nanocomposite membrane. SP-IL attains an enhanced conductivity of 7.2 mS cm^{-1} at 120 °C, more than 14 times of that of SP (0.47 mS cm^{-1}) under identical condition. This should be resulted from the additional proton-hopping sites from IL, as supported by the high inherent conduction ability [57]. Meanwhile, the basic group in IL may form base–acid pair with $–SO_3H$ in SPEEK, activating the conduction ability of $–SO_3H$ and therefore promoting the anhydrous conduction. In comparison with SP-IL (IL uptake: 43.0%, conductivity: 2 mS cm^{-1}), SP-GO-2.5%-IL with similar IL uptake (45.3%) achieves an elevated conductivity of 8.3 mS cm^{-1}. Furthermore, SP-VGO-2.5%-IL with lower IL uptake (39.7%) attains a higher conductivity of 7.4 mS cm^{-1}. The improved proton transfer property should be resulted from the continuous IL distribution along interface channels, which paves long-range paths for efficient proton transfer. This is different from our previous study, in which polymer capsule is utilized to improve the IL uptake of composite membrane [58]. The constructed channels related to 0D nanofiller are relatively tortuous and short range, and only, high IL loading can confer high conductivity. Figure 4.31b also reveals that changing GO content can effectively regulate IL loading amount and subsequent conductivity. For example, the conductivity of SP-GO-*X*-IL increases in the order of SP-GO-10%-IL < SP-GO-2.5%-IL < SP-GO-5%-IL < SP-GO-7.5%-IL, well in consistent with the order of IL uptake. Meanwhile, for nanocomposite membrane, the IL loading amount is found to govern the proton conductivity, and the anhydrous conductivity elevates from 9.7 to 17.2 mS cm^{-1} as the IL loading amount increases from 50% to 73.7% for SP-VGO-*X*-IL. It is interesting to note that SP-SGO-2.5%-IL and SP-SGO-5%-IL with relatively low IL uptake (50.0 and 64.3%) achieve higher proton conductivity (9.7 and 14.3 mS cm^{-1}) than those of SP-VGO-5%-IL and SP-VGO-7.5%-IL (9.5 and 13.6 mS cm^{-1}) with IL uptake of 52.8% and 66.5%, respectively. These should result from the enrichment of IL at SPEEK-SGO interface, and the formed broad channels (see SEM and FFV results) serve as lower energy barrier paths for proton conduction.

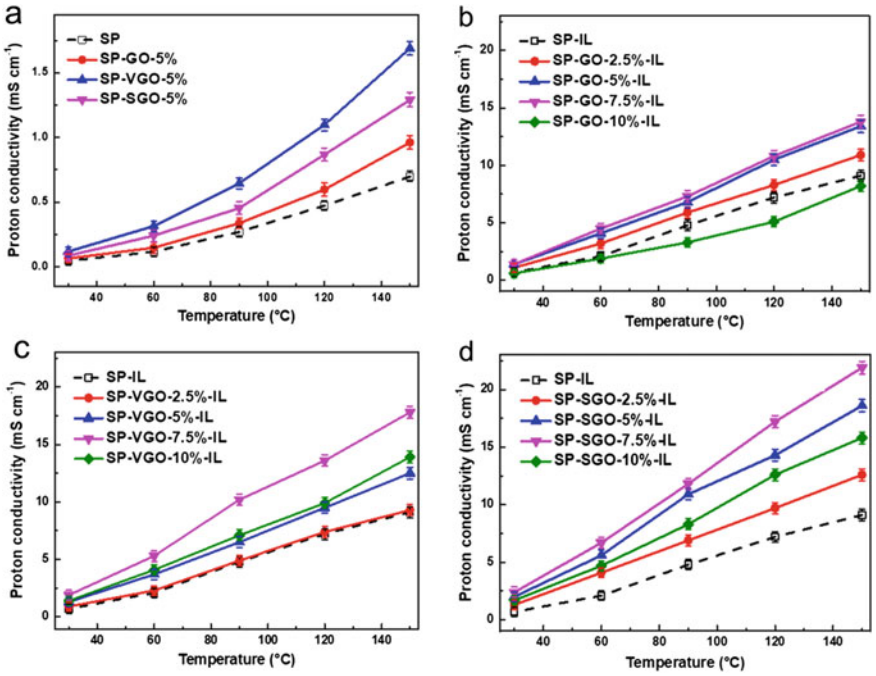

Fig. 4.31 Temperature-dependent proton conductivity of **a** IL-free membrane, **b** SP-GO-*X*-IL, **c** SP-VGO-*X*-IL, and **d** SP-SGO-*X*-IL. Copyright (2016), American Chemical Society [50]

For another, Fig. 4.31b also exhibits that all membranes display continuous conductivity increase with temperature. The conductivity of SP-GO-5%-IL increases from 1.4 to 13.4 mS cm^{-1} as the temperature elevates from 30 to 150 °C. The prompted mobility of proton-hopping sites should be the main contributor for this. Figure 4.31c–d reveals that the anhydrous conductivity of VGO-incorporated and SGO-incorporated nanocomposite membrane displays similar tendency with the increase of filler loading amount and temperature. Note that, SP-SGO-7.5%-IL attains the maximum conductivity of 21.9 mS cm^{-1} at 150 °C, which is 2.4 times of that of SP-IL (9.1 mS cm^{-1}) under identical condition. It should be noted that this value is much higher than that of commercial Nafion (1.0 mS cm^{-1}), and one of the highest anhydrous conductivity reported in literatures.

For IL-filled PEM, the IL leaching, which will result in conductivity reduction, is a bothersome issue that hampers the practical application for IL-filled membranes. IL loss and IL retention of as-prepared membrane was tested under an extreme condition (immersing membrane into water) [32, 43, 59]. In addition to SPEEK control membrane, SP-GO-5%, SP-VGO-5%, and SP-SGO-5%, which contain relatively high filler content an possess good filler dispersity, were selected as representatives. For better comparison, the IL uptake of all membranes is tuned to be the same (about 70%) by controlling IL treatment time and temperature. Figure 4.32a depicts the

dynamic IL loss curve of membranes as a function of time, which reveals that all membranes display two-stage IL release: fast IL release at the beginning 30 min and slow IL release from 30 to 240 min (reaching a constant value). Within IL-filled nanocomposite, the IL might exist in two state like water: free state and bound state. The former is corresponding to IL having weak or no interaction with polymer matrix, which has strong mobility; the latter is corresponding to IL having strong interaction with polymer matrix, which has inhibited mobility. Accordingly, it is speculated that: the fast IL release may be mainly ascribed to the release of free-state IL. After this stage, the release of bound IL gives a slow loss process (i.e., the second stage). In comparison with SP-IL, incorporating GO affords nanocomposite membrane lower IL loss. For instance, the constant IL loss decreases from 85.5% for SP-IL to 81.3% for SP-GO-5%-IL. The decreased IL loss is possibly attributed to the formed nanodomains along GO surface, which confine the IL through capillary force. The good compatibility with SPEEK confers VGO-incorporated membrane compact interfacial domains (that is narrower storage domains) and hence lower IL loss. SP-VGO-5%-IL attains a constant IL loss of 80.4%. In comparison, SP-SGO-5%-IL achieves a constant IL loss of 76.9%, which is the lowest of as-prepared membranes with 5% filler loading amount. Considering the large interfacial domain, this should result from the $–SO_3H$ groups along SPEEK-SGO interface, which generates strong electrostatic attraction with imidazole-type IL. This interaction could, on the one hand, make more IL aggregate in the formed channels during IL diffusion, on the other hand, create more bound-state IL. Like the result in Fig. 4.32a, the IL retention decreases obviously at the beginning 30 min and then reaches a constant value for all membranes. For the four types of IL-filled membranes, the value of constant IL retention reduces in the order of SP-SGO-*X*-IL > SP-VGO-*X*-IL > SP-GO-*X*-IL > SP-IL (Fig. 4.32b). The IL leaching will decrease the amount of proton-hopping sites and thus weaken the proton conduction ability of membrane. Figure 4.32c shows the anhydrous conductivity of IL-filled membrane after IL leaching. SP-IL with constant IL retention of 9.9% achieves a conductivity of 2.57 mS cm^{-1} at 150 °C. In comparison, nanocomposite membrane achieves elevated anhydrous conductivity due to the higher content of IL in membrane, especially at SPEEK-filler interfacial domain. For example, the conductivity after IL leaching of SP-GO-*X*-IL, SP-VGO-*X*-IL, and SP-GO-*X*-IL increases to 3.37, 3.60, and 4.71 mS cm^{-1}, respectively. Lin et al. utilized imidazolium-modified SiO_2 and mesoporous SiO_2 to improve the anhydrous conductivity and IL retention of polymer membrane, which attains the maximum conductivity of 10 and 12 mS cm^{-1} (160 °C) with IL retention of about 5.8% and 8.0%, respectively [60, 61]. In comparison, the values obtained in this work are acceptable, possibly ascribed to the long-range interfacial paths constructed by 2D FGO/GO. Collectively, these imply that the anhydrous conductivity is IL loading amount and distribution controllable for IL-filled nanocomposite, and incorporating functional GO could simultaneously improve IL uptake and IL retention by constructing nano-confined domain.

In conclusion, we attempt a facile approach to improve IL uptake and retention of polymer membrane by adding functional GO species for efficient anhydrous proton conduction. Within nanocomposite membrane, the GO species construct numerous

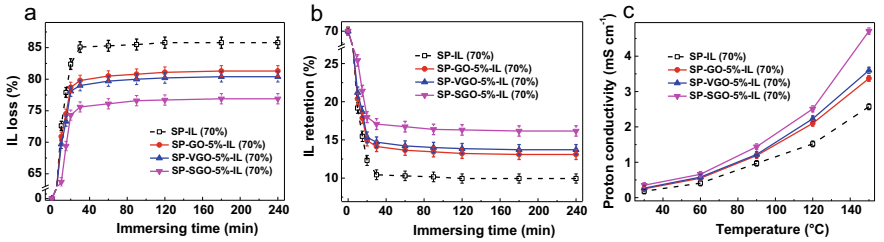

Fig. 4.32 Time-dependent **a** IL loss and **b** IL retention of membranes, **c** temperature-dependent anhydrous conductivity of membranes after immersing in water. Copyright (2016), American Chemical Society [50]

interfacial domain, which provides additional space for IL storage. Benefitted from the high aspect ratio and surface area of filler, the stored IL forms long-range transfer paths and therefore endows nanocomposite membrane with elevated anhydrous proton conductivity. Altering the functional group could efficiently regulate the interface structure and thus IL uptake and distribution, which determines the conduction property of IL-filled composite. In addition, the confined effect of interfacial domain offers nanocomposite membrane improved IL retention ability via capillary force and would be further strengthened at the presence of strong attraction from functional groups on channel surface. Collectively, the high IL uptake and retention ability confers improved anhydrous conductivity and long-time operation stability to nanocomposite membrane. While more efforts should be devoted to avoiding any loss of IL from membrane to ensure the practical application in fuel cell, for example, highly cross-linked membrane surface, surface coating by inorganic material, etc.

4.7 Composite Membrane with Ionic Liquid and Polymer Microcapsule

Silica microsphere with diameter of ~ 400 nm was fabricated based on Stöber method [62]. TEOS was incorporated into the mixture of ethanol, water, and aqueous solution of ammonium hydroxide with strong stirring at 30 °C for 24 h. Then, excess MPS was incorporated into above mixture for reacting for another 24 h to modify the silica with carbon–carbon double bond. The coating of polyelectrolyte layer on MPS-silica microsphere was conducted by distillation-precipitation polymerization [63, 64]. In a dried 100 mL flask that was attached to a fractionating column, Liebig condenser, and receiver, 0.30 g of MPS-silica particle was added into 80 mL acetonitrile with ultrasonication. MAA (0.5 mL), EGDMA (0.5 mL), and AIBN (0.02 g, 2 wt% relative to the comonomers) were then dispersed in the MPS-silica solution. The mixture was heated to boiling state, and then, the solvent was distilled from the reaction system. After 40 mL of acetonitrile was distilled out, the reaction was ended, and the resultant microsphere was purified by three cycles of ultracentrifugation, decanting, and

resuspension in acetonitrile. Two-stage polymerization with the same monomer and crosslinker content was performed to confer the polyelectrolyte shell with adequate thickness for supporting the capsule structure. The fabricated microsphere was etched by HF solution (10 wt%) for 2 h followed by several centrifugation/washing cycles in water till neutral pH. The resultant polyelectrolyte microcapsule was named as PMC. The methacrylic acid polyelectrolyte microsphere was fabricated by two-stage direct distillation-precipitation polymerization of MAA and EGDMA. The volume ratio of MAA and EGDMA was 1:1, the same as that of PMCs The resultant polyelectrolyte microsphere was named as PMS.

SPEEK was fabricated via post-sulfonation of PEEK. The sulfonation degree of prepared SPEEK was computed to be 65% through titration method. SPEEK control membrane was prepared through solution-casting method: SPEEK (0.75 g) was dispersed into DMF (10 g) at 25 °C and then stirred vigorously for 12 h. The mixture was casted onto a glass plate and dried first at 60 °C for 12 h, then at 80 °C for 8 h. The resultant membrane was named as SP.

IL-free membrane: certain amount of PMC or PMS (3% ~ 12%) was dispersed in DMF (10.0 g) solution with ultrasonic for 8 h at room temperature. Then, SPEEK (0.75 g) was incorporated into the above solution and stirred vigorously for another 12 h at room temperature. The resultant solution was casted onto a glass plate and dried at 60 °C in an oven for 12 h followed by drying at 80 °C for another 12 h. The resultant membrane was named as SP-PMC-*X* or SP-PMS-*X*, representing PMC or PMS as the filler, where *X* ($X = 3$, 6, 9, or 12) was the weight ratio of the filler to SPEEK.

The as-prepared membrane (4×4 cm^2) was used to prepare IL-filled composite membrane. The IL-free membrane was immersed in ionic liquid at a given temperature and ultrasonic power. After immersing in IL for a certain time, the membrane was taken out, and the surface IL was removed. Afterward, the membrane was dried in vacuum oven at 60 °C until a constant weight.

PMC and PMS were fabricated via distillation-precipitation polymerization method. MAA and EGDMA, rather than divinylbenzene, were selected because of the potential of providing: (i) cross-linking and flexible shell, which can neatly regulate the flowing in or out of IL; (ii) $-CO_2H$ groups, which can generate strong interaction with IL. The morphology of PMC and PMS was detected by TEM and shown in Fig. 4.33. The PMC is clearly observed by well-defined capsule structure with dense shell and large lumen. The lumen size is ~ 280 nm, and the shell thickness is ~ 140 nm, which is robust enough to support the hollow structure. The PMS also has well-defined shape with smooth surface, and the diameter is ~ 520 nm, close to that of PMC. During the polymerization, the monomer concentration and heating rate for PMC and PMS is controlled to ensure a moderate and uniform growth, without aggregation of the resultant capsule and sphere.

Homogeneous filler dispersion is essential for high-performance membrane because of the potential of producing more polymer-filler interfaces and offering more possibility of surface-induced tailoring of membrane morphology [65, 66]. The dispersion of PMC/PMS within the membran was detected by SEM, as shown in Fig. 4.34. The cross-sectional SEM images reveal that SP-PMC-*X* and SP-PMS-*X* are

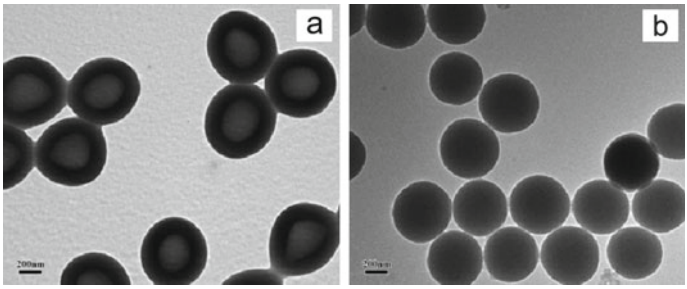

Fig. 4.33 TEM image of **a** PMC and **b** PMS. Copyright (2015), Elsevier [61]

relatively dense, uniform, and defect free. The fillers are homogeneously dispersed in membrane without obvious agglomeration. In addition, PMC with large lumen is clearly observed in Fig. 4.34b and d, which maintains the pristine structure. The lumen is observed possibly due to the partially break during freeze fracture in liquid nitrogen. In comparison with SP-PMC-*X* and SP-PMS-*X* (Fig. 4.34a and b), clear continuous channels are observed in SP-PMC-*X*-IL and SP-PMS-*X*-IL (Fig. 4.34c and d), in which the gray region and black region are corresponding to SPEEK and IL, respectively. Such phenomena suggest that the ILs are mainly stored in the ionic cluster of SPEEK driven by the interaction from $-SO_3H$ group. As a result, the aggregation of IL broadens the cluster into interconnected channel. Notably, for SP-PMC-*X*-IL (Fig. 4.34d), IL can be detected clearly in the lumen of PMC (region within red dash line), confirming the potential of PMC as IL reservoir. The IL-enriched channel would confer continuous paths for proton hopping, and the IL-filled PMC would provide the composite membrane high IL uptake and retention.

The amphiphilic feature of SPEEK chain endows SPEEK-based membrane with distinct nanophase-separation structure between the hydrophobic and hydrophilic domains, in which the sulfonic acid groups aggregate into ionic clusters. This structure could be detected by SAXS technology, and the SAXS pattern of as-prepared membrane was shown in Fig. 4.35. It is found that SPEEK control membrane displays a typical scattering peak at $q = 0.24\ \text{nm}^{-1}$, indicating the existence of the self-organized ionic cluster [67, 68]. In comparison, incorporating PMC decreases the q value of SP to $0.23\ \text{nm}^{-1}$ for SP-PMC-6%. Given that the Bragg spacing (d) is related to q based on the equation: $d = 2\pi/q$, where the d refers to the inter-cluster distance and indicates the size of ionic cluster [69], the reduction of q value implies the increase of cluster size. Such phenomena is reasonably ascribed to the repulsive interaction between PMC and SPEEK phase, which affords composite membrane high entropic driving force for phase separation [70]. Incorporating PMS endows SP-PMS-*X* with a similar tendency, as verified by the reduction of q value of SP-PMS-*X*. These results demonstrate that the same surface structure of PMC and PMS allows a similar influence on the segment configuration of SPEEK. Furthermore, increasing the PMS/PMC content leads to a further reduction of q value that is the larger cluster size. The effect of incorporating IL on structure of composite membrane is shown in

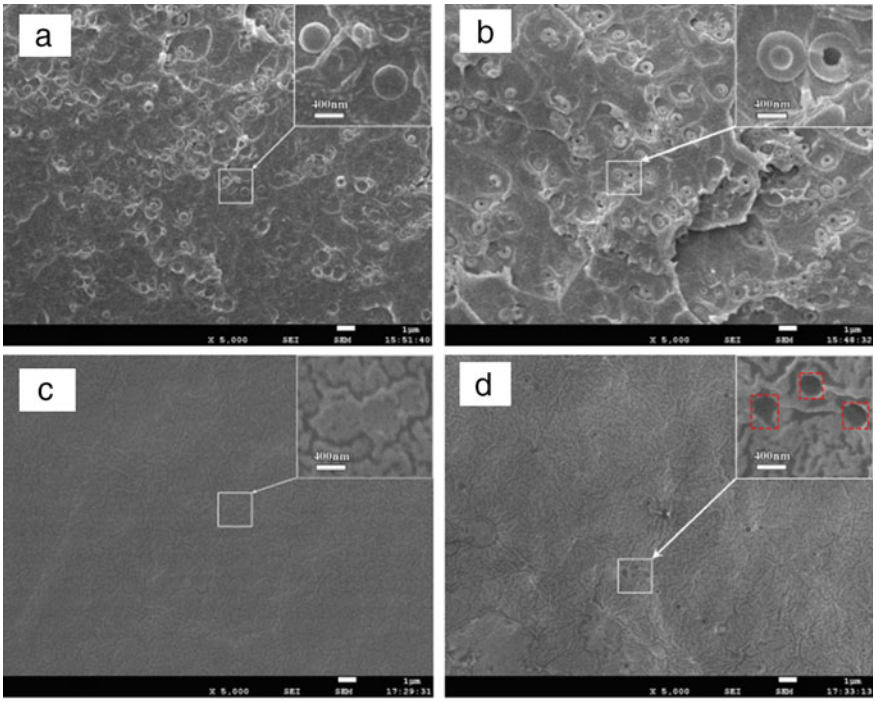

Fig. 4.34 Cross-sectional SEM image of **a** SP-PMS-6%, **b** SP-PMC-6%, **c** SP-PMS-6%-IL, and **d** SP-PMC-6%-IL. Copyright (2015), Elsevier [61]

Fig. 4.35b. It is found that the incorporation of IL shifts the scattering peak to a small value, and no peak can be observed in the range of 0.1 ~ 0.3 nm^{-1}. Similar results have been observed in other SPEEK-based membranes [26, 71, 72]. The reduction of q value is possibly ascribed to the enrichment of IL in hydrophilic cluster, which boardens the cluster and then forms interconnected channels.

To further explore the influence of PMC/PMS and IL on the structure of SPEEK matrix, the membrane was subjected to WXRD analysis. Figure 4.36 reveals that all membranes exhibit broad crystalline band at $2\theta = 9 \sim 21°$, related to the ordered stacking of hydrophobic backbone [9]. In comparison with SPEEK control membrane, SP-PMC-6% (Fig. 4.36a) shows an intensity decline of this band. Such phenomenon is reasonably attributed to the presence of PMC, which hinders the crystallization of hydrophobic backbone through mutual interaction and space interference. The incorporation of PMS gives a similar regulation on the segment configuration of SPEEK phase, and this finding is in consistent with the result in SAXS. In addition, increasing the PMC/PMS content would confer a further reduction of peak intensity. As detected in Fig. 4.36b, incorporating IL obviously weakens the crystallization peak of composite membrane, which should result from the plasticizing effect of IL on hydrophobic domain of SPEEK. The plasticizing effect would weaken the

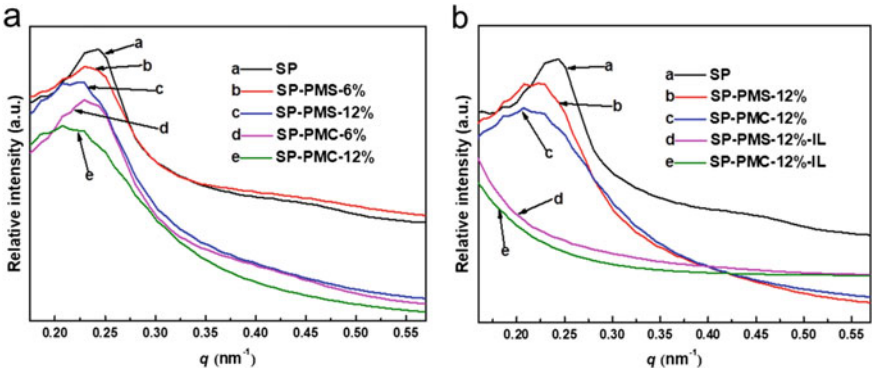

Fig. 4.35 SAXS pattern of membrane. Copyright (2015), Elsevier [61]

interaction among backbone and thus destroy the ordered stacking, making composite membrane more flexible.

Anhydrous conductivity of PEM is a key parameter for fuel cell performance, including the operational voltage and current output. Anhydrous conductivity of as-prepared membranes at 30 ~ 150 °C was tested, and the results were shown in Fig. 4.37. It is found that SP, SP-PMS-*X*, and SP-PMC-*X* display weak anhydrous conduction ability. The conductivity is below 0.7 mS cm^{-1} at150 °C, which is much lower than those at hydrated condition (about 100 mS cm^{-1}). This is due to the absence of water molecule, which acts as proton carrier and meanwhile could facilitate the dissociation of H^+ from the acid group ($–SO_3H$ or $–CO_2H$). Accordingly, the $–SO_3H$/$–CO_2H$ groups in membrane may lose the conduction ability. Incorporating IL affords the membrane additional proton-hopping sites (i.e., imidazole and ionic liquid) and meanwhile activates proton conduction groups ($–SO_3H$, $–CO_2H$) in the form of acid–base pairs. These two features could significantly improve the proton transfer ability of composite membrane [30]. SP-IL exhibits an increased

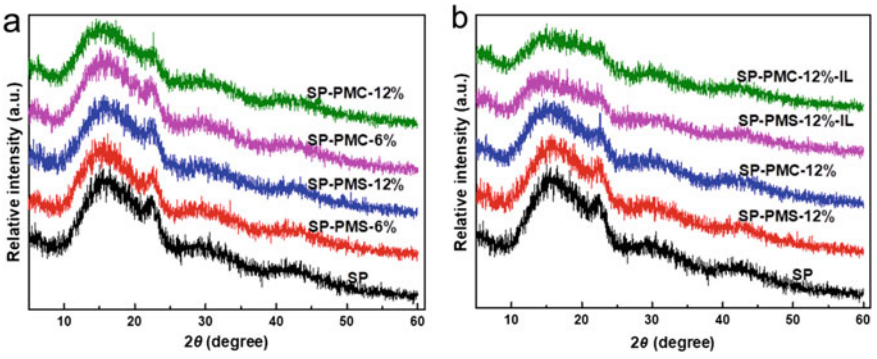

Fig. 4.36 WXRD pattern of membrane. Copyright (2015), Elsevier [61]

conductivity of 8.9 mS cm^{-1} at 120 °C, 63 of that of SP (0.14 mS cm^{-1}). In comparison with SP-IL, SP-PMC-*X*-IL achieves much higher anhydrous conductivity, and 3% PMC affords a 92% augment in conductivity to composite membrane (17.1 mS cm^{-1}). It is known that $–CO_2H$ groups possesses lower dissociation degree than $–SO_3H$ groups. Incorporating carboxyl-based filler would decrease the ion-exchange capacity of SPEEK membrane, which in turn decreases the Grotthuss-type transfer. Therefore, the augment of anhydrous conductivity of SP-PMC-*X*-IL is attributed to the increased IL uptake, which provides more anhydrous hopping sites for proton jumping. Increasing PMC content would further elevate the IL uptake and the anhydrous conductivity. For instance, the conductivity gradually increases to 18.0, 20.9, and 24.3 mS cm^{-1} as the PMC content increases to 6%, 9%, and 12%, respectively. For another, Fig. 4.37a also reveals that all membranes display continuous conductivity increase with temperature. The conductivity of SP-PMC-9%-IL increases from 3.9 to 29.8 mS cm^{-1} when the temperature elevates from 30 to 150 °C. The prompted mobility of proton carrier should be the main contributor for this increase. In comparison with PMC-incorporated composite membrane, the anhydrous conductivity of PMS-incorporated composite membrane displays similar tendency with the increase of filler content and testing temperature (Fig. 4.37b). Figure 4.37c clearly reveals that the conductivity of SP-PMC-*X*-IL is higher than those of SP-PMS-*X*-IL under identical condition, probably because of the higher IL uptake in SP-PMC-X-IL. Note that SP-PMC-12%-IL achieves the maximum anhydrous conductivity of 33.7 mS cm^{-1} at 150 °C, which is 2.6 times of that of SP-IL (13.2 mS cm^{-1}) under identical condition and much higher than that of commercial Nafion (1.0 mS cm^{-1}) [73]. Although the highest anhydrous conductivity in this work (33.7 mS cm^{-1} at 150 °C) cannot rival that of polybenzimidazole-H_3PO_4 membrane, the acidic SPEEK matrix allows higher low-temperature proton conductivity, faster oxygen reduction kinetics, and lower sensibility to oxidative degradation by peroxides [74, 75]. Consequently, this work may pave a new avenue toward technologically attractive PEM.

For IL-based PEM, IL leaching caused by vapor or liquid water is a great challenge. To investigate the IL retention ability, composite membrane with same IL uptake was prepared by controlling the IL treatment time and temperature. Then, the dynamic IL loss and IL retention of the resultant membrane was tested at an extreme condition (immersing membrane in water). Figure 4.38a and b depicts the dynamic IL loss curves of SP-IL, SP-PMC-*X*-IL, and SP-PMS-*X*-IL as a function of time. It is found that all membranes display two-stage IL release: the fast IL release at the beginning 60 min and a slow IL release from 60 to 240 min (reaching constant value, the corresponding IL retention value is defined as “steady-state IL retention” in this work). Similar to water, the IL in membrane may exist in two states (free state and bound state). The former is corresponding to the IL with free mobility, which has weak interaction with polymer matrix and mainly locates in the center of ionic channels (like free water). The latter is corresponding to the IL with restricted mobility, which has strong interaction with polymer matrix and mainly locates at the side of ionic channels (like bound water). Accordingly, the fast IL release in the first stage is mainly resulted from the release of free-state IL. In the second stage, the retained IL is

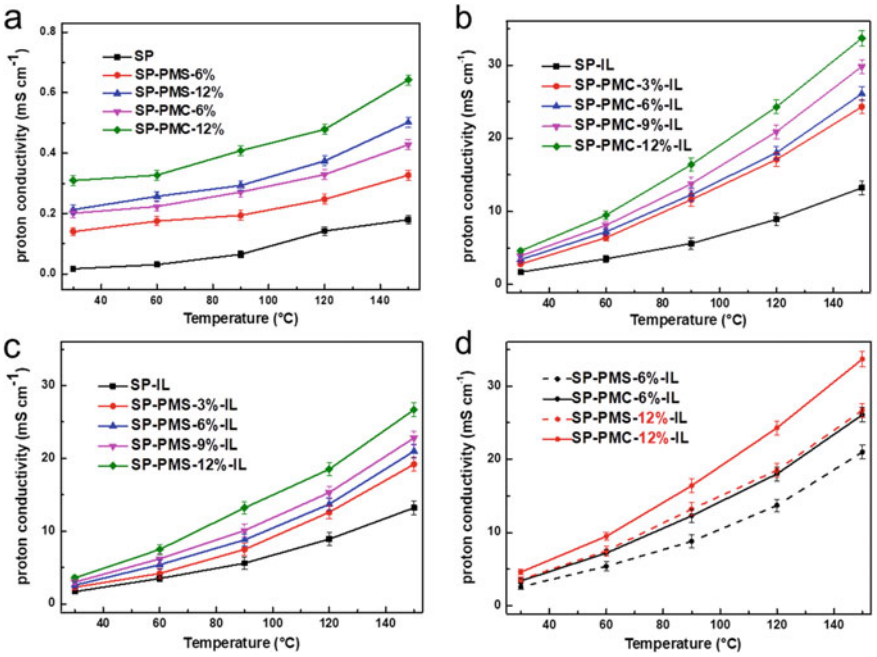

Fig. 4.37 Temperature-dependent proton conductivity of **a** IL-free membrane, **b** SP-PMC-*X*-IL, **c** SP-PMS-*X*-IL, and **d** the comparison of SP-PMC-*X*-IL and SP-PMS-*X*-IL. Copyright (2015), Elsevier [61]

mainly in bound state. Therefore, the IL content of composite membrane keeps almost constant with testing time, which is significantly different from the case of PMC-enabled water retention. Although PMC has been proved temporarily effective as water reservoir within ionomer membrane, they tend to constantly release water, and hence, the problem of proton conductivity decline could not be thoroughly addressed. Helped by the strong electrostatic interaction between IL and capsule wall, as well as the much larger kinetic diameter than water, the mass transfer resistance of IL through capsule wall is much higher than that of water. In this way, PMC within ionomer membrane could serve as a kind of "permanently" effective IL reservoir, rather than temporarily. This interesting finding implies the possibility of thoroughly addressing the excessive IL release issue.

More detailed information could be obtained from Fig. 4.38a–c. In comparison with SP-IL, SP-PMC-*X*-IL and SP-PMS-*X*-IL exhibit lower IL loss during the first stage, possibly because that the capillary force at polymer-filler interfacial area retards the free-state IL release. Consequently, the constant data at the second stage for SP-PMC-*X*-IL and SP-PMS-*X*-IL are lower than those of SP-IL. For instance, the steady-state IL loss reduces from 78.8% for SP-IL to 66.6 and 47.3% for SP-PMS-12%-IL and SP-PMC-12%-IL, respectively. For composite membrane, Fig. 4.37c reveals that the final IL loss of SP-PMC-*X*-IL is much lower than that of

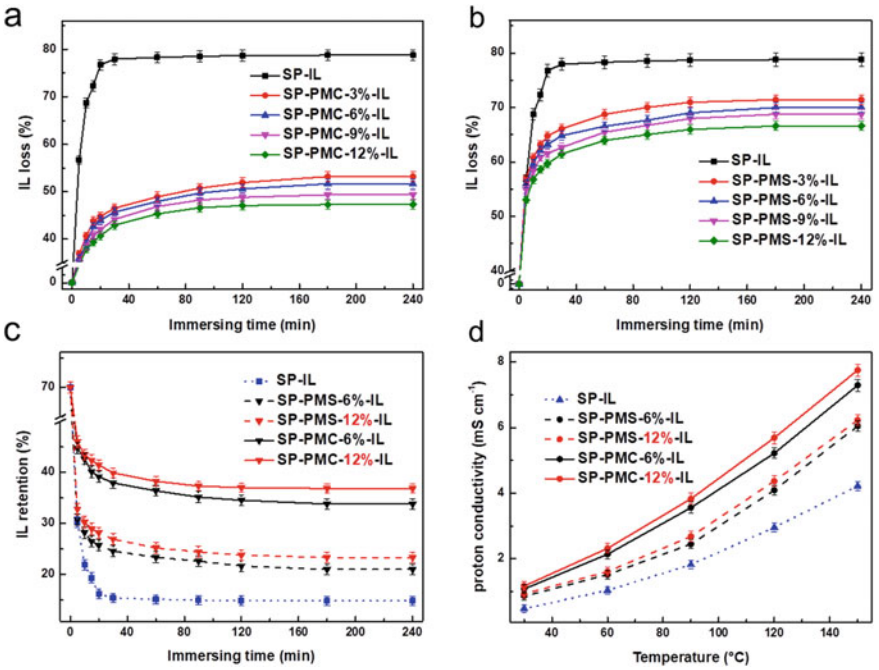

Fig. 4.38 Time-dependent IL loss of **a** SP-PMC-*X*-IL, **b** SP-PMS-*X*-IL; the comparison of **c** IL retention between SP-PMC-*X*-IL and SP-PMS-*X*-IL, and **d** temperature-dependent anhydrous conductivity of composite membrane after immersing in water. Copyright (2015), Elsevier [61]

SP-PMS-*X*-IL, even SP-PMC-6%-IL (51.7%) achieves lower steady-state loss value than that of SP-PMS-12%-IL (66.6%). Such results suggest a IL-state switching within PMC. When migrating from the lumen to the shell, free-state IL would be partially converted into bound-state IL, resulting from the interaction between imidazole group and carboxyl group, which is a common phenomenon found in human physiology to maintain homeostasis [76]. For the three type of membrane, the steady-state IL retention reduces in the order of SP-PMC-*X*-IL > SP-PMS-*X*-IL > SP-IL under identical condition (Fig. 4.38c). Additionally, SP-IL with different IL uptake is prepared for adjunctive leaching test. It is found that composite membrane with high IL uptake achieves higher IL retention, and similar finding is also found in other literature [77]. The higher IL retention is probably due to that: for the composite membrane with high IL uptake, IL is induced deeply into the ionic cluster and thus generates larger SPEEK-IL interfacial area and more bound-state IL. In this way, the increased proportion of bound-state IL confers high IL retention on composite membrane with high IL uptake. These phenomena could powerfully verify our above hypothesis (free-state ILs and bound-state ILs).

Figure 4.38d shows the proton conductivity of composite membrane after IL leaching. After leaching, the SP-IL with steady-state IL retention of 14.8% achieves a conductivity of 4.22 mS cm^{-1}. In comparison, the incorporation of PMS confers

SP-PMS-6%-IL and SP-PMS-12%-IL higher conductivity of 6.05 and 6.23 mS cm^{-1}, respectively. The improved anhydrous conduction ability should result from the high steady-state IL retention, which provides more proton-hopping sites. Incorporating PMC would further elevate the IL retention ability of membrane and thus enhance the anhydrous conductivity (Fig. 4.38). For example, the conductivity of SP-PMC-6%-IL and SP-PMC-12%-IL is 7.29 and 7.75 mS cm^{-1}, respectively. Additionally, the presence of PMC, which is similar to the vacuole in plant cell, could liberate IL into SPEEK matrix and thus render membrane a stable IL environment. Collectively, these imply that the anhydrous conductivity is IL loading amount controllable, and the SP-PMC-*X*-IL has fascinating IL retention and proton conduction property (Fig. 4.39).

In summary, a facile approach for enhancing the IL retention of membrane is developed by incorporating PMC into SPEEK matrix. PMC possesses the following merits: (i) the lumen of PMC acts as the IL reservoir, ensuring higher IL uptake and (ii) the highly cross-linked shell of PMC manipulates the IL release, mimicking the cytoplasm storage mechanism in cell and endowing an enhanced IL retention ability. The IL donates sufficient anhydrous hopping sites (e.g., imidazole, acid–base pair, IL) to composite membrane, resulting in the elevated anhydrous proton conductivity. Particularly, the composite membrane containing 12% PMC achieves a high steady-state IL retention of 36.9% after leaching in liquid water, which is

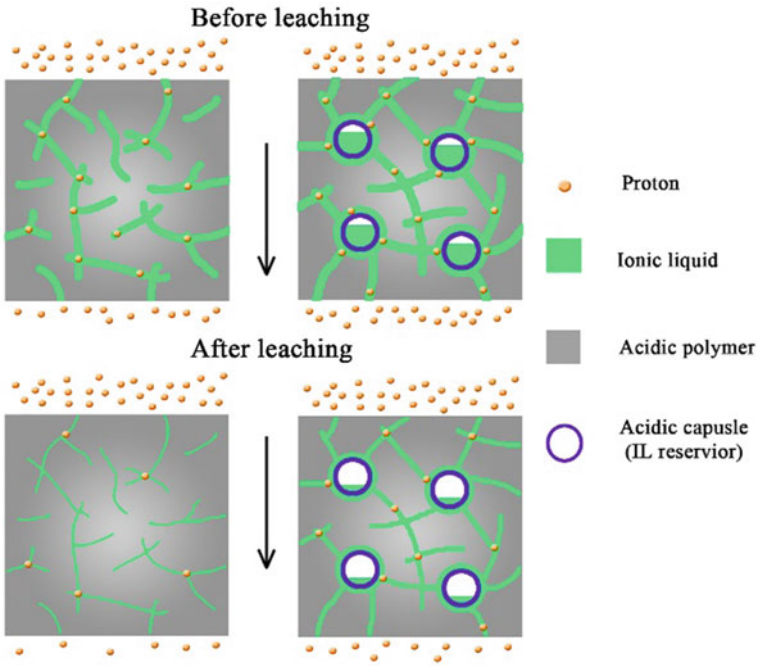

Fig. 4.39 Schematic structure and proton transfer of membrane before and after IL leaching. Copyright (2015), Elsevier [61]

twice more than that of SPEEK control membrane. This affords a 84% enhancement of anhydrous conductivity to composite membrane. Considering the versatility of capsule synthesis method, more delicate capsules with tunable hierarchical structure and functional group are expected to be designed and synthesized for IL-based PEM.

4.8 Composite Membrane with Quantum Dot

QD and hybrid membrane preparation: the quantum dot (QD) was prepared by one-step microwave-assisted pyrolysis. Typically, 0.96 g citric acid and 540 μL diethylenetriamine were dissolved in ultra-purified water (2.0 g) with ultrasonic for 5 min at room temperature (~22 °C). Afterward, the mixture was heated in a microwave oven at 750 W for 5 min. The product was washed with ethanol (98 wt%) several times to remove residual small molecule, followed by dispersing in water and freeze drying of the aqueous solution for 48 h. The product was named as polymer-like quantum dot (PQD). While for GO-quantum dot (GQD) with greater carbonation, the mixed solvent of ultra-purified water and glycerol was selected for higher reaction temperatures above 100 °C. The mass of ultra-purified water and glycerol was 1.0 and 1.0 g and 0.5 and 1.5 g, for GQD1 and GQD3, respectively.

Nafion control and hybrid membranes were prepared by solution-casting method. Nafion solution was heated in a vacuum oven at 60 °C for about 24 h to obtain a dry Nafion resin that was then re-dissolved in dimethylacetamide (DMAC) under vigorous stirring to obtain a homogeneous Nafion/DMAC solution. QDs were dispersed in DMAC under ultrasonic treatment for 2 h at room temperature then introduced to Nafion/DMAC solution under stirring and ultrasonic treatment for 8 and 4 h, respectively. The resultant mixture was casted onto a glass plate and dried at 80 °C in a vacuum oven for 12 h followed by drying at 120 °C for another 4 h. The membrane was peeled from the glass plate and kept in deionized water. The hybrid membrane was named as RN-PQD-X, RN-GQD1-X, or RN-GQD3-X, where *X* (*X* = 1, 2, 5, 10, or 15%) was the mass-ratio of the filler to Nafion. For characterization and testing, all membranes were pre-treated by soaking in 3% (w/w) H_2O_2 aqueous solution at 80 °C for 1 h followed by rinsing with water at 80 °C for 1 h, soaking in 1 M H_2SO_4 at 80 °C for 1 h, and a final rinse with deionized water until neutral pH. The Nafion control membrane was designated as RN.

The QDs were prepared via one-pot, microwave-assisted condensation of citric acid and diethylenetriamine, which enabled facile regulation of QD chemical components by adjusting the reaction solvent. Hydrophilic PQD (Fig. 4.40a) was fabricated using water as a solvent to ensure a carbonization-free condensation and thereby generate evenly dispersed $–CO_2H$ and $–NH–/–NH_2$ groups. Hydrophobic GQD (Fig. 4.40b) was prepared by carbonizing the O–/N– containing groups using a glycerol/water mixture as a solvent to generate higher reaction temperature (exceeding 100 °C) under microwave irradiation [78]. Two types of GQD with moderate (GQD1), and high (GQD3), carbonization degrees were prepared by setting the glycerol/water ratio to 1:1 and 3:1, respectively. TEM image, Fig. 4.40c, reveals the clear lattice

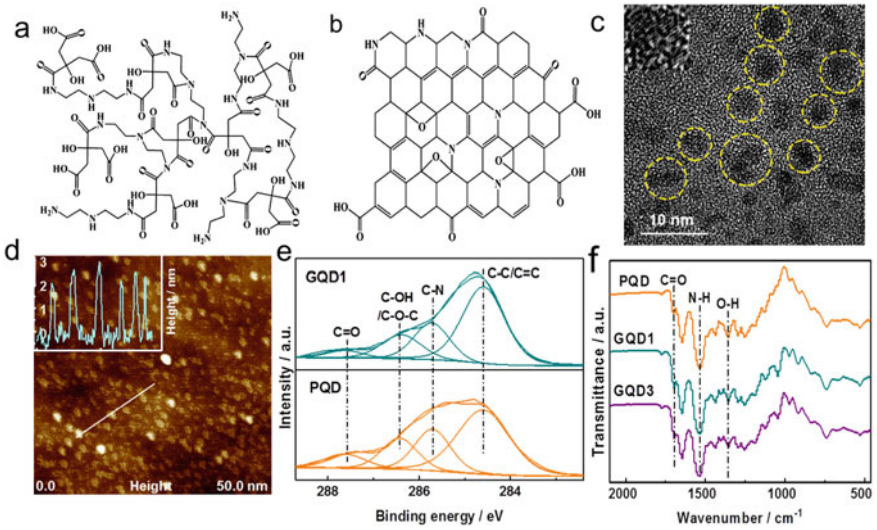

Fig. 4.40 Chemical structure of hydrophilic PQD **a** and hydrophobic GQD **b**. **c** TEM image of GQD1 (inset: high-resolution TEM image of single GQD1). **d** AFM topography image of GQD1 (inset: height profile along the white line). **e** C 1 s spectra of PQD and GQD1. **f** FTIR spectra of QDs. Copyright (2018), John Wiley and Sons [20]

structure of GQD1 with a size of 2 ~ 5 nm [79]. Atomic force microscopy (AFM) image, Fig. 4.40d, reveals the GO-like structure with a (regular) height of (2.5 ± 0.4) nm. High-resolution TEM showed that GQD3 with greater carbonization possesses clearer lattice fringes. XPS (Fig. 4.40e) and FTIR (Fig. 4.40f) illustrate clearly the wide variation of functional groups on QDs with the carbonization degree. The deconvolution of C 1 s band confirms the decrease of C=O/C–O bonds and increase of C–C/C=C bands for GQD as compared to PQD. Together, the nanoscale size and tailored surface functional groups of QDs herald significant promise for molecular-level hybridization, which is difficult to realize with conventional fillers.

Nafion control membrane was prepared by recasting Nafion solution and designated as RN. Then, QDs were uniformly dispersed in Nafion solution to prepare hybrid membranes. These were referred to as RN-QD-*X*, in which *X* is the loading quantity of QDs (Fig. 4.41). Tapping-mode AFM and SAXS were used to probe the nanophase-separation structure. RN showed a well-defined "fingerprint image" of surface morphology under hydrated condition, in which dark and bright areas represent, respectively, hydrophilic ionic nanophase and hydrophobic backbone nanophase (Fig. 4.42a) [79, 80]. This distinctive hierarchical structure is formed through the entropy-driven self-assembly of amphipathic Nafion chains coupled with a chain pre-arrangement in casting solution. Apart from a slight diminishing, the "fingerprint image" structure of Nafion is retained after incorporating QDs, especially

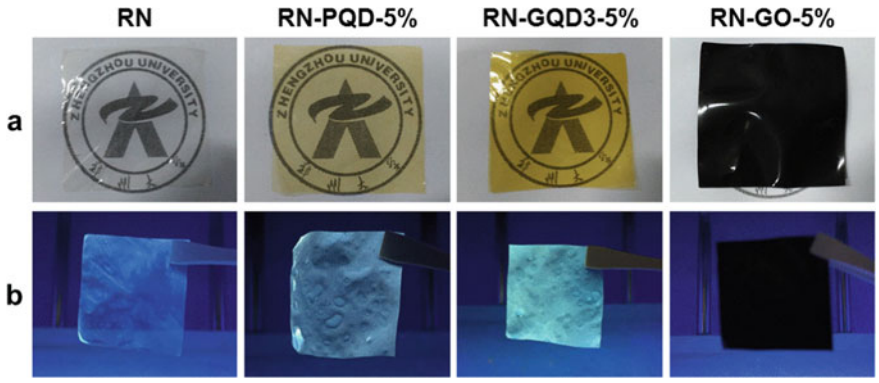

Fig. 4.41 **a** Photographs of dry membranes under daylight. **b** Photographs of wetting membranes under 365 nm UV. Copyright (2018), John Wiley and Sons [20]

under low loading level (< 5 wt%). For RN-GO-5%, it is difficult to discern continuous ionic nanophase that has been cut into isolated large-sized domains by GO sheets.

SAXS findings further confirm the weak alteration on the overall topology of Nafion by QDs. Compared with RN, only, slight shift of ionomer peak can be observed when adding 5 wt.% QDs, while incorporation of GO led to a significant q shift (Fig. 4.42b). The result is due to the significant interference of GO with Nafion self-assembly [81]. This can also be observed in cross-sectional SMS images (Fig. 4.42c), and the uniform Nafion matrix is macroscopically cut into isolated domains by GO sheets. QDs therefore show significant potential for molecular-level hybridization in nanophase-separated material with feeble alteration of the overall topology because of the matched structural size.

Also, important is the distribution of QDs in the nanophases. WXRD pattern exhibits a broad diffraction peak at $2\theta = 12 \sim 22°$. This peak can be deconvoluted into $2\theta = 16.0°$ and 17.5° and is attributed to, respectively, the amorphous and crystalline scattering of the backbone nanophase [57, 82]. Figure 4.43a reveals the co-existence of these two domains in RN and RN-QD-*X*. The crystallinity for RN is computed to be 20.7%. Contrarily, GQDs generate strong interference with backbone nanophase, and the crystallinity value of RN-GQD1-5% is 16.7%. For RN-GQD3-5%, this reduces further to 12.3%, nearly that of RN-GO-5% at 10.5%. It can be deduced therefore that PQD is located mainly in the hydrophilic ionic nanophase, whereas GQD tends to stay in the hydrophobic backbone nanophase. For PQD, the ample O–/N– containing hydrophilic groups impart strong chemical affinity with the $–SO_3H$ groups in Nafion side chain. It is postulated that the complete nanophase separation in RN-QD-*X*, its small size, excellent dispersion, and strong interactions, might permit PQD to 'subordinately assemble' along with Nafion side chain, and then be brought into, and be enriched in, the ionic nanophase. Similarly, GQD3 can form strong affinity with poly(tetrafluoroethylene) backbone. These then are covered within the backbone nanophase subordinated with Nafion backbone and thereby

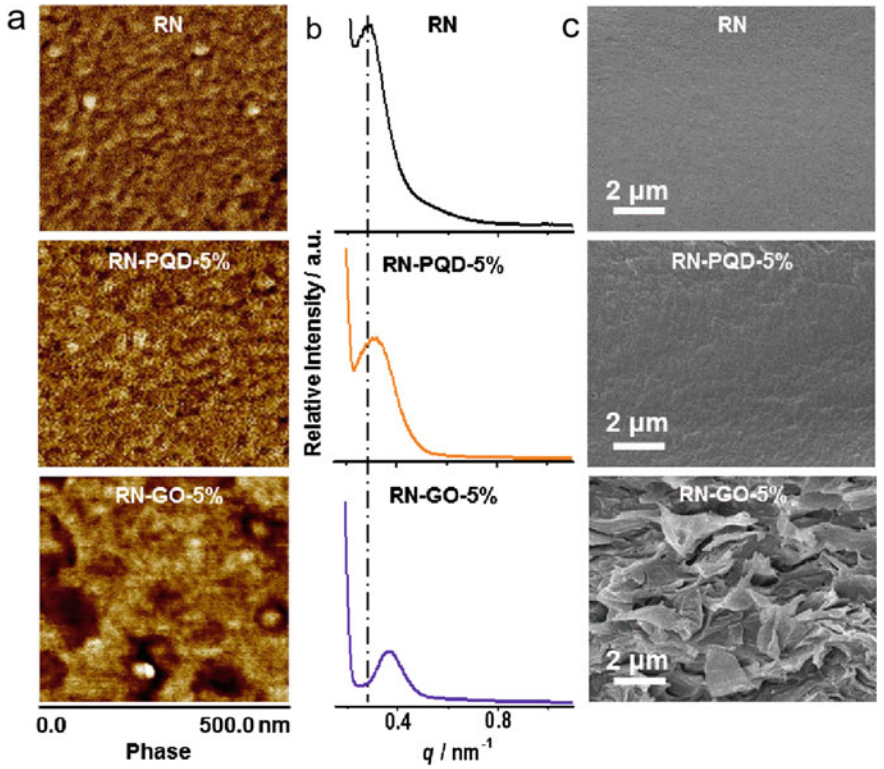

Fig. 4.42 Microstructural characterization of membranes. **a** Tapping-mode AFM phase images of the hydrated membranes. **b** SAXS patterns of the membranes. **c** Cross-sectional SEM images of the membranes. Copyright (2018), John Wiley and Sons [20]

disturb the crystalline structure of backbone domains. The entry of GQD3 makes these generate close influence to the micro-sized GO that breaks the bicontinuous nanophase of Nafion. GQD1 might distribute in both nanophases because of the bi-affinities with side chain and backbone.

The precise distribution of QDs in specific nanophase was validated through DSC measurement, in which the thermal relaxation of backbone nanophase ($T_{g,m}$) and ionic nanophase ($T_{g,c}$) generated two different endothermic peaks [83, 84]. As is shown in Fig. 4.43b, RN gives peaks for $T_{g,m}$ at 154 °C and $T_{g,c}$ at 230 °C. By comparison, RN-PQD-X exhibits a similar $T_{g,m}$, but a significant down-shift of $T_{g,c}$ to 215 °C. This can be attributed to the presence of PQDs that weaken the intrinsic acid–acid interactions in the ionic nanophase of Nafion. In contrast, RN-GQD3-5% displays a significant reduction in $T_{g,m}$ to 133 °C, as a result of the disturbance of GQDs on the backbone nanophase. The synchronous down-shift of $T_{g,m}$ and $T_{g,c}$ for RN-GQD1-5% strongly infers the co-existence of GQD1 in ionic and backbone nanophases. TEM images, Fig. 4.44a–c, illustrate the nanophase separation of these membranes, in which the dark and bright areas correspond to, respectively, the

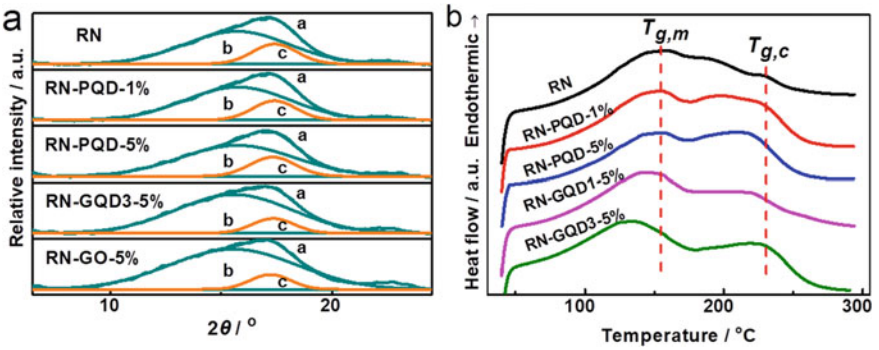

Fig. 4.43 **a** WXRD patterns of the membranes. **b** DSC thermograms of the membranes. Copyright (2018), John Wiley and Sons [20]

ionic and backbone nanophases [15, 77]. RN-PQD-5% shows similar morphology to RN but with deeper, dark domains, inferring impregnation of PQDs in the ionic nanophase. GQD3s appear distinctive difference in the image of RN-GQD3-5%, suggesting these are mainly located in the backbone nanophase. Together, these findings demonstrate that QDs with tailored surface functional groups can be precisely distributed in the specific nanophase.

A possible formation mechanism for molecular-level hybridization was investigated. FTIR spectra of RN, RN-PQD-5%, and RN-GQD3-5% in the forms of casting solution and dry membrane were researched. In DMAC solution (Fig. 4.45a), the –SO_3H groups in Nafion chains give characteristic bands for O–H (2937 dimethylacetamide (cm^{-1}) and O=S=O (1225 and 1058 cm^{-1}). The significant reduction of band intensity for RN-PQD-5% suggests the emergence of strong interactions between –SO_3H and PQDs [85, 86]. This finding confirms that the PQDs have automatically recognized the –SO_3H side chains, and then, they subordinately assemble during DMAC evaporation driven by the side chains into the ionic nanophase (Fig. 4.46c). This hypothesis is validated by the FTIR spectra of dry membranes (Fig. 4.45b).

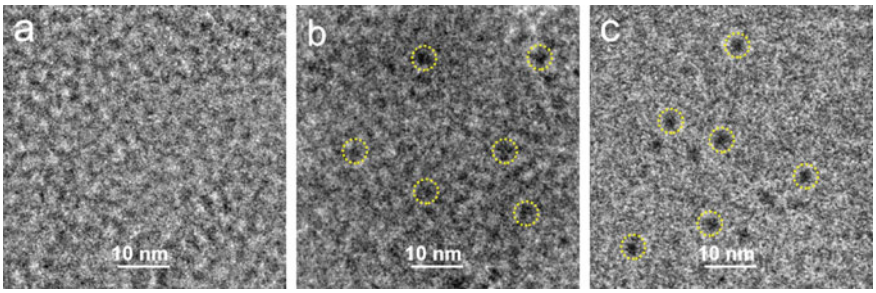

Fig. 4.44 **a–c** TEM images for RN, RN-PQD-5%, and RN-GQD3-5%, respectively. Copyright (2018), John Wiley and Sons [20]

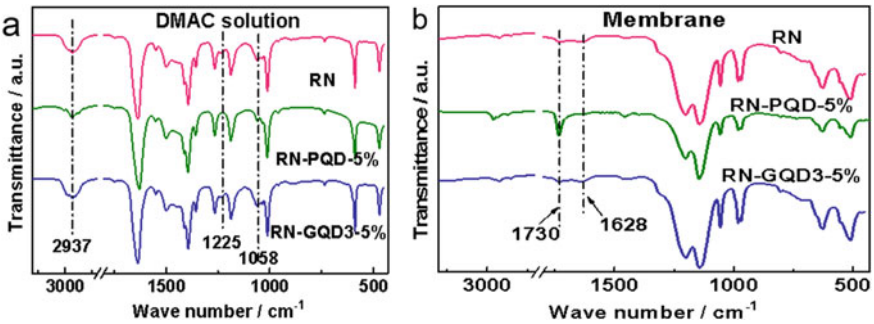

Fig. 4.45 **a**, **b** FTIR spectra of membranes in, respectively, DMAC solution and membrane form. Copyright (2018), John Wiley and Sons [20]

This reveals that the band intensity for S–OH (1628 cm^{-1}) descends, while that for bending vibration of O–H deformation (1730 cm^{-1}) broadens in the spectrum of RN-PQD-5%. This suggests strong intermolecular hydrogen bonding between PQD and $–SO_3H$ groups [87]. While for RN-GQD3-5%, a weak variation in these bands was observed, whether in solution or in the membrane. Accordingly, we propose a "subordinate assembly" based on the result that the QDs form ordered stacking in one specific nanophase, that is, subordinated with the self-assembly of host substrate through selective interactions. Considering the detrimental change in the bicontinuous nanostructure with alteration of assembly environments, this subordinate assembly is shown to be an efficient procedure to realize molecular-level hybridization of nanophase-separated membrane.

The molecular-level hybridization of QDs in Nafion matrix evidently influences membrane macroscopic properties. These features are required for transparent and flame-retardant materials where the crystallinity of specific nanophase needs to be effectively controlled [88, 89]. These results show that molecular-level hybridization with desired filler distribution has potential to independently regulate properties of hierarchical nanostructures.

The selective hybridization of PQD in ionic nanophase gives a hybrid membrane with highly increased proton conduction and fuel cell performance, as is shown in Figs. 4.47 and 4.48. RN gives a conductivity of 147 mS cm^{-1} at 80 °C and 100% RH (Fig. 4.48a). This significant increase is the result of the presence of PQDs in the ionic nanophase, that, on the one hand, increase the water content, and on the other provide additional hydrogen-bond donors (the abundant functional groups). These collectively contribute to well-developed water-mediated hydrogen-bonded transfer networks, where protons can pass through via fast rotation and re-orientation (Grotthuss mechanism). Therefore, the conduction barrier is decreased (E_a 12.4 vs. 14.0 kJ mol^{-1} of RN, Fig. 4.47a) [27]. Confirmation of this hypothesis is provided by the humidity-dependent conductivity performance presented as Fig. 4.48b. As expected, the membranes display a significant increase in proton conductivity as a function of RH. This confirms the importance of the connectivity of ionic nanophases and hydrogen-bond networks on short-range proton migration, which interrupt at low

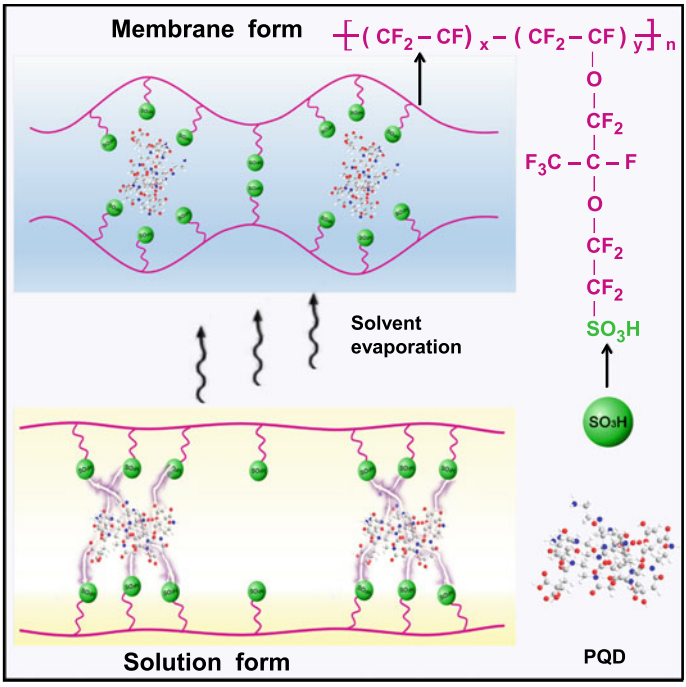

Fig. 4.46 Schematic of subordinate assembly of PQD in casting solution. Copyright (2018), John Wiley and Sons [20]

RH. This underscores a weakened solvent dependence of RN-PQD-5% for proton conduction due to modification by PQD, which provides abundant hydrogen-bond donors and strong water bonding sites (–CO_2H, hydration energy − 8.79 vs. − 5.19 kJ mol^{-1} of –SO_3H) [30]. For RN-GQD3-5%, it gives similar conduction performance to RN but with a slight increase under all testing conditions (Fig. 4.48a and b). These findings result from the fact that GQD3s are located in the backbone nanophase and permit an unaltered microenvironment of the conduction ionic nanophase. They serve only as weak conduction paths (Fig. 4.47b). In contrast, the addition of GO leads to a reduction in conductivity for Nafion, due likely to interruption and isolation of the ionic nanophase.

The hydrogen fuel cell performance was tested under 60 °C and 75% RH. Figure 4.48c reveals that the open-circuit voltage of all the membranes is above 0.9 V highlighting an acceptable gas barrier ability. The maximum current density and power density of RN were 1.05 A cm^{-2} and 255 mW cm^{-2}, respectively. By comparison, RN−PQD−5% showed boosted cell performance with a maximum current density of 1.56 A cm^{-2} and power density of 407 mW cm^{-2}. This increased performance is, in part, from a boosted proton conduction that reduces the electrolyte resistance and also accelerates the cathodic reaction [11].

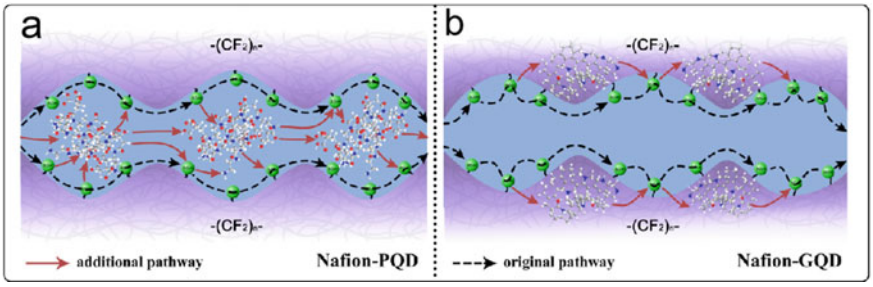

Fig. 4.47 Schematic of proton transfer in RN–PQD–X and RN–GQD–X, respectively. Copyright (2018), John Wiley and Sons [20]

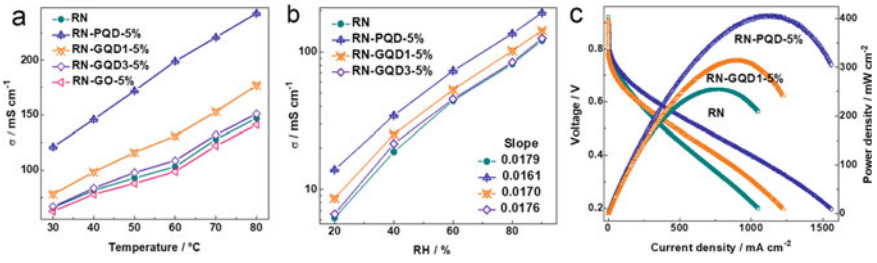

Fig. 4.48 **a** Temperature-dependent proton conductivities of the membranes under 100% RH. **b** Humidity-dependent proton conductivities of the membranes at 80 °C (the slope was obtained by linear fitting of conductivities under different RH). **c** Single cell performance of the membrane with H_2/O_2 operated under 60 °C and 75% RH. The flux rates of H_2 and O_2 are, respectively, 80 and 120 mL min^{-1}. Copyright (2018), John Wiley and Sons [20]

In summary, we have demonstrated that QDs can provide a molecular-level hybridization into ionic or backbone nanophases while maintaining Nafion hierarchical topology. The adjustable chemical affinities, together with the matched structural size, allow the 2 ~ 5 nm QDs to selectively interact with different blocks of Nafion chains in casting solution, then, driving these to subordinate assembly with the self-assembly of Nafion chains. The precise filler distribution, i.e., hydrophilic PQD mainly in the ionic nanophase and hydrophobic GQD3 mainly in the backbone nanophase, brings about efficient regulation of membrane microstructure and performance. In particular, PQDs in the ionic nanophase allow these to act as increased proton conduction sites without losing mechanical stability. This significantly increases the proton conduction and hydrogen fuel cell output power of the Nafion membrane. GQD3s in the backbone nanophase confer strong water uptake and swelling capabilities on the membrane. Molecular-level hybridization therefore holds significant promise to increase process efficiencies and cost savings. Further, our demonstration of molecular-level hybridization by QDs should be applicable universally because QDs can be tailored to bear various functional groups to precisely enter any nanophase of hierarchical nanostructures.

References

1. Z. Jiang, Z. Jiang, Plasma techniques for the fabrication of polymer electrolyte membranes for fuel cells. J. Membr. Sci. **456**, 85–106 (2014)
2. M. Hasani-Sadrabadi, E. Dashtimoghadam, N. Mokarramd, F. Majedi, K. Jacob, Triple-layer proton exchange membranes based on chitosan biopolymer with reduced methanol crossover for high-performance direct methanol fuel cells application. Polymer **53**, 2643–2651 (2012)
3. B. Choi, Y. Huh, Y. Park, D. Jung, W. Hong, Enhanced transport properties in polymer electrolyte composite membranes with GO sheets. Carbon **50**, 5395–5402 (2012)
4. A. Argun, J. Ashcraft, P. Hammond, Highly conductive, methanol resistant polyelectrolyte multilayers. Adv. Mater. **20**, 1539–1543 (2008)
5. B. Vinayan, R. Nagar, N. Rajalakshmi, S. Ramaprabhu, Novel platinum-cobalt alloy nanoparticles dispersed on nitrogen-doped graphene as a cathode electrocatalyst for PEMFC applications. Adv. Func. Mater. **22**, 3519–3526 (2012)
6. Z. Yao, Z. Zhang, L. Wu, T. Xu, Novel sulfonated polyimides proton-exchange membranes via a facile polyacylation approach of imide monomers. J. Membr. Sci. **455**, 1–6 (2014)
7. M. Hickner, H. Ghassemi, Y. Kim, B. Einsla, J. McGrath, Alternative polymer systems for proton exchange membranes (PEMs). Chem. Rev. **104**, 4587–4612 (2004)
8. P. Venkatesan, S. Dharmalingam, Characterization and performance study on chitosan-functionalized multi walled carbon nano tube as separator in microbial fuel cell. J. Membr. Sci. **435**, 92–98 (2013)
9. H. Zhang, C. Ma, J. Wang, X. Wang, H. Bai, J. Liu, Enhancement of proton conductivity of polymer electrolyte membrane enabled by sulfonated nanotubes. Int. J. Hydrogen Energy **39**, 974–986 (2014)
10. H. Liao, K. Zhang, G. Xiao, D. Yan, High performance sulfonated poly(phthalazinone ether phosphine oxide)s for proton exchange membranes. J. Membr. Sci. **447**, 43–49 (2013)
11. K. Mauritz, R. Moore, State of understanding of Nafion. Chem. Rev. **104**, 4535–4586 (2004)
12. N. Nadermann, E. Davis, K. Page, C. Stafford, E. Chan, Using indentation to quantify transport properties of nanophase-segregated polymer thin films. Adv. Mater. **27**, 4924–4930 (2015)
13. K. Kreuer, G. Portale, A critical revision of the nano-morphology of proton conducting ionomers and polyelectrolytes for fuel cell applications. Adv. Func. Mater. **23**, 5390–5397 (2013)
14. C. Park, S. Lee, D. Hwang, D. Shin, D. Cho, K. Lee, T. Kim, M. Lee, D. Kim, C. Doherty, A. Thornton, A. Hill, M. Guiver, Y. Lee, Nanocrack-regulated self-humidifying membranes. Nature **532**, 480–483 (2016)
15. N. Li, C. Wang, S. Lee, C. Park, Y. Lee, M. Guiver, Enhancement of proton transport by nanochannels in comb-shaped copoly(arylene ether sulfone)s. Angew. Chem. Int. Ed. **50**, 9158–9161 (2011)
16. J. Wang, X. Yue, Z. Zhang, Z. Yang, Y. Li, H. Zhang, X. Yang, H. Wu, Z. Jiang, Enhancement of proton conduction at low humidity by incorporating imidazole microcapsules into polymer electrolyte membranes. Adv. Func. Mater. **22**, 4539–4546 (2012)
17. A. Anantaraman, C. Gardner, Studies on ion-exchange membranes. Part 1. Effect of humidity on the conductivity of Nafion. J. Electroanal. Chem. **414**, 115–120 (1996)
18. Y. Li, G. He, S. Wang, S. Yu, F. Pan, H. Wu, Z. Jiang, Recent advances in the fabrication of advanced composite membranes. J. Mater. Chem. A **1**, 10058–10077 (2013)
19. S. Kango, S. Kalia, A. Celli, J. Njuguna, Y. Habibi, R. Kumar, Surface modification of inorganic nanoparticles for development of organic-inorganic nanocomposites—a review. Prog. Polym. Sci. **38**, 1232–1261 (2013)
20. W. Wu, Y. Li, J. Liu, J. Wang, Y. He, K. Davey, S. Qiao, Molecular-level hybridization of Nafion with quantum dots for highly enhanced proton conduction. Adv. Mater. **30**, 1707516 (2018)
21. Y. Kim, K. Ketpang, S. Jaritphun, J. Park, S. Shanmugam, A polyoxometalate coupled GO-Nafion composite membrane for fuel cells operating at low relative humidity. J. Mater. Chem. A **3**, 8148–8155 (2015)

22. Z. Chai, C. Wang, H. Zhang, C. Doherty, B. Ladewig, A. Hill, H. Wang, Nafion-carbon nanocomposite membranes prepared using hydrothermal carbonization for proton-exchange-membrane fuel cells. Adv. Func. Mater. **20**, 4394–4399 (2010)
23. H. Pan, Y. Zhang, H. Pu, Z. Chang, Organic–inorganic hybrid proton exchange membrane based on polyhedral oligomeric silsesquioxanes and sulfonated polyimides containing benzimidazole. J. Power Sources **263**, 195–202 (2014)
24. S. Kango, S. Kalia, A. Celli, J. Njuguna, Y. Habibi, R. Kumar, Surface modification of inorganic nanoparticles for development of organic-inorganic nanocomposites—A review. Prog. Polym. Sci. **38**, 1232–1261 (2013)
25. K. Park, S. Kim, J. Chun, D. Jo, B. Chun, W. Jang, G. Kang, S. Kim, K. Lee, Composite membranes based on a sulfonated poly(arylene ether sulfone) and proton-conducting hybrid silica particles for high temperature PEMFCs. Int. J. Hydrogen Energy **36**, 10891–10900 (2011)
26. D. Marcano, D. Kosynkin, J. Berlin, A. Sinitskii, Z. Sun, A. Slesarev, L. Alemany, W. Lu, J. Tour, Improved synthesis of graphene oxide. ACS Nano **4**, 4806–4814 (2010)
27. J. Wang, H. Zhang, X. Yang, S. Jiang, W. Lv, Z. Jiang, S. Qiao, Enhanced water retention by using polymeric microcapsules to confer high proton conductivity on membranes at low humidity. Adv. Func. Mater. **21**, 971–978 (2011)
28. Y. Liu, J. Wang, H. Zhang, C. Ma, J. Liu, S. Cao, X. Zhang, Enhancement of proton conductivity of chitosan membrane enabled by sulfonated graphene oxide under both hydrated and anhydrous conditions. J. Power Sources **269**, 898–911 (2014)
29. Y. He, J. Wang, H. Zhang, T. Zhang, B. Zhang, S. Cao, J. Liu, Polydopamine-modified graphene oxide nanocomposite membrane for proton exchange membrane fuel cell under anhydrous conditions. J. Mater. Chem. A **2**, 9548–9558 (2014)
30. L. Vilčiauskas, M. Tuckerman, G. Bester, S. Paddison, K. Kreuer, The mechanism of proton conduction in phosphoric acid. Nat. Chem. **4**, 461–466 (2012)
31. S. Peighambardoust, S. Rowshanzamir, M. Amjadi, Review of the proton exchange membranes for fuel cell applications. Int. J. Hydrogen Energy **35**, 9349–9384 (2010)
32. H. Zhang, T. Zhang, J. Wang, F. Pei, Y. He, J. Liu, Enhanced proton conductivity of sulfonated poly(ether ether ketone) membrane embedded by dopamine-modified nanotubes for proton exchange membrane fuel cell. Fuel Cells **13**, 1155–1165 (2013)
33. X. Zhang, Z. Hu, Y. Pu, S. Chen, J. Ling, H. Bi, S. Chen, L. Wang, K. Okamoto, Preparation and properties of novel sulfonated poly(p-phenylene-co-aryl ether ketone)s for polymer electrolyte fuel cell applications. J. Power Sources **216**, 261–268 (2012)
34. M. Kang, M. Lee, Anhydrous solid proton conductors based on perfluorosulfonic ionomer with polymeric solvent for polymer electrolyte fuel cell. Electrochem. Commun. **11**, 457–460 (2009)
35. G. Liu, H. Zhang, X. Yang, Y. Wang, Facile synthesis of silica/polymer hybrid microspheres and hollow polymer microspheres. Polymer **48**, 5896–5904 (2007)
36. L. Li, J. Zhang, Y. Wang, Sulfonated poly(ether ether ketone) membranes for direct methanol fuel cell. J. Membr. Sci. **226**, 159–167 (2003)
37. L. Zhao, Y. Li, H. Zhang, W. Wu, J. Liu, J. Wang, Constructing proton-conductive highways within an ionomer membrane by embedding sulfonated polymer brush modified graphene oxide. J. Power Sources **286**, 445–457 (2015)
38. H. Tang, G. Ehlert, Y. Lin, H. Sodano, Highly efficient synthesis of graphene nanocomposites. Nano Lett. **12**, 84–90 (2012)
39. H. Zarrin, D. Higgins, Y. Jun, Z. Chen, M. Fowler, Functionalized graphene oxide nanocomposite membrane for low humidity and high temperature proton exchange membrane fuel cells. J. Phys. Chem. C **115**, 20774–20781 (2011)
40. A. Mishra, S. Bose, T. Kuila, N. Kim, J. Lee, Silicate-based polymer-nanocomposite membranes for polymer electrolyte membrane fuel cells. Prog. Polym. Sci. **37**, 842–869 (2012)
41. J. Hou, H. Yu, L. Wang, D. Xing, Z. Hou, P. Ming, Z. Shao, B. Yi, Conductivity of aromatic-based proton exchange membranes at subzero temperatures. J. Power Sources **180**, 232–237 (2008)

42. J. Wang, H. Bai, J. Zhang, L. Zhao, P. Chen, Y. Li, J. Liu, Acid-base block copolymer brushes grafted graphene oxide to enhance proton conduction of polymer electrolyte membrane. J. Membr. Sci. **531**, 47–58 (2017)
43. K. Kreuer, Proton conductivity: materials and applications. Chem. Mater. **8**, 610–641 (1996)
44. D. Neugebauer, Two decades of molecular brushes by ATRP. Polymer **72**, 413–421 (2015)
45. H. Zhang, W. Wu, J. Wang, T. Zhang, B. Shi, J. Liu, S. Cao, Enhanced anhydrous proton conductivity of polymer electrolyte membrane enabled by facile ionic liquid-based hoping pathways. J. Membr. Sci. **476**, 136–147 (2015)
46. B. Li, B. Yu, Q. Ye, F. Zhou, Tapping the potential of polymer brushes through synthesis. Acc. Chem. Res. **48**, 229–237 (2015)
47. B. Yameen, A. Kaltbeitzel, A. Langer, F. Müller, U. Gösele, W. Knoll, O. Azzaroni, Highly proton-conducting self-humidifying microchannels generated by copolymer brushes on a scaffold. Angew. Chem. Int. Ed. **48**, 3124–3128 (2009)
48. R. Farina, N. Laugel, P. Pincusc, M. Tirrell, Brushes of strong polyelectrolytes in mixed mono- nd tri-valent ionic media at fixed total ionic strengths. Soft Matter **9**, 10458–10472 (2013)
49. J. Wang, H. Bai, H. Zhang, L. Zhao, H. Chen, Y. Li, Anhydrous proton exchange membrane of sulfonated poly(ether ether ketone) enabled by polydopamine-modified silica nanoparticles. Electrochim. Acta **152**, 443–455 (2015)
50. W. Wu, Y. Li, P. Chen, J. Liu, J. Wang, H. Zhang, Constructing ionic liquid-filled proton transfer channels within nanocomposite membrane by using functionalized graphene oxide. ACS Appl. Mater. Interfaces **8**, 588–599 (2016)
51. M. Schuster, W. Meyer, M. Schuster, K. Kreuer, Toward a new type of anhydrous organic proton conductor based on immobilized imidazole. Chem. Mater. **16**, 329–337 (2004)
52. Z. Li, W. Dai, L. Yu, L. Liu, J. Xi, X. Qiu, L. Chen, Properties investigation of sulfonated poly(ether ether ketone)/polyacrylonitrile acid−base blend membrane for vanadium redox flow battery application. ACS Appl. Mater. Interfaces. **6**, 18885–18893 (2014)
53. G. He, J. Zhao, S. Hu, L. Li, Z. Li, Y. Li, Z. Li, H. Wu, X. Yang, Z. Jiang, Functionalized carbon nanotube via distillation precipitation polymerization and its application in Nafion-based composite membranes. ACS Appl. Mater. Interfaces **6**, 15291–15301 (2014)
54. S. Sekhon, J. Park, J. Baek, S. Yim, T. Yang, C. Kim, Small-angle X-ray scattering study of water free fuel cell membranes containing ionic liquids. Chem. Mater. **22**, 803–812 (2010)
55. A. Sunda, Ammonium-based protic ionic liquid doped Nafion membranes as anhydrous fuel cell electrolytes. J. Mater. Chem. A **3**, 12905–12912 (2015)
56. S. Yi, F. Zhang, W. Li, C. Huang, H. Zhang, M. Pan, Anhydrous elevated-temperature polymer electrolyte membranes based on ionic liquids. J. Membr. Sci. **366**, 349–355 (2011)
57. P. Dimitrova, K. Friedrich, U. Stimming, B. Vogt, Modified Nafion®-based membranes for use in direct methanol fuel cells. Solid State Ionics **150**, 115–122 (2002)
58. L. Jheng, S. Hsu, T. Tsai, W. Chang, Novel symmetric polybenzimidazole membrane for high temperature proton exchange membrane fuel cells. J Mater. Chem. A **2**, 4225–4233 (2014)
59. K. Feng, B. Tang, P. Wu, "Evaporating" graphene oxide sheets (GOSs) for rolled up goss and its applications in proton exchange membrane fuel cell. ACS Appl. Mater. Interfaces **5**, 1481–1488 (2013)
60. A. Mishra, T. Kuila, D. Kim, H. Kim, J. Lee, Protic ionic liquid-functionalized mesoporous silica-based hybrid membranes for proton exchange membrane fuel cells. J. Mater. Chem. **22**, 24366–24372 (2012)
61. H. Zhang, W. Wu, Y. Li, Y. Liu, J. Wang, B. Zhang, J. Liu, Polyelectrolyte microcapsules as ionic liquid reservoirs within ionomer membrane to confer high anhydrous proton conductivity. J. Power Sources **279**, 667–677 (2015)
62. W. Stöber, A. Fink, Controlled growth of monodisperse silica spheres in the micron size range. J. Colloid Interface Sci. **26**, 62–69 (1986)
63. G. He, Y. Li, Z. Li, L. Nie, H. Wu, X. Yang, Y. Zhao, Z. Jiang, Enhancing water retention and low-humidity proton conductivity of sulfonated poly(ether ether ketone) composite membrane enabled by the polymer-microcapsules with controllable hydrophilicity-hydrophobicity. J. Power Sources **248**, 951–961 (2014)

64. G. Li, H. Möhwald, D. Shchukin, Precipitation polymerization for fabrication of complex core-shell hybrid particles and hollow structures. Chem. Soc. Rev. **42**, 3628–3646 (2013)
65. N. Zhang, B. Wang, Y. Zhang, F. Bu, Y. Cui, X. Li, C. Zhao, H. Na, Mechanically reinforced phosphoric acid doped quaternized poly(ether ether ketone) membranes via cross-linking with functionalized graphene oxide. Chem. Commun. **50**, 15381–15384 (2014)
66. J. Song, S. Lee, H. Woo, D. Shin, J. Sohn, Y. Lee, J. Shin, EB-crosslinked SPEEK electrolyte membrane with 1,4-butanediol divinyl ether/triallyl isocyanurate for fuel cell application. J. Membr. Sci. **469**, 209–215 (2014)
67. N. Takimoto, L. Wu, A. Ohira, Y. Takeoka, M. Rikukawa, Hydration behavior of perfluorinated and hydrocarbon-type proton exchange membranes: relationship between morphology and proton conduction. Polymer **50**, 534–540 (2009)
68. B. Yang, A. Manthiram, Comparison of the small angle X-ray scattering study of sulfonated poly(etheretherketone) and Nafion membranes for direct methanol fuel cells. J. Power Sources **153**, 29–35 (2006)
69. J. Wang, S. Jiang, H. Zhang, W. Lv, X. Yang, Z. Jiang, Enhancing proton conduction and methanol barrier performance of sulfonated poly(ether ether ketone) membrane by incorporated polymer carboxylic acid spheres. J. Membr. Sci. **364**, 253–262 (2010)
70. T. Peckham, S. Holdcroft, Structure-morphology-property relationships of non-perfluorinated proton-conducting membranes. Adv. Mater. **22**, 4667–4690 (2010)
71. Y. Li, S. Wang, G. He, H. Wu, F. Pan, Z. Jiang, Facilitated transport of small molecules and ions for energy-efficient membranes. Chem. Soc. Rev. **44**, 103–118 (2015)
72. J. Jalili, S. Borsacchi, V. Tricoli, Proton conducting membranes in fully anhydrous conditions at elevated temperature: effect of nitrilotris (methylenephosphonic acid) incorporation into Nafion and poly(styrenesulfonic acid). J. Membr. Sci. **469**, 162–173 (2014)
73. A. Kusoglu, A. Weber, New insights into perfluorinated sulfonic-acid ionomers. Chem. Rev. **117**, 987–1104 (2017)
74. J. Pan, C. Chen, Y. Li, L. Wang, L. Tan, G. Li, X. Tang, L. Xiao, J. Lu, L. Zhuang, Constructing ionic highway in alkaline polymer electrolytes. Energy Environ. Sci. **7**, 354–362 (2014)
75. T. Norsten, M. Guiver, J. Murphy, T. Astill, T. Navessin, S. Holdcroft, B. Frankamp, V. Rotello, J. Ding, Highly fluorinated comb-shaped copolymers as proton exchange membranes (pems): improving pem properties through rational design. Adv. Func. Mater. **16**, 1814–1820 (2006)
76. Y. Chen, M. Thorn, S. Christensen, C. Versek, A. Poe, R. Hayward, M. Tuominen, S. Thayumanavan, Enhancement of anhydrous proton transport by supramolecular nanochannels in comb polymers. Nat. Chem. **2**, 503–510 (2010)
77. B. Bae, T. Yoda, K. Miyatake, H. Uchida, M. Watanabe, Proton-conductive aromatic ionomers containing highly sulfonated blocks for high-temperature-operable fuel cells. Angew. Chem. Int. Ed. **49**, 317–322 (2010)
78. S. Zhu, Q. Meng, L. Wang, J. Zhang, Y. Song, H. Jin, K. Zhang, H. Sun, H. Wang, B. Yang, Highly photoluminescent carbon dots for multicolor patterning, sensors, and bioimaging. Angew. Chem. Int. Ed. **52**, 3953–3962 (2013)
79. A. Tomalia, A. Naylor, W. Goddard III., Starburst dendrimers: molecular-level control of size, shape, surface chemistry, topology, and flexibility from atoms to macroscopic matter. Angew. Chem. Int. Ed. **29**, 138–145 (1990)
80. M. L. Einsla, Y. S. Kim, M. Hawley, H. S. Lee, J. E. McGrath, B. Liu, M. D. Guiver, B. S. Pivovar, Toward improved conductivity of sulfonated aromatic proton exchange membranes at low relative humidity. Chem. Mater. **20**, 5636 (2008)
81. G. Choi, J. Hong, Y. Park, D. Jung, W. Hong, P. Hammond, H. Park, Innovative polymer nanocomposite electrolytes: nanoscale manipulation of ion channels by functionalized graphenes. ACS Nano **5**, 5167–5174 (2011)
82. P. Antonucci, A. Aricò, P. Cretì, E. Ramunni, V. Antonucci, Investigation of a direct methanol fuel cell based on a composite Nafion®-silica electrolyte for high temperature operation. Solid State Ionics **125**, 431–437 (1999)
83. R. Moore, C. Martin, Chemical and morphological properties of solution-cast perfluorosulfonate ionomers. Macromolecules **21**, 1334–1340 (1988)

84. T. Kyu, M. Hashiyama, A. Eisenberg, Dynamic mechanical studies of partially ionized and neutralized Nafion polymers. Can. J. Chem. **61**, 680–687 (1983)
85. S. Gahlot, P.P. Sharma, V. Kulshrestha, P.K. Jha, SGO/SPES-Based Highly conducting polymer electrolyte membranes for fuel cell application. ACS Appl. Mater. Interfaces. **6**, 5595–5601 (2014)
86. H. Beydaghi, M. Javanbakht, E. Kowsari, Synthesis and characterization of poly(vinyl alcohol)/sulfonated graphene oxide nanocomposite membranes for use in proton exchange membrane fuel cells (PEMFCs). Ind. Eng. Chem. Res. **53**, 16621–16632 (2014)
87. R. Kumar, C. Xu, K. Scott, Graphite oxide/Nafion composite membranes for polymer electrolyte fuel cells. RSC Adv. **2**, 8777–8878 (2012)
88. Z. Zhang, C. Bao, W. Yao, S. Ma, L. Zhang, S. Hou, Influence of deposition temperature on the crystallinity of Al-doped ZnO thin films at glass substrates prepared by RF magnetron sputtering method. Superlattices Microstruct. **49**, 644–653 (2011)
89. D. Lee, H. Yang, S. Park, W. Kim, Nafion/Graphene oxide composite membranes for low humidifying polymer electrolyte membrane fuel cell. J. Membr. Sci. **452**, 20–28 (2014)

Chapter 5
Lamellar and Nanofiber-Based Proton Exchange Membranes for Hydrogen Fuel Cell

Jianlong Lin, Wenjia Wu, and Jingtao Wang

5.1 Introduction

Hydrogen fuel cell, as a typical chemical-to-electrical energy conversion device, has been used in a series of applications, such as power plant, aviation, and automobile [1–4]. As the core component, the performance of PEM determines the hydrogen fuel cell efficiency. According to the proton transfer mechanism of PEM, the formation of continuous proton conduction pathways is vital to increase membrane proton conductivity [5]. However, an inherent problem for traditional polymer membranes is that, due to the complex chain structure and weak interaction, the channel structure is often unsatisfactory in connectivity and stability, especially under harsh environment, such as high temperature and low humidity [6, 7]. Incorporating nanofiller to prepare hybrid or composite membrane is considered as a facile approach to interconnect the intrinsic deadends of polymer electrolyte and construct additional pathways along filler surface, and related researches have been introduced in Chap. 4. However, the common fillers are nanoparticles, nanotubes, nanorods, or nanosheets, which tend to aggregate at high loading contents, thus limiting their efficiency in constructing continuous pathways. Therefore, it is highly desired to exploit advanced strategies to overcome above problems.

Recently, lamellar membrane and nanofiber composite membrane (NFCMs) have showed great potential for utilization as advanced PEMs [6–9]. Lamellar membrane with regular and ordered layered structure is anticipated to confer well-defined and

J. Lin · W. Wu · J. Wang (✉)
School of Chemical Engineering, Zhengzhou University, Zhengzhou 450001, P. R. China
e-mail: jingtaowang@zzu.edu.cn

W. Wu
e-mail: wenjiawu@zzu.edu.cn

J. Wang
Henan Institute of Advanced Technology, Zhengzhou University, Zhengzhou 450003, P. R. China

J. Wang and W. Wu (eds.), *Functional Membranes for High Efficiency Molecule and Ion Transport*, https://doi.org/10.1007/978-981-19-8155-5_5

stable proton transfer channels. Particularly, GO membrane with ample oxygen-containing groups (−OH, $-CO_2H$) has demonstrated the potential for fast proton migration [6]. He et al. fabricated a nacre-inspired GO lamellar membrane and realized a high in-plane conductivity of 222 mS cm^{-1} at 30 °C, 2.9 times of that of Nafion [7]. For NFCM, the large surface area of nanofiber together with the enriched functional groups at nanofiber-matrix interface could act as long-range proton transfer pathways, imparting NFCM high in-plane proton conductivity [8, 9]. Compared with the conventional homogeneous membrane, the interfacial transfer pathways are more stable, which impart NFCM high conductivity even under low RH. However, these lamellar membranes and NFCMs suffer from an inherent drawback of transfer anisotropy, because of the oriented geometric arrangement [10, 11]. However, the fuel cell performances are mainly determined by vertical conduction, i.e., proton transfer from anode to cathode of fuel cell. This greatly limits their practical application in hydrogen fuel cell. In this chapter, some important advances in lamellar and nanofiber-based PEMs are introduced, including lamellar GO-bacterial cellulose membrane, lamellar GO-quantum dot membrane, nanofiber composite membrane, quantum dot incorporated nanofiber composite membrane, and porous nanofiber composite membrane. The microstructure and physicochemical property of these composite membranes are investigated in detail, and the performances are evaluated in terms of proton conduction, structural stability, and application in hydrogen fuel cell.

5.2 Lamellar GO-Bacterial Cellulose Membrane

Here, phosphorylated bacterial cellulose (PBC_4) was fabricated as follows: 2.0 g bacterial cellulose (BC) powder was dispersed in 100 mL DMF with 40 g urea and stirred for 1 h. Afterward, 20.0 g phosphoric acid was incorporated dropwise. The mixture was then placed in a 130 °C oil bath for phosphorylation. After cooling, the mixture was purified with in turn a mixture of water and 1-propanol, 0.1 mol L^{-1} hydrochloric acid, and water. Finally, the product was obtained through lyophilization and ball-milling. Graphite powder was oxidized to synthesize GO based on the Hummers' method [12]. DGO nanosheet was fabricated based on the strategy in literature [13].

The DGO@PBC_4 composite membrane was prepared as follows: for fabricating stable PBC_4 dispersion, 0.5 g PBC_4 was dispersed in 500 mL water/formamide solution (1:4 v/v) under ultrasonic at 300 W for 2 h. Next, 25 mL DGO dispersion (1 mg mL^{-1}) was mixed with 2 mL PBC_4 dispersion (1 mg mL^{-1}) and then ultrasonicated for 30 min. The DGO@PBC_4 was then obtained by filtrating the mixture and drying for 24 h at 35 °C. Using the above method, DGO@PBC_4-X, ($X = 1$, 2, 3, and 4) denoted the weight percentage of PBC_4.

DGO nanosheet was fabricated by self-polymerization of dopamine on GO surface. GO displays a typical sheet structure with the average lateral size of ~3 μm and the thickness of ~0.89 nm. In comparison with DGO, adhesion of PBC_4 brings

two new characteristic peaks at 1204 and 973 cm^{-1}, related to the P=O and P−OH groups [14, 15], while the peak intensity corresponding to $-NH_2/-NH-$ groups (1607 cm^{-1}) weakens obviously for DGO@PBC_4-1 and DGO@PBC_4-3 [16] indicating the formation of electrostatic interaction between PBC_4 and DGO nanosheets. This is beneficial to the construction of layer-by-layer structural lamellar composite membrane (Fig. 5.1).

Cross-sectional SEM image in Fig. 5.2a exhibits that DGO membrane displays a compact lamellar structure. In comparison, the cross-section of DGO@PBC_n-3 maintains the lamellar structure (Fig. 5.2b). Surficial SEM images reveal that the surface of DGO@PBC_4-3 becomes rough, and obvious fibrous structure could be observed (Fig. 5.2b). In atomic force microscopy (AFM) image (Fig. 5.2c, d), obvious fibrous structures are detected on the surface of DGO@PBC_n-3.

Figure 5.3a reveals that the binding energy for pyrrolic N atoms increases from 400.5 eV for DGO to 400.7 and 401.5 eV for DGO@PBC_4-1 and DGO@PBC_4-3, respectively. This energy shift implies the electron distribution change and the generation of acid–base interaction. These findings hint the formation of layer-by-layer structure with anchored acid–base pairs in these lamellar composite membrane. On the basis of the peak area ratios, the P content in DGO@PBC_4-1 and DGO@PBC_4-3 is computed to be 1.6 and 8.6 wt%, respectively, corresponding to the $-P=O(OH)_2$ group content of 4.2 and 22.5 wt% (Fig. 5.3b). The intercalation of PBC_n with high surface area and ample $-P=O(OH)_2$ groups would impart DGO@PBC_n-*X* continuous proton transfer paths and enhanced interlayer interactions.

The strong acid–base interaction between PBC_n and DGO nanosheet then endows DGO@PBC_n-*X* with highly enhanced water stability. Figure 5.3c reveals that, the GO membrane breaks into small fragments after immersing in water for 14 d, while DGO@PBC_4-3 maintains the original structure. After harsh stirring at speed of 500 r min^{-1} for 5 min, DGO@PBC_4-3 still maintains original structure. This phenomenon should be ascribed to the strong acid–base interaction between PBC_4 and DGO nanosheet, which effectively prevents the nanosheets from exfoliating from each other. This speculation is testified by XRD result (Fig. 5.3d). In comparison with the obviously increased *d*-spacing of GO membrane (from 0.75 nm at dry condition to 1.56 nm at wet condition), DGO membrane shows a smaller *d*-spacing increase from 0.86 nm to 1.51 nm, because of the surface adhesion character of polydopamine. Similarly, DGO@PBC_4-1 also shows an augment in *d*-spacing from 1.34

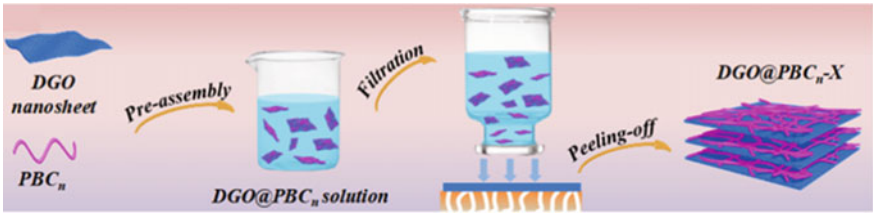

Fig. 5.1 Schematic illustration of the preparation of DGO@PBC_n-*X*. Copyright (2020), Elsevier [93]

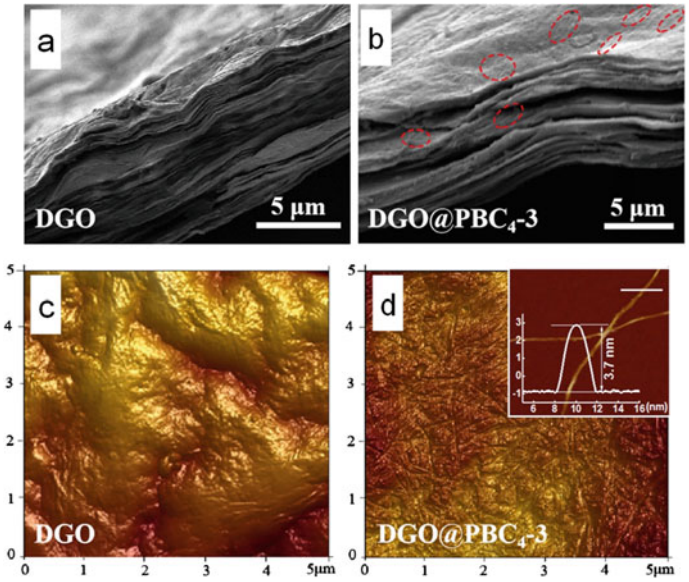

Fig. 5.2 Cross-sectional SEM images of **a** DGO and **b** DGO@PBC_4-3. AFM images of **c** DGO and **d** DGO@PBC_4-3. Copyright (2020), Elsevier [93]

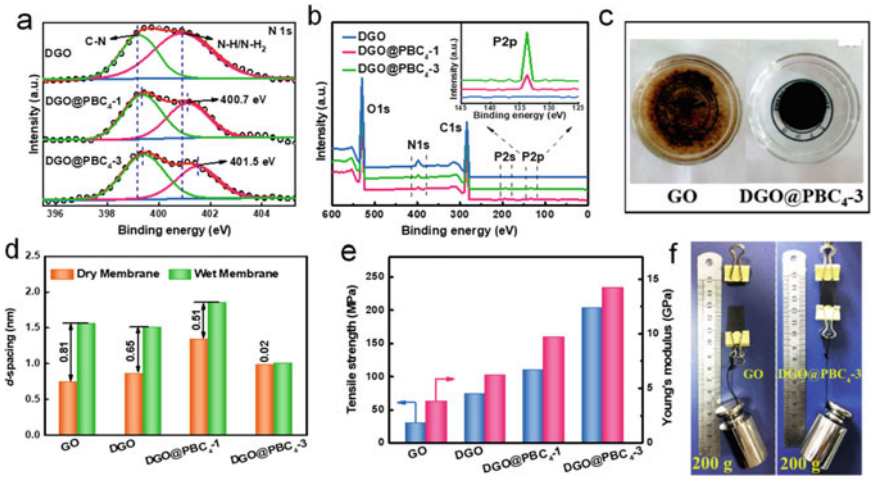

Fig. 5.3 **a** High-resolution XPS N 1 s spectra of as-prepared membranes. **b** Full-scan XPS spectra of as-prepared membranes (insert: amplification of P 2*p* peak). **c** Photograph of GO and DGO@PBC_4-3 after immersing in water for 14 *d* and stirring at speed of 500 r min^{-1} for 5 min. **d** *d*-spacing of as-prepared membranes at dry and wet conditions (the values are computed with XRD results). **e** Mechanical property of as-prepared membranes. **f** Comparison of mechanical strength of GO and DGO@PBC_4-3. Copyright (2020), Elsevier [93]

to 1.85 nm, while the increased value is less than DGO membrane (0.65 nm), and especially, the *d*-spacing of DGO@PBC_4-3 increases by only 0.02 nm. These further verify the effect of acid–base interaction on improving water stability. The mechanical property in Fig. 5.3e exhibits that GO membrane displays a tensile strength of 30.1 MPa and an elastic modulus of 3.8 GPa. In comparison, the tensile strength and elastic modulus of DGO membrane elevate to 73.4 MPa and 6.2 GPa, respectively, while the formation of strong acid–base interaction confers DGO@PBC_4-*X* obviously enhanced mechanical property, and the mechanical property improves with PBC_4 content. The tensile strength and elastic modulus of DGO@PBC_4-3 reach up to 203.5 MPa and 14.2 GPa, respectively, which are ~5.8 and ~2.7 times higher than that of GO membrane. Macroscopically, DGO@PBC_4-3 with thickness of 21 μm and width of 13 mm is robust enough to hold up 200 g mass (Fig. 5.3f).

The ample acid–base pairs at fiber-nanosheet interface then act as rapid transfer pathways, conferring lamellar composite membrane significantly improved proton conduction property. Figure 5.4a exhibits that the in-plane conductivity of all membranes increases with the elevating of temperature (30–90 °C). GO and DGO membranes show in-plane conductivity of 62.4 and 72.2 mS cm^{-1} at 90 °C and 100% RH, respectively. In comparison, the in-plane proton conductivity of DGO@PBC_4-1 elevates to 129.2 mS cm^{-1}. Meanwhile, the in-plane proton conductivity elevates with PBC_4 content. Especially, the in-plane proton conductivity of DGO@PBC_4-3 reaches up to 215.2 mS cm^{-1}, ~3.5 times of that of GO membrane. Such obvious conductivity enhancement should originate from the generated acid–base pairs at fiber-nanosheet interface, which act as low-energy barrier proton transfer pathways [17, 18]. All membranes exhibit reduced conductivity under D_2O vapor (vs. H_2O vapor), because of the involvement of heavier deuterium atom (vs. proton) through Grotthuss-type transport [19]. In comparison, DGO@PBC_4-3 displays a more obvious conductivity reduction of 61.2% under D_2O vapor, as compared with 34.4% and 39.9% for GO and DGO membrane, respectively (Fig. 5.4b). This phenomenon indicates that the formed acid–base pairs along nanochannel enable more proportion of Grotthuss-type transport in DGO@PBC_4-3 membrane. Next, the through-plane proton conductivity of membrane, which determines the fuel cell performance, was evaluated at different temperatures (Fig. 5.4c). The through-plane proton conductivity of GO and DGO membrane is 4.03 and 6.60 mS cm^{-1} under 90 °C and 100% RH, respectively. By comparison, DGO@PBC_4-3 obtains ~10 times' improvement of through-plane conductivity as compared with GO membrane, reaching up to 43.9 mS cm^{-1}. Notably, the conductivity improvement in vertical direction is more obvious than that in parallel direction (a 2.4-fold).

The membrane was then assembled into MEA for evaluating the hydrogen fuel cell performance. The open-circuit voltage of all membranes is above 0.9 V, indicating a satisfactory gas barrier property (Fig. 5.5a) [20]. GO membrane acquires the maximum power density and current density of 79.9 mW cm^{-1} and 305.3 mA cm^{-1}, respectively. By comparison, DGO membrane exhibits improved maximum power density of 109.7 mW cm^{-1} and current density of 394.4 mA cm^{-1}, due to the enhanced conductivity. Furthermore, the constructed acid–base pairs in interlayer give DGO@PBC significantly promoted fuel cell performances. For example,

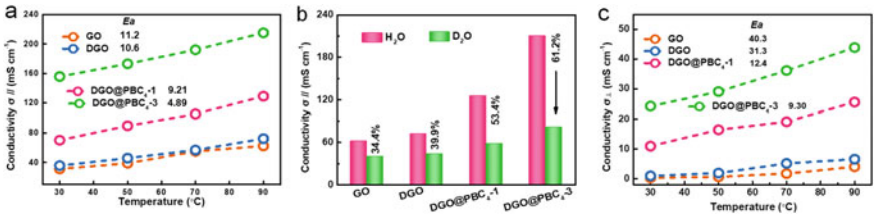

Fig. 5.4 **a** Temperature-dependent in-plane proton conductivity ($\sigma_{\parallel}$) at 100% RH. **b** Temperature-dependent through-plane proton conductivity ($\sigma_{\perp}$) at 100% RH. **c** Weight loss and through-plane proton conductivity of DGO@PBC_4-3 in 30 °C water over time. Copyright (2020), Elsevier [93]

DGO@PBC_4-3 obtains the maximum power density of 182.9 mW cm^{-1} and current density of 674.8 mA cm^{-1}, 128.9% and 121.0% higher than those of GO membrane. The stability of MEA assembled with GO and DGO@PBC_4-3 membrane was measured at a current of 30 mA cm^{-1} for 24 h. As displayed in Fig. 5.5b, the voltage of fuel cell assembled with GO membrane decreases by ~4.2%, originating from the structure deformation under operating condition [21]. In comparison, the excellent structure stability imparts the MEA assembled with DGO@PBC_4-3 almost no voltage loss, which holds great potential for practical application.

Accordingly, we have demonstrated a joint improvement of proton conductivity and water stability of GO-based lamellar membranes, by constructing layer-by-layer structured lamellar composite membrane wtih PBC and DGO nanosheet. The formed acid–base pairs between PBC and DGO nanosheets work as low-energy barrier proton transfer paths. DGO@PBC attains an in-plane proton conductivity of 215.2 mS cm^{-1}, 244.9% higher than that of GO membrane. Moreover, it obtains more obvious enhancement in through-plane proton conductivity by almost 9 times higher than that of GO membrane. Consequently, the transfer anisotropy coefficient obviously reduces, and the hydrogen fuel cell performance increases by over 120%. Moreover, the acid–base pairs efficiently improve the interactions between adjacent

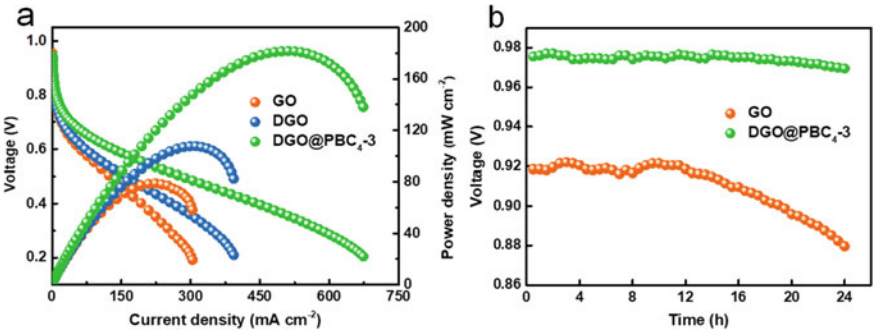

Fig. 5.5 **a** Single-cell performance of as-prepared membranes at 60 °C and 100% RH. **b** Stability of MEA at 30 mA cm^{-1} for 24 h. Copyright (2020), Elsevier [93]

GO nanosheets, enabling the lamellar composite membrane almost no breakdown or delamination in water, acid, and basic solutions even after 14 *d*. Furthermore, the lamellar composite membrane acquires high tensile strength of 203.5 MPa. The constructed layer-by-layer structure with strong interlayer interaction may pave a way to designing high-performance lamellar membranes.

5.3 Lamellar GO-Quantum Dot Membrane

GO nanosheet was fabricated by the improved Hummers' method [12]. DGO nanosheet was fabricated through dopamine self-polymerization on the surface of GO nanosheet. Concretely, GO powder (5.0 g) was added into 100 mL dopamine hydrochloride solution (2 g L^{-1}) and stirred for 4 h. The pH value was controlled to 8.5 with HCl and Tris. Then, DGO powder was attained by repeated centrifugation and wash and then freeze-drying for 48 h [22]. Two kinds of QD (PQD and C-PQD) were synthesized through microwave-assisted polycondensation [23]. Specifically, 0.96 g CA, 540 μL DETA, and 2.0 g water were mixed by ultrasonic treatment for 5 min, and then put in microwave oven at 750 W for 5 min. Afterward, the product was fully washed with ethanol and freeze-dried for 48 h to obtain PQD powder. C-PQD was fabricated via the same method but with the glycerol (0.5 g) and water (1.5 g) mix solution instead of water as solvent.

GO and DGO membranes were prepared by vacuum-filtrating the GO or DGO solution (35 mL, 1 g L^{-1}) with Millipore membrane as support. For SDF membrane, the QD precursors (CA and DETA) were firstly intercalated in the interlayer of DGO membrane by vacuum filtration for 20 min. The optimal concentration of precursor solution was about 0.016 mol L^{-1}, since low precursor concentration resulted in the failure of growing enough PQD, while high precursor concentration would hamper the solution entrance into the interlayer because of the high viscosity. Then, the membrane was immersed in water and heated with a microwave oven at 750 W for 30 s, where the polycondensation reaction occurred to form SDF structure. Two kinds of SDF membrane with different PQD contents were fabricated and named as SDF-1 and SDF-4. For comparison, 45 μL DETA and 0.08 g CA were dispersed in 6.25 g glycerol and 18.75 g water to prepare SDF-C membrane with part of functional groups carbonized. Ultimately, all membranes were dried in vacuum oven for 24 h and peeled off from Millipore membrane to obtain free-standing membrane.

Here, SDF membrane was fabricated through in-situ growth of PQD on $-NH_2$/$-NH-$ groups of DGO nanosheet with CA and DETA as precursors, as shown in Fig. 5.6. DGO nanosheet was fabricated through dopamine self-polymerization on the surface of GO nanosheet. Then, DGO nanosheets were assembled into DGO membrane via vacuum filtration. The precursors (CA and DETA) were then evenly intercalated into the interlayer spacing of DGO membrane via fine-tuning vacuum filtration pressure, followed by microwave-assisted polycondensation for obtaining SDF membrane. For this method, the control of precursor concentration could effectively regulate PQD content, and two types of SDF membrane with different PQD

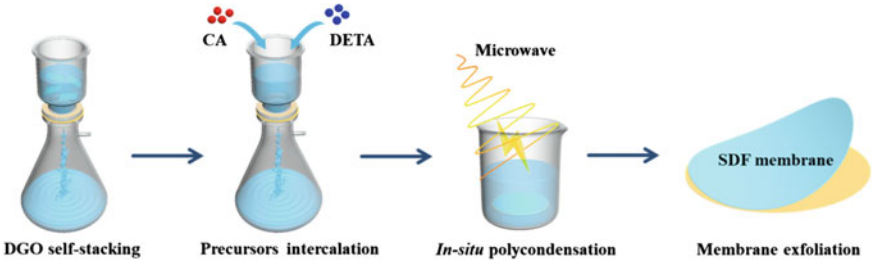

Fig. 5.6 Schematic preparation of SDF membrane. Copyright (2020), Royal Society of Chemistry [94]

content were prepared and named as SDF-1 and SDF-4. SDF-4 membrane was chosen as a representative due to the high PQD content. GO and DGO pristine membranes were also prepared for comparison.

Cross-sectional TEM image in Fig. 5.7a reveals that DGO membrane possesses compact lamellar structure with regular interlayer spacing. By comparison, SDF-4 membrane shows looser lamellar structure with half-full interlayer spacing (Fig. 5.7b). This indicates the presence of PQD in interlayer spacing, which can be directly testified by the obvious left shift of (002) peak in XRD pattern (Fig. 5.7c). With the augment of PQD content, the peak position varies from $2\theta = 10.01°$ to 7.02°, related to the *d*-spacing changes from 0.88 nm for DGO membrane to 1.26 nm for SDF-4 membrane.

Then, violent mechanical pulverization and ultrasonic treatment were conducted for SDF-4 membrane for obtaining SDF-4 nanosheet, which was then used to detect the distribution and size of formed PQDs. TEM image in Fig. 5.8a shows that ample and uniformly distributed dark domains (outlined in yellow) appear on SDF-4 nanosheet as compared with DGO nanosheet, implying the uniform growth of PQD in the interlayer spacing of SDF-4 membrane. High-resolution TEM image with obvious lattice in Fig. 5.8b reveals that the lateral size of PQD is 2–5 nm. AFM image in Fig. 5.8c reveals that the height of PQD is 1–2 nm. Note that, compared

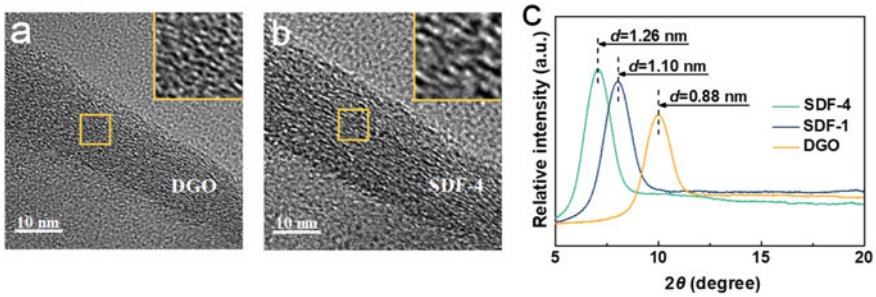

Fig. 5.7 Cross-sectional TEM image of **a** DGO and **b** SDF-4 membranes. **c** XRD pattern of as-prepared membranes. Copyright (2020), Royal Society of Chemistry [94]

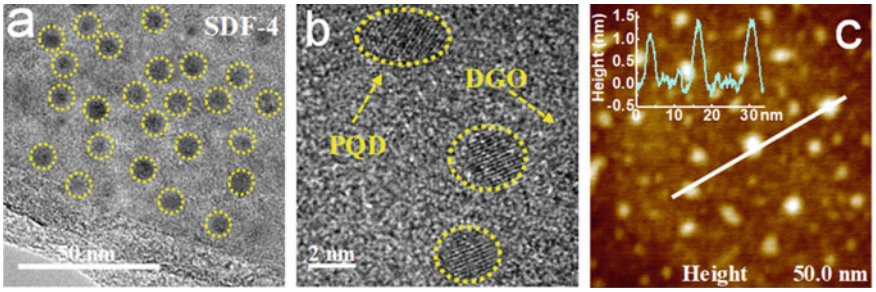

Fig. 5.8 **a** TEM image, **b** high-resolution TEM image, and **c** AFM image of SDF-4 nanosheet. Copyright (2020), Royal Society of Chemistry [94]

with PQD grown in open space, PQD grown in SDF membrane displays decreased size but more regular structure, probably resulting from that the confined effect of nanoscale interlayer spacing which influences the growth of PQD.

Also important is elucidating the binding form between PQD and DGO nanosheet in SDF membrane. The carboxyl groups in CA could react with amino groups on DGO nanosheet into amide bond during PQD growth. Therefore, PQD could act as nanocross-linkers and assist the construction of framework structure. Figure 5.9a displays that, a new peak at 288.5 eV corresponding to N−C=O is found for SDF-4 membrane when compared with DGO membrane [24], indicating the reaction between carboxyl groups in CA, and amino groups in DGO nanosheet and DETA. These demonstrate that the framework structure forms via covalent cross-linking by PQD (Fig. 5.9b), similar to COF.

The cross-linked framework structure then imparts SDF membrane outstanding structure stability (Fig. 5.10). SDF membrane could maintain their structure integrity after ultrasonic for 4 h, while DGO membrane breaks up completely (Fig. 5.10a). XRD patterns in Fig. 5.10b exhibit that DGO membrane acquires a sharp *d*-spacing

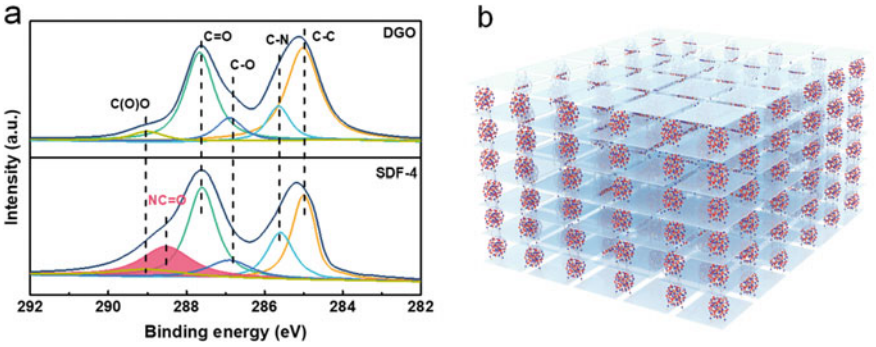

Fig. 5.9 **a** XPS C 1 s spectra of DGO and SDF-4 membrane. **b** Schematic structure of SDF membrane. Copyright (2020), Royal Society of Chemistry [94]

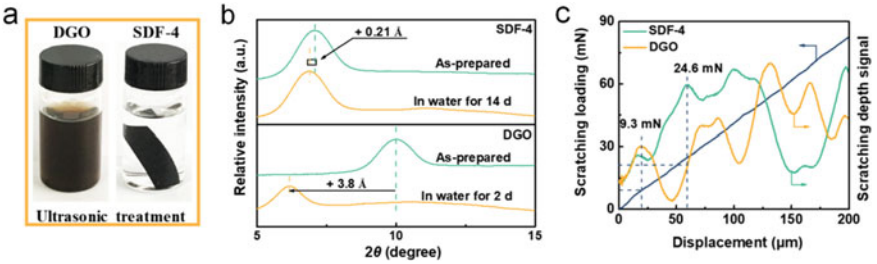

Fig. 5.10 **a** Stability testing result of DGO and SDF-4 membrane after ultrasonic for 4 h. **b** XRD patterns of DGO and SDF-4 membrane in dry and wet state. **c** Nanoscratch result of DGO and SDF-4 membrane. Copyright (2020), Royal Society of Chemistry [94]

increase of 3.8 Å after immersing in water for 2 *d*. In comparison, only 0.2 Å increase is detected for SDF-4 membrane after immersing in water for 14 *d* (Fig. 5.10b). In order to quantify the interlayer force, nanoscratch was utilized through recording dynamic loading with scratch distance (Fig. 5.10c) [25]. It is found that SDF-4 membrane displays a critical loading of 24.6 mN, ~1.6 times higher than that of DGO membrane (9.3 mN). This performance is superior to most GO-based membranes, highlighting the unique advantage of SDF membrane.

Proton conductivity, a vital parameter determining fuel cell performance, of SDF membrane was measured and displayed in Fig. 5.11. Similar to the reported GO-based lamellar membranes [6, 26], GO and DGO membranes show low vertical conductivity of 1.6 and 4.9 mS cm^{-1} at 80 °C and 100% RH, respectively, due to the lack of cross-layer transfer path (Fig. 5.11a). In comparison, SDF membrane attains highly enhanced conductivity, reaching up to 54.6 mS cm^{-1}, which is ~10 times higher than that of DGO membrane and close to Nafion membrane. Such obvious enhancement possibly originates from the regular SDF structure, where conductive PQD bridges the adjacent DGO nanosheets. Meanwhile, the ample hydrophilic groups (i.e., $–NH_2$, $–CO_2H$, and –OH) in PQD confer well-developed water-mediated hydrogen-bonded transfer networks, where proton could go through via fast rotation and reorientation (Grotthuss mechanism). In this way, similar to other frameworks, regular, continuous, and efficient transfer paths are constructed in the whole membrane. These paths could effectively transfer proton and reduce the energy barrier for cross-layer transport. This could be testified by the 50% reduction of E_a from 0.154 eV for DGO membrane to 0.075 eV for SDF-4 membrane. For this framework structure, PQD uses the conductive groups as bridge to prompt the cross-layer transfer. Therefore, the proton conduction ability of membrane should be influenced by the number of conductive groups on PQD. To verify this speculation, a referenced SDF-C membrane was fabricated, in which part of the conductive groups in PQD was carbonized through the incorporation of small amount of glycerol in the reaction solvent (i.e., water) to elevate the polycondensation temperature. In comparsion with SDF-4 membrane, SDF-C membrane displays 74% reduction in proton conductivity and 50% increase in E_a (Fig. 5.11b). The reduction in proton conductivity for SDF-C membrane should

be ascribed to the carbonization and therefore the decreased number of conductive groups on PQD. This further highlights the unique advantage of SDF membrane.

The SDF membrane also displays other PQD-dependent proton conduction property. Since the proton conduction ability of PQD stems from the hydrophilic groups ($-CO_2H$, $-NH_2$, $-OH$), the proton conductivity of SDF membrane shows obvious dependence on water (Fig. 5.11c). All the membranes display gradual augment of proton conductivity with testing RH, especially SDF-4 membrane obtains much larger slope (0.37) than DGO membrane (0.023). These indicate that PQD endows membrane with stronger water absorption capacity. Besides, the PQD content also obviously affects proton transport efficiency. With PQD content increases, the proton conductivity elevates from 36.8 to 54.6 mS cm^{-1} for SDF-1 membrane and SDF-4 membrane at 80 °C and 100% RH, respectively. Then, the horizontal conductivity of as-prepared membranes was tested to evaluate the transfer anisotropy. Similar to most reported lamellar membranes [27], DGO membrane displays severe transfer anisotropy with anisotropy coefficient (defined as $\sigma_{\parallel}/\sigma_{\perp}$) of 17.3 (Fig. 5.11d). For

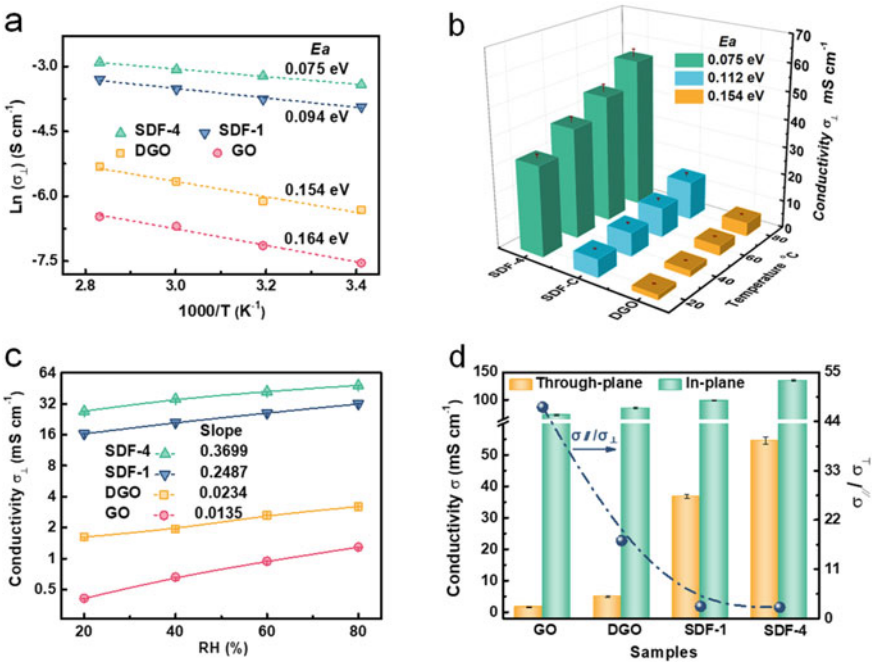

Fig. 5.11 **a** Arrhenius plot of vertical conductivity at 100% RH. **b** Temperature-dependent vertical conductivity of as-prepared membranes at 100% RH. **c** Humidity-dependent vertical conductivity at 80 °C (the slope was attained by linear-fitting conductivity with RH). **d** Transfer anisotropy coefficient ($\sigma_{\parallel}/\sigma_{\perp}$) of as-prepared membranes at 80 °C and 100% RH. Copyright (2020), Royal Society of Chemistry [94]

SDF membrane, the presence of interlayer conductive groups also elevates the horizontal conductivity and decreases the E_a value for horizontal conduction. Nevertheless, the augment is less obvious than that in vertical direction. Therefore, the transfer anisotropy coefficient of SDF membrane is sharply reduced. SDF-4 membrane acquires a low transfer anisotropy coefficient of 2.5, much lower than most reported lamellar membranes.

Finally, the as-prepared membrane was assembled into MEA for evaluating the hydrogen fuel cell performance. Figure 5.12a reveals that the open-circuit voltage of all membranes is above 0.9 V, suggesting an acceptable gas barrier property. Similar to reported lamellar membranes [28], DGO membrane shows inferior fuel cell performances with maximum current density and power density of 180 mA cm^{-1} and 51 mW cm^{-1}, respectively. In comparison, SDF membrane achieves significant improvement in fuel cell performance. Particularly, SDF-4 membrane acquires the maximum current density of 570 mA cm^{-1} and power density of 157 mW cm^{-1}, 216% and 208% higher than those of DGO membrane, respectively. This enhancement should result from the high vertical conductivity of SDF membrane, which enables fast chemical-to-energy conversion. Likewise, SDF-4 membrane exhibits better device performance than SDF-1 membrane. Furthermore, the robust structure stability imparts outstanding durability for SDF-based MEA in single cell (Fig. 5.12b). After 12 h stability testing at 40 mA cm^{-1}, SDF-4 membrane displays almost no change in voltage (~0.94 V), while the voltage for DGO membrane assembled MEA decreases from 0.90 V to 0.85 V.

In conclusion, we have demonstrated the design and fabrication of a SDF membrane wtih DGO nanosheet and PQD as building blocks, through an in situ microwave-assisted polycondensation method for the first time. DGO nanosheets assemble into highly regular lamellar structure, in which PQDs evenly cross-link the adjacent DGO nanosheets in the interlayer spacing. In this way, the PQDs act as bridges for efficient cross-layer proton conduction. As a result, the novel SDF membrane attains significantly enhanced vertical proton conductivity and fuel cell performance. Specifically, SDF-4 membrane provides a vertical conductivity

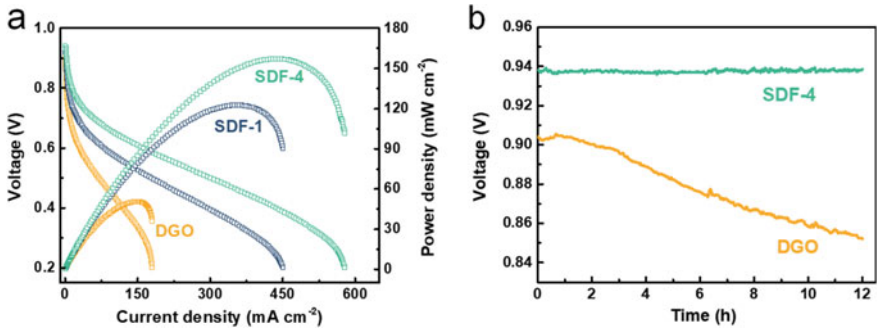

Fig. 5.12 **a** Single-cell performance of membranes at 60 °C and 100% RH. **b** Durability of the assembled MEA at 40 mA cm^{-1}. Copyright (2020), Royal Society of Chemistry [94]

of 54.6 mS cm^{-1} at 80 °C and 100% RH (more than 10 times higher than that of DGO membrane) and a low transfer anisotropy coefficient of 2.5, superior to most reported GO-based membranes. This then brings 208% improvement in fuel cell out-power. Additionally, the proton conductivity of SDF membrane exhibits obvious dependence on PQD. Importantly, the regular covalent framework structure endows SDF membrane with excellent structure stability and operation stability, permitting great potential for practical application. This strategy of constructing framework structure with 2D nanosheet and 0D PQD may open up a new avenue for developing high-performance framework materials.

5.4 Nanofiber-Based Composite Membrane

PVA (7 wt%) was dispersed in water at 60 °C with vigorous stirring for 1 h [29]. TEOS solution (40 wt%) was prepared by dispersing TEOS in the mixture of ethanol, water, and HCl (molar ratio, 3: 8: 0.03), followed by stirring at 60 °C for 1 h. Then, the PVA solution was added dropwise into the TEOS solution with same weight, and the mixture was fully mixed for 1 h with vigorous stirring at 60 °C. The prepared electrospinning solution was incorporated into a plastic disposable syringe with a 0.7 mm I.D. needle, and then pumped through a Teflon tube with a syringe pump (LEAD FLUID, TYD01) at a rate of 0.0125 mL min^{-1}. A high-voltage power supply (Tianjin Dongwen, DW-N503-4ACDE) provided 15 kV potential to the needle. The needle-to-collector distance was controlled at 20 cm, and the rotating speed of collector was set as 10 rpm. The average thickness of NF–OH mat was ~20 μm, which was regulated to be almost constant by the same electrospinning time.

Then, NF–OH was immersed in a mixture of ethanol (160 mL), water (10 mL), and aqueous solution of ammonium (15 mL) with drastic shaking at 25 °C for 24 h. Then, APTES or MPTMS (1.0 mL) was added into the mixture and shaked for another 24 h. The APTES-modified NF–OH was washed with water followed by vacuum-drying to obtain NF–NH_2 [30]. The MPTMS-modified NF–OH was washed with water and then oxygenized with 30% v/v H_2O_2 for 4 h at 50 °C to attain NF–SO_3H [31]. The thickness of NF–NH_2 and NF–SO_3H was about 20 μm, similar to that of NF–OH. Note that the modification occurred mainly on the surface of nanofiber and could not form extra layer.

SPEEK was synthesized based on the method in literature, and the sulfonation degree was controlled to be 65.6% [32]. SPEEK (4.5 wt%) was dispersed in DMF with vigorous stirring for 6 h. Then, the SPEEK solution was poured on the NF–OH, NF–NH_2, or NF–SO_3H mat on a clean glass bar, which was fully dried firstly at 60 °C for 12 h and then at 80 °C for another 12 h to attain a NFCM. The resultant NFCM was named as SP/NF–OH, SP/NF–NH_2, or SP/NF–SO_3H.

A certain amount of CS (1 wt%) was dispersed in acetic acid aqueous solution (1 wt%) with vigorous stirring at 60 °C for 2 h. Then, the CS solution was poured on the NF–OH, NF–NH_2, or NF–SO_3H mat on a clean glass, which was then dried for 72 h at room temperature to obtain a NFCM. Then, the NFCM was immersed in

H_2SO_4 (1 M) for 24 h to fully cross-link the CS matrix, followed by fully washing with water until pH reaches 7.0 to remove the residual acid (H_2SO_4 and acetic acid). By titration and elemental analysis, the membranes were found to be thoroughly cross-linked, and the loading amount of sulfuric acid in per mass CS was around 3.06 mmol g^{-1}, similar to the result in the literature [33]. The resultant NFCM was vacuum-dried at room temperature for 24 h and named as CS/NF–OH, CS/NF–NH_2, or CS/NF–SO_3H. The average thickness of NFCM was ~40 μm.

For comparison, SPEEK and CS control membrane was prepared through solution casting method. SPEEK (9 wt%) was dispersed in DMF to obtain homogeneous casting solution, which was casted onto a glass plate and dried firstly at 60 °C for 12 h and then at 80 °C for another 12 h. The above-mentioned defoaming CS solution was casted onto a clean glass plate and dried for 72 h at room temperature. Then, the CS membrane was cross-linked and washed using the same procedure as that of NFCM (Fig. 5.13).

SEM image in Fig. 5.14a reveals that the NF–OH nanofibers interlace with each other and form a 3D multi-layered interpenetrating fibrous network. The nanofibers show an average diameter of 290 nm bearing oval beads with a diameter of about 880 nm, which may be formed driven by the surface tension [34]. From TGA results, the SiO_2 content is computed to be ~24% in NF–OH [35]. After surface modification, there is no obvious change in morphology, indicating that the modified layer is ultrathin.

The FTIR spectra of nanofiber mat in Fig. 5.15a show a characteristic peak at 1070 cm^{-1} for all the mats, because of the superposition of 1095 cm^{-1} (Si–O–Si) and 1045 cm^{-1} (Si–O–C). The appearance of Si–O–C originates from the covalent cross-linking between Si–OH group from hydrolyzed TEOS and C–OH group from PVA.

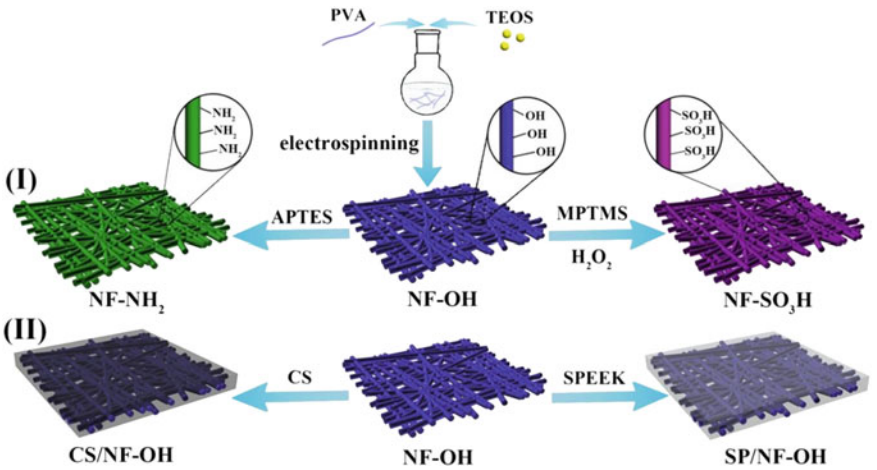

Fig. 5.13 Schematic preparation of nanofiber and NFCM: **I** electrospinning and surface modification of NF–OH nanofiber mat; **II** preparation of NFCM. Copyright (2015), Royal Society of Chemistry [66]

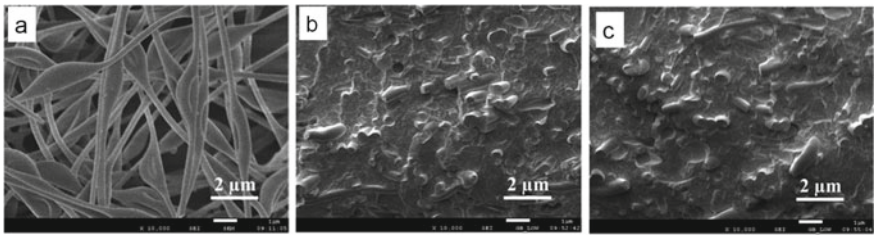

Fig. 5.14 SEM image of **a** surface of NF–OH, **b** cross-section of CS/NF–SO_3H, and **c** cross-section of SP/NF–NH_2. Copyright (2015), Royal Society of Chemistry [66]

This feature affords nanofiber elevated structural stability and low water swelling. After being modified with APTES, the grafting of –NH_2 groups gives rise to three characteristic peaks at 863, 697, and 1550 cm^{-1} for NF–NH_2, corresponding to the out-of-plane bending and stretching vibration of N–H. For NF–SO_3H, the characteristic peak related to O=S=O of –SO_3H group at 1075 cm^{-1} is overlapped by the broad band at 1070 cm^{-1} [36–38]. Figure 5.15b indicates that SPEEK control membrane displays the characteristic peaks for O=S=O of –SO_3H at 1225, 1081, and 1025 cm^{-1}. After being incorporated into nanofiber mat, SPEEK-filled NFCM exhibits the same but weak characteristic peaks due to the decrease of SPEEK content. Different from SP/NF-OH and SP/NF-SO_3H, a new peak at 903 cm^{-1} (red star) is observed in the spectrum of SP/NF-NH_2, which is ascribed to the symmetric stretching of –S–O– [39]. This phenomenon suggests that the acid group of SPEEK and the base group of matrix may assemble into acid–base pair (–SO^{3-}…$^{+}H_3N$–) along nanofiber surface [37].

The amphiphilic feature allows SPEEK chain to assemble into ionic cluster, which can be detected by SAXS. The q value of SPEEK control membrane is 0.228 $Å^{-1}$ as shown in Fig. 5.16a. The addition into nanofiber mat results in sharply reduced q value (around 0.035 $Å^{-1}$). This is because that SPEEK chains are restrained and

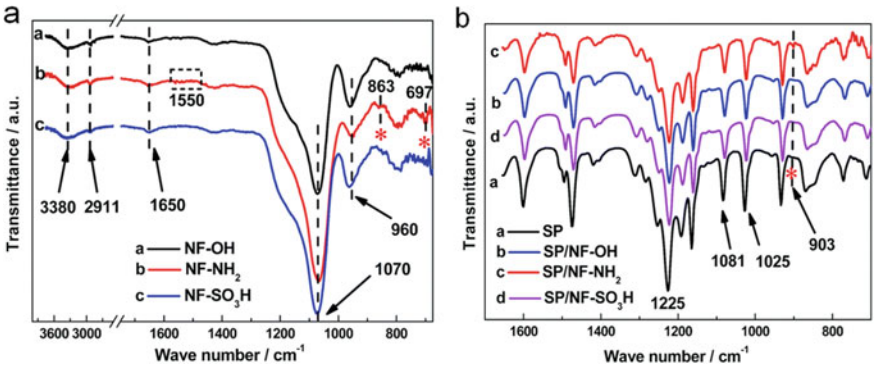

Fig. 5.15 FTIR spectra of **a** nanofiber and **b** SPEEK-filled NFCM. Copyright (2015), Royal Society of Chemistry [66]

interfered; therefore, the nanophase separation process could not develop completely, and smaller cluster is formed. The chain packing and mobility are critical for proton transfer ability of polymer membrane, which can be probed by DSC technique. T_d is related to the endothermic peak, corresponding to the relaxation process occurring in polymer phase that releases residual stress and facilitates structural reorganization [40]. An obvious increase of T_d (above 234 °C) is observed when SPEEK is incorporated into nanofiber mat. This is beneficial from the bicontinuous-phase structure of NFCM, in which the chain mobility of SPEEK is suppressed by the backbone of nanofiber network. For SP/NF–OH, the hydrogen-bonding interaction between $–SO_3H$ group and –OH group affords it admirable T_d at 239.8 °C. In comparison, the repulsive force between $–SO_3H$ group of nanofiber and matrix in SP/NF–SO_3H promotes the chain mobility and thus reduces the T_d to 234.3 °C, whereas the electrostatic attraction within the acid–base pairs endows SP/NF–NH_2 with the highest T_d of 241.7 °C [41]. Excellent mechanical stability is vital for PEM, which can be evaluated with stress–strain curve. Figure 5.16c indicates that SPEEK membrane possesses acceptable mechanical stability with a tensile strength of 33.3 MPa and elongation at break above 30%. In comparison, SPEEK-filled NFCM exhibits favorable tensile strength of 38.9–44.3 MPa due to the reinforcement by nanofibrous framework. Meanwhile, the inorganic component in nanofiber obviously decreases the flexibility of NFCM, resulting in the reduction of elongation at break to the range of 8.0%–9.8%. Similarly, CS-filled NFCM shows higher tensile strength and lower elongation at break when compared with CS control membrane. In particular, CS/NF–SO_3H displays the highest tensile strength, because of the strong electrostatic attraction at the interfacial region.

Fenton's test is a common method utilized for detecting the radical oxidative stability of PEM. During the operation in fuel cell, radicals like HO^- and HOO^- will attack the membrane and lead to degradation. As shown in Table 5.1, SPEEK membrane shows inferior oxidative stability, and it resolves after soaking in Fenton's reagent for 1 h. This is mainly ascribed to the sulfonic acid groups on polymer chain, which leads to the water uptake and diffusion of peroxide and the derived radicals into membrane [42]. In comparison, SPEEK-filled NFCM exhibits much better oxidative stability, with a retained weight of above 80%. This possibly results from the fact that

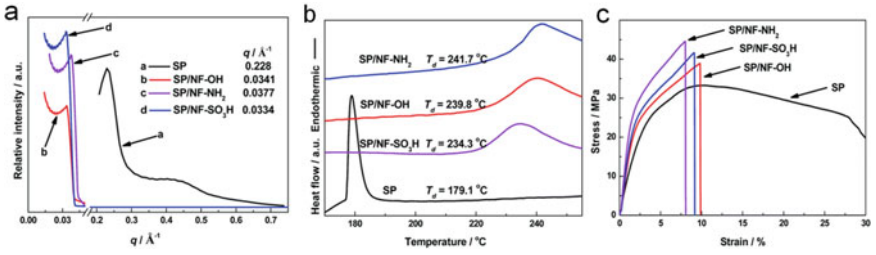

Fig. 5.16 **a** SAXS patterns, **b** DSC, and **c** stress–strain curves of SPEEK-filled NFCM. Copyright (2015), Royal Society of Chemistry [66]

Table 5.1 *IEC* and proton conduction property of NFCM

Membrane	*IEC* (mmol g^{-1})	Proton conductivity (mS cm^{-1})		E_a value (kJ mol^{-1})		Carrier type	Category
		65 °C 100% RH	120 °C 0% RH	100% RH	0% RH		
SP	1.84	30.1	0.957	13.94	21.81	–	–
SP/NF-OH	1.13	28.9	0.768	16.43	23.94	Acid-inert	I
SP/NF-NH_2	1.02	93.8	27.0	10.30	16.29	Acid–base	III
SP/NF-SO_3H	1.47	56.5	20.4	12.15	20.45	Acid-acid	II
CS	0.198	19.8	1.14	11.17	14.44	–	–
CS/NF-OH	0.114	17.9	0.924	14.07	17.06	Base-inert	I
CS/NF-NH_2	0.171	22.2	18.0	10.34	13.95	Base-base	II
CS/NF-SO_3H	0.281	65.6	23. 7	8.71	9.94	Base-acid	III

Copyright (2015), Royal Society of Chemistry [66]

the nanofiber-containing silica could prevent the attack of radical on the polar groups in polymer matrix. Similarly, the low retained weight of CS membrane (79.6%) is obviously enhanced to above 90% for CS-filled NFCM.

The *IEC* value (Table 5.1) of SPEEK (DS = 65.6%) and CS control membrane is 1.84 and 0.198 mmol g^{-1}, which results from the dissociation of $–SO_3H$ group and the protonated NH^{3+}, respectively. The values are in accordance with those in literatures [43]. For NFCM containing I-type proton carrier, the *IEC* value is lower than control membrane due to the addition of neutral nanofiber mat. For example, SP/NF–OH shows an *IEC* value of 1.13 mmol g^{-1}. In comparison, the grafting of functional group on nanofiber mat affords higher *IEC* value to the NFCM containing II-type carrier (e.g., SP/NF–SO_3H: 1.47 mmol g^{-1}). Considering the higher *IEC* value of NF–NH_2 (0.169 mmol g^{-1}) than that of NF–OH (0.005 mmol g^{-1}), it is interesting to find that SP/NF–NH_2 (III-type proton carrier) shows an even lower *IEC* value (1.02 mmol g^{-1}) than SP/NF–OH (1.13 mmol g^{-1}). This finding corroborates the generation of acid–base pairs driven by electrostatic attractive force, which reduces the H^+ dissociation from the pair during titration process. CS-filled NFCM displays a quite close *IEC* value to SPEEK-filled NFCM.

In order to investigate the effect of proton carrier on conduction property, proton conductivity of NFCM under hydrated condition (temperature: 25–65 °C) and low humidity (temperature: 25–120 °C) and the corresponding E_a value were systematically tested. The results in Table 5.1 reveal that SPEEK and CS control membrane displays acceptable hydrated conductivity of 30.1 and 19.8 mS cm^{-1} at 65 °C, which are close to the results in literature [44]. Note that proton transports through CS membrane by the protonated NH^{3+} and the ion bonded $SO_4{}^{2-}$ via Grotthuss mechanism. The incorporation of nanofiber mat into casting membrane will make the

functional groups from nanofiber and matrix work synergistically. Specifically, for I-type proton carrier, the neutral component dilutes the density of conductive group and decreases the valid number in membrane, thus resulting in depressed proton conduction property. For instance, SP/NF–OH obtains a conductivity of 28.9 mS cm^{-1}, lower than that of SPEEK control membrane. In comparison, II-type proton carrier donates more proton hopping sites and therefore higher conductivity to NFCM under identical condition (e.g., SP/NF–SO_3H: 56.5 mS cm^{-1}). Particularly, III-type proton carrier exhibits a distinct induction effect, which stimulates the rearrangement and enrichment of acidic and basic groups on nanofiber surface to assemble into acid–base pairs. Within these acid–base pairs, the electrostatic attraction can induce an optimum orientation of water network and promote the protonation/deprotonation and therefore the proton hopping. In this way, III-type proton carrier could work as facile path for ultrafast proton conduction. Consequently, the type of hybrid proton carrier and the match of different functional groups play critical role in proton transfer: (i) for I-type proton carrier (acid-neutral or base-neutral), the lack of functional group and the subsequent interaction result in the inferior proton conduction ability; (ii) for II-type proton carrier (acid-acid or base–base), the abundant functional groups donate acceptable proton conduction ability; (iii) for III-type proton carrier (acid–base or base-acid), the favorable matching of acidic and basic groups and the generated attraction provide the highest conductivity via synergistic mechanism.

To further explore the transfer property of the three type of proton carrier, the proton conduction barrier was calculated in the form of activation energy (Table 5.1). It is found that NFCM with I-type proton carrier shows higher E_a value as compared to those of control membranes, indicating the higher transfer barrier. For instance, SP/NF–OH possesses an E_a value of 16.43 kJ mol^{-1}, higher than that of SPEEK control membrane (13.94 kJ mol^{-1}). For II-type proton carrier, the relatively high carrier content affords lower proton hopping barrier and E_a value (e.g., SP/NF–SO_3H: 12.15 kJ mol^{-1}). In comparison, III-type proton carrier enables NFCM to efficiently transfer proton via low-energy barrier manner, and SP/NF–NH_2 possesses the lowest E_a value (10.30 kJ mol^{-1}) among the SPEEK-filled NFCM. Similarly, CS/NF–SO_3H achieves the lowest E_a value of 8.71 kJ mol^{-1} among the CS-filled NFCM, and it is also comparable to Nafion (7.30 kJ mol^{-1}).

The temperature-dependent conductivity at hydrated condition shown in Fig. 5.17a, b reveals that all membranes exhibit gradual increased conductivity with the temperature elevates from 25 to 65 °C. This conductivity should be ascribed to the promoted polymer chain motion at high temperature, which decreases the enthalpy change during proton hopping. For example, the conductivity of SPEEK control membrane increases from 0.0152 to 0.0301 S cm^{-1}. In comparison, NFCM containing II- or III-type proton carrier possesses higher conductivity than SPEEK control membrane at all temperatures, meanwhile obeys the order of SP/NF–OH < SPEEK < SP/NF–SO_3H < SP/NF–NH_2. With the temperature elevates from 25 to 65 °C, the conductivity increases from 0.013 to 0.029 S cm^{-1}, from 0.031 to 0.056 S cm^{-1}, and from 0.059 to 0.094 S cm^{-1} for SP/NF–OH, SP/NF–SO_3H, and SP/NF–NH_2, respectively. Note that the hydrated conductivity of NFCM containing III-type proton carrier is comparable to those in literature [45].

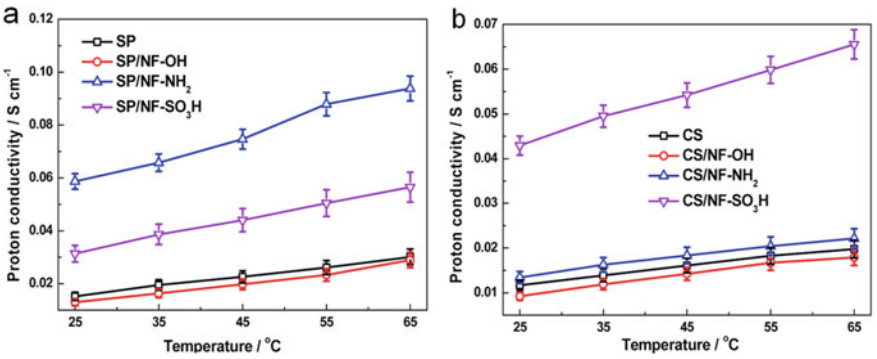

Fig. 5.17 Temperature-dependent hydrated conductivity of (a) SPEEK-filled membrane and (b) CS-filled membrane. Copyright (2015), Royal Society of Chemistry [66]

In comparison, the conductivity of SPEEK and CS control membrane under low humidity is 0.957 and 1.140 mS cm^{-1} at 120 °C, respectively, which are close to those in literature [46]. Because of the lack of water, the proton conductivity in low humidity condition reduces significantly as compared with those in hydrated condition [47]. The proton transfer is mainly via Grotthuss mechanism, which is advantageous to investigate the inherent transfer property of proton carrier. For I-type proton carrier, the dilution effect of functional group leads to the low proton conductivity. For example, the addition of CS matrix into NF–OH reduces the conductivity to 0.924 mS cm^{-1} as shown in Fig. 5.18. In comparison, II-type proton carrier containing more conduction groups donates more continuous proton transfer paths at interfacial region [48]. And CS/NF–NH_2 achieves a high conductivity of 17.97 mS cm^{-1} at 120 °C. For III-type proton carrier, the ample functional groups in form of acid–base pair (–SO_3H/–NH_2) serve as effective proton hopping sites, and the synergistic effect allows the constructed paths to transfer proton rapidly [49]. This feature affords CS/NF–SO_3H high conductivity of 23.67 mS cm^{-1} at 120 °C, almost 21 times of that of CS control membrane at low humidity. Therefore, it is reasonable to state that III-type proton carrier exhibits more distinct advantages in low humidity. In particular, III-type proton carrier endows NFCM with superior conduction property in low humidity as compared to those in literature [50].

Table 5.1 reveals that the E_a value in low humidity is higher than those in hydrated condition, implying the critical role of water in vehicle-type proton transport. This also indicates that the proton conduction in low humidity mainly relies on Grotthuss mechanism. The E_a value of CS control membrane in low humidity is 14.44 kJ mol^{-1}. I-type proton carrier provides relatively deficient conduction groups to NFCM and thus leads to the higher transfer barrier (*e.g.*, CS/NF–OH: 17.06 kJ mol^{-1}). For II-type proton carrier, the increase in conduction group content gives NFCM lower E_a value (*e.g.*, CS/NF–NH_2: 13.95 kJ mol^{-1}). In contrast, III-type proton carrier (acid–base pair) possesses distinct synergistic effect, which brings the lowest E_a value

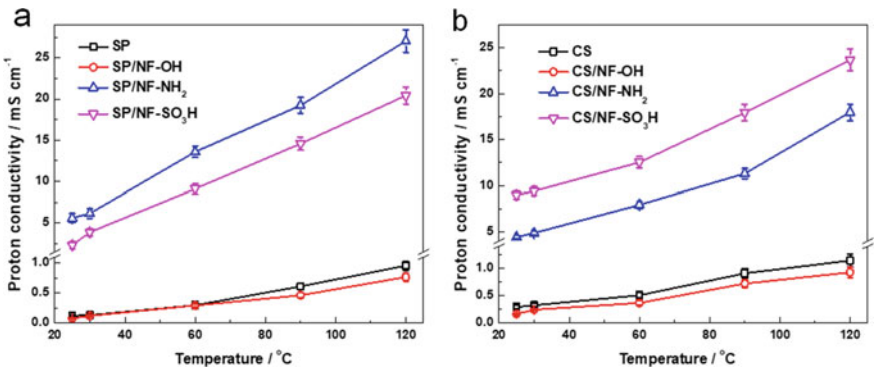

Fig. 5.18 Temperature-dependent anhydrous conductivity of (a) SPEEK-filled membrane and (b) CS-filled membrane. Copyright (2015), Royal Society of Chemistry [66]

(9.94 kJ mol^{-1}) to CS/NF–SO_3H. In comparison, it is found that the effect of carrier type on transfer behavior of SPEEK-filled NFCM is close to that of CS-filled NFCM.

By comparing the E_a and proton conductivity of three types of proton carrier under both 100% RH and low humidity, III-type proton carrier (acid–base pair) shows optimal property with low E_a value, high proton conductivity, and excellent operational stability resulted from the synergistic effect. This suggests the importance of matching different functional groups and the subsequent proton carriers on proton transfer. The investigation on proton carrier herein might pave a way for deeply understanding proton transfer and for the design of high-performance PEM.

The single-cell performance of SPEEK-filled NFCM at 120 °C and low humidity was tested to further investigate the difference of the three types of proton carrier. The thickness of these three membranes is kept almost the same, and the MEA was fabricated in the same manner to ensure a good comparison of the inherent performance of the membrane. As shown in Fig. 5.19, the open-circuit voltage of all cells is above 0.92 V, implying low gas (H_2 and O_2) crossover of the membranes. SPEEK control membrane attains the maximum current density and power density of 318.4 mA cm^{-2} and 86.9 mW cm^{-2}, respectively. In comparison, SP/NF–OH shows inferior performance because of the low proton conductivity. SP/NF–SO_3H possesses ample conduction groups and higher proton conductivity, thus brings improved maximum current density (395.9 mA cm^{-2}) and maximum power density (107.9 mW cm^{-2}). Acid–base pair affords a more obvious prompting effect, and SP/NF–NH_2 displays a 49% augment in maximum current density (475.8 mA cm^{-2}) coupled with a 63% augment in maximum power density (143.4 mW cm^{-2}) as compared to SPEEK control membrane. In addition, the *OCV* of cell is 1.01 V, higher than 0.96 V of the cell using SPEEK control membrane and very close to that of Nafion. The higher proton conductivity should be responsible for the cell performance enhancement of SP/NF–NH_2, which offers lower electrolyte resistance and faster reduction reaction in the cathode of fuel cell [51].

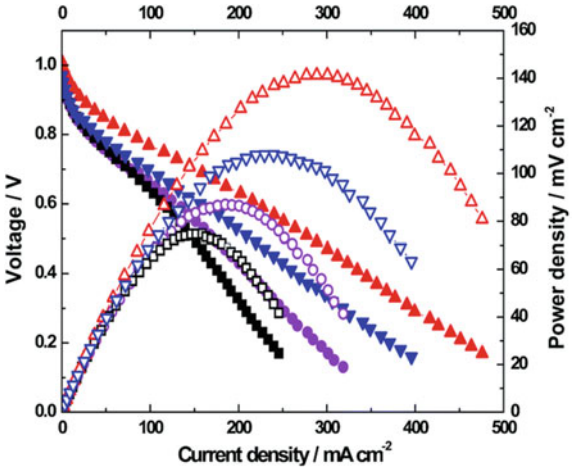

Fig. 5.19 Single-cell performance of SPEEK control membrane and SPEEK-filled NFCM at 120 °C and anhydrous condition (□:SP/NF-OH, ○:SPEEK, ▽:SP/NF-SO_3H, △: SP/NF-NH_2). Copyright (2015), Royal Society of Chemistry [66]

In conclusion, we have designed six kinds of nanofibrous composite membranes with different type of proton carrier, which are divided into three types: I-type (acid-neutral and base-neutral), II-type (acid-acid and base–base), and III-type (acid–base and base-acid). The proton conductivity increases in the order of I < II < III. There is no obvious synergistic interaction in I and II-type composite proton carriers. In comparison, the electrostatic attraction within III-type proton carrier shows distinct advantages by facilitating the protonation and deprotonation process, thus brings low-energy barrier hopping sites. Practically, SP/NF–NH_2 shows the highest hydrated conductivity of 93.8 mS cm^{-1} (65 °C) and a conductivity of 20.4 mS cm^{-1} in low humidity (120 °C) among SPEEK-filled NFCM, which are 2.1 and 20.3 times higher than those of corresponding control membranes, respectively. Therefore, the different combination of group leads to various results, among which the effective interaction and synergistic effect within proton carriers are essential to the ultrafast proton conduction through membrane. In addition, the superior proton conduction ability of III-type proton carrier confers favorable H_2/O_2 cell performance. Moreover, the electrostatic interaction within III-type proton carrier inhibits the chain mobility of polymer, thus affording NFCM admirable thermal, mechanical, and oxidative stability.

5.5 Nanofiber-Based Composite Membrane with Dual Transfer Pathways

SPEEK was fabricated based on the procedure in literature [52]. During the sulfonation, the DS of SPEEK was controlled by regulating the sulfonation time. Four types of SPEEK with DS of 58.2%, 66.1%, 74.4%, and 82.0% were attained when the sulfonation time was 7.5, 9.0, 10.0, and 10.5 h, respectively. SPEEK with DS of

66.1% was selected to be electrospun into nanofiber. The detailed electrospinning process was the same with that in previous study [53].

SHNT was synthesized via distillation-precipitation polymerization method [54]: HNT (5.0 g) was dispersed in the mixture of ethanol (150 mL), water (15 mL), and aqueous solution of ammonium (12 mL) under stirring at room temperature for 24 h. Then, MPS (1.0 mL) was added in the resultant mixture and stirred for another 24 h. Afterward, the MPS-modified HNT was purified by three cycles of centrifugation and followed by drying in a vacuum oven at 50 °C. MPS-modified HNT (0.30 g), St (0.40 mL), SS (0.40 mL), and AIBN (0.016 g) were dispersed into acetonitrile (80 mL) in a dried three-necked flask. The above mixture was heated and kept under boiling state until half acetonitrile was distilled out. Afterward, the hybrid HNT was purified by centrifugation and washing with acetonitrile. The resultant hybrid HNT was treated with 0.1 M HCl to exchange the Na^+ in $–SO_3Na$ with H^+. Then halloysite nanotube bearing sulfonated polyelectrolyte brush was obtained after being dried in a vacuum oven at 50 °C till constant weight. PVA (7 wt%) was dissolved in de-ionized water at 60 °C under stirring for 1 h [55]. TEOS solution (40 wt%) was made by dissolving TEOS in the mixture of ethanol, water, and HCl (molar ratio, 3:8:0.03) followed by stirring at 60 °C for 1 h. Afterward, the PVA solution was gradually added into the TEOS solution (weight ratio, 1:1), and the mixture was thoroughly mixed for 1 h under stirring at 60 °C. The obtained electrospinning solution was loaded in a plastic disposable syringe with a 0.7 mm I.D. needle, and then pumped through a Teflon tube with a syringe pump (LEAD FLUID, TYD01) at the rate of 0.0125 mL min^{-1}. A high-voltage power supply (Tianjin Dongwen, DW-N503-4ACDE) provided 15 kV potential to the needle. The needle-to-collector distance was fixed at 20 cm, and the rotating speed of the collector was set at 10 rpm. The obtained nanofiber mat was named as NF-OH, and the thickness was controlled almost the same by the time allowed for deposition.

Afterward, NF-OH mat (6 cm^2 × 6 cm^2) was immersed in aqueous dopamine solution (100 mL, 2.0 mg mL^{-1}) for 24 h at (25 ± 1) °C under stirring. The pH value of the solution was controlled by Tris and HCl to 7.5, 8.5, or 9.5. The obtained nanofiber mats were designated as NF-PDA-*Y*, where *Y* indicated the pH value of the aqueous dopamine solution. Thereafter, NF-PDA-*Y* was washed with de-ionized water repeatedly, followed by drying at room temperature in oven overnight.

CS (1.5 g) was dissolved in acetic acid aqueous solution (2%, 40 mL) under stirring at 80 °C. Simultaneously, certain amounts of nanotubes (HNTs or SHNTs) were dispersed into acetic acid aqueous solution (2%, 35 mL) with ultrasonic treatment for 30 min. These two parts of solution were then mixed and stirred vigorously at 80 °C for another 2 h. After degasification, the above homogenous solution was cast onto a clean glass plate with a piece of SPEEK nanofiber mat placed in advance and dried at room temperature to obtain a membrane. The membrane was then immersed in 1.0 M H_2SO_4 for 24 h for complete cross-linking and then extensively rinsed with water to remove the residual H_2SO_4. Finally, the membrane was dried under vacuum at 30 °C for 48 h. The resulting membranes were designated as CS/SPNF/HNTs-*X* or CS/SPNF/SHNTs-*X* representing HNTs or SHNTs as the fillers, where *X* ($X = 0$, 2.5, 5, 7.5, or 10) represented the weight percentage of nanotubes to CS. CS casting

membrane was fabricated in exactly the same way as above without incorporating nanotubes and nanofibers. It should be pointed out that membrane thickness was in the range of 43–58 μm.

Four kinds of SPEEK (4.5 wt%) with the DSs of 58.2%, 66.1%, 74.4%, and 82.0% were dissolved in DMF under stirring for 6 h, respectively. Afterward, the SPEEK solution was filled into the NF-OH or NF-PDA-*Y* mat on a clean glass bar, which was thoroughly dried firstly at 60 °C for 12 h and then at 80 °C for another 12 h to obtain NFCMs. The resultant NFCMs were named as SP-*Z*/NF-OH or SP-*Z*/NF-PDA-*Y*, where *Z* referred to the DS of SPEEK. For comparison, SPEEK (DS = 66.1%) casting membranes were fabricated via solution casting method. SPEEK (9 wt%) was dissolved in DMF to obtain homogeneous casting solution, which was cast onto a glass plate and dried firstly at 60 °C for 12 h and then at 80 °C for another 12 h. The obtained SPEEK casting membrane was named as SP-66 (Fig. 5.20).

SPEEK (sulfonation degree, 66.1%) nanofiber was fabricated by electrospinning method, and the SEM image was shown in Fig. 5.21a, which reveals that the average diameter is around 140 nm. Nanofibers possessing smooth surface lap with each other and form three-dimensional interpenetrating network, beneficial to establish bicontinuous structure. After grafting the brush, uniform polymeric brush with average thickness of about 10 nm can be observed on SHNT surface in Fig. 5.21b, and SHNT keeps tubular structure without obvious destruction. The chemical structure and weight content of polyelectrolyte brush on SHNT are determined by FTIR and TGA analyses, which reveal that sulfonated polyelectrolyte brushes are introduced on SHNT with the weight percentage of approximately 7.4% [56].

SHNT (or HNT) is mixed with CS matrix and then embedded into SPEEK nanofiber mat to prepare NFCMs via solution casting method. The cross-sectional SEM image (Fig. 5.21c) suggests that NFCM is dense and uniform without obvious

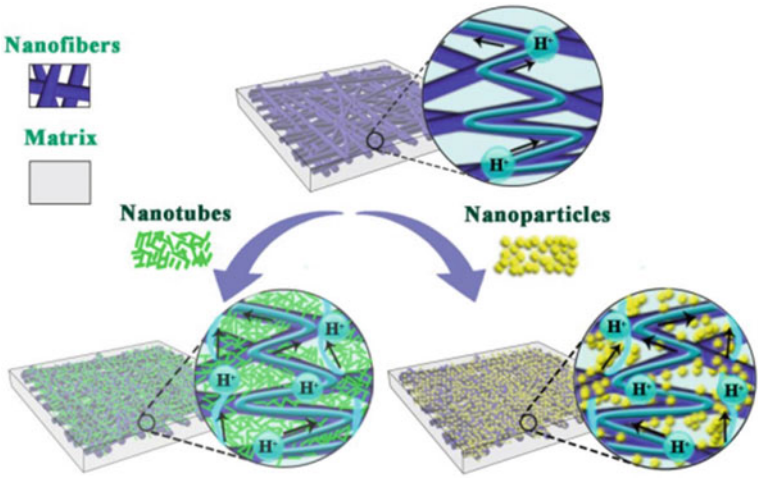

Fig. 5.20 Schematic synthesis of SPEEK nanofiber. Copyright (2016), Elsevier [95]

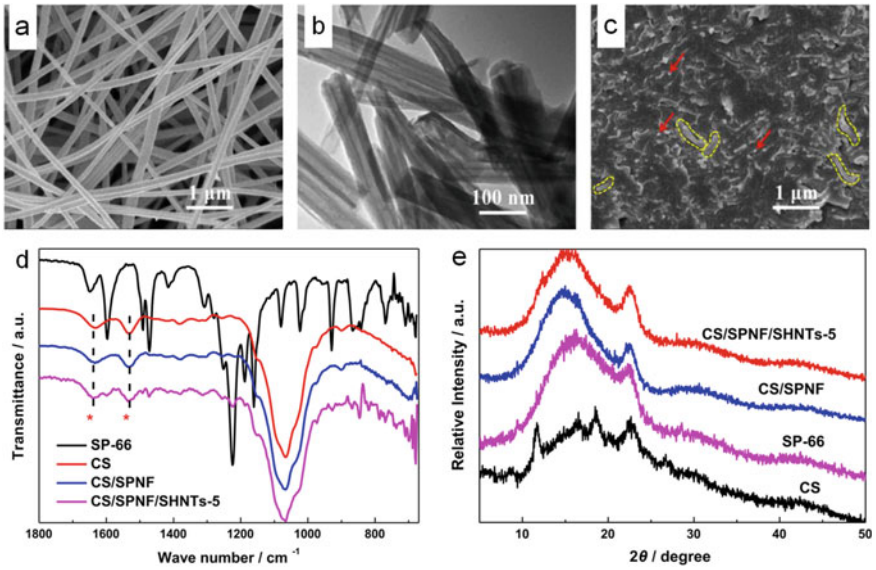

Fig. 5.21 **a** SEM image of SPEEK nanofiber, **b** TEM image of SHNT, **c** cross-sectional SEM image of CS/SPNF/SHNT-5, **d** FTIR, and **e** XRD of membrane. Copyright (2016), Elsevier [95]

defect. SPEEK nanofiber (yellow circle) and SHNT (red arrow) maintain their pristine structure and homogeneously disperse within the whole NFCM. SHNT displays a favorable dispersion in CS matrix without agglomeration and void. The sulfonated polyelectrolyte brush should contribute to this observation, which generates strong and extensive electrostatic attraction with CS matrix ($–NH_2$ groups). Meanwhile, these attraction might drive the brush to insert into CS matrix with the aid of brush motion, forming wide CS-filler interfacial domain.

FTIR spectra in Fig. 5.21d show that SPEEK displays the peaks at 1219, 1076, and 1020 cm^{-1} corresponding to $-SO_3H$ group, and CS membrane exhibits the characteristic peaks at 1649 and 1538 cm^{-1}, which are attributed to amide I and amide II groups, respectively. By comparison, CS/SPNF and CS/SPNF/SHNTs-5 remain these characteristic peaks in their spectra [57]. There is no new peak appearing, interpreting that they are physically mixed with no covalent peak among CS, SPNF, and SHNT. This might imply that CS and SPNF/SHNT are bridged by acid–base pair rather than quaternary ammonium [58]. It is noted that the characteristic peaks of SPEEK and SHNT could not be distinguished, probably because they are wrapped within CS matrix [57]. Also, the interaction interferes with the chain stacking of NFCM, as determined by XRD. Figure 5.21e reveals that CS casting membrane displays three characteristic peaks at $2\theta = 18.7, 21.3, 24.6°$ corresponding to the semicrystalline structure of CS matrix [59]. However, these distinct peaks disappear for CS/SPNF, implying the semicrystalline structure of CS reduces or even disappears when being incorporated in nanofiber mat. This finding is probably due to the interference of electrostatic attraction and steric effect from the mat, which breaks

the ordered arrangement of CS linkage by inhibiting CS chain motion. Similarly, the spectrum of CS/SPNF/SHNT-*X* shows no semicrystalline peak of CS matrix.

Thermal stability of membrane was investigated by TGA and DSC. Figure 5.22a shows that all membranes exhibit three-stage weight losses: (i) the first one is the evaporation of water molecule from membrane around 30–200 °C; (ii) the second stage is the polymer side-chain pyrolysis around 220–330 °C; and (iii) the third stage is the polymer backbone degradation around 480–800 °C. The char yield at 800 °C is 46.2% and 1.78% for SPEEK and CS casting membrane, respectively, which comes to 12.6% for CS/SPNF. Upon incorporating SHNT, the char yield increases to 21.0% for CS/SPNF/SHNTs-5. DSC result in Fig. 5.22b suggests that the T_d of SPEEK and CS casting membrane is 179.0 °C and 218.4 °C, respectively. In comparison, CS/SPNF shows higher T_d of 228.7 °C; adding nanofiller (SHNT) into NFCM further enhances the stability of CS/SPNF/SHNTs-5 with the T_d of 233.4 °C. The elevated T_d and char yield may indicate the improvement of thermal stability of NFCM upon SHNT incorporation. The enhanced thermal stability of NFCM corroborates the reinforcement of membrane by the bicontinuous phase structure and the hybridization of inorganic filler [45]. The result of mechanical property shows that the SHNT incorporation also elevates the tensile strength of CS/SPNF at both dry and wet states (see Fig. 5.22c, d). This reinforcement could also be observed by the behavior of water uptake and swelling degree of NFCM (Fig. 5.22e, f). CS casting membrane possesses the water uptake of 70.7% under 25 °C, and it reduces to 60.2% when being incorporated into SPNF mat. As expected, CS/SPNF/SHNTs-5 displays much lower water uptake of 50.7%. Like water uptake, area swelling of membrane decreases in the order of CS > CS/SPNF > CS/SPNF/SHNTs-*X* (Fig. 5.22f). Meanwhile due to the acceleration of chain motion as the temperature elevates, all membranes display gradually increased water uptake and area swelling [60]. CS/SPNF/SHNTs-*X* shows the best swelling-resistant ability, especially at elevated temperatures. With the temperature increasing from 25 to 80 °C, the enhancement of swelling for CS/SPNF/SHNTs-5 is 79.1%, while this value is 103.0% for CS casting membrane.

Proton conduction, determining the operational voltage and current output of fuel cell, is one essential property for PEM. Proton conduction in PEM generally obeys two mechanism [61]: vehicle mechanism, which assumes that proton combines with solvent molecule to yield hydronium ions (H_3O^+, $H_5O_2^+$, $H_9O_4^+$) and then diffuses as a whole; Grotthuss mechanism, which is related to the proton hopping from one solvent molecule or conducting carrier to a neighboring one. Proton conductivity of membrane at both hydrated (100% RH) and anhydrous (0% RH) condition is depicted in Fig. 5.23. The hydrated conductivity in Fig. 5.23a reveals that CS casting membrane attains a conductivity of about 25.68 mS cm^{-1} at 90 °C and 100% RH, close to the result in literature [62]. For CS/SPNF, its conductivity elevates to 86.11 mS cm^{-1}, 2.2 times of that of CS-SPEEK blending membrane (around 38.92 mS cm^{-1}) [63]. This observation is in accordance with previous study and should be attributed to the long-range proton conduction paths on nanofiber surface, where the formed acid–base pairs act as facile hopping sites and efficiently transport proton along the interfacial paths. Considering the reduced water content (corresponding to vehicle-type transfer), these results suggest that Grotthuss-type proton

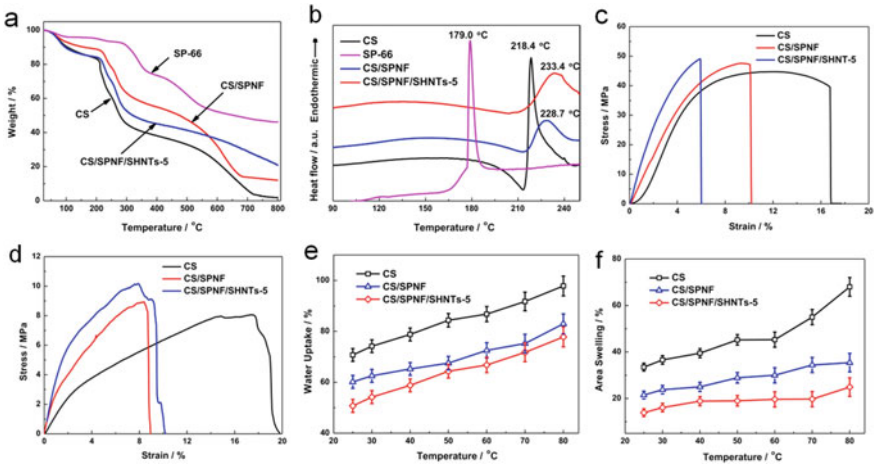

Fig. 5.22 **a** TGA, **b** DSC, **c** stress–strain curves in dry state, **d** stress–strain curves in wet state, **e** water uptake, and **f** area swelling of membranes. Copyright (2016), Elsevier [95]

conduction of two kinds of polymer could be markedly elevated by forming nanofibrous composite membrane rather than blending membrane. The electrostatic attraction allows the conducting groups being enriched onto nanofiber surface, together with the large specific surface area of nanofiber, offering efficient interfacial paths to NFCM. For the incorporated CS matrix, it is interesting to find that its conduction ability could be obviously enhanced after the addition of nanofiller (SHNT). Figure 5.23a reveals that 5% SHNT affords a 36.7% enhancement of conductivity for CS/SPNF/SHNTs-5 (117.69 mS cm^{-1}) compared with that of CS/SPNF. This should be resulted from that SHNT (i) forms additional SHNT/CS interface and thus new interfacial proton-conducting paths by means of $-SO_3H$ groups on nanotube surface; (ii) forms acid–base pairs ($-SO_3^-\ldots H_3N^+-$) with CS chain at interfacial region, decreasing the energy barrier of $-NH_2$ groups in CS matrix for proton transfer. About the interfacial conduction paths, it would be further analyzed in anhydrous proton conductivity part in detail. At anhydrous condition, membrane displays identical but more obvious conduction variation behavior. Under this condition, proton could transfer only through Grotthuss mechanism, and carrier site and transfer path are the critical factor for proton conduction. As shown in Fig. 5.23c, CS casting membrane displays relatively low anhydrous proton conductivity of 0.35 mS cm^{-1} at 100 °C. After being incorporated in nanofiber mat, CS/SPNF attains a 20.3 time increase of anhydrous conductivity to 7.10 mS cm^{-1} under 100 °C. This is mainly attributed to the following aspects: (i) SPEEK possesses higher ion exchange capacity and proton conduction ability, which would enhance the whole proton transfer property; (ii) the formed interfacial region could serve as continuous proton paths, in which $-SO_3H$ and $-NH_2$ groups would be enriched and assembled into acid–base pairs, working as efficient hopping sites. Upon addition of SHNT, CS/SPNF/SHNTs-5 achieves a further enhanced conductivity of 19.95 mS cm^{-1}, almost 2.8 times of

that of CS/SPNF. This conduction intensification indicates the obvious promotion function of nanofiller; that is, additional interface emerges along SHNT and the $-SO_3H$ groups combined with $-NH_2$ groups of CS into $-SO_3^-\cdots H_3N^+-$ pairs. It should be noted that the achieved anhydrous conductivity of CS/SPNF/SHNTs-*X* is among the best conductivity reported in literatures. Collectively, these results reveal that the constructed dual-interfacial proton-conducting paths confer efficient proton transfer property on NFCM. In this study, the acid–base pairs are different from those fabricated by the low-molecule acid or base with free mobility, which are easy to form quaternary ammonium. By comparison, these acid and base groups are anchored on polymer chains or nanotube, their motion would be inhibited, and the reaction to quaternary ammonium might be diminished [64].

For polymer matrix, with the increase of SHNT content, more transfer paths are constructed and then afford higher conductivity to NFCM. For instance, the conductivity of CS/SPNF/SHNTs-*X* increases from 12.04 to 21.95 mS cm^{-1} at 100 °C when the SHNT content increases from 2.5% to 7.5%. For all membranes, the hydrated conductivity grows with the increase of temperature (within the testing range). While under anhydrous condition, the conductivity decreases from 0.59 to 0.33 mS cm^{-1}

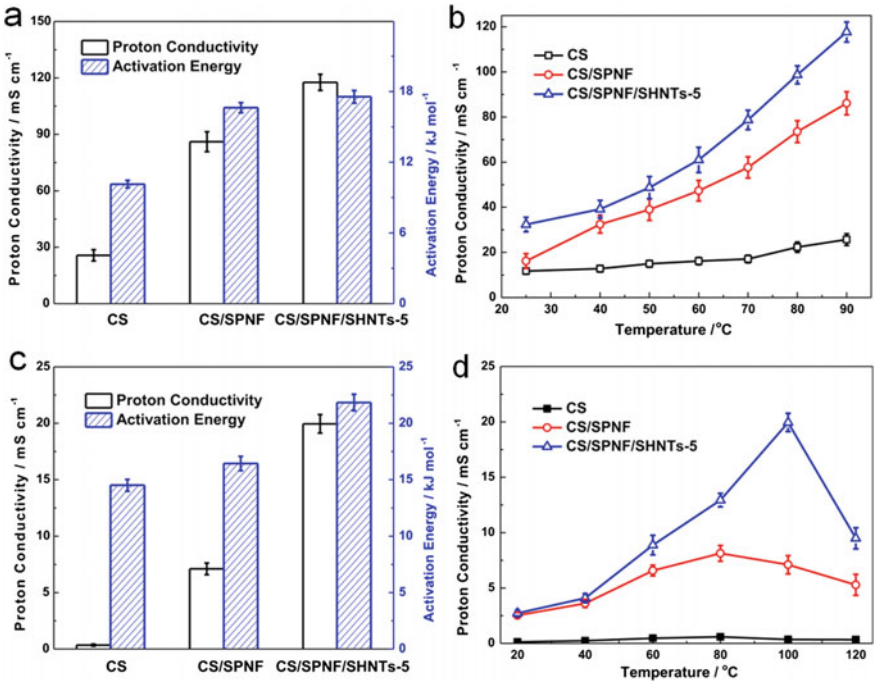

Fig. 5.23 **a** Hydrated proton conductivity at 90 °C and energy activation value of membrane. **b** Temperature-dependent conductivity of membrane under 100% RH. **c** Anhydrous proton conductivity at 100 °C and energy activation value of membrane. **d** Temperature-dependent conductivity of membrane under 0% RH. Copyright (2016), Elsevier [95]

and from 8.13 to 5.28 mS cm^{-1} for CS and CS/SPNF when further increasing the temperature from 80 °C to 120 °C, respectively. This phenomenon might result from the evaporation of bonded water from membrane. In comparison, CS/SPNF/SHNTs-5 does not show conductivity decrease until above 100 °C, exhibiting reduced conductivity from 19.95 to 9.49 mS cm^{-1} when the temperature increases from 100 °C to 120 °C. It is reasonable to state that SHNT endows the CS/SPNF/SHNTs-*X* with enhanced proton conduction property, possibly because of the capillary force of SHNT, which gives better water retention ability to SHNTs-filled membrane [65].

Temperature-dependent conductivity curves are also utilized to calculate E_a, which is a parameter for exploring proton transfer mechanism. E_a value for proton transfer could be employed to evaluate the transfer mechanism: the E_a value for vehicle-type transfer is less than 9.0 kJ mol^{-1}, and it alters to 14.3−39.8 kJ mol^{-1} for Grotthuss-type transfer. CS casting membrane displays the E_a value of 10.1 kJ mol^{-1} under hydrated condition, lower than that for the Grotthuss mechanism alone, indicating that the Grotthuss and vehicle mechanism co-exist [66]. The incorporation of SPEEK nanofiber increases the E_a value of CS/SPNF to 16.6 kJ mol^{-1}, while adding SHNT further improves the E_a value to 17.6 kJ mol^{-1} for CS/SPNF/SHNTs-5. The incorporation of SPEEK nanofiber and SHNT provides additional hopping sites and thus facilitates the proton transport by Grotthuss mechanism. The E_a increase might suggest that Grotthuss mechanism tends to be the primary route for proton conduction in NFCM due to the formed facile continuous paths. Similar finding has been reported in other PEMs. Under anhydrous conduction, the E_a value of these membrane displays similar tendency and increases in the order of CS (14.5 kJ mol^{-1}) < CS/SPNF (16.4 kJ mol^{-1}) < CS/SPNF/SHNTs-5 (21.8 kJ mol^{-1}). For each membrane, the absence of water makes the E_a value under anhydrous conduction higher than that under hydrated conduction.

This study mainly attempts to find a facile approach for enhancing the proton conduction ability of NFCM by tuning the microstructure of the incorporated polymer matrix. From the above researches, it is found that (i) the incorporation of nanofiller into polymer matrix effectively reinforces the thermal and structural stability of NFCM; (ii) the formation of additional hopping paths within polymer matrix efficiently enhances the proton conduction ability of NFCM, especially at anhydrous condition. To investigate and verify the universality of this approach, another kind of NFCM with polydopamine nanoparticle as nanofiller is prepared and named as SP-*Z*/NF-PDA-*Y*, where *Z* and *Y* represent SPEEK sulfonation degree and the pH at which polydopamine self-assembled, respectively.

NF-OH nanofiber mat was fabricated and then modified via the convenient self-polymerization of dopamine under mild conditions. SEM image in Fig. 5.24a shows that NF-OH nanofiber is smooth with an average diameter of 290 nm bearing oval beads with the diameter of about 880 nm, close to the morphology in literature and formed by surface tension. NF-PDA remains the nanofiber structure but is coated with a PDA layer and plenty of PDA particles, which are probably resulted from long-time polymerization [67]. The size of particle is several decades of nanometer. The presence of PDA layer and particle gives rise to lower char yield at 800 °C

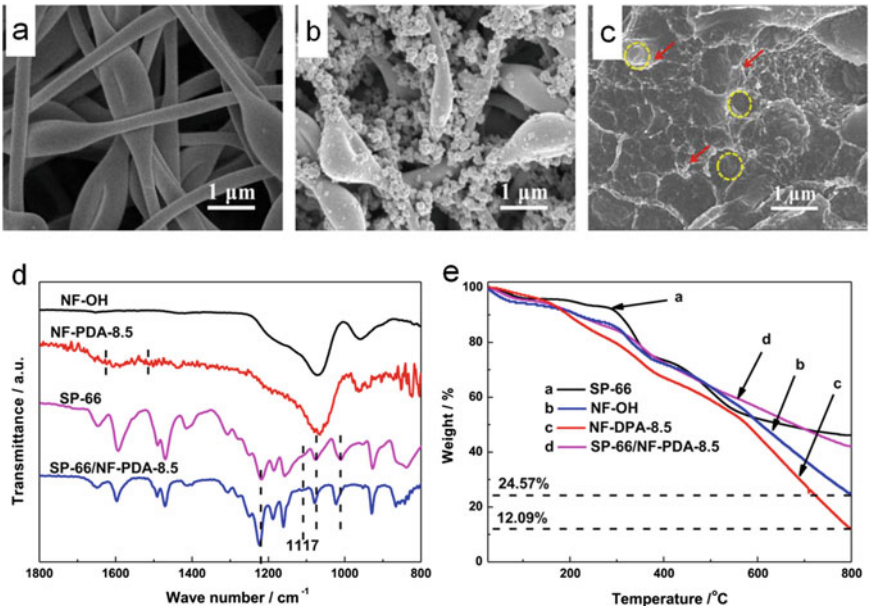

Fig. 5.24 SEM image of **a** NF-OH, **b** NF-PDA, **c** SP/NF-PDA-8.5, **d** FTIR spectra, and **e** TGA curves of membrane. Copyright (2016), Elsevier [95]

(Fig. 5.24e). The content of deposited PDA on NF-OH is calculated to be around 17.28%, 49.63%, and 51.01% for NF-PDA-7.5, NF-PDA-8.5, and NF-PDA-9.5.

SPEEK matrix is then incorporated into NF-OH and NF-PDA to prepare NFCM. SEM image in Fig. 5.24c shows that nanofiber (yellow circle) homogeneously disperses throughout the cross-section of membrane. PDA particle (red arrow) is still attached to nanofiber surface and combines well with polymer matrix driven by electrostatic interaction. The interaction induces the formation of acid–base pairs ($–SO_3^-…^+H_3N^-$) at nanofiber surface and particle surface from the acidic group of SPEEK and the basic group of PDA, as verified by the new FTIR peak at 1117 cm^{-1} (–S–O–) (Fig. 5.24d).

Benefiting from the attraction, NFCM achieves acceptable thermal stability as shown in their TGA and DSC curves (Figs. 5.24d and 5.25a). SP-66 shows a decomposition temperature (T_d) of about 179 °C, and it shifts to 241.5 °C when just being confined in NF-PDA. And NFCM also remains more char yield at 800 °C than that for SP-66. SAXS result in Fig. 5.25b indicates that the formation of acid–base pair inhibits chain motion and the consequent self-assembly of SPEEK to ion cluster, and the ion-channel size and free volume cavity in SP-66/NF-PDA-*Y* are enlarged. *IEC* values in Table 5.2 reveal that SP-66/NF-OH exhibits a lower *IEC* value of 1.13 mmol g^{-1} than SP-66 (1.85 mmol g^{-1}) due to the dilution effect of NF-OH on $–SO_3H$ groups. In spite of coating PDA bearing $–NH_2$ and –NH– groups, SP-66/NF-PDA-*Y* shows lower *IEC* values of 1.02, 0.95, or 0.98 mmol g^{-1} (corresponding to

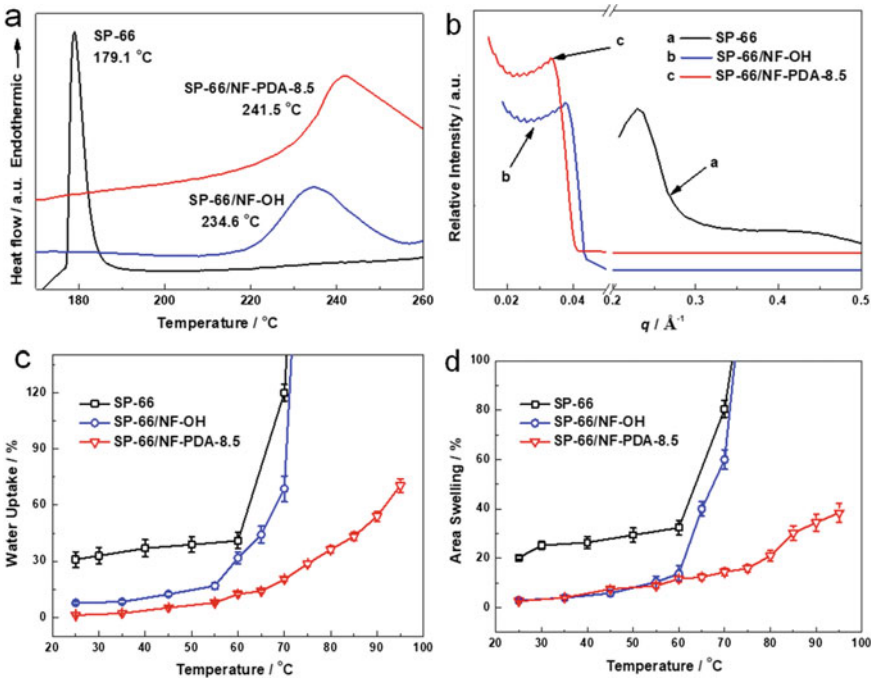

Fig. 5.25 **a** DSC, **b** SAXS, **c** water uptake, and **d** area swelling of membrane. Copyright (2016), Elsevier [95]

pH = 7.5, 8.5, or 9.5) due to the formation of acid–base pair from proton exchange group.

Water uptake of SP-66 is 31.0% at 25 °C (Fig. 5.25c), in consistent with the result in literature [68]. When confined in NF-OH, water uptake sharply decreases to 7.9% for SP-66/NF-OH. In comparison, SP-66/NF-PDA-8.5 displays much lower water uptake of about 2% at 25 °C. Such phenomenon should be ascribed to the electrostatic interaction between SPEEK and PDA as well as the strong steric effect of polydopamine particle, suppressing the chain mobility of SPEEK for water absorption. Although all membranes display gradual enhancement of water uptaking capability with temperature, SP-*Z*/NF-PDA-*Y* achieves much lower water uptake and area swelling. For example, SP-66 and SP-66/NF-OH are already dissolved in water solution when the temperature exceeds 70 °C, while SP-66/NF-PDA-*Y* shows acceptable structural stability with water uptake and area swelling below 85% and 60% at even 90 °C, respectively. These data should be competitive for practical application in fuel cell when compared with other well-developed PEMs [69]. It should be noted that the amount of acid–base pairs, thermal and structural property, and microstructure of NFCM could be tuned by the sulfonation degree of SPEEK and/or the loading amount of PDA.

Table 5.2 *IEC*, water uptake, area swelling, and proton conduction property of membrane

Membrane	*IEC* (mmol g^{-1})	Water uptake (%)	Area swelling (%)	Proton conductivity (mS cm^{-1})	
		70 °C	70 °C	60 °C, 100% RH	100 °C, 0% RH
CS	0.20	91.7	55.0	16.2	0.4
CS/SPNF	0.73	75.2	34.4	47.3	7.1
CS/SPNF/HNTs-1.5	0.71	72.5	32.3	38.6	5.1
CS/SPNF/HNTs-5	0.70	67.5	29.0	34.3	4.6
CS/SPNF/HNTs-7.5	0.69	65.2	19.7	31.0	4.3
CS/SPNF/HNTs-10	0.68	70.5	30.0	28.8	4.2
CS/SPNF/SHNTs-1.5	0.74	73.5	28.9	50.0	12.0
CS/SPNF/SHNTs-5	0.75	70.5	19.6	61.0	20.0
CS/SPNF/SHNTs-7.5	0.77	69.2	18.3	78.7	22.0
CS/SPNF/SHNTs-10	0.78	71.7	25.3	55.0	12.9
SP-66	1.85	120	80.6	30.1	0.8
SP-66/NF-OH	1.13	68.8	60.0	29.0	0.6
SP-66/NF-PDA-7.5	1.02	26.0	25.2	67.5	3.1
SP-66/NF-PDA-9.5	0.98	21.9	23.2	75.5	4.1
SP-58/NF-PDA-8.5	0.85	17.3	13.3	81.6	5.2
SP-66/NF-PDA-8.5	0.95	20.5	14.5	89.2	5.6
SP-74/NF-PDA-8.5	1.13	24.9	20.3	105.8	5.7
SP-82/NF-PDA-8.5	1.28	30.1	26.0	127.0	6.3

The hydrated proton conductivity at different temperatures is shown in Fig. 5.26b. SP-66 attains a conductivity of about 3.15 mS cm^{-1} at 20 °C, and by comparison, SP-66/NF-OH attains a close conductivity of 2.58 mS cm^{-1} in spite of the weakly conductive NF-OH. This should be ascribed to the enriched $–SO_3H$ groups in SPEEK matrix into interfacial paths induced by the –OH groups on nanofiber surface. Meanwhile, the decreased crystalline degree reduces the energy barrier for proton transfer within the matrix and thus helps the proton migration. In comparison, the modification of NF-OH into NF-PDA-*X* bearing PDA layer and nanoparticle improves the proton conductivity of SP-66/NF-PDA-7.5 to 3.92 mS cm^{-1} with an enhancement of 24.4%. This might be because that the nanoparticle tunes the chain mobility and stacking of the polymer matrix and creates new nanoparticle/matrix interface, thus providing additional proton-conducting paths. By increasing the content of PDA, SP-66/NF-PDA-8.5 and SP-66/NF-PDA-9.5 acquire much higher conductivity of 7.27 and 4.73 mS cm^{-1}, with the enhancement of 130.8% and 50.2%, respectively. Similarly, increasing the sulfonation degree of SPEEK could also improve the proton conductivity of NFCM. Considering the relatively low water uptake and swelling

degree, the enhanced conductivity should result from the increase of Grotthuss-type proton transfer. The formed acid–base pairs act as efficient hopping sites along nanofiber surface and particle surface, forming two conducting paths. Meanwhile, the more distinct difference is achieved when the membrane is tested under anhydrous condition, and SP-66/NF-PDA-8.5 acquires an 8.0 times increment of proton conductivity from 0.96 mS cm^{-1} (SP-66) to 7.70 mS cm^{-1} at 100 °C, while the conductivity of SP-66/NF-OH is only 0.77 mS cm^{-1} under identical condition (Fig. 5.26b). The proton conduction ability continuously elevates with the temperature due to the promoted motion of hopping sites. However, the high-energy barrier for Grotthuss-type transfer makes the NFCM display higher E_a value. For example, the E_a value for SP-66, SP-66/NF-OH, and SP-66/NF-PDA-8.5 is 13.5, 15.9, and 20.8 kJ mol^{-1} under hydrous condition, respectively, and they alter to 21.8, 22.3, and 28.2 kJ mol^{-1} under anhydrous condition (Fig. 5.26c, d). Meanwhile, favorable structural stability endows membrane with excellent conductivity stability.

Table 5.2 summarizes the *IEC*, water uptake, area swelling, and proton conductivity of two kinds of NFCM, and it could be found that SPEEK-filled NFCM exhibits higher proton conductivity under hydrated condition because of the unique nanophase

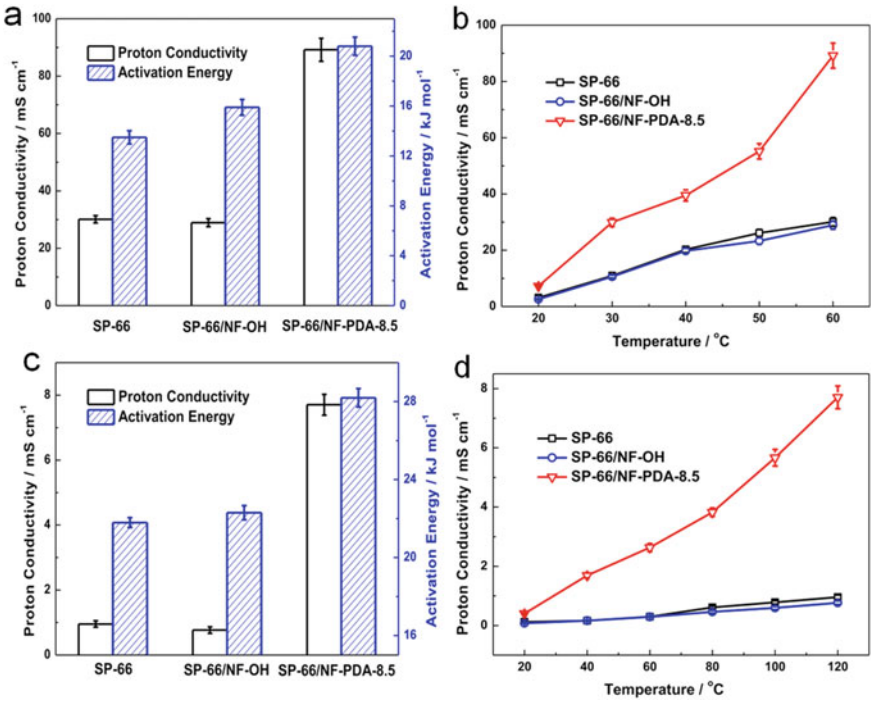

Fig. 5.26 **a** Hydrated proton conductivity at 60 °C and energy activation value of membrane. **b** Temperature-dependent conductivity of membrane under 100% RH. **c** Anhydrous proton conductivity at 120 °C and energy activation value of membrane. **d** Temperature-dependent conductivity of membrane under 0% RH. Copyright (2016), Elsevier [95]

separation of SPEEK, while CS-filled NFCM shows favorable anhydrous proton conductivity, which originates from the more distinctly arranged acid–base pairs. Beneficial from the organic–inorganic hybrid structure of NF-PDA, the relevant NFCM attains high swelling resistance ability.

In conclusion, we report an attempt for highly conductive nanofibrous composite membrane by incorporating nanofiller (nanotube or nanoparticle) into polymer matrix, followed by incorporating them into nanofiber mat. The systemic characterizations of NFCM confirm that the plenty of acid–base pairs are assembled onto the surface of nanofiber and nanofiller, improving the thermal and structural stability of NFCM by inhibiting the motion of polymer chain. In addition, these pairs offer facile dual-interfacial conduction paths to NFCM by means of the overlapped nanofiber and high surface area nanofiller, thus donating much higher proton conductivity to NFCM, especially under anhydrous environment. Meanwhile, the microstructure and transfer property of NFCM could be tuned by the content of nanofiller or the loading of conductive groups on polymer. Both the two kinds of NFCM (CS/SPNF/SHNTs-*X* and SP-*Z*/NF-PDA-*Y*) achieve obviously enhanced proton conduction ability due to the incorporation of nanofiller (nanotube and nanoparticle) under hydrated and anhydrous conditions, which are also much higher than those of the pristine casting membrane. Considering the facile preparation process and obvious enhanced performance, the present study on the construction of dual-interfacial pathways might provide a potential strategy on the design of nanofibrous composite membrane with controlled transfer property for various application.

5.6 Quantum Dot-Incorporated Nanofiber-Based Composite Membrane

QDs were prepared by microwave-assisted condensation of CA and DETA. PQD: CA (0.96 g) was fully dissolved in water (2.0 g). Then, DETA (540 μL) was added to the above solution. After ultrasonic treatment for 5 min, the mixture was heated in a microwave oven at 750 W for another 5 min. The products were rinsed in ethanol for several times to remove residual small molecules and were dispersed in water. Finally, the aqueous solution was freeze-dried for 48 h to get the resultant PQD. GQD: CA (0.96 g) was mixed uniformly with a mixed solvent composed of glycerol (1.5 g) and water (0.5 g). The mixed solvent ensured higher reaction temperatures (above 100 °C) and thus carbonized the O−/N−containing groups under microwave radiation. And the subsequent preparation steps were similar to those described in PQD.

Hybrid nanofiber mats were fabricated by blend spinning of QDs and SPEEK: required amount of SPEEK (1.0 g) was dissolved in DMF (2.7 g) and THF (1.2 g) under agitation for 4 h at room temperature. Simultaneously, a certain amount of QDs and DMF (2 g) was mixed together and did an agitation and ultrasonic treatment alternately an hour each. Then, SPEEK solution was poured into QDs solution and

continued to stir for 24 h to get homogeneous electrospinning solution. The obtained solution was electrospun at 25 kV with the tip-to-collector distance and feed rate of 20 cm and 0.0005 mm min^{-1}, respectively. Finally, nanofiber mats were collected on a rotating drum covering with aluminum foil. The resultant hybrid nanofiber mats with various weight ratios of QDs and SPEEK were abbreviated as SP/PQD-*X* (*X* = 20%) and SP/GQD-*X* (*X* = 20%), respectively. For comparison, neat SPEEK electrospun mat without QDs was also prepared similarly and denoted as SP.

The composite membranes were fabricated by the solution casting method [70]. CS (1.0 g) was added to acetic acid aqueous solution (1:99 weight ratio for acetic acid and water), and the mixture was heated at 60 °C until dissolved. Then, the nanofiber mat was placed on a clean glass plate fitted with edge, and the above CS solution was cautiously added, dropwise, into mat and allowed it dry naturally. The casting and drying processes were repeated several times, in order to ensure that the nanofiber mat was well embedded in CS matrix, while without extra CS layer. Meanwhile, compared with the casting process of directly impregnating nanofiber into CS solution, this process could effectively avoid the destruction of closely contacted nanofiber structure caused by CS solution swelling and intercalation. The membrane was transferred into 1 M H_2SO_4 solution and cross-linked. After a period of 24 h, the membrane was washed with water for three times followed by drying at 60 °C and denoted as CS/SP/PQD or CS/SP/GQD. Pure membrane without QDs was also fabricated via the same procedure and was abbreviated as CS/SP.

The QDs were prepared via one-pot, microwave-assisted condensation of citric acid and diethylenetriamine. We have synthesized two kinds of QDs (PQD and GQD) with different carbonation degree as nanofillers, for evaluating the effect of functional groups on nanofiber structure and proton conduction. A series of hybrid nanofiber mats were prepared by electrospinning QDs and SPEEK blend solution (Fig. 5.27). The electrospinning solution was obtained by pouring SPEEK solution into QDs solution.

Figures 5.28a–c show the photographic images of SP, SP/PQD-10%, and SP/GQD-10% under daylight and 365 nm UV. Compared with SP, the color of

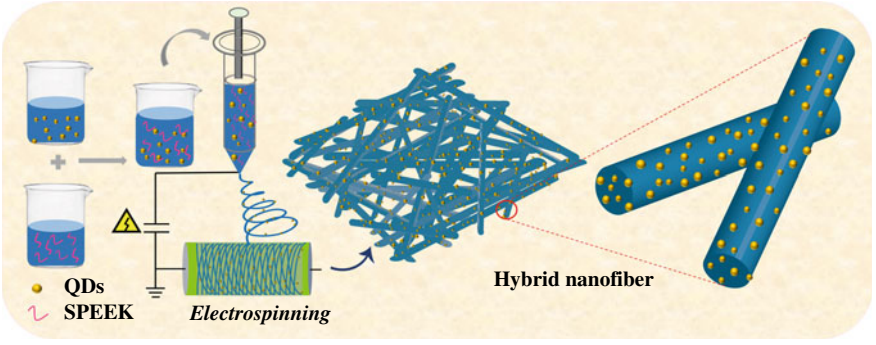

Fig. 5.27 Schematic illustration of electrospinning of hybrid nanofiber. Copyright (2020), Elsevier [96]

hybrid nanofiber becomes dark under daylight, and distinct photoluminescence effect is observed for SP/PQD-10% and SP/GQD-10% under 365 nm UV. SEM images of the hybrid nanofibers indicate the retention of their fibrous morphology after the incorporation of QDs (Figs. 5.28d–f). The uniform diameter of SP/PQD-*X* further confirms the homogeneous dispersion of PQD in nanofiber due to the matched structural size. Meantime, it is observed that the surfaces of SP and SP/PQD nanofiber are smooth. In comparison, the surface of SP/GQD becomes rough with uneven diameter. These phenomena should result from the higher carbonation degree of GQD and thus inferior compatibility with SPEEK, while it should note that, the diameter of nanofiber decreases after PQD incorporation (Fig. 5.28e) and further decreases with the increase of PQD loading amount. This decrease should originate from the functional groups in PQD, which elevates the charge density of electrospinning solution and thus strengthens the elongation force imposed on the jet [71]. Collectively, these phenomena demonstrate the presence and uniform distribution of QDs in hybrid nanofiber mat, which could contribute to the construction of continuous conduction pathways at QDs-SPEEK interfaces.

Next, HNFCMs were fabricated by embedding CS matrix into the hybrid nanofiber mats. The surficial and cross-sectional SEM images of CS/SP/PQD-10% are shown in Fig 5.29a, b, respectively, where the closely linked and defect-free morphologies indicate the strong interfacial interaction between hybrid nanofiber and CS matrix [72, 73]. Such interaction was then detected by DSC analysis, as depicted in Fig. 5.29c. The temperature of DSC endothermic peak for pure CS is 218.4 °C, while the temperature increases to 229.1 °C for CS/SP. This should be attributed to the formed acid–base pairs along the surface of SP nanofiber, which restrain the chain mobility of CS [74–76]. The hypothesis can be verified by the variation of DSC endothermic peak of HNFCMs. The lower content of surficial $–SO_3H$ groups of SP/GQD-10% gives a decreased temperature at 226.2 °C. This decrease results from the reduction of acid–base pairs at the nanofiber-matrix interface. Likewise, CS/SP/PQD-10% attains a

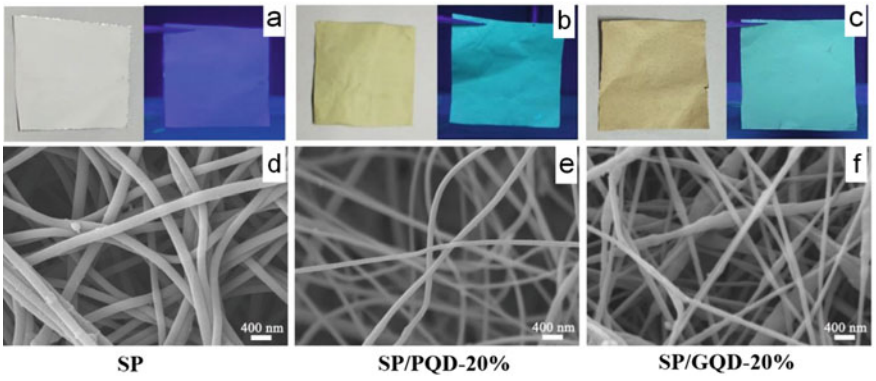

Fig. 5.28 Photographic images of **a** SP, **b** SP/PQD-10%, and **c** SP/GQD-10% under daylight (left) and 365 nm UV (right). SEM images of **d** SP, **e** SP/PQD-10%, and **f** SP/GQD-10%. Copyright (2020), Elsevier [96]

further decreased temperature of DSC endothermic peak at 223.7 °C. These findings are in accordance with the variation of *IEC* values of membranes (Fig. 5.29d). Compared with nanofiber, NFCMs show obviously reduction in *IEC* value because of the formation of acid–base pairs at the nanofiber-matrix interface. For instance, the *IEC* values of CS/SP, CS/SP/GQD-10%, and CS/SP/PQD-10% are reduced by 48%, 45%, and 34%, respectively, to 0.65, 0.54, and 0.47 mmol g^{-1}. The more striking reduction of *IEC* value for CS/SP roots in the more proportion of $–SO_3H$ groups on the surface of SP nanofiber. The water uptake and area swelling of CS/SP are 64% and 59%, respectively. By comparison, CS/SP/PQD-*X* obtains increased water uptake but decreased area swelling. For example, the water uptake and area swelling of CS/SP/PQD-30% are 85% and 46%, which are, respectively, 33% higher and 22% lower, than those of CS/SP. These phenomena can be attributed to the abundant hydrophilic functional groups ($–CO_2H$ and $–NH–/–NH_2$) in PQD and inhibited chain mobility of CS matrix.

The presence of PQD inside nanofiber highly enhances the proton conduction properties of HNFCMs, especially at vertical direction. The through-plane conductivity of HNFCMs under 100% RH is displayed in Fig. 5.30a. CS/SP obtains a through-plane conductivity of 158 mS cm^{-1} at 90 °C and 100% RH. In comparison,

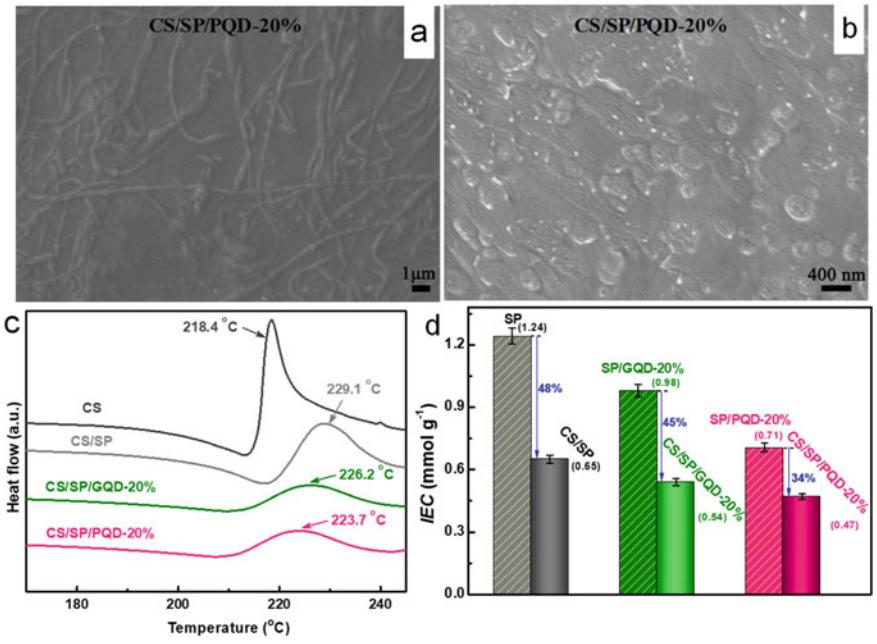

Fig. 5.29 **a** Surfacial and **b** cross-sectional SEM images of CS/SP/PQD-10%. **c** DSC curves of CS, CS/SP, CS/SP/PQD-10%, and CS/SP/GQD-10%. **d** Comparison of *IEC* values between nanofiber (SP, SP/GQD-10%, and SP/PQD-10%) and corresponding membrane (CS/SP, CS/SP/GQD-10%, and CS/SP/PQD-10%). Copyright (2020), Elsevier [96]

the incorporation of PQD confers HNFCMs significantly enhanced through-plane proton conduction ability, and CS/SP/PQD-10% attains a through-plane conductivity of 327 mS cm^{-1} at 90 °C and 100% RH. With the increase of PQD loading amount, the through-plane conductivity further increases. The conductivity of CS/SP/PQD-30% reaches 456 mS cm^{-1}, almost 3 times of that of CS/SP. These phenomena should result from the formed acid–base pairs between the filled PQD and the trapped $–SO_3H$ groups inside nanofiber, as well as the inherent acid–base pairs in PQD. As for these pairs, electrostatic interactions between the linked donors ($–SO_3H$/–COOH) and acceptors (–NH–/$–NH_2$) would promote the protonation/deprotonation process. In such a way, protons could shuttle rapidly via the low-barrier acid–base transfer pathways in through-plane direction. Then, the transfer E_a was calculated by fitting temperature-dependent conductivity. Figure 5.30a shows that E_a value sharply decreases from 15.8 kJ mol^{-1} for CS/SP to 7.82 kJ mol^{-1} for CS/SP/PQD-30%. Furthermore, these low-barrier pathways allow HNFCMs exhibiting superior proton conduction ability under low RH. CS/SP/PQD-30% obtains a through-plane conductivity of 166 mS cm^{-1} at 80 °C and 20% RH, which is 163% higher than that of CS/SP (63 mS cm^{-1}) under identical conditions (Fig. 5.30b). As plotted in Fig. 5.30c, compared with CS/SP, the E_a values decrease sharply for HNFCMs both at vertical and parallel directions. Notably, the reduction at vertical direction is more obvious than that at parallel direction. The E_a values for CS/SP at vertical direction and parallel direction are 24.2 and 13.5 kJ mol^{-1}, respectively. Compared with CS/SP, the E_a value for CS/SP/PQD-30% at vertical direction decreases by 66.0%, to 8.23 kJ mol^{-1}, while the E_a value at parallel direction decreases by 62.7%, to 5.03 kJ mol^{-1}. As a result, the transfer anisotropy coefficient ($\sigma_{\parallel}/\sigma_{\perp}$) of HNFCMs reduces significantly. Figure 5.30d depicts that the transfer anisotropy coefficient sharply decreases to 1.39 for CS/SP/PQD-30% from 2.46 for CS/SP.

The highly enhanced through-plane proton conduction then permits HNFCMs excellent hydrogen fuel cell performances. For better comparison, CS/SP, CS/SP/PQD-10%, and CS/SP/GQD-10% are selected to evaluate the fuel cell performances, and the current (I)−voltage (V) polarization and power density curves at 60 °C are shown in Fig. 5.31. Under 75% RH condition, CS/SP achieves maximum current and power density of 1242 mA cm^{-1} and 382 mW cm^{-1}, respectively. In comparison, HNFCMs obtain significantly enhanced fuel cell performances. CS/SP/GQD-10% possesses maximum current and power density of 1910 mA cm^{-1} and 570 mW cm^{-1}, respectively, while CS/SP/PQD-10% exhibits further increased maximum current (2364 mA cm^{-1}) and power density (775 mW cm^{-1}), which are 90% and 100% improvement than those of CS/SP. Notably, the maximum current and power density of CS/SP/PQD-10% are 2.4 and 2.6 times, respectively, of those of Nafion 117 (1003 mA cm^{-1} and 296 mW cm^{-1}). The variation in maximum current and power density positively correlates with their through-plane conductivity, indicating the function of QDs on reducing the electrolyte resistance [75, 77]. Next, the fuel cell performances under low humidity, which are critical for the development of elevated temperature hydrogen fuel cell, are also probed as shown in Fig. 5.5b. Under 0% RH, the HNFCMs also show remarkable fuel cell performances. Compared with CS/SP, both the maximum current density and the maximum power

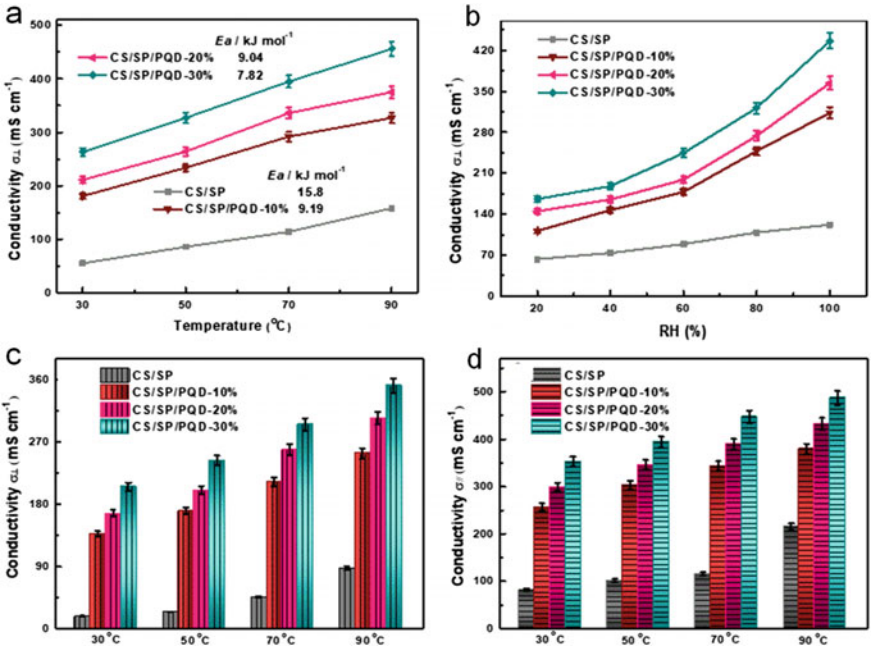

Fig. 5.30 **a** Through-plane conductivity ($\sigma_{\perp}$) measured at 100% RH and different temperatures. **b** Through-plane conductivity ($\sigma_{\perp}$) measured at 80 °C and different RH. **c** Through-plane conductivity ($\sigma_{\perp}$) measured at 0% RH and different temperatures. **d** In-plane conductivity ($\sigma_{\parallel}$) measured at 0% RH and different temperatures. Copyright (2020), Elsevier [96]

density of CS/SP/PQD − 10% increase by 47.0% (1377 vs. 937 mA cm^{-1} and 413 vs. 282 mW cm^{-1}, respectively).

In summary, we demonstrate a fabrication of novel hybrid SPEEK nanofiber mat by uniformly dispersing QDs, followed by incorporating CS matrix to prepare

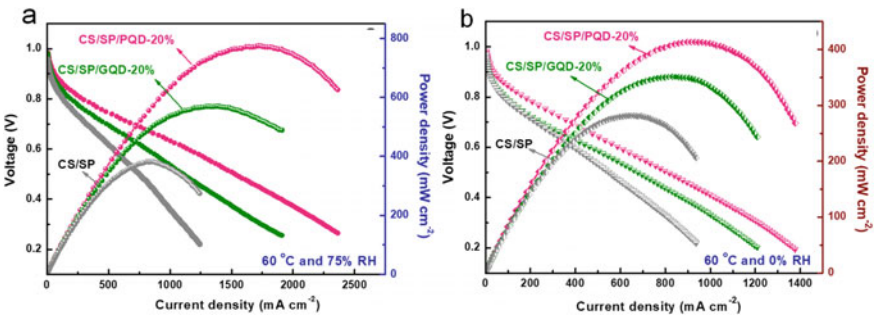

Fig. 5.31 Fuel cell polarization curves and power density curves of CS/SP, CS/SP/PQD—10%, and CS/SP/GQD—10% measured at: **a** 60 °C, 75% RH; **b** 60 °C, 0% RH. Copyright (2020), Elsevier [96]

HNFCM. The 2–5 nm structural size makes QDs ideal candidate over common nanofillers for hybridizing the nanofiber. Moreover, the –NH–/–NH_2 groups in QDs induce a transfer of –SO_3H groups of SPEEK from the nanofiber surface to interior and then form ordered acid–base pairs. Together with the abundant –CO_2H groups, these permit HNFCM significantly enhanced through-plane conductivity and decreased transfer anisotropy. Particularly, CS/SP/PQD-30% shows a nearly 200% enhancement of through-plane conductivity over CS/SP, reaching 456 mS cm^{-1} at 90 °C and 100% RH. The transfer anisotropy of CS/SP/PQD-30%, thus, reduces from 2.46 for CS/SP to 1.39. Importantly, the maximum power density and current density of HNFCM reach up to 775 mW cm^{-2} and 2364 mA cm^{-2}, respectively (60 °C and 75% RH), which are 100 and 90% higher than those of CS/SP. Considering the tailorable chemical composition of QDs, this study may offer a strategy to conquer the transfer anisotropy of NFCM, helpful to expand the application scope of nanofiber-based materials in energy-related fields.

5.7 Porous Nanofiber-Based Composite Membrane

The preparation process of electrospinning solution comprised the following steps: first, the 7 wt% PVA solution was obtained by dissolving a specific mass of solid PVA into water, and the mixture was gently stirred at 60 °C for 1 h, followed by adding quantitative PEI (the mass ratio of PVA and PEI was 1:1) with continuous stirring for 30 min. Simultaneously, a certain amount ILs and H_2O (2.0 g) were mixed together and stirred for 12 h to ensure that ILs uniformly self-assemble into micelles. Afterward, IL solution was dispersed in the above solution with stirring for 12 h to get a resultant electrospinning solution. The solution was then electrospun at 25 kV for 12 h with a feed rate of 0.5 μm min^{-1} and a working distance of 15 cm. The obtained nanofiber mats were cross-linked by GA vapor at 40 °C and then immersed into 5% (v/v) (for [C_2mim][Tf_2N] micelles as the template) or 15% (v/v) (for [C_8mim][Tf_2N] micelles as the template) methanol solution for 24 h at 25 °C to remove the IL micelles. Finally, porous nanofibers were attained by vacuum cryodesiccation for 24 h and denoted as PVA/PEI/$C_{X\text{-}Y}$, where C_X ($X = 2$ and 8) represented the ILs of [C_2mim][Tf_2N] and [C8mim][Tf_2N], respectively, and Y ($Y = 10$, 20, and 30 wt%) referred to the ILs loading amount. For comparison, nonporous nanofibers without adding ILs were prepared using the similar method and designated as PVA/PEI.

SPEEK was first fabricated according to the method in literature, and the sulfonation degree was set to be 70% [78]. Then SPEEK solution (4.5 wt%) was prepared by dissolving SPEEK powders in DMF. In this study, both NFCM and PNFCM were prepared by casting SPEEK solution into nanofiber mats. Concretely, SPEEK solution was casted on the nanofiber mats dropwise, followed by vacuum-drying at 60 °C for 12 h and then 80 °C for another 12 h. The casting and drying processes were repeated several times, in order to ensure that the nanofiber mats were well embedded in SPEEK matrix, while without extra SPEEK layer. It is worth mentioning that,

the PNFCM should qualitatively possess lower nanofiber mass loading and higher SPEEK mass loading when compared with NFCM because of the porous structure. The obtained membranes were denoted as SP@PVA/PEI/$C_{X\text{-}Y}$. For comparison, the dense composite membrane was also fabricated similarly and abbreviated as SP@PVA/PEI. SPEEK control membrane (SP) was prepared according to method in literature [79]. The average thickness of as-prepared membranes was in the range of 83–90 μm.

The porous nanofibers were fabricated via the union of electrospinning and emulsion template method, as shown in Scheme 1. Firstly, the hydrophobic IL were added into water under vigorous agitation, so as to make ILs fully assemble into micelles. Then, the IL emulsion was incorporated into the well-dispersed PVA/PEI solution with strong stir, for ensuring the homogeneous distribution of IL micelles in electrospinning solution. Here, two kinds of ILs with different hydrophobicity, long alkyl chain contained [C_8mim][Tf_2N] and short alkyl chain contained [C_2mim][Tf_2N], were chosen for elucidating the mechanism of nanopore formation. After electrospinning, the nanofiber mats were exposed to GA vapor for a cross-linked structure and thus adequate water stability. The cross-linked nanofiber mats were then immersed in methanol solution to exchange IL micelles. Afterward, the nanofiber mats were exposed to freeze-drying, for removing solvents and retaining solvent-occupied nanopores. The maximum IL loading amount of 30 wt% was selected, because higher IL loading amount would lead to unacceptable mechanical strength of nanofiber (Fig. 5.32).

SEM image in Fig. 5.33a reveals that PVA/PEI/C_2-30 possesses uniformly distributed nanopores with size of 15–40 nm. High-magnification SEM image shows that the nanopores form interpenetrating nanochannels inside the nanofiber (Fig. 5.33b). Cross-sectional TEM image of PVA/PEI/C_2-30 further confirms the

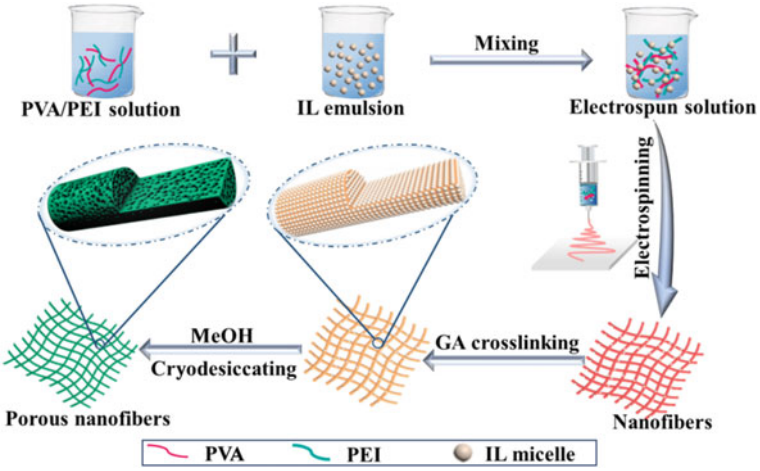

Fig. 5.32 Schematic illustration of the synthesis of porous nanofibers. Copyright (2020), Royal Society of Chemistry [11]

above findings, where the nanopores form interpenetrating networks (Fig. 5.33c). Compared with PVA/PEI/C_2-30, PVA/PEI/C_8-30 presents larger nanopores with size of 20–50 nm. This phenomenon should be attributed to the difference in alkyl chain length and thus the hydrophobicity of ILs. [C_8mim][Tf_2N] with longer alkyl chain and stronger hydrophobicity tends to form larger micelle in water-based electrospinning solution when compared to [C_2mim][Tf_2N]. This can be demonstrated by the optical photographs and microscope images of electrospinning solution (Fig. 5.33d). The PVA/PEI/C_2-30 solution is translucent with a turbidity of 57 nephelometric turbidity unit (NTU), and the IL micelles are uniformly dispersed with an average diameter of 15−40 nm. In comparison, PVA/PEI/C_8-30 solution presents higher turbidity of 70 NTU and larger micelles with size of 20–50 nm.

Figure 5.33e reveals that PVA/PEI exhibits a transitional isotherm behavior between type-II and type-IV, with a small hysteresis loop (P/P_o: from 0.7 to 0.98) and low surface area (7.35 $m^2\ g^{-1}$), which indicates the absence of nanopores. By contrast, porous nanofibers show type-IV isotherm behaviors with larger hysteresis loops (P/P_o: 0.4–0.9). These demonstrate the presence of tubular nanopores [80–82]. The existence of nanopores significantly enhances the surface area and total pore volume of porous nanofibers. PVA/PEI/C_2-10% attains a surface area of 22.47 $m^2\ g^{-1}$ and total pore volume of 0.093 $cm^3\ g^{-1}$. Furthermore, increasing the IL loading amount elevates the surface area and total pore volume. The surface area and total pore volume of PVA/PEI/C_2-30% increase to 78.83 $m^2\ g^{-1}$ and 0.287 $cm^3\ g^{-1}$, respectively. Meanwhile, the nanopore size also increases with IL loading amount. The average pore size increases from 17.1 nm for PVA/PEI/C_2-10% to 34.8 nm for

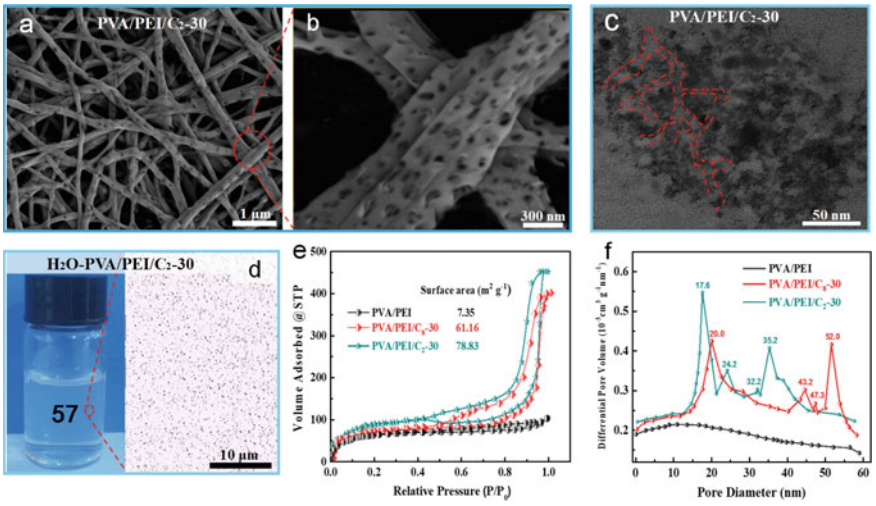

Fig. 5.33 **a**, **b** SEM images of PVA/PEI/C_2-30. **c** Cross-sectional TEM image of PVA/PEI/C_2-30. **d** Optical photograph and microscope image of PVA/PEI/C_2-30 electrospinning solution. **e** Nitrogen adsorption/desorption isotherms. **f** Pore size distribution curves of PVA/PEI, PVA/PEI/C_2-30, and PVA/PEI/C_8-30. Copyright (2020), Royal Society of Chemistry [11]

PVA/PEI/C_2-30. Compared with PVA/PEI/C_2-*Y*, the stronger hydrophobicity and larger IL micelles of [C_8mim][Tf_2N] confer PVA/PEI/C_8-*Y* larger nanopores. The average pore size of PVA/PEI/C_8-30 reaches 45.0 nm. These interconnected, large nanopores would permit a full and uniform entrance of SPEEK matrix and thus better through-plane proton conduction of composite membrane.

Cross-sectional TEM image of sliced SP@PVA/PEI/C_2-30 further demonstrates the entrance of SPEEK matrix into nanopores (Fig. 5.34a). Within the nanopore, obvious nanophase separation structure of SPEEK matrix is observed (Fig. 5.34b), where the dark and bright areas represent the ionic and backbone nanophases, respectively [83, 84]. Besides, the ionic nanophase is found to aggregate mainly along the nanopore wall. This indicates the generation of interfacial interaction between SP and PVA/PEI, which is verified by FTIR results (Fig. 5.34c). Compared with SP, SP@PVA/PEI displays a new characteristic peak at 947 cm^{-1}, corresponding to the symmetric stretching of –S–O–. Such finding is ascribed to the base groups (−NH−/−NH_2) in PEI that enable aggregation and dissociation of –SO_3H along nanofiber-matrix interface and the formation of acid–base pairs [85]. Compared with SP@PVA/PEI, the peak intensity of –S–O– is enhanced for PNFCM and further enhanced with IL loading amount (from 10 to 30%) due to the increased BET surface area and thus interfacial area. The strong interfacial interaction also restrains the motility of SPEEK chain [86, 87]. DSC curves in Fig. 5.34d show that the endothermic peak for dense SP is at 211 °C, which elevates to 215 °C for SP@PVA/PEI. In comparison, the temperature further increases for PNFCM. For example, the temperature increases in the order of SP@PVA/PEI/C_2-10% (219 °C) < SP@PVA/PEI/C_2-10 (223 °C) < SP@PVA/PEI/C_2-30 (229 °C). The formation of acid–base pairs then induces variation of *IEC* values of membranes [88]. Collectively, these results demonstrate that the interconnected, large nanopores of as-prepared nanofibers permit a full and uniform entrance of SPEEK matrix and thus the formation of 3D interpenetrating nanopore networks with enriched acid–base pairs.

Figure 5.35a exhibits the through-plane conductivity of SP@PVA/PEI and SP@PVA/PEI/C_2-*Y* at 100% RH as a function of temperature. SP@PVA/PEI attains a through-plane conductivity of 103 mS cm^{-1} at 80 °C and 100% RH. By comparison, SP@PVA/PEI/C_2-*Y* obtains highly enhanced through-plane conductivity, and the conductivity increases with IL loading amount. The through-plane conductivity of SP@PVA/PEI/C_2-30 reaches 561 mS cm^{-1}, which is 4.4 times higher than that of SP@PVA/PEI and superior to most of existing membranes. Considering the decreased *IEC* value and moderately enhanced water uptake, such drastic improvement in conduction should be mainly attributed to the 3D interpenetrating nanopore networks and the enriched acid–base pairs, which serve as low-energy barrier transfer highways in vertical direction. This speculation can be verified by the variation of E_a, which markedly decreases from 0.137 eV for SP@PVA/PEI to 0.076 eV for SP@PVA/PEI/C_2-30. SP@PVA/PEI/C_2-*Y* also exhibits highly enhanced through-plane conductivity under low humidity. Figure 5.35b shows that the through-plane conductivity of SP@PVA/PEI at 80 °C and 20% RH is only 34 mS cm^{-1}. In comparison, SP@PVA/PEI/C_2-30 achieves more than 10 times enhancement in conduction, reaching 370 mS cm^{-1}. Through a linear fitting of through-plane conductivity to

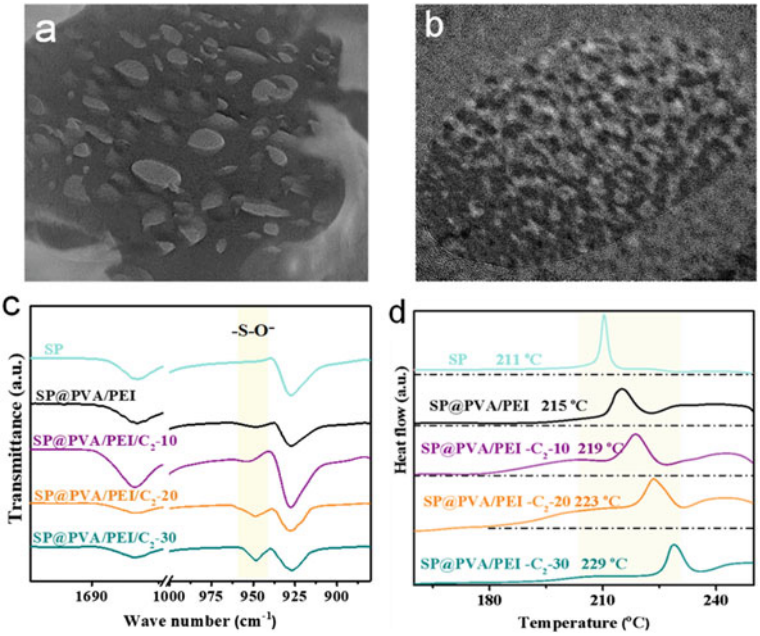

Fig. 5.34 Cross-sectional TEM images of SP@PVA/PEI/C_2-30 for **a** single nanofiber and **b** single nanopore. **c** FTIR spectra and **d** DSC curves of SP, SP@PVA/PEI, and SP@PVA/PEI/C_2-*Y*. Copyright (2020), Royal Society of Chemistry [11]

humidity, the slop is observed to descend from 1.65 for SP@PVA/PEI to 1.40 for SP@PVA/PEI/C_2-30, implying a weak dependence of proton conduction on water. This should be ascribed to the presence of abundant acid–base pairs within nanopore networks, which enables more proportion of Grotthuss-type proton migration in SP@PVA/PEI/C_2-30. This can be confirmed by a deuterium-related experiment (Fig. 5.35c). Both SP@PVA/PEI and SP@PVA/PEI/C_2-*Y* show decreased conductivity under D_2O atmosphere when compared with that under H_2O atmosphere, because of the involvement of heavier deuterium atom (*vs.* proton) in Grotthuss-type migration. Compared with SP@PVA/PEI (39.1%), SP@PVA/PEI/C_2-*Y* displays a higher reduction: 73.3% for SP@PVA/C_2-30. These suggest the more proportion of Grotthuss-type migration in SP@PVA/PEI/C_2-*Y*. The above hypothesis can be testified by the comparison of E_a under 0% RH and 100% RH (Fig. 5.35d). It is found that the conduction E_a for SP@PVA/PEI decreases by 25.1%, from 0.183 eV under 0% RH to 0.137 eV under 100% RH. By comparison, SP@PVA/PEI/C_2-30 displays a slight reduction of 7.3%, from 0.082 eV to 0.076 eV. These further confirm the more proportion of Grotthuss-type migration in SP@PVA PVA/PEI/C_2-*Y* under hydrated conditions.

Time-dependent conductivity at different RH in Fig. 5.35e reveals that SP@PVA/PEI/C_2-*Y* can reach faster balance (compared with SP@PVA/PEI) at each RH, indicating the stronger water absorbing ability of SP@PVA/PEI/C_2-*Y*.

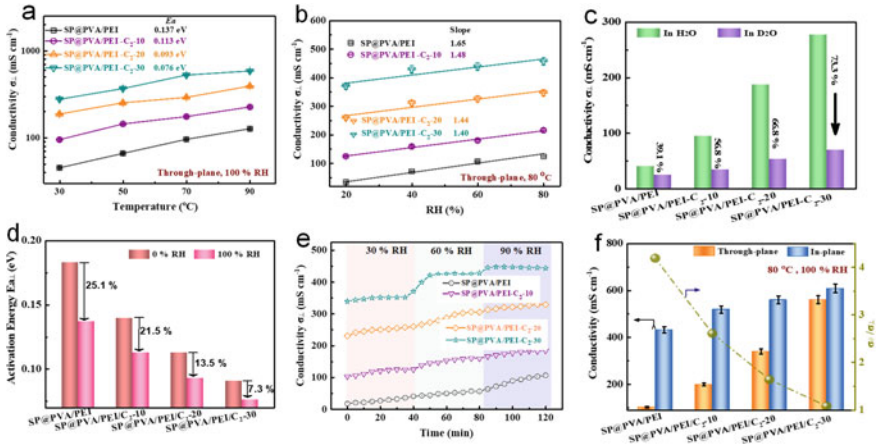

Fig. 5.35 Proton conduction properties of SP@PVA/PEI and SP@PVA/PEI/C_2-*Y*: **a** Temperature-dependent through-plane conductivity ($\sigma_{\perp}$) under 100% RH. **b** RH-dependent through-plane conductivity ($\sigma_{\perp}$) at 80 °C. **c** Proton conductivities under H_2O and D_2O vapor at 30 °C. **d** Comparison of transfer E_a under 0% RH and 100% RH at 80 °C. **e** Time-dependent through-plane conductivity ($\sigma_{\perp}$) under different RH at 80 °C for 120 min. **f** Transfer anisotropy coefficient ($\sigma_{\parallel}/\sigma_{\perp}$) at 80 °C and 100% RH. Copyright (2020), Royal Society of Chemistry [11]

In order to elucidate the underlying reason, water state was calculated from DSC curves. SP@PVA/PEI/C_2-30 achieves a significantly high-bound water ratio of 92.9%, which is much higher than that of SP@PVA/PEI (33.8%), highlighting the stronger water bonding ability. Figure 5.35f shows that the in-plane conductivity of SP@PVA/PEI/C_2-*Y* is also obviously enhanced when compared with SP@PVA/PEI, and the conductivity increases with IL loading amount. For example, the in-plane conductivity of SP@PVA/PEI/C_2-30 reaches 644 mS cm^{-1} under 80 °C and 100% RH, 39% higher than that of SP@PVA/PEI (463 mS cm^{-1}). However, this augment is inferior to that of through-plane direction (440%). As a result, the transfer anisotropy coefficient of SP@PVA/PEI/C_2-*Y* is significantly reduced. SP@PVA/PEI attains a transfer anisotropy coefficient of 4.19 at 80 °C and 100% RH. In comparison, the transfer anisotropy coefficient of SP@PVA/PEI/-C_2-30 drastically reduces to 1.08, ranking one of the lowest values for NFCM.

In order to investigate the effect of pore structure on proton conduction, proton conductivity and transfer anisotropy of SP@PVA/PEI/C_8-*Y* were also measured and compared with SP@PVA/PEI/C_2-*Y* systematically. Figure 5.36a reveals that SP@PVA/PEI/C_8-30 obtains a 285% enhancement in through-plane conductivity (~397 mS cm^{-1} at 80 °C and 100% RH) when compared with SP@PVA/PEI. And the E_a reduces from 0.137 eV for SP@PVA/PEI to 0.091 eV for SP@PVA/PEI/C_8-30 (Fig. 5.36a). Figure 5.36b shows that SP@PVA/PEI/C_8-*Y* also obtains elevated through-plane conductivity under low humidity and displays weaker dependence of proton conduction on humidity. SP@PVA/PEI/C_8-30 acquires a through-plane conductivity of 288 mS cm^{-1} at 80 °C and 20% RH, 7.5 times higher than

that of SP@PVA/PEI. Meantime, the slope of SP@PVA/PEI/C_8-30 decreases to 1.44, indicating weakened water dependence of proton conduction. Similarly, SP@PVA/PEI/C_8-30 achieves an ultralow transfer anisotropy value of 1.49 at 80 °C and 100% RH (Fig. 5.36c). Collectively, these performances are inferior to those of SP@PVA/PEI/C_2-*Y*, because of the smaller BET surface area and thereby fewer vertical transfer pathways of SP@PVA/PEI/C_8-*Y*. Additionally, SP was prepared and the conductivity was measured. The control membrane attains a through-plane proton conductivity of 45 mS cm^{-1} and in-plane proton conductivity of 50 mS cm^{-1} at 80 °C and 100% RH. And the transfer anisotropy coefficient is ~1.11, which suggests an almost isotropous proton transfer in SP. Compared with SP, SP@PVA/PEI obtains a much higher in-plane proton conductivity (463 mS cm^{-1}) due to the constructed transfer pathways along nanofiber-matrix interfaces in parallel direction, while the through-plane proton conductivity is 103 mS cm^{-1}, and therefore, like most NFCMs, SP@PVA/PEI has higher transfer anisotropy coefficient (4.19) than SP. As for PNFCM, the presence of 3D interpenetrating nanopore networks and the enriched acid–base pairs obviously enhance through-plane conduction and thereby reduce the transfer anisotropy coefficient. For instance, SP@PVA/PEI/C_2-30 shows the transfer anisotropy coefficient of 1.08, comparable to SP.

Hydrogen fuel cell performances of the membranes were measured at 60 °C. Figure 5.37 reveals that the open-circuit voltages of all membranes are above 0.9 V, implying acceptable gas barrier ability. For further confirmation, the hydrogen and oxygen permeabilities of as-prepared membranes at different temperatures were measured. Under 80% RH, the maximum current density and power density of SP@PVA/PEI are 960 mA cm^{-1} and 246 mW cm^{-1}, respectively (Fig. 5.37a). Compared with SP@PVA/PEI, SP@PVA/PEI/C_8-30 exhibits boosted fuel cell performances with maximum current density of 1637 mA cm^{-1} and power density of 524 mW cm^{-1}. The drastic improvement derives from the significantly enhanced through-plane proton conduction and thus accelerated cathode reaction. In comparison, SP@PVA/PEI/C_2-30 attains further enhanced fuel cell performance because of the better through-plane proton conduction property. The maximum current density and power density elevate to 1998 mA cm^{-1} and 723 mW cm^{-1}, respectively, which

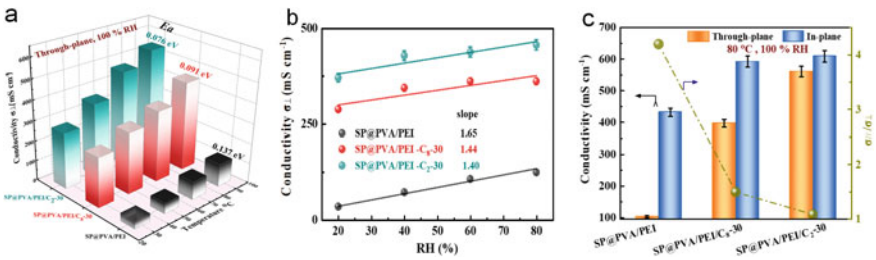

Fig. 5.36 Proton conduction properties of SP@PVA/PEI, SP@PVA/PEI/C_8-30, and SP@PVA/PEI/C_2-30: **a** Temperature-dependent through-plane conductivity ($\sigma_\perp$) under 100% RH. **b** RH-dependent through-plane conductivity ($\sigma_\perp$) at 80 °C. **c** Transfer anisotropy coefficient ($\sigma_\parallel/\sigma_\perp$) at 80 °C and 100% RH. Copyright (2020), Royal Society of Chemistry [11]

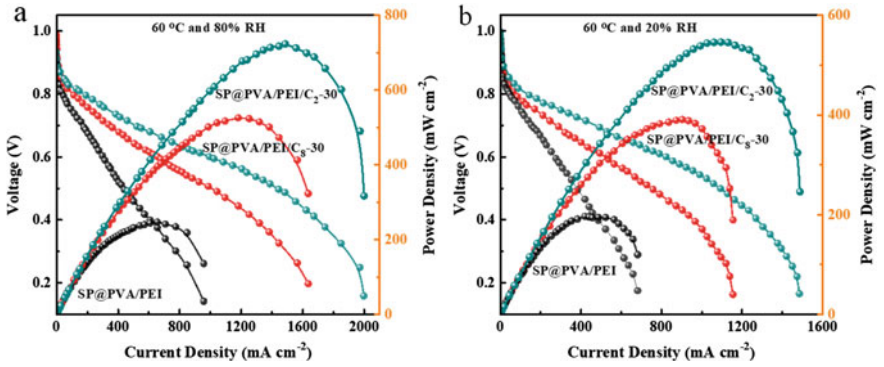

Fig. 5.37 Hydrogen fuel cell performances of SP@PVA/PEI, SP@PVA/PEI/C_8-30, and SP@PVA/PEI/C_2-30 at 60 °C: **a** under 80% RH and **b** under 20% RH. Copyright (2020), Royal Society of Chemistry [11]

are 1.1 and 2.0 times higher than SP@PVA/PEI. PNFCMs also exhibit enhanced fuel cell performances under low humidity. Under 20% RH, SP@PVA/PEI/C_2-30 achieves the maximum current density and power density of 1487 mA cm^{-1} and 546 mW cm^{-1}, respectively, which are 1.2 and 1.8 times higher than those of SP@PVA/PEI (Fig. 5.37b). Significantly, these performances are superior to most of NFCMs, highlighting the advantages of 3D interpenetrating nanopore networks in as-prepared PNFCMs [89–92].

In summary, we demonstrate a strategy for significantly enhancing the through-plane proton conduction and reducing transfer anisotropy of NFCMs, enabled by building 3D interpenetrating nanopore networks inside the nanofiber. Within the water-based electrospinning solution (PVA/PEI), hydrophobic ILs can self-assemble into 15–50 nm micelles. These IL micelles then act as templates and permit the formation of interconnected, large nanopores (average pore size: 17–45 nm), followed by full entrance of SPEEK matrix. The constructed 3D interpenetrating nanopore networks and the enriched acid–base pairs, serving as proton transfer highways in vertical direction, remarkably boost the through-plane proton conduction and H_2 fuel cell performances of PNFCMs. SP@PVA/PEI/C_2-30 achieves an ultra-high through-plane conductivity of 561 mS cm^{-1} at 80 °C and 100% RH, 440% higher than that of SP@PVA/PEI, and superior to most of the reported works. The transfer anisotropy coefficient dramatically decreases to 1.08 for SP@PVA/PEI/C_2-30 from 4.19 for SP@PVA/PEI, realizing an almost isotropic proton conduction. The maximum current density and power density of SP@PVA/PEI/C_2-30 reach, respectively, 1998 mA cm^{-1} and 723 mW cm^{-1}, 1.1 and 2.0 times higher than those of SP@PVA/PEI. Meanwhile, PNFCMs also display excellent mechanical property and operational stability. Furthermore, the as-prepared porous nanofibers with 3D interpenetrating nanopore networks, featuring high BET surface area and mechanical stability, should be attractive in many fields, including adsorption, catalysis, energy storage, etc.

References

1. A. Ozden, S. Shahgaldi, X. Li, F. Hamdullahpur, A review of gas diffusion layers for proton exchange membrane fuel cells-with a focus on characteristics, characterization techniques, materials and designs. Prog. Energy Combust. Sci. **74**, 50–102 (2019)
2. J. Kim, M. Jo, S. Nam, A review of polymer-nanocomposite electrolyte membranes for fuel cell application. J. Ind. Eng. Chem. **21**, 36–52 (2015)
3. C. Park, C. Lee, M. Guiver, Y. Lee, Sulfonated hydrocarbon membranes for medium-temperature and low-humidity proton exchange membrane fuel cells (PEMFCs). Prog. Polym. Sci. **36**, 1443–1498 (2011)
4. C. Park, S. Lee, D. Hwang, D. Shin, D. Cho, K. Lee, T. Kim, T. Kim, M. Lee, D. Kim, C. Doherty, A. Thornton, A. Hill, M. Guiver, Y. Lee, Nanocrack-regulated self-humidifying membranes. Nature **532**, 480–483 (2016)
5. N. Li, S. Lee, Y. Liu, Y. Lee, M. Guiver, A new class of highly-conducting polymer electrolyte membranes: aromatic ABA triblock copolymers. Energy Environ. Sci. **5**, 5346–5355 (2012)
6. B. Shi, H. Wu, J. Shen, L. Cao, X. He, Y. Ma, Y. Li, J. Li, M. Xu, X. Mao, M. Qiu, H. Geng, P. Yang, Z. Jiang, Control of edge/in-plane interactions toward robust, highly proton conductive graphene oxide membranes. ACS Nano **13**, 10366–10375 (2019)
7. G. He, M. Xu, J. Zhao, S. Jiang, S. Wang, Z. Li, X. He, T. Huang, M. Cao, H. Wu, M. Guiver, Z. Jiang, Bioinspired ultrastrong solid electrolytes with fast proton conduction along 2D channels. Adv. Meter. **29**, 1605898 (2017)
8. D. Liu, J. Ashcraft, M. Mannarino, M. Silberstein, A. Argun, G. Rutledge, M. Boyce, P. Hammond, Spray layer-by-Layer electrospun composite proton exchange membranes. Adv. Func. Mater. **23**, 3087–3095 (2013)
9. Y. Yao, Z. Lin, Y. Li, M. Alcoutlabi, H. Hamouda, X. Zhang, Superacidic electrospun fiber-nafion hybrid proton exchange membranes. Adv. Energy Mater. **1**, 1133–1140 (2011)
10. A. Koltonow, J. Huang, Two-dimensional Nanofluidics. Science **351**, 1395–1397 (2016)
11. Y. Zhang, X. Zhang, P. Li, W. Wu, J. Lin, J. Wang, L. Qu, H. Zhang, Porous nanofiber composite membrane with 3D interpenetrating networks towards ultrafast and isotropic proton conduction. J. Mater. Chem. A **8**, 5128–5137 (2020)
12. D. Marcano, D. Kosynkin, J. Berlin, A. Sinitskii, Z. Sun, A. Slesarev, L. Alemany, W. Lu, J. Tour, Improved synthesis of graphene oxide. ACS Nano **4**, 4806–4814 (2010)
13. Y. Xu, M. Wu, S. Yu, Y. Zhao, C. Gao, J. Shen, Ultrathin and stable graphene oxide film via intercalation polymerization of polydopamine for preparation of digital inkjet printing dye. J. Membr. Sci. **586**, 15–22 (2019)
14. T. Oshima, K. Kondo, K. Ohto, K. Inoue, Y. Baba, Preparation of phosphorylated bacterial cellulose as an adsorbent for metal ions. React. Funct. Polym. **68**, 376–383 (2008)
15. H. Zhang, Q. Hu, X. Zheng, Y. Yin, H. Wu, Z. Jiang, Incorporating phosphoric acid-functionalized polydopamine into Nafion polymer by in situ sol-gel method for enhanced proton conductivity. J. Membr. Sci. **570**, 236–244 (2019)
16. P. Chaturvedi, I. Vlassiouk, D. Cullen, A. Rondinone, N. Lavrik, S. Smirnov, Ionic conductance through graphene: assessing its applicability as a proton selective membrane. ACS Nano **13**, 12109–12119 (2019)
17. L. Nie, J. Wang, T. Xu, H. Dong, H. Wu, Z. Jiang, Enhancing proton conduction under low humidity by incorporating core-shell polymeric phosphonic acid submicrospheres into sulfonated poly (ether ether ketone) membrane. J. Power Sour. **213**, 1–9 (2012)
18. L. Cao, X. He, Z. Jiang, X. Li, Y. Li, Y. Ren, L. Yang, H. Wu, Channel-facilitated molecule and ion transport across polymer composite membranes. Chem. Soc. Rev. **46**, 6725–6745 (2017)
19. F. Yang, G. Xu, Y. Dou, B. Wang, H. Zhang, H. Wu, W. Zhou, J. Li, B. Chen, A flexible metal-organic framework with a high density of sulfonic acid sites for proton conduction. Nat. Energy **2**, 877–883 (2017)
20. T. Gür, Review of electrical energy storage technologies, materials and systems: challenges and prospects for large-scale grid storage. Energy Environ. Sci. **11**, 2696–2767 (2018)

21. H. Zhang, T. Zhang, J. Wang, F. Pei, Y. He, J. Liu, Enhanced proton conductivity of sulfonated poly (ether ether ketone) membrane embedded by dopamine-modified nanotubes for proton exchange membrane fuel cell. Fuel Cells **13**, 1155–1165 (2013)
22. Y. He, J. Wang, H. Zhang, T. Zhang, B. Zhang, S. Cao, J. Liu, Polydopamine-modified graphene oxide nanocomposite membrane for proton exchange membrane fuel cell under anhydrous conditions. J. Mater. Chem. A **2**, 9548–9558 (2014)
23. W. Wu, Y. Li, J. Liu, J. Wang, Y. He, K. Davey, S. Qiao, Molecular-level hybridization of Nafion with quantum dots for highly enhanced proton conduction. Adv. Mater. **30**, 1707516 (2018)
24. Y. Nam, J. Choi, K. Kang, D. Kim, H. Jung, Enhanced stability of laminated graphene oxide membranes for nanofiltration via interstitial amide bonding. ACS Appl. Mater. Interfaces **8**, 27376–27382 (2016)
25. M. Zhang, Y. Mao, G. Liu, G. Liu, Y. Fan, W. Jin, Molecular bridges stabilize graphene oxide membranes in water. Angew. Chem. Int. Ed. **59**, 1689–1695 (2020)
26. J. Wang, H. Zhang, Z. Jiang, X. Yang, L. Xiao, Tuning the performance of direct methanol fuel cell membranes by embedding multifunctional inorganic submicrospheres into polymer matrix. J. Power Sour. **188**, 64–74 (2009)
27. L. Cao, H. Wu, P. Yang, X. He, J. Li, Y. Li, M. Xu, M. Qiu, Z. Jiang, Graphene oxide-based solid electrolytes with 3D prepercolating pathways for efficient proton transport. Adv. Func. Mater. **28**, 1804944 (2018)
28. T. Bayer, R. Selyanchyn, S. Fujikawa, K. Sasaki, S.M. Lyth, Spray-painted graphene oxide membrane fuel cells. J. Membr. Sci. **541**, 347–357 (2017)
29. T. Pirzada, S. Arvidson, C. Saquing, S. Shah, S. Khan, Unexpected bilayer formation in langmuir films of nucleolipids. Langmuir **28**, 5834–5844 (2012)
30. M. Irani, A. Keshtkar, M. Moosavian, Comparative study on PVA/silica membrane functionalized with mercapto and amine groups for adsorption of Cu(II) from aqueous solutions. Chem. Eng. J. **32**, 200–202 (2012)
31. R. Guo, X. Ma, C. Hu, Z. Jiang, Polymer, disease-modifying effects of neural regeneration peptide 2945 in the GAERS. Model Absence Epilepsy **48**, 2939–2945 (2007)
32. J. Wang, X. Yue, Z. Zhang, Z. Yang, Y. Li, H. Zhang, X. Yang, Z. Jiang, Enhancement of proton conduction at low humidity by incorporating imidazole microcapsules into polymer electrolyte membranes. Adv. Funct. Mater. **22**, 4539–4546 (2012)
33. Z. Cui, Y. Xiang, J. Si, M. Yang, Q. Zhang, T. Zhang, Ionic interactions between sulfuric acid and chitosan membranes. Carbohyd. Polym. **73**, 111–116 (2008)
34. K. Lee, H. Kim, H. Bang, Y. Jung, S.G. Lee, Conductivity model and photoacoustic FT-IR surface depth profiling of heterogeneous polymers. Polymer **44**, 4029–4034 (2003)
35. J. Wang, H. Bai, H. Zhang, L. Zhao, H. Chen, Y. Li, Anhydrous proton exchange membrane of sulfonated poly(ether ether ketone) enabled by polydopamine-modified silica nanoparticles. Electrochim. Acta **152**, 443–455 (2015)
36. L. Zhao, Y. Li, H. Zhang, W. Wu, J. Liu, J. Wang, Constructing proton-conductive highways within an ionomer membrane by embedding sulfonated polymer brush modified graphene oxide. J. Power Sour. **286**, 445–457 (2015)
37. K. Yamazaki, Y. Tang, H. Kawakami, Proton conductivity and stability of low-IEC sulfonated block copolyimide membrane. J. Membr. Sci. **362**, 234–240 (2010)
38. X. Li, X. Hao, D. Xu, G. Zhang, S. Zhong, H. Na, D. Wang, Fabrication of sulfonated poly(ether ether ketone ketone) membranes with high proton conductivity. J. Membr. Sci. **281**, 1–6 (2006)
39. Z. Chai, C. Wang, H. Zhang, C. Doherty, B. Ladewig, A. Hill, H. Wang, Nafion-carbon nanocomposite membranes prepared using hydrothermal carbonization for proton-exchange-membrane fuel cells. Adv. Func. Mater. **20**, 4394–4399 (2010)
40. V.D. Notoa, M. Pigaa, G.A. Giffina, G. Pace, Rapid determination of 16S ribosomal RNA sequences for phylogenetic analyses. J. Membr. Sci. **390–391**, 58–67 (2012)
41. S. Gahlot, P.P. Sharma, V. Kulshrestha, P.K. Jha, SGO/SPES-Based Highly conducting polymer electrolyte membranes for fuel cell application. ACS Appl. Mater. Interfaces **6**, 5595–5601 (2014)

42. F. Ding, S. Wang, M. Xiao, X. Li, Y. Meng, Fabrication and properties of cross-linked sulfonated fluorene-containing poly(arylene ether ketone) for proton exchange membrane. J. Power Sour. **170**, 20–27 (2007)
43. Z.M. Cui, W. Xing, C.P. Liu, J.H. Liao, H. Zhang, Chitosan/heteropolyacid composite membranes for direct methanol fuel cell. J. Power Sour. **188**, 24–29 (2009)
44. P. Xing, G.P. Robertson, M.D. Guiver, S.D. Mikhailenko, K. Wang, S. Kaliaguine, Synthesis and characterization of sulfonated poly(ether ether ketone) for proton exchange membranes. J. Membr. Sci. **229**, 95–106 (2004)
45. G. He, L. Nie, X. Han, H. Dong, Y. Li, H. Wu, X. He, J. Hu, Z. Jiang, Constructing facile proton-conduction pathway within sulfonated poly(ether ether ketone) membrane by incorporating poly(phosphonic acid)/silica nanotubes. J. Power Sour. **259**, 203–212 (2014)
46. Q. Che, B. Sun, R. He, Preparation and characterization of new anhydrous, conducting membranes based on composites of ionic liquid trifluoroacetic propylamine and polymers of sulfonated poly (ether ether) ketone or polyvinylidenefluoride. Electrochim. Acta **53**, 4428–4434 (2008)
47. X. Chen, D. Wong, S. Yakovlev, K.M. Beers, K.H. Downing, N.P. Balsara, Effect of morphology of nanoscale hydrated channels on proton conductivity in block copolymer electrolyte membranes. Nano Lett. **14**, 4058–4064 (2014)
48. T. Tamura, R. Takemori, H. Kawakami, Proton conductive properties of composite membranes containing uniaxially aligned ultrafine electrospun polyimide nanofiber. J. Power Sour. **217**, 135–141 (2012)
49. J. Zheng, J. Tian, D. Wu, M. Gu, W. Xu, C. Wang, F. Gao, M. Engelhard, J. Zhang, J. Liu, J. Xiao, Lewis acid-base interactions between polysulfides and metal organic framework in lithium sulfur batteries. Nano Lett. **14**, 2345–2352 (2014)
50. N. Abhishek, P. Bijay, K. Vinod, Aliphatic-aromatic sulphonated polyimide and acid functionalized polysilsesquioxane composite membranes for fuel cell applications. J. Mater. Chem. A **21**, 4117–4124 (2011)
51. M. Jun, Y. Cao, J. Kim, Solvent casting effects of sulfonated poly(ether ether ketone) for Polymer electrolyte membrane fuel cell. J. Membr. Sci. **396**, 32–37 (2012)
52. H. Cong, J. Chen, S. Yu, Graphene-based macroscopic assemblies and architectures: an emerging material system. Chem. Soc. Rev. **43**, 7295–7325 (2014)
53. J. Shin, S. Won, L. Jeong, S. Bae, B. Chan, J. Ho, W. Ho, Effect of organosoluble salts on the nanofibrous structure of electrospun poly(3-hydroxybutyrate-co-3-hydroxyvalerate). Int. J. Biol. Macromol. **34**, 249–256 (2004)
54. P. Li, W. Wu, J. Liu, B. Shi, Y. Du, Y. Li, J. Wang, Investigating the nanostructures and proton transfer properties of Nafion-GO hybrid membranes. J. Membr. Sci. **555**, 327–336 (2018)
55. T. Kajita, H. Tanaka, A. Noro, Y. Matsushita, N. Nakamura, Acidic liquid-swollen polymer membranes exhibiting anhydrous proton conductivity higher than 100 mS cm^{-1} at around 100 °C. J. Mater. Chem. A **7**, 15585 (2019)
56. Y. Yin, H. Wang, L. Cao, Z. Li, Z. Li, M. Gang, Sulfonated poly (ether ether ketone)-based hybrid membranes containing graphene oxide with acid-base pairs for direct methanol fuel cells. Electrochim. Acta **203**, 178–188 (2016)
57. J. Liang, J. Ge, K. Wu, Q. Zhang, J. Wang, Z. Ye, Sulfonated polyaryletherketone with pendant benzimidazole groups for proton exchange membranes. J. Membr. Sci. **204**, 117626 (2019)
58. J. Zhang, J. Zhang, H. Bai, Q. Tan, H. Wang, B. He, Y. Xiang, S. Lu, A new high temperature polymer electrolyte membrane based on tri-functional group grafted polysulfone for fuel cell application. J. Membr. Sci. **572**, 496–503 (2019)
59. Y. Yang, X. He, P. Zhang, Y. Andaloussi, H. Zhang, Z. Jiang, Y. Chen, S. Ma, P. Cheng, Z. Zhang, Predisposed intrinsic and extrinsic proton conduction in robust covalent organic frameworks for hydrogen fuel cell application. Angew. Chem. Int. Ed. **32**, 56–67 (2019)
60. J. Wang, Y. He, L. Zhao, Y. Li, S. Cao, B. Zhang, H. Zhang, Enhanced proton conductivities of nanofibrous composite membranes enabled by acid-base pairs under hydrated and anhydrous conditions. J. Membr. Sci. **482**, 1–12 (2015)

61. G. He, J. Zhao, S. Hu, L. Li, Z. Li, Y. Li, Z. Jiang, Functionalized carbon nanotube via distillation precipitation polymerization and its application in Nafion-based composite membranes. ACS Appl. Mater. Interfaces **6**, 15291–15301 (2014)
62. T. Pirzada, S. Arvidson, C. Saquing, S. Shah, S. Khan, Hybrid silica-PVA nanofibers via sol-gel electrospinning. Langmuir **28**, 5834–5844 (2012)
63. Y. Liu, J. Wang, H. Zhang, C. Ma, J. Liu, S. Cao, X. Zhang, Enhancement of proton conductivity of chitosan membrane enabled by sulfonated graphene oxide under both hydrated and anhydrous conditions. J. Power Sour. **269**, 898–911 (2014)
64. J. Wang, Y. Zhao, W. Hou, J. Geng, L. Xiao, H. Wu, Z. Jiang, Simultaneously enhanced methanol barrier and proton conductive properties of phosphorylated titanate nanotubes embedded nanocomposite membranes. J. Power Sour. **195**, 1015–1023 (2010)
65. H. Bai, H. Zhang, Y. He, J. Liu, B. Zhang, J. Wang, Enhanced proton conduction of chitosan membrane enabled by halloysite nanotubes bearing sulfonate polyelectrolyte brushes. J. Membr. Sci. **454**, 220–232 (2014)
66. Y. He, H. Zhang, Y. Li, J. Wang, L. Ma, W. Zhang, J. Liu, Synergistic proton transfer through nanofibrous composite membranes by suitably combining proton carriers from the nanofiber mat and pore-filling matrix. J. Mater. Chem. A **3**, 21832–21841 (2015)
67. Z. Li, Y. Du, Z. Zhang, D. Pang, Preparation and characterization of CdS quantum dots chitosan biocomposite. React. Funct. Polym. **55**, 35–43 (2003)
68. J. Won, H. Lee, J. Lim, J. Kim, Y. Hong, S. Lee, Anomalous behavior of proton transport and dimensional stability of sulfonated poly(arylene ether sulfone) nonwoven/silicate composite proton exchange membrane with dual phase co-continuous morphology. J. Membr. Sci. **450**, 235–241 (2014)
69. I. Shabani, M. Hasani-Sadrabadi, V. Haddadi-Asl, M. Soleimani, Nanofiber-based polyelectrolytes as novel membranes for fuel cell applications. J. Membr. Sci. **368**, 233–240 (2011)
70. B. Lee, H. Park, H. Back, K. Lee, Novel film-casting method for high-performance flexible polymer electrodes. Adv. Funct. Mater. **21**, 487–493 (2011)
71. J. Choi, K. Lee, R. Wycisk, P. Pintauro, P. Mather, Nanofiber network ion-exchange membranes. Macromolecules **41**, 4569–4572 (2008)
72. S. Zhong, X. Cui, T. Fu, H. Na, Modification of sulfonated poly(ether ether ketone) proton exchange membrane for reducing methanol crossover. J. Power Sour. **180**, 23–28 (2008)
73. D. Wu, T. Xu, L. Wu, Y. Wu, Hybrid acid-base polymer membranes prepared for application in fuel cells. J. Power Sour. **186**, 286–292 (2009)
74. B. Lin, B. Qiu, L. Qiu, Z. Si, F. Chu, X. Chen, F. Yan, Imidazolium-functionalized SiO_2 nanoparticle doped proton conducting membranes for anhydrous proton exchange membrane applications. Fuel Cells **13**, 72–78 (2013)
75. J. Wang, H. Zhang, X. Yang, S. Jiang, W. Lv, Z. Jiang, S. Qiao, Enhanced water retention by using polymeric microcapsules to confer high proton conductivity on membranes at low humidity. Adv. Func. Mater. **21**, 971–978 (2011)
76. W. Liu, Y. Li, X. Meng, G. Liu, S. Hu, F. Pan, X. Cao, Embedding dopamine nanoaggregates into a poly(dimethylsiloxane) membrane to confer controlled interactions and free volume for enhanced separation performance. J. Mater. Chem. A **1**, 3713–3723 (2013)
77. H. Wang, X. Xu, N. Johnson, N. Dandala, H. Ji, High proton conductivity of water channels in a highly ordered nanowire. Angew. Chem. Int. Ed. **123**, 12746–12749 (2011)
78. Y. Fu, L. Liu, L. Zhang, W. Wang, Highly conductive one-dimensional nanofibers: silvered electrospun silica nanofibers via poly (dopamine) functionalization. ACS Appl. Mater. Interfaces **6**, 5105–5112 (2014)
79. W. Liu, S. Wang, M. Xiao, D. Han, Y. Meng, A proton exchange membrane fabricated from a chemically heterogeneous nonwoven with sandwich structure by the program-controlled co-electrospinning process. Chem. Commun. **48**, 3415–3417 (2012)
80. W. Wu, Y. Li, P. Chen, J. Liu, J. Wang, H. Zhang, Constructing ionic liquid-filled proton transfer channels within nanocomposite membrane by using functionalized graphene oxide. ACS Appl. Mater. Interfaces **8**, 588–599 (2016)

81. L. Chen, X. Zhang, H. Liang, M. Kong, Q. Guan, P. Chen, A. Wu, S. Yu, Synthesis of nitrogen-doped porous carbon nanofibers as an efficient electrode material for supercapacitors. ACS Nano **6**, 7092–7102 (2012)
82. C. Zhang, X. Wang, J. Lin, B. Ding, J. Yu, N. Pan, Nanoporous polystyrene fibers functionalized by polyethyleneimine for enhanced formaldehyde sensing. Sens. Actuators B Chem. **152**, 316–323 (2011)
83. Y. Zhang, J. Guan, X. Wang, J. Yu, B. Ding, Balsam pear skin like porous polyacrylonitrile nanofibrous membranes grafted with polyethyleneimine for postcombustion CO_2 capture. ACS Appl. Mater. Interfaces **9**, 41087–41098 (2017)
84. T. Hasegawa, A. Béléké, M. Mizuhata, Membrane modification by liquid phase deposition using small amount of TiO_2 for high-temperature operation of polymer electrolyte fuel cells. J. Power Sour. **233**, 148–156 (2013)
85. N. Li, C. Wang, S. Lee, C. Park, Y. Lee, M. Guiver, Enhancement of proton transport by nanochannels in comb-shaped copoly(arylene ether sulfone)s. Angew. Chem. Int. Ed. **123**, 9324–9327 (2011)
86. W. Jia, K. Feng, B. Tang, P. Wu, β-Cyclodextrin modified silica nanoparticles for Nafion based proton exchange membranes with significantly enhanced transport properties. J. Mater. Chem. A **3**, 15607–15615 (2015)
87. Y. Wang, S. Li, S. Hsiao, W. Liao, P. Chen, S. Yang, C. Hu, Integration of tailored reduced graphene oxide nanosheets and electrospun polyamide-66 nanofabrics for a flexible supercapacitor with high-volume-and high-area-specific capacitance. Carbon **73**, 87–98 (2014)
88. S. Cheruthazhekatt, T. Pijpers, G. Harding, V. Mathot, H. Pasch, Multidimensional analysis of the complex composition of impact polypropylene copolymers: combination of TREF, SEC-FTIR-HPer DSC, and high temperature 2D-LC. Macromolecules **45**, 5866–5880 (2012)
89. J. Wang, P. Li, Y. Zhang, Y. Liu, W. Wu, J. Liu, Porous Nafion nanofiber composite membrane with vertical pathways for efficient through-plane proton conduction. J. Membr. Sci. **585**, 157–165 (2019)
90. C. Boaretti, L. Pasquini, R. Sood, S. Giancola, A. Donnadio, M. Roso, Mechanically stable nanofibrous SPEEK/Aquivion® composite membranes for fuel cell applications. J. Membr. Sci. **545**, 66–74 (2018)
91. D. Yu, S. Yoon, T. Kim, J. Lee, J. Lee, Y. Hong, Properties of sulfonated poly(arylene ether sulfone)/electrospun nonwoven polyacrylonitrile composite membrane for proton exchange membrane fuel cells. J. Membr. Sci. **446**, 212–219 (2013)
92. H. Li, Y. Lee, J. Lai, Y. Liu, Composite membranes of Nafion and poly(styrene sulfonic acid)-grafted poly(vinylidene fluoride) electrospun nanofiber mats for fuel cells. J. Membr. Sci. **466**, 238–245 (2014)
93. J. Wang, Y. Liu, J. Dang, G. Zhou, Y. Wang, Y. Zhang, L. Qu, W. Wu, Lamellar composite membrane with acid-base pair anchored layer-by-layer structure towards highly enhanced conductivity and stability. J. Membr. Sci. **602**, 117978 (2020)
94. J. Lin, J. Dang, G. Zhou, W. Wu, Y. Liu, Y. Zhang, J. Wang, Sheet-dot-framework membrane towards efficient proton conduction and outstanding stability. J. Mater. Chem. A **8**, 10822–10830 (2020)
95. H. Zhang, Y. He, J. Zhang, L. Ma, Y. Li, J. Wang, Constructing dual-interfacial proton-conducting pathways in nanofibrous composite membrane for efficient proton transfer. J. Membr. Sci. **505**, 108–118 (2016)
96. P. Li, J. Dang, W. Wu, J. Lin, Z. Zhou, J. Zhang, J. Wang, Nanofiber composite membrane using quantum dot hybridized SPEEK nanofiber for efficient through-plane proton conduction. J. Membr. Sci. **609**, 118198 (2020)

Chapter 6
Composite Separator or Electrolyte for Lithium–Sulfur Battery

Weijie Kou, Jiajia Huang, and Wenjia Wu

6.1 Introduction

The development and utilization of high-performance and high-energy–density battery is indispensable to meet the ever-increasing demands in advanced energy storage system [1–5]. Particularly, lithium–sulfur (Li–S) battery is considered to be the most promising next-generation battery due to high theoretical capacity (1675 mAh g^{-1}), high theoretical energy density (2600 Wh kg^{-1}), and low cost [4–7]. Unfortunately, the rapid capacity fading and poor cycling life of Li–S battery, resulting from severe polysulfide shuttle effect, limit the application and development [7–9]. Numerous studies have been devoted to addressing the polysulfide shuttle effect, including functionalization of cathode structure or composition [10, 11], modification of separators [12, 13], and design of solid-state electrolytes [14, 15]. Among them, anchoring polysulfides through designing functionalized cathode structure or composition is an effective way to alleviate the polysulfide shuttle effect. However, the addition of redundant inactive materials in cathode usually reduces the energy density of battery [16]. Moreover, functionalizing cathode materials by doping heteroatoms would sacrifice electrical conductivity of cathode and cannot effectively suppress polysulfide shuttling [17, 18].

A simple and effective strategy of modifying a functional layer on the separator, as a key component of the battery to avoid direct contact between cathode and anode, can overcome the polysulfide shuttle effect [19, 20]. Benefiting from the potential strong interactions with polysulfide, strongly polar inorganic materials, including metal oxides [21, 22], metal sulfides [23], and Ti_3C_2 [24], could be used as modifiers of separator for suppressing polysulfide shuttling. Meanwhile, it is also an effective method to modify a polymer layer with anion groups, such as $-CO_2H$ or $-SO_3H$, on the surface of separator [25]. On the other hand, although many advances

W. Kou · J. Huang · W. Wu (✉)
School of Chemical Engineering, Zhengzhou University, Zhengzhou 450001, P. R. China
e-mail: wenjiawu@zzu.edu.cn

J. Wang and W. Wu (eds.), *Functional Membranes for High Efficiency Molecule and Ion Transport*, https://doi.org/10.1007/978-981-19-8155-5_6

were reported in improving the performance of Li–S batteries, the polysulfide shuttle effect and the formation of lithium dendrites in liquid electrolytes remain serious challenges for Li–S batteries [26]. Replacing liquid electrolyte with solid electrolyte can effectively eliminate polysulfide shuttle and enable stable cycling for all-solid-state Li–S batteries [27, 28]. A good solid electrolyte must possess high ionic conductivity, good compatibility with lithium anode, wide electrochemical window, and physicochemical stability [29].

In this chapter, we introduce the electronegative modified separator with semi-fused pores [30] and sheet-polymer laminar film as ideal modification layer [31] for composite separators in liquid Li–S batteries and asymmetry-structure LLTO composite electrolyte [32] and laminar vermiculite composite electrolyte [33] in all-solid-state Li–S batteries. Then, the microstructure and electrochemical properties of these composite separators and electrolytes are investigated in detail.

6.2 Lithiated Nanofiber-Functionalized Separator

Electrospinning technology was performed for the preparation of nanofiber-functionalized separator. 2,2′-Benzidinedisulfonic acid (BDSA) and polyacrylic acid (PAA) were added into Nafion solution and stirred at 60 °C to prepare homogeneous Nafion/PAA electrospinning solution, where the mass fractions were controlled at 5% for PAA and 0.5% for BDSA. The polypropylene (PP) separator was covered over the collector, and the distance between collector and needle was controlled to 20 cm. Next, the above electrospinning solution was injected into a syringe, followed by electrospinning with a rate of 0.030 mL min^{-1} at 10 kV. Finally, after 12-h heat treatment at 100 °C, the Nafion/PAA nanofiber mat-modified separator (NP mat/PP) was successfully prepared. Specially, to balance the modification effect and energy density, the loading of Nafion/PAA mat on separator was kept at ~0.30 mg cm^{-2}.

Sulfonated poly(ether ether ketone) (SPEEK) was prepared using the method in literature [34]. The sulfonation degree of SPEEK was kept at 78% by sulfonating PEEK for 10 h. Afterward, the as-prepared SPEEK was dissolved in *N*, *N*-dimethylformamide and stirred for 12 h to obtain a 20 wt.% SPEEK electrospinning solution. Similarly, the above solution was operated with a rate of 0.020 mL min^{-1} at 25 kV. Finally, after drying at 60 °C for 12 h, the SPEEK nanofiber mat-modified PP separator (SP mat/PP) was obtained and the mass loading was also kept at ~0.30 mg cm^{-2}.

Subsequently, these fiber mat-modified separators were further lithiated to prepare lithiated nanofiber-functionalized separators. Concretely, 0.1 M LiOH solution was prepared by dissolving a certain amount of $LiOH{\cdot}H_2O$ into the mixture of water and ethanol (9:1 w/w). Then, the NP mat/PP separator was put into LiOH solution and fully soaked for 6 h at room temperature. Finally, after the processes of rinsing with ultra-purified water and drying for 24 h at 60 °C, the Nafion/PAA-Li network-modified separator (NP-Li/PP) was successfully prepared. And the areal mass loading of Nafion/PAA-Li increased to ~0.32 mg cm^{-2}. Furthermore, the Li^+ content of the

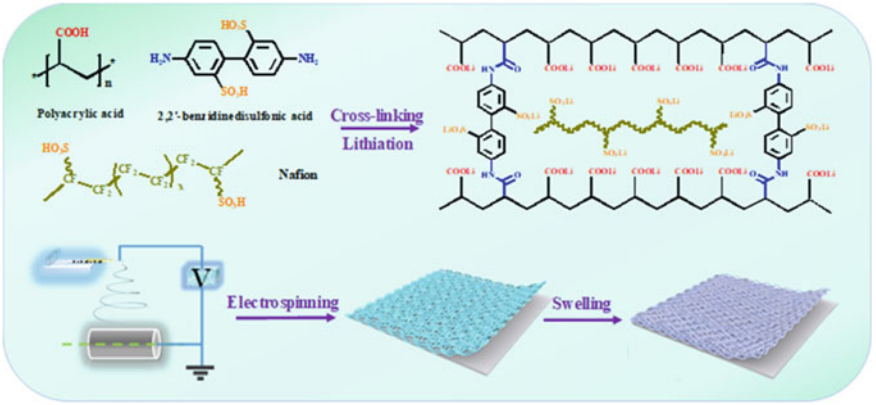

Fig. 6.1 Schematic illustration of the fabrication process of NP-Li/PP separator. Copyright (2019), American Chemical Society [30]

prepared NP-Li/PP was evaluated through acid–base titration [19]. The NP-Li/PP was immersed in 2 M NaCl solution for 48-h deprotonation process and then being titrated using the 0.01 M standard NaOH solution. Similarly, SPEEK-Li network-modified separator (SP-Li/PP) with a mass loading of ~0.32 mg cm^{-2} was synthesized through the same method.

Additionally, Nafion/PAA-Li-coated (NP-coated/PP) and SPEEK-Li-coated (SP-coated/PP) separators were prepared by electrospinning technology. The Nafion/PAA blend solution was drop-casted on PP separator and dried at 60 °C for 6 h. The area mass of Nafion/PAA-coated layer was controlled about 0.40 mg cm^{-2}. To obtain the NP-coated/PP separator, the modified separator with Nafion/PAA coating was immersed in LiOH aqueous solution (0.1 M) at 25 °C, rinsed with water, and dried at 50 °C for 12 h. Using the same process fabricated SP-coated/PP separator. Figure 6.1 shows the fabrication process of the NP-Li/PP separator.

Due to the lack of sufficient chain entanglement, pure Nafion solution cannot be directly used for electrospinning to prepare nanofibers [35]. PAA was added to solve the above problems, and the addition of PAA also introduced more anionic groups. The $-CO_2H$ groups on PAA react with the crosslinker BDSA to enhance the structural stability of nanofibers. Nafion/PAA nanofibers were prepared by heat treatment at 100 °C using a PP separator as a carrier. The NP mat/PP separator exhibits higher thermal dimensional stability as compared to the PP separator.

Scanning electron microscopy (SEM) was used to characterize the surface morphology of these modified separators. The nanofibers are intertwined to form large interspaces on the micron-scale, so that the polysulfide shuttle might not be effectively prevented. To suture these interspaces, the nanofibers are fused with lithiation treatment. Through pre-experiment, the treatment time was chosen as 6 h, and optimized structure was obtained. Figure 6.2a shows that the porous fiber mat forms a relatively compact semi-fused pores fiber network. Meanwhile, as shown in Fig. 6.2b, fiber mat exhibits a thickness of 600 nm.

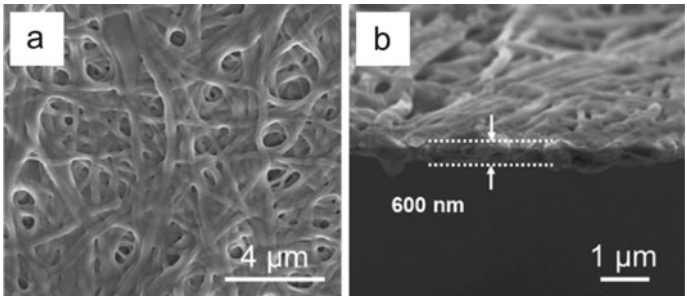

Fig. 6.2 The structural characterization of separators. **a** Surface SEM image of NP-Li/PP. **b** Cross-section SEM image of NP-Li. Copyright (2019), American Chemical Society [30]

The chemical structure of this modification layer is tested by Fourier transform infrared (FTIR). Figure 6.3a shows that the characteristic band of PAA is C=O at 1707 cm^{-1}. Nafion brings the characteristic bands for C−O−C at 981 cm^{-1}, C−F at 1159 cm^{-1}, and O=S=O at 1056 and 1229 cm^{-1} [36, 37]. These results prove the presence of $–CO_2H$ and $–SO_3H$ groups on the modified separators. Moreover, after thermal crosslinking, NP mat displays two new bands for amide I of carbonyl stretching at 1648 cm^{-1} and amide II of N−H bending at 1530 cm^{-1} [19]. This indicates that BDSA has successfully crosslinked PAA chains. As shown in Fig. 6.3b, further evidence is supplied by thermogravimetric analysis (TGA) curves. In the range of 30–120 °C, the weight loss of uncrosslinked NP mat is larger than that of crosslinked NP mat because of the water escape of PAA and BDSA during amidation reaction. And a new peak of DTG curve appears at 90 °C, accordingly. Crosslinking significantly improves the water-resistant and solvent-resistant abilities, enabling the NP-Li/PP separator to keep fiber structure after lithiation. In Fig. 6.3a, due to the introduction of Li^+, the characteristic bands of NP-Li modification layer at 1229 and 1707 cm^{-1} show obvious red shift, indicating that $-SO_3Li$ and $-CO_2Li$ are formed, respectively [25, 37]. Further, exchange of Li^+ and H^+ hinders PAA dehydrating action, so the weight loss process of NP-Li modification layer is different, especially before 430 °C.

The impedance plots were carried out to calculate Li^+ conductivities of separators (Fig. 6.4a) [38, 39]. Note that the porous structure of separator enables Li^+ transfer through electrolyte; thus, PP separator shows a high conductivity of 9.5×10^{-4} S cm^{-1} (Fig. 6.4b). In contrast, the NP mat possesses a large number of $–SO_3H$ and $–CO_2H$ groups. These negatively charged anion groups act as sites for the Li^+ transport through the Coulombic interactions [20, 40], and the Li^+ in the electrolyte interacts with the unshared electron pairs in anion groups, which facilitates the Li^+ transport [19, 41]. In addition, the presence of interspaces and the improvement of electrolyte affinity also promote Li^+ conduction. Therefore, the Li^+ conductivity of NP mat/PP separator reaches as high as 1.4×10^{-3} S cm^{-1}. For NP-Li/PP separator, the process of lithiation increases the exposed anion groups and introduces additional Li^+. Besides, the semi-fused pores can provide a low-barrier path for Li^+ transport.

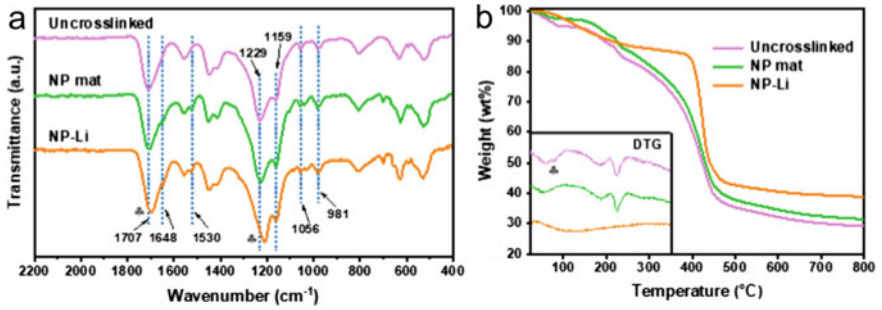

Fig. 6.3 **a** FTIR spectra of modification layers. **b** TGA curves of modification layers. Copyright (2019), American Chemical Society [30]

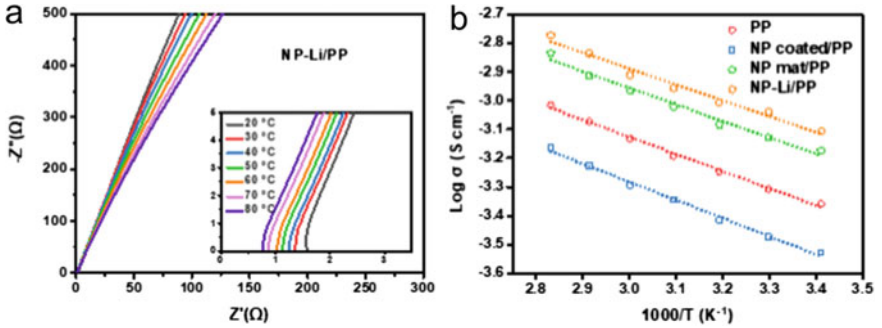

Fig. 6.4 **a** The impedance plots of NP-Li/PP separators at different temperatures. **b** Temperature-dependent ionic conductivities. Copyright (2019), American Chemical Society [30]

Thus, the Li^+ conductivity of NP-Li/PP separator is further improved to 1.7×10^{-3} S cm^{-1}.

As depicted in Fig. 6.5, EIS of the cells is collected. At high frequency, each EIS profile shows a semicircle corresponding to charge-transfer resistance (R_{ct}) [11, 42]. The NP-Li/PP separator assembled cell shows a lower R_{ct} of around 32 Ω, which is only 34.7% of that with PP separator (92 Ω). This is attributed to the improved separator/electrode interface and enhanced Li^+ conduction. Similarly, the R_{ct} of cell with NP mat/PP separator shows the decreased R_{ct} of 45 Ω. In contrast, because of the increased resistance of Li^+ diffusion, NP-coated/PP separator displays the highest R_{ct} of 101 Ω.

The cells' rate performance from 0.1 to 3.0C is tested (Fig. 6.6a). At 0.1, 0.2, 0.5, 1.0, 2.0, and 3.0C, the capacities of cell with PP separator display 909, 720, 591, 479, 217, and 197 mAh g^{-1}, respectively, which are the minimum at the same rate among all cells. This is due to the loss of active sulfur which results in severe polysulfide shuttle. By contrast, the capacities of the cells using NP-Li/PP separator at the corresponding rates are 1321, 1150, 1042, 945, 849, and 730 mAh g^{-1}, respectively. Especially, at high rate of 3.0C, the cell capacity is 3.7 times of that of the cell with PP

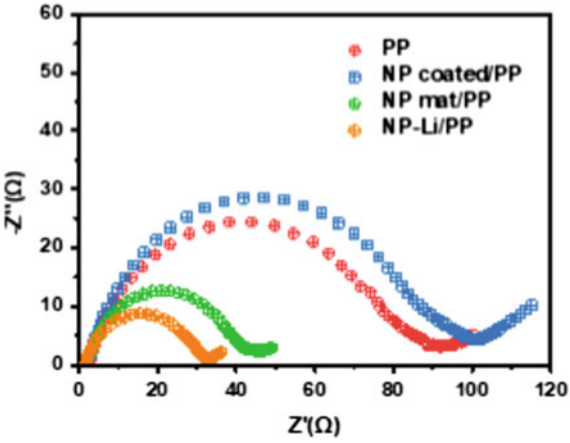

Fig. 6.5 EIS profiles of the cells with different separators. Copyright (2019), American Chemical Society [30]

separator. When the current returns to 0.2C, capacity is restored to 90% of its initial capacity, which is also more than the cell with PP separator (83%). The significant improvement in rate performance is mainly due to the functions of promoting Li^+ conduction and preventing polysulfide shuttle by NP-Li/PP separator. This can also be proved by the improved cell performance using NP mat/PP separator. Although the R_{ct} of the cell with NP-coated/PP separator is slightly higher, the discharge capacities of the cell with PP separator are better than that of the NP-coated/PP separator because of its good polysulfide inhibition performance. However, compared to the cells with NP-Li separators and NP mat/PP, with the gradual increase in the current rate, the capacity decreases rapidly. Especially, at 3.0C, the capacity is only 423 mAh g^{-1}, which is 33% of the initial capacity at 0.1C. At high rates, the reduction of capacities is attributed to the high impedance of the cell and the poor Li^+ conductivity. In addition, Fig. 6.6b shows that the cell with NP-Li/PP separator corresponding charge–discharge profiles display well-defined profiles with one charge plateau and two discharge plateaus.

The cells with different separators were assembled to evaluate the long-term cycling stability. As shown in Fig. 6.7, the initial capacities of the cells with PP, NP-coated/PP, NP mat/PP, and NP-Li/PP separators are 608, 730, 870, and 977 mAh g^{-1}, respectively. As the number of cycles increases, the capacity of the cell with PP separator decreases rapidly and finally fails in the 605th cycle. This is mainly due to the rampant polysulfide shuttle [18, 43]. And the capacity of 220 mAh g^{-1} is reserved, corresponding to a capacity decay of 0.106% per cycle. At the same time, when the battery fails, Coulomb efficiency decreases to 90%. In comparison, the cell with NP-Li/PP separator displays remarkable cycle stability with a reversible capacity of 748 mAh g^{-1} after 1000 cycles and the Coulomb efficiency is over 99%.

Then, the cycled cells were disassembled to further reveal the function of NP-Li/PP separator (Fig. 6.8). Owing to the elevated solvent-resistant ability of NP-Li/PP separator during crosslinking, it is easily separated from the disassembled cell, which indicates that NP-Li/PP separator can keep its structure stable during cycling. In

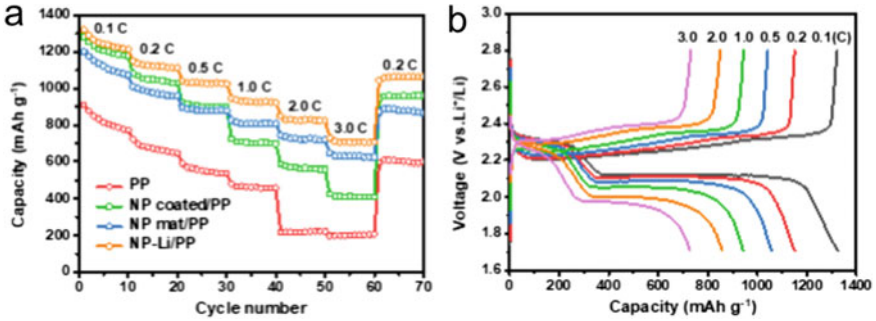

Fig. 6.6 **a** Rate performances of the cells with different separators. **b** Charge–discharge curves of the cell with NP-Li/PP separator at different rates. Copyright (2019), American Chemical Society [30]

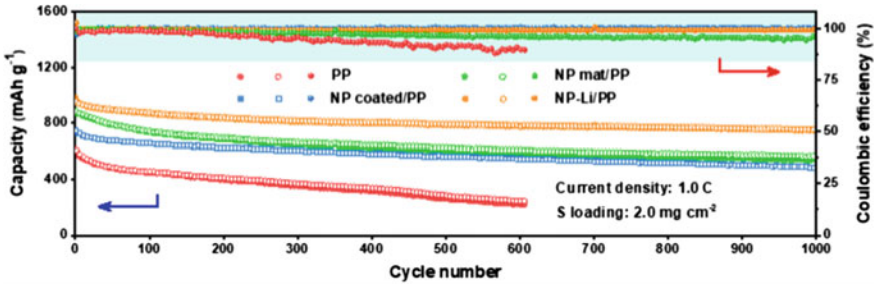

Fig. 6.7 Long-term cycling stability of the cells with different separators. Copyright (2019), American Chemical Society [30]

addition, there is slight discoloration on the surface of NP-Li/PP separator in Fig. 6.8b. As shown in Fig. 6.8d, e, the surface of cycled Li anode displays a relatively smooth morphology, and the S signal is weak in the corresponding EDS elemental mapping. In comparison, after cell cycling, the surface of PP separator is seriously polluted by dissolved polysulfide (Fig. 6.8a). Because of the rampant polysulfide shuttle, the surface of cycled Li anode is serious corrosion, and there is a strong S signal on the surface of the lithium anode (Fig. 6.8c, d). These results further demonstrate that NP-Li/PP separator can effectively suppress the shuttle effect and enhance the cycling performances of cell.

In conclusion, an electronegative NP-Li/PP nanofiber composite separator with semi-fused pores is designed and prepared for high-performance Li–S battery. The modified separator prepared by electrospinning possesses numerous $–CO_2H$ and $–SO_3H$ functional groups and compact physical structure, which effectively inhibit the polysulfide shuttle effect due to the electrostatic repulsion and physical barrier. In addition, the abundant anion groups afford innumerable carrier sites for the transmitting of positively charged Li^+, and special semi-fused pores serve as low-barrier transport pathways. Therefore, at room temperature, Li^+ conductivity can reach as

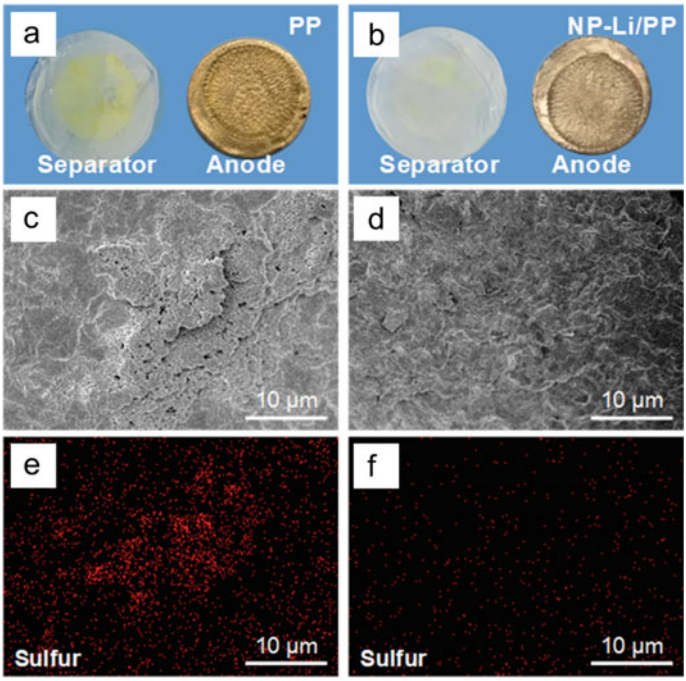

Fig. 6.8 Photographs of disassembled cells with **a** PP and **b** NP-Li/PP separators after long-term cycling test. The top sides of these separators were faced toward cathodes. Surface SEM images of the cycled Li anodes with **c** PP and **d** NP-Li/PP separators. Corresponding sulfur elemental maps of the cycled Li anodes with **e** PP and **f** NP-Li/PP separators. Copyright (2019), American Chemical Society [30]

high as 10^{-3} S cm^{-1}. Owing to this NP-Li/PP separator, the Li−S cell shows excellent electrochemical performances, containing outstanding cycling stability, high-rate performance of 730 mAh g^{-1} at 3.0C, and superb long-cycle life with decay rate of 0.023% at 1.0C during 1000 cycles. What's more, as an example, aiming to confirm the generality of this modification strategy, SPEEK-modified separators are also prepared and investigated. This study proposes a new strategy for targeted structure design and rational material selection of battery separator, representing an approach toward highly stable Li–S batteries.

6.3 Lamellar $Ti_3C_2T_x$-Nafion-Functionalized Separator

MAX (Ti_3AlC_2) powder was synthesized according to the method in literature. MAX powder was etched to obtain MXene ($Ti_3C_2T_x$) nanosheets. Firstly, LiF (1.0 g) was dissolved in HCl (20 mL, 9.0 mol L^{-1}) to form the uniform solution in a Teflon beaker. Afterward, Ti_3AlC_2 (1.0 g) was slowly added to the above solution at 35 °C, followed

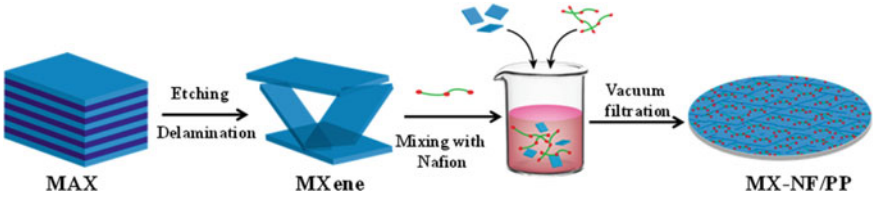

Fig. 6.9 The modification process of MX-NF/PP separator. Copyright (2019), Elsevier [31]

by stirring for 24 h to obtain the multilayered MXene. Then, the multilayered MXene was washed with ultra-purified water for 3 times and freeze-dried for 12 h. Next, the multilayered MXene (0.1 g) was added to ultra-purified water (25 mL) and then sonicated for 20 min in Ar atmosphere to obtain MXene nanosheet solution. Finally, the solution was centrifuged at 3500 rpm for 1 h to remove the non-peeled MAX powder. The obtained MXene nanosheet solution (0.5 mg mL^{-1}) was used to modify the separator.

The modification process of separator is shown in Fig. 6.9. Concretely, the obtained MXene nanosheet solution (4 mL) and Nafion solution (0.3 mL) were mixed into the water/ethanol mixture (95.7 mL, v/v = 3:7), followed by stirring for 10 min to obtain the uniform solution. Afterward, the modified PP separator was prepared by filtrating the obtained uniform solution on one side of the PP separator and drying for 12 h at 40 °C. Then, the modified separator was cut into circular piece, which was named as MXene-Nafion/PP (MX-NF/PP). Similarly, the fabrication of MXene/PP (MX/PP) was same as MX-NF/PP without using Nafion solution. Nafion solution was coated on PP separator to fabricate Nafion/PP (NF/PP). MXene@Nafion/PP (MX@NF/PP) was fabricated by firstly filtering MXene and then coating Nafion. Additionally, GO-Nafion/PP (GO-NF/PP) was fabricated by filtrating the GO dispersion. The modification layer was controlled with a loading of 0.2 mg cm^{-2}.

During the mixing of MXene sheets and Nafion solution in water–ethanol mixture, Nafion chains possess a lot of –F and $–SO_3H$ groups, which will form hydrogen bonds with the –OH on MXene (Fig. 6.10). Thus, Nafion chains will self-assemble on the surface of MXene. And the obtained product was named as MX-NF.

Then, MX-NF/PP separator was prepared by filtrating the above MX-NF solution on the PP separator. Afterward, MX/PP, NF/PP, and MX@NF/PP separators were fabricated by the filtration and coating methods. Herein, commercial PP separator with long-narrow pores (~200 nm) was used as the substrate. By comparison, the surface of NF/PP separator can be completely coated by Nafion. However, there are some micropores (the size of ~40 nm) those still exist in the Nafion modification layer. Although increasing Nafion loading can form a dense modification layer, the internal resistance will also increase [44]. Differently, the surface of MX/PP separator displays a defect-free film, which is formed by MXene modification layer under appropriate loading. However, the surface of MX/PP separator is rough, which indicates that MXene sheets are dis-orderly stacked and stacked pores are created in

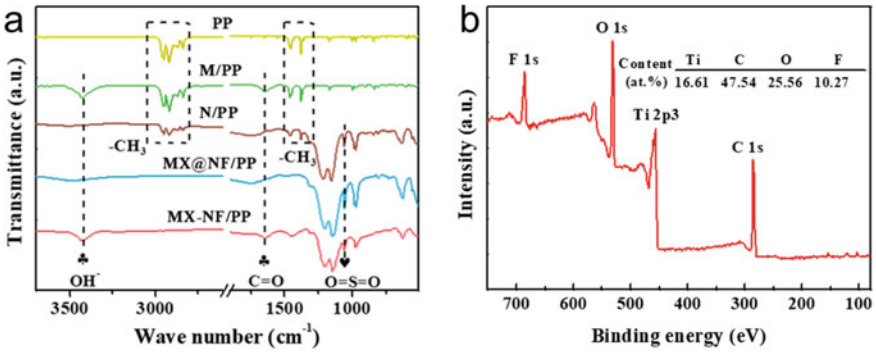

Fig. 6.10 **a** FTIR spectra of PP, NF/PP, MX/PP, MX@NF/PP, and MX-NF/PP separators. **b** XPS survey spectrum of MXene. Copyright (2019), Elsevier [31]

modification layer. Additionally, owing to the poor interaction between MXene and PP separator, MXene modification layer tends to peel off the PP separator. This is a general problem for modifying the inorganic layer. Interestingly, if using MXene as a support layer, Nafion can easily form a defect-free layer. Thus, MX@NF/PP separator reveals a uniform and smooth surface. Compared with MX/PP, after the self-assembly of Nafion and MXene sheets, an evolutionary modification layer (MX-NF) is formed on the surface of PP separator. Scanning electron microscopy (SEM) image in Fig. 6.11a shows that MX-NF is a uniform and smooth modification layer on PP separator. In addition, the energy-dispersive X-ray spectroscopy (EDS) mappings (S and Ti) display that MXene and Nafion are uniformly dispersed on the surface of MX-NF/PP separator (Fig. 6.11b). Meanwhile, MX-NF on the surface of PP separator displays a highly ordered layer-by-layer laminar structure (Fig. 6.11d). This is mainly due to Nafion acting as a surfactant to evenly disperse MX-NF sheets, and then, MX-NF is orderly stacked to form a regular structure during the filtration process. Importantly, the thickness of MX-NF modification layer is ~1.0 μm, and it adheres to PP separator (Fig. 6.11c). This is mainly due to the introduction of Nafion, which enhances the compatibility of PP separator and MXene sheets.

The ability of inhibiting the polysulfide shuttle is one key parameter for the separator of Li–S batteries. 0.1 M of Li_2S_6 THF solution is used for polysulfide permeation experiments [13, 45]. As shown in Fig. 6.12a, PP separator is unable to inhibit the polysulfide shuttle due to the long-narrow pores (~200 nm). It can be seen that Li_2S_6 begins to diffuse in the permeation side, and the system achieves balance at 48 h with a deep yellow. Compared with PP separator, the MX-NF-modified PP separator can effectively inhibit the polysulfide shuttle, and the color of the right side has barely changed after 48 h in Fig. 6.12b. This is mainly attributed to the MX-NF-modified layer possessing superiority nanostructure, which is a defect-free and uniform rejection layer. And the Nafion and MXene sheets might play the synergistic role in inhibiting polysulfide shuttle by electrostatic repulsion and physical resistance.

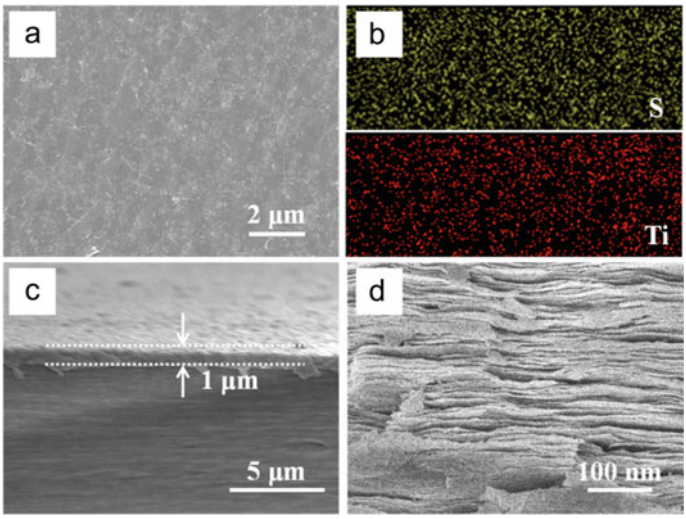

Fig. 6.11 **a** Surface SEM image of MX-NF/PP separator. **b** The EDS elemental (S and Ti) mappings of MX-NF/PP separator. **c** Low- and **d** high-magnification SEM images of cross-sectional MX-NF/PP separator. Copyright (2019), Elsevier [31]

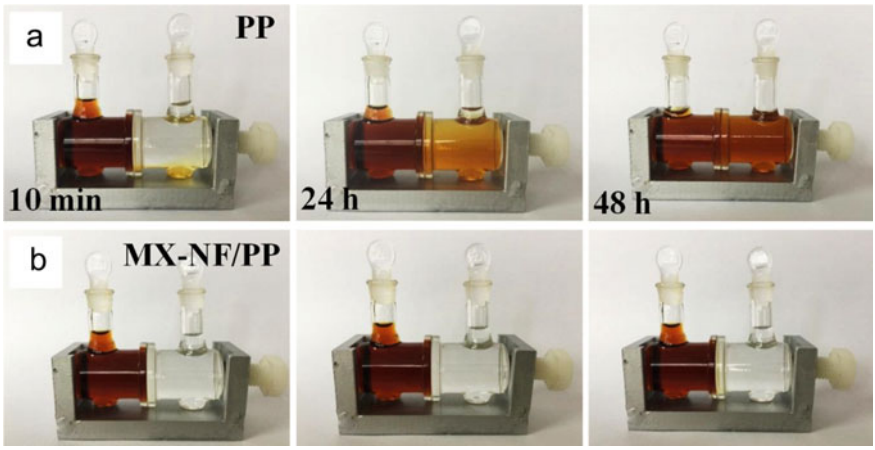

Fig. 6.12 Polysulfide permeation of **a** PP and **b** MX-NF/PP separators. Copyright (2019), Elsevier [31]

To further reveal the effectiveness of MX-NF/PP separator in inhibiting the polysulfide shuttle, carbon black with weak entrapment of polysulfides was chosen as the sulfur hosts [13]. The MX-NF/PP and PP separators were assembled into cells to evaluate the galvanostatic discharge/charge performances at 0.2C. As shown in Fig. 6.13a, the cell with PP separator possesses a lower initial discharge capacity of 825 mAh g^{-1}. In comparison, MX-NF/PP cell displays an initial discharge capacity

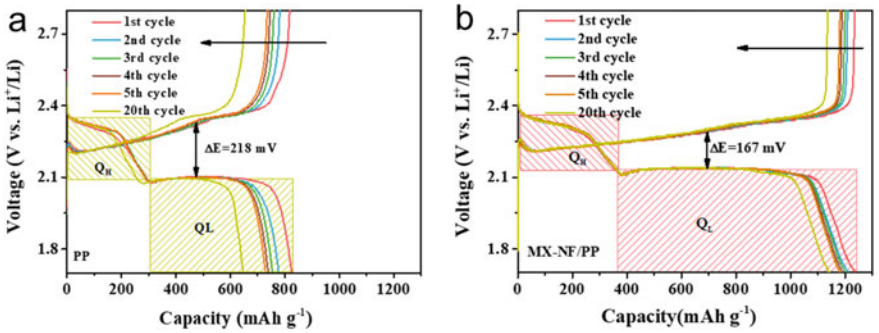

Fig. 6.13 Discharge/charge curves of PP cell **a** and MX-NF/PP cell **b** at 0.2C. Copyright (2019), Elsevier [31]

of 1234 mAh g^{-1}, 50% higher than that of PP cell (Fig. 6.13b). This is mainly due to the fact that the MX-NF modification layer can effectively inhibit the polysulfide shuttle, which leads to an elevated discharge capacity. Similarly, the initial discharge capacity of NF/PP, MX/PP, and MX@NF/PP cells are 113.6%, 125.9%, and 133.3% of that of PP cell, respectively. Obviously, the initial discharge capacity of cells, a key parameter for high capacity Li–S batteries, is related to the ability of inhibiting the polysulfide shuttle [46]. MXene sheets in MX-NF/PP and MX/PP separators possess fast electron conduction ability, which will act as an expanded current collector to promote the re-utilization of polysulfides [47, 48]. Additionally, the initial discharge capacity of MX-NF/PP cell is superior to other cells with most inorganic modification layers (e.g., graphene-CNT-nickel, MoS_2, and rGO@MoS_2) and organic modification layers (e.g., polyacrylic acid and Nafion) in literatures [40, 49–52], which highlights the superiority of MX-NF modification layer.

Then, the utilization rate of soluble S is calculated, which directly reflects the ability of inhibiting the polysulfide shuttle of separator. As shown in Fig. 6.13, the reduction reactions between sulfur and soluble polysulfides (S → Li_2S_4, theoretical capacity: 419 mAh g^{-1}) occur at high plateau discharge capacity (Q_H), where suffers from serious shuttle effect [16]. For the low plateau discharge capacity (Q_L), it represents that soluble polysulfides are further reduced to lithium sulfide (Li_2S_4 → Li_2S, theoretical capacity: 1256 mAh g^{-1}) [53]. Because Q_H is one third as much as Q_L in theory, the value of $Q_L/3$ Q_H is used to express the utilization of soluble S. Figure 6.13b shows a reduction of 19 mAh g^{-1} for the discharge capacity of MX-NF/PP cell, which is only 13.7% and 39.6% of PP cell (139 mAh g^{-1}) and MX@NF/PP cell (48 mAh g^{-1}), proving that MX-NF/PP separator can effectively inhibit the polysulfide shuttle. Additionally, there are dense solid polysulfides on the surface of PP separator. In comparison, a smaller amount of polysulfides can be observed on the surface of NF/PP, MX/PP, and MX@NF/PP separators. Differently, there are no obvious polysulfides on the surface of MX-NF/PP separator, which indicates the outstanding ability of MX-NF/PP separator in inhibiting polysulfide shuttle.

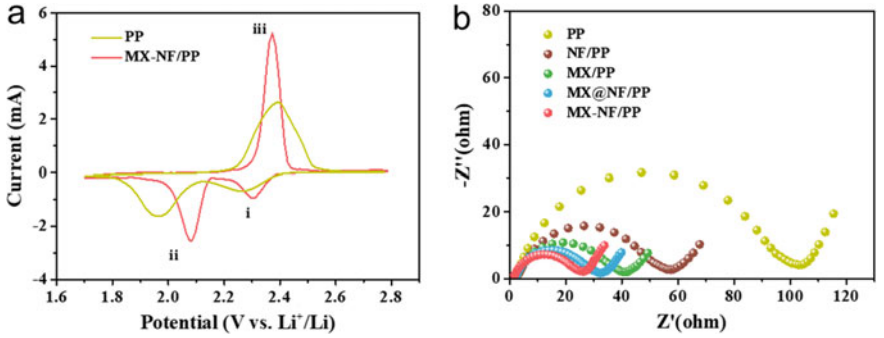

Fig. 6.14 **a** The CV curves of PP and MX-NF/PP cells. **b** The Nyquist plots of the cells assembled with different separators. Copyright (2019), Elsevier [31]

Cyclic voltammetry (CV) and electrochemical impedance spectroscopy (EIS) tests were used to explore the redox kinetics of the cells assembled by PP and MX-NF/PP separators [17]. As shown in Fig. 6.14a, the CV curves of PP and MX-NF/PP cells all display three typical peaks at around 2.30 (i), 2.05 V (ii), and 2.40 V (iii). The first two peaks appear in the cathodic scans, which are mainly due to that the solid S_8 is reduced to soluble polysulfides (Li_2S_n, $4 \leq n \leq 8$) and insoluble products (Li_2S_2, Li_2S). The last peak in the anodic scans corresponds to the converse oxidation process (i.e., Li_2S_2/Li_2S to Li_2S_{4-8} and to sulfur) [54, 55]. The peak ii and peak iii exist potential difference, which can be used to reveal the rate of redox kinetics to some extent [56]. These results suggest that MX-NF/PP cell exhibits rapid redox reactions and low internal resistance, which is derived from the rapid electron/ion transfer and reformative electrolyte wettability of modified layer [17, 57]. The Nyquist plots in Fig. 6.14b show the further evidence about rapid redox reactions and low internal resistance. The bulk resistance of MX-NF/PP cell is 25.4 Ω, which is much less than that of PP cell (103.5 Ω). And the bulk resistances of other cells assembled with NF/PP, MX/PP, MX@NF/PP separators are 57.8 Ω, 41.4 Ω, and 32.1 Ω, respectively.

MX-NF/PP cell possesses rapid redox kinetics and excellent polysulfide inhibition ability, which is expected to significantly improve the rate performance. The cell assembled with PP separator displays discharge capacities of 825, 675, 590, 213, and 195 mAh g^{-1} at 0.2, 0.5, 1.0, 2.0, and 3.0C, respectively. And the rate performances of cells assembled with NF/PP, MX/PP, and MX@NF/PP separators are moderately improved. In comparison, for MX-NF/PP cell, the discharge capacities at 0.2, 0.5, 1.0, 2.0, and 3.0C are 1234, 1027, 916, 859, and 794 mAh g^{-1}, respectively, which are superior to other cells. Furthermore, the cells assembled with PP, NF/PP, MX/PP, and MX@NF/PP separators display the discharge capacities of 195, 313, 537, and 637 mAh g^{-1} at 3.0C, respectively. The gradually increased capacities are mainly attributed to the decrease in internal resistance. Note that the capacity of MX-NF/PP cell is 794 mAh g^{-1} at 3.0C, which is higher than that of other cells. This also indicates that MX-NF/PP cell possesses rapid redox kinetics and lowest internal resistance. When the current density rate come back to 0.2C, the capacity retention of

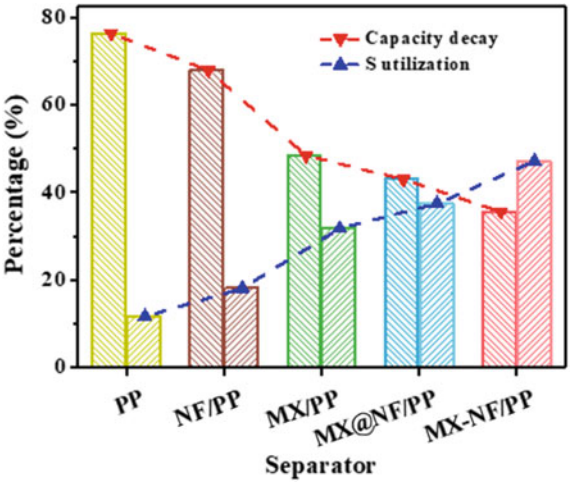

Fig. 6.15 The S utilization and capacity decay of different cells. Copyright (2019), Elsevier [31]

PP separator assembled cell (discharge capacity at 0.2C/initial discharge capacity at 0.2C) is 62.3%. In comparison, for MX-NF/PP cell, the capacity retention reaches to 82.3%, which indicates excellent rate performances for MX-NF/PP cell [58]. And the capacity retentions of NF/PP, MX/PP, and MX@NF/PP cells are only 70.2%, 72.1%, and 78.6%, respectively, which are lower than that of MX-NF/PP cell. Additionally, the capacity decay (compared with initial capacity) and S utilization (compared with theoretical capacity) of those cells at 3.0C were calculated to further highlight the excellent rate performance of MX-NF/PP cell. As shown in Fig. 6.15, the S utilization of MX-NF/PP cell is 47.1%, which is higher than that of PP cell (11.6%), MX/PP cell (31.7%), and MX@NF/PP cell (37.4%). Moreover, the capacity decay of MX-NF/PP cell (35.6%) is lower than MX@NF/PP cell (43.0%), MX/PP cell (48.5%), NF/PP cell (67.9%), and PP cell (76.4%). These results indicate that the cell assembled with MX-NP/PP separator possesses an excellent rate performance.

The ability of separators on inhibiting the polysulfide shuttle is a core factor for improving the long-life cycling performance of battery [13, 23]. Figure 6.16 shows that the cell assembled with PP separator displays a low initial capacity of 671 mAh g^{-1} and a capacity of 249 mAh g^{-1} after 590 cycles at 0.5C with a low capacity retention of 37.1%. By contrast, the cell assembled with MX-NF/PP separator displays an excellent cycling performance with a discharge capacity of 645 mAh g^{-1} after 1000 cycles at 1.0C and a higher capacity retention of 70.1% (the initial discharge capacity: 920 mAh g^{-1}). For MX@NF/PP separator, the assembled cell possesses a capacity retention of 47.2% (the initial discharge capacity: 880 mAh g^{-1}, the capacity after 1000 cycles: 415 mAh g^{-1}). In addition, more perfecter Coulombic efficiency appears in the cell assembled with MX-NF/PP separator than MX@NF/PP and PP cells. The excellent cycling performance of MX-NF/PP cell indicates that S-species are fully utilized, and a capacity decay of 0.03% per cycle is therefore achieved.

In conclusion, a MX-NF/PP functionalized separator with superior performances was fabricated by filtering layer-by-layer MXene nanosheets and Nafion solution

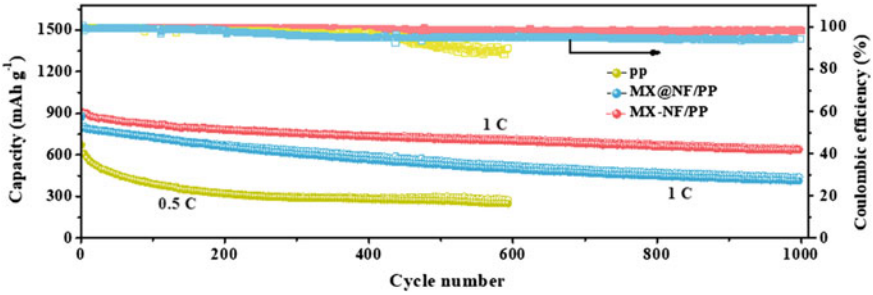

Fig. 6.16 Long-term cycling performances of PP cell at 0.5C, MX@NF/PP cell at 1.0C, and MX-NF/PP cell at 1.0C. Copyright (2019), Elsevier [31]

on PP separator. MX-NF/PP separator can effectively inhibit the polysulfide shuttle and promote the re-utilization of polysulfides. Therefore, the assembled Li–S battery displays a high initial discharge capacity of 1234 mAh g^{-1} and an excellent long-life cycling performance at 1.0C (capacity decay of 0.03% per cycle over 1000 cycles). These enhanced performances are mainly attributed to the synergistic effect of Nafion and MXene nanosheets. Nafion acts as a surfactant to evenly disperse MX-NF sheets, and then, MX-NF is orderly stacked on PP separator to form a regular structure, which can be effectively against polysulfides and realize re-utilization of such species. In addition, the MX-NF modification layer can inhibit the polysulfide shuttle and transport Li^+ by electrostatically repulses. This study proposes a strategy of sheet-polymer modification layer for designing high-performance Li–S batteries.

6.4 Asymmetry-Structure LLTO Composite Electrolyte

$Li_{0.33}La_{0.557}TiO_3$ (LLTO) nanoparticles (LP) were obtained by sol–gel method in literatures [59, 60]. Preparation of asymmetric LLTO framework (ALF) was based on breath figure method by sintering asymmetric PS template which contains LLTO precursors [61]. Firstly, $LiNO_3$, $La(NO_3)_3{\cdot}6H_2O$, and $Ti(OC_4H_9)_4$ were weighted according to the stoichiometric ratio, and then, they were dissolved in the mixture solution of anhydrous ethanol and acetic acid (volume ratio of 8:2) and stirred for 20 min to obtain a precursor solution. Then, the obtained precursor solution was added into trichloromethane (TCM) solution which contains 10 wt% PS, followed by stirring for 24 h to form a homogeneous solution. Afterward, the obtained homogeneous solution was dripped on the quartz plate (humidity > 99%) and dried for 3 h at 60 °C to acquire PS template. Next, the high ionic conductivity of asymmetric LLTO framework was obtained by sintering PS template at 1000 °C for 2 h in the air [62].

Next is using solution-dripping method to prepare the PEO/LiTFSI/ALF (PLALF) electrolyte. Firstly, the LiTFSI and PEO were weighed with molar ratio of Li^+:EO

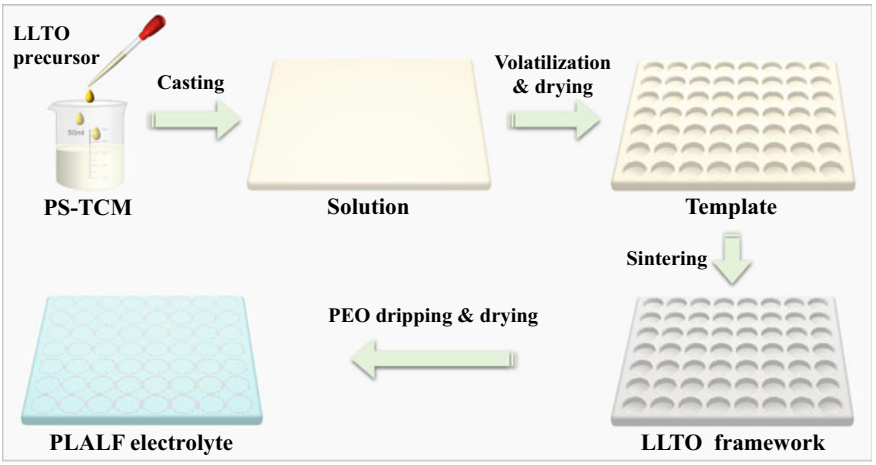

Fig. 6.17 Synthetic diagram of the preparation of PLALF electrolyte. Copyright (2021), Elsevier [32]

to be 1:18, and then, they were dissolved in acetonitrile, followed by stirring to form homogenized solution. Then, the obtained solution was dripped on the above asymmetric LLTO framework. Afterward, the obtained product was dried at 60 °C for 2 h. Repeating the above process ensures that PEO is completely filled into the asymmetric LLTO framework. Figure 6.17 shows the preparation process of the PLALF electrolyte.

PEO/LiTFSI/LP (PLLP) electrolyte was prepared by solution casting method. Concretely, LiTFSI, PEO, and LLTO nanoparticles were added into acetonitrile and stirred to form homogenized casting solution (the molar ratio of Li^+:EO to be 1:18). Then, the obtained casting solution was casted on polytetrafluoroethylene plates, followed by drying at 50 °C for 48 h to ensure that the solvent evaporates completely. Similarly, PEO/LiTFSI (PL) electrolyte was obtained by the same method without LLTO nanoparticles. All operations are performed in argon-filled glove box.

SEM images in Fig. 6.18a, b show that the obtained PS template containing LLTO precursor possesses the obvious asymmetric structure with the dense side and porous side. After sintering the PS template, asymmetric LLTO framework was obtained. Figure 6.18c, d shows that LLTO framework has an obvious asymmetric structure with the dense side and porous side. The prepared LLTO framework was then impregnated with PEO/LiTFSI to fabricate PLALF electrolyte. Meanwhile, a thin PEO layer (~1 μm) was coated on each side of electrolyte to ensure the better contact of electrode and electrolyte. Unlike LLTO framework, the surface of PLALF electrolyte (porous layer, named as PLALF-P) displays a barely visible pore structure (Fig. 6.19a), which suggests that LLTO framework can be well wetted with polymer. Additionally, after coating PEO, the other side of PLALF (dense layer, named as PLALF-D) possesses a dense and smooth surface (Fig. 6.19b).

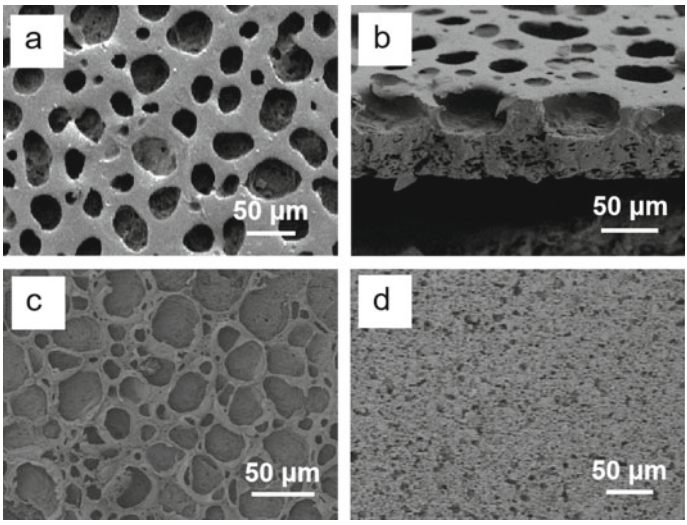

Fig. 6.18 Surface (**a**) and cross-sectional (**b**) SEM images of PS template containing LLTO precursor. Surface SEM images of LLTO framework **c** porous side and **d** dense side surface. Copyright (2021), Elsevier [32]

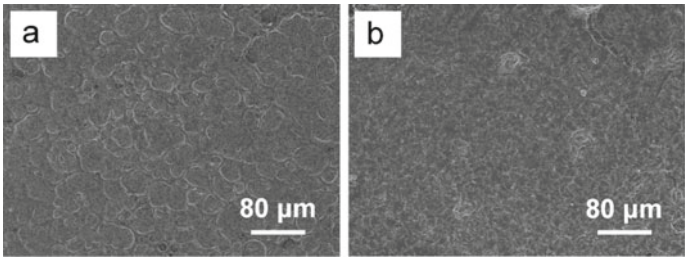

Fig. 6.19 Surface SEM images of PLALF-P (**a**) and PLALF-D (**b**). Copyright (2021), Elsevier [32]

The prepared PLALF electrolyte displays excellent flexibility and easy foldability (Fig. 6.20a, b). Figure 6.20c shows that the crystallinity of PEO is reduced due to the addition of LLTO nanoparticles [63, 64]. Similarly, PLALF electrolyte displays that the crystallization peak of PEO is sharply weakened. This decrease in crystallinity should be attributed to the confinement effect of LLTO framework, which effectively inhibits the crystallization of PEO [65]. The high compressive strength of electrolyte is crucial to reduce the risk of dendrite-induced short circuit in battery [66, 67]. Nanoindentation test can simulate the Li dendrite growth and is used to examine the compressive properties of the prepared electrolytes. As is shown in Fig. 6.20d, the PL electrolyte displays the maximal displacement of 4910 nm and the final depth after unloading of 3258 nm. By contrast, the dense side of PLALF electrolyte (PLALF-D)

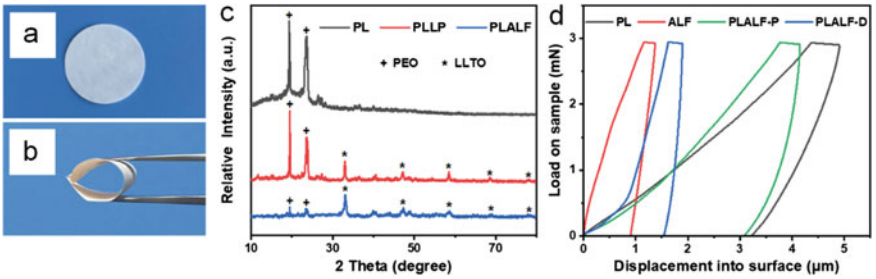

Fig. 6.20 **a**, **b** Photographs of PLALF electrolyte. **c** XRD patterns of PLALF, PLLP, and PL electrolytes. **d** Load–displacement curves of PLALF, PLLP, and PL electrolytes under nanoindentation test. Copyright (2021), Elsevier [32]

shows the maximal displacement and the final depth after unloading of 1895 and 1546 nm, respectively, which are similar with ALF. In addition, the porous side of PLALF electrolyte (PLALF-P) exhibits the maximal displacement of 4151 nm and the final depth after unloading of 3107 nm, which are similar with PL electrolyte. These results indicate that the ALF possesses unique advantage in enhancing the compressive strength of PLALF electrolyte, which can effectively inhibit Li dendrite growth. Note that the initial loading curve of the dense side of PLALF electrolyte (<1 μm) is similar with the loading curve of PL electrolyte, while the final loading curve (>1 μm) is similar with the loading curve of LLTO framework. This indicates that the thickness of PEO layer is about 1 μm (the dense side of PLALF electrolyte). The coating of thin PEO layers on each side of PLALF electrolyte will enhance the contact of electrode and electrolyte, which is significant for reducing interface impedance. Additionally, the thin PEO layer can also prevent the LLTO from reacting with Li anode, which benefits to enhance the interface stability [68–70].

Figure 6.21a shows the ionic conductivity of PLALF, PLLP, and PL electrolytes at different temperatures. PL electrolyte exhibits low ionic conductivities of 3.73 $\times$ 10^{-6} and 3.65 $\times$ 10^{-4} S cm^{-1} at 30 and 60 °C, respectively, which are similar to previous reports [71, 72]. In addition, the activation energy of PL electrolyte changes strongly at temperatures above and below the melting point of PEO due to PEO crystallization [73]. By contrast, the ionic conductivities of PLLP electrolyte are up to 2.89 $\times$ 10^{-5} and 6.41 $\times$ 10^{-4} S cm^{-1} at 30 and 60 °C, respectively. The ionic conductivity enhancement is because LLTO nanoparticles provide rapid Li^+ transfer pathways and reduce the crystallization of PEO. However, LLTO nanoparticles are discrete distribution in PLLP electrolyte, which cannot provide a continuous Li^+ transport pathway, and thus, the conductivity enhancement is limited. LLTO framework, providing a continuous Li^+ transport pathway, will greatly enhance ion conductivity and reduce the activation energy [64, 65, 74, 75]. Thus, the ionic conductivity of PLALF electrolyte is increased to 1.49 $\times$ 10^{-4} S cm^{-1} at 30 °C, which is 5.2 and 40.0 times that of PLLP and PL electrolytes, respectively. It is worth noting that the activation energy for PLALF electrolyte does not change significantly.

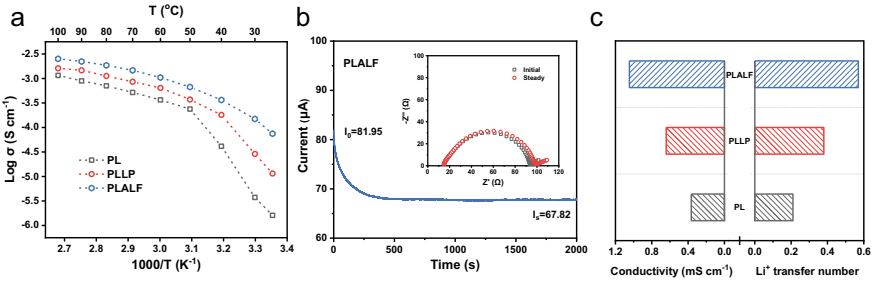

Fig. 6.21 **a** Temperature-dependent conductivities of PLALF, PLLP, and PL electrolytes. **b** The chronoamperometry curves of PLALF electrolyte at 60 °C (inset: AC impedance curves of the corresponding cells before and after polarization) **c** Li^+ transference number and ionic conductivity of PLALF, PLLP, and PL electrolytes at 60 °C. Copyright (2021), Elsevier [32]

Li^+ transference number (t_{Li+}) is also an important parameter for solid-state electrolyte. In general, the Li^+ transference number of polymer-based electrolyte is low, which is caused by the coexistence of anion and cation that move oppositely under the electric field in the system [76, 77]. Figure 6.21c displays that the t_{Li+} of PL electrolyte is 0.21. In comparison, PLLP electrolyte exhibits a t_{Li+} value of 0.38. After adding LLTO nanoparticles, the improvement of t_{Li+} is not obvious because LLTO has low loading amount with discrete distribution in PLLP electrolyte. For PLALF electrolyte, possessing continuous Li^+ transport path provided by LLTO framework achieves a t_{Li+} value of 0.57, which is much higher than that of PLLP and PL electrolytes. A higher t_{Li+} value will efficiency improve the charge transfer of electrolyte and thus reduce the concentration polarization [78, 79].

Li|PLALF|Li cell was assembled to explore the stability of Li electrode and electrolyte during the cycling. As shown in Fig. 6.22, Li|PLALF|Li cell exhibits stable plating/stripping behavior under different current densities. It can be seen that Li|PLALF|Li cell displays a voltage profile of 8 mV at 0.05 mA cm^{-2}, which is lower than those of Li|PL|Li and Li|PLLP|Li cells (30 and 16 mV). This is because of the continuous Li^+ transport path of LLTO framework, which endows PLALF electrolyte with low internal resistance. When the current density increases to 0.10 mA cm^{-2}, the Li|PL|Li cell shows a sharp drop in voltage after 30 h of cycling. This phenomenon mainly results from the uneven deposition of Li^+ and the less mechanical strength of the electrolyte, which cannot inhibit Li dendrite growth [67, 80]. Similarly, Li|PLLP|Li cell exhibits the same phenomenon under 0.20 mA cm^{-2}. By contrast, Li|PLALF|Li cell displays stable voltage profiles without short circuits for 600 h. This improved stability is mainly due to the dense layer of LLTO framework and hence uniform Li-ion deposition and improved compressive strength of PLALF electrolyte. Thus, PLALF electrolyte can effectively act as a physical barrier to inhibit Li dendrite growth.

Next, the prepared electrolytes were assembled into Li–S cells to investigate the stability of the electrolytes. Figure 6.23a shows that the S|PLLP|Li and S|PL|Li cells exhibit the initial capacities of 1131.4 and 987.9 mAh g^{-1} at 0.05C and

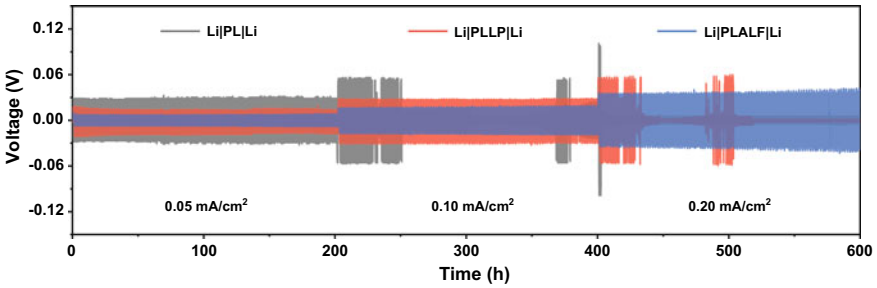

Fig. 6.22 Long-term cycling of Li|PL|Li, Li|PLLP|Li, and Li|PLALF|Li symmetrical cells at 60 °C. Copyright (2021), Elsevier [32]

60 °C, respectively. In contrast, S|PLALF|Li cell displays a higher initial capacity of 1234.6 mAh g^{-1} because of the higher ionic conductivity for PLALF electrolyte [81]. As shown in Fig. 6.23b, S|PLALF|Li cell exhibits flat and long voltage plateaus, which indicates that uncompromising polarization occurs during the charging and discharging processes. Differently, S|PL|Li cell suffers from micro short circuit after 10 cycles, which is mainly due to the fact that PL electrolyte possesses the inferior ability of inhibiting Li dendrite growth. And abundant Li dendrites are found on the cycled Li anode (Fig. 6.24a). S|PLLP|Li is able to operate 60 cycles because the addition of LLTO nanoparticles endows PLLP electrolyte with higher ionic conductivity, which will improve cycle performance of cell. However, S|PLLP|Li occurs short circuit after 63 cycles owing to the Li dendrite growth on the surface of Li anode (Fig. 6.24b). Figure 6.24c shows that the surface of cycled Li anode of S|PLALF|Li cell displays no obvious Li dendrite growth. This is mainly because PLALF electrolyte possesses the excellent ability of uniform Li-ion deposition and high compressive strength. This also endows S|PLALF|Li cell with excellent cycling performance. The cell possesses a discharge capacity of 907.6 mAh g^{-1} after 100 cycles with a Coulombic efficiency of ~99%. Additionally, XPS was used to explore the stability between PLALF electrolyte and Li anode. Figure 6.25 shows that the XPS Ti 2p spectrum displays two peaks at 463.9 and 458.1 eV, which correspond to the $p_{1/2}$ and $p_{3/2}$ peaks of Ti^{4+}, respectively. This indicates PLALF electrolyte is stable during the cell cycling [68].

In conclusion, breath figure method is used to fabricate the LLTO framework with an asymmetric structure, and then, the LLTO framework is impregnated with PEO to form composite electrolyte. The LLTO framework provides a rapid Li^+ transport path, which can effectively promote Li^+ transport in PLALF electrolyte. Thus, the electrolyte achieves a high ionic conductivity and t_{Li+}: 1.05×10^{-3} S cm^{-1} and 0.57 at 60 °C. Additionally, the dense layer of LLTO framework can give uniform Li-ion deposition and improve the compressive strength of PLALF electrolyte. Thus, PLALF electrolyte can effectively act as a physical barrier to inhibit Li dendrite growth. Consequently, the PLALF electrolyte assembled Li–S battery displays an excellent cycling performance. S|PLALF|Li cell displays an initial discharge capacity of 1234.6 mAh g^{-1}. Moreover, it can be cycled stably for 100 cycles at 0.05C and

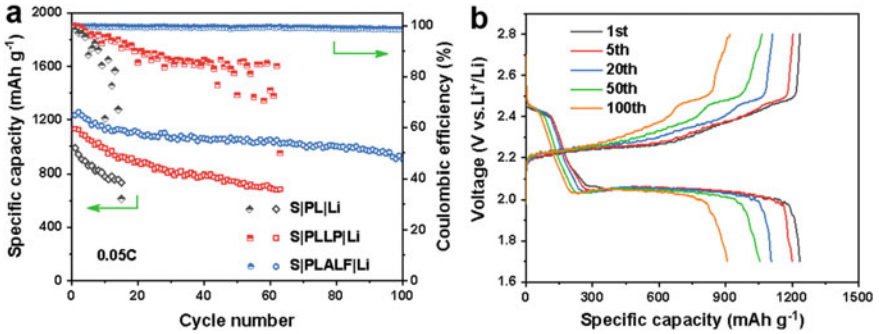

Fig. 6.23 **a** Cycling performances of PLALF, PLLP, and PL electrolytes assembled cells. **b** Discharge–charge profiles of PLALF electrolyte assembled cell. Copyright (2021), Elsevier [32]

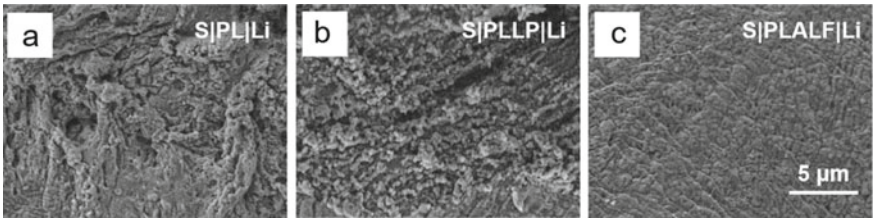

Fig. 6.24 SEM surface images of the cycled Li anode of PLALF, PLLP, and PL electrolytes assembled cells. Copyright (2021), Elsevier [32]

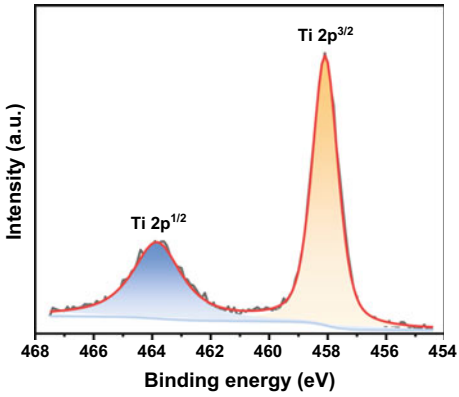

Fig. 6.25 The XPS Ti 2p spectra collected from PLALF electrolyte after charge/discharge cycling. Copyright (2021), Elsevier [32]

60 °C (Coulombic efficiency: ~99%). The design strategy of asymmetrically structured SSE might provide a new way to design the next-generation high-performance Li–S battery.

6.5 Laminar Vermiculite Composite Electrolyte

The vermiculite (Vr) nanosheets were obtained by a two-step ion exchange method. Firstly, Vr (0.5 g) and saturated NaCl solution (100 mL) were mixed and stirred for 24 h at 120 °C to obtain Na-exchanged vermiculite. Then, the obtained product was washed by 5 times with water to remove excess ions. Afterward, the washed product and LiCl solution (2 M, 100 mL) were mixed and stirred for 48 h at 120 °C to obtain Li-exchanged vermiculite. Then, the product was washed by 3 times, followed by sonication for 20 min and centrifugation at 8000 rpm for 15 min to obtain Vr nanosheets. Finally, Vr nanosheets were filtrated into laminar Vr framework on a support (anodic aluminum oxide, AAO) and then dried at 200 °C for 12 h.

Then, laminar composite solid electrolyte was fabricated by a swelling and filtration method, and as shown in Fig. 6.26, the obtained laminar Vr framework was swelled in acetonitrile (C_2H_3N) solution for 1 h to ensure that the framework possesses a large interlayer distance. Afterward, PEO and LiTFSI were dissolved in acetonitrile to form a uniform solution (0.1 wt%), and then, the solution was filtrated into the interlayer of the laminar Vr framework to obtain the laminar composite solid polymer electrolyte. Notably, the thickness of electrolyte was determined by the amount of Vr nanosheets and PEO-LiTFSI, and the obtained electrolytes were named as Vr/PEO-LCSE-X (X: thickness, μm).

Figure 6.27a shows that laminar Vr framework displays smooth and complete surface structure without obvious cracks. Additionally, laminar Vr framework possesses a typical laminar structure with regular interlayer channels (Fig. 6.27b). Next, PEO-LiTFSI uniform solution was filtrated into the interlayer spacing of the swelled laminar Vr framework to obtain Vr/PEO-LCSE. Cross-sectional SEM

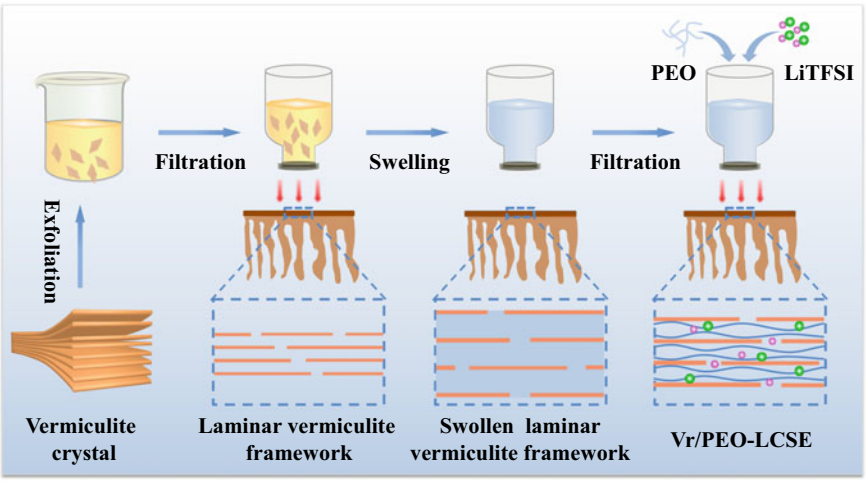

Fig. 6.26 Synthetic diagram of the preparation of Vr/PEO-LCSE. Copyright (2020), Royal Society of Chemistry [33]

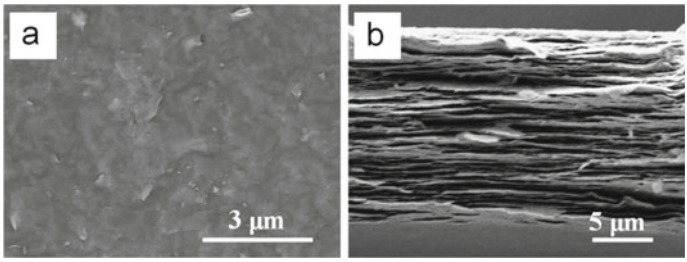

Fig. 6.27 **a** Surface and **b** cross-sectional SEM images of laminar Vr framework. Copyright (2020), Royal Society of Chemistry [33]

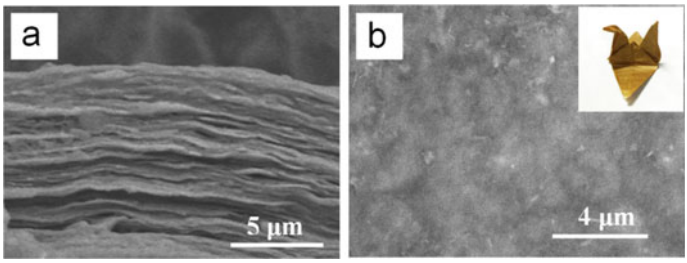

Fig. 6.28 **a** Cross-sectional and **b** Surface SEM images of Vr/PEO-LCSE (inset is a paper crane folded by Vr/PEO-LCSE). Copyright (2020), Royal Society of Chemistry [33]

image in Fig. 6.28a shows that PEO-LiTFSI could be effectively filled and evenly distributed in the interlayer of laminar Vr framework. Additionally, Fig. 6.28b shows that Vr/PEO-LCSE displays a smoother surface than that of laminar Vr framework. Collectively, these results indicate that the swelling and filtration processes could ensure the uniform entrance and distribution of PEO-LiTFSI in the interlayer spacing of laminar Vr framework.

Meanwhile, solution casting method was used to fabricate pure PEO electrolyte (PEO-SPE) and Vr-PEO composite electrolyte (Vr/PEO-CSPE) for comparison. Fourier transform infrared (FTIR) was used to analyze the dissociation degree of LiTFSI. As shown in Fig. 6.29a, the peak of Vr/PEO-LCSE, Vr/PEO-CSPE, and PEO-SPE can be deconvoluted into free $TFSI^-$ and bonded LiTFSI ion pairs at ~740 and ~746 cm^{-1}, respectively [82–84]. The dissociation degree of LiTFSI in PEO-SPE is 83.7%. For Vr/PEO-CSPE, the dissociation degree increases to 88.9% because Vr nanosheets and LiTFSI exist in the Lewis acid–base interaction, which promotes dissociation of LiTFSI [67, 85]. By contrast, Vr/PEO-LCSE displays a higher LiTFSI dissociation degree of 95.7%. This is because the laminar structure provides more sufficient contact between nanosheets and LiTFSI, which further promotes dissociation of LiTFSI.

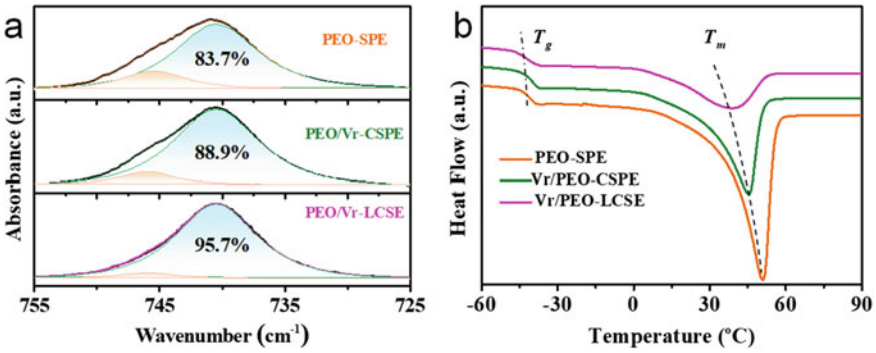

Fig. 6.29 **a** FTIR spectra of Vr/PEO-LCSE, Vr/PEO-CSPE, and PEO-SPE (725–755 cm^{-1}). **b** DSC profiles of Vr/PEO-LCSE, Vr/PEO-CSPE, and PEO-SPE. Copyright (2020), Royal Society of Chemistry [33]

DSC was used to analyze hermodynamic properties of the electrolytes. As shown in Fig. 6.29b, PEO-SPE exhibits the melting point (T_m) and glass transition temperature (T_g) of 50 and −40 °C, respectively [73, 86]. For Vr/PEO-CSPE, the T_m and T_g decrease to 45 and −42 °C, respectively. This is because adding Vr nanosheets reduces the crystallinity of polymer and improves the chain motility of PEO. By contrast, Vr/PEO-LCSE displays the further lower T_m and T_g of 39 and −44 °C, respectively. And the crystallinity of Vr/PEO-LCSE is calculated to be 28%, which is lower than those of PEO-SPE (45%) and Vr/PEO-CSPE (34%). These results indicate that the vacuum-filtration process of PEO matrix into nanoconfined interlayer of laminar Vr framework can facilitate the stretching of PEO chain and thus improve the chain mobility [87]. Low crystallization and high chain motility will endow PEO with rapid transport ability for Li^+.

Generally, lower crystallinity means weaker mechanical strength [88]. However, the strong rigidity of Vr nanosheets and the typical brick-and-mortar architecture, as well as the hydrogen-bonding interactions between C−O−C on PEO and −OH on Vr (Fig. 6.30a), endow Vr/PEO-LCSE with outstanding mechanical strength [69, 89]. Nanoindentation test, simulating the Li dendrite growth, is used to examine the compressive properties of the fabricated electrolytes [67, 75, 83]. As shown in Fig. 6.30b, PEO-SPE displays the compressive strength of around 20 MPa. For Vr/PEO-CSPE, the compressive strength increases to 31 MPa. This is because adding Vr nanosheets improves the compressive strength of CSPE. By contrast, Vr/PEO-LCSE exhibits a compressive strength of 131 MPa, which is 2.2 and 4.5 times higher than those of Vr/PEO-CSPE and PEO-SPE. Additionally, Vr/PEO-LCSE also displays outstanding flexibility (Fig. 6.28b). Those phenomena indicate that Vr/PEO-LCSE possesses excellent flexibility and high mechanical strength.

Figure 6.31a shows the ionic conductivity of the fabricated electrolytes. PEO-SPE displays a low ionic conductivity of 9.62×10^{-7} S cm^{-1} at 25 °C. After adding Vr nanosheets, the ionic conductivity of Vr/PEO-CSPE increases to 4.51×10^{-6} S cm^{-1} at 25 °C. This is because the added nanosheets reduce the crystallinity

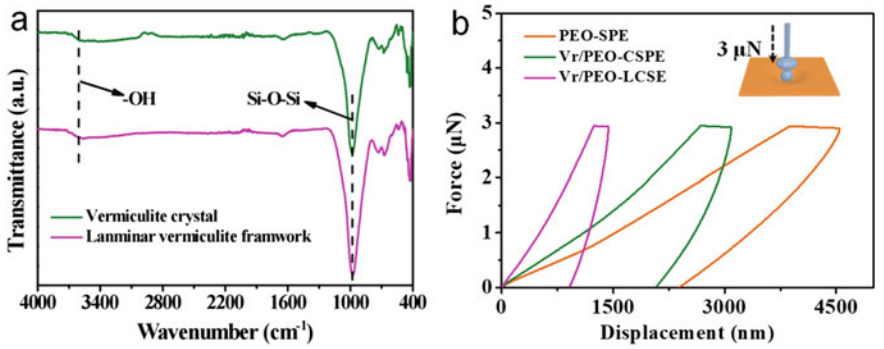

Fig. 6.30 **a** FTIR spectra of laminar Vr framework and Vr crystal. **b** Load–displacement curves of Vr/PEO-LCSE, Vr/PEO-CSPE, and PEO-SPE under nanoindentation test. Copyright (2020), Royal Society of Chemistry [33]

of polymer and improve the chain motility of PEO. By contrast, Vr/PEO-LCSE achieves a high ionic conductivity of 1.22×10^{-5} S cm^{-1} at 25 °C, which is 11.6 times higher than that of PEO-SPE. Because laminar Vr framework possesses the poor ionic conductivity, the conductivity enhancement might come from the confined PEO-LiTFSI in the interlayer spacing of laminar Vr framework. The confinement effect promotes dissociation of LiTFSI (dissociation degree: Vr/PEO-LCSE, 95.7% *vs.* PEO-SPE, 83.7%) and reduces the crystallinity of PEO (Vr/PEO-LCSE, 28% *vs.* PEO-SPE, 45%). Thus, Vr/PEO-LCSE obtains a high ionic conductivity value.

The area-specific-resistance (ASR) is also a key parameter directly reflecting the rate performance and the internal resistance of cell [90, 91]. As shown in Fig. 6.31b, Vr/PEO-CSPE and PEO-SPE (thickness ~100 μm) display the ASR of 1124 and 3332 Ω cm^2 at 30 °C, respectively. By contrast, Vr/PEO-LCSE exhibits an ultralow ASR of 66 Ω cm^2 at 30 °C, which is 50 times lower than that of PEO-SPE. This is because Vr/PEO-LCSE possesses ultrathin thickness of 10 μm and high ionic conductivity.

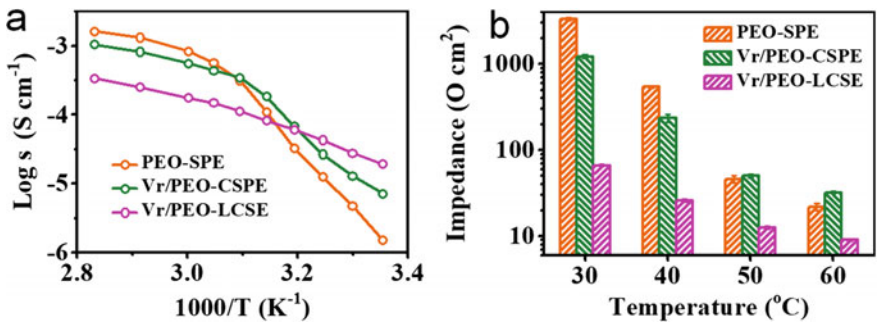

Fig. 6.31 **a** Temperature-dependent conductivities of Vr/PEO-LCSE, Vr/PEO-CSPE, and PEO-SPE. **b** The ASR of Vr/PEO-LCSE, Vr/PEO-CSPE, and PEO-SPE at different temperature. Copyright (2020), Royal Society of Chemistry [33]

Additionally, the ionic conductivities of the electrolytes increase significantly when increasing the temperature. For instance, the ionic conductivity of Vr/PEO-LCSE increases to 1.11 × 10^{-4} S cm^{-1} at 60 °C, which is 7 times higher than that at 30 °C. By contrast, PEO-SPE and Vr/PEO-CSPE display more obvious conductivity enhancement. Vr/PEO-CSPE and PEO-SPE achieve the ionic conductivities of 3.10 × 10^{-4} and 4.50 × 10^{-4} S cm^{-1} at 60 °C, respectively. Although the ionic conductivities of Vr/PEO-CSPE (35 times) and PEO-SPE (151 times) are improved obviously, the ASR values of Vr/PEO-CSPE (32 Ω cm^2) and PEO-SPE (22 Ω cm^2) are still higher than Vr/PEO-LCSE (9 Ω cm^2) at 60 °C.

Li symmetric cells were assembled to explore the cycling stability of the prepared electrolytes [68, 92]. As shown in Fig. 6.32, all the assembled Li symmetric cells display stable voltage profiles with 0.05 mA cm^{-2} at 60 °C. Li|Vr/PEO-LCSE|Li cell exhibits overpotential (14 mV), which is lower than that of Li|Vr/PEO-CSPE|Li cell (29 mV) and Li|PEO-SPE|Li cell (21 mV). This is because Vr/PEO-LCSE possesses low ASR value. However, Li|PEO-SPE|Li cell occurs short circuit after cycling for 30 h with the current density of 0.1 mA cm^{-2}. This is because of the low t^+-induced uneven deposition of lithium and poor mechanical strength of PEO-SPE [93, 94]. By contrast, Li|Vr/PEO-CSPE|Li cell can operate for 200 h at 0.1 mA cm^{-2}, because the added Vr nanosheets increase the t^+ and mechanical strength of electrolyte, while Li|Vr/PEO-CSPE|Li cell suffers short circuit after cycling 60 h with 0.2 mA cm^{-2}. By contrast, Li|Vr/PEO-LCSE|Li cell can be cycled stably with different current densities. This is because of the high mechanical strength and t^+ of Vr/PEO-LCSE. Those results indicate that Vr/PEO-LCSE-assembled cell possesses outstanding cycling performance, which further demonstrates the high t^+ and small ASR of Vr/PEO-LCSE.

To further evaluate cycling performance, the fabricated electrolytes were assembled into Li−S cell. Figure 6.33 shows that the assembled cells display two characteristic reaction plateaus in the discharge curves, corresponding to the results in literatures [95–97]. As shown in Fig. 6.33a, S|PEO-SPE|Li cell exhibits initial charge and discharge capacities of 1364 and 836 mAh g^{-1}, respectively, which are lower than the theoretical capacity of 1675 mAh g^{-1}. While S|PEO-SPE|Li cell displays

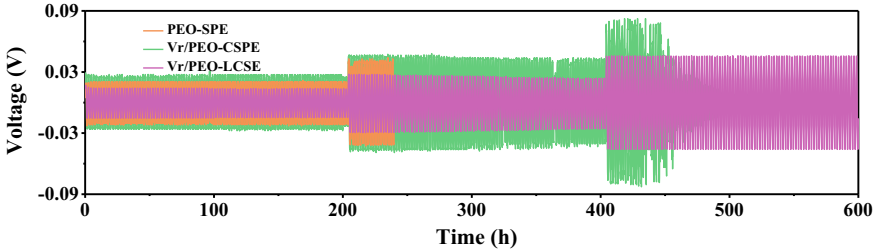

Fig. 6.32 Galvanostatic cycling performances of Li|Vr/PEO-LCSE|Li, Li|Vr/PEO-LCSE|Li, and Li|PEO-SPE|Li cells with different current densities at 60 °C. Copyright (2020), Royal Society of Chemistry [33]

overcharge phenomenon during the 6th cycle. This is mainly due to the side reaction between polysulfides and Li anode [95, 98]. For Vr/PEO-CSPE, the presence of Vr nanosheets can effectively inhibit the polysulfide shuttle; thus, the assembled cell exhibits the initial capacity of 1141 mAh g^{-1} (Fig. 6.33b). By contrast, the layer-by-layer stacked Vr nanosheets endow LCSE with better polysulfide inhibition ability. S|Vr/PEO-LCSE|Li cell displays a higher initial capacity of 1254 mAh g^{-1} (Fig. 6.33c). Additionally, Vr/PEO-LCSE also possesses high t^+ and mechanical strength, which ensures S|Vr/PEO-LCSE|Li cell an excellent cycling stability. S|Vr/PEO-LCSE|Li exhibits the high capacity of 1017 mAh g^{-1} at 0.05 C after 150 cycles and a high Coulombic efficiency of 95%.

Generally, the internal resistance is also an important parameter impacting the rate performance of cells [99]. The EIS impedance spectra exhibit a typical semicircle and the intercept of real axis at high frequency, corresponding to the charge-transfer resistance (R_{ct}) and ohmic resistance (R_o), respectively (Fig. 6.34a) [100, 101]. Li|Vr/PEO-LCSE|S cell displays R_o of 10 Ω, which is close to those of S|Vr/PEO-CSPE|Li (14 Ω) and S|PEO-SPE|Li (12 Ω) cells. However, S|Vr/PEO-LCSE|Li exhibits a low R_{ct} value of 22 Ω, which is lower than those of S|Vr/PEO-CSPE|Li (74 Ω) and S|PEO-SPE|Li (121 Ω) cells. This is because Vr/PEO-LCSE possesses the small ASR. Additionally, considering that the impedance of cells also is influenced by the dissolution and shutting of lithium polysulfides, the cycled cells

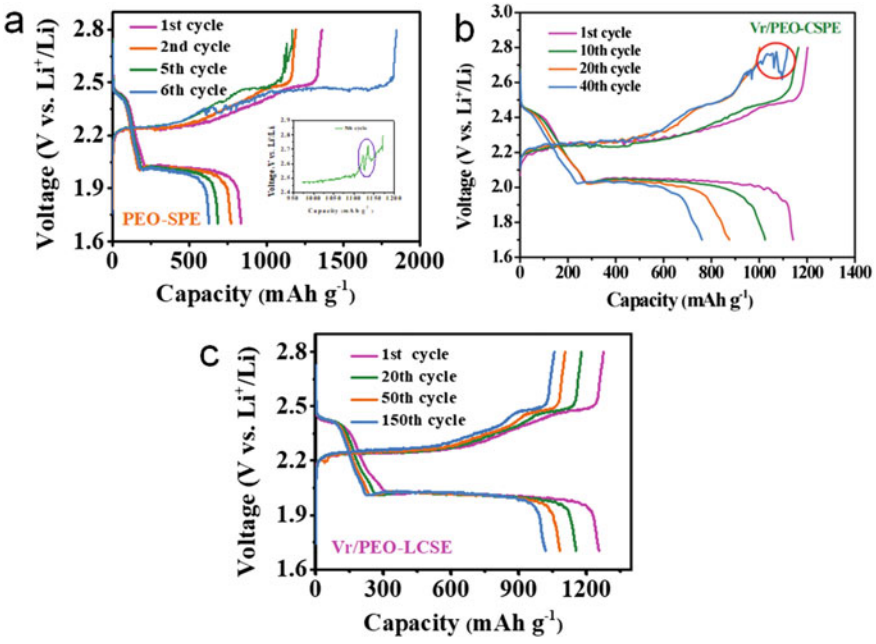

Fig. 6.33 Discharge/charge curves of **a** S|PEO-SPE|Li, **b** S|Vr/PEO-CSPE|Li, and **c** S|Vr/PEO-LCSE|Li cells at 0.05 C. Copyright (2020), Royal Society of Chemistry [33]

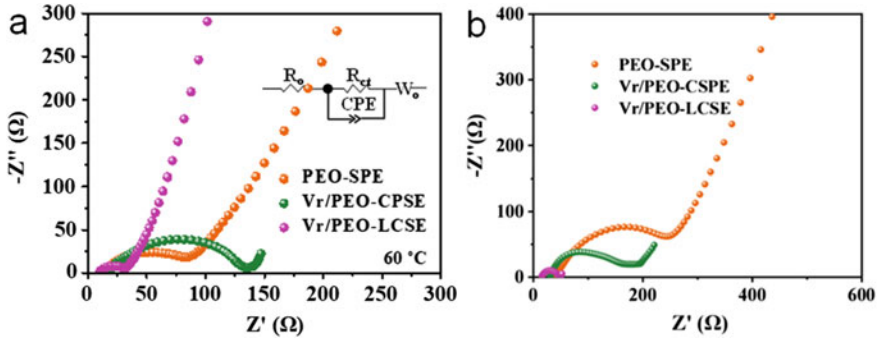

Fig. 6.34 **a** The initial EIS impedance spectra and **b** EIS impedance spectra after 5 cycles of S|Vr/PEO-LCSE|Li, S|Vr/PEO-CSPE|Li, and S|PEO-SPE|Li cells at 60 °C. Copyright (2020), Royal Society of Chemistry [33]

are tested by EIS impedance spectra. As shown in Fig. 6.34b, S|Vr/PEO-CSPE|Li and S|PEO-SPE|Li cells display the R_{ct} values of 158 and 223 Ω, respectively. The increase in R_{ct} value is mainly due to polysulfide shuttle. By contrast, owing to outstanding polysulfide-inhibiting ability, Vr/PEO-LCSE-assembled cell displays a small change from 22 to 34 Ω.

The outstanding polysulfide-inhibiting ability, high mechanical strength, as well as low internal resistance of Vr/PEO-LCSE endow the assembled S|Vr/PEO-LCSE|Li cell with excellent rate performance. Figure 6.35a shows that the discharge curves of S|Vr/PEO-LCSE|Li cell exhibit two characteristic reaction plateaus at different rates, which indicates the reversible and rapid redox reactions. Additionally, S|Vr/PEO-LCSE|Li cell displays high capacity under different current densities in Fig. 6.35b (the capacities at 0.05C and 0.2C are 1252 and 1000 mAh g^{-1}, respectively). Moreover, when the current density comes back to 0.05C, the discharge capacity of S|Vr/PEO-LCSE|Li cell returns to 1100 mAh g^{-1}. By contrast, S|Vr/PEO-CSPE|Li cell occurs short circuit when the current density increases to 0.1C.

In conclusion, we fabricated a 10-μm-thick laminar composite solid electrolyte with high mechanical strength and ionic conductivity. Concretely, Vr nanosheets are assembled into laminar Vr framework by vacuum-filtration process, and then, PEO-LiTFSI is intercalated into the interlayer channels of laminar Vr framework by a swelling and filtration method. The confinement effect of regular interlayer channels promotes dissociation of LiTFSI and reduces the crystallinity of PEO. Thus, the ionic conductivity of Vr/PEO-LCSE is greatly enhanced (1.22×10^{-5} S cm^{-1} at 25 °C). Additionally, owing to the thin thickness, Vr/PEO-LCSE possesses an ultralow ASR of 66 Ω cm^2 at 30 °C, which is about 50 times lower than that of PEO-SPE. Meanwhile, the typical brick-and-mortar architecture together with the strong rigidity of Vr nanosheet endows Vr/PEO-LCSE with high mechanical strength. The outstanding polysulfide-inhibiting ability, excellent mechanical strength, and high t^+ impart Li|Vr/PEO-LCSE|S cell excellent cycling performance. The assembled S|Vr/PEO-LCSE|Li cell displays a high initial capacity of 1254 mAh g^{-1}, and a

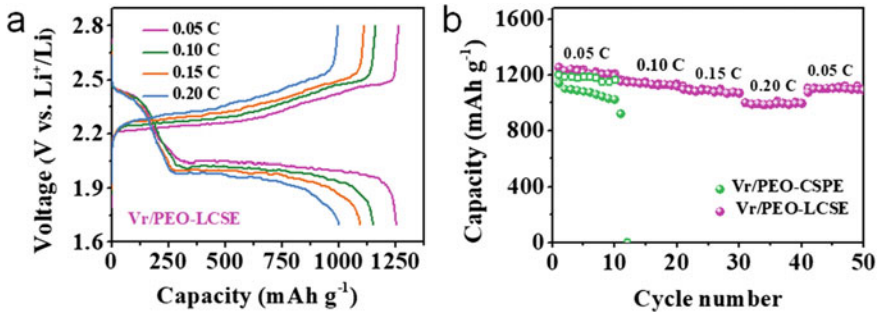

Fig. 6.35 **a** Discharge/charge curves of S|Vr/PEO-LCSE|Li cell with different current densities. **b** The cycling performance of S|Vr/PEO-LCSE|Li cell with different current densities. Copyright (2020), Royal Society of Chemistry [33]

capacity retention of 1017 mAh g^{-1} after 150 cycles. This study might propose a strategy of laminar composite solid electrolyte for designing high-performance Li–S batteries.

References

1. P.G. Bruce, S.A. Freunberger, L.J. Hardwick, J.M. Tarascon, Li–O_2 and Li–S batteries with high energy storage. Nat. Mater. **11**, 19–29 (2012)
2. J. Ran, H. Wang, H. Jin, C. Ling, X. Zhang, H. Ju, L. Jing, J. Wang, R. Zheng, S.Z. Qiao, Metallic MoN ultrathin nanosheets boosting high performance photocatalytic H_2 production. J. Mater. Chem. A **6**, 23278–23282 (2018)
3. T. Zhao, J. Zhang, Z. Du, Y. Liu, G. Zhou, J. Wang, Dopamine-derived N-doped carbon decorated titanium carbide composite for enhanced supercapacitive performance. Electrochim. Acta **254**, 308–319 (2017)
4. Y. Yan, C. Cheng, L. Zhang, Y. Li, J. Lu, Deciphering the reaction mechanism of lithium–sulfur batteries by in situ/operando synchrotron-based characterization techniques. Adv. Energy Mater. **9**, 1900148 (2019)
5. H.J. Peng, J.Q. Huang, X.B. Cheng, Q. Zhang, Review on high-loading and high-energy lithium–sulfur batteries. Adv. Energy Mater. **7**, 1700260 (2017)
6. Y. Zhao, Y. Ye, F. Wu, Y. Li, R. Chen, Anode interface engineering and architecture design for high-performance lithium–sulfur batteries. Adv. Mater. **31**, 1806532 (2019)
7. D. Lei, K. Shi, H. Ye, Z. Wan, Y. Wang, L. Shen, B. Li, Q.H. Yang, F. Kang, Y.B. He, Progress and perspective of solid-state lithium–sulfur batteries. Adv. Func. Mater. **28**, 1707570 (2018)
8. J. Xie, H.J. Peng, J.Q. Huang, W.T. Xu, X. Chen, Q. Zhang, A supramolecular capsule for reversible polysulfide storage/delivery in lithium–sulfur batteries. Angew. Chem. Int. Ed. **56**, 16223–16227 (2017)
9. C. Ye, Y. Jiao, A.D. Slattery, K. Davey, H. Wang, S.Z. Qiao, 2D MoN-VN heterostructure to regulate polysulfides for highly efficient lithium–sulfur batteries. Angew. Chem. Int. Ed. **57**, 16703–16707 (2018)
10. F. Pei, L. Lin, D. Ou, Z. Zheng, S. Mo, X. Fang, N. Zheng, Self-supporting sulfur cathodes enabled by two-dimensional carbon yolk-shell nanosheets for high-energy-density lithium–sulfur batteries. Nat. Commun. **8**, 482 (2017)

11. T. Zhao, P. Zhai, Z. Yang, J. Wang, L. Qu, F. Du, J. Wang, Self-supporting $Ti_3C_2T_x$ foam/S cathodes with high sulfur loading for high-energy-density lithium–sulfur batteries. Nanoscale **10**, 22954–22962 (2018)
12. Y.C. Jeong, J.H. Kim, S. Nam, C.R. Park, S.J. Yang, Rational design of nanostructured functional interlayer/separator for advanced Li–S batteries. Adv. Func. Mater. **28**, 1707411 (2018)
13. F. Pei, L. Lin, A. Fu, S. Mo, D. Ou, X. Fang, N. Zheng, A two-dimensional porous carbon-modified ceparator for high-energy-density Li–S batteries. Joule **2**, 323–336 (2018)
14. L. Wang, Y. Ye, N. Chen, Y. Huang, L. Li, F. Wu, R. Chen, Development and challenges of functional electrolytes for high-performance lithium–sulfur batteries. Adv. Func. Mater. **28**, 1800919 (2018)
15. J. Zheng, G. Ji, X. Fan, J. Chen, Q. Li, H. Wang, Y. Yang, K.C. Demella, S.R. Raghavan, C. Wang. High-fluorinated electrolytes for Li–S batteries. Adv. Energy Mater. 1803774 (2019)
16. Y. Yang, J. Zhang, Highly stable lithium–sulfur batteries based on laponite nanosheet-coated Celgard separators. Adv. Energy Mater. **8**, 1801778 (2018)
17. L. Kong, B.Q. Li, H.J. Peng, R. Zhang, J. Xie, J.Q. Huang, Q. Zhang, Porphyrin-derived graphene-based nanosheets enabling strong polysulfide chemisorption and rapid kinetics in lithium–sulfur batteries. Adv. Energy Mater. **8**, 1800849 (2018)
18. S. Tu, X. Chen, X. Zhao, M. Cheng, P. Xiong, Y. He, Q. Zhang, Y. Xu, A polysulfide-immobilizing polymer retards the shuttling of polysulfide intermediates in lithium–sulfur batteries. Adv. Mater. **30**, 1804581 (2018)
19. X. Luo, X. Lu, G. Zhou, X. Zhao, Y. Ouyang, X. Zhu, Y.E. Miao, T. Liu, Ion-selective polyamide acid nanofiber separators for high-rate and stable lithium−sulfur batteries. ACS Appl. Mater. Interfaces. **10**, 42198–42206 (2018)
20. J.Q. Huang, T.Z. Zhuang, Q. Zhang, H.J. Peng, C.M. Chen, F. Wei, Permselective graphene oxide membrane for highly stable and anti-self-discharge lithium−sulfur batteries. ACS Nano **9**, 3002–3011 (2015)
21. Y. Song, W. Zhao, X. Zhu, L. Zhang, Q. Li, F. Ding, Z. Liu, J. Sun, Vanadium dioxide-graphene composite with ultrafast anchoring behavior of polysulfides for lithium–sulfur batteries. ACS Appl. Mater. Interfaces **10**, 15733–15741 (2018)
22. Y. Zhou, G. Hu, W. Zhang, Q. Li, Z. Zhao, Y. Zhao, F. Li, F. Geng, Cationic two-dimensional sheets for an ultralight electrostatic polysulfide trap toward high-performance lithium–sulfur batteries. Energy Storage Mater. **9**, 39–46 (2017)
23. X. Gao, X. Yang, M. Li, Q. Sun, J. Liang, J. Luo, J. Wang, W. Li, J. Liang, Y. Liu, S. Wang, Y. Hu, Q. Xiao, Y. Li, T.K. Sham, X. Sun, Cobalt-doped SnS_2 with dual active centers of synergistic absorption-catalysis effect for high-S loading Li–S batteries. Adv. Func. Mater. **29**, 1806724 (2019)
24. J. Song, D. Su, X. Xie, X. Guo, W. Bao, G. Shao, G. Wang, Immobilizing polysulfides with MXene-functionalized separators for stable lithium–sulfur batteries. ACS Appl. Mater. Interfaces **8**, 29427–29433 (2016)
25. K. Jiang, S. Gao, R. Wang, M. Jiang, J. Han, T. Gu, M. Liu, S. Cheng, K. Wang, Lithium sulfonate/carboxylate-anchored polyvinyl alcohol separators for lithium–sulfur batteries. ACS Appl. Mater. Interfaces. **10**, 18310–18315 (2018)
26. Z.W. Seh, Y. Sun, Q. Zhang, Y. Cui, Designing high-energy lithium–sulfur batteries. Chem. Soc. Rev. **45**, 5605–5634 (2016)
27. X. Wang, X. Hao, Y. Xia, Y. Liang, X. Xia, J. Tu, A polyacrylonitrile (PAN)-based double-layer multifunctional gel polymer electrolyte for lithium–sulfur batteries. J. Membr. Sci. **582**, 37–47 (2019)
28. X. Yao, N. Huang, F. Han, Q. Zhang, H. Wan, J.P. Mwizerwa, C. Wang, X. Xu, High-performance all-solid-state lithium–sulfur batteries enabled by amorphous sulfur-coated reduced graphene oxide cathodes. Adv. Energy Mater. **7**, 1602923 (2017)
29. Z. Lin, C. Liang, Lithium–sulfur batteries: from liquid to solid cells. J. Mater. Chem. A **3**, 936–958 (2014)

30. J. Wang, M. Li, C. Liu, Y. Liu, T. Zhao, P. Zhai, J. Wang, An electronegative modified separator with semifused pores as a selective barrier for highly stable lithium–sulfur batteries. Ind. Eng. Chem. Res. **58**, 14538–14547 (2019)
31. J. Wang, P. Zhai, T. Zhao, M. Li, Z. Yang, H. Zhang, J. Huang, Laminar MXene-Nafion-modified separator with highly inhibited shuttle effect for long-life lithium–sulfur batteries. Electrochim. Acta **320**, 134558 (2019)
32. W. Kou, J. Wang, W. Li, R. Lv, N. Peng, W. Wu, J. Wang, Asymmetry-structure electrolyte with rapid Li^+ transfer pathway towards high-performance all-solid-state lithium–sulfur battery. J. Membr. Sci. **634**, 119432 (2021)
33. P. Zhai, N. Peng, Z. Sun, W. Wu, W. Kou, G. Cui, K. Zhao, J. Wang, Thin laminar composite solid electrolyte with high ionic conductivity and mechanical strength towards advanced all-solid-state lithium–sulfur battery. J. Mater. Chem. A **8**, 23344–23353 (2020)
34. J. Wang, X. Yue, Z. Zhang, Z. Yang, Y. Li, H. Zhang, X. Yang, H. Wu, Z. Jiang, Enhancement of proton conduction at low humidity by incorporating imidazole microcapsules into polymer electrolyte membranes. Adv. Func. Mater. **22**, 4539–4546 (2012)
35. H. Chen, J.D. Snyder, Y.A. Elabd, Electrospinning and solution properties of Nafion and poly (acrylic acid). Macromolecules **41**, 128–135 (2008)
36. H. Tang, S. Peikang, S.P. Jiang, F. Wang, M. Pan, A degradation study of Nafion proton exchange membrane of PEM fuel cells. J. Power Sour. **170**, 85–92 (2007)
37. I. Bauer, S. Thieme, J. Brückner, H. Althues, S. Kaskel, Reduced polysulfide shuttle in lithium–sulfur batteries using Nafion-based separators. J. Power Sour. **251**, 417–422 (2014)
38. Y. Zang, F. Pei, J. Huang, Z. Fu, G. Xu, X. Fang, Large-area preparation of crack-free crystalline microporous conductive membrane to upgrade high energy lithium–sulfur batteries. Adv. Energy Mater. **8**, 1802052 (2018)
39. S. Ali, M. Waqas, X. Jing, N. Chen, D. Chen, J. Xiong, W. He, Carbon−tungsten disulfide composite bilayer separator for high-performance lithium–sulfur batteries. ACS Appl. Mater. Interfaces. **10**, 39417–39421 (2018)
40. J.Q. Huang, Q. Zhang, H.J. Peng, X.Y. Liu, W.Z. Qian, F. Wei, Ionic shield for polysulfides towards highly-stable lithium–sulfur batteries. Energy Environ. Sci. **7**, 347–353 (2014)
41. C.E. Lin, H. Zhang, Y.Z. Song, Y. Zhang, J.J. Yuan, B.K. Zhu, Carboxylated polyimide separator with excellent lithium ion transport properties for a high-power density lithium-ion battery. J. Mater. Chem. A **6**, 991–998 (2018)
42. M. Yan, H. Chen, Y. Yu, H. Zhao, C.F. Li, Z.Y. Hu, P. Wu, L. Chen, H. Wang, D. Peng, H. Gao, T. Hasan, Y. Li, B.L. Su, 3D ferroconcrete-like aminated carbon nanotubes network anchoring sulfur for advanced lithium–sulfur batteries. Adv. Energy Mater. **8**, 1801066 (2018)
43. J. Park, B.C. Yu, J.S. Park, J.W. Choi, C. Kim, Y.E. Sung, J.B. Goodenough, Tungsten disulfide catalysts supported on a carbon cloth interlayer for high performance Li–S battery. Adv. Energy Mater. **7**, 1602567 (2017)
44. T.Z. Zhuang, J.Q. Huang, H.J. Peng, L.Y. He, X.B. Cheng, C.M. Chen, Q. Zhang, Rational integration of polypropylene/graphene oxide/Nafion as ternary-layered separator to retard the shuttle of polysulfides for lithium–sulfur batteries. Small **12**, 381–389 (2016)
45. Y. Song, S. Zhao, Y. Chen, J. Cai, J. Li, Q. Yang, J. Sun, Z. Liu, Enhanced sulfur redox and polysulfide regulation via porous VN-modified separator for Li–S batteries. ACS Appl. Mater. Interfaces. **11**, 5687–5694 (2019)
46. J.Y. Hwang, H.M. Kim, S. Shin, Y.K. Sun, Designing a high-performance lithium–sulfur batteries based on layered double hydroxides-carbon nanotubes composite cathode and a dual-functional graphene-polypropylene-Al_2O_3 separator. Adv. Func. Mater. **28**, 1704294 (2018)
47. C. (John) Zhang, S.H. Park, A. Seral-Ascaso, S. Barwich, N. McEvoy, C.S. Boland, J.N. Coleman, Y. Gogotsi, V. Nicolosi, High capacity silicon anodes enabled by MXene viscous aqueous ink. Nat. Commun. **10**, 849 (2019)
48. W. Cai, G. Li, K. Zhang, G. Xiao, C. Wang, K. Ye, Z. Chen, Y. Zhu, Y. Qian, Conductive nanocrystalline niobium carbide as high-efficiency polysulfides tamer for lithium–sulfur batteries. Adv. Func. Mater. **28**, 1704865 (2018)

49. Z.A. Ghazi, X. He, A.M. Khattak, N.A. Khan, B. Liang, A. Iqbal, J. Wang, H. Sin, L. Li, Z. Tang, MoS_2/Celgard separator as efficient polysulfide barrier for long-life lithium–sulfur batteries. Adv. Mater. **29**, 1606817 (2017)
50. L. Tan, X. Li, Z. Wang, H. Guo, J. Wang, Lightweight reduced graphene oxide@MoS_2 interlayer as polysulfide barrier for high-performance lithium–sulfur batteries. ACS Appl. Mater. Interfaces. **10**, 3707–3713 (2018)
51. G. Gnana Kumar, S.H. Chung, T. Raj Kumar, A. Manthiram, Three-dimensional graphene-carbon nanotube-Ni hierarchical architecture as a polysulfide trap for lithium–sulfur batteries. ACS Appl. Mater. Interfaces **10**, 20627–20634 (2018)
52. S. Song, L. Shi, S. Lu, Y. Pang, Y. Wang, M. Zhu, D. Ding, S. Ding, A new polysulfide blocker-poly (acrylic acid) modified separator for improved performance of lithium–sulfur battery. J. Membr. Sci. **563**, 277–283 (2018)
53. Y.S. Su, Y. Fu, T. Cochell, A. Manthiram, A strategic approach to recharging lithium–sulphur batteries for long cycle life. Nat. Commun. **4**, 2985 (2013)
54. Z. Wang, M. Feng, H. Sun, G. Li, Q. Fu, H. Li, J. Liu, L. Sun, A. Mauger, C.M. Julien, H. Xie, Z. Chen, Constructing metal-free and cost-effective multifunctional separator for high-performance lithium–sulfur batteries. Nano Energy **59**, 390–398 (2019)
55. Y.T. Liu, D.D. Han, L. Wang, G.R. Li, S. Liu, X.P. Gao, $NiCo_2O_4$ nanofibers as carbon-free sulfur immobilizer to fabricate sulfur-based composite with high volumetric capacity for lithium–sulfur battery. Adv. Energy Mater. **9**, 1803477 (2019)
56. D.B. Babu, K. Giribabu, K. Ramesha, Permselective SPEEK/Nafion composite-coated separator as a potential polysulfide crossover barrier layer for Li–S batteries. ACS Appl. Mater. Interfaces. **10**, 19721–19729 (2018)
57. T. Lei, W. Chen, Y. Hu, W. Lv, X. Lv, Y. Yan, J. Huang, Y. Jiao, J. Chu, C. Yan, C. Wu, Q. Li, W. He, J. Xiong, A nonflammable and thermotolerant separator suppresses polysulfide dissolution for safe and long-cycle lithium–sulfur batteries. Adv. Energy Mater. **8**, 1802441 (2018)
58. W. Yang, J. Xiao, Y. Ma, S. Cui, P. Zhang, P. Zhai, L. Meng, X. Wang, Y. Wei, Z. Du, B. Li, Z. Sun, S. Yang, Q. Zhang, Y. Gong, Tin intercalated ultrathin MoO_3 nanoribbons for advanced lithium–sulfur batteries. Adv. Energy Mater. **9**, 1803137 (2019)
59. X. Wang, Y. Zhang, X. Zhang, T. Liu, Y.H. Lin, L. Li, Y. Shen, C.W. Nan. Lithium-salt-rich PEO/$Li_{0.3}La_{0.557}TiO_3$ interpenetrating composite electrolyte with three-dimensional ceramic nano-backbone for all-solid-state lithium-ion batteries. ACS Appl. Mater. Interfaces **10**, 24791–24798 (2018)
60. J. Bae, Y. Li, J. Zhang, X. Zhou, F. Zhao, Y. Shi, J.B. Goodenough, G. Yu, A 3D nanostructured hydrogel-framework-derived high-performance composite polymer lithium-ion electrolyte. Angew. Chem. Int. Ed. **57**, 2096–2100 (2018)
61. G. Widawski, M. Rawiso, B. François, Self-organized honeycomb morphology of star-polymer polystyrene films. Nature **369**, 387–389 (1994)
62. R. Jim, A. Campo, M.L. Calzada, J. Sanz, S.D. Kobylianska, S.O. Solopan, A.G. Belous. Lithium $La_{0.57}Li_{0.33}TiO_3$ perovskite and $Li_{1.3}Al_{0.3}Ti_{1.7}(PO_4)_3$ Li-NASICON supported thick films electrolytes prepared by tape casting method. J. Electrochem. Soc. **163**, A1653–A1659 (2016)
63. Z. Xie, Z. Wu, X. An, X. Yue, P. Xiaokaiti, A. Yoshida, A. Abudula, G. Guan, A sandwich-type composite polymer electrolyte for all-solid-state lithium metal batteries with high areal capacity and cycling stability. J. Membr. Sci. **596**, 117739 (2020)
64. S. Li, S.Q. Zhang, L. Shen, Q. Liu, J.B. Ma, W. Lv, Y.B. He, Q.H. Yang, Progress and perspective of ceramic/polymer composite solid electrolytes for lithium batteries. Adv. Sci. **7**, 1903088 (2020)
65. C. Liu, J. Wang, W. Kou, Z. Yang, P. Zhai, Y. Liu, W. Wu, J. Wang, A flexible, ion-conducting solid electrolyte with vertically bicontinuous transfer channels toward high performance all-solid-state lithium batteries. Chem. Eng. J. **404**, 126517 (2021)
66. D. Cao, X. Sun, Q. Li, A. Natan, P. Xiang, H. Zhu, Lithium dendrite in all-solid-state batteries: growth mechanisms, suppression strategies, and characterizations. Matter **3**, 57–94 (2020)

67. W. Tang, S. Tang, C. Zhang, Q. Ma, Q. Xiang, Y.W. Yang, J. Luo, Simultaneously enhancing the thermal stability, mechanical modulus, and electrochemical performance of solid polymer electrolytes by incorporating 2D sheets. Adv. Energy Mater. **8**, 1800866 (2018)
68. Z. Jiang, H. Xie, S. Wang, X. Song, X. Yao, H. Wang, Perovskite membranes with vertically aligned microchannels for all-solid-state lithium batteries. Adv. Energy Mater. **8**, 1801433 (2018)
69. A. Li, X. Liao, H. Zhang, L. Shi, P. Wang, Q. Cheng, J. Borovilas, Z. Li, W. Huang, Z. Fu, M. Dontigny, K. Zaghib, K. Myers, X. Chuan, X. Chen, Y. Yang, Nacre-inspired composite electrolytes for load-bearing solid-state lithium-metal batteries. Adv. Mater. **32**, 1905517 (2020)
70. H.W. Kim, J. Han, Y.J. Lim, Y.S. Choi, E. Lee, Y. Kim, 3D ion-conducting, scalable, and mechanically reinforced ceramic film for high voltage solid-state batteries. Adv. Func. Mater. **31**, 2002008 (2020)
71. D. Zhou, D. Shanmukaraj, A. Tkacheva, M. Armand, G. Wang, Polymer electrolytes for lithium-based batteries: advances and prospects. Chem **5**, 2326–2352 (2019)
72. Z. Xiao, B. Zhou, J. Wang, C. Zuo, D. He, X. Xie, Z. Xue, PEO-based electrolytes blended with star polymers with precisely imprinted polymeric pseudo-crown ether cavities for alkali metal ion batteries. J. Membr. Sci. **576**, 182–189 (2019)
73. Z. Wan, D. Lei, W. Yang, C. Liu, K. Shi, X. Hao, L. Shen, W. Lv, B. Li, Q.H. Yang, F. Kang, Y.B. He, Low resistance–integrated all-solid-state battery achieved by $Li_7La_3Zr_2O_{12}$ nanowire upgrading polyethylene oxide (PEO) composite electrolyte and PEO cathode binder. Adv. Func. Mater. **29**, 1805301 (2019)
74. X. Wang, H. Zhai, B. Qie, Q. Cheng, A. Li, J. Borovilas, B. Xu, C. Shi, T. Jin, X. Liao, Y. Li, X. He, S. Du, Y. Fu, M. Dontigny, K. Zaghib, Y. Yang, Rechargeable solid-state lithium metal batteries with vertically aligned ceramic nanoparticle/polymer composite electrolyte. Nano Energy **60**, 205–212 (2019)
75. H. Zhai, P. Xu, M. Ning, Q. Cheng, J. Mandal, Y. Yang, A flexible solid composite electrolyte with vertically aligned and connected ion-conducting nanoparticles for lithium batteries. Nano Lett. **17**, 3182–3187 (2017)
76. K.M. Diederichsen, E.J. McShane, B.D. McCloskey, Promising routes to a high Li^+ transference number electrolyte for lithium ion batteries. ACS Energy Lett. **2**, 2563–2575 (2017)
77. B.M. Savoie, M.A. Webb, T.F. Miller, Enhancing cation diffusion and suppressing anion diffusion via lewis-acidic polymer electrolytes. J. Phys. Chem. Lett. **8**, 641–646 (2017)
78. H. Zhang, C. Li, M. Piszcz, E. Coya, T. Rojo, L.M. Rodriguez-Martinez, M. Armand, Z. Zhou, Single lithium-ion conducting solid polymer electrolytes: advances and perspectives. Chem. Soc. Rev. **46**, 797–815 (2017)
79. D.H. Kim, S. Hwang, J.J. Cho, S. Yu, S. Kim, J. Jeon, K.H. Ahn, C. Lee, H.K. Song, H. Lee, Toward fast operation of lithium batteries: ion activity as the factor to determine the concentration polarization. ACS Energy Lett. **4**, 1265–1270 (2019)
80. Y. Li, D. Cao, W. Arnold, Y. Ren, C. Liu, J.B. Jasinski, T. Druffel, Y. Cao, H. Zhu, H. Wang, Regulated lithium ionic flux through well-aligned channels for lithium dendrite inhibition in solid-state batteries. Energy Storage Mater. **31**, 344–351 (2020)
81. X. Judez, H. Zhang, C. Li, G.G. Eshetu, Y. Zhang, J.A. González-Marcos, M. Armand, L.M. Rodriguez-Martinez, Polymer-rich composite electrolytes for all-solid-state Li–S cells. J. Phys. Chem. Lett. **8**, 3473–3477 (2017)
82. N. Wu, P.H. Chien, Y. Li, A. Dolocan, H. Xu, B. Xu, N.S. Grundish, H. Jin, Y.Y. Hu, J.B. Goodenough, Fast Li^+ conduction mechanism and interfacial chemistry of a NASICON/polymer composite electrolyte. J. Am. Chem. Soc. **142**, 2497–2505 (2020)
83. D. Lin, P.Y. Yuen, Y. Liu, W. Liu, N. Liu, R.H. Dauskardt, Y. Cui, A silica-aerogel-reinforced composite polymer electrolyte with high ionic conductivity and high modulus. Adv. Mater. **30**, 1802661 (2018)
84. N. Wu, P.H. Chien, Y. Qian, Y. Li, H. Xu, N.S. Grundish, B. Xu, H. Jin, Y.Y. Hu, G. Yu, J.B. Goodenough, Enhanced surface interactions enable fast Li^+ conduction in oxide/polymer composite electrolyte. Angew. Chem. Int. Ed. **59**, 4131–4137 (2020)

85. W. Tang, S. Tang, X. Guan, X. Zhang, Q. Xiang, J. Luo, High-performance solid polymer electrolytes filled with vertically aligned 2D materials. Adv. Func. Mater. **29**, 1900648 (2019)
86. Q. Zhao, X. Liu, S. Stalin, K. Khan, L.A. Archer, Solid-state polymer electrolytes with in-built fast interfacial transport for secondary lithium batteries. Nat. Energy **4**, 365–373 (2019)
87. J. Wan, J. Xie, X. Kong, Z. Liu, K. Liu, F. Shi, A. Pei, H. Chen, W. Chen, J. Chen, X. Zhang, L. Zong, J. Wang, L.Q. Chen, J. Qin, Y. Cui, Ultrathin, flexible, solid polymer composite electrolyte enabled with aligned nanoporous host for lithium batteries. Nat. Nanotechnol. **14**, 705–711 (2019)
88. J. Lopez, D.G. Mackanic, Y. Cui, Z. Bao, Designing polymers for advanced battery chemistries. Nat. Rev. Mater. **4**, 312–330 (2019)
89. G. He, M. Xu, J. Zhao, S. Jiang, S. Wang, Z. Li, X. He, T. Huang, M. Cao, H. Wu, M.D. Guiver, Z. Jiang, Bioinspired ultrastrong solid electrolytes with fast proton conduction along 2D channels. Adv. Mater. **29**, 1605898 (2017)
90. N. Zhao, W. Khokhar, Z. Bi, C. Shi, X. Guo, L.Z. Fan, C.W. Nan, Solid garnet batteries. Joule **3**, 1190–1199 (2019)
91. X. Chen, W. He, L.X. Ding, S. Wang, H. Wang, Enhancing interfacial contact in all solid state batteries with a cathode-supported solid electrolyte membrane framework. Energy Environ. Sci. **12**, 938–944 (2019)
92. Z. Jiang, S. Wang, X. Chen, W. Yang, X. Yao, X. Hu, Q. Han, H. Wang, Tape-casting $Li_{0.34}La_{0.56}TiO_3$ ceramic electrolyte films permit high energy density of lithium-metal batteries. Adv. Mater. **32**, 1906221 (2020)
93. Z. Sun, Y. Li, S. Zhang, L. Shi, H. Wu, H. Bu, S. Ding, g-C_3N_4 nanosheets enhanced solid polymer electrolytes with excellent electrochemical performance, mechanical properties, and thermal stability. J. Mater. Chem. A **7**, 11069–11076 (2019)
94. L. Chen, W. Li, L.Z. Fan, C.W. Nan, Q. Zhang, Intercalated electrolyte with high transference number for dendrite-free solid-state lithium batteries. Adv. Func. Mater. **29**, 1901047 (2019)
95. X. Gao, X. Zheng, J. Wang, Z. Zhang, X. Xiao, J. Wan, Y. Ye, L.Y. Chou, H.K. Lee, J. Wang, R.A. Vila, Y. Yang, P. Zhang, L.W. Wang, Y. Cui, Incorporating the nanoscale encapsulation concept from liquid electrolytes into solid-state lithium–sulfur batteries. Nano Lett. **20**, 5496–5503 (2020)
96. M. Jana, R. Xu, X.B. Cheng, J.S. Yeon, J.M. Park, J.Q. Huang, Q. Zhang, H.S. Park, Rational design of two-dimensional nanomaterials for lithium–sulfur batteries. Energy Environ. Sci. **13**, 1049–1075 (2020)
97. G.G. Eshetu, X. Judez, C. Li, M. Martinez-Ibanez, I. Gracia, O. Bondarchuk, J. Carrasco, L.M. Rodriguez-Martinez, H. Zhang, M. Armand, Ultrahigh performance all solid-state lithium sulfur batteries: salt anion's chemistry-induced anomalous synergistic effect. J. Am. Chem. Soc. **140**, 9921–9933 (2018)
98. Y.X. Song, Y. Shi, J. Wan, S.Y. Lang, X.C. Hu, H.J. Yan, B. Liu, Y.G. Guo, R. Wen, L.J. Wan, Direct tracking of the polysulfide shuttling and interfacial evolution in all-solid-state lithium–sulfur batteries: a degradation mechanism study. Energy Environ. Sci. **12**, 2496–2506 (2019)
99. S. Randau, D.A. Weber, O. Kötz, R. Koerver, P. Braun, A. Weber, E. Ivers-Tiffée, T. Adermann, J. Kulisch, W.G. Zeier, F.H. Richter, J. Janek, Benchmarking the performance of all-solid-state lithium batteries. Nat. Energy **5**, 259–270 (2020)
100. W. Shen, K. Li, Y. Lv, T. Xu, D. Wei, Z. Liu, Highly-safe and ultra-stable all-flexible gel polymer lithium ion batteries aiming for scalable applications. Adv. Energy Mater. **10**, 1904281 (2020)
101. S. Zekoll, C. Marriner-Edwards, A.K.O. Hekselman, J. Kasemchainan, C. Kuss, D.E.J. Armstrong, D. Cai, R.J. Wallace, F.H. Richter, J.H.J. Thijssen, P.G. Bruce, Hybrid electrolytes with 3D bicontinuous ordered ceramic and polymer microchannels for all-solid-state batteries. Energy Environ. Sci. **11**, 185–201 (2018)

Chapter 7
Composite Electrolyte for All-Solid-State Lithium Battery

Jie Zhang, Yafang Zhang, and Jingtao Wang

7.1 Introduction

All-solid-state lithium batteries (ASSLBs) have been considered as next-generation energy storage devices owing to the remarkable energy density and high safety as compared with conventional batteries [1, 2]. Solid-state electrolytes (SSEs) are the key component of ASSLBs, and their ionic conductivity and mechanical stability directly determine the battery performance [3]. Generally, the SSEs can be divided into inorganic ceramic electrolyte and polymer electrolyte [3–5].

Among the reported SSEs, solid polymer electrolytes, represented by poly(ethylene oxide) (PEO), possess the advantages of high processability, flexibility, and low cost [6]. However, the strong crystallinity limits its Li-ion conductivity (10^{-8}–10^{-6} S cm^{-1} at room temperature) [4]. Recently, the strategy of preparing hybrid polymer electrolytes using nanofillers and polymer matrix can maximize the advantages of nanomaterials and polymer matrix, which can effectively improve the ionic conductivity and stability of SSEs [7–9]. In general, the addition of highly stable inorganic nanosheets (e.g., graphene oxide, montmorillonite, montmorillonite, MXene, and boron nitride) into PEO matrix can significantly improve the mechanical strength of SSEs, although the crystallinity of polymer matrix is reduced [10–13]. Meanwhile, the organic–inorganic interfaces formed in the electrolyte can provide high-efficiency pathways for Li^+ transfer and thus endow the electrolyte with high ionic conductivity [14]. For instance, Luo and co-workers used vermiculite nanosheets to prepare composite polymer electrolyte [15], which utilized the

J. Zhang · Y. Zhang · J. Wang (✉)
School of Chemical Engineering, Zhengzhou University, Zhengzhou 450001, P. R. China
e-mail: jingtaowang@zzu.edu.cn

J. Wang
Henan Institute of Advanced Technology, Zhengzhou University, Zhengzhou 450003, P. R. China

J. Wang and W. Wu (eds.), *Functional Membranes for High Efficiency Molecule and Ion Transport*, https://doi.org/10.1007/978-981-19-8155-5_7

functional groups on functionalized nanosheets to improve the interfacial Li^+ conductivity. Thus, a high ionic conductivity of 2.9×10^{-5} S cm^{-1} was achieved at room temperature.

On the other hand, inorganic ceramic electrolytes with surface oxygen vacancy and periodic crystal structure possess excellent ionic conductivity, wide electrochemical windows, and outstanding stability [3, 16, 17]. Despite the excellent Li^+ transfer performance of inorganic ceramic electrolytes, large thicknesses are usually required to ensure the mechanical stability of electrolytes owing to mechanical brittleness [18]. Meanwhile, the large interfacial resistance between the electrolyte and electrodes also limits the battery performance. Organic–inorganic composite could subtly combine the excellent ionic conductivity of inorganic electrolyte with the excellent compatibility and processability of polymer electrolyte to enhance the Li^+ transfer capacity and mechanical stability of electrolyte [19, 20]. Nevertheless, the advantages of fast ionic conductor cannot be fully maximized in composite electrolyte due to the tendency of ceramic particles to agglomerate and the difficulty of forming continuous transfer pathways [21]. Therefore, the electrolytes with bicontinuous phase structure, including metal–organic frameworks (MOFs) [22], covalent organic frameworks (COFs) [23], and ceramic networks [24], have exhibited enormous competitiveness. These structures show intrinsic advantages of high specific surface areas, tailorable porosity, and continuous transfer channels [25]. For instance, Zekoll et al. constructed a solid electrolyte with continuous transfer pathways using 3D ceramic framework, which exhibited high ionic conductivity (1.6×10^{-4} S cm^{-1} at 25 °C) and excellent mechanical stability [26].

In this chapter, we introduce lithiated polydopamine-modified GO nanosheet (LiDGO) hybrid polymer electrolyte [27], poly(ethylene glycol) grafted polymer-like quantum dots (PPQDs) hybrid polymer electrolyte [28], composite electrolyte with PEO-threaded MOF nanosheets [29], 3D LLTO framework/PEO composite electrolyte [30], 2D thin LLTO framework/PEO composite electrolyte [31], and 2D lamellar LLTO/Vr composite electrolyte [32] for all-solid-state lithium batteries. The microstructure and electrochemical properties of these composite electrolytes are investigated in detail.

7.2 Composite Electrolyte with Lithiated GO

GO nanosheets were prepared by improved Hummers' method, in which graphite powders were oxidized and exfoliated [33]. 2.0 g GO nanosheets were added to 2 mg mL^{-1} dopamine-containing aqueous solution, immersed in Tris and HCl controlled solution at pH = 8.5, and stirred for 3 h at room temperature to obtain DGO nanosheets. DGO powders were then obtained by centrifugation at 9000 rpm [34]. Then, the above DGO powders were added to LiOH solution (1 M). After stirring for 48 h, it was washed with deionized water for several times and centrifuged at 9000 rpm to collect the powder and ensure no residual LiOH. After freeze-drying for 48 h, LiDGO powders were successfully prepared.

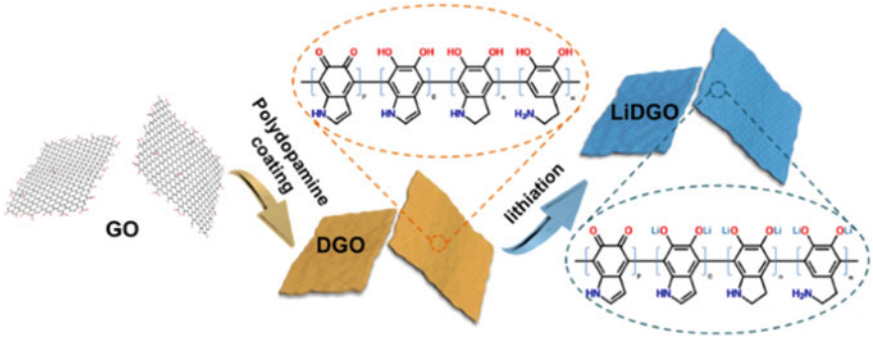

Fig. 7.1 Preparation process of LiDGO nanosheet. Copyright (2021), Elsevier [27]

According to the solution casting technique, solid-state polymer electrolytes (SPEs) were obtained. PEO was mixed with bis(trifluoromethane)sulfonamide lithium salt (LiTFSI) (EO/Li = 20: 1) in acetonitrile. LiDGO, GO, or DGO was dissolved in acetonitrile. These two solutions were mixed and stirred for 12 h to obtain casting solution, and then cast on a polytetrafluoroethylene plate. After drying for 48 h at 50 °C in a vacuum oven, the SPEs were prepared. All SPEs were stored in the glove box filled with argon.

Figure 7.1 shows that LiDGO nanosheets were obtained by lithiation of anchored Ar-OH groups on DGO nanosheets. DGO nanosheets were prepared through the self-polymerization of dopamine on the surface of GO nanosheets [35–37]. Then, lithium ions were introduced to the surface of nanosheets by replacing hydrogen on hydroxide radicals with lithium ions. Considering that the LiDGO nanosheets are completely cleaned after lithiation process, strong interaction between Li^+ and DGO nanosheet is speculated.

Considering the mechanical stability and ionic conductivity, LiDGO nanosheets were added to PEO-LiTFSI casting solution with a loading capacity of 6 wt% to prepare SPE. At the same time, GO and DGO nanosheets were added into SPE, respectively, for comparison. Figure 7.2a, b demonstrates that the LiDGO nanosheets are uniformly distributed in the polymer matrix, and no obvious agglomeration of nanosheet is observed. And the SPE has an average thickness of about 120 μm.

This organic–inorganic hybridization combines the advantage of the flexibility of PEO and dimensional stability of LiDGO, resulting in excellent mechanical properties of PEO/LiTFSI/LiDGO. After poking treatment and exposure to violent stretching, PEO/LiTFSI/LiDGO can retain its integrality (Fig. 7.3a). As shown in Fig. 7.3b, stress–strain testing result exhibits that the tensile strength and elongation at break of PEO/LiTFSI/LiDGO are 1.25 MPa and 936%, respectively, 2.4 times and 1.3 times higher than those of blank PEO/LiTFSI. The hardness and modulus of PEO/LiTFSI/LiDGO are 1.4 times and 1.5 times higher than those of blank PEO/LiTFSI, respectively. These mechanical properties will help as-prepared SPE to improve the inhibition ability of lithium dendrite growth [38–40].

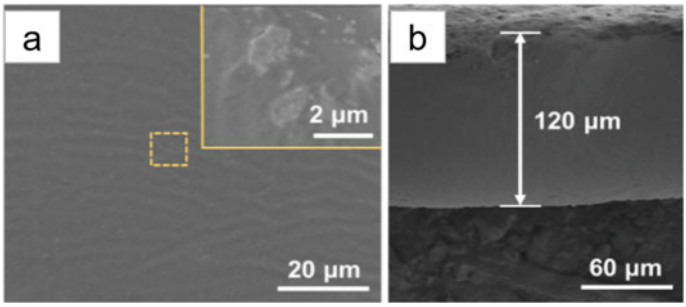

Fig. 7.2 **a** Surficial SEM image of PEO/LiTFSI/LiDGO. **b** Cross-sectional SEM image of PEO/LiTFSI/LiDGO. Copyright (2021), Elsevier [27]

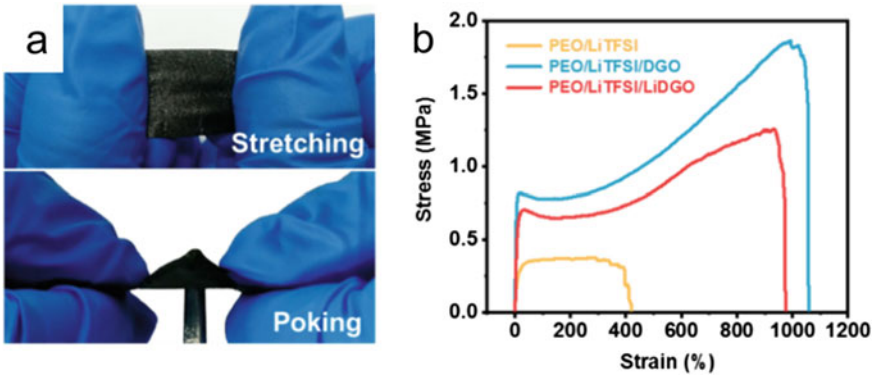

Fig. 7.3 **a** Undergoing stretching and poking of photographs of PEO/LiTFSI/LiDGO. **b** Stress–strain curves of PEO/LiTFSI/LiDGO, PEO/LiTFSI/DGO, and PEO/LiTFSI electrolytes. Copyright (2021), Elsevier [27]

It is worth noting that the mechanical property of PEO/LiTFSI/DGO is superior to that of PEO/LiTFSI/LiDGO due to the strong hydrogen bond interactions between PEO chains and DGO nanosheets, which is weakened by the presence of lithium ions in PEO/LiTFSI/LiDGO. The results of differential scanning calorimetry (DSC) could confirm this speculation. Compared with PEO/LiTFSI/DGO, the melting point (T_m) and glass transition temperature (T_g) of PEO/LiTFSI/LiDGO decline by 2.0 °C and 1.6 °C, respectively (Fig. 7.4a, b). These indicate that the LiDGO-PEO interactions are weakened and the motility of PEO chain is enhanced. The crystallinity of PEO in electrolyte was calculated according to the melting enthalpy [41]. X-ray diffractometry (XRD) results further prove that the chain motility of PEO/LiTFSI/LiDGO is stronger than that of PEO/LiTFSI/DGO, which shows obviously lower peak intensity than PEO/LiTFSI and PEO/LiTFSI/DGO [42]. The ionic conductivity of the SPE can be enhanced through newly formed amorphous regions and the construction of organic–inorganic interfaces in PEO.

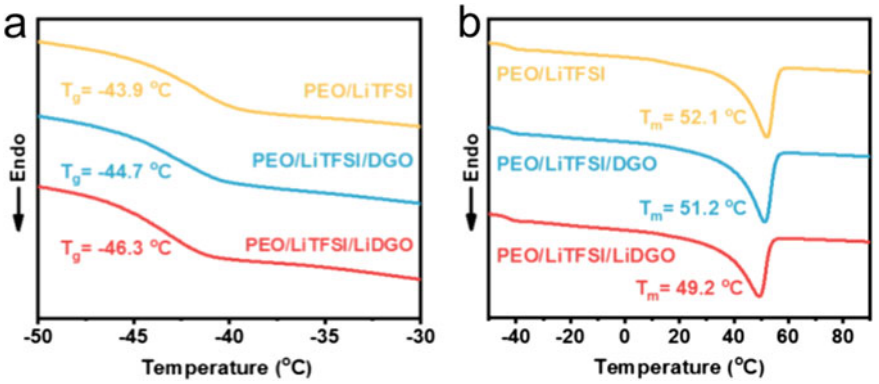

Fig. 7.4 The DSC thermograms of PEO/LiTFSI/LiDGO, PEO/LiTFSI/DGO, and PEO/LiTFSI at **a** –30 to –50 °C and **b** 90 to –50 °C. Copyright (2021), Elsevier [27]

Figure 7.5 displays the ionic conductivities of the as-prepared electrolytes. At 30 °C, the ionic conductivity of PEO/LiTFSI is 3.2×10^{-6} S cm^{-1}, and the conductivity increases with the increase of testing temperature. The addition of nanosheets enhances ionic conduction of SPE as compared with PEO/LiTFSI. At 30 °C, the ionic conductivity of PEO/LiTFSI/LiDGO and PEO/LiTFSI/DGO reaches 3.4×10^{-5} and 9.9×10^{-6} S cm^{-1}, which are ten and two times higher than that of PEO/LiTFSI, respectively. The enhanced conductivity mainly results from the construction of long-range interfacial transfer channels in SPE and the reduction of crystallinity, which provide low-energy-barrier pathways for fast Li-ion conduction.

Activation energy (E_a) data confirm this speculation. The E_a value of electrolytes below T_m is obtained through fitting ionic conductivity data of electrolytes at different temperatures, which are then calculated using Arrhenius equation [43]. For PEO/LiTFSI, PEO/LiTFSI/DGO, and PEO/LiTFSI/LiDGO electrolytes, the E_a value below T_m is 1.59, 1.34, and 1.19 eV, respectively. In addition, according to Vogel-Tamman-Fulcher equation, the E_a value of electrolytes above T_m is obtained

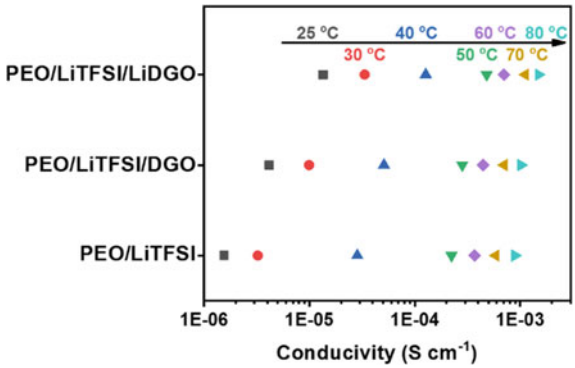

Fig. 7.5 The ionic conductivities of PEO/LiTFSI/LiDGO, PEO/LiTFSI/DGO, and PEO/LiTFSI electrolytes. Copyright (2021), Elsevier [27]

[44, 45]. Compared to the E_a value for PEO/LiTFSI above T_m (0.10 eV), the value for PEO/LiTFSI/DGO decreases to 0.09 eV. E_a value of PEO/LiTFSI/DGO may be reduced due to the construction of long-range interfacial transfer channels. However, the *Ea* value of PEO/LiTFSI/LiDGO is further decreased to 0.08 eV when it has the same nanosheet loading amount as PEO/LiTFSI/DGO. We hypothesize that the decrease of E_a value for PEO/LiTFSI/LiDGO is due to free Li^+ concentration augment. This is because ionic conductivity of solid-state electrolyte depends not only on the continuity of conduction pathway, but also on the concentration of lithium ion in the conduction pathway. Therefore, Fourier transform infrared (FTIR) was used to detect the degree of dissociation of lithium salts, in which the bonded LiTFSI ion pairs and free $TFSI^-$ correspond to peaks at ~744 cm^{-1} and ~739 cm^{-1}, respectively [46–48]. The LiTFSI dissociation degree for PEO/LiTFSI/DGO increases to 88.7% compared with that of PEO/LiTFSI (81.1%). This phenomenon may be due to existence of DGO in SPE, in which abundant amine and hydroxyl groups on DGO could promote LiTFSI to dissociate into more free lithium ions through Lewis acid–base interactions. For PEO/LiTFSI/LiDGO, the dissociation degree of LiTFSI further improves to 95.7% as compared with PEO/LiTFSI/DGO. PEO/LiTFSI/LiDGO has the same loading amount of nanosheet but higher ionic conductivity (3.4×10^{-5}). The conductivity is much higher than that of PEO/LiTFSI/DGO (9.9×10^{-6} S cm^{-1}), indicating that PEO/LiTFSI/LiDGO has a higher LiTFSI dissociation degree. This is related to the lithiation of DGO. The hydroxyl and amine groups on DGO have Lewis acid–base interactions with LiTFSI to promote its dissociation, thus providing a large amount of Li^+ on the surface of LiDGO. And the zeta potential vibration of LiDGO nanosheet further confirms this phenomenon, as seen from Fig. 7.6b. In acetonitrile solution, when the weight ratio of LiTFSI-LiDGO increases from 0 to 12, the zeta potential of LiDGO nanosheet changes from –40 to 20 mV. These indicate that the concentration of Li^+ in LiDGO-PEO interface is effectively elevated owing to the enrichment of free Li^+ on surface of LiDGO rather than the random distribution in PEO matrix [44, 49]. Therefore, the ionic conductivity and Li^+ transference number of PEO/LiTFSI/LiDGO are significantly enhanced by the locally enriched free Li^+ and the constructed long-range interfacial transfer channels.

Then, in order to evaluate the operation stability during Li plating/stripping process, the electrolytes were assembled into Li symmetrical cells. And there are significant lithium dendrites on the Li electrode surface, which are attributed to the difference of the ionic conductivity induced by crystal in electrolyte, Li^+ heterogeneous deposition on Li electrode, as well as the weak mechanical and structural stability of PEO/LiTFSI electrolyte [50, 51]. In comparison, Fig. 7.7 shows that the addition of LiDGO and DGO nanosheets significantly improves mechanical strength and reduces the crystallinity of SPEs. Therefore, the cycling performances of batteries are improved dramatically. The cell assembled with PEO/LiTFSI/DGO electrolyte possesses better mechanical property, but poor battery cycling performance as compared with PEO/LiTFSI/LiDGO. Specially, serious short circuit occurs after cycling for 880 h in PEO/LiTFSI/DGO cell. This is attributed to the higher crystallinity in PEO/LiTFSI/DGO electrolyte, which leads to heterogeneous Li^+ deposition on Li electrode, resulting in the uncontrolled formation of

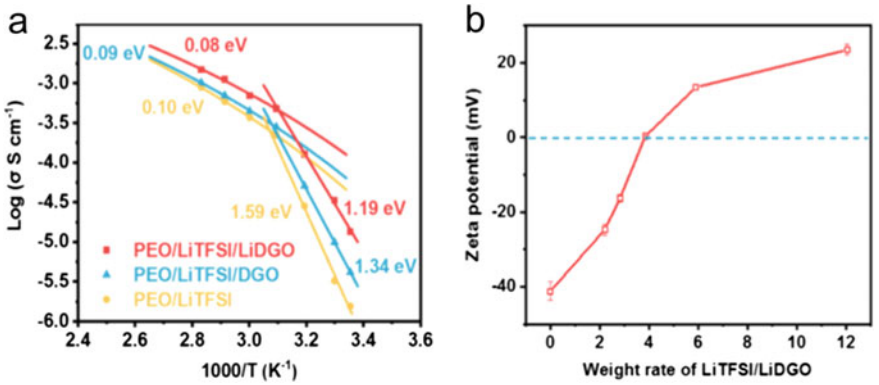

Fig. 7.6 **a** The Arrhenius plots of PEO/LiTFSI/LiDGO, PEO/LiTFSI/DGO, and PEO/LiTFSI. **b** Zeta potential of LiDGO nanosheets in acetonitrile suspension as a weight ratios function of LiTFSI/LiDGO. Copyright (2021), Elsevier [27]

lithium dendrite growth. Generally, the cell assembled with PEO/LiTFSI/LiDGO exhibits no short circuit during the 1000 h cycling, and there is no obvious lithium dendrite on corresponding Li electrode. The symmetrical cell assembled with PEO/LiTFSI/LiDGO shows excellent electrochemical performance, even when the charge/discharge duration is extended and the operating current density is increased. The Li|PEO/LiTFSI|Li symmetrical cell encounters short circuit at 98 h at 0.2 mA cm^{-2}, and Li|PEO/LiTFSI/DGO|Li symmetrical cell suffers short circuit for 134 h at 0.4 mA cm^{-2}. By comparison, the Li|PEO/LiTFSI/LiDGO|Li symmetrical cell could work normally for 200 h at 0.4 mA cm^{-2}. Moreover, during cycling, the overpotential of Li|PEO/LiTFSI/LiDGO|Li symmetrical cell is lower than those of Li|PEO/LiTFSI|Li and Li|PEO/LiTFSI/DGO|Li symmetrical cells. Such findings are attributed to the fact that the assembled cell with PEO/LiTFSI/LiDGO possesses high Li^+ transference number and ionic conductivity, and also good electrochemical stability.

As shown in Fig. 7.8a, the capacity of LFP|PEO/LiTFSI|Li cell decreases rapidly at 45 °C and 0.5C, and after 200 cycles, the discharge capacity decreases from 157 to 139 mAh g^{-1}. In comparison, after 200 cycles, the discharge capacity of LFP|PEO/LiTFSI/LiDGO|Li cell is 156 mAh g^{-1} and a capacity retention of over 98% is achieved. Figure 7.8b exhibits that the polarization voltage of LFP|PEO/LiTFSI/LiDGO|Li cell is only 0.23 V after 200 cycles, which is basically the same as that at 100 cycles. Compared with that of LFP|PEO/LiTFSI|Li cell (0.28 V after 200 cycles), the polarization voltage declines significantly. These results indicate that PEO/LiTFSI/LiDGO displays excellent electrochemical stability. Meanwhile, the rate performance of the cell assembled with PEO/LiTFSI/LiDGO is also improved due to the reduction of concentration polarization in the cell, resulting from the high Li^+ transference number and ionic conductivity [52]. Figure 7.8c shows that the discharge capacity of cell assembled with PEO/LiTFSI electrolyte decreases sharply as the rate increases. In comparison, LFP|PEO/LiTFSI/LiDGO|Li

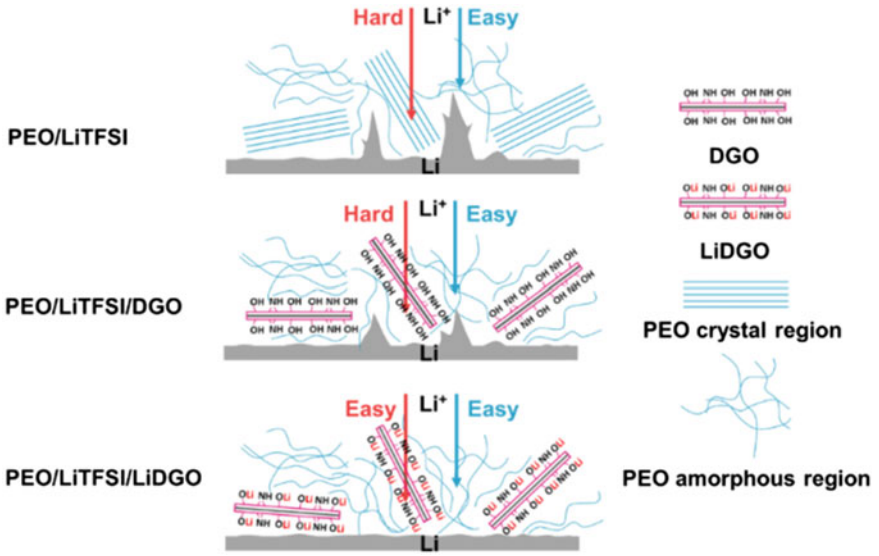

Fig. 7.7 The schematic diagram of Li deposition behaviors in different batteries. Copyright (2021), Elsevier [27]

cell presents better battery rate performances. And the discharge capacities of 161, 153, 149, 146, 143, 138, 132, and 125 mAh g^{-1} are achieved at 0.2, 0.5, 0.8, 1, 1.2, 1.5, 1.8, and 2.0C, respectively. At the same time, Fig. 7.8d shows that the polarization voltage of LFP|PEO/LiTFSI/LiDGO|Li cell displays the small change tendency as the rate increase. It is worth noting that the rate and cycling performances of LFP|PEO/LiTFSI/LiDGO|Li cell are superior to those of most reported SPEs.

In addition, NCM523|PEO/LiTFSI/LiDGO|Li cell was assembled and operated with high-voltage window of 2.7–4.3 V. Figure 7.9a shows that NCM523|PEO/LiTFSI/LiDGO|Li cell is activated after 11 cycles under 0.2C. The cell has high discharge capacity of 128 mAh g^{-1} and low polarization at 0.5C after 100 cycles. The discharge capacity of cell reaches to 60 mAh g^{-1} even under a high rate of 3C (Fig. 7.9b). These indicate that PEO/LiTFSI/LiDGO displays a good electrochemical stability at high voltage and has broad application prospect in high-performance power rechargeable Li batteries.

In addition, Fig. 7.10 shows that the LFP|PEO/LiTFSI/LiDGO|Li pouch cell could power LEDs even after corner cut or folding, demonstrating the potential utilization of PEO/LiTFSI/LiDGO in safe and flexible solid-state batteries.

In conclusion, a functionalized PEO/LiTFSI/LiDGO polymer electrolyte is prepared by combining PEO matrix with LiDGO nanosheets prepared by lithium synthesis of anchored Ar-OH on DGO nanosheets. PEO/LiTFSI/LiDGO has highly enhanced mechanical stability, probably attributed to the good dispersibility of nanosheets and the inherent advantages of organic–inorganic hybridization. At the

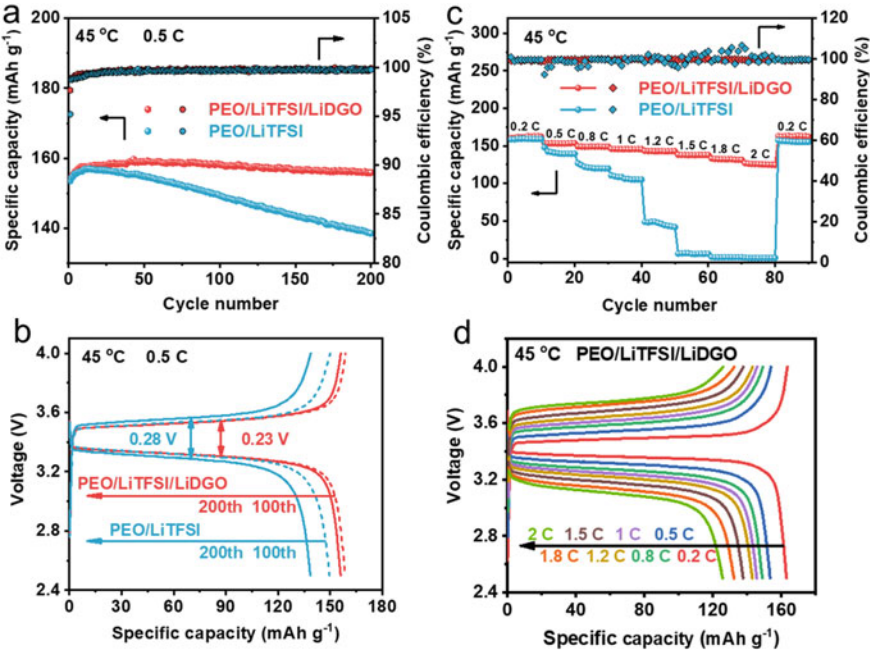

Fig. 7.8 Performances of all-solid-state cell. **a** The Coulombic efficiency and special capacity of LFP/Li cells as function of cycle number at 0.5C. **b** The charge/discharge curves of LFP/Li cells at 100th and 200th cycles. **c** The rate performances of LFP/Li cells at various rates. **d** The initial charge/discharge curves of cell assembled with PEO/LiTFSI/LiDGO at various rates. Copyright (2021), Elsevier [27]

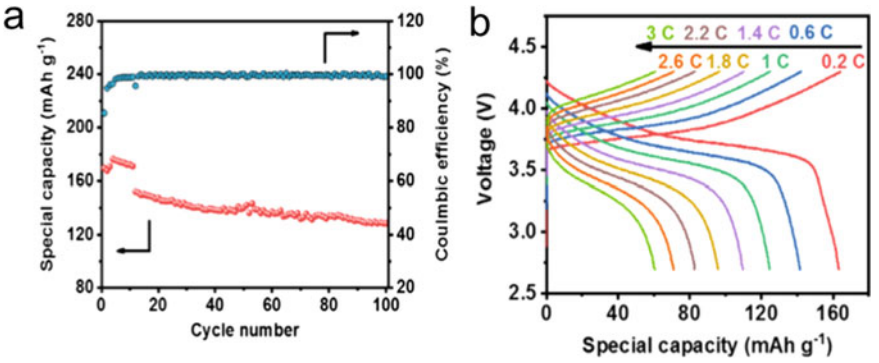

Fig. 7.9 **a** The cycling performance of NCM523|PEO/LiTFSI/LiDGO|Li cell. **b** The initial charge/discharge curves at various rates. Copyright (2021), Elsevier [27]

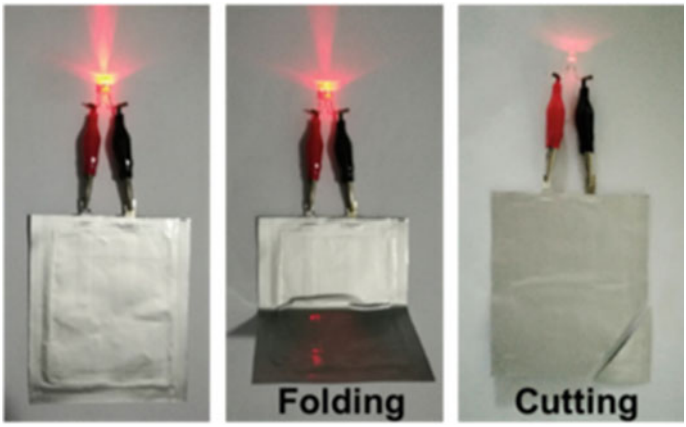

Fig. 7.10 Optical photograph of the solid-state Li/LFP pouch cell operated with folding and cutting. Copyright (2021), Elsevier [27]

same time, the introduction of LiDGO nanosheets significantly enhances concentration of local Li^+ and elevates dissociation degree of lithium salt at PEO-LiDGO interfaces. The highly enhanced Li^+ transference number and ionic conductivity for PEO/LiTFSI/LiDGO are ascribed to the conduction of long-range conductive highways of Li^+ with locally concentrated lithium ions. The discharge capacity after 200 cycles of the all-solid-state Li/LFP batteries is as high as 156 mAh g^{-1}, and the capacity retention is over 98%. This strategy may open up a new way to solve the balance problem between mechanical stability and ionic conductivity of SPEs.

7.3 Composite Electrolyte with Quantum Dot

Polymer-like quantum dots (PQDs) were prepared using literature method [53]. By optimizing PQD synthesis method, poly(ethylene glycol) grafted polymer-like quantum dots (PPQDs) were obtained. First step is to dissolve 0.96 g citric acid in 2.0 mL water. Meanwhile, ultrasonic treatment of 400 μL poly(ethylene glycol) diglycidyl ether (PEGDGE) and 540 μL diethylenetriamine was conducted at room temperature for 30 min, followed by heating to open the epoxy ring at 90 °C for 12 h [54, 55]. Then, the above solution was added to citric acid aqueous solution and mixed with ultrasonic for 30 min and microwave with 750 W for 2 min. Remaining unreacted small molecules were washed with 98% W/W ethanol for several times, followed by freeze-drying for 48 h to obtain yellow PPQDs powder (Fig. 7.11).

Solid-state polymer electrolytes (SPEs) were obtained using solution casting method. PPQDs, PEO, and LiTFSI were added in acetonitrile to prepare casting solution and casted on a custom polytetrafluoroethylene (PTFE) mold. The above solution was dried for 24 h in an atmosphere of argon at 30 °C, followed by drying

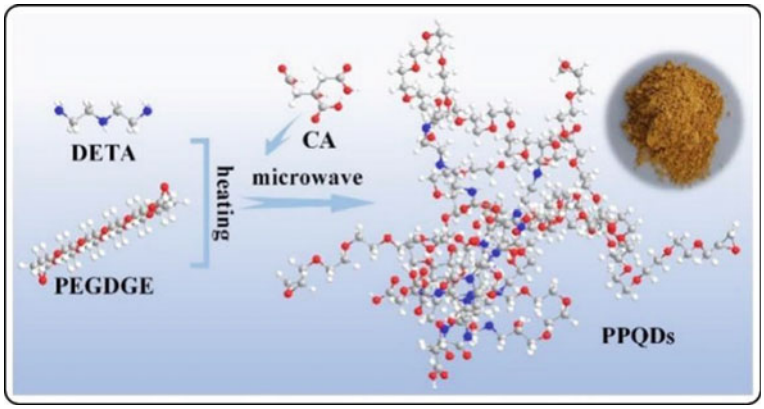

Fig. 7.11 PPQDs formation diagram. Copyright (2021), Elsevier [28]

for 24 h in a vacuum oven at 60 °C to obtain electrolyte. These pre-prepared SPEs are named as PEO/LiTFSI (0 wt% PPQDs) and PEO/LiTFSI/PPQDs (0–10 wt% PPQDs) based on the content of PPQDs. And under the same condition, PEO/LiTFSI/PQDs were also prepared. Here, EO/Li^+ molar ratio was controlled at 18:1 in all SPEs.

As shown in Fig. 7.12a, TEM image shows a lateral size of 2–3 nm for PPQDs. By grafting PEG onto PPQDs, new O–H and C–N groups and rich ether oxygen groups are introduced. Compared with PQDs, the corresponding peak integral area of PPQDs increases with the content of C–OH, C–O–C, and C–N bands, as shown in Fig. 7.12b. These collectively prove that PPQDs possess more functional groups, smaller size, and stronger interactions with PEO and lithium salts.

Then, PEO/LiTFSI/PPQDs were prepared by solution casting method. In Fig. 7.13d, cross-sectional SEM image determines that these SPEs have a thickness of around 100 μm. It is noteworthy that the solution casting of PPQDs remains

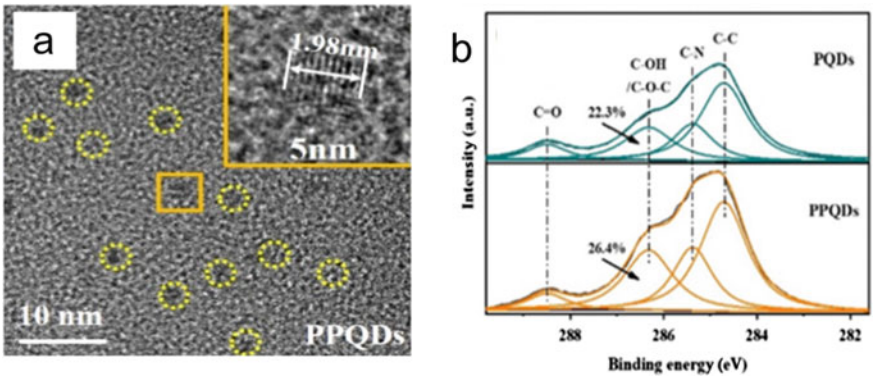

Fig. 7.12 **a** TEM image and high-resolution TEM image of PPQDs. **b** PQDs and PPQDs C 1s spectra. Copyright (2021), Elsevier [28]

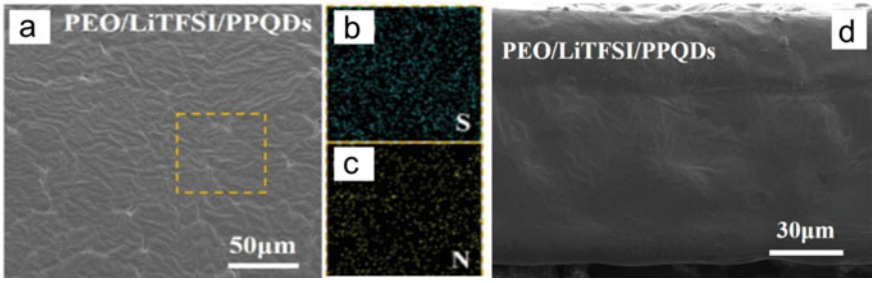

Fig. 7.13 **a** Surface SEM image of PEO/LiTFSI/PPQDs. EDS mappings of **b** S element and **c** N element on PEO/LiTFSI/PPQDs surface. **d** Cross-sectional SEM image of PEO/LiTFSI/PPQDs. Copyright (2021), Elsevier [28]

stable after long-term storage, while the solution casting of PQDs precipitates. This indicates that the compatibility between PPQDs and PEO is enhanced after grafting PEGDGE. In Fig. 7.13a, after adding PPQDs into PEO matrix, the surface SEM image of PEO/LiTFSI/PPQDs shows a smooth and uniform surface. This implies that PPQDs is evenly dispersed in PEO electrolyte due to its hydrophilic surface groups and molecular-scale size, resulting in rich PPQD-PEO interfaces and destruction of orderly PEO chain arrangement [56–59]. In addition, the PEO chain local recombination is inhibited owing to the strong hydrogen bonds formed by abundant amino and hydroxyl groups in PPQDs and the PEO chain [60]. In Fig. 7.13b, c, the uniform distribution of PPQDs in PEO matrix could be further verified by the mapping images of energy dispersion (EDS).

The electrolyte crystallization was directly determined by XRD. Figure 7.14 shows that the PEO/LiTFSI/PPQDs have the smallest characteristic diffraction peak intensity and the largest half-peak full width, implying lowest crystallinity. In addition, the intensity in XRD patterns of crystalline and amorphous phase are independent [42, 61, 62]. And the crystallinity of PEO/LiTFSI/PPQDs is 28.1% lower than that of PEO/LiTFSI (37.0%), because the PEO crystallization is effectively inhibited by the rich interfaces of PPQD-PEO.

Then, in Fig. 7.15a, b, the thermodynamic properties of different SPEs were studied by DSC analysis. By adding PPQDs, a lower enthalpy of melting (ΔH_m, 52.8 J g^{-1} vs. 71.7 J g^{-1} of PEO/LiTFSI) is detected, which corresponds to a lower crystallinity for PEO/LiTFSI/PPQDs electrolyte. According to the theoretical calculation, the crystallinity of PEO/LiTFSI/PPQDs is the lowest, $\chi_c = 28.5\%$, which is consistent with the XRD result. Compared with PEO/LiTFSI/PPQDs, the crystallinity of PEO/LiTFSI/PQDs is ~33% by the calculation of ΔH_m and XRD data, indicating the outstanding advantages for PPQDs. In addition, Fig. 7.15b also shows that the low glass transition temperature (T_g) of –45.6 °C further supports the low crystallinity of PEO/LiTFSI/PPQD. These results confirm that PPQDs are effective nanofillers to suppress PEO chain arrangement and crystallinity.

High flexibility and mechanical strength reduce the risk of battery short circuit by inhibiting Li dendrites. Figure 7.16a shows that the maximum displacement of

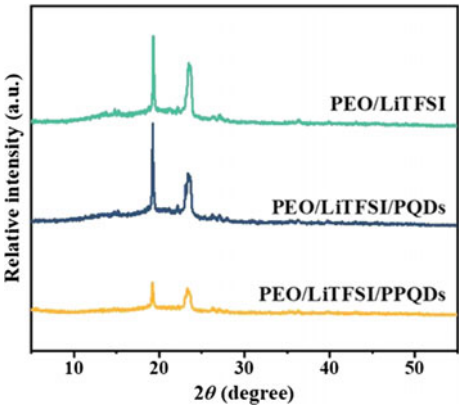

Fig. 7.14 XRD patterns of different SPEs. Copyright (2021), Elsevier [28]

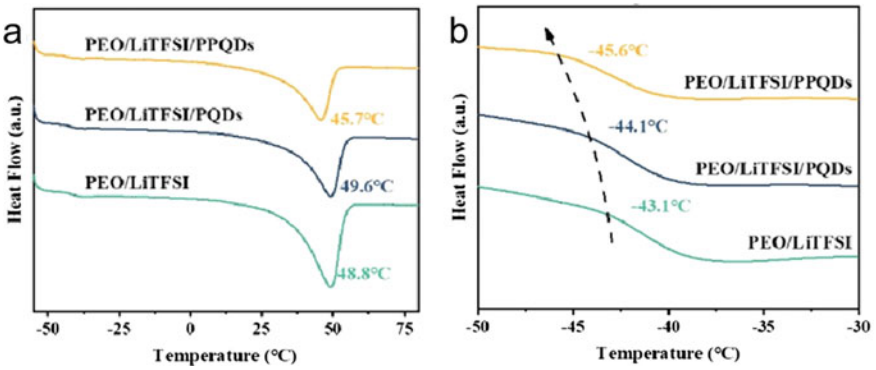

Fig. 7.15 **a** DSC heating curves of SPEs from 80 to –55 °C. **b** DSC heating curves of SPEs from –30 to –50 °C. Copyright (2021), Elsevier [28]

PEO/LiTFSI/PPQDs load–displacement curve is 2909 nm, which is 13% and 31% lower than that of PEO/LiTFSI/PQDs and PEO/LiTFSI under nanoindentation experiment, respectively. This shows that PEO/LiTFSI/PPQDs possess high mechanical modulus, which is consistent with the tensile testing results. It should be noted that PEO/LiTFSI/PPQDs has an elongation at break of 1095%, which is 25% and 46% higher than PEO/LiTFSI and PEO/LiTFSI/PQDs, respectively (Fig. 7.16b), indicating the good flexibility.

Figure 7.17 implies the ionic conductivities of different SPEs. In Fig. 7.17a, ionic conductivities of PEO/LiTFSI are 2.72×10^{-4} S cm^{-1} at 60 °C and 3.33×10^{-6} S cm^{-1} at 30 °C. By comparison, the ionic conductivities of PEO/LiTFSI/PPQDs reach 1.07×10^{-3} S cm^{-1} at 60 °C and 5.53×10^{-5} S cm^{-1} at 30 °C, which are much higher than those of PEO/LiTFSI. This significant improvement is due to the precise regulation of chemical microenvironment of PEO matrix by PPQDs, i.e., ion conductive groups, ionic coupling, and crystallinity [63, 64]. The reduction of

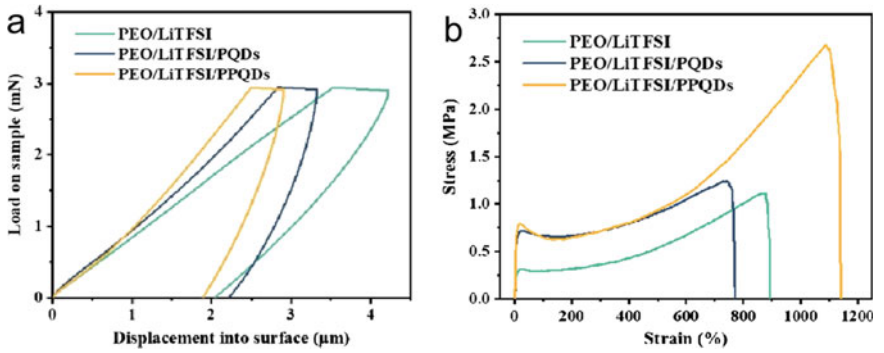

Fig. 7.16 **a** Load–displacement curves under nanoindentation test for different SPEs. **b** Stress–strain curves for different SPEs. Copyright (2021), Elsevier [28]

crystallinity provides high PEO chain mobility. Lithium salt and hydroxyl groups on PPQDs would produce strong Lewis acid–base interaction, which makes the dissociation rate reach 95.7%, providing more free Li^+ [46, 65, 66]. In addition, PPQDs can attract free Li^+ through Lewis base groups (e.g., C–O–C, C=O) and thus more free Li^+ can be quickly transferred by polyethylene glycol brushes [64]. Under the same loading, molecular-scale PPQDs can produce more interfaces of PPQD-PEO and continuous vertical networks for ion transfer when compared with large-size fillers. They collectively construct efficient networks for Li^+ transfer. In addition, in Fig. 7.17a, the E_a values of PEO/LiTFSI/PPQDs electrolyte obtained by Arrhenius fitting (1.178 eV) and Vogel-Tamman-Fulcher fitting (0.071 eV) are much lower than those of PEO/LiTFSI electrolyte (1.719 and 0.098 eV), also confirming the rapid transfer of Li^+ for PEO/LiTFSI/PPQDs electrolyte [15, 44].

As shown in Fig. 7.18a, symmetrical cells were assembled and operated at 60 °C at different current densities to evaluate the electrochemical stability of electrolyte.

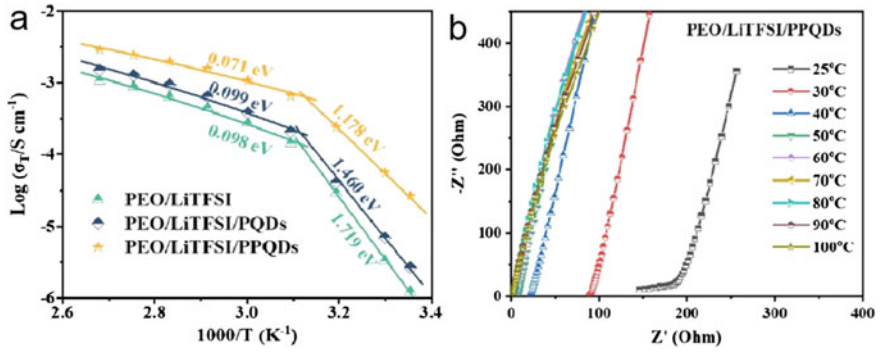

Fig. 7.17 **a** Activation energy and ionic conductivity of different SPEs. **b** Impedance spectroscopy at different temperatures of SPEs. Copyright (2021), Elsevier [28]

At 0.05 mA cm^{-2}, the Li|PEO/LiTFSI/PPQDs|Li symmetric cell displays a polarization voltage of 17 mV, much lower than that of Li|PEO/LiTFSI|Li cell (34 mV) and Li|PEO/LiTFSI/PQDs|Li cell (25 mV). It shows that PEO/LiTFSI/PPQDs have excellent interfacial contact and low internal resistance [10, 16, 67]. Notably, the voltage with Li|PEO/LiTFSI/PQD|Li or Li|PEO/LiTFSI|Li cells shows a larger irreversible drop at 0.1 and 0.2 mA cm^{-2}, respectively. This is caused by the dendrite-induced short circuits, resulting from the poor mechanical stability and uneven Li^+ deposition in Li|PEO/LiTFSI/PQD|Li and Li|PEO/LiTFSI|Li cells. SEM images of lithium surface after cycling, as shown in Fig. 7.18b, c, further verify the reason of short circuits in Li|PEO/LiTFSI/PQD|Li and Li|PEO/LiTFSI|Li cells. Under different current densities, Li|PEO/LiTFSI/PPQDs|Li cell can cycle for 1000 h and stay stable due to the efficient conduction ability of ion in PEO/LiTFSI/PPQDs, which leads to more uniform deposition of Li^+ and thus inhibits the growth of Li dendrite [67]. In Fig. 7.18d, SEM image shows compact, smooth, and uniform lithium electrode after cycling, which further confirms the high stability for Li|PEO/LiTFSI/PPQD|Li cell. In addition, the cell assembled with PEO/LiTFSI/PPQDs can continuously operate with stable overpotential for 1000 h at 60 °C and 0.2 mA cm^{-2}, supporting the stability of PEO/LiTFSI/PPQDs. Therefore, the addition of PPQDs improves the ionic conductivity, flexibility, and mechanical strength of PEO/LiTFSI/PPQDs, thus ensuring excellent battery cycling stability.

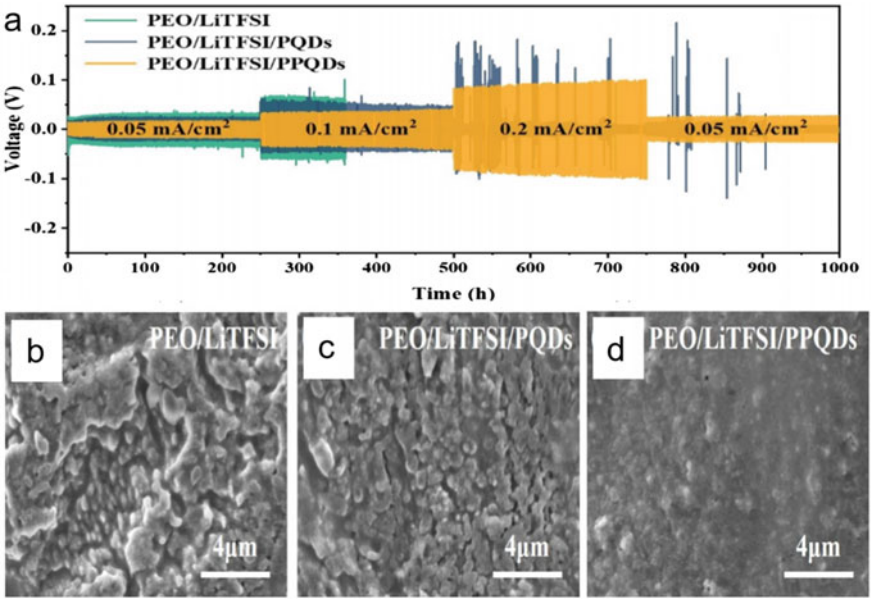

Fig. 7.18 **a** Voltage profiles under different current density at 60 °C for Li|SPEs|Li symmetric cells. The Li electrodes surface SEM images after cycling about 1000 h obtained from **b** Li|PEO/LiTFSI|Li cell, **c** Li|PEO/LiTFSI/PQDs|Li cell, and **d** Li|PEO/LiTFSI/PPQDs|Li cell. Copyright (2021), Elsevier [28]

Based on the LFP|SPEs|Li cell using different electrolytes, battery performances were evaluated. In Fig. 7.19a, c, the capacity of LFP|PEO/LiTFSI/PPQDs|Li cell only reduces to ~146 mAh g^{-1} after 150 cycles under 1.0C. The excellent cycling stability of LFP|PEO/LiTFSI/PPQDs|Li cell is attributed to the good interfacial compatibility with electrodes, excellent physicochemical stability, and high ionic conductivity of PEO/LiTFSI/PPQDs. Furthermore, the low polarization voltage platform implies rapid Li^+ transfer capacity in PEO/LiTFSI/PPQDs [68–70]. To further highlight the advantages of PEO/LiTFSI/PPQDs, rate performances of different cells are evaluated. Notably, rate performance of LFP|PEO/LiTFSI/PPQDs|Li cell exhibits a high capacity of 142.2 mAh g^{-1} at 4.5C. When the rate returns to 0.5C, the discharge capacity recovers to 158.4 mAh g^{-1}, indicating that the LFP|PEO/LiTFSI/PPQDs|Li cell has excellent stability [70]. On the contrary, the discharge capacities of LFP|PEO/LiTFSI|Li and LFP|PEO/LiTFSI/PQDs|Li cells degrade significantly at 2.0C. This indicates that PEO/LiTFSI and PEO/LiTFSI/PQDs cannot operate at high rate, caused by low ionic conductivity and high battery polarization. The outstanding rate and cycling performances for LFP|PEO/LiTFSI/PPQDs|Li cells are attributed to structure stability and high Li^+ conduction of PEO/LiTFSI/PPQDs electrolyte.

As shown in Fig. 7.20a, the general applicability is demonstrated by the anticipant charge–discharge capacities of LFP|PEO/LiTFSI/PPQDs|Li pouch cell. It is

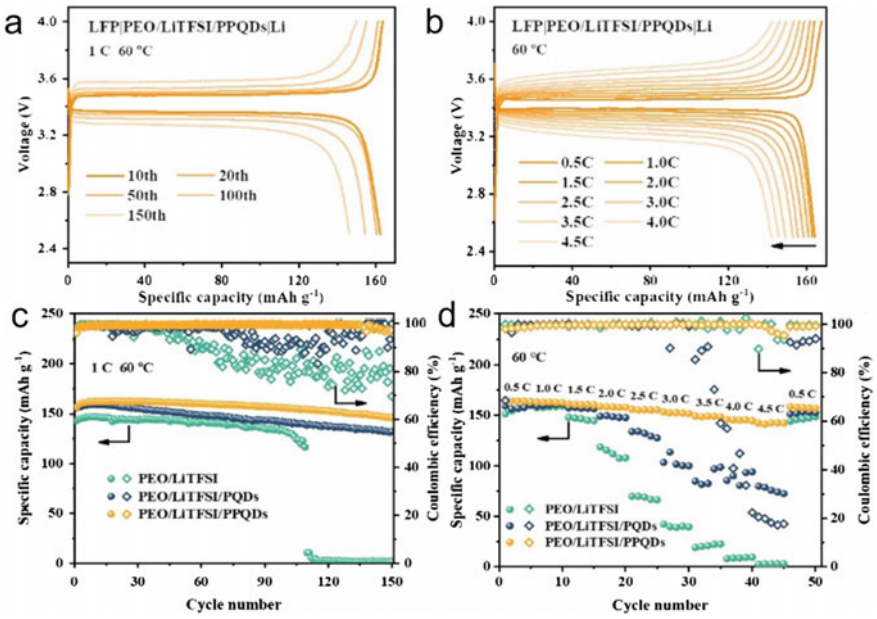

Fig. 7.19 **a** Charge–discharge voltage profiles at 1.0C and 60 °C for LFP|PEO/LiTFSI/PPQDs|Li cell. **b** Charge–discharge voltage profiles of LFP|PEO/LiTFSI/PPQDs|Li cell at 60 °C under various rates. **c** Cycling performances at 1.0C and 60 °C for LFP|SPEs|Li cells. **d** Rate performances at 60 °C for LFP|SPEs|Li cells. Copyright (2021), Elsevier [28]

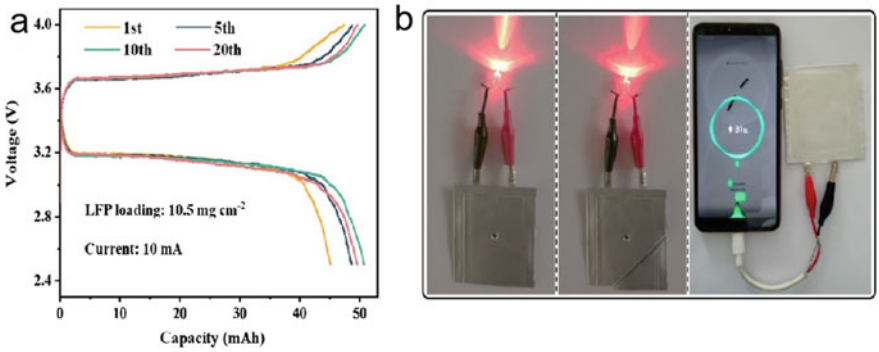

Fig. 7.20 **a** Pouch cell cycling performance of LFP|PEO/LiTFSI/PPQDs|Li. **b** Powering a phone and lighting light-emitting diode inset of all-solid-state pouch lithium batteries. Copyright (2021), Elsevier [28]

worth noting that LFP|PEO/LiTFSI/PPQDs|Li pouch cell can still light up the LED even with corner cut and nail penetration and can be acted as a successful mobile power supply (Fig. 7.20b). These results mean that the battery safety is significantly improved by using PEO/LiTFSI/PPQDs, paving the way for the development of flexible wearable batteries in the future.

In conclusion, PEG-grafted polymer-like quantum dots are synthesized as nanofillers, which possess rich functional groups and good interface compatibility with PEO chain. PPQDs are evenly dispersed in the electrolyte to form rich PPQD-PEO networks. And the lithium salt dissociation increases to 96.6%, which is attributed to the strong interaction of Lewis acid–base at the PPQD-PEO interface. Thus, continuous vertical networks for Li^+ transfer are constructed in the PEO/LiTFSI/PPQDs electrolyte, and the ionic conductivities of 1.07×10^{-3} S cm^{-1} at 60 °C and 5.53×10^{-5} S cm^{-1} at 30 °C are achieved. Meanwhile, the excellent flexibility and mechanical stability of the electrolyte are attributed to the hydrogen bond network formed by the PEO chains and PPQDs. Therefore, LFP|PEO/LiTFSI/PPQDs|Li cell displays excellent cycling stability of ~146 mAh g^{-1} at 60 °C and 1.0C after 150 cycles and rate performance of ~142 mAh g^{-1} under at 60 °C and 4.5C. In addition, such molecular-level fillers with abundant designable surface groups might exhibit great application and development potential for hydrogen-based fuel cell and all-solid-state lithium battery.

7.4 Composite Electrolyte with PEO-Threaded MOF Nanosheets

MOF nanosheets were prepared on the basis of the method in literature [71]. Firstly, 0.75 mmol 4,4′-biphenyldicarbonyl chloride was dispersed in the solution of water

(2 mL), C_2H_5OH (2 mL), and *N*,*N*-dimethylformamide (24 mL). Then, 0.8 mL triethanolamine was added to the solution. Afterward, 0.375 mmol $NiCl_2 \cdot 6H_2O$ and 0.375 mmol $CoCl_2 \cdot 6H_2O$, dissolved in 4 mL *N*,*N*-dimethylformamide, respectively, were injected into the mixture solution and stirred at 20 °C for 20 min. After that, the colloidal suspension was ultrasonicated under airtight condition for 20 h. In the end, the products were washed by 3 times by centrifugation with ethanol and subsequently dried at 25 °C, represented by MB nanosheet. Then, by replacing 4,4′-biphenyldicarbonyl chloride with TPDC, MC nanosheet was synthesized. In addition, except that 4,4′-biphenyldicarbonyl chloride was replaced by benzenedicarboxylic acid and triethanolamine was added after the injection of metal salts, the preparation step of MA nanosheet was identical to MB nanosheet's step. The lengths of A, B, and C are 6.9, 11.1, and 15.7 Å, respectively.

For the synthesis of $–NH_2$ group-modified MOF nanosheets, the nanosheets were first uniformly decentralized in 30 mL ethanol. Then, superfluous KH540 was injected slowly in the even solution. After stirring at 40 °C for 6 h, the functionalized nanosheet suspension was prepared through centrifugation and then washed by ethanol for 3 times aiming to get rid of excess reactant. Finally, at room temperature, the $–NH_2$-modified MOF nanosheet was dried for 24 h in a vacuum oven.

The laminar composite solid electrolyte (LCSE) was synthesized by a two-step method: self-assembly and low-pressure filtrating, as shown in Fig. 7.21. The polymer can disperse uniformly in the lower and upper layers of LCSE. First, MOF nanosheets and PEO-LiTFSI with equal quality were added into acetonitrile and stirred for 4 h. Then, at room temperature, this solution was ultrasonic for 4 h, aiming to drive PEO to enter in the pores. Subsequently, the thin LCSE was prepared by filtrating the solution at low pressure on a Nylon membrane. In the end, at room temperature, the LCSE was dried for 24 h and then peeled from Nylon membrane to get the self-supporting electrolyte (PEO@N-M*X* LCSE). The preparation step of PEO chain intercalated LCSE (PEO/N-MB LCSE) was alike to PEO@N-MB LCSE step, except that N-MB nanosheet suspension and PEO-LiTFSI-acetonitrile solution were mixed directly and then filtrated.

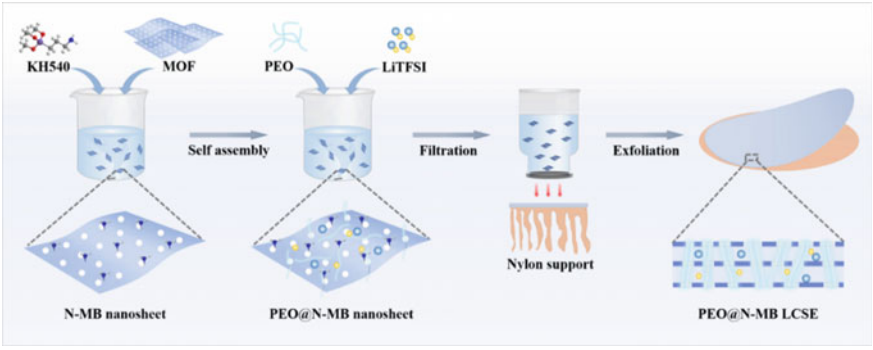

Fig. 7.21 Schematic fabrication of PEO@N-MB LCSE. Copyright (2022), John Wiley and Sons [29]

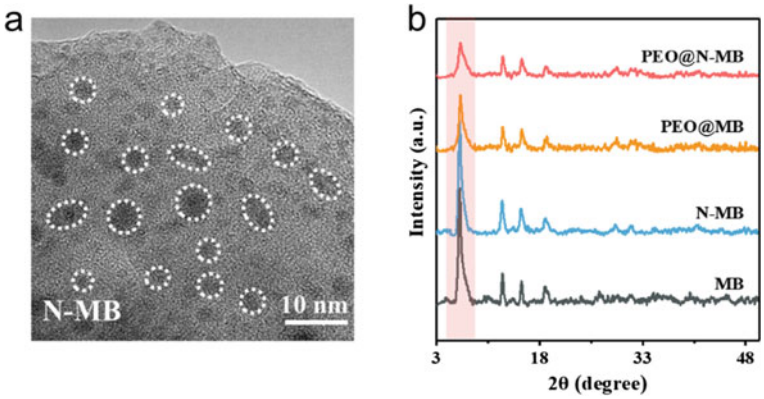

Fig. 7.22 **a** High-resolution TEM image of single N-MB nanosheet. **b** XRD patterns of PEO@N-MB, PEO@MB, N-MB, and MB nanosheets. Copyright (2022), John Wiley and Sons [29]

MOF nanosheet was fabricated by a solution of organic ligands and metal atoms using ultrasonication [71, 72]. In order to facilitate the interaction between PEO chains and MOF nanosheets and enhance the entrance of PEO into the pores of MOF nanosheets, the nanosheets were modified by silane coupling agent for grafting $–NH_2$ functional groups. TEM images in Fig. 7.22a show uniform MOF nanosheets with 2–5 nm diameter and well-distributed pores.

Then, by the two-step method, PEO-threaded MOF LCSE (PEO@N-MB LCSE) was fabricated. Firstly, the $–NH_2$-modified MOF nanosheets were pre-assembled with PEO chains in acetonitrile to prepare PEO-threaded MOF nanosheets (PEO@N-MB). Then, XRD was used to explore the structure of them. Figure 7.22b exhibits that, for PEO@N-MB nanosheet, the peak strength at 6.5° is apparently reduced. This variation should be attributed to the disturbance derived by the PEO chains in the pores of MOF nanosheets [73]. Remarkably, PEO@N-MB nanosheets show smaller pore volume and weaker XRD peak intensity in contrast with PEO@MB nanosheets. This should result from the powerful hydrogen-bonding interactions between $–NH_2$ groups in the pores and ether oxygen groups on PEO chains, which make more PEO chains to enter into the pores of nanosheets.

Then, the PEO@N-MB nanosheet was filtrated on a Nylon membrane to prepare thin and self-supporting PEO@N-MB LCSE. In order to get defect-free stacking of even PEO@N-MB nanosheet and facilitate PEO chain to enter in the pores of nanosheets, a filtration step at low pressure was employed. Cross-sectional SEM image (Fig. 7.23a) exhibits that PEO@N-MB LCSE owns sequential layered structure which is 7.5 μm in thickness. Remarkably, the interlayer spacing of PEO@N-MB LCSE is alike to that of layered MOF framework, apparently lower than that of PEO intercalated LCSE (PEO/N-MB LCSE). These results show that most PEO chains entered into the pores rather than gathering in the channels. The porosity of PEO@N-MB LCSE was tested by BET measurement in order to confirm the

above viewpoint. Compared with PEO@N-MB nanosheet, Fig. 7.23b shows remarkably reduced porosity of PEO@N-MB LCSE. This demonstrates that, during low-pressure filtration step, PEO chains fill the pores of PEO@N-MB LCSE. Similarly, these results prove the successful preparation of MOF laminar solid electrolyte with PEO-threaded structure.

PEO@N-MB LCSE attains a high ionic conductivity owing to the PEO-threaded structure. Figure 7.24a shows that the ionic conduction of PEO@N-MB LCSE (3.97×10^{-5} S cm^{-1}) at room temperature is about 25 times higher than that of SPE (1.51×10^{-6} S cm^{-1}). On one hand, this significant advancement should be ascribed to the PEO chains inside the pores of MOF nanosheets, which give many transport paths. On the other hand, the pore confinement effect endows PEO with high chain motility, which allows fast Li^+ transport. PEO/N-MB LCSE with chemical component and alike lamellar structure exhibits a low ionic conductivity (6.30×10^{-6} S cm^{-1}), which deeply emphasizes the advantage of this PEO-threaded structure.

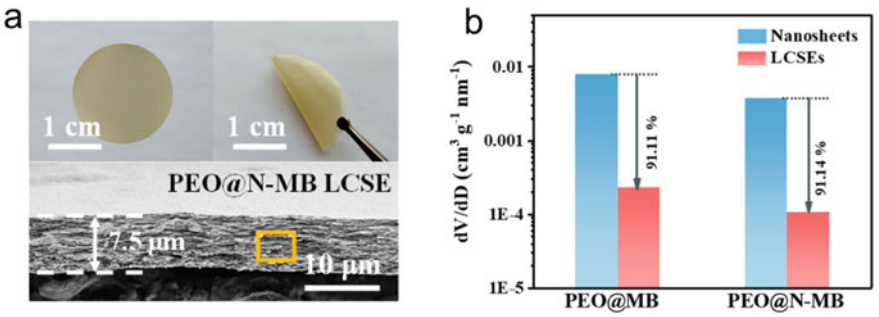

Fig. 7.23 **a** Optical and cross-sectional SEM images of PEO@N-MB LCSE. **b** Porosity of PEO@N-MB LCSE, PEO@MB LCSE, PEO@N-MB nanosheets, and PEO@MB nanosheets. Copyright (2022), John Wiley and Sons [29]

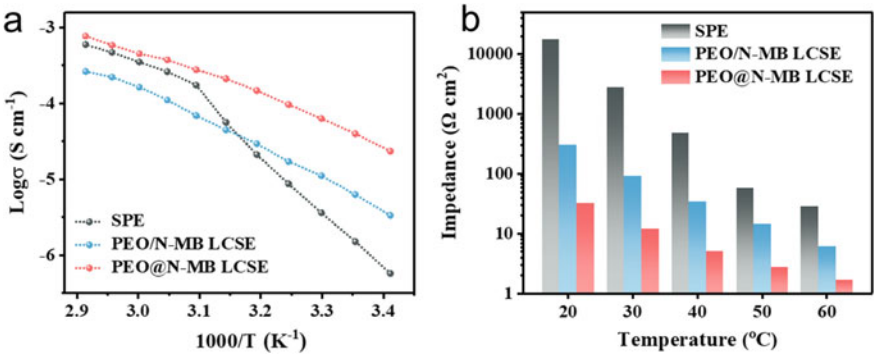

Fig. 7.24 **a** Ionic conductivity of PEO/N-MB, PEO@N-MB LCSE, and SPE. **b** ASR of PEO/N-MB, PEO@N-MB LCSE, and SPE. Copyright (2022), John Wiley and Sons [29]

PEO@N-MB LCSE owns a low area-specific resistance because of the higher ion conduction and indifferent thickness (12 Ω cm^2) at room temperature, which is two orders of magnitude lower than SPE as shown in Fig. 7.24b. Moreover, ionic transference number (t_{Li+}) was described. The ionic transference number of PEO@N-MB LCSE reaches as high as 0.6, which is much higher than those of PEO/N-MB LCSE (0.43) and SPE (0.22). These discoveries emphasize the PEO-threaded structure with advanced chain motility, building high-efficiency transmission channels in the perpendicular direction of PEO@N-MB LCSE.

In the previous study, the chain motility and function of PEO inside the pores of nanosheets are crucially important for ionic conductivity. In order to research this detailedly, the aperture of nanosheets was tested through altering the lengths of ligands [74–76], aiming for the regulation of PEO chain configuration and purity in the pores of nanosheets. The change of pore size is proved through rejection test employing dye molecules in different sizes, which is the same as the result of aperture attained by BET test. The PEO-threaded pores were checked, as shown in Fig. 7.25a. In contrast with N-M*X* nanosheets, the specific surface area decreases by 77.70%, 45.92%, and 67.04% for PEO@N-MC, PEO@N-MA, and PEO@N-MB nanosheets, respectively. As MOF nanosheets have the similar weight proportion (about 50 wt%), the specific surface area of PEO@N-MC nanosheet sharply decreases, which demonstrates that more PEO chains entered into the pores as compared with N-MB and N-MA nanosheets. The diffraction peak strength of PEO@N-MC nanosheet is apparently decreased as compared to those of PEO@N-MB and PEO@N-MA nanosheets, as shown in Fig. 7.22b. And the *d*-spacing change of PEO@N-MC LCSE is smaller as compared with PEO@N-MB LCSE and PEO@N-MA LCSE (Fig. 7.25b), which again confirms the above viewpoint.

The ion conduction of three different LCSEs was measured detailedly. For PEO@N-MA LCSE, the ionic conductivity at 25 °C reaches 1.11 × 10^{-5} S cm^{-1} (Fig. 7.26b). In contrast, for PEO@N-MB LCSE, owning to the fact that more PEO

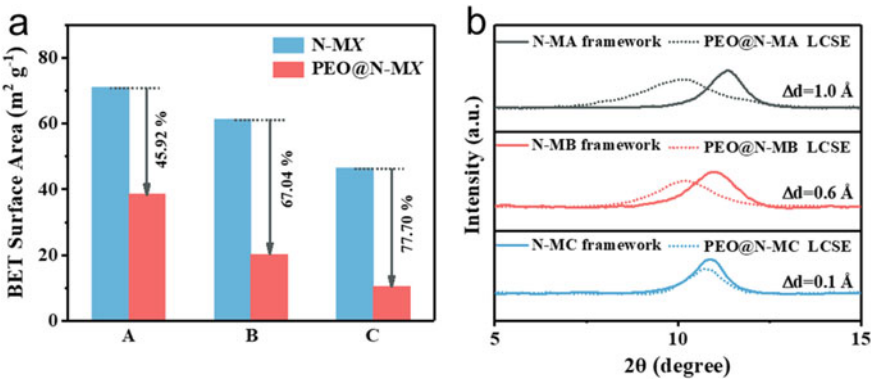

Fig. 7.25 **a** Specific surface areas of PEO@N-MX and N-MX nanosheets. **b** XRD patterns of PEO@N-MX LCSEs and N-MX frameworks. Copyright (2022), John Wiley and Sons [29]

chains enter into the pores, the ionic conductivity reaches 3.97 × 10^{-5} S cm^{-1}, as shown in Fig. 7.26a. For PEO@N-MC LCSE, the conductivity achieves 1.96 × 10^{-5} S cm^{-1}, despite the more PEO than other in the pores. In order to further research this finding, on the basis of the temperature-dependent conductivity curves, the transfer activation energy is calculated. It is shown that PEO@N-MC LCSE has a higher activation energy (0.123 eV) as compared with PEO@N-MB LCSE (0.114 eV), which demonstrates a high Li^+ transfer energy barrier in the former [3, 77]. These are attributed to the disorder packing of PEO chains, making Li^+ transfer paths tedious.

Because of low crystallinity of polymer chains in confined spacing, the effect on ionic conductivity can be ignored [78], and the PEO chain conformation was explored. FTIR results of PEO@N-MC, PEO@N-MB, and PEO@N-MA LCSEs were explored. The characteristic peaks of PEO at 1342, 2882, and 2945 cm^{-1} (Fig. 7.26c) correspond to wagging vibrations, symmetric stretching, and asymmetric stretching of C–H [79–81]. With the growth of PEO chains in the pores of MOF nanosheets, the peak strengths assigned to wagging vibrations and asymmetrical stretching of carbon-hydrogen bond are decreased, demonstrating the disorder degree of PEO chain [78, 82].

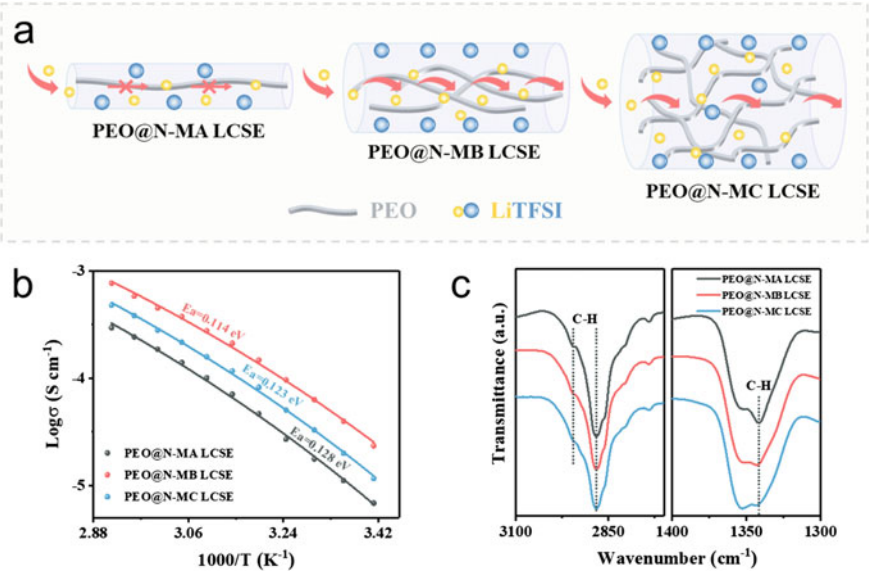

Fig. 7.26 **a** Concept schemes of the ion conduction of PEO@N-MB, PEO@N-MC, and PEO@N-MA LCSEs. **b** Ionic conductivity at different temperatures for PEO@N-MB, PEO@N-MC, and PEO@N-MA LCSEs. **c** FTIR absorption spectra of PEO@N-MC, PEO@N-MB, and PEO@N-MA LCSEs. Copyright (2022), John Wiley and Sons [29]

As shown in Fig. 7.27a, lithium symmetric cells were assembled and researched at 60 °C on disparate current densities. Under 0.1 mA cm^{-2}, the voltages of Li|PEO/N-MB LCSE|Li and Li|SPE|Li symmetric cells show stability at 24 and 31 mV, respectively, while they suffer irreversible and large drop when current density increases to 0.4 and 0.2 mA cm^{-2}. These suggest internal short circuit resulting from the poor mechanical strength and uneven Li^+ deposition. In comparison, as the current densities increases from 0.1 to 0.4 mA cm^{-2}, the cell using PEO@N-MB LCSE can run for 800 h stably. Particularly, the overpotentials reach 45 and 22 mV at 0.2 and 0.1 mA cm^{-2}, respectively. For Li|PEO@N-MB LCSE|Li, the overpotential reaches 83 mV even at 0.4 mA cm^{-2}. The outstanding cycling performance should result from two reasons: Firstly, the outstanding ionic conductivity makes even Li^+ deposition on the lithium metal surface and, secondly, the outstanding mechanical strength of electrolyte prevents the lithium dendrite growth efficiently. Furthermore, the electrochemical stability is assessed through LSV measurement, as shown in Fig. 7.27b. Compared with SPE (4.1 V) and PEO/N-MB LCSE (4.6 V), PEO@N-MB LCSE shows a high decomposition voltage (5.1 V). This observation resulted from the pores, which efficiently stop PEO from reacting with lithium metal. What's more, the powerful hydrogen-bonding interactions between $–NH_2$ functional groups of MOF nanosheets and ether oxygen of PEO chains could also prevent PEO from decomposing [83]. These also demonstrate that PEO@N-MB LCSE has great potential in high-voltage electrode materials.

$LiFePO_4$/Li batteries were assembled to test the rate performances and cycling performances. Figure 7.28a exhibits the cycling performances of different cells at 60 °C under 0.5C. After 74 cycles, the discharge capacity sharply drops from 130 to 0 mAh g^{-1} for LFP|SPE|Li cell owing to the low ionic conductivity of SPE. The discharge capacity of LFP/Li cell using PEO/N-MB LCSE drops from 140 to 115 mAh g^{-1} with a retention of 82% after 150 cycles. The promoted cycling performance is ascribed to PEO/N-MB LCSE's thin thickness and the increased lithium-ion conduction. In comparison, owing to the excellent structural stability and highest ion conduction, LFP/Li cell using PEO@N-MB LCSE owns a retention of 94% after 150 cycles and the highest initial discharge capacity (148 mAh g^{-1}).

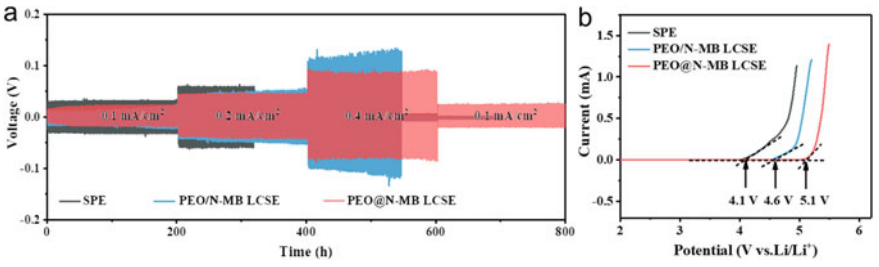

Fig. 7.27 **a** Galvanostatic cycling curves of lithium symmetric cells with SPE, PEO@N-MB, and PEO/N-MB LCSEs on different current densities at 60 °C. **b** Linear sweep voltammetry curves at 60 °C of the different electrolytes at scanning rate of 1 mV s^{-1}. Copyright (2022), John Wiley and Sons [29]

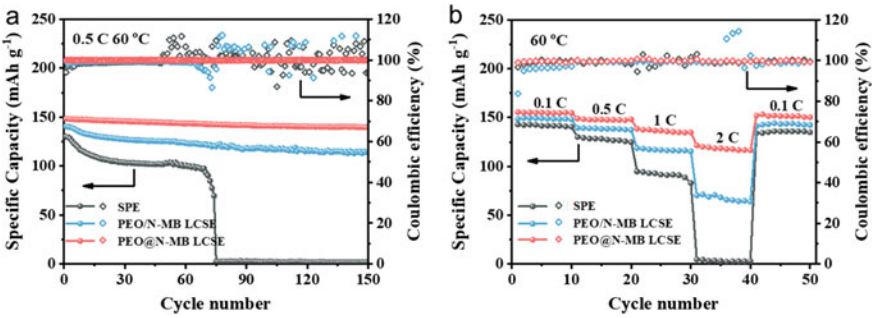

Fig. 7.28 Electrochemical performances of all-solid-state lithium battery. **a** Cycling performances of the different cells under 0.5C at 60 °C. **b** Rate performances of the different cells under various rates at 60 °C. Copyright (2022), John Wiley and Sons [29]

Additionally, the rate performances of different cells were also explored (Fig. 7.28b). The LFP|SPE|Li cell has inferior Coulomb efficiency and a low discharge capacity. For LFP/Li cell using SPE, the discharge capacity drops dramatically, especially at 2.0C. For LFP/Li cell using PEO/N-MB LCSE, the discharge capacity sustains apparent recession at 2.0C while the discharge capacity of LFP/Li cell using PEO@N-MB LCSE reaches 116, 134, 148, and 154 mAh g^{-1} at 2.0, 1.0, 0.5, and 0.1C, respectively, much higher than that of LFP|SPE|Li and LFP|PEO/N-MB LCSE|Li cells under the same condition. Significantly, for LFP/Li cell using PEO@N-MB LCSE, the discharge capacity comes back to 152 mAh g^{-1} (98.7% of the initial discharge capacity) as the current density recovers to 0.1C. These results suggest that PEO@N-MB LCSE attains outstanding stability.

In conclusion, we show the preparation and design of thin LCSE employing MOF nanosheets with PEO threading structure, as building-block through the filtration at low-pressure way. The pores are modified by $–NH_2$ functional groups to guide PEO chain entering in the pores of nanosheets through powerful hydrogen-bonding interactions between $–NH_2$ functional group and ether oxygen of PEO. Through the interactions, the threaded-PEO chains combine with the surrounding MOF nanosheets, providing PEO@N-MB LCSE (7.5 μm-thick) with outstanding mechanical stability. Furthermore, the confinement function advances the chain motility and promotes the stretching of PEO chains, endowing PEO@N-MB LCSE with improved ion conduction (3.97×10^{-5} S cm^{-1}), that is 25 times higher than PEO electrolyte. By this way, the trade-off effect is resolved between mechanical stability and ionic conductivity for PEO-based and MOF-based electrolytes. Significantly, the battery using PEO@N-MB LCSE shows a retention of 94% after 150 cycles and an outstanding initial capacity (148 mA h g^{-1}). Noticeably, we research the function of different pore sizes on the preparation of threaded-PEO chains. Then, we also confirm the superiority of synergistic function between *cis*-PEO and *trans*-PEO in promoting ionic conductivity. The excellent design approach and concept are possible to be employed to prepare other materials with polymer matrices and various aperture materials, which have great potential for ion separation, gas separation, and hydrogen-based fuel cell.

7.5 Composite Electrolyte with LLTO Framework

$Li_{0.33}La_{0.557}TiO_3$ (LLTO) framework was synthesized by sol–gel method. Generally, $Ti(OC_4H_9)_4$ (10.00 g), $La(NO_3)_3 \cdot 6H_2O$ (7.08 g), and $LiNO_3$ (0.74 g) were dissolved in ethanol (10 mL) and stirred at 50 °C for 10 min to obtain the precursor solution [21]. Considering the thin structure and interconnected porous of nylon, it was selected as a template to prepare the LLTO framework. Subsequently, the precursor solution was mixed into nylon filter for gel permeation. Then by stirring constantly, a viscous gel was obtained. The gel-permeated nylon was dried and calcined at 1000 °C for 2 h in air under a heating rate of 1 °C min^{-1}. LLTO nanoparticles were prepared by the method of ball milling.

By solution-dripping method, PEO-LLTO framework (PLLF) electrolyte was prepared. LiTFSI and PEO were dried overnight at 100 °C and 60 °C in vacuum, respectively. LiTFSI and PEO (the molar ratio of EO to LiTFSI is 18:1) were dissolved in anhydrous acetonitrile and stirred for 4 h. Then, the solution (concentration of 1.0 g L^{-1}) was slowly dripped into the LLTO framework and then dried in a 60 °C vacuum oven to remove acetonitrile completely. The drying and dripping processes were repeated many times till the bottom and top of LLTO framework were completely embedded in the PEO matrix. In addition, adding different loadings of LLTO nanoparticles into the LiTFSI and PEO solution (the molar ratio of EO to Li is 18:1) was conducted. And then, the casting solution was fully mixed and stirred for 5 h, then poured onto PTFE plate. After drying at 40 °C in a vacuum, the PEO-LLTO nanoparticle (PLLN) electrolyte was prepared. All the processes of experiments were implemented in a dry glove box with argon gas. The solution of LiTFSI and PEO was completely mixed and then cast onto the PTFE plate. After drying at 40 °C, the PEO (PL) electrolyte was obtained in vacuum. The processes of experiments were carried out in a glove box with argon gas. In Fig. 7.29, the synthesis procedure of PLLF electrolyte and LLTO framework is schematically illustrated.

As shown in Fig. 7.30a, the SEM image displays the PLLF electrolyte microstructure. It is observed that the LLTO framework with porous structure turns into dense electrolyte with well-organized wrinkles, implying that the PEO matrix has been infiltrated into LLTO framework. This can be supported by dimming the bright lines,

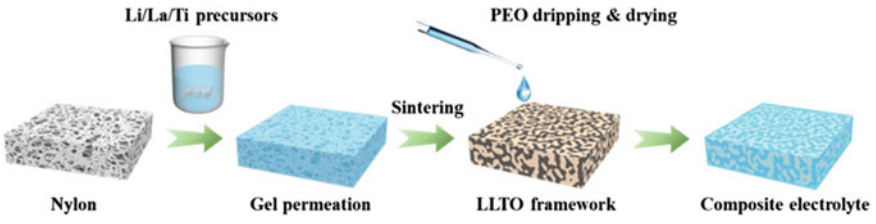

Fig. 7.29 Schematic diagram of the synthesis process of PLLF electrolyte and LLTO framework. Copyright (2021), Elsevier [30]

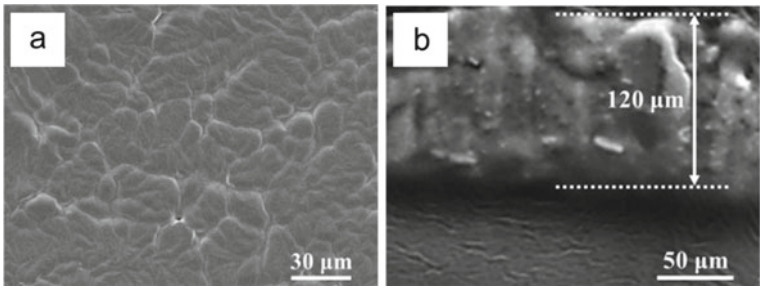

Fig. 7.30 Proofs for the synthesis of PLLF electrolyte. **a** Surface and **b** cross-sectional SEM images of PLLF electrolyte. Copyright (2021), Elsevier [30]

corresponding to the wrinkles above in the optical image [44]. In LLTO framework, the penetration of PEO is directly confirmed by cross-sectional SEM image (Fig. 7.30b), which results in uniform and dense electrolyte. This suggests that the constructed PLLF electrolyte has a structure of vertical bicontinuous phase: confined PEO and LLTO framework. Moreover, the thickness of LLTO framework is about 100 μm, which is slightly thinner than the 120 μm of PLLF electrolyte. The excess thickness manifests that the surface of PLLF electrolyte forms a thin PEO layer. The polymer layer can restrain the side reactions between lithium anode and LLTO, and it can hold the potential to improve stability at electrolyte interface [16, 18, 84]. Herein, large pores of LLTO framework (1–2 μm) are taken to ensure the complete entrance of PEO matrix, and therefore, it has a vertical bicontinuous phase structure. But other frameworks, like MOF and COF, fail to do so [22–24].

Thermal behaviors and chemical features of these electrolytes were researched by thermogravimetric analysis (TGA) and FTIR. The characteristic peaks of PLLF, PLLN, and PL electrolytes are fundamentally coincident as shown in FTIR [85], indicating an adequate coupling between LLTO and PEO in the fabricating process (Fig. 7.31a). Furthermore, in Fig. 7.31b, the TGA curves indicate that PL electrolyte goes through weight loss for two stages, including the evaporation of water at the first stage (below 100 °C), and the decomposition of lithium salt and PEO at the second stage (380–450 °C). Here, during TGA test, the moisture might be from the water in the air [44]. By contrast, PLLF electrolyte shows a similar TGA curve but with a lower weight loss as compared to PL electrolyte at the second stage, implying that the LLTO framework has splendid thermal stability. The residuals for PLLF and PL electrolytes are 65.2 wt% and 6.4 wt%, respectively. Thus, in PLLF electrolyte, the weight ratio of LLTO framework is about 63 wt%.

For solid electrolyte, Li^+ transference number and ionic conductivity are both important indicators. The ionic conductivities of PLLN and PL electrolytes are 2.35×10^{-5} and 2.85×10^{-6} S cm^{-1} at 25 °C, respectively, as shown in Fig. 7.32a. This finding indicates that the LLTO nanoparticles improve its transfer ability probably because of the reduction of PEO crystallization. By contrast, the ionic conductivity of PLLF electrolyte is 2.04×10^{-4} S cm^{-1}, 8.7, and 71.6 times greater than that of PLLN and PL electrolytes. And the conductivity remarkably precedes a lot of

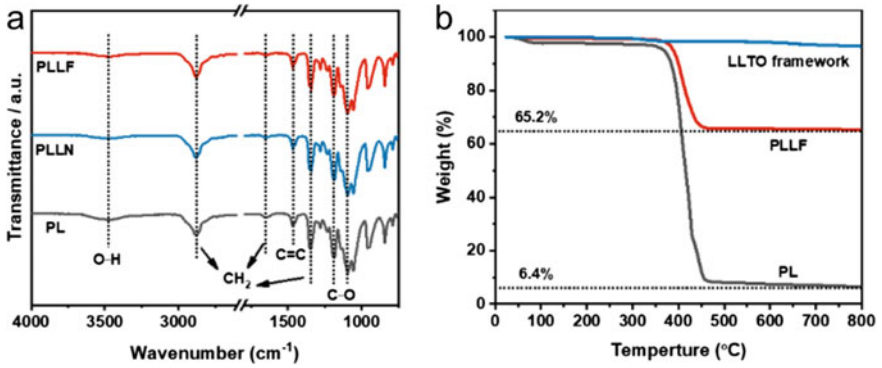

Fig. 7.31 **a** FTIR spectra of PLLF, PL, and PLLN electrolytes. **b** TGA curves of PLLF electrolytes, PL electrolytes, and LLTO framework. Copyright (2021), Elsevier [30]

electrolytes, particularly composite electrolytes, which emphasizes the advantages of structural advantage of the conductive PEO and LLTO [26].

Here, at 40 °C, the temperature turning points appear for PLLN electrolytes (Fig. 7.32b). In comparison with PL electrolyte, the reduction proves the effect of LLTO nanoparticles, which enhances the chain motion and reduces the PEO crystallization, thereby enhancing the transfer ability at relatively low temperature [86]. Moreover, the ionic conductivity of PLLN electrolyte climbs up and then declines as the LLTO mass ratio increases. In PLLN electrolyte, the decreased conductivity at high LLTO mass ratio is due to the agglomeration of substantial LLTO nanoparticles, which reduces the Li^+ transfer ability and diminishes the inhibition effect on PEO crystallization [87] while the related curve shows a straight line without distinct turning point between temperature and ionic conductivity of PLLF electrolyte. This

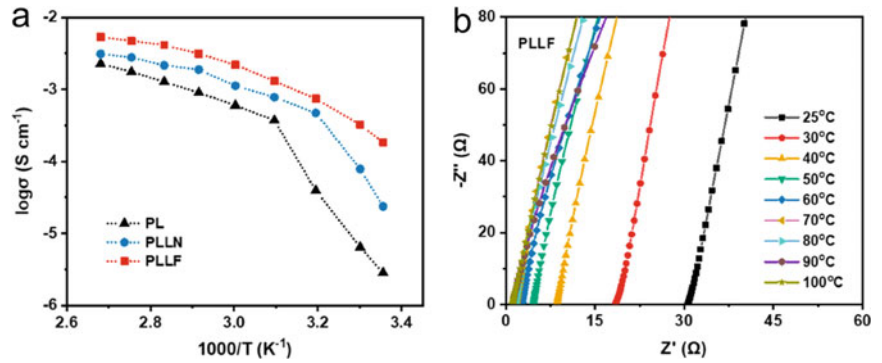

Fig. 7.32 **a** Ionic conductivity of PLLF, PLLN, and PL electrolytes at various temperatures. **b** The impedance spectra of PLLF electrolyte sandwiched by two stainless steels from 25 °C to 100 °C. Ionic conductivity is calculated through the corresponding impedance data. Copyright (2021), Elsevier [30]

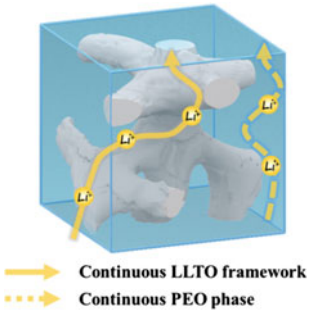

Fig. 7.33 Schematic diagram of possible Li^+ conduction pathways in the PLLF electrolyte with some vertically bicontinuous transmission channels. Copyright (2021), Elsevier [30]

indicates that in this electrolyte, the Li^+ transfer follows the continuous rapid ion transfer mode [87], which implies that the limited PEO phase shows greatly improved transfer ability when compared with PLLF and PL electrolytes. Here, through a vertical bicontinuous transfer channels (particularly the LLTO framework), PLLF electrolyte acquires outstanding ionic conductivity.

Based on electrolyte structure and ionic conductivity, there are three possible transfer channels (Fig. 7.33) in this as-prepared PLLF electrolyte: PEO-LLTO interface, LLTO framework, and PEO phase [88, 89]. To test this speculation, more characteristics including the segmental motion of PEO, the crystallization, and the existence of lithium ions were conducted.

High-resolution solid-state nuclear magnetic resonance spectrometry (Li NMR) clearly exhibits three Li^+ local environments (Fig. 7.34a): PEO-LLTO interface, LLTO framework, and lithium salts in PEO phase [89, 90]. The ^6Li resonances at 2.5 and –0.3 ppm correspond to LiTFSI in LLTO framework and PEO phase, respectively. Except for these two signals, at 1.8 ppm, the PEO-LLTO interface with a characteristic signal is obtained. This implies that under this bicontinuous phase structure, both PEO and LLTO phases can transfer Li^+ effectively.

Then, the XRD performs the crystallization behavior of PEO as shown in Fig. 7.34b. It is observed that all of the diffraction peaks belong to LLTO and PEO phases present in the curve of PLLF and PLLN electrolytes. While it implies that the peak intensity of PEO phase at 23.4° and 19.0° shows prominent alteration in comparison with the excellent crystallinity in PL electrolyte. The LLTO nanoparticles are added which have steric reference to the PEO chains for reducing PEO crystallinity [88, 90, 91]. By contrast, under close chemical component, the PEO matrix exhibits much lower crystallinity degree in PLLF electrolyte. This implies that in LLTO framework the crystallization behavior of PEO is extremely inhibited, and the restricted PEO chains are difficult to condense into ordered packages. Different from the low crystallinity of PEO phase, PLLF electrolyte shows distinctly elevated crystallinity for LLTO phase relative to PLLN electrolyte, implying the well-crystallized LLTO framework [21, 92]. The weak crystallinity of PEO and the strong crystallinity of LLTO are both conducive to Li^+ conduction, and these also highlight the structural advantage of this PLLF electrolyte.

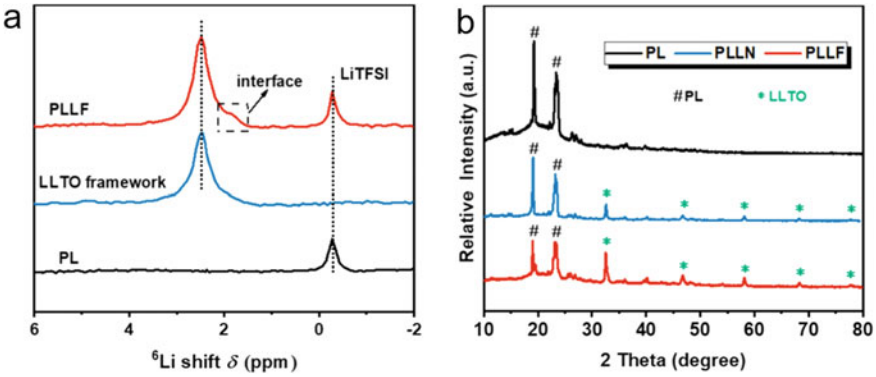

Fig. 7.34 Ion transfer characteristics of PLLF, PLLN, and PL electrolytes. **a** ^{6}Li NMR spectra of LLTO framework, PLLF, and PL electrolytes. **b** XRD patterns of PLLF, PLLN, and PL electrolytes. Copyright (2021), Elsevier [30]

Heterogeneous Li^+ deposition often forms dendrites on the surface of lithium anode during the operation process of lithium stripping/plating. The interface stability between solid electrolyte and anode determines the electrochemical performance of battery [10]. The constant-current cycling performance was performed at a current density of 0.1, 0.2, and 0.4 mA cm^{-2} at 60 °C (Fig. 7.35). The stability of Li/PLLN/Li and Li/PL/Li symmetric batteries are 28.5 mV and 41.5 mV at 0.1 mA cm^{-2}, respectively, which is higher than that of Li/PLLF/Li (20.3 mV). As the current density rises to 0.2 mA cm^{-2}, the voltage of the Li/PL/Li battery increases sharply and then suddenly drops to 0 V, suggesting a short circuit caused by lithium dendrites which pierce the electrolyte [86]. This is because of the poor mechanical stability of the electrolyte and the uneven deposition of Li^+ on the electrolyte–electrode. The others keep a steady voltage. In addition, when the current density is 0.4 mA cm^{-2}, Li/PLLN/Li symmetric cells stop working due to uneven deposition of interfacial lithium ions at high current densities. This implies that the interface between PLLN electrolyte and Li electrode is unstable. Meanwhile, the voltage of the Li/ PLLF/Li battery fluctuates slightly and there is no significant polarization. This means that Li^+ ions are evenly distributed within the electrolyte because of its double continuous transfer channels in vertical direction, which afford uniform deposition at interface and efficient Li^+ transfer [17, 93].

All-solid-state LFP/Li cells were assembled to evaluate rate performance and cycling performance. Figure 7.36 shows the cycling performance at 1.0C and 60 °C. After 150 cycles, the discharge capacity of LFP/PLLF/Li battery decreases to 154.7 mAh g^{-1} with a retention rate of 97.2%. In comparison, the discharge capacities of LFP/PLLN/Li and LFP/PL/Li cells decrease to 137.2 mAh g^{-1} and 2.6 mAh g^{-1}, with only 88.5% and 1.9% retention, respectively. The superior cycling performance and increased capacity are probably ascribed to the synergistic effect of Li^+ conduction frame and sealed PEO, which enhance the ion transfer capacity, and the interconnect structure also improves cycling stability. The LLTO framework enables superior

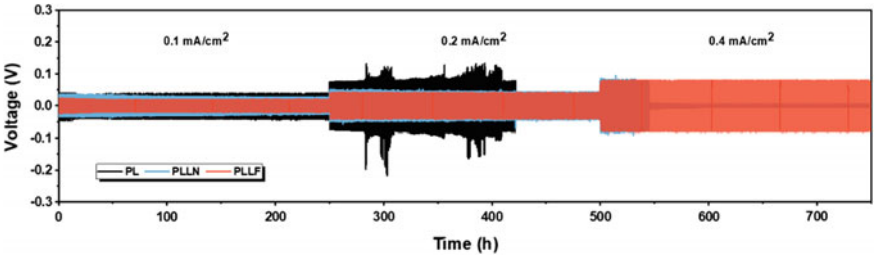

Fig. 7.35 Galvanostatic cycling performance of Li/PLLF/Li, Li/PLLN/Li, and Li/PL/Li symmetrical cells with different current densities at 60 °C. Copyright (2021), Elsevier [30]

Li^+ transport capabilities through its vertically continuous channels. At the same time, the limited PEO phase with low crystallinity also helps the rapid Li^+ transfer with the helped of enhanced chain movement [45, 94]. Therefore, in comparison with the other two cells, LFP/PLLF/Li cells show significantly enhanced electrochemical performance. In addition, the charge–discharge curves of LFP/PLLF/Li cells remain stable, while the polarization voltage rises gently, and the capacity decreases mildly at the current density of 1.0C. And this demonstrates the excellent stability and lithium-ion transfer of the vertical bicontinuous phase structure.

Moreover, Fig. 7.37 shows the original, 1st, 30th, and 70th cycle's impedance spectra of LFP/PLLF/Li cells at 1.0C and 60 °C. What is noteworthy is that the interfacial resistance of LFP/PLLF/Li cells changes slightly during the cycling (from 41.9 Ω at 1st cycle to 55.7 Ω at 70th cycle). This suggests that the PLLF electrolyte-Li electrode interface can maintain stable and consistent contact during the cycling without Li dendrite growth. This finding is in accordance with the constant-current cycle, as confirmed by the SEM image of the surface near Li electrode. The excellent cycling performance of LFP/PLLF/Li batteries proves the interface stability of PLLF electrolyte-Li electrodes [10, 95].

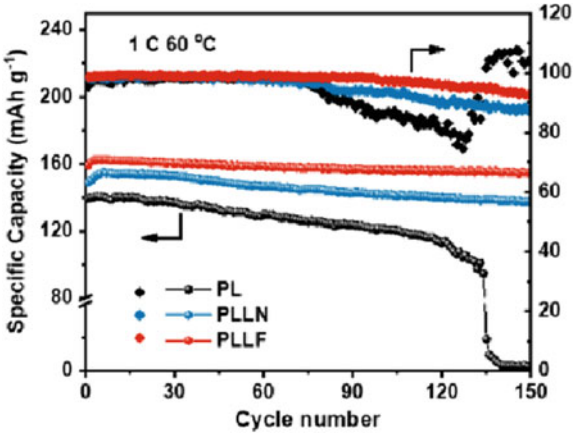

Fig. 7.36 The cycling performance of all-solid-state cells with various electrolytes. Copyright (2021), Elsevier [30]

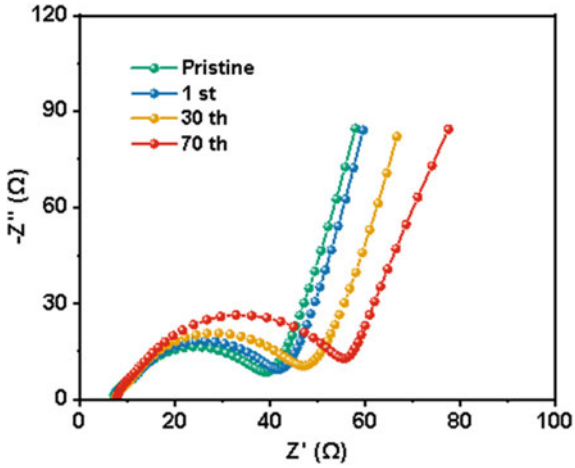

Fig. 7.37 AC impedance spectra of LFP/PLLF/Li cell after different cycles. Copyright (2021), Elsevier [30]

In conclusion, we have demonstrated a method to dramatically enhance Li^+ conductivity and improve electrolyte structure stability by constructing vertical dual-continuous transfer channels using PEO and LLTO framework. The vertically continuous frame and airtight PEO act as high-efficiency Li^+ transfer pathways, significantly improving the ion conduction property of electrolytes. Particularly, at 25 °C, PLLF electrolyte attains excellent ionic conductivity of 2.04×10^{-4} S cm^{-1}, about 72 times higher than that of PL electrolyte and better than the majority of reported electrolytes. Besides, the PLLF electrolyte shows excellent interfacial compatibility and structural stability due to its stably interconnect network. After 150 cycles, the LFP/PLLF/Li cell demonstrates excellent cycling stability (154.7 mAh g^{-1}) and an ultra-high retention rate (97.2%). In consequence, this framework-based electrolyte with high structural stability, featuring superior conductivity and vertically bicontinuous phase structure, should be instrumental for providing a path to construct the next-generation devices for energy storage.

7.6 Composite Electrolyte with LLZO Nanosheets

$Li_7La_3Zr_2O_{12}$ (LLZO) nanosheets were synthesized using two-step sintering approach and subsequent liquid-phase exfoliation. Firstly, sucrose (0.50 g), $ZrO(NO_3)_2$ (0.46 g), $La(NO_3)_3{\cdot}6H_2O$ (1.30 g), and $LiNO_3$ (0.58 g) were dissolved in deionized water (70 mL), in which the pH value was kept at 1.5. The above precursor solutions were subsequently sintered at 250 °C and 850 °C for 4 h and 2 h, respectively [96]. The calcined product was added to an acetonitrile solution (80 mL) and stirred at room temperature for 12 h, followed by sonication for 10 min. To obtain uniformly dispersed LLZO nanosheets, the above solution was centrifuged at 1000 rpm for 15 min to remove unexfoliated particles.

LLZO laminar inorganic solid electrolyte (LLISE) was obtained by the suction filtration method. Firstly, layered LLZO frameworks were prepared by filtering the solution of LLZO nanosheets onto nylon substrates. Secondly, the binder for configuring LLZO nanosheets is a small amount of PEO and LiTFSI (18:1, EO/Li molar ratio) which was dissolved in acetonitrile. The above solution was suction filtered in a layered LLZO framework and then dried in an argon-filled glovebox for 24 h. Finally, in order to obtain LLISE, autoclaving at 80 °C for 10 min was required. Here, the concentration of LLZO nanosheets was utilized to control the thickness of LLISE. LLISE-x (x = thickness, μm) represents the LLISE with different thicknesses. In order to obtain LN/PEO CSEs with a thickness of 140 μm, a PEO-LiTFSI-acetonitrile solution (EO/Li molar ratio of 18:1) was first prepared, and LLZO nanosheets with different contents were added into above solution. Next, the mixed solution was stirred at room temperature for 10 h, and then, it was cast on a polytetrafluoroethylene (PTFE) plate and finally dried under an argon atmosphere at normal pressure and 40 °C for 12 h, followed by dried at 55 °C under vacuum for 12 h. It is worth noting that the above operations were all carried out in a glovebox filled with argon gas.

LLZO nanosheets were synthesized using two-step sintering manner and subsequently liquid-phase exfoliation. It can be seen from the AFM images (Fig. 7.38a) that LLZO nanosheets are about 4.5 nm thick and have lateral dimension of 3–5 μm. In order to verify the good crystallinity of the LLZO nanosheets, high-magnification TEM image (Fig. 7.38b) was taken, and the results show that the nanosheets have clearer and more ordered lattice fringes [97]. These results confirm the successful preparation of LLZO nanosheets.

Figure 7.39 shows the preparation process of LLISE. In order to obtain the layered LLZO framework, vacuum filtration is employed to assemble the resultant LLZO nanosheets into a film, followed by dispersing the solution on a nylon substrate and vacuum filtration to facilitate its film formation. It is worth noting that in order to obtain uniform and defect-free stacking of LLZO nanosheets on the base membrane, it is necessary to employ a low-pressure and uniform suction filtration. Then, the small amount of PEO-LiTFSI-acetonitrile solution was drawn into the interlayer by

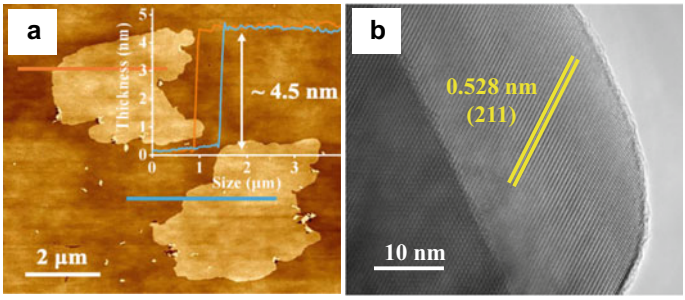

Fig. 7.38 **a** AFM image of LLZO nanosheets with corresponding height profiles and **b** high-magnification TEM image of LLZO nanosheets. Copyright (2022), Elsevier [31]

utilizing the layered structure of the LLZO framework, which was dried in an argon-filled glovebox for one day to obtain LLISE. In the above operation, it is necessary to ensure that the acetonitrile in the structure is completely removed. In the end, in order to improve the interlayer contact and obtain a denser film, hot pressing at 80 °C is utilized. PEO plays three main roles in LLISE: (1) It acts as a binder to improve the mechanical properties of the electrolyte; (2) the presence of PEO makes the surface of the garnet electrolyte smoother and improves the contact between the separator and the positive electrode and the lithium metal negative electrode [98]; and (3) it provides necessary sites for the transfer of lithium ions between layers. LLISE surface is smoother than that of the layered framework as shown by SEM image in Fig. 7.40a. The thickness of the LLISE is about 20 μm (Fig. 7.40b) as revealed by the cross-sectional SEM image. Different thicknesses of LLISEs were prepared to study the effect of thickness on lithium-ion migration, and the thinnest LLISE can reach 12 μm.

Ionic conductivity is an important reference to measure the quality of electrolytes. A comparison of LN/PEO CSE (140 μm) and LLZO particles (200 μm) highlights

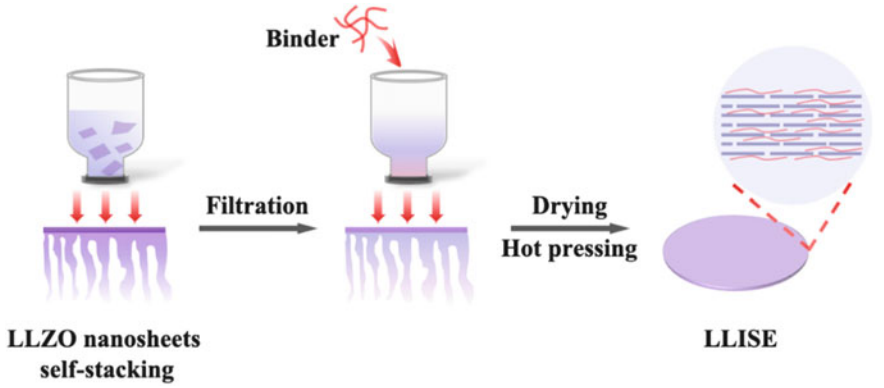

Fig. 7.39 Flowchart for the preparation of LLISE. Copyright (2022), Elsevier [31]

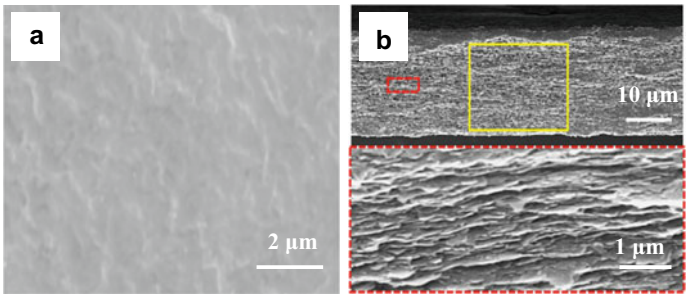

Fig. 7.40 **a** Surface SEM images of LLISE. **b** Cross-sectional SEM images of LLISE at different magnifications. Copyright (2022), Elsevier [31]

the strengths of LLISE as a framework material. The ionic conductivity of LN/PEO CSE at 25 °C is 1.61 × 10^{-5} S cm^{-1} while the ionic conductivity of LLZO pellet at 25 °C is 1.02 × 10^{-5} S cm^{-1}. By comparison, it can be seen that the ionic conductivity of LLISE-12 at 25 °C is 1.04 × 10^{-4} S cm^{-1}, which is 5.5 times and 9.2 times higher than that of LN/PEO CSE and LLZO pellet, respectively. The continuous transport path, low grain boundary resistance, and short diffusion distance of LLZO enable its Li-ion conductivity [45, 94, 99]. At the same time, in Fig. 7.41a, the Arrhenius ionic conductivity plots of as-prepared electrolytes are conducted. Comparing with LN/PEO CSE, LLISE-12 and LLZO pellet electrolytes show no significant change in transfer activation energy (E_a) below and above the melting temperature of PEO. The above phenomena suggest that the lithium-ion transfer in LLISE-12 and LLZO pellet is dominated by the LLZO phase, and a small amount of PEO in the LLISE interlayer does not significantly alter the performance of LLZO [18]. LLISE-12 possesses a low Li-ion transfer activation energy (0.36 eV), much lower than that of LN/PEO CSE (1.22 eV), due to the continuous LLZO transfer pathways. However, as for LLZO pellet, although the LLZO phase is continuous, its E_a (0.38 eV) is higher than that of LLISE-12. This should be attributed to the fact that LLZO pellet has large grain boundary resistance and thick film thickness. As shown in Fig. 7.41b, grain boundary resistance measurements of LLISE-12 and LLZO pellet were performed in the frequency range from 1 MHz to 0.1 Hz. The grain boundary resistance of LLZO particles is calculated to be 1847.5 Ω cm^2 by the equivalent circuit calculation, which is related to the semicircle and grain boundary resistance at high frequencies. In contrast, LLISE-12 has a weaker grain boundary capacitive reactance signal due to its low grain boundary resistance, so no obvious semicircle is observed [100]. LLISEs with different thicknesses were prepared, and the ionic conductivity of each thickness is measured to show the effect of thickness on Li-ion conductivity (Fig. 7.41c). The ionic conductivities of LLISEs with the thicknesses of 140, 60, and 20 μm at 25 °C are 2.53 × 10^{-5}, 5.71 × 10^{-5}, and 8.48 × 10^{-5} S cm^{-1}, respectively. When the thickness of LLISE changes from 12 μm to 140 μm, the ionic conductivity is dropped by 76%. The above data indicate that thin electrolyte has superior ionic conductivity [101, 102]. This is because the short diffusion distance of lithium ions and the reduction of grain boundary resistance can significantly improve the ionic conductivity.

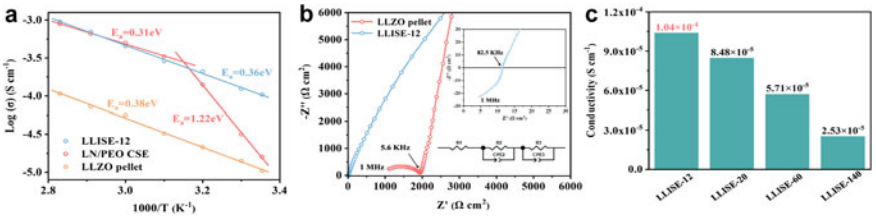

Fig. 7.41 **a** The ionic conductivities of LLZO pellet, LN/PEO CSE, and LLISE-12. **b** EIS of LLISE-12 and LLZO pellet with frequency ranging from 1 MHz to 0.1 Hz at 25 °C. **c** The ionic conductivities of LLISE-140, LLISE-60, LLISE-20, and LLISE-12. Copyright (2022), Elsevier [31]

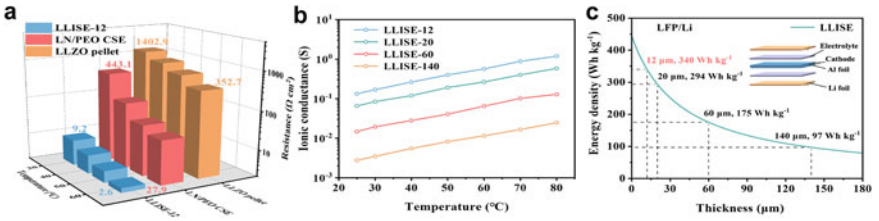

Fig. 7.42 **a** The temperature-dependent ASR of LLZO pellet, LN/PEO CSE, and LLISE-12. **b** The temperature-dependent ionic conductances of LLISE-140, LLISE-60, LLISE-20, and LLISE-12. **c** Gravimetric energy density as a function of thickness of LLISE employing LFP cathode (inset shows an idea pouch cell model). Copyright (2022), Elsevier [31]

Area-specific resistance (ASR) is an effective parameter to measure the internal resistance of the cell [103, 104]. The ASR value of LN/PEO CSE is 443.1 Ω cm^2 at 30 °C, while it of LLZO particles is 1402.9 Ω cm^2 at 30 °C (Fig. 7.42a). At 30 °C, the LLISE-12 achieves an ultra-low ASR (9.2 Ω cm^2), which is more than 150 times lower than that of LLZO pellet, mainly due to its thin thickness and high ionic conductivity. Due to the different thickness of each electrolyte, the ionic conductance becomes a more direct measure of the energy density of ASSLBs [101, 103]. The corresponding ionic conductances of LLISE at different thicknesses are shown in Fig. 7.42b. Among them, the highest ionic conductance of LLISE-12 at 30 °C is 0.17 S, which is twice that of LLISE-20, 9 times of that of LLISE-60, and 48 times of that of LLISE-140. Shorter lithium-ion diffusion distance and reduced grain boundary resistance help the realization of such high ionic conductance. Figure 7.42c shows the idea of pouch cell model calculation of LLISE gravimetric energy density, which provides guidance for the design of ASSLBs. The gravimetric energy density of LLISE-12 can reach 340 Wh kg^{-1} when the electrolyte thickness is 12 μm. It is worth noting that when compared with other types of electrolytes, the combined performance of LLISE is better in both ionic conductance and energy density.

In order to evaluate the stability of the as-prepared SSE in lithium stripping and electroplating reactions, lithium symmetric batteries were assembled. The cycling test was performed at 0.2 mA cm^{-2} at 60 °C. The choice of LLISE-20 to assemble the battery is because of its better overall performance. The LN/PEO CSE is shorted after 184 h as shown in Fig. 7.43a. By comparison, it can be seen that LLISE-20 has better cycling stability, the cycling time is as long as 1500 h, and the overpotential is as low as about 28 mV. The long-term cycling stability of LLISE-20 is due to its good mechanical strength and high electrical conductivity, which enables uniform deposition of Li ions at the interface [45]. According to the SEM image, it can be seen that a large number of irregular lithium dendrites appear on the surface of the lithium electrode cycled in the LN/PEO CSE. Conversely, as shown in Fig. 7.43b, c, the Li sheet surface of the Li/LLISE-20/Li symmetric cell is smooth and defect-free. The above experimental results indicate a high ionic conductivity of LLISE-20 due to its short diffusion distance, continuous transport path, and low grain boundary

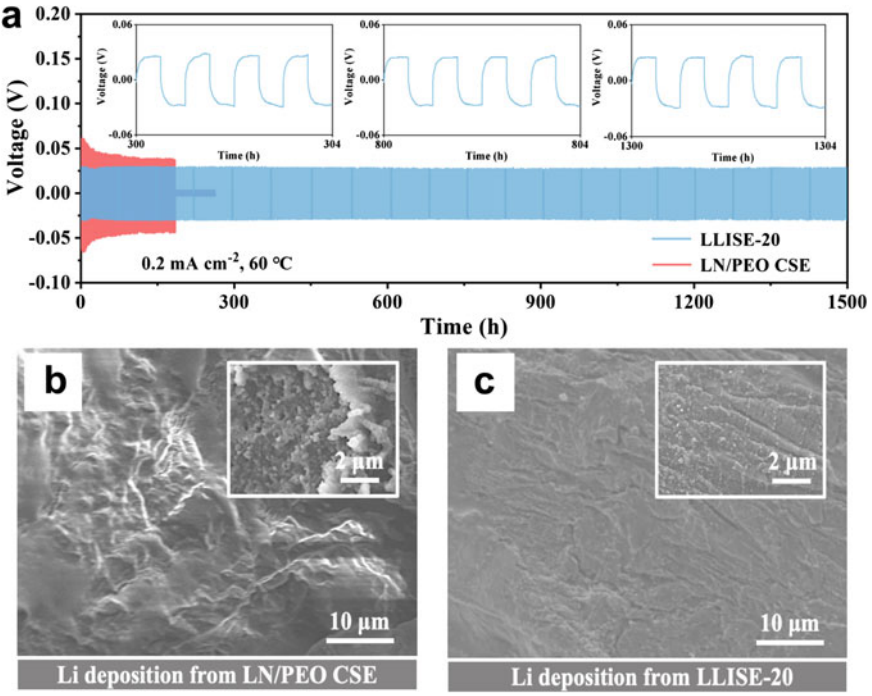

Fig. 7.43 **a** Long-term cycling of Li/LN/PEO CSE/Li and Li/LLISE-20/Li cells at 60 °C (inset shows voltage profiles of Li/LLISE-20/Li at 300, 800, and 1300 h, respectively). **b** and **c** Surface SEM images of Li cathode after lithium plating/stripping in Li/LN/PEO CSE/Li and Li/LLISE-20/Li cells (inset reveals zoomed-in SEM images). Copyright (2022), Elsevier [31]

resistance of LLZO, thus enabling uniform deposition of Li ions at the interface. Finally, this affords high Li-ion migration number (0.91) to LLISE-20 [105].

In order to test the mechanical strength of LN/PEO CSE, PEO/LiTFSI, and LLISE electrolytes and verify the ability of SSEs in inhibiting the growth of lithium dendrites, nanoindentation technology was selected to simulate the growth of lithium dendrites [15]. The compressive strength of LLISE-20 is 3.2 GPa, which is about 10 times higher than that of LN/PEO CSE, as shown in Fig. 7.44a, b. It is worth noting that PEO is easily penetrated by the indenter because the maximum loading force applied in the nanoindentation test is only 3 mN. Therefore, the layered framework formed by LLZO nanosheets enhances the compressive strength of LLISE-20.

Long-cycling and rate performance tests were performed by assembling the LFP/SSE/Li cells. As shown in Fig. 7.45a, they are the cycling performances of the battery at 0.5C at 60 °C. Among them, the battery assembled with LLISE-20 has better cycling performance, while the LFP/LN/PEO CSE/Li battery-assembled battery has a sharp capacity decline after 92 cycles. The battery assembled with LLISE-20 remains stable after 200 cycles, and the capacity decay per cycle is not higher than 0.05%. Its initial discharge capacity is 164.2 mAh g^{-1}, and its Coulombic

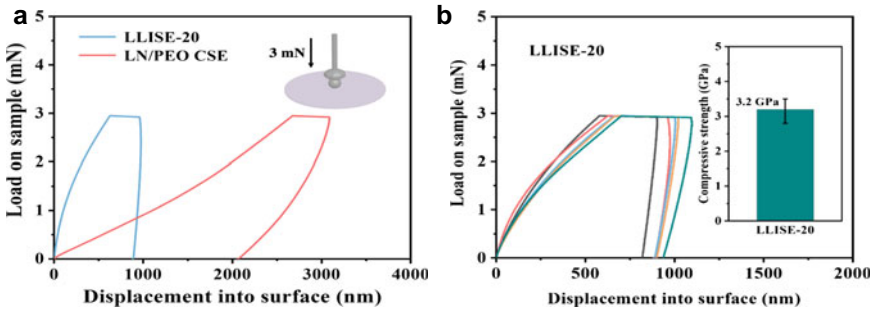

Fig. 7.44 **a** Load–displacement curves of LN/PEO CSE and LLISE-20 under nanoindentation test. **b** Load–displacement curves of LLISE-20 under nanoindentation test (inset displays the error bar of compressive strength). Copyright (2022), Elsevier [31]

efficiency is close to 100% after long-term cycling charge–discharge. By comparing the cycling performance of LFP/LLISE-20/Li battery and LN/PEO CSE battery at 60 °C at 0.5C, it can be seen that the electrochemical performance of LLISE-20 is relatively stable, as shown in Fig. 7.45b. From the above results, the excellent long-cycle performance of the LFP/LLISE-20/Li full cell should be attributed to the short and continuous transport path of LLZO, which results in its high ionic conductivity and good physicochemical stability. In addition, after 150 cycles, the LFP/LLISE-20/Li battery exhibits a Coulombic efficiency of 95.2% and a discharge capacity of 142.2 mAh g^{-1}. The above cycling data is measured at a lower operating temperature of 45 °C, and a plateau of low polarization voltage can be observed as shown in Fig. 7.45c, d. The excellent cycle performance of LFP/LLISE-20/Li cell can be further confirmed by the above data.

The rate performance of the cell is shown in Fig. 7.46a. The LFP/LLISE-20/Li cell provides high discharge capacity of 164.2, 161.4, 158.7, 148.2, and 123.5 mAh g^{-1} when cycling at 0.1, 0.2, 0.4, 0.6, and 1.0C, respectively. However, the discharge capacity of the LN/PEO CSE battery decreases significantly from 0.6C to 1.0C. LFP/LLISE-20/Li cell displays an excellent cycling performance with a discharge capacity of 162.8 mAh g^{-1}, and 99.1% of initial capacity was maintained when the rate returns to 0.1C. The voltage curves at different rates show that LFP/LLISE-20/Li obtains a plateau with low polarization voltage as shown in Fig. 7.46b. The above experimental data show that LLISE-20 has good contact with the electrode interface, high ionic conductivity, and stable physical and chemical properties, which lead to the superior rate performance for LFP/LLISE-20/Li battery. The above experimental phenomena also indicate that the layered ISE in ASSLB has great potential for practical application.

In conclusion, LLZO nanosheets with a thickness of about 4.5 nm and lateral dimensions of 3–5 μm were successfully fabricated, and on this basis, thin (12 μm) and defect-free LLISEs were fabricated. The high ionic conductivity of LLISE is due to the low grain boundary resistance, short diffusion distance, and continuous transport path of LLZO. The ionic conductivity of LLISE at 30 °C is 1.30×10^{-4} S

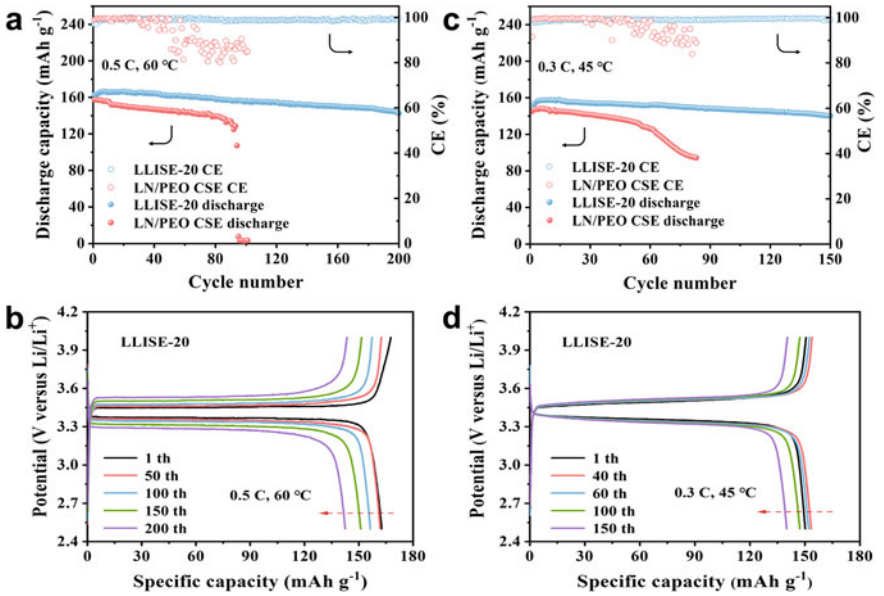

Fig. 7.45 All-solid-state LFP/Li battery performances. **a** Cycling performances of the cells assembled with different electrolytes at 60 °C under 0.5C. **b** Charge–discharge profiles of LFP/LLISE-20/Li cell at 60 °C under 0.5C. **c** Cycling performances of the cells assembled with different electrolytes at 45 °C under 0.3C. **d** Charge–discharge profiles of LFP/LLISE-20/Li cell at 45 °C under 0.3C. Copyright (2022), Elsevier [31]

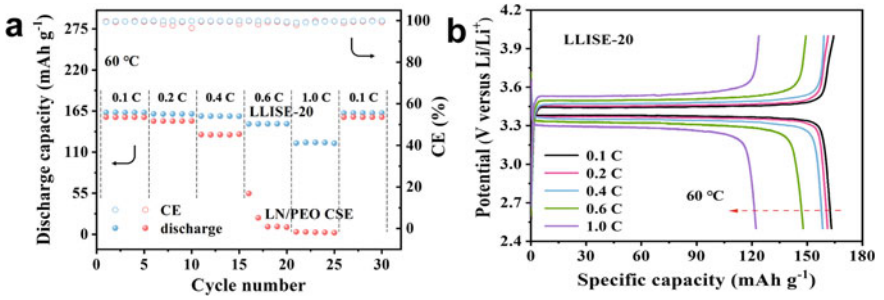

Fig. 7.46 All-solid-state LFP/Li cell performances. **a** Rate performances of the cells assembled with different electrolytes at 60 °C under different rates. **b** Charge–discharge profiles of LFP/LLISE-20/Li cell at 60 °C under different rates. Copyright (2022), Elsevier [31]

cm^{-1}, which is an order of magnitude higher than that of LLZO pellets (>200 μm) prepared by cold pressing. Notably, compared to most reported SSEs, LLISE has high ionic conductivity (0.17 S) and high-energy density of 340 Wh kg^{-1} at 30 °C due to its thin thickness. At the same time, the compressive strength of LLISE is as high as 3.2 GPa when its thickness is 20 μm. The assembled Li/LLISE/Li cell

can cycle stably over 1500 h with a low polarization under 0.2 mA cm^{-2} and 60 °C. Furthermore, the LFP/LLISE/Li cell displays an excellent cycling performance with a discharge capacity of 143 mAh g^{-1} after 200 cycles with low capacity decay of 0.05% per cycle at 0.5C and 60 °C. High-performance SSEs can be fabricated through the self-stacking of ISE nanosheets, which hold promise for the development of advanced solid-state electrolytes.

7.7 Laminar LLTO/Vr Composite Electrolyte

Vermiculite (Vr) nanosheets were prepared using two-step ion exchange method [106]. Laminar LLTO/Vr composite electrolytes (Vr-LLTO LISE) were fabricated by a method that consists of swelling filtration and sintering, as shown in Fig. 7.47. Firstly, Vr laminar framework was obtained by filtrating the Vr nanosheets. Subsequently, the Vr laminar framework was swelled in ethanol to get a larger interlayer spacing. Then, precursor solution was prepared by solving the inorganic salt ($(NO_3)_3 \cdot 6H_2O$, $Ti(OC_4H_9)_4$, and $LiNO_3$) with certain concentration in the mixture solution of anhydrous ethanol and acetic acid (volume ratio of 8:2), which was filtrated into Vr laminar framework. Afterward, Vr-LLTO LISE was obtained for drying at 60 °C for 3 h, sintering for 2 h at 1000 °C, and then annealing. LLTO nanoparticles were obtained by the sol–gel method [30]. For the preparation of LLTO pellet, the LLTO nanoparticles were hot-pressed in a graphite die at 1000 °C with a pressure of 40 MPa for 2 h in argon atmosphere. To enhance the interface contact between electrolyte and electrodes, a thin layer of PEO-LiTFSI (EO: $Li^+ = 16$: 1) was coated on the electrolyte surface and then dried at 50 °C. Next, a slight pressure was employed to promote the interface contact at 80 °C [99].

Vr laminar framework was obtained by filtrating Vr nanosheets. Constant-rate and low-pressure filtration manner were employed to help rigid Vr nanosheets building ordered laminar framework. Subsequently, hydrophilic Vr laminar framework was swollen in low-concentration precursors, and the vacuum filtration process is to let

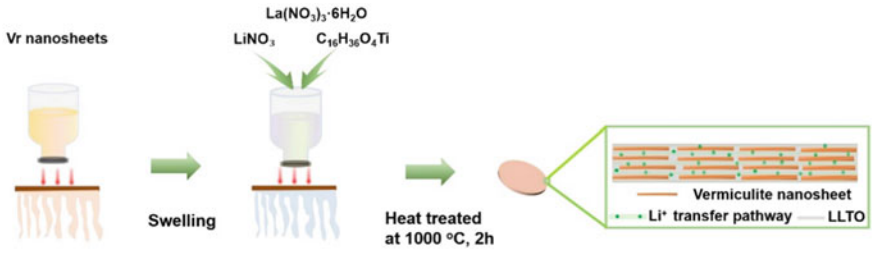

Fig. 7.47 Synthetic diagram of Vr-LLTO LISE preparation. Copyright (2021), John Wiley and Sons [32]

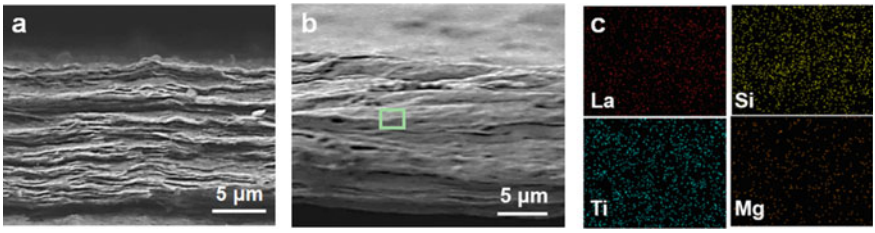

Fig. 7.48 Cross-sectional SEM image of **a** Vr laminar framework and **b** Vr-LLTO LISE. **c** Cross-sectional SEM image of Vr-LLTO LISE corresponding EDS mappings of La, Si, Ti, and Mg elements. Copyright (2021), John Wiley and Sons [32]

precursors continuously and uniformly distribute in interlayer channels. Finally, Vr-LLTO LISE was obtained by annealing and traditional sintering process. As shown in Fig. 7.48a, b, the thickness of Vr-LLTO LISE increases from 13 to 15 μm, due to the growth of LLTO crystals in interlayer channels. La, Si, Ti, and Mg elements are uniformly dispersed throughout the Vr-LLTO LISE, which indicates that the LLTO crystals are uniformly distributed in the interlayer channels (Fig. 7.48c).

Then, the arrangement and morphology of LLTO crystals in Vr-LLTO LISE are explored. TEM images display that the Vr-LLTO LISE has an ordered 2D laminar structure, where the bright and dark areas correspond to the LLTO crystal and Vr nanosheet, respectively (Fig. 7.49a). Importantly, under high-resolution TEM images, the LLTO crystals have no detectable void and structural defect, implying that the LLTO crystals are continuously arranged in the interlayer channels. Besides, the distance is 0.274 nm between adjacent fringes (Fig. 7.49b). This corresponds to LLTO crystal (110) plane, which means that LLTO crystal preferentially grows along the [001] direction (i.e., *c*-axis) in interlayer channels. Moreover, in LLTO crystal, the fastest direction for Li^+ transfer is the *c*-axis due to the large number of vacancies in La-poor layer [107, 108]. In contrast, LLTO crystal grown in open spacing shows obvious defects due to the infinite growth in different directions. However, as shown in Fig. 7.49c, there are various crystal planes [e.g., (101), (110), and (001)] in LLTO nanoparticles. In general, these findings indicate that the 2D channel confinement effect promotes the ordered arrangement and growth of LLTO crystals, thereby reducing structural defects.

In confined 2D channels, the exploration of LLTO crystal growth mechanism is also important. To this end, another two laminar frameworks composed of rigid, hydrophobic g-C_3N_4 and flexible, hydrophilic GO, were also manufactured for crystal growth. In Fig. 7.50a, XRD results show that the (001)/(110) peak intensity ratio of LLTO crystal is 13.7% when growing in open spacing. In contrast, the proportions of LLTO crystals grown in the Vr, GO, and g-C_3N_4 laminar frameworks are 9.8%, 12.9%, and 13.4%, respectively. It can be seen that the peak intensity ratio decreases, which means that when growing in confined spacing, LLTO crystals preferentially grow along the *c*-axis, and the proportion of (001) crystal plane perpendicular to *c*-axis is decreased [109, 110]. LLTO crystals grown in laminar frameworks

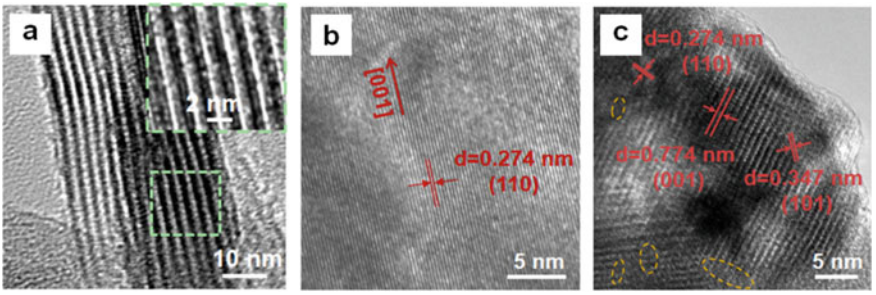

Fig. 7.49 **a** High-magnification TEM images of Vr-LLTO LISE cross-sectional. **b** High-resolution TEM images of surface slice of Vr-LLTO LISE. **c** High-resolution TEM images of LLTO nanoparticle (yellow circles areas are structural defects). Copyright (2021), John Wiley and Sons [32]

composed of rigid and hydrophilic Vr nanosheets have the lowest (001)/(110) peak intensity ratio, which means that hydrophilicity and rigidity are important for uniform and prior growth of LLTO crystals in 2D channels. The Raman peaks in Fig. 7.50c show that the peak of LLTO pellet at 146.8 cm^{-1} corresponds to vibration of Ti–O bond in the *a*-*b* plane, and the peak at 553.4 cm^{-1} corresponds to the vibration of Ti–O bond on the *c*-axis of Ti-O_6 [111]. In the spectrum of Vr-LLTO LISE, the corresponding peaks red-shift to 140.9 cm^{-1} and blue-shift to 572.4 cm^{-1}, respectively. In confined interlayer channel, the growth of LLTO crystals along *a*-axis and *b*-axis is limited, while the growth of LLTO crystals along *c*-axis is almost unaffected. As shown in Fig. 7.50b, 2D wide-angle XRD results provide further evidence. Compared to LLTO pellet, the (101) crystal plane of Vr-LLTO LISE displays a brighter ring, which means that more (101) crystal planes are formed along the *c*-axis.

As depicted In Fig. 7.51c, the ionic conductivity of LLTO pellet is close to the data in the literature, which is 1.77×10^{-5} S cm^{-1} at 30 °C [112]. In contrast, the ionic conductivity of Vr-LLTO LISE reaches 8.22×10^{-5} S cm^{-1} at 30 °C, which is 364% higher than that of LLTO pellet. The increase in ionic conductivity is

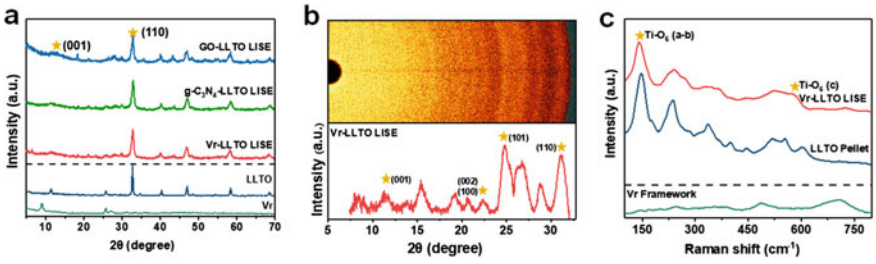

Fig. 7.50 **a** XRD patterns of GO-LLTO LISE, g-C_3N_4-LLTO LISE, Vr-LLTO LISE, LLTO, and Vr laminar framework. **b** 2D wide-angle X-ray diffraction patterns of Vr-LLTO LISE. **c** Raman spectra of Vr laminar framework, LLTO pellet, and Vr-LLTO LISE. Copyright (2021), John Wiley and Sons [32]

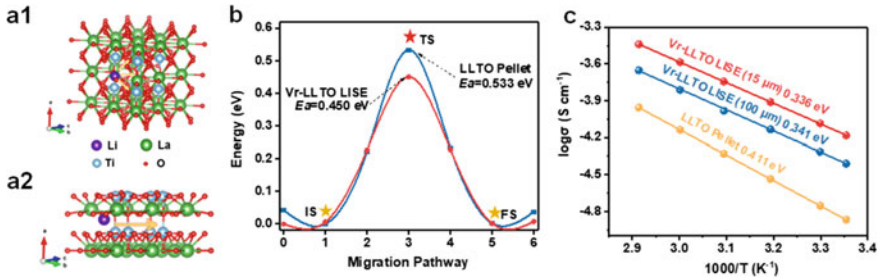

Fig. 7.51 **a1** Li^+ transport diagram in 3D LLTO crystal. **a2** Li^+ transport diagram in 2D LLTO crystal. **b** Energy profiles of the Li^+ transport pathways in LLTO pellet and Vr-LLTO LISE. **c** Conductivity of LLTO pellet and Vr-LLTO LISE with thicknesses of 15 and 100 μm, respectively. Copyright (2021), John Wiley and Sons [32]

owing to the ordered arrangement of LLTO crystals, which reduce inherent structural defects and lower grain boundary resistance. The activation energies of LLTO pellet (0.411 eV) and Vr-LLTO LISE (0.336 eV) provides direct evidence, which is close to grain boundary and bulk activation energies, respectively [16]. This indicates that the main transport mechanism in Vr-LLTO LISE is similar to the bulk Li^+ transfer of LLTO, which highlights the advantages of LLTO crystal grown in confined spacing. LLTO pellet and Vr-LLTO LISE with the same thickness (100 μm) were prepared for comparison. As LLTO crystals are orderly arranged in the electrolyte, the thicker Vr-LLTO LISE gains a low activation energy value (0.341 eV).

Further, Li^+ transport mechanism was investigated in Vr-LLTO LISE using density functional theory (DFT) simulations. Li^+ transport energy barrier was calculated. Fig. 7.51a1 is a geometric model of 3D LLTO crystals grown in open space, and 2D LLTO crystals grown in confined spacing are shown in Fig. 7.51a2. In LLTO crystals, the La-poor layer and La-rich layer are alternately stacked. For 2D LLTO crystals grown in confined spacing, the ordered and large-size crystals along the *c*-axis act as the fast transport channel of Li^+. However, due to the existence of different crystal planes, the transport direction of Li^+ in 3D LLTO crystals is random. As shown in Fig. 7.51b, the transport energy distributions in the 2D and 3D LLTO crystals prove this statement. The energy barriers of 2D and 3D LLTO crystal are 0.450 eV and 0.553 eV, respectively. This proved that the energy barrier of Li^+ passing through the *c*-axis is lower than that passing through the *a*-axis and *b*-axis, and the transport of Li^+ is mainly along *c*-axis in the 2D LLTO crystal.

Vr-LLTO LISE displays excellent mechanical stability. As shown in Fig. 7.52a, the lithium dendrite growth process was simulated by nanoindentation test to evaluate the Vr-LLTO LISE mechanical stability. A good compressive modulus of 1.24 GPa is obtained for Vr-LLTO LISE with the thickness of only 15 μm. Furthermore, the final depth and maximal displacement after unloading of the Vr-LLTO LISE reach 748 and 1120 nm, respectively, higher than those of LLTO pellet (582 and 664 nm). This demonstrates that Vr-LLTO LISE has good flexibility. In Fig. 7.52b, the interlayer force was directly quantified using nanoscratch. The critical loading of Vr-LLTO

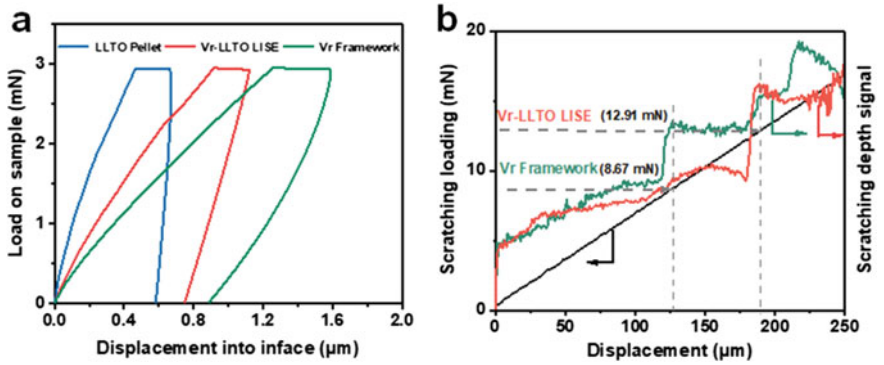

Fig. 7.52 **a** Under nanoindentation test, load–displacement curves of LLTO pellet, Vr-LLTO LISE, Vr laminar framework. **b** Nano crack results of Vr-LLTO LISE and Vr laminar framework. Copyright (2021), John Wiley and Sons [32]

LISE is 49% higher than that of Vr laminar framework (8.67 mN), indicating that the interlayer force is stronger.

As shown in Fig. 7.53, voltage profiles of the lithium stripping/plating behaviors at 60 °C in lithium symmetrical batteries were tested. It can be seen that at a current density of 0.2 mA cm^{-2}, the lithium symmetrical battery with LLTO pellet has a high overpotential of about 68 mV, coupled with a short circuit at 252 h. In contrast, the lithium symmetric battery with Vr-LLTO LISE can be stably cycled for over 1200 h with a low overpotential of about 50 mV. Then, in order to calculate the critical current densities, the symmetric batteries of LLTO pellet and Vr-LLTO LISE were measured.

LFP/Li batteries with LLTO pellet, Vr-LLTO LISE (15 μm), and Vr-LLTO LISE (100 μm) electrolytes were assembled and tested at 60 °C to evaluate the rate and cycling performances. LLTO pellet-assembled battery appears short circuit after 47

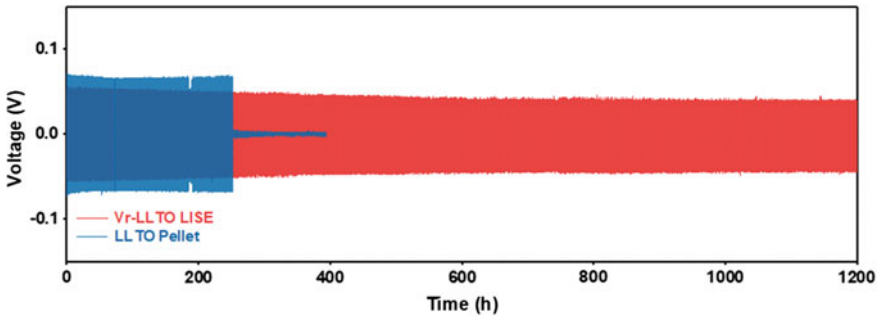

Fig. 7.53 LLTO pellet and Vr-LLTO LISE-assembled Li symmetric batteries cycling performance under 0.2 mA cm^{-2} at 60 °C. Copyright (2021), John Wiley and Sons [32]

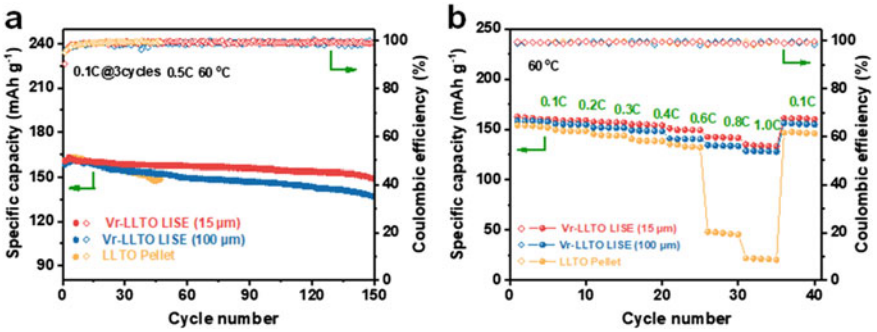

Fig. 7.54 **a** Cycling performances (0.1C in the first three cycles and 0.5C in the latter cycles) and **b** rate performances of different batteries assembled with LLTO pellet and 15 μm- and 100 μm-thick Vr-LLTO LISE at 60 °C. Copyright (2021), John Wiley and Sons [32]

cycles due to serious structural defects (Fig. 7.54a). In contrast, the discharge capacities of 15 μm- and 100 μm-thick Vr-LLTO LISEs reach 148.9 and 137 mAh g^{-1} after 150 cycles, respectively. The battery assembled with Vr-LLTO LISE with 15 μm thickness shows only 0.057% capacity reduction per cycle, proving its excellent cycling performance. The LFP/Vr-LLTO LISE (15 μm)/Li batteries operated at 60 °C exhibit discharge capacities of 162.3, 158.7, 156.8, 153.9, 149.7, 140.3, and 131.5 mAh g^{-1} at 0.1, 0.2, 0.3, 0.4, 0.6, 0.8, and 1.0C, respectively (Fig. 7.54b). And a capacity of 159.8 mAh g^{-1} could be recovered when the rate resets to 0.1C, showing good cycling stability and reversibility. Overall, the excellent rate and cycling performances demonstrate Vr-LLTO LISE has great application in ASSLBs.

In conclusion, we report the preparation of defect-free, oriented, and large-size 2D LLTO crystal, through controlling the arrangement and growth of crystal in confined spacing. Due to the ordered arrangement of LLTO crystals, the structural defects are efficiently eliminated, endowing Vr-LLTO LISE with ultrafast Li^+ transport. At 30 °C, the synthesized Vr-LLTO LISE with a thickness of 15 μm exhibits a high ionic conductance of 87.2 mS and high ionic conductivity of 8.22×10^{-5} S cm^{-1}, outperforming most reported LLTO-based electrolytes. Furthermore, the Vr laminar framework with linking by covalent bonds exhibits good toughness, which provides excellent mechanical properties for Vr-LLTO LISE. Under 0.5C at 60 °C, the assembled LFP/Li battery can still achieve a high capacity of 148.9 mAh g^{-1} after 150 cycles and the capacity decay of each cycle is only 0.057%, showing excellent cycling stability. Theoretical calculation and experimental results show that the transfer and growth mechanisms of LLTO crystals in confined spacing are established. The 2D confinement effect of hydrophilic and rigid channel enables the long-range, ordered arrangement of LLTO crystals along *c*-axis, which then eliminate structural defects, construct a fast Li^+ transfer path, and promote Li^+ conduction. The 2D LLTO crystal with controlled arrangement and growth of LLTO crystals in confined spacing provides a promising method for design of ultrafast Li^+ transfer devices.

References

1. D. Lin, Y. Liu, Y. Cui, Reviving the lithium metal anode for high-energy batteries. Nat. Nanotechnol. **12**, 194–206 (2017)
2. A. Manthiram, X. Yu, S. Wang, Lithium battery chemistries enabled by solid-state electrolytes. Nat. Rev. Mater. **2**, 16103 (2017)
3. S. Xia, X. Wu, Z. Zhang, Y. Cui, W. Liu, Practical challenges and future perspectives of all-solid-state lithium-metal batteries. Chemistry **5**, 753–785 (2019)
4. D. Zhou, D. Shanmukaraj, A. Tkacheva, M. Armand, G. Wang, Polymer electrolytes for lithium-based batteries: advances and prospects. Chemistry **5**, 2326–2352 (2019)
5. L. Xu, J. Li, W. Deng, H. Shuai, S. Li, Z. Xu, J. Li, H. Hou, H. Peng, G. Zou, X. Ji, Garnet solid electrolyte for advanced all-solid-state Li batteries. Adv. Energy Mater. **11**, 2000648 (2020)
6. J.W. Fergus, Ceramic and polymeric solid electrolytes for lithium-ion batteries. J. Power Sour. **195**, 4554–4569 (2010)
7. F. Lv, Z. Wang, L. Shi, J. Zhu, K. Edström, J. Mindemark, S. Yuan, Challenges and development of composite solid-state electrolytes for high-performance lithium ion batteries. J. Power Sour. **441**, 227175 (2019)
8. E. Bakangura, L. Wu, L. Ge, Z. Yang, T. Xu, Progress in polymer science mixed matrix proton exchange membranes for fuel cells: state of the art and perspectives. Prog. Polym. Sci. **57**, 103–152 (2016)
9. Y. Li, G. He, S. Wang, S. Yu, F. Pan, H. Wu, Z. Jiang, Recent advances in the fabrication of advanced composite membranes. J. Mater. Chem. A **35**, 10058–10077 (2013)
10. L. Chen, W. Li, L.Z. Fan, C.W. Nan, Q. Zhang, Intercalated electrolyte with high transference number for dendrite-free solid-state lithium batteries. Adv. Func. Mater. **29**, 1901047 (2019)
11. Z. Zhang, R.G. Antonio, K.L. Choy, Boron nitride enhanced polymer/salt hybrid electrolytes for all-solid-state lithium ion batteries. J. Power Sour. **435**, 226736 (2019)
12. Y.S. Ye, H. Wang, S.G. Bi, Y. Xue, Z.G. Xue, X.P. Zhou, X.L. Xie, Y.W. Mai, High performance composite polymer electrolytes using polymeric ionic liquid-functionalized graphene molecular brushes. J. Mater. Chem. A **3**, 18064–18073 (2015)
13. Q. Pan, Y. Zheng, S. Kota, W. Huang, S. Wang, H. Qi, S. Kim, Y. Tu, M.W. Barsoum, C.Y. Li, 2D MXene-containing polymer electrolytes for all-solid-state lithium metal batteries. Nanoscale Adv. **1**, 395–402 (2019)
14. W. Liu, S.W. Lee, D. Lin, F. Shi, S. Wang, A.D. Sendek, Y. Cui, Enhancing ionic conductivity in composite polymer electrolytes with well-aligned ceramic nanowires. Nat. Energy **2**, 17035 (2017)
15. W. Tang, S. Tang, C. Zhang, Q. Ma, Q. Xiang, Y.W. Yang, J. Luo, Simultaneously enhancing the thermal stability, mechanical modulus, and electrochemical performance of solid polymer electrolytes by incorporating 2D sheets. Adv. Energy Mater. **8**, 1800866 (2018)
16. Z. Jiang, H. Xie, S. Wang, X. Song, X. Yao, H. Wang, Perovskite membranes with vertically aligned microchannels for all-solid-state lithium batteries. Adv. Energy Mater. **8**, 1801433 (2018)
17. K. Fu, Y. Gong, G.T. Hitz, D.W. McOwen, Y. Li, S. Xu, Y. Wen, L. Zhang, C. Wang, G. Pastel, J. Dai, B. Liu, H. Xie, Y. Yao, E.D. Wachsman, L. Hu, Three-dimensional bilayer garnet solid electrolyte based high energy density lithium metal-sulfur batteries. Energy Environ. Sci. **10**, 1568–1575 (2017)
18. A. Li, X. Liao, H. Zhang, L. Shi, P. Wang, Q. Cheng, J. Borovilas, Z. Li, W. Huang, Z. Fu, M. Dontigny, K. Zaghib, K. Myers, X. Chuan, X. Chen, Y. Yang, Nacre-inspired composite electrolytes for load-bearing solid-state lithium-metal batteries. Adv. Mater. **32**, 1905517 (2020)
19. M.J. Palmer, S. Kalnaus, M.B. Dixit, A.S. Westover, K.B. Hatzell, N.J. Dudney, X.C. Chen, A three-dimensional interconnected polymer/ceramic composite as a thin film solid electrolyte. Energy Storage Mater. **26**, 242–249 (2020)

20. J. Ding, R. Xu, C. Yan, Y. Xiao, Y. Liang, H. Yuan, J. Huang, Integrated lithium metal anode protected by composite solid electrolyte film enables stable quasi-solid-state lithium metal batteries. Chin. Chem. Lett. **31**, 2339–2342 (2020)
21. W. Liu, N. Liu, J. Sun, P.C. Hsu, Y. Li, H.W. Lee, Y. Cui, Ionic conductivity enhancement of polymer electrolytes with ceramic nanowire fillers. Nano Lett. **15**, 2740–2745 (2015)
22. C. Gerbaldi, J.R. Nair, M.A. Kulandainathan, R.S. Kumar, C. Ferrara, P. Mustarelli, A.M. Stephan, Innovative high performing metal organic framework (MOF)-laden nanocomposite polymer electrolytes for all-solid-state lithium batteries. J. Mater. Chem. A **2**, 9948–9954 (2014)
23. K. Jeong, S. Park, G.Y. Jung, S.H. Kim, Y.H. Lee, S.K. Kwak, S.Y. Lee, Solvent-free, single lithium-ion conducting covalent organic frameworks. J. Am. Chem. Soc. **141**, 5880–5885 (2019)
24. J. Bae, Y. Li, F. Zhao, X. Zhou, Y. Ding, G. Yu, Designing 3D nanostructured garnet frameworks for enhancing ionic conductivity and flexibility in composite polymer electrolytes for lithium batteries. Energy Storage Mater. **15**, 46–52 (2018)
25. Y. Gong, K. Fu, S. Xu, J. Dai, T.R. Hamann, L. Zhang, G.T. Hitz, Z. Fu, Z. Ma, D.W. McOwen, X. Han, L. Hu, E.D. Wachsman, Lithium-ion conductive ceramic textile: a new architecture for flexible solid-state lithium metal batteries. Mater. Today **21**, 594–601 (2018)
26. S. Zekoll, C. Marriner-Edwards, A.K.O. Hekselman, J. Kasemchainan, C. Kuss, D.E.J. Armstrong, D. Cai, R.J. Wallace, F.H. Richter, J.H.J. Thijssen, P.G. Bruce, Hybrid electrolytes with 3D bicontinuous ordered ceramic and polymer microchannels for all-solid-state batteries. Energy Environ. Sci. **11**, 185–201 (2018)
27. Z. Yang, Z. Sun, C. Liu, Y. Li, G. Zhou, S. Zuo, J. Wang, W. Wu, Lithiated nanosheets hybridized solid polymer electrolyte to construct Li^+ conduction highways for advanced all-solid-state lithium battery. J. Power Sour. **484**, 229287 (2021)
28. W. Kou, R. Lv, S. Zuo, Z. Yang, J. Huang, W. Wu, J. Wang, Hybridizing polymer electrolyte with poly(ethylene glycol) grafted polymer-like quantum dots for all-solid-state lithium batteries. J. Membr. Sci. **618**, 118702 (2021)
29. N. Peng, W. Kou, W. Wu, S. Guo, Y. Wang, J. Wang. Laminar composite solid electrolyte with poly(ethylene oxide)-threaded metal-organic framework nanosheets for high-performance all-solid-state lithium battery. Energy Environ. Mater. **0**, 1–10 (2021)
30. C. Liu, J. Wang, W. Kou, Z. Yang, P. Zhai, Y. Liu, W. Wu, J. Wang, A flexible, ion-conducting solid electrolyte with vertically bicontinuous transfer channels toward high performance all-solid-state lithium batteries. Chem. Eng. J. **404**, 126517 (2021)
31. S. Guo, W. Kou, W. Wu, R. Lv, Z. Yang, J. Wang, Thin laminar inorganic solid electrolyte with high ionic conductance towards high-performance all-solid-state lithium battery. Chem. Eng. J. **427**, 131948 (2022)
32. R. Lv, W. Kou, S. Guo, W. Wu, Y. Zhang, Y. Wang. J. Wang. Preparing two-dimensional ordered $Li_{0.33}La_{0.557}TiO_3$ crystal in interlayer channel of thin laminar inorganic solid-state electrolyte towards ultrafast Li^+ transfer. Angewandte Chemie International Edition, **61**, e202114220 (2022)
33. D.C. Marcano, D.V. Kosynkin, J.M. Berlin, A. Sinitskii, Z. Sun, A. Slesarev, L.B. Alemany, W. Lu, J.M. Tour, Improved synthesis of graphene oxide. ACS Nano **4**, 4806–4814 (2010)
34. Y. He, J. Wang, H. Zhang, T. Zhang, B. Zhang, S. Cao, J. Liu, Polydopamine-modified graphene oxide nanocomposite membrane for proton exchange membrane fuel cell under anhydrous conditions. J. Mater. Chem. A **2**, 9548–9558 (2014)
35. Y. Liu, K. Ai, L. Lu, Polydopamine and its derivative materials: synthesis and promising applications in energy, environmental, and biomedical fields. Chem. Rev. **114**, 5057–5115 (2014)
36. J.H. Ryu, P.B. Messersmith, H. Lee, Polydopamine surface chemistry: a decade of discovery. ACS Appl. Mater. Interfaces **10**, 7523–7540 (2018)
37. S.M. Kang, S. Park, D. Kim, S.Y. Park, R.S. Ruoff, H. Lee, Simultaneous reduction and surface functionalization of graphene oxide by mussel-inspired chemistry. Adv. Func. Mater. **21**, 108–112 (2011)

38. Y.T. Weng, H.W. Liu, A. Pei, F.F. Shi, H. Wang, C.Y. Lin, S.S. Huang, L.Y. Su, J.P. Hsu, C.C. Fang, Y. Cui, N.L. Wu, An ultrathin ionomer interphase for high efficiency lithium anode in carbonate based electrolyte. Nat. Commun. **10**, 5824 (2019)
39. J. Shim, H.J. Kim, B.G. Kim, Y.S. Kim, D.G. Kim, J.C. Lee, 2D boron nitride nanoflakes as a multifunctional additive in gel polymer electrolytes for safe, long cycle life and high rate lithium metal batteries. Energy Environ. Sci. **10**, 1911–1916 (2017)
40. J. Wan, J. Xie, D.G. Mackanic, W. Burke, Z. Bao, Y. Cui, Status, promises, and challenges of nanocomposite solid-state electrolytes for safe and high performance lithium batteries. Mater. Today Nano **4**, 1–16 (2018)
41. B. Chen, Z. Huang, X. Chen, Y. Zhao, Q. Xu, P. Long, S. Chen, X. Xu, A new composite solid electrolyte PEO/$Li_{10}GeP_2S_{12}$/SN for all-solid-state lithium battery. Electrochim. Acta **210**, 905–914 (2016)
42. H. Chen, D. Adekoya, L. Hencz, J. Ma, S. Chen, C. Yan, H. Zhao, G. Cui, S. Zhang, Stable seamless interfaces and rapid ionic conductivity of Ca-CeO_2/LiTFSI/PEO composite electrolyte for high-rate and high-voltage all-solid-state battery. Adv. Energy Mater. **10**, 2000049 (2020)
43. X. Wang, Y. Zhang, X. Zhang, T. Liu, Y.H. Lin, L. Li, Y. Shen, C.W. Nan, Lithium-salt-rich PEO/$Li_{0.3}La_{0.557}TiO_3$ interpenetrating composite electrolyte with three-dimensional ceramic nano-backbone for all-solid-state lithium-ion batteries. ACS Appl. Mater. Interfaces **10**, 24791–24798 (2018)
44. Y. Lin, X. Wang, J. Liu, J.D. Miller, Natural halloysite nano-clay electrolyte for advanced all-solid-state lithium-sulfur batteries. Nano Energy **31**, 478–485 (2017)
45. J. Wu, Z. Rao, Z. Cheng, L. Yuan, Z. Li, Y. Huang, Ultrathin, flexible polymer electrolyte for cost-effective fabrication of all-solid-state lithium metal batteries. Adv. Energy Mater. **9**, 1902767 (2019)
46. D. Lin, P.Y. Yuen, Y. Liu, W. Liu, N. Liu, R.H. Dauskardt, Y. Cui, A silica-aerogel-reinforced composite polymer electrolyte with high ionic conductivity and high modulus. Adv. Mater. **30**, 1802661 (2018)
47. L. Edman, Ion association and ion solvation effects at the crystalline-amorphous phase transition in PEO-LiTFSI. J. Phys. Chem. B **104**, 7254–7258 (2000)
48. I. Rey, P. Johansson, J. Lindgren, J.C. Lassègues, J. Grondin, L. Servant, Spectroscopic and theoretical study of $(CF_3SO_2)_2N^-$ ($TFSI^-$) and $(CF_3SO_2)_2NH$ (HTFSI). J. Phys. Chem. A **102**, 3249–3258 (1998)
49. C. Ma, K. Dai, H. Hou, X. Ji, L. Chen, D.G. Ivey, W. Wei, High ion-conducting solid-state composite electrolytes with carbon quantum dot nanofillers. Adv. Sci. **5**, 1700996 (2018)
50. J. Ma, B. Chen, L. Wang, G. Cui, Progress and prospect on failure mechanisms of solid-state lithium batteries. J. Power Sour. **392**, 94–115 (2018)
51. B.J. Xiao, How lithium dendrites form in liquid batteries. Sci. **366**, 426–428 (2019)
52. Q. Zhang, K. Liu, F. Ding, X. Liu, Recent advances in solid polymer electrolytes for lithium batteries. Nano Res. **10**, 4139–4174 (2017)
53. W. Wu, Y. Li, J. Liu, J. Wang, Y. He, K. Davey, S.Z. Qiao, Molecular-level hybridization of Nafion with quantum dots for highly enhanced proton conduction. Adv. Mater. **30**, 1707516 (2018)
54. Q. Lu, Y.B. He, Q. Yu, B. Li, Y.V. Kaneti, Y. Yao, F. Kang, Q.H. Yang, Dendrite-free, high-rate, long-life lithium metal batteries with a 3D cross-linked network polymer electrolyte. Adv. Mater. **29**, 1604460 (2017)
55. Y. Zhu, J. Cao, H. Chen, Q. Yu, B. Li, High electrochemical stability of a 3D cross-linked network PEO@nano-SiO_2 composite polymer electrolyte for lithium metal batteries. J. Mater. Chem. A **7**, 6832–6839 (2019)
56. Z. Xiao, B. Zhou, J. Wang, C. Zuo, D. He, X. Xie, Z. Xue, PEO-based electrolytes blended with star polymers with precisely imprinted polymeric pseudo-crown ether cavities for alkali metal ion batteries. J. Membr. Sci. **576**, 182–189 (2019)
57. J. Hu, W. Wang, B. Zhou, Y. Feng, X. Xie, Z. Xue, Poly (ethylene oxide)-based composite polymer electrolytes embedding with ionic bond modified nanoparticles for all-solid-state lithium-ion battery. J. Membr. Sci. **575**, 200–208 (2019)

58. X. Zhou, H. Jiang, H. Zheng, Y. Sun, X. Liang, H. Xiang, Nonflammable hybrid solid electrolyte membrane for a solid-state lithium battery compatible with conventional porous electrodes. J. Membr. Sci. **603**, 117820 (2020)
59. L. Liu, J. Lyu, J. Mo, H. Yan, L. Xu, P. Peng, J. Li, B. Jiang, L. Chu, M. Li, Comprehensively-upgraded polymer electrolytes by multifunctional aramid nanofibers for stable all-solid-state Li-ion batteries. Nano Energy **69**, 104398 (2020)
60. Z. Zou, Y. Li, Z. Lu, D. Wang, Y. Cui, B. Guo, Y. Li, X. Liang, J. Feng, H. Li, C.W. Nan, M. Armand, L. Chen, K. Xu, S. Shi, Mobile ions in composite solids. Chem. Rev. **120**, 4169–4221 (2020)
61. N.S. Murthy, H. Minor, General procedure for evaluating amorphous scattering and crystallinity from X-ray diffraction scans of semicrystalline polymers. Polymer **31**, 996–1002 (1989)
62. T.H. Lee, F.Y.C. Boey, K.A. Khor, X-ray diffraction analysis technique for determining the polymer crystallinity in a polyphenylene sulfide composite. Polym. Compos. **16**, 481–488 (1995)
63. N. Lago, O. Garcia-Calvo, J.M. Lopezdelamo, T. Rojo, M. Armand, All-solid-state lithium-ion batteries with grafted ceramic nanoparticles dispersed in solid polymer electrolytes. Chemsuschem **8**, 3039–3043 (2015)
64. S. Li, K. Jiang, J. Wang, C. Zuo, Y.H. Jo, D. He, X. Xie, Z. Xue, Molecular brush with dense PEG side chains: design of a well-defined polymer electrolyte for lithium-ion batteries. Macromolecules **52**, 7234–7243 (2019)
65. Q. Zhou, J. Ma, S. Dong, X. Li, G. Cui, Intermolecular chemistry in solid polymer electrolytes for high-energy-density lithium batteries. Adv. Mater. **31**, 1902029 (2019)
66. Z. Wang, X. Huang, L. Chen, Understanding of effects of nano-Al_2O_3 particles on ionic conductivity of composite polymer electrolytes. Electrochem. Solid-State Lett. **6**, E40–E44 (2003)
67. T. Li, P. Shi, R. Zhang, H. Liu, X.B. Cheng, Q. Zhang, Dendrite-free sandwiched ultrathin lithium metal anode with even lithium plating and stripping behavior. Nano Res. **12**, 2224–2229 (2019)
68. J. Wang, M. Li, C. Liu, Y. Liu, T. Zhao, P. Zhai, J. Wang, An electronegative modified separator with semifused pores as a selective barrier for highly stable lithium-sulfur batteries. Ind. Eng. Chem. Res. **58**, 14538–14547 (2019)
69. J. Zhang, C. Ma, Q. Xia, J. Liu, Z. Ding, M. Xu, L. Chen, W. Wei, Composite electrolyte membranes incorporating viscous copolymers with cellulose for high performance lithium-ion batteries. J. Membr. Sci. **497**, 259–269 (2016)
70. Z. Xie, Z. Wu, X. An, X. Yue, P. Xiaokaiti, A. Yoshida, A. Abudula, G. Guan, A sandwich-type composite polymer electrolyte for all-solid-state lithium metal batteries with high areal capacity and cycling stability. J. Membr. Sci. **596**, 117739 (2020)
71. S. Zhao, Y. Wang, J. Dong, C.T. He, H. Yin, P. An, K. Zhao, X. Zhang, C. Gao, L. Zhang, J. Lv, J. Wang, J. Zhang, A.M. Khattak, N.A. Khan, Z. Wei, J. Zhang, S. Liu, H. Zhao, Z. Tang, Ultrathin metal–organic framework nanosheets for electrocatalytic oxygen evolution. Nat. Energy **1**, 16184 (2016)
72. Y. Wang, Y. Liu, H. Wang, W. Liu, Y. Li, J. Zhang, H. Hou, J. Yang, Ultrathin NiCo-MOF Nanosheets for High-Performance Supercapacitor Electrodes. ACS Appl. Energy Mater. **2**, 2063–2071 (2019)
73. Z. Guo, Y. Zhang, Y. Dong, J. Li, S. Li, P. Shao, X. Feng, B. Wang, Fast ion transport pathway provided by polyethylene glycol confined in covalent organic frameworks. J. Am. Chem. Soc. **141**, 1923–1927 (2019)
74. H. Deng, C.J. Doonan, H. Furukawa, R.B. Ferreira, J. Towne, C.B. Knobler, B. Wang, O.M. Yaghi, Multiple functional groups of varying ratios in metal-organic frameworks. Science **327**, 846–850 (2010)
75. M. Eddaoudi, J. Kim, N. Rosi, D. Vodak, J. Wachter, M. O'Keeffe, O.M. Yaghi, Systematic design of pore size and functionality in isoreticular MOFs and their application in methane storage. Science **295**, 469–472 (2002)

76. S. Yuan, L. Huang, Z. Huang, D. Sun, J.S. Qin, L. Feng, J. Li, X. Zou, T. Cagin, H.C. Zhou, Continuous variation of lattice dimensions and pore sizes in metal−organic frameworks. J. Am. Chem. Soc. **142**, 4732–4738 (2020)
77. H. Qin, K. Fu, Y. Zhang, Y. Ye, M. Song, Y. Kuang, S.H. Jang, F. Jiang, L. Cui, Flexible nanocellulose enhanced Li^+ conducting membrane for solid polymer electrolyte. Energy Storage Mater. **28**, 293–299 (2020)
78. X. Zhang, J. Xie, F. Shi, D. Lin, Y. Liu, W. Liu, A. Pei, Y. Gong, H. Wang, K. Liu, Y. Xiang, Y. Cui, Vertically aligned and continuous nanoscale ceramic−polymer interfaces in composite solid polymer electrolytes for enhanced ionic conductivity. Nano Lett. **18**, 3829–3838 (2018)
79. S. Ramesh, T.F. Yuen, C.J. Shen, Conductivity and FTIR studies on PEO–LiX [X: $CF_3SO_3^-$, SO_4^{2-}] polymer electrolytes. Spectrochim. Acta Part A Mol. Biomol. Spectrosc. **69**, 670–675 (2008)
80. L.H. Sim, S.N. Gan, C.H. Chan, R. Yahya, ATR-FTIR studies on ion interaction of lithium perchlorate in polyacrylate/poly (ethylene oxide) blends. Spectrochim. Acta Part A Mol. Biomol. Spectrosc. **76**, 287–292 (2010)
81. M. Marcinek, M. Ciosek, G. Zukowska, W. Wieczorek, K.R. Jeffrey, J.R. Stevens, The impact of end groups on ionic interactions in low molecular weight Al_2O_3–polyether–$LiClO_4$ electrolytes. Solid State Ionics **171**, 69–80 (2004)
82. Y. Suzuki, H. Duran, M. Steinhart, H.J. Butt, G. Floudas, Homogeneous crystallization and local dynamics of poly (ethylene oxide) (PEO) confined to nanoporous alumina. Soft Matter **9**, 2621–2628 (2013)
83. H. Huo, B. Wu, T. Zhang, X. Zheng, L. Ge, T. Xu, X. Guo, X. Sun, Anion-immobilized polymer electrolyte achieved by cationic metal-organic framework filler for dendrite-free solid-state batteries. Energy Storage Mater. **18**, 59–67 (2019)
84. Z. Yang, H. Yuan, C. Zhou, Y. Wu, W. Tang, S. Sang, H. Liu, Facile interfacial adhesion enabled LATP-based solid-state lithium metal battery. Chem. Eng. J. **392**, 123650 (2020)
85. R. Li, S. Guo, L. Yu, L. Wang, D. Wu, Y. Li, X. Hu, Morphosynthesis of 3D macroporous garnet frameworks and perfusion of polymer-stabilized lithium salts for flexible solid-state hybrid electrolytes. Adv. Mater. Interfaces **6**, 1900200 (2019)
86. Z. Wan, D. Lei, W. Yang, C. Liu, K. Shi, X. Hao, L. Shen, W. Lv, B. Li, Q.H. Yang, F. Kang, Y.B. He, Low resistance-integrated all-solid-state battery achieved by $Li_7La_3Zr_2O_{12}$ nanowire upgrading polyethylene oxide (PEO) composite electrolyte and PEO cathode binder. Adv. Func. Mater. **29**, 1805301 (2019)
87. J. Bae, Y. Li, J. Zhang, X. Zhou, F. Zhao, Y. Shi, J.B. Goodenough, G. Yu, A 3D nanostructured hydrogel-framework-derived high-performance composite polymer lithium-ion electrolyte. Angew. Chem. Int. Ed. **57**, 2096–2100 (2018)
88. C.Z. Zhao, X.Q. Zhang, X.B. Cheng, R. Zhang, R. Xu, P.Y. Chen, H.J. Peng, J.Q. Huang, Q. Zhang, An anion-immobilized composite electrolyte for dendrite-free lithium metal anodes. Proc. Natl. Acad. Sci. **114**, 11069–11074 (2017)
89. J. Zheng, M. Tang, Y.Y. Hu, Lithium ion pathway within $Li_7La_3Zr_2O_{12}$ polyethylene oxide composite electrolytes. Angew. Chem. Int. Ed. **128**, 12726–12730 (2016)
90. N. Wu, P.H. Chien, Y. Qian, Y. Li, H. Xu, N.S. Grundish, B. Xu, H. Jin, Y.Y. Hu, G. Yu, J.B. Goodenough, Enhanced surface interactions enable fast Li^+ conduction in oxide/polymer composite electrolyte. Angew. Chem. Int. Ed. **59**, 4131–4137 (2020)
91. K. He, J. Zha, P. Du, S. H. Cheng, C. Liu, Z. Dang, R.K.Y. Li. Tailored high cycling performance in a solid polymer electrolyte with perovskite-type $Li_{0.33}La_{0.557}TiO_3$ nanofibers for all-solid-state lithium ion batteries. Dalton Trans. **48**, 3263–3269 (2019)
92. P. Zhu, C. Yan, M. Dirican, J. Zhu, J. Zang, R.K. Selvan, C.C. Chung, H. Jia, Y. Li, Y. Kiyak, N. Wu, X. Zhang, $Li_{0.33}La_{0.557}TiO_3$ ceramic nanofiber-enhanced polyethylene oxide-based composite polymer electrolytes for all-solid-state lithium batteries. J. Mater. Chem. A, **6**, 4279–4285 (2018)
93. Y. Zhao, S. Hao, L. Su, Z. Ma, G. Shao, Hierarchical Cu fibers induced Li uniform nucleation for dendrite-free lithium metal anode. Chem. Eng. J. **392**, 123691 (2020)

94. J. Wan, J. Xie, X. Kong, Z. Liu, K. Liu, F. Shi, A. Pei, H. Chen, W. Chen, J. Chen, X. Zhang, L. Zong, J. Wang, L. Chen, J. Qin, Y. Cui, Ultrathin, flexible, solid polymer composite electrolyte enabled with aligned nanoporous host for lithium batteries. Nat. Nanotechnol. **14**, 705–711 (2019)
95. T. Jiang, P. He, G. Wang, Y. Shen, C.W. Nan, L.Z. Fan, Solvent-free synthesis of thin, flexible, nonflammable garnet-based composite solid electrolyte for all-solid-state lithium batteries. Adv. Energy Mater. **10**, 1903376 (2020)
96. A.A. AbdelHamid, J.L. Cheong, J.Y. Ying, $Li_7La_3Zr_2O_{12}$ sheet-based framework for high-performance lithium-sulfur hybrid quasi-solid battery. Nano Energy **71**, 104633 (2020)
97. W. Li, C. Sun, J. Jin, Y. Li, C. Chen, Z. Wen, Realization of the Li^+ domain diffusion effect via constructing molecular brushes on the LLZTO surface and its application in all-solid-state lithium batteries. J. Mater. Chem. A **7**, 27304–27312 (2019)
98. K.J. Kim, M. Balaish, M. Wadaguchi, L. Kong, J.L.M. Rupp, Solid-state Li-metal batteries: challenges and horizons of oxide and sulfide solid electrolytes and their interfaces. Adv. Energy Mater. **11**, 2002689 (2021)
99. Z. Jiang, S. Wang, X. Chen, W. Yang, X. Yao, X. Hu, Q. Han, H. Wang, Tape-casting $Li_{0.34}La_{0.56}TiO_3$ ceramic electrolyte films permit high energy density of lithium-metal batteries. Adv. Mater. **32**, 1906221 (2020)
100. S. Jung, H. Gwon, G. Yoon, L.J. Miara, V. Lacivita, J. Kim, Pliable lithium superionic conductor for all-solid-state batteries. ACS Energy Lett. **6**, 2006–2015 (2021)
101. X. Yang, K.R. Adair, X. Gao, X. Sun, Recent advances and perspectives on thin electrolytes for high-energy-density solid-state lithium batteries. Energy Environ. Sci. **14**, 643–671 (2021)
102. J. Wu, L. Yuan, W. Zhang, Z. Li, X. Xie, Y. Huang, Reducing the thickness of solid-state electrolyte membranes for high-energy lithium batteries. Energy Environ. Sci. **14**, 12–36 (2021)
103. N. Zhao, W. Khokhar, Z. Bi, C. Shi, X. Guo, L.Z. Fan, C.W. Nan, Solid garnet batteries. Joule **3**, 1190–1199 (2019)
104. X. Chen, W. He, L.X. Ding, S. Wang, H. Wang, Enhancing interfacial contact in all solid state batteries with a cathode-supported solid electrolyte membrane framework. Energy Environ. Sci. **12**, 938–944 (2019)
105. H. Huo, X. Li, Y. Sun, X. Lin, K.D. Davis, J. Liang, X. Gao, R. Li, H. Huang, X. Guo, X. Sun, Li_2CO_3 effects: new insights into polymer/garnet electrolytes for dendrite-free solid lithium batteries. Nano Energy **73**, 104836 (2020)
106. J.J. Shao, K. Raidongia, A.R. Koltonow, J. Huang, Self-assembled two-dimensional nanofluidic proton channels with high thermal stability. Nat. Commun. **6**, 7602 (2015)
107. C.H. Chen, J. Du, Lithium ion diffusion mechanism in lithium lanthanum titanate solid-state electrolytes from atomistic simulations. J. Am. Ceram. Soc. **98**, 534–542 (2014)
108. X. Wang, H. Wang, Y. Zhou, Y. Liu, B. Li, X. Zhou, H. Shen, Confined-space synthesis of single crystal TiO_2 nanowires in atmospheric vessel at low temperature: a generalized approach. Sci. Rep. **5**, 8129 (2015)
109. X. Gao, C.A.J. Fisher, T. Kimura, Y.H. Ikuhara, H. Moriwake, A. Kuwabara, H. Oki, T. Tojigamori, R. Huang, Y. Ikuhara, Lithium atom and A-site vacancy distributions in lanthanum lithium titanate. Chem. Mater. **25**, 1607–1614 (2013)
110. A.A. AbdelHamid, Y. Yu, J. Yang, J.Y. Ying, Generalized synthesis of metal oxide nanosheets and their application as Li-ion battery anodes. Adv. Mater. **29**, 1701427 (2017)
111. M. Romero, R. Faccio, S. Vázquez, S. Davyt, Á. W. Mombrú, Experimental and theoretical Raman study on the structure and microstructure of $Li_{0.30}La_{0.57}TiO_3$ electrolyte prepared by the sol-gel method in acetic medium. Ceram. Int. **42**, 15414–15422 (2016)
112. M.J. Wang, J.B. Wolfenstine, J. Sakamoto, Mixed electronic and ionic conduction properties of lithium lanthanum titanate. Adv. Func. Mater. **30**, 1909140 (2020)